

F.M. Mazzolani
R. Zandonini
editors



The Line 5 of the national research program funded by the network ReLUIIS in the period 2005-2008 focused on the development of innovative approaches for the design of steel and composite steel-concrete structural systems, under the chairmanship of Federico Mazzolani and Riccardo Zandonini. This book collects the main outcomes of the research activity developed by twelve research groups of the following Universities: Ancona; Chieti-Pescara; Milano; Molise; Napoli (Federico II-Engineering and Architecture Faculties, Second University); Pisa; Salerno; Sannio; Trento; Trieste. The studies were mainly devoted to three significant areas: moment resisting frames, braced frames, bridges.

The development of innovative approaches for the design
of steel and composite steel-concrete structural systems

The Line 5 of the ReLUIIS-DPC 2005-2008 Project

The development of innovative approaches for the design of steel and composite steel-concrete structural systems

The Line 5 of the ReLUIIS-DPC 2005-2008 Project

Federico M. Mazzolani
Riccardo Zandonini
editors



ISBN 978-88-89972-25-0



The Development
of Innovative Approaches
for the Design of Steel and Composite
Steel-Concrete Structural Systems

The Line 5
of the ReLUIS-DPC 2005-2008 Project

F.M. Mazzolani, R. Zandonini
editors



ISBN 978-88-89972-25-0

© 2011 Doppiavoce
Napoli
www.doppiavoce.it

Tutti i diritti riservati.
È vietata ogni riproduzione.

Opera in libero accesso, secondo i termini indicati nel sito www.doppiavoce.it.

CONTENTS

<i>Foreword</i>	V
“All-steel” Buckling Restrained Braces for Seismic Upgrading of Existing RC Buildings	1
<i>Federico M. Mazzolani, Gaetano Della Corte, Mario D’Aniello</i>	
Rotation Capacity and Classification Criteria of Steel Beams	37
<i>Raffaele Landolfo, Mario D’Aniello, Manuela Brescia, Susanna Tortorelli</i>	
Metal Shear Panels for Improving the Seismic Behaviour of Framed Buildings	89
<i>Gianfranco De Matteis, Giuseppe Brando, Antonio Formisano, Federico M. Mazzolani</i>	
Seismic Performance Evaluation of Steel Moment Resisting Frames Using Adaptive Pushover	155
<i>Massimiliano Ferraioli, Angelo Lavino, Alberto Maria Avossa, Alberto Mandara</i>	
Ultimate Behaviour of Steel-Concrete Composite Bridge Piers	187
<i>Fabio Iannone, Luigi Mastrandrea, Rosario Montuori, Vincenzo Piluso, Gianvittorio Rizzano</i>	
Seismic Behavior and Design Rules for Steel Bridges	227
<i>Giuseppe Chellini, Francesco Vittorio Lippi, Walter Salvatore</i>	
Analysis Procedures of the Low Cycle Fatigue Behaviour for Structural Elements and Connections	261
<i>Carlo A. Castiglioni, Alberto Drei</i>	
Tests and Analysis of Structures and Joints for Steel-Concrete Moment-Resisting Frames and Steel-Concrete Box-girder Bridges	307
<i>Oreste S. Bursi, Fabio Ferrario, Raffaele Pucinotti, Nicola Tondini, Riccardo Zandonini</i>	

Rotation Capacity and Classification Criteria for Composite Members	347
<i>Marisa Pecce, Francesca Ceroni, Luigi Di Sarno</i>	
Steel Braced Frames with Viscoelastic or Elastoplastic Structural Dampers	373
<i>Andrea Dall'Asta, Luigino Dezi, Graziano Leoni, Laura Ragni, Alessandro Zona</i>	
Numerical Modelling and Seismic Assessment of Steel and Steel-Concrete Composite Frames	409
<i>Claudio Amadio, Maurizio Bella, Vanessa Bertoni, Lorenzo Macorini</i>	

FOREWORD

In the past decade there was an increasing research effort aimed at improving concepts, methods and design practice in seismic engineering. Italian studies gave a significant contribution to the remarkable achievements.

The national research program funded by the network Reluis certainly represented the core of the Italian work in the period 2005-2008, covering all the main issues relevant to the enhancement of seismic resistant design. In particular, the Line 5 of this program focused on the development of innovative approaches for the design of steel and composite steel-concrete structural systems.

This book collects the main outcomes of the research activity developed in that period under the Line 5, which comprised the following twelve research groups.

- RU 1: University of Naples Federico II – Faculty of Engineering; research coordinator: Federico M. Mazzolani; Topic: *Design criteria and response assessment of buckling restrained braces.*
- RU 2: University of Naples Federico II – Faculty of Architecture; research coordinator: Raffaele Landolfo; Topic: *Rotation capacity and classification of steel members.*
- RU 3: University of Chieti-Pescara; research coordinator: Gianfranco De Matteis; Topic: *Design criteria and response assessment of metal shear panels.*
- RU 4: Second University of Naples; research coordinator: Alberto Mandara; Topic: *Design criteria of steel moment resisting frames and methods of nonlinear analysis.*
- RU 5: University of Salerno; research coordinator: Vincenzo Piluso; Topic: *Design criteria and response assessment of composite steel-concrete bridge piers.*
- RU 6: University of Pisa; research coordinator: Walter Salvatore; Topic: *Design criteria and response assessment of steel bridges.*
- RU 7: Polytechnic of Milan; research coordinator: Carlo A. Castiglioni; Topic: *Procedures to assess low-cycle fatigue of steel members and connections.*
- RU 8: University of Trento; research coordinators: Riccardo Zandonini and Oreste Bursi; Topic: *Design-by-testing for buildings and bridges*
- RU 9: University of Sannio; research coordinator: Maria Rosaria Pecce; Topic: *Rotation capacity and classification of composite elements.*

- RU 10: University of Molise; research coordinator: Giovanni Fabbrocino; Topic: *Methods for structural analysis of composite steel-concrete structures.*
- RU 11: University of Ancona; research coordinator: Luigi Dezi; Topic: *Composite frames with dissipative braces.*
- RU 12: University of Trieste; research coordinator: Claudio Amadio; Topic: *Degrading hysteresis models and fragility curves of frames with composite semi-continuous joints.*

The studies of the above research units were mainly devoted to three significant areas: moment resisting frames, braced frames, bridges. More in detail, the main issues dealt with can be summarized as follows:

- *Moment resisting frames:* methods for measuring the plastic rotation of members and joints, classification criteria of members under cycling loading; optimal design of beam-to-column and column-to-foundation joints; energy dissipation of frames with partially encased columns; assessment of design methods based on the capacity design philosophy; influence of walls on the frame seismic response.
- *Braced frames:* energy dissipation capacity and seismic reliability of structural systems with standard bracings and with innovative high ductility bracings; new types of bracings, different for material and structural detailing; assessment of design methods for braced structures based on the capacity design philosophy.
- *Bridges:* assessment of the seismic response of steel and composite steel-concrete bridges aimed at developing design rules to be incorporated in the codes; assessment of the remaining life of existing bridges; fragility curves.

All these studies were carried out by maximizing the synergies among the research groups, leading to advances, sometimes very significant, in the knowledge improvement. They may be considered as a rich background, where further developments of the current Codes can find sound bases.

The reader will certainly find a number of fairly interesting new results. Furthermore, he will get a vivid sensation of the great vitality of the Italian research in the area of steel and composite steel-concrete structures in seismic areas.

Federico M. Mazzolani
Riccardo Zandonini

“ALL-STEEL” BUCKLING RESTRAINED BRACES FOR SEISMIC UPGRADING OF EXISTING RC BUILDINGS

Federico M. Mazzolani, Gaetano Della Corte, Mario D’Aniello

Department of Structural Engineering, University of Naples Federico II, Naples, Italy

Abstract. Buckling Restrained Braces (BRBs), differently from conventional braces, do not exhibit appreciable difference between the tensile and compression capacity and no strength degradation under compressive and cyclic loading. Since lateral and local buckling behaviour modes are restrained, large inelastic capacities are attainable. Hence, BRBs may represent an efficient and reliable solution for reducing the seismic vulnerability of buildings. This consideration aimed the course of the present research. Indeed, this paper shows and discusses the results of experimental tests on the response of real reinforced concrete (RC) buildings equipped with three different “all-steel” BRBs. In particular, the tested devices have been designed to be demountable, consisting in a rectangular steel plate and a restraining steel sleeve, composed by two omega shapes, which are bolted together. The main characteristic of these braces consists in the possibility to hide them within the space between the facing and the backing of masonry infill walls commonly used for RC buildings. The experimental tests were carried out beyond the design target performance in order to analyze the final condition of the devices. The results showed that the investigated systems are cheap, simple, efficient, robust devices, suitable for the intended applications.

Keywords: Buckling Restrained Braces, experimental tests, ductility, over-strength, seismic upgrading.

1. INTRODUCTION

Seismic retrofitting of existing buildings requires taking into account several different factors, such as architectural constraints, the cost due to the possibility to close the building (or part of it) for the duration of the retrofit work, or having to heavily reinforce existing framing due to the increased seismic demands the retrofit strategy may place on it. Referring to the structural needs, it seems that the limitation of lateral displacement in buildings under seismic action and the capacity to resist horizontal actions can be considered as the main concerns for structural designers.

Among the possible solutions to retrofit an existing structure, bracing systems are a simple and effective retrofit system, especially when story drifts

need to be limited. Concentric brace frames (CBFs) can be considered as one of the most efficient structural systems for resisting lateral forces due to wind and earthquakes. However, this structural system is not been considered ductile by building codes and past design practices. In fact, when the braces are subjected to large compressive forces they exhibit buckling deformation with substantial strength and stiffness deterioration. Consequently, CBFs are characterized by a pinched hysteresis loop, with relatively small earthquake energy absorption capacity. The concentration of strain, which occurs when braces buckle, increases the likelihood of fracture after a few cycles of loading.

These problems can be avoided if buckling of a steel brace is restrained and the same strength is ensured both in tension and compression. In this way, the energy absorption of the brace significantly increases and the hysteresis loop become compact and round. These requirements led researchers to develop a new type of brace called buckling-restrained brace (BRB), which is a relatively recent development in the field of seismic resistant steel structures (Brown et al., 2001; Black et al., 2002; Chen, 2002; Wada & Nakashima, 2004; Xie, 2005; Tsai et al., 2004; Wada & Watanabe, 2004).

This chapter shows the main results of an experimental research aiming to investigate the response of “all-steel” BRBs, which may be designed to be demountable. This aspect implies that is possible to design these systems to be inspected, so that it is possible to control their condition after each seismic event and, if necessary, the yielded steel core could be replaced by a new one. To do this the restraining tubes should be connected by bolted steel connections. Moreover an ‘all-steel’ BRB is lighter than an ‘unbonded’ one; this implies a technical and economical advantage during the assembling. These considerations motivated the research presented herein that was addressed to study a special “all-steel” demountable BRB, designed to improve the seismic response of existing buildings.

Three different BRB prototypes (hereinafter called type A, B and C, respectively) have been analyzed. The main characteristic of the tested devices is the possibility to hide them within the space between the two panels of masonry infill walls commonly used for claddings of RC buildings. Tests have been performed on a real two-story reinforced concrete (RC) building equipped with the novel BRBs. In particular, the buildings have been subjected to cyclic loading histories, which resemble the one typically used to experimentally validate BRBs in the laboratory. The main outcomes are presented and discussed.

2. BUCKLING-RESTRAINED BRACES

Generality

Figure 1 shows the parts that constitute a common BRB:

1. Axial force-carrying unit (usually called “core”);

2. Sleeve or buckling-restraining unit (encasing member which may be of steel, concrete or composite), whose function is to restrain the core buckling;
3. Separation unit between brace and buckling-restraining units, which ensures that the core can freely slide inside the buckling-restraining unit and that the transverse expansion of the brace can take place when the brace yields in compression.

The core is further into three zones:

- i) the yielding zone, that has a reduced cross section area within the zone of lateral restraint provided by the sleeve (zone A);
- ii) the transition zones, which have a larger cross-section area than the one of the yielding zone and is similarly restrained (zone B);
- iii) the connection zones, which extend past the sleeve and connect to the frame (zone C).

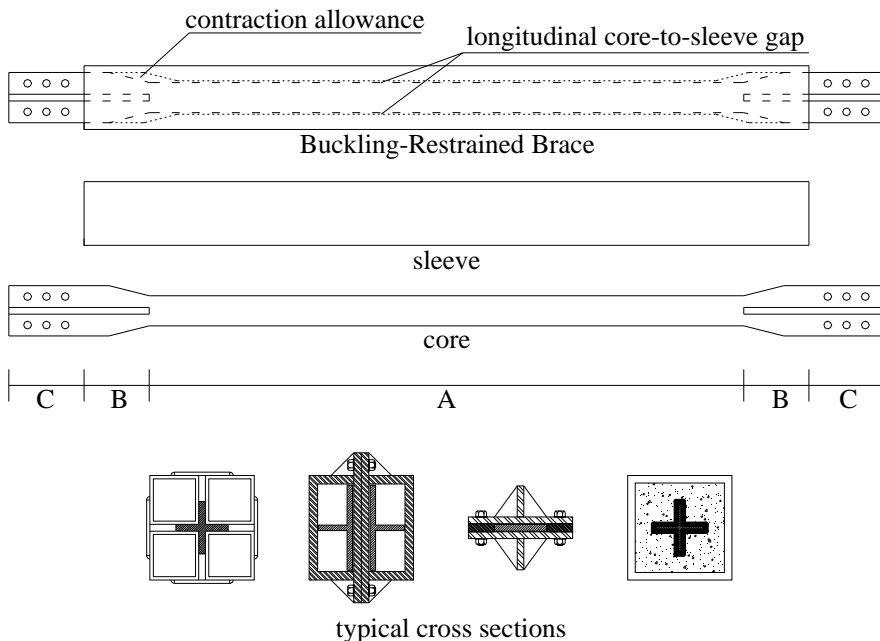


Figure 1. The Typical layout of common BRBs.

The detailing of interface between core and sleeve takes a key role to characterize the BRB performance. Indeed, in order to avoid the transmission of axial load from core to sleeve some debonding materials need to be employed as a separation unit in case concrete is used as infilling material (“unbounded” braces). Otherwise, a gap should be kept between the two units (“all-steel” braces).

Evolution of BRB typologies at the light of existing literature

One of the first proposal to inhibit global buckling of braces in compression was developed in Japan in the 1970s to 1980s, which consisted in a system having the steel braces (made of steel flat plates) sandwiched between a pair of precast reinforced concrete panels (Xie, 2005). Extending this concept various developments on BRBs with a steel core confined by a steel casing were made in Japan in the 1980s to 1990s. In that period the early type of BRB, which consisted of a conventional brace encased in a square steel pipe filled with mortar, was tested. These braces were characterized by few stable hysteretic characteristics, because of the transverse deformation of the mortar resulted in permanent void space that were large enough to allow local buckling (Xie, 2005). This concept was further refined by Fujimoto et al. (1988), Watanabe et al. (1988) and Wada et al. (1998) and lead to the so called unbonded brace. It consists in a ductile steel core (rectangular or cruciform plates, circular rods, etc.) either in a continuous concrete filled tube.

Watanabe et al. (1988) studied the influence of the ratio between the Euler buckling load (N_E) of the sleeve and the actual yield force (N_y) of the internal steel core (N_E/N_y). Test results showed that specimen designed with $N_E/N_y < 1$ buckled globally in compression, while the remaining three specimens exhibited stable and symmetric hysteresis under both tension and compression. Afterwards they suggested that for practical applications the N_E/N_y ratio be at least equal to 1.5.

Nagao & Takahashi (1990) developed a BRB composed of a wide flange section encased in a reinforced concrete member and experimentally evaluated the stiffness and strength requirements of the concrete casing. Kuwahara & Tada (1993), Manabe et al. (1996), Suzuki et al. (1994), Shimizu et al. (1997) studied the use of an “all-steel” BRB, adopting hollow steel tube as restraining unit. However, the simplicity of its design and the outstanding performance of the unbonded brace have attracted the interest of industry and have been made commercially available by Nippon Steel Corporation. Up today, more than 300 buildings have been equipped with ‘unbonded’ braces manufactured by Nippon Steel Corporation. In particular, after several tests carried out in 1999 at the University of California, Berkeley, the technology has also been implemented in the US, by utilizing BRBs for the seismic retrofitting of the UC Davis Plant and Environmental Sciences. Another significant example is the Wallace F. Bennett Federal Building (Salt Lake City, Utah, USA).

All-steel BRBs: summary of key design issues

Among the key elements characterizing an “all-steel” BRB, the sleeve casing has a crucial role. It has to be designed to avoid overall buckling of the device without resisting any significant axial load, as well. The buckling-restraining mechanism is strictly related to the flexural stiffness of the sleeve. Watanabe et

al. (1988) suggested that the steel casing should be designed for a sufficient flexural stiffness such that:

$$\frac{N_E}{N_y} \geq \alpha > 1 \quad (1)$$

where N_E is the Euler buckling load, N_y is the core plastic strength and α takes into account imperfections.

However, the device has to be stable up to the maximum core axial strength. Indeed, the peak core strength is appreciably larger than N_y because of strain hardening and residual friction forces between the core and the sleeve.

Hence, Watanabe et al. (1988) proposed to fix α factor equal to 1.5. This value is obtained assuming an increase of the compressive brace strength of about 30% as respect to the yield strength and a safety factor of 0.9. Under these assumptions the stability criterion may be rewritten as follows:

$$\frac{0.9N_E}{1.3N_y} \geq 1 \Rightarrow \frac{N_E}{N_y} \geq 1.5 \quad (2)$$

The stability criterion expressed by Eq. (2) is generally applied to any type of BRB. In case of “all-steel” BRBs it is important to detail each part constituting the sleeve. Indeed, in order to effectively restrain the yielding core, the sleeve must be designed to prevent the local plastic flexural deformation of the plates constituting the sleeve. This implies that the sleeve has to possess adequate flexural strength and stiffness under the forces T induced by the buckled core waves at the maximum expected storey drift (Fig. 2). The transverse forces T may be computed from the static balance illustrated in Figure 3, where N_p is the plastic axial core strength and l'_n is the length of the buckling wave. The latter may be obtained equalling the load related to the higher buckling mode, activated in the inner core, to the axial core strength. Then the number of buckling waves may be calculated as follows:

$$n = \sqrt{\frac{L_c^2 \cdot N_{max}}{\pi^2 EI_c}} \quad (3)$$

where L_c is the core length and I_c is the relevant second moment of area.

Hence, indicating by ($l_n = L_c/n$) the length of buckling wave in the elastic field and assuming that their number do not vary when the core yields, the length of the buckling wave in the plastic field l'_n is given by the following Equation:

$$l'_n = l_n - \varepsilon_{pc} \frac{L_c}{n} = \frac{L_c(1 - \varepsilon_{pc})}{n} \quad (4)$$

where the axial core deformation ε_{pc} represents a design parameter related to the BRB design axial deformation.

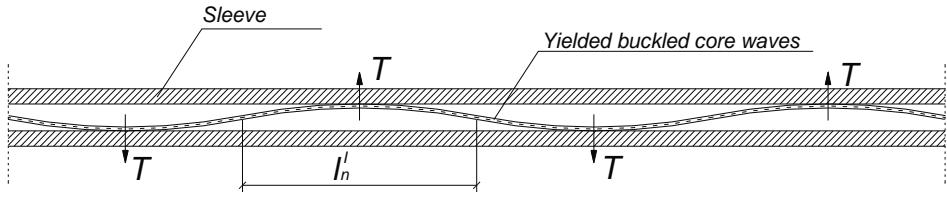


Figure 2. Yielded buckled core waves and punching transverse forces.

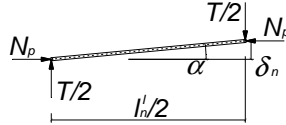


Figure 3. Static rotational balance of inner core in buckled shape.

“All-steel” can be designed as a demountable device. This is typically achieved by using bolted connections between two or more parts of the restraining sleeve. Using the elastic stability theory (Timoshenko and Gere, 1961), it can be found that the required strength R_{req} of the tie connection can be expressed in the following form (Tsai et al., 2004a):

$$R_{req} = \frac{3}{L_{tube}} \left(\frac{N_{max}}{2} - N_{cr} \right) \cdot \left(\frac{B \cdot f_y}{E} + e \right) \quad (5)$$

where L_{tube} is the length of the buckling restraining sleeve, N_{max} is the maximum axial core strength, N_{cr} is the critical eccentric load of the single longitudinal element constituting the sleeve, B is the width of the short side of the rectangular tube, E is Young’s modulus of steel, f_y is yield stress of steel constituting the sleeve, e is the load eccentricity measured from the neutral axis of the single longitudinal element constituting the sleeve.

Besides having satisfied the above-illustrated overall and local stability criteria, another aspect should be taken into account in order to prevent the sleeve buckling. Indeed, it is fundamental detailing the sleeve assembling the layout in order to avoid any possibility to transfer axial load from the core to the restraining system. Such bearing action would, unexpectedly and spuriously, increase the compressive capacity of the brace beyond the expected design strength, which is not desirable from the viewpoint of capacity design and increases the possibility of an unbalanced load in case a chevron-bracing configuration is used. Moreover, this functioning may be dangerous and disadvantageous, because the device would behave as a conventional classic brace, affected by overall buckling if the axial load increases. Therefore, a separation unit between core braces and buckling-restraining units should be designed in order to ensure that the brace can slide freely inside the buckling-restraining unit and

that transverse expansion of the brace can take place when the brace yields in compression. In addition, since the core length changes when the BRB yields, in order to permit inelastic deformations of the steel core the ends of the sleeve and the transition zone between the restrained yielding and non-yielding segment are detailed to avoid direct bearing between the steel core and the sleeve, providing a supplementary longitudinal reserve of space.

Finally, the end-connections have to be also designed to avoid modes of overall instability of the bracing member. In this sense, Nakamura et al. (2000) suggested that the following criterion should be satisfied:

$$N_{e,trans} = \frac{\pi^2 EI_{trans}}{(KL_b)^2} \geq N_{max} \quad (6)$$

where N_{max} is the maximum axial capacity of core plate, EI_{trans} is the flexural stiffness of the core member at a section near the end of the steel tube and KL_b is the effective (or equivalent) length, where K is usually assumed equal to 1 and L_b is two times the length measured from the theoretical brace node to the end of the sleeve.

3. FRAMEWORK OF THE RESEARCH ACTIVITY

The research activity consisted of a series of full-scale tests on a reinforced concrete (RC) building (Fig. 4), located in Bagnoli (Naples, Italy), in the area where the plants of the previous steel mill named ILVA (former Italsider) have been destined to demolition. The possibility to perform collapse tests on existing structures must be considered as a precious and unique opportunity to improve the knowledge on the real behaviour of structures.

Three experimental tests, each of them with a different BRB prototype, have been investigated.

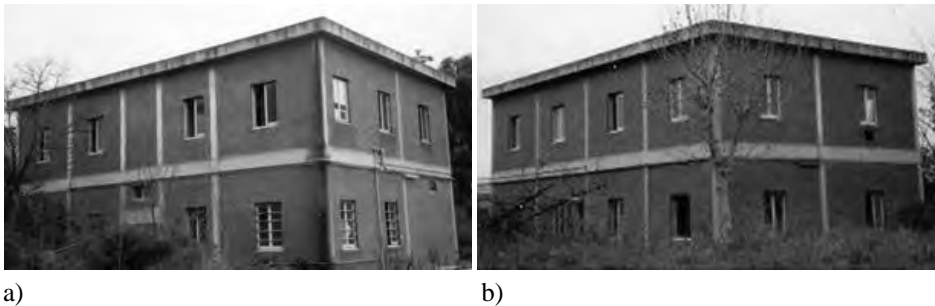


Figure 4. The tested building: N-W side (a), S-E side (b).

4. EXPERIMENTAL TESTS

Experimental layout and test setup

The tested building is rectangular in plan (18.50 m x 12.00 m), on two floors, with first and second floor heights equal to 4.60 m and 8.95 m. Figure 5a shows the plan location of the braces (highlighted with the dashed lines). Figure 5b shows the vertical location of the BRBs, which were applied only at the first floor, which is the one strongly damaged during two former tests on the building (Della Corte et al., 2008).

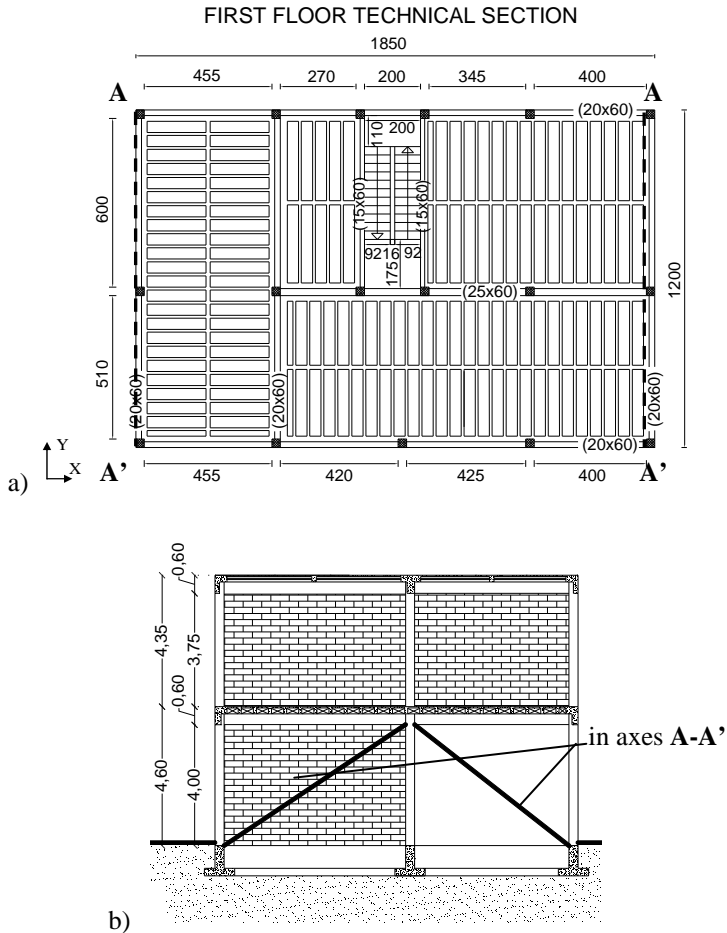


Figure 5. The building to be equipped with BRBs: a) structural plan; b) brace configuration.

Indeed, this RC building has initially been tested in its original conditions by lateral loading up to severe damage of both structural frame members and infill walls (Della Corte et al., 2008). Lateral loads have been applied according to an inverted triangular distribution. After the first experimental test the structure was re-centred, repaired and upgraded by means of C-FRP in the form of Near Surface Mounted Bars (NSM-B). Both tests showed the formation of a weak story at the first floor. Detailed information about the first two tests can be found in Della Corte et al. (2008).

After these tests, the structure has been partially repaired and re-centred and three different BRB systems have been designed and tested separately and subsequently. In particular, the novel BRBs were designed to be hidden inside the free space usually found between the facing and the backing of masonry infill walls commonly used for cladding of RC buildings. In order to demonstrate the feasibility to hide the device into the claddings, for the first test of this experimental series the masonry cladding has been reconstructed in one bay (Figures 6a,b and c show intermediate construction phases).

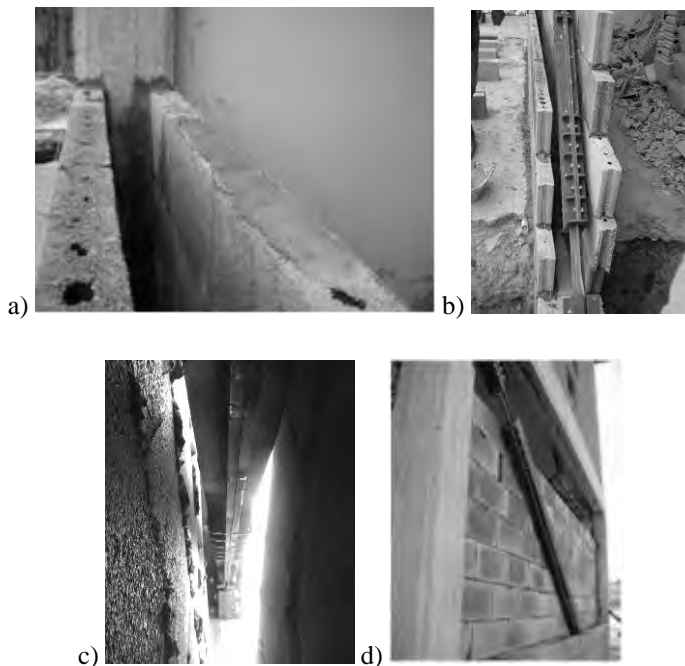


Figure 6. Example of a BRB inside masonry claddings.

The building has been subjected to a horizontal inverted triangular force distribution which simulates an action of seismic nature.

The test set-up consisted of a reacting steel structure with a push-pull system made of six hydraulic jacks used for applying the load in two opposite directions (Figs. 7a, b, c, d, e).

Figure 7a illustrates a view of both the reacting frame and the loading jacks used for applying the lateral force.

The jacks have a maximum stroke of ± 30 cm and a maximum load equal to 496 kN in compression and 264 kN in tension (corresponding to a total force of 2976 kN and 1584 kN respectively in push and in pull action). They have been connected to a hydraulic pump by means of a circuit in order to guarantee always the same pressure in all the jacks. The latter have been located at a height of 7.31 m and spaced horizontally 3.64 m on centers. The lateral load has been transferred to the two slabs of the building through a steel trussed structure (Fig. 7b).

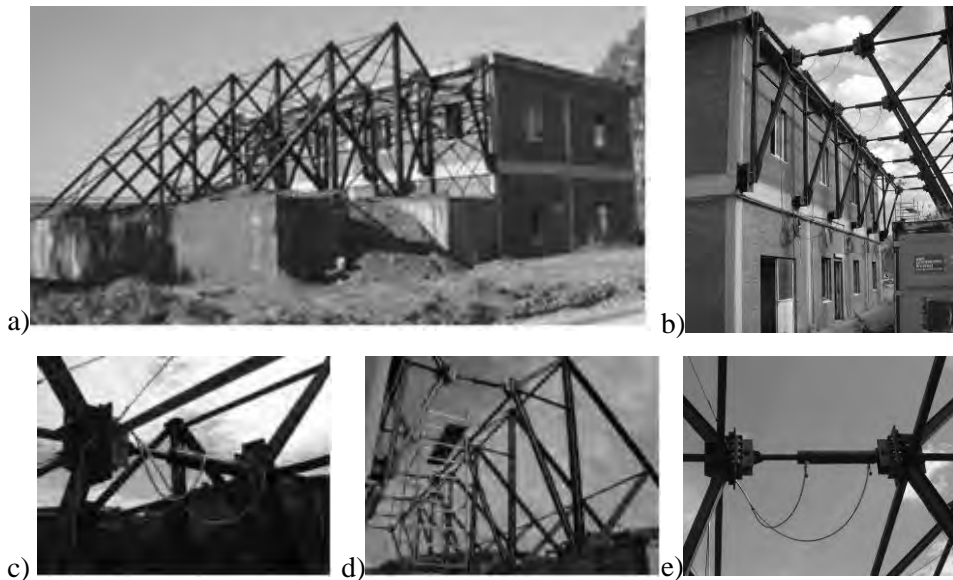


Figure 7. Reacting structure and hydraulic jacks.

Storey displacements were monitored by using a diastimeter Zeiss-Trimble S10 (Fig. 8a) and reflecting prisms (Fig. 8b). Six measuring points (i.e. six reflecting prisms) were fixed in correspondence of the two building stories, three at the first floor and three at the second floor (Fig. 8c). These measuring points allow measuring the average story translation and rotation about the vertical axis. In addition, for the last test axial BRB total deformation has been measured by means of a linear potentiometer spanning the brace ends (Fig. 9).



Figure 8. Location of station and reflecting targets.

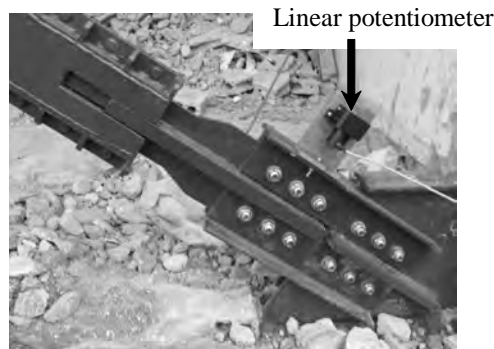


Figure 9. BRB axial deformation measuring system..

The strengthened structure was subjected to a cyclic loading history up to the development of a clear collapse mechanism. The loading protocols adopted for the tests can be considered as a compromise between technical operative-ness and scientific needs. In fact, starting from the loading protocols suggested by AISC (2005) seismic provisions, for the sake of inexpensiveness, the adopted protocols are characterized by a smaller number of cycles and also slightly adjusted. Figure 10 shows the applied loading protocols in terms of interstorey drift ratios. In the Figure, type A,B and C refers to three different BRB prototypes that have been tested.

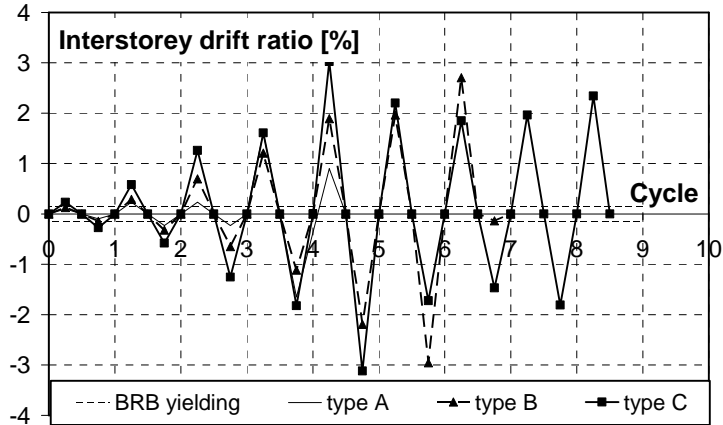


Figure 10. Applied loading protocols.

Description of the BRB specimens

The concept of the novel device descends from the experience matured within the ILVA-IDEM project (Della Corte & Mazzolani, 2006; Mazzolani et al., 2009), where two types of BRBs have been studied. The first type was made using two restraining rectangular tubes, fully welded together with steel plates; the second type was demountable, being made again with two restraining rectangular tubes but joined together by means of bolted steel connections.

The new tested BRB prototypes (henceforth called type A, B and C) have also been designed to be demountable, but they differ in some aspects both from the progenitor and among them.

One difference with the former BRBs was in the buckling-restraining unit, as it can be easily recognized by comparing Figure 11 to 12. Indeed, the restraining unit was made by two omega-shaped built-up sections, which were joined together by means of bolted stitch connections. As it is shown in Figure 12, two longitudinal bars on each side stiffen the two omega-shaped sections of the sleeve, providing the required restraining action to the core. This arrangement permitted to reduce the transverse size of the sleeve thus allowing to hide the brace between the two panels of masonry claddings commonly adopted for RC buildings. Indeed, the transverse size of the sleeve reduced from 130 mm of BRBs designed for the first series of tests (Fig.11) to 94 mm of BRB type A and type B, up to 92 mm of BRB type C. Notwithstanding, the sleeves were designed with a minimum ratio N_E/N_y equal to 2.06, which is the value adopted also for the devices tested in the previous experimental series. In addition, BRBs were designed to limit local and overall buckling of the steel core for deformations corresponding to a design story drift ratio θ_d equal to 2%.

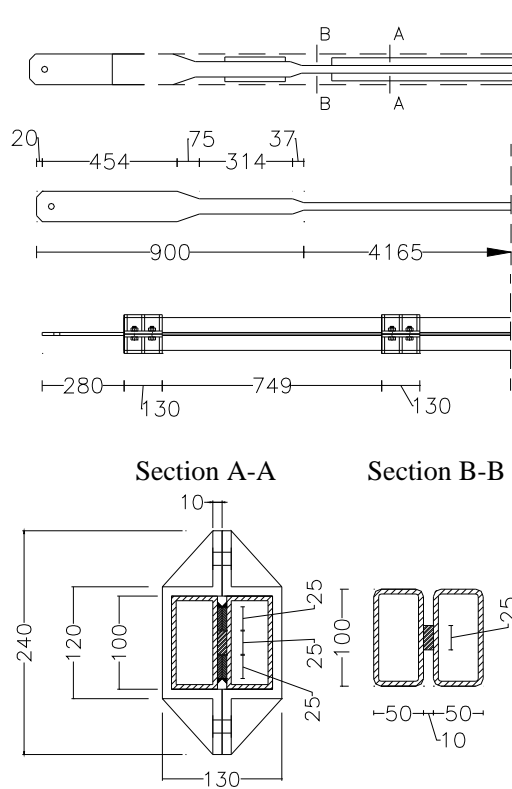


Figure 11. Geometry and details of a BRB tested within the ILVA-IDEM project (Mazzolani et al., 2009).

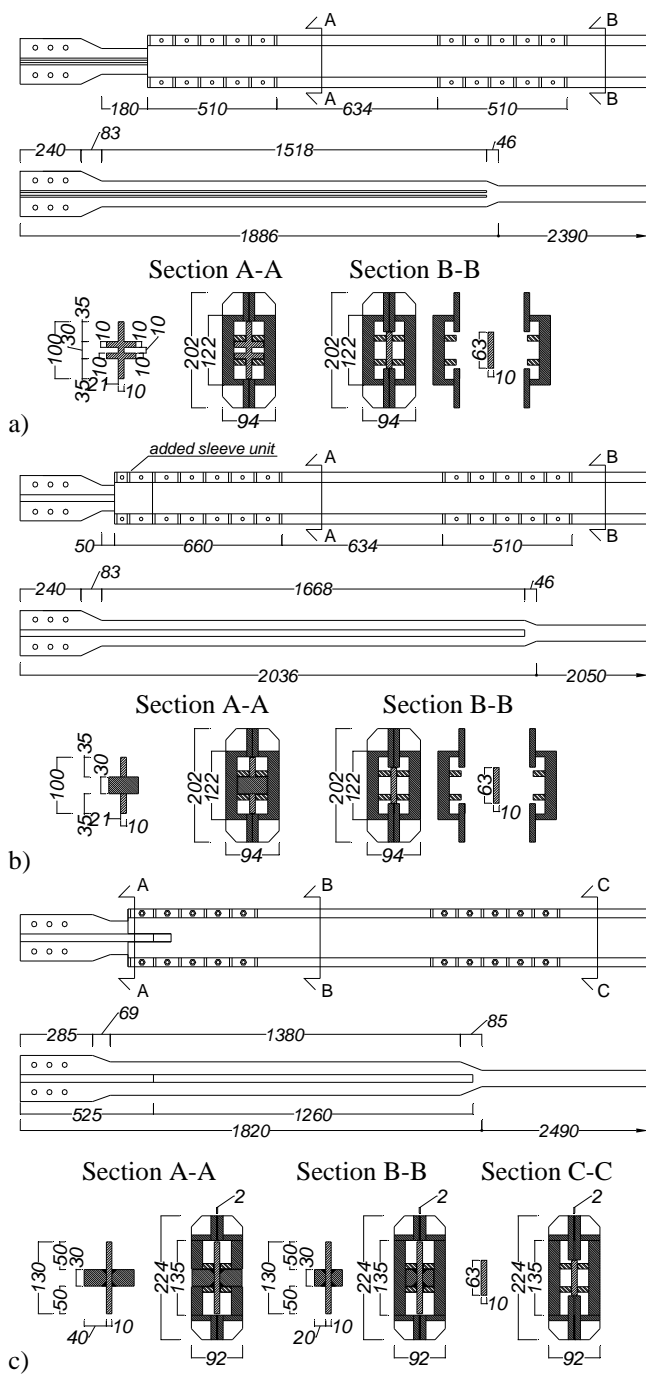


Figure 12. Geometry and details of BRB type A (a), Type B (b) and Type C (c).

One aspect of differentiation between examined BRBs is the ratio between the core length (L_c) and the total BRB length (L), which was 0.39 for type A, 0.33 for type B and 0.40 for type C.

Another aspect of differentiation was the inner clearance between the yielding core and the restraining sleeve. Indeed, BRB type A was designed with an inner clearance between the yielding core and the restraining sleeve equal to 1 mm per core side. Instead, in case of type B and type C the clearance was fixed equal to 2 mm per core side.

Furthermore, the tested prototypes differed in terms of the length and stiffeners of the unrestrained end portions of the core, as shown in Figures 12 a, b, c.

Finally, it must be noted that, in the last test, the RC building has been equipped with the novel BRBs (type C) in one bay and classic concentric braces (CCBs) in the adjacent bay. In such a way, it was possible to compare the performance of BRBs and CCBs and to highlight the benefits related to the use of BRBs. The CCBs have been designed to have the minimum tensile axial strength to preserve the compressive force regime in the intermediate column. Moreover, the CCBs have been designed with a normalized slenderness $\bar{\lambda}$ not larger than 2. As a result, the selected brace was a circular tube (101.6 mm x 2 mm), characterized by a cross section of class 2 according to Eurocode 3 (CEN, 2004) and a normalized slenderness $\bar{\lambda} = 1.8$.

Prototype A: experimental results

In case of BRB type A the tested structure exhibited a stable response up to a maximum interstorey drift ratio of about 1.25% (Figure 13a), which corresponded to a local-distorsional buckling failure of the unrestrained end portion of the steel core. The corresponding ductility was $\mu = \theta_{max}/\theta_y = 6.94$ (Figure 13b). For larger deformation demand, the local-distorsional buckling failure of the unrestrained non-yielding end-plate produced strength degradation.

Figure 14 summarizes the damage pattern. In particular, Figure 14a shows the tensile brace elongation. Figure 14b shows the collapse of the external facing wall caused by buckling of the BRB. Figure 14c shows the unrestrained end portion of the brace in its final buckled configuration and the failure of welds between the stiffener plates and the tapered core plate.

Moreover, it is interesting to examine the final state of BRBs which were demounted after the test. Figure 14d shows the presence of the Lüder lines tilted of about 45° testifying yielding of the inner core. However, no plastic buckling wave was observed along the core after the test. In addition, no damages occurred in the steel built up sleeve, as shown in Figure 14e. Thus, all sleeves of these devices have been used again to restrain the core of the specimens of prototype B.

The reasons generating the undesired buckling failure of BRBs may be found in the negative synergy of two combined events: (i) the actual yield

stress for the steel of the core plate was appreciably larger than the expected value; (ii) the inner clearance between the yielding core and the restraining sleeve was measured equal to 0.5 mm, which is lower than the design value of 1 mm per core side. In addition, it must be noted that the fillet welds between the stiffeners and the tapered unrestrained end portion of the core were erroneously made as discontinuous, contrary to the design prescription.

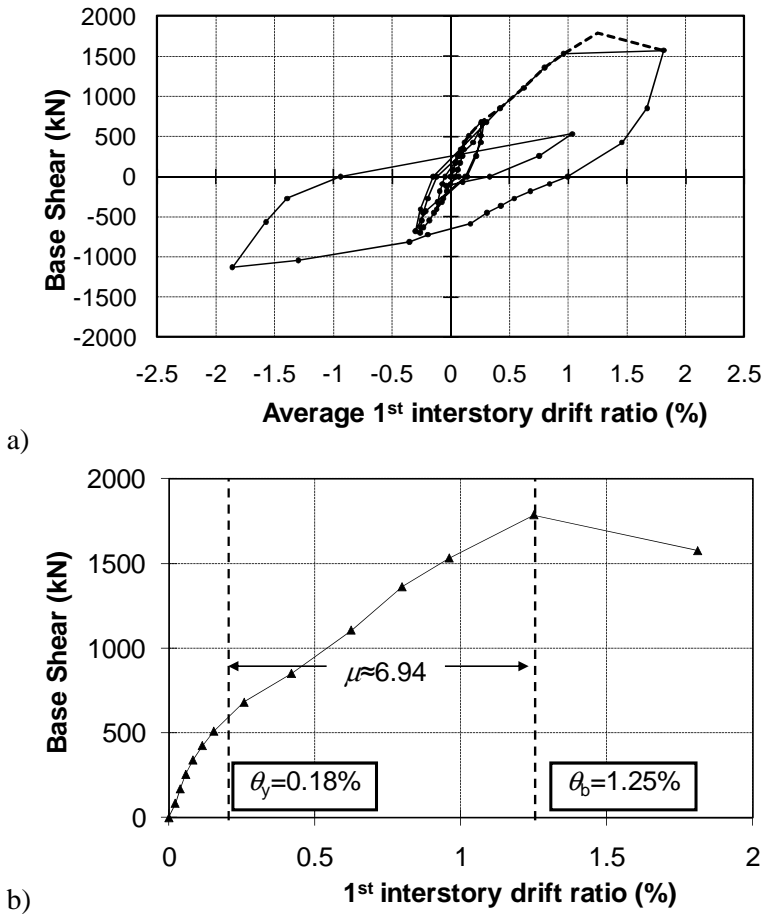


Figure 13. BRB type A: overall response.

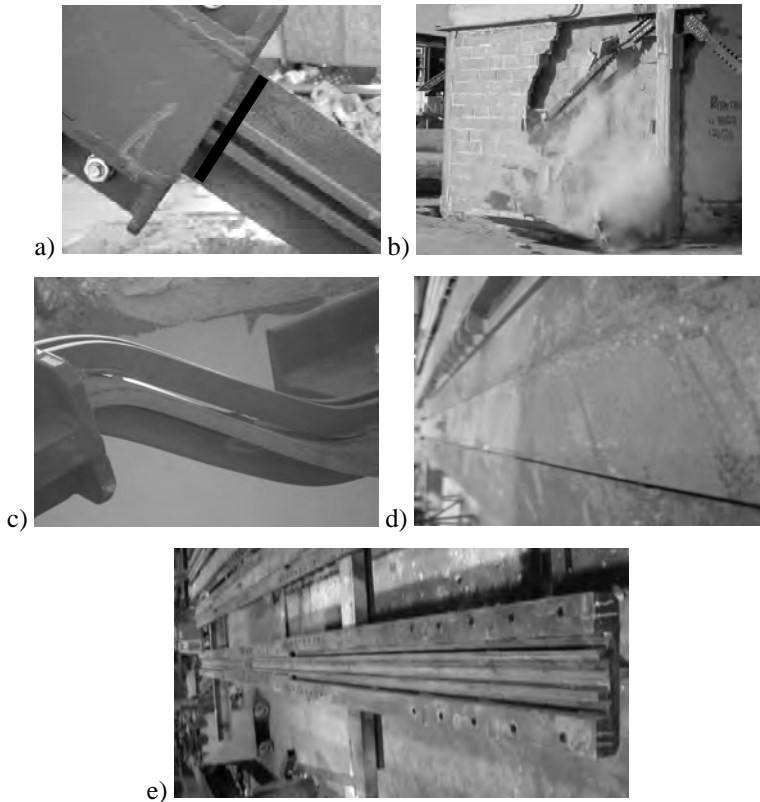


Figure 14. BRB type A: damage pattern.

Prototype B: experimental results

BRB type B showed a satisfactory overall performance, characterized by stable and symmetric hysteresis loops. As it can be noted in Figure 15a, the tested device showed a symmetric response in the interstorey drift range of $\pm 1.5\%$, with a minimum ductility capacity of about $\mu = 10.50$ (Figures 15b). In particular, the experimental test was completed in conjunction with the end of the core free stroke.

The performance of type B may be summarized into three different phases, as follows:

Phase 1): The devices exhibited a stable and symmetric response; the inner core yielded both in tension and in compression (Fig. 16a) and high levels of plastic deformations were reached; the sleeve did not show any significant deformation.

Phase 2): The sleeve exhibited localized deformations induced by the punching forces “T”, described in Figure 2.

Phase 3): After having exceeded the core free length working stroke, the sleeve carried an axial compression force (Fig. 16b). This event sparked off two possible phenomena: i) overall buckling of the whole device (Fig. 16f); ii) an increase of local sleeve deformations exhibited in phase 2 (Figs. 16c,d).

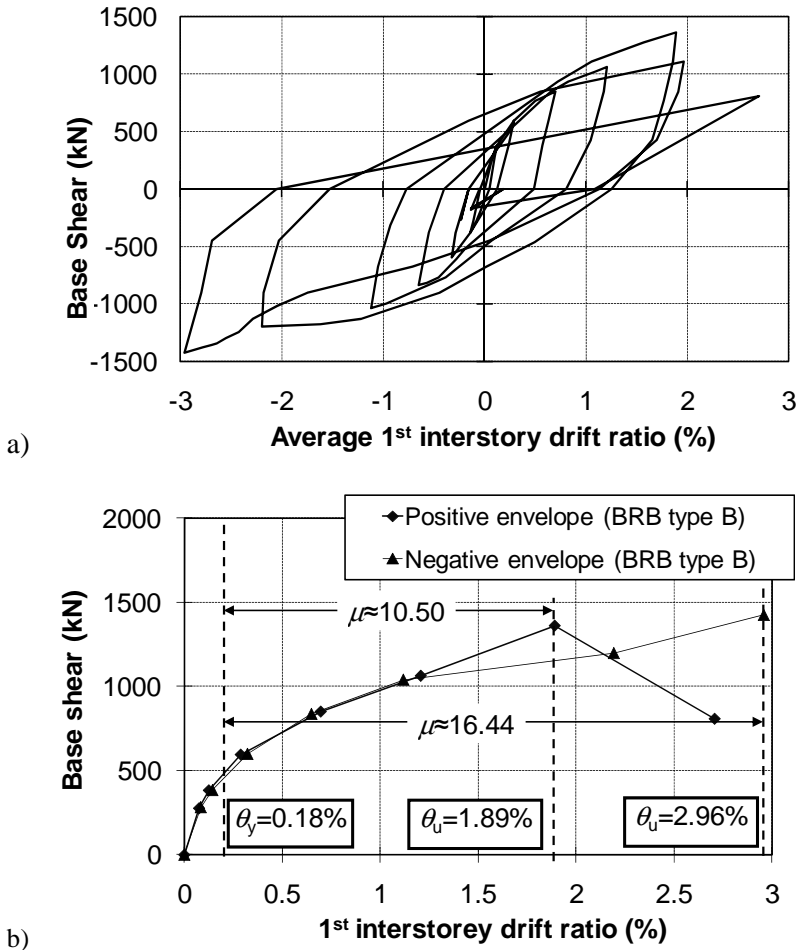


Figure 15. BRB type B: overall response.

In general, the occurrence of the phase 2 can be inferred to be directly related to both the clearance between the sleeve and the core (which influences the value of the “*T*” forces) and the local strength and stiffness of the plates constituting the sleeve. In case the phase 2 comes out, then in phase 3 the device exhibit only the increase of the sleeve plastic deformations and the inner core attains the final buckled configuration as a sort of accordion shape (Fig.

16g). In the studied cases these phenomena have been recognized for three devices over the four tested and they occurred starting from an interstorey drift ratio equal to 1.88% of the storey height. If the phenomena described in phase 2 are absent, the device directly exhibits the overall buckling (Fig. 16 f). These considerations are strengthened by having observed and measured a-posteriori the core-to-sleeve clearance of the tested devices. Indeed, in case of the BRB exhibited overall buckling the clearance was 1 mm per core side, which is lower than the designed value 2 mm per core side. The latter value was instead confirmed in the other three devices. For these BRBs the so-called “accordion” deformed shape has been observed as being particularly evident (Fig. 16 g). The “*T*” forces, calculated by means of the static balance shown in Figure 3, were about 2.5% of core yielding force. The number of buckling waves calculated with Eq. (3) has been confirmed by the experimental evidence. Indeed, the calculated number was 10, which was exactly the number of semi-waves shown by one BRB, while the remaining two BRBs exhibited a close number of 11 semi-waves.

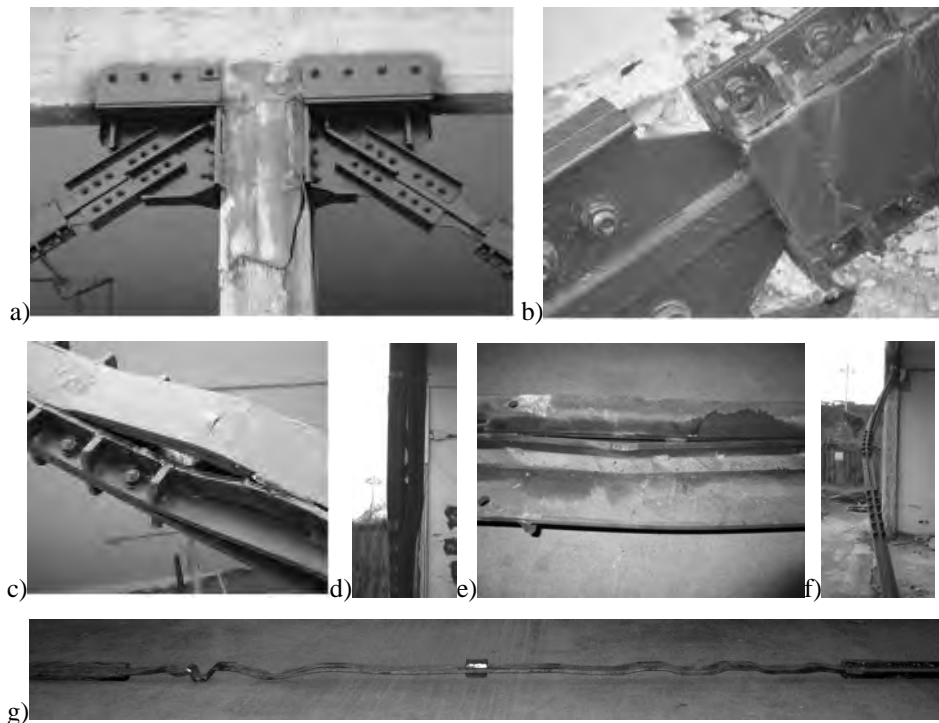


Figure 16. BRB type B: damage pattern.

Prototype C: experimental results

BRBs type C showed an excellent overall response, characterized by the complete efficiency as a ductile fuse up to the design value of the maximum interstorey drift ratio. Indeed, as highlighted in Figure 17, the tested prototype showed a fully stable and symmetric response in the design interstorey drift range ($\pm 2\%$) and allowed to reach in a stable manner the maximum allowable interstorey drift of $\pm 3\%$. Moreover, it is worth noting that the loading program applied to the type 5 (Fig. 10) was more severe than the one used for the other devices. Indeed, fully reversed interstorey drift ratios of 1.0%, 1.5%, 3.0% and continuing with cycles at 1.5% up to the core fracture were imposed. The residual capacity exhibited in the final cycles is shown in Figure 17b.

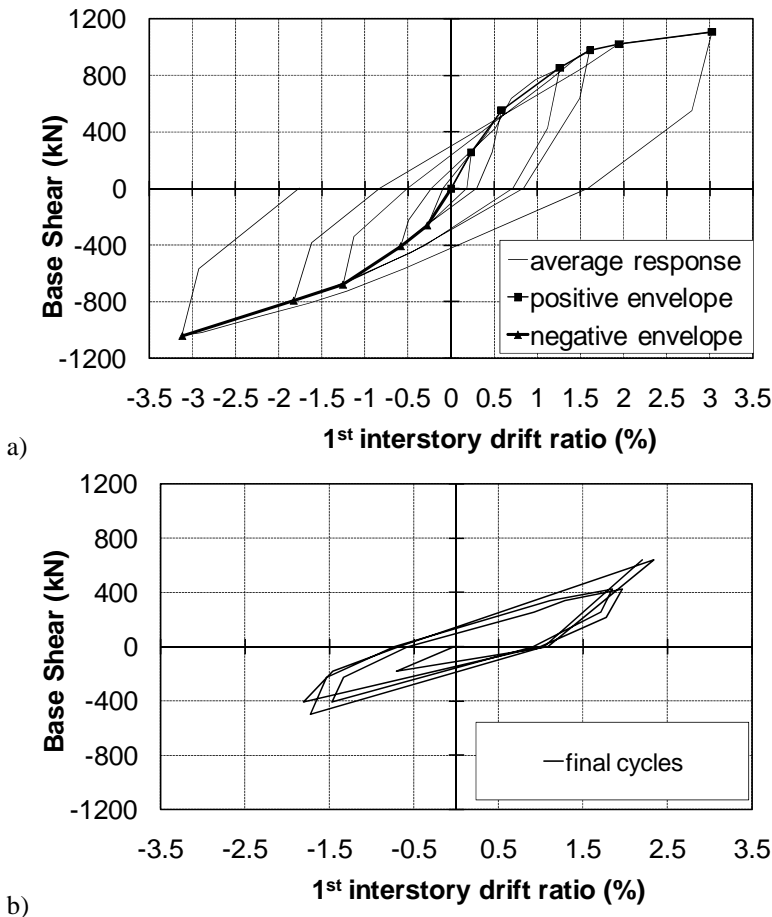


Figure 17. Measured base shear vs. first interstorey drift ratio.

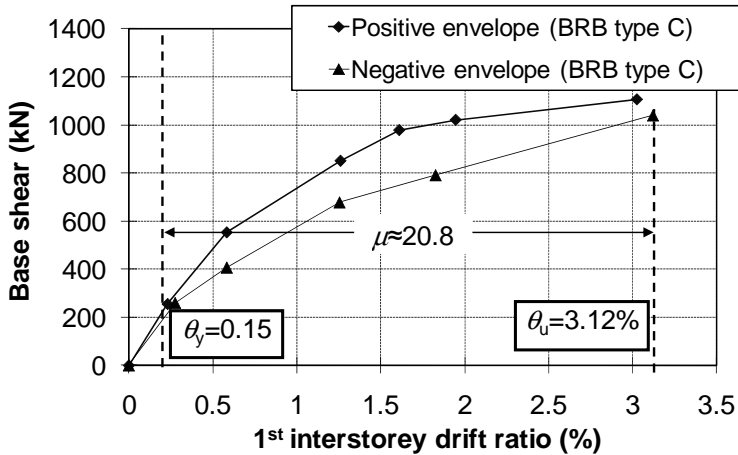


Figure 18. Envelope curves.

Notwithstanding the presence of CCBs, which affected the overall response in terms of loss of strength and stiffness because of their global buckling in compression, it is worth to note that the cyclic response was satisfactory stable. The degrading behaviour of CCBs may be recognized by comparing the envelope curves of the cyclic response. Indeed, analyzing the plot of Figure 18, the positive envelope curve, which is representative of the structure with BRBs in compression and CCBs in tension, exhibit a lateral strength and stiffness larger than the ones of the negative envelope curve, where the BRBs are in tension and the CCBs are in compression (which means in their buckled configuration). The tested structure reached a maximum interstorey drift of about 3.12 % and a maximum ductility $\mu = 20.8$.



Figure 19. Damage pattern: -0.2% of interstorey drift ratio.

The first non-linear event occurred at an interstorey drift of 0.2%, when CCBs buckled in compression while BRB prototypes were in tension (Fig. 19).

Subsequently, up to 2% of imposed interstorey drift ratio the BRBs perfectly behaved both in tension and in compression and no sign of damage to the sleeve was observed. The whole braced structure is shown in its lateral deformed shape (as respect to the vertical white line) in Figure 20a, while Figure 20b shows the predictable BRB response in compression.

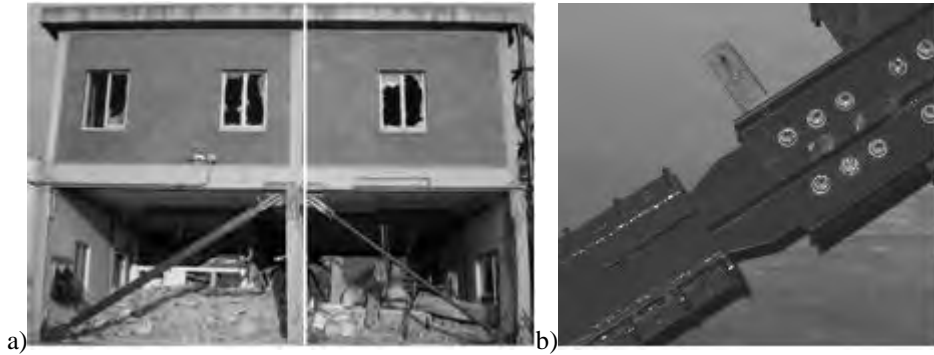


Figure 20. Damage pattern: +2% of interstorey drift ratio.

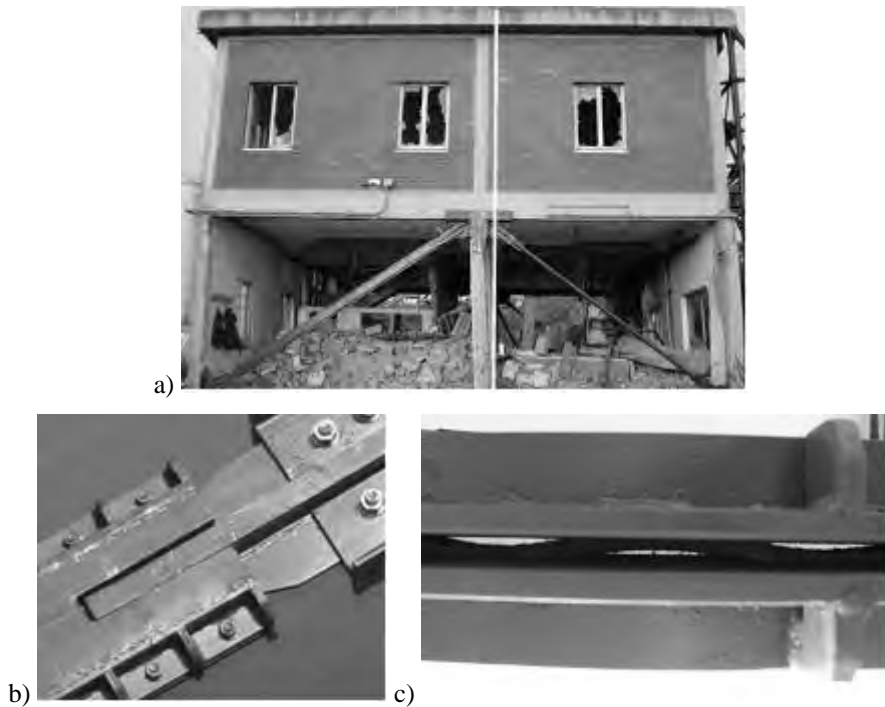


Figure 21. Damage pattern: +3% of interstorey drift ratio.

When the storey displacements increased from 2% to 3% of the first storey height, the occurrence of local damage to the sleeve was observed, with the detachment of the two parts constituting the bolted sleeve due to the “*T*” punching forces generated by the buckled core plate. In detail, at a 3% interstorey drift ratio (Figure 21a) both BRBs reached the end of their core working stroke (Fig. 21b), while the separation between the sleeve components became very apparent (Fig. 21c), testifying the typical formation of the high-order buckling waves along the inner steel core. At the same time, CCBs did not straighten in tension, showing a residual buckled shape. On the other hand, loading up to a negative interstorey drift equal to -3% (Fig. 22a) both BRBs perfectly behaved in tension (Fig. 22b), while the buckled CCBs showed a significant plastic hinging in the cross-section at middle length (Figs. 22c,d). In particular, the first cracking in the plastic hinge zone of both CCBs was recognized at 2.22% of interstorey drift ratio.

Finally, the test continued applying fully reversed storey displacements in the range of $\pm 1.5\%$ of the first storey height, up to the core fracture. In particular, three and half cycles were necessary to lead the core to fracture.

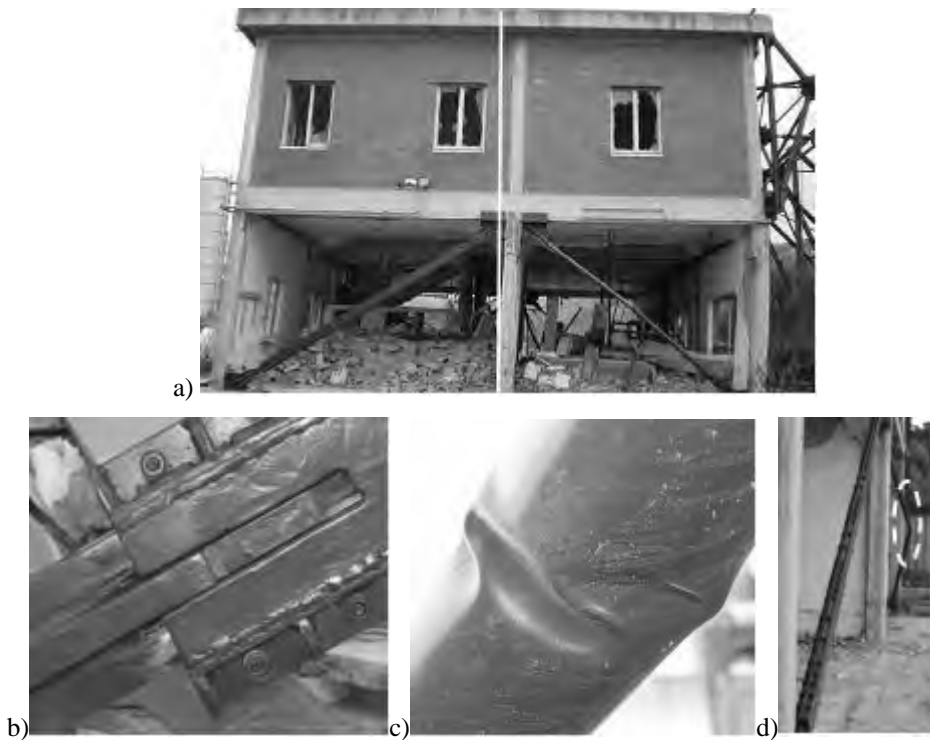


Figure 22. Damage pattern: -3% of interstorey drift ratio.

Test comparison

The brace prototypes showed a satisfactory global response, as highlighted by Figure 23, even if the performance of the first type was impaired by buckling of the unrestrained end portions. The local details adopted for BRB types B and C improved both their behaviour and “robustness”. The excellent experimental performance confirmed the effectiveness of the chosen technological and geometrical adjustments. The type C exhibited the best behaviour, with large overall ductility (range of $\pm 3\%$ of interstorey drift). It is worth noting that the lateral stiffness of the building equipped with BRB type C is lower than those of the other tests because of the simultaneous presence of CCBs, which did not have the same axial stiffness of BRBs.

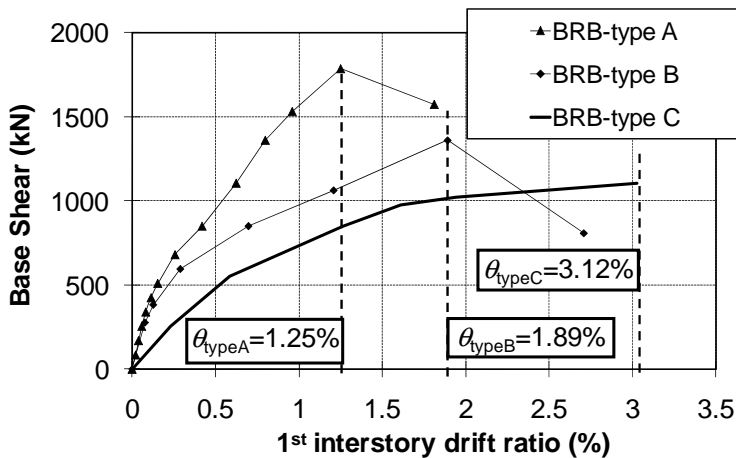


Figure 23. Comparison of response positive envelopes.

The experimental activity highlighted that the end parts of BRBs need special care in the detailing. In addition, an adequate control of the manufacturing process is important.

5. NUMERICAL MODELS

Generality

The numerical modelling of the tested two-story RC building involves several aspects to be taken into account, such as the presence of non structural elements (as claddings and partition walls), the influence of stairwells and the damage accumulation in the RC members after each experimental test.

A discussion about the modelling issues of the original masonry-infilled RC building, including the effect of the staircase structure, is presented in Della

Corte et al., 2008. Hereinafter, the numerical modelling of the damaged RC structure equipped with BRBs is discussed and validated by comparison with the experimental results shown in previous Sections.

Numerical modelling assumptions

Modelling the lateral response of the bare RC structure severely damaged and locally repaired after the second experimental test was a crucial phase of the modelling study. In fact, this physical condition has been assumed as the initial state of the RC building for the design of the first BRB prototype.

The following modelling assumptions were adopted:

- neglect the staircase: in fact, after the first two experimental tests on the bare RC building the staircase structure appeared to be very heavily damaged;
- take into account cracking of concrete: in fact, after the first tests a significant and spread cracking was observed into columns. This phenomenon was schematized reducing both the gross moment of inertia and the shear area of columns up to 40% of the initial values;
- place the plastic hinges in their actual position, as highlighted by the on-site survey: in fact, because of the presence of infill walls the position of plastic hinges was moved in some perimeter columns from their base towards the central part;
- reduce the flexural and shear capacity of the damaged internal columns (external perimeter columns were repaired, as shown in Fig. 24).

The residual flexural capacity of damaged columns has been calculated assuming, as shown in Figure 25b, that the moment resisting cross section was composed by a central concrete core and by the steel longitudinal rebars. In particular, the inner concrete core has been defined thanks to the data measured coming from the geometrical survey performed after the second testing, resulting that the spalled concrete was on the average about two times the original cover of longitudinal steel rebars.

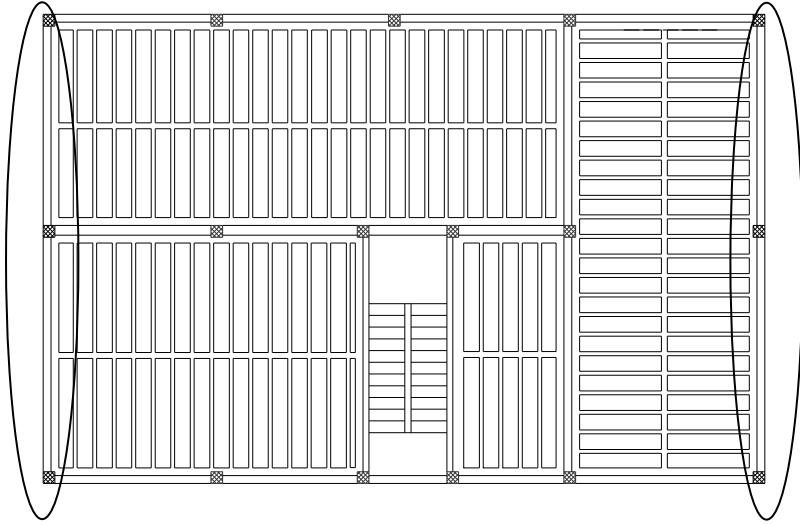


Figure 24. Position of the repaired columns (the red columns were not repaired).

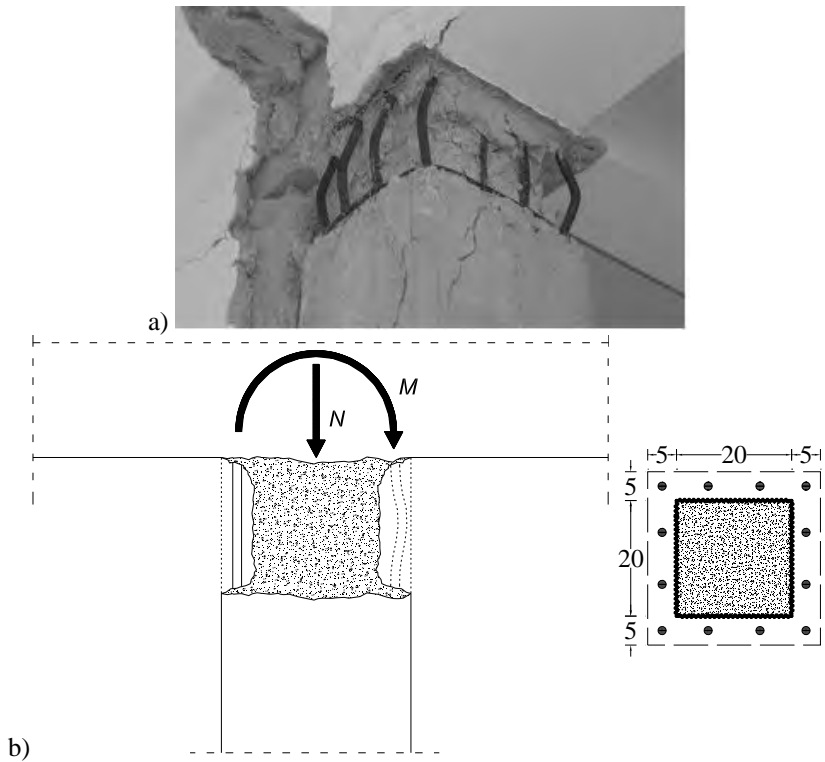


Figure 25. Modelling assumptions for the damaged RC columns: actual state after testing (a), calculation model (b).

The presence of the rebuilt masonry infill facing walls was taken into account for the test with BRBs type A (Fig. 26). The masonry infill walls have been schematized as two equivalent diagonal struts by means of the model presented by Al-Chaar (2002).

BRBs have been modelled as truss elements by means of the so-called “non-linear links” available in SAP2000. Their non-linear hysteretic properties have been reproduced adopting the Bouc-Wen model (1976), suggested by Black (2002). In particular, the model parameters (“ n ”, which is a dimensionless quantity that control the shape of the hysteretic loop and the post-yield to elastic stiffness ratio “ K ”) have been assumed with values equal to those usually suggested for unbonded BRBs (i.e. $n = 1$, which implies a smooth transition from the elastic to the post-yielding regime, and $K = 0.025$).

For the simulation of the test on BRBs type C the presence of diagonal CCBs had to be taken into account. The axial force-deformation relationship given by Georgescu (1996) has been adopted in order to model the buckling response.

The above modelling hypotheses led to satisfactorily reproduce the experimental global response, as shown in Figures 27 to 29. It is worth to notice that the deviations of numerical results from the experimental response curve are mainly due to the difficulties to properly model the damages to the RC structure induced by previous tests.

It is interesting to note that the 1st interstorey response is not affected by the presence of the rebuilt perimeter masonry infill walls. Figure 27c shows the comparison of the experimental envelope response curves with those obtained by a calibrated model with and without masonry infill walls. In fact, the numerical model highlights that the perimeter masonry infill walls contribute for only about 10% to the 1st storey lateral capacity.

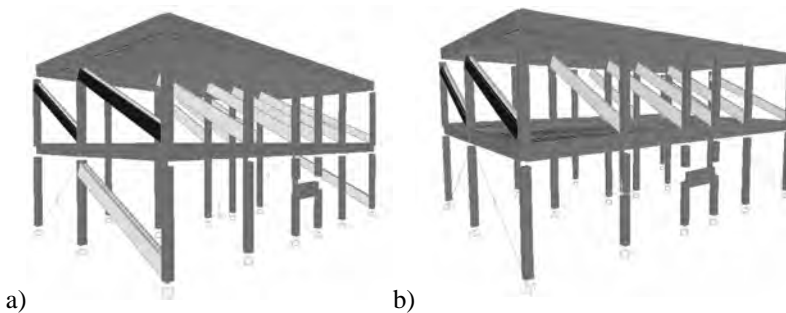


Figure 26. Calibrated numerical model of the masonry infilled RC structure equipped with BRBs prototype A (a) and with prototypes B or C (b).

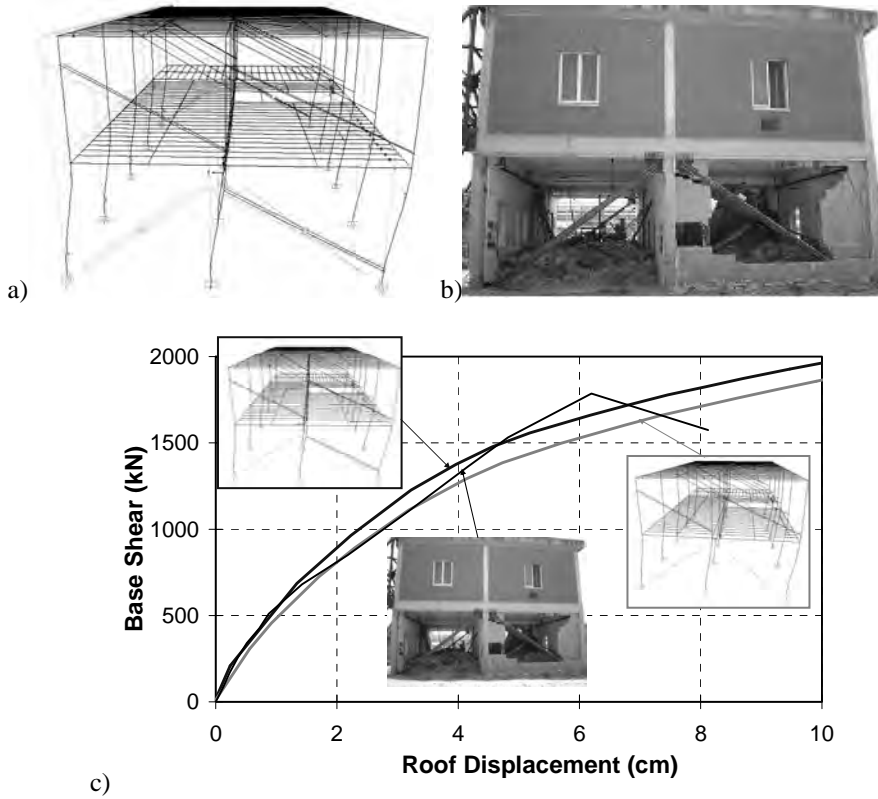


Figure 27. Experimental vs. numerical response: simulated mechanism (a); observed mechanism (b); backbone response curves. (BRB Type A).

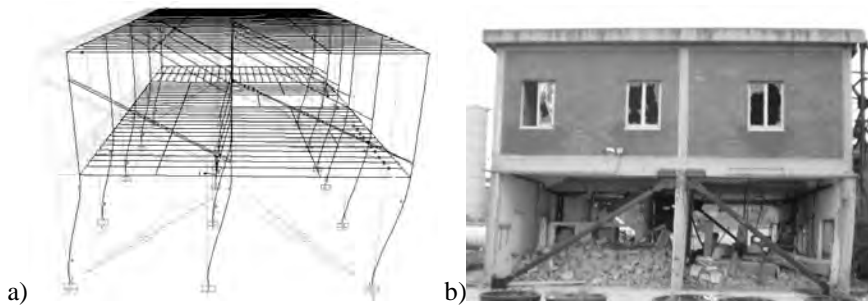


Figure 28a,b. Experimental vs. numerical response of the RC structure equipped with the BRB type B: simulated mechanism (a); observed mechanism (b); backbone response curves (c) (continued).

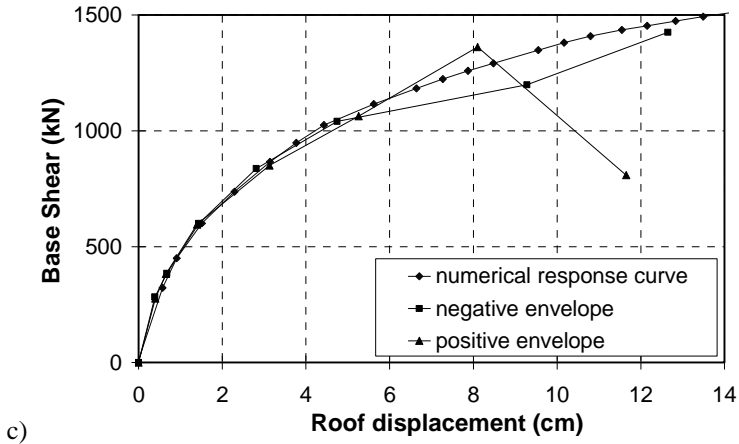


Figure 28c. Experimental vs. numerical response of the RC structure equipped with the BRB type B: simulated mechanism (a); observed mechanism (b); backbone response curves (c).

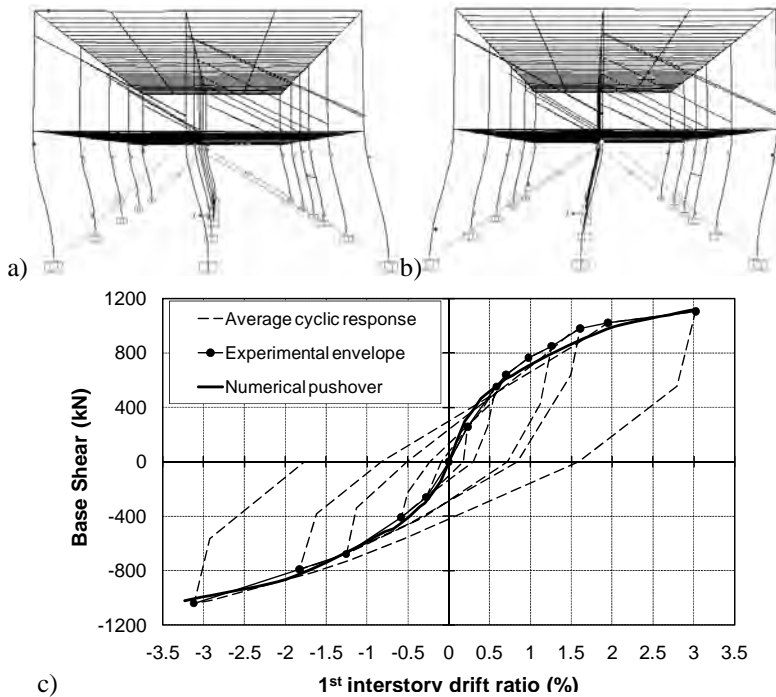
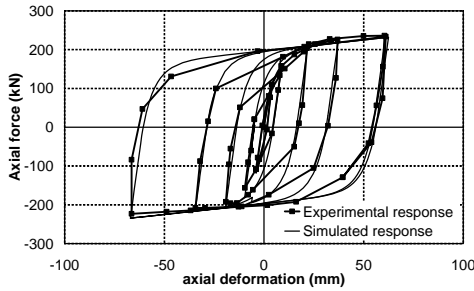
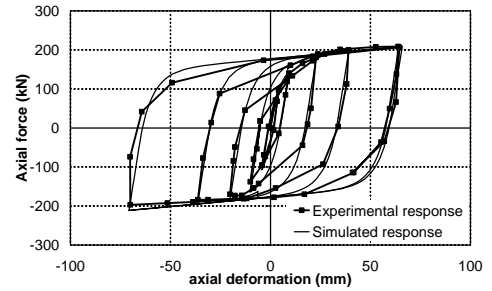


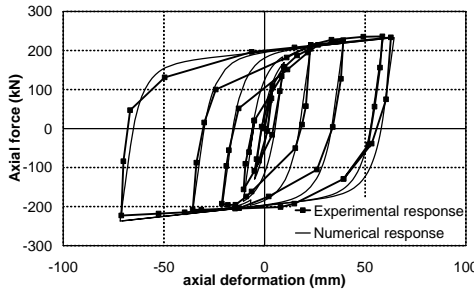
Figure 29. Experimental vs. numerical response of the tested RC structure equipped with BRBs type C and CCBs: simulated failure mechanism: a) pushover in negative direction; b) pushover in positive direction.



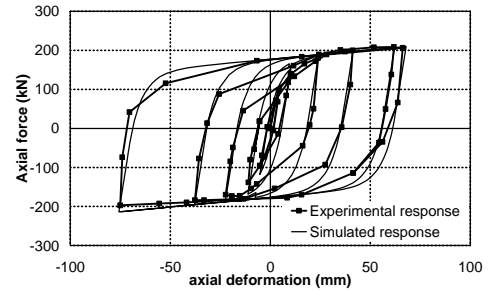
Specimen in the short bay – West side



Specimen in the long bay – West side



Specimen in the short bay – East side



Specimen in the long bay – East side

Figure 30. Experimental vs. numerical response of the BRBs type B.

The simulated BRB axial force vs. displacement response has been compared to that observed experimentally. The comparison is carried out for maximum drift ratios of $\pm 1.5\%$, i.e. the range of stable BRB response. The latter has been deduced from the experimental overall response curves by subtracting the fraction from the measured total base shear resistance given by the RC frame (calculated by the numerical simulation), then, sharing the remaining lateral force among the braces depending on their strength. As shown by Figures 30, the simulated response curves adequately match those exhibited experimentally.

CONCLUSIONS

This paper shows and discusses the main results from a two-phase experimental program devoted to analyze the behaviour of “all steel” buckling restrained braces to improve the seismic capacity of existing RC buildings. Indeed, two novel series of “all-steel” BRBs have been tested. The second group of prototypes is characterized by the possibility to hide the brace inside masonry claddings.

Experimental results demonstrate that “all-steel” BRBs can deliver ductile, stable, and repeatable hysteretic behaviour.

The Bouc–Wen model was used to approximate the inelastic behaviour of the devices. Coherently to the literature (Black et al., 2002), a single set of calibrated model parameters was found to satisfactorily predict the cyclic and transient behaviour of the BRBs when subjected to a variety of loading histories.

This work showed that the performance of “all-steel” BRBs depends on some local details. Indeed, based on test results it was recognized that:

- Wrong connection details usually leads to undesired local-distortional buckling modes of failure, which may impair the correct performance of the device.
- Properly designed, fabricated and erected BRBs showed excellent cyclic inelastic response.
- Even when undesired failure modes occurred, RC frames equipped with BRBs showed superior performance over bare RC frames or frames with classic braces.

ACKNOWLEDGEMENTS

The financial support of the following subjects is gratefully acknowledged:

- The Italian Civil Protection: ReLUIS Project – Task 5 “Development of innovative approaches to design steel and composite steel-concrete structures”
- The Italian Ministry for Research and Education (MIUR): PRIN 2005-2007 project “Innovative techniques and strategies for seismic upgrading of existing RC structures”.
- The European Commission: PROHITECH project “Earthquake Protection of Historical Buildings by Reversible Mixed Technologies”.

REFERENCES

- AISC/SEAOC [2001]. “Recommended Provisions for Buckling-Restrained Braced Frames,” American Institute of Steel Construction/Structural Engineers Association of California Task Group.
- Al-Chaar, G., [2002]. Evaluating Strength and Stiffness of Unreinforced Masonry Infill Structures. US Army Corps of Engineers – Engineer Research and Development Center.
- American Institute of Steel Construction, Inc. (AISC), [2005]. Seismic provisions for structural steel buildings. Standard ANSI/AISC 341-05. Chicago (IL, USA).
- Antonucci, R., Calducci, F, Castellano, M.G., Donà, F. [2006]. Pre-casted RC Buildings with Buckling Restrained Braces: the Example of the New Building of the Faculty of Engineering in Ancona. Proceedings of the 2nd International Fib Congress, Naples (Italy).

- Black, C., Makris, N., Aiken, I., [2002]. Component testing, stability analysis and characterization of buckling restrained braces. PEER Report 2002/08, Pacific Earthquake Engineering Research Center, University of California at Berkeley.
- Brown, A.P., Aiken, I.D., Jafarzadeh, F.J., [2001]. Buckling Restrained Braces Provide the Key to the Seismic Retrofit of the Wallace F. Bennett Federal Building. Modern Steel Construction.
- Carden, L., Itani, A., Buckle, I. & Aiken, I. [2004]. Buckling Restrained Braces for Ductile end cross frames in steel plate girder bridges. Proceedings of the 13th World Conference on Earthquake Engineering, Canada.
- CEN (European Committee for Standardization), [2004]. Eurocode 3 – Design of steel structures – Part 1.1: General rules and rules for buildings. EN 1993-1-1, Bruxelles.
- Chen, C.H., [2002]. Recent advances of seismic design of steel building in Taiwan. International training programs for seismic design of building structures, Taiwan
- Chen, C.H., Hsiao, P.C., Lai, J.W., Lin, S.L., Weng, Y.T. & Tsai, K.C., [2004]. Pseudo-dynamic test of a full-scale CFT/BRB frame: Part2- Construction and testing. Proceedings of the 13th World Conference on Earthquake Engineering, Canada.
- Chopra, A. [2000]. Dynamics of structures: Theory and Applications to Earthquake Engineering, Prentice Hall
- D'Aniello, M., Della Corte, G. & Mazzolani, F.M., [2006]. Seismic Upgrading of RC Buildings by Steel Eccentric Braces: Experimental Results vs Numerical Modeling. Proceedings of the STESSA Conference, Yokohama, Japan, 14-17 August.
- D'Aniello, M., Della Corte, G., Mazzolani, F.M., [2007]. A special type of buckling-restrained brace for seismic retrofitting of RC buildings: design and testing. Proc. of XXI C.T.A. Conference, Catania (Italy).
- D'Aniello, M., Della Corte, G., Mazzolani, F.M., [2009]. Un controvento speciale ad instabilità impedita per il consolidamento sismico di edifici in c.a.. Costruzioni Metalliche, Gennaio-Febbraio, pp. 47-56.
- Della Corte, G., Faggiano, B., Mazzolani, F.M., [2003]. Innovative steel bracing systems for seismic upgrading of reinforced concrete structures: planning of a testing program. Atti del XIX Congresso CTA, Genova, 28-30 settembre, Vol. 1, pp. 317-330.
- Della Corte, G., D'Aniello, M., Mazzolani, F.M., [2005]. Seismic upgrading of RC buildings using buckling restrained braces: full-scale experimental tests. Atti del XX Congresso CTA (Collegio dei Tecnici dell'Acciaio), Ischia, 26-28 settembre.
- Della Corte G., Mazzolani F.M. [2006]. Full-scale tests of advanced seismic upgrading techniques for RC structures. Proceedings of the Second fib Congress, Naples, Italy, 5-8 June 2006, paper No. 0432.
- Della Corte, G., Fiorino, L., Mazzolani, F.M., [2008]. Lateral loading tests on a real RC building including masonry infill panels with and without FRP strengthening. Journal of Materials in Civil Engineering, ASCE, Vol. 20, No. 6.
- De Sortis, A., Antonacci, E., Vestroni, F. [2005]. "Dynamic identification of a masonry building using forced vibration tests", Engineering Structures vol. 27 155–165.
- Eurocode 2 [2005]. Design of concrete structures – part 1-1: General rules for buildings.
- Eurocode 3 [2005]. Design of steel structures – part 1-1: General rules for buildings.

- Fahnestock L.A., Sause R., Ricles J.M. [2003]. Analytical and experimental studies on buckling restrained braced composite frames. Proceedings of the International workshop on Steel and Concrete Composite Construction (IWSCCC-2003), October, 8-9, Taipei, pp. 177-188.
- FEMA 356 [2000]. Prestandard and commentary for the Seismic Rehabilitation of Buildings. Building seismic safety Council for the Federal Emergency Management Agency, Washington.
- Fujimoto, M., Wada, A., Saeki, E., Watanabe, A. and Hitomi, Y. [1988]. A study on the unbonded brace encased in buckling-restraining concrete and steel tube, *Journal of Structural Engineering*, 034B, 249–258
- Inoue, K, Sawaizumi, S, Higashibata, Y., [2001]. Stiffening requirements for unbonded braces encased in concrete panels. *Journal of Structural Engineering*, ASCE;127(6):712–9.
- Iwata, M., Kato, T. & Wada, A., [2000]. “Buckling-restrained braces as hysteretic dampers,” Proceedings of Third International Conference on Behavior of Steel Structures in Seismic Areas (STESSA 2000), Montreal, Canada, pp.33-38.
- Iwata, M., Murai, M. [2006]. “Buckling behavior of the core plate on buckling-restrained braces”. *Steel – a New and Traditional Material for Building*, Proceedings of international Conference, Poiana Brasov (Romania) 20-22 September. Taylor & Francis Group, London.
- Kimura, K., Takeda, Y., Yoshioka, K., Furuya, N. and Takemoto, Y. [1976]. “An experimental study on braces encased in steel tube and mortar,” Annual Meeting of the Architectural Institute of Japan.
- Kuwahara, S. and Tada, M. [1993]. A study on stiffening capacity of double-tube members, *Journal of Structural and Construction Engineering*, 445, 151–158
- Manabe, N., Shimokawa, H., Kamitani, M, Morino, S. and Kawaguchi, J. [1996]. Elasto-plastic behavior of flat-bar brace stiffened by square steel tube, *Summaries of Technical Papers of Annual Meeting*, Architectural Institute of Japan, pp. 783–784
- Maheri, Sahebi. [1997]. Use of steel bracing in reinforced concrete frames. *Engineering structures* vol. 19, No. 12, pp. 1018-1024, 1997.
- Martelli A. [2006] Modern seismic protection systems for civil and industrial structures. An advanced approach to earthquake risk scenarios, with applications to different European towns; 2006.
Downloadable at: http://www.samco.org/network/download_area/paper_martelli.pdf.
- Mazzolani, F.M., (Ed.) [2006]. Seismic upgrading of RC buildings by advanced techniques. The ILVA-IDEM research project. Polimettrica, Italy.
- Mazzolani, F.M., Della Corte, G., D’Aniello, M. [2009]. Experimental analysis of steel dissipative bracing systems for seismic upgrading. *Journal of Civil Engineering and Management* 15(1): 7-19.
- Merritt, S., Uang, C.M. and Benzoni, G. [2003a], Subassemblage testing of corebrace buckling-restrained braces, Report No. TR-2003/01, University of California, San Diego, La Jolla, CA.
- Merritt, S., Uang, C.M. and Benzoni, G. [2003b]. Subassemblage testing of star seismic buckling restrained braces, Report No. TR-2003/04, University of California, San Diego, La Jolla, CA.

- Merritt, S., Uang, C.M. and Benzoni, G. [2003c]. Uniaxial testing of associated bracing buckling-restrained braces, Report No. TR-2003/05, University of California, San Diego, La Jolla, CA.
- Mochizuki, S., Murata, Y., Andou, N. & Takahashi, S., [1979]. Experimental study on buckling of unbonded braces under axial forces: Parts 1 and 2. Summaries of technical papers of annual meeting. Architectural Institute of Japan; p. 1623–6.
- Mochizuki, S., Murata, Y., Andou, N. & Takahashi, S., [1980]. Experimental study on buckling of unbonded braces under axial forces: Part 3. Summaries of technical papers of annual meeting. Architectural Institute of Japan; p. 1913–4.
- Mochizuki, S., Murata, Y., Andou, N. & Takahashi, S. [1982]. Experimental study on buckling of unbonded braces under axial forces: Part 4. Summaries of technical papers of annual meeting. Architectural Institute of Japan; p. 2263–4.
- Nagao, N. and Takahashi, S. [1990]. A study on the elasto-plastic behavior of unbonded composite bracing (Part 1: experiments on isolated members under cyclic loading), *Journal of Structural Engineering*, 415, 105–115.
- Nakamura, H., Maeda, Y., Sasaki, T., Wada, A., Takeuchi, T., Nakata, Y. and Iwata, M. [2000]. Fatigue properties of practical-scale unbonded braces, *Nippon Steel Technical Report*, 82(July), 51–57.
- Nishimoto, K., Nakata, Y., Kimura, I., Aiken, I., Yamada, S. & Wada, A., [2004]. Sub-assembly testing of large buckling restrained unbonded braces. *Proceedings of the 13th World Conference on Earthquake Engineering*, Canada.
- Ren, W.X., Zong, Z.H. [2004]. “Output-only modal parameter identification of civil engineering structures”, *Structural Engineering and Mechanics*, Vol. 17, No. 3-4
- Richardson, M.H. [1986]. “Global frequency & damping estimates from frequency response measurements”, 4rd IMAC Conference, Los Angeles, CA February.
- Richardson, M.H. [1999]. “Structural Dynamics Measurements”, *Spectral Dynamics* – April 11-16.
- Sabelli, R., Mahin, S., Chang, C. [2003]. Seismic demands on steel braced frame buildings with buckling-restrained braces. *Engineering Structures*, Vol. 25 (5).
- Sabelli R., Aiken I. [2004]. U.S. building-code provisions for buckling-restrained braced frames: basis and development. *Proceedings of the 13th World Conference on Earthquake Engineering*, Vancouver, Canada, CD-ROM: paper no. 1828.
- Sabelli, R., Lopez, W., [2005]. Design of Buckling Restrainted Braced frames.
- Shimizu, T., Fujisawa, K., Uemura, K. and Inoue, I. [1997]. Design method to prevent buckling of low yield strength steel tube brace and fracturing of joints (Parts 1 and 2), *Summaries of Technical Papers of Annual Meeting*, Architectural Institute of Japan, pp. 781–784
- Suzuki, N., Asano, R. Tohata, Y., Sasaki, T. and Segawa, T. [1994]. Experimental study on the H-section steel brace encased in RC or steel tube, *Summaries of Technical Papers of Annual Meeting*, Architectural Institute of Japan, pp. 1621–1622
- Tsai K.C., Huang Y.C. [2002]. Experimental responses of large scale BRB frames. Report No. CEER/R91-03, Center for Earthquake Engineering Research.
- Tsai, K.C., Lai, J.W., Hwang, Y.C., Lin, S.L. & Weng, Y.T. [2004,a]. Research and application of double-core buckling restrained braces in Taiwan. *Proceedings of the 13th World Conference on Earthquake Engineering*, Canada.

- Tsai, K.C., Weng, Y.T., Lin, S.L. & Goel, S. [2004,b]. Pseudo-dynamic test of a full-scale CFT/BRB frame: Part1-Performance Based Design. Proceedings of the 13th World Conference on Earthquake Engineering, Canada.
- Wada, A., Saeki, E., Takeuch, T., Watanabe, A. [1989]. Development of unbonded brace Column (A Nippon Steel Publication), No.115 1989.12
- Wada, A., Saeki, E., Takeuchi, T. and Watanabe, A. [1998]. Development of unbonded brace, Nippon Steel Corporation Building Construction and Urban Development Division, Tokyo, Japan.
- Wada, A., Nakashima, M. [2004]. From infancy to maturity of buckling restrained braces research. Proceedings of the 13th World Conference on Earthquake Engineering, Vancouver, Canada, CD-ROM: paper no. 1732.
- Wakabayashi, M., Nakamura, T., Katagihara, A., Yogoyama, H. & Morisono, T., [1973]. Experimental study on the elastoplastic behavior of braces enclosed by precast concrete panels under horizontal cyclic loading – Parts 1 & 2. Summaries of technical papers of annual meeting, vol. 6. Kinki Branch of the Architectural Institute of Japan; p. 121–8
- Watanabe, A., Hitomi, Y., Saeki, E., Wada, A. & Fujimoto M. [1988]. Properties of brace encased in buckling-restraining concrete and steel tube. In: Proc. of ninth world conf. on earthquake eng. vol. IV. p. 719–24.
- Xie, Q. [2005]. State of the art of buckling-restrained braces in Asia. Journal of Constructional Steel Research, vol. 61 p. 727–748.

ROTATION CAPACITY AND CLASSIFICATION CRITERIA OF STEEL BEAMS

Raffaele Landolfo, Mario D'Aniello, Manuela Brescia, Susanna Tortorelli

*Department of Constructions and Mathematical Methods in Architecture,
University of Naples Federico II, Naples, Italy*

Abstract. Rotation capacity of steel beams is parameter of significant importance for plastic and seismic analysis and design of steel moment resisting structures. In the former case it influences the plastic bending moment redistribution. In the second case, rotation capacity of steel beams is the source of ductility allowing the attainment of a globally ductile behaviour of the structure. Thus the determination of rotation capacity of steel structures is a crucial issue. The flexural requirements for plastic design of steel sections in modern international design codes (e.g. EN 1993:1-1, EN 1993:1-8, AISC 2005, etc.) provide misleading emphasis on local buckling as the primary strain-weakening effect, focusing on local slenderness ratios, but neglecting important physical parameters as the variation of bending moment along the member length and the hysteretic behaviour of the steel constituting the beam. With the aim of quantify and predict the flexural capacity of steel members an experimental campaign on a wide range of cross section typologies (I sections, Square and Rectangular Hollow sections) was planned. Different local slenderness (flange over thickness and web over thickness) ratios have been selected in order to integrate the data early available in literature. The rotation capacities measured in these tests are examined in terms of standard local and lateral buckling parameters. The importance of different parameters is assessed and the effectiveness of the code provisions and theoretical models of literature is analyzed with comparison to the experimental results.

Keywords: rotation capacity, ductility, moment resisting frames, cross section classification.

1. INTRODUCTION

The rotation capacity is the fundamental structural property that is assumed in plastic and seismic design of building structures. Indeed, in plastic design the member should be capable of forming plastic hinges, which must rotate until the collapse mechanism is reached without dropping its moment capacity. Thus the required redistribution of bending moments is assured. The total rotation of the beam plastic hinge in a collapse mechanism is the rotation demand of the structure, which varies for different structural configurations, loading arrange-

ments, geometry, material strengths and level of seismicity and has been widely studied in the literature, particularly for continuous beams and frames (Driscoll, 1958; Kerfoot, 1965; ASCE Plastic design in steel, 1971).

In the earthquake-resistant design, this rotation capacity is essential to assure that a determined portion of the input seismic energy shall be dissipated by plastic behaviour.

It is generally accepted in design practice that steel members behave in ductile manner with a good rotation capacity. Unfortunately, this idea has become a myth among the practitioner engineers. The flexural behaviour of steel beams can be impaired by the occurrence of local and/or overall buckling phenomena, such as the plastic buckling of compression parts or by inelastic flexural-torsional buckling. Both the EN1993:1-1 (EC3) and EN1998-1 (EC8) do not provide rational and concise requirements, but only vague and qualitative provisions. Indeed, EC3, Section 5.4.3(2), states that "*Plastic global analysis may be used where the members are capable of sufficient rotation capacity to enable the required redistributions of bending moments to develop*". Analogously, EC8, Section 6.5.3(1)P, outlines that "*Sufficient local ductility of members which dissipate energy in compression or bending shall be ensured by restricting the width-thickness ratio b/t according to the cross-sectional classes specified in EN 1993-1-1:2004, 5.5.*" thus referring entirely to the EC3.

However, to perform a reliable structural analysis is essential to quantify clearly what 'sufficient rotation capacity' or 'sufficient local ductility' mean.

In any case, EC3 provides the subdivisions of cross-sections into four classes, depending on the properties of compression elements. For plastic global analysis, EC3 requires that all members containing plastic hinges shall have class 1 ductility. For seismic analysis according to EC8, the cross section classes defined in EC3 are related to the selected behaviour factors: class 1 for $q > 4$, class 2 for $2 < q \leq 4$, and class 3 for $q \leq 2$. This procedure is very useful for design purposes, but the classification contains many weaknesses. The main criticism of the EC3 classification, especially for what concerns the seismic application, refers to the consideration of a very few number of parameters, selected only between material and cross-section factors, the very important member characteristics being ignored, such as, flange-web interaction, member slenderness, moment gradient, lateral restraints, cyclic loading, etc. In particular, the cyclic loading of members under seismic action is fundamentally different from the monotonic one under static loading. With this regard it is important to underline that the EC3 classification is basically derived from the results of monotonic experimental tests. This aspect highlights again the weakness of EC3 classification for seismic application. In order to give an idea of this statement, it is worth noting that the comparison of the width-to-thickness limits in the EC3 and AISC reveals considerable differences in the case of rectangular and circular tubular members. The limits of seismically-compact sections in AISC are significantly more severe than those corresponding to Class 1

used in EC3 and EC8. Since the ductility capacity and susceptibility to fracture are directly related to the occurrence of local buckling, it seems necessary to conduct further assessment of the adequacy of Class 1 sections to satisfy the cyclic demands imposed under prevalent seismic conditions.

Another aspect neglected by EC3 classification is the flexural overstrength of steel beams, which has a key role in application of hierarchy criteria for seismic design. Indeed, EC8 consider a uniform overstrength factor equal to 1.1 for all types of members, thus underestimating the ultimate strength in all compact members. This factor is not explicitly defined in EN 1998-1. Although it can represent the strain-hardening of dissipative regions, some authors (Fardis et al., 2005) consider the 1.1 factor as a “safety factor”. In both cases it is inadequate to predict the actual flexural behaviour of steel beams.

Therefore, classification of member ductility accounting for both cross-section slenderness and member slenderness were proposed by several authors (Mazzolani & Piluso, 1992; Gioncu & Mazzolani, 1995; Gioncu & Mazzolani, 2002) for I and H shaped members.

For seismic application the subdivision of members into ductility classes is necessary because, as before mentioned, the rotation capacity influences the behavioural factor of the structure. At the same time, the subdivision of the members into overstrength classes is necessary in order to apply the capacity design criteria both to local level (connections among dissipative and not dissipative zones), and to global level (overstrength of non-dissipative members). The twofold classification of the steel members in ductility and overstrength classes is the most appropriate approach for the seismic applications.

The late Italian code for seismic design OPCM 3274 substitute the EC3 concept of cross-section behavioural classes by the concept of member behavioural classes (Mazzolani & Piluso, 1993). Although this criterion is the most appropriate to classify the flexural response of steel beams, the new Italian code NTC 2008 reintroduced the EC3 approach, for uniformity and consistency with the European code.

In spite of the current code, a theoretical and experimental activity was carried out in the framework of Reluis project (2005-2008) (<http://www.reluis.it/>) in order to develop reliable design formulas based on the member behavioural concept, owing to the effectiveness of this approach. Therefore, a wide range of cross section typologies (I sections, Square and Rectangular Hollow sections) has been investigated and the influence of geometrical and mechanical parameters are analyzed.

2. ROTATION CAPACITY

Generality

The plastic behaviour of a structure system depends on moment redistribution. The achievement of a predicted collapse load is related to the distribution of

plastic hinges, being the zones where the full plastic moment is reached, and to the plastic rotation which other hinges can develop elsewhere. Hence, a good behaviour of a plastic hinge requires a good amount of ductility, in addition to its strength requirement. The rotation capacity (R) is the rational measure of the flexural ductility of steel beams, being the ability of a cross-section to satisfy the rotation requirement. R may be defined by two commonly ways. One is evaluated from the moment–curvature relationship and the other is based on the moment–rotation behaviour. Both approaches define the rotation capacity as a non-dimensional parameter, whose meaning is described in Figure 1, where the generalized moment-rotation curve for a section capable of sustaining plastic deformation (Class I or compact section, according to EC3) is plotted.

The moment–curvature based approach has been widely utilized in the literature for the study of cold-formed steel sections (Korol & Hudoba, 1972; Hasan & Hancock, 1989; Zhao & Hancock, 1991; Wilkinson & Hancock, 1998) in a four-point bending arrangement. According to this philosophy R is defined by the following equation:

$$R = \frac{\chi_u}{\chi_p} - 1 \quad (1)$$

where χ_p is evaluated as M_p/EI and χ_u is the limiting curvature at which the moment resistance drops back below M_p .

Similarly, the definition of R based on the moment–rotation relationship has been commonly used in the literature (Rondal et al., 1995; Sedlacek et al., 1995, 1998). Rotation capacity based on the moment–rotation relationship is defined by the following:

$$R = \frac{\theta_u}{\theta_p} - 1 \quad (2)$$

being θ_p the rotation corresponding to the flexural yielding and θ_u the ultimate beam rotation, as shown in Figure 1.

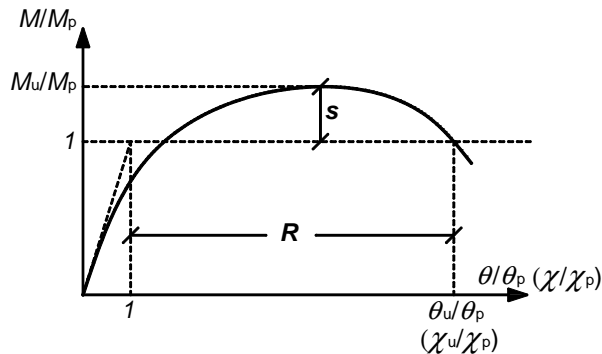


Figure 1. Generalized moment-rotation curve for a steel beam.

Owing to its clarity, the moment-rotation approach is the most effective and useful for experimental purposes. This measure was already proposed by Schleich et al. (1998) who pointed out the easiness by which it may be obtained from the output of structural analysis programs. This is the reason induced the most of research in using it. However, its value depends not only on the cross section but also on the moment gradient (loading and boundary conditions) and length of the element.

Predictive methods of the Rotation Capacity

In general, R can be directly obtained from experimental tests, measuring and calculating the rotations θ_u and θ_p . However, several methods to evaluate the beam rotation capacity are proposed by different authors, which can be grouped in the following methods:

- Theoretical methods: the evaluation of the rotational capacity is based on the approximate theoretical evaluation of the relationship moment-curvature of the section and on the theoretical analysis of the instability phenomena (particularly the local instability of the compressed flange). Indeed, both the effects derived from the geometric configuration of the section and the mechanical imperfections are neglected, although they affect the flexural curvature. Under this hypothesis, the theoretical investigation of the relationship moment - curvature can be addressed assuming an ideal section made of two concentrated masses. This approach has been adopted by Kato (1988, 1989, 1990) also in the analysis of the capacity of deformation of tubular square and circular sections. In any case, the equivalent section has the same area of the actual section, while its height is calculated imposing the equivalence of the two sections in terms of plastic moment. Moreover, Kato theory neglects the rotation due to the part of the member still in elastic field, thus assuming a rigid-perfectly plastic-hardening behaviour;
- Semi-empirical methods: differently from theoretical methods the local buckling phenomena are obtained experimentally. Indeed, in semi-empirical methods the moment-curvature relationship of the section depends on the experimental measurements of the critical stress, which corresponds to the local buckling of the flange in compression. Kato proposed a procedure (Kato, 1988, 1989, 1990) to determine the rotation capacity. This theory is obtained assuming an ideal section made of two equivalent flanges characterized by a rigid-perfectly plastic-hardening material. The equivalency is maintained by equating the full plastic moment and axial strength for both actual and ideal sections. From the integration of member curvature simple equations of R are given for different level of axial force as function of two parameters, which are “ ρ ” and “ s ”. The former is the ratio between the axial force (N) and the axial strength (N_{pl}). The second is the normalized critical stress, given by the ratio between the critical stress (f_{cr}) and the yield

- stress (f_y). Kato proposed also a procedure (Kato, 1988, 1989, 1990) to determine the parameter “ s ” as a function of flange and web slenderness.
- Empirical methods: based on statistic analyses of a large number of data obtained by experimental tests or on numerical simulations. Several empirical relationships for the evaluation of the rotation capacity of steel members have been proposed in the scientific literature. Kato & Akiyama (1980, 1981) have proposed a simplified moment-rotation relationship constituted by three linear branches for members subjected to a bi-triangular distribution of the bending moment. This equation has been obtained interpolating the experimental results performed by Fukuchi (1969), Kato et al. (1973, 1976), Lukey & Adams (1969), Suzuki et al. (1974). Nakamura (1988) proposed a different equation for rotation capacity obtained by having processed the results of 121 tests carried out on beams having different lateral torsional-slenderness. The Spangemacher & Sedlacek (1992) proposed a method based on the results obtained from F.E.M. simulations. Particularly, they carried out a parametric numerical study, analyzing separately the influence of all parameter a time.

Rotation Capacity in modern codes

In modern steel design codes for plastic design, national reference values for rotation capacity have been established on the basis of available analytical, experimental and numerical studies. Design rules have then been developed with reference to this rotation capacity. Indeed, after plastic design was introduced, Driscoll (1957, 1958) evaluated the rotation capacity required to achieve plastic collapse in a wide range of continuous beams and portals made of wide flange profiles, and concluded that the required R could be equal to 12 in the worst cases. Recently, this requirement has been relaxed because of the following influences:

- (a) the flexibility of the connections, particularly bolted splices, increases the rotation in critical regions;
- (b) tests on complete structures showed that the rate of strain weakening is less marked than in tests on statically determinate elements, where the energy absorbed in the testing equipment may be significant;
- (c) improved resistance associated with strain hardening.

Kemp (1985) has first recommended lower limits of rotation capacity ($R > 5$ and $R > 3$) to be used for different limit states in the South African Code for plastic design, whereas Yura et al. (1978) have already proposed $R > 3$ in the draft American LRFD Code. Nowadays, the North American standard has assumed a rotation capacity of 3 to be sufficient for most civil engineering structures as indicated in Yura et al. (1978) and AISC 2005 a,b. This rotation capacity of three is based on limiting the flange strain to four times the yield strain. The North American standard has then derived their limiting width-to-thickness ratios for compact sections on the basis of this value.

Similarly, in the background document to the European standard, Bild et al. (1989) and Sedlacek & Feldmann (1995) investigated and summarized the rotation requirements for three-span continuous beams and single bay frames under point loads. They concluded that a rotation capacity equal to 3 is sufficient and corresponding limiting width-to-thickness ratios for Class 1 sections were developed.

Several studies were addressed also for cold-formed structural hollow sections. Korol & Hudoba (1972) recommended a rotation capacity equal to 4 for plastic design. To satisfy this requirement some design rules for limiting width-to-thickness ratios were then developed. This rotation capacity was further adopted by Hasan & Hancock (1989), Zhao & Hancock (1991) and Wilkinson & Hancock (1998). In Europe Stranghoner et al. (1994) performed parametric studies into the rotation requirements on square, rectangular and circular hollow sections on a three-span continuous beam subjected to a point load in the central span.

The investigated factors included beam geometry, loading, cross-section, material and serviceability requirements. Results demonstrated a rotation capacity of 3 is sufficient.

3. FLEXURAL OVERSTRENGTH

Generality

The flexural overstrength (s) is the measure of the maximum bending capacity of steel beams. According to Kemp (1985), Kato (1989) and Mazzolani & Piluso (1992). It could be intended as the ratio between the critical stress (f_{cr}) occurring at the local buckling and the yielding stress (f_y), namely given by the following equation:

$$s = \frac{f_{cr}}{f_y} \quad (3)$$

Conversely, s may be defined in terms of bending moments by the following equation:

$$s = \frac{M_u}{M_p} \quad (4)$$

where M_u is the peak bending moment experienced by the beam and M_p is the beam plastic bending moment. This approach is described in Figure 1.

Predictive methods of the flexural overstrength

In general, s can be directly obtained from experimental tests, measuring and calculating the maximum bending moment M_u and the plastic moment M_p .

However, several methods to evaluate the beam rotation capacity are proposed by different authors, which can be grouped in the following methods:

- *Theoretical method*: the evaluation of the flexural overstrength is based on the theoretical evaluation of the critical strain occurring in the compressed flange when it buckled in plastic field. Kemp (1985) proposed a theoretical solution for an ideal I beam made of a perfectly plastic material, assuming that the critical strain could occur in the middle of the plastic zone. In addition the extension of plastic zone is considered to be equal to the semi-wave buckling length, as confirmed by the study of Lay & Galambos (1965).
- *Semi-empirical method*: this approach provide the overstrength on the basis of experimental results, taking into account also mechanical parameters in addition to the geometrical slenderness. Indeed, the critical stress is influenced also by the relative restraint among the web and the flange and also by the stress distribution across the section depth. Besides, the theoretical analyses does not take into account the effects due to the stress gradient related to the variation of bending moment along the beam length. These effects have been early underlined by tests performed by Kuhlmann (1989), which showed that for I and H beams the buckling length of the flange is approximately 1.20 times larger the flange width (b_f). The influence of the stress gradient on the critical stress depends on the ratio b_f/L (being L the distance from the zero point to the maximum of the bending moment diagram).

Mazzolani & Piluso (1992) introduced this parameter. They provided a new formulation of s by processing the experimental results given by Kemp (1985), Kato (1988, 1989) and Kuhlmann (1989) through a multiple regression.

- *Empirical method*: Kato (1988, 1989, 1990) proposed empirical equations to predict the flexural overstrength based on the results of 68 tests carried out on “stub-columns” specimens having different steel grades and local (flange and web) slenderness. The normalized overstrength s was obtained by a multiple regression as function of the flange and web slenderness for each grade of steel

The analyzed procedures have to be integrated with the control of the conditions that determines the flexural-torsional instability.

Flexural overstrength in current codes

In modern steel design codes the value of flexural overstrength is provided only for seismic design, owing to the need to apply the hierarchy criterion.

According to AISC 341-05 the beam flexural overstrength is equal to $1.1R_y$, being 1.1 the factor to take into account the strain hardening and other possible overstrength, while R_y is ratio of the expected yield stress to the specified minimum yield stress (R_y varies in the range 1.1 to 1.5, depending on steel grade). The factor 1.1 has been obtained from the wide experimental research

devoted to provide qualified moment-resisting connections during the SAC project (FEMA 350). Tests showed that this value is adequate to the overstrength that beams belonging to frames designed according to the code could experience.

The new Italian code NTC'08 and the EC8 proposed a similar equation. Indeed, the flexural overstrength is 1.1 γ_{ov} , thus assuming the same factor 1.1 for the strain hardening, while the factor γ_{ov} takes into account the variability of yield stress of steel. EC8 does not provide a criterion for an appropriate evaluation of γ_{ov} , but suggests the use of $\gamma_{ov}=1.25$. This assumption leads to a local overstrength factor equal to $\gamma_{ov} \odot 1.1=1.375$, which has an important role not only in the connection design but also in the application of capacity design at global level. In fact, in the case of moment resisting frame structures, the columns shall be verified under seismic actions considering the following combination:

$$S_{Ed} = S_{Ed,G} + 1.1\gamma_{ov}\Omega S_{Ed,E} \quad (5)$$

where:

$S_{Ed,G}$ represents the resistances (the compression force, the bending moment and shear force) in the column due to the non-seismic actions;

$S_{Ed,E}$ represents the resistances (the compression force, the bending moment and shear force) in the column due to the design seismic action;

γ_{ov} is the overstrength factor defined in (2);

Ω is the minimum value of

$$\Omega_i = \frac{M_{pl,Rd,i}}{M_{Ed,i}} \quad (4)$$

of all beams in which dissipative zones are located; $M_{Ed,i}$ is the design value of the bending moment in beam i in the seismic design situation and $M_{pl,Rd,i}$ is the corresponding plastic moment.

It is worth noting that all current codes assumed a constant value of the hardening factor, that is not related with the class of the transversal cross section. Only the late Italian code OPCM 3274, nowadays no longer in use, overcome this limit. Indeed, in this code the flexural overstrength was provided using the s factor suggested by Mazzolani & Piluso (1992). In detail, for I section subjected to axial and/or flexural loads, considering usual steel types, the overstrength factor s can be calculated by means of the following analytical formulation:

$$s = \frac{1}{0.695 + 1.632 \cdot \lambda_f^2 + 0.062 \cdot \lambda_w^2 - 0.602 \cdot \frac{b_f}{L^*}} \leq \min \left\{ \frac{f_u}{f_y}; 1.25 \right\} \quad (5)$$

being:

$$\lambda_f = \frac{b_f}{2 \cdot t_f} \sqrt{\frac{f_y}{E}} \quad \text{the flange slenderness}$$

$$\lambda_w = \frac{d_{w,e}}{t_w} \sqrt{\frac{f_y}{E}} \quad \text{the web slenderness}$$

b_f the flange width;

L^* the distance between the plastic hinge and the point of zero moment;

$$d_{w,e} = \frac{1}{2} \left(1 + \frac{A}{A_w} \rho \right) d_w \quad \text{the parameter which takes into account the influence}$$

of the axial load because it represents the compressed part of the beam web.

In OPCM 3274 the application of capacity design to local level is given by the following equation:

$$M_{jRd} \geq s \gamma_{ov} M_{bRd} \quad (6)$$

where the γ_{ov} factor is not unique, but it is defined for every steel type as indicated in Table 1.

Table 1. γ_{ov} values for different steel type (OPCM 3274).

Steel	γ_{ov}
S235	1.2
S275	1.15
S355	1.1

Consequently, contrary to the EC8, for which the necessary overstrength at the local level is constant (37.5%) and independent from the steel type and from of the transversal cross-section, the OPCM 3274 local overstrength depends on γ_{ov} and s factors. Particularly, in the most unfavourable situation, the necessary overstrength according to the OPCM 3274 reaches the value of about 50% ($\gamma_{ov}=1.2$; $s=s_{\max}=1.25$).

As far as the capacity design at global level (beam-column) is concerned, the OPCM 3274 requires its control only if the structural system is designed in high ductility. In this case the columns have to be verified considering the most unfavourable combination of the axial load and bending moments:

$$S_{c,Sd} = S_{c,Sd,G} + \alpha S_{c,Sd,E} \quad (7)$$

where:

$S_{c,Sd,G}$ represents the resistance (the compression force, the bending moment and shear force) in the column due to the non-seismic actions;

$S_{c,Sd,E}$ represents the resistance (the compression force, the bending moment and shear force) in the column due to the design seismic action;

α is the minimum value of α_i of all beams connected to the examined column:

$$\alpha_i = \min \left\{ \frac{\gamma_{ov} S_i M_{b,pl,Rd,i} - M_{b,Sd,G,i}}{M_{b,Sd,E,i}}; q \right\} \quad (8)$$

where $M_{b,pl,Rd,i}$ is the plastic moment value for i beam, $M_{b,Sd,G,i}$ is the bending moment value due only to vertical actions, $M_{b,Sd,E,i}$ is the design bending moment value due to seismic actions.

A comparison between the EC8 and the OPCM 3274, regarding the application of the capacity design at global level, shows that, first of all, both codes require the amplification of the internal actions produced by the seismic input on the column, through a coefficient.

In the EC8, since the local overstrength is constant, the coefficient is $1.1\gamma_{ov}\Omega$; while in the OPCM 3274 it is also dependent on the variability of the local overstrength. In addition, in the case of the EC8, the coefficient Ω is calculated neglecting vertical loads contribution, which are, instead, taken into account in the α expression. Nevertheless, with reference to ordinary structures, this discordance does not involve a significant difference respect to OPCM 3274. Besides, small variations of these multipliers do not behave substantial differences in the choice of the adopted profiles, because of the great discontinuity of the available commercial sections.

4. PLASTIC BENDING FAILURE MECHANISM OF BEAMS

As experimentally observed, the shape of failure mechanisms depends on the type of loading, the boundary conditions and the geometry of beams.

In general, as observed experimentally, the plastic rotation can be limited by flexural-torsional instability, local buckling or brittle fracture of members.

The yield mechanism shapes of an I beam can be classified according to the following criteria.

- a) According to the type of loading;
- b) According to the positions of the intersecting lines of the web and the flanges, the so-called “yield-line” or “throat-lines” (Rasmussen & Hancock, 1998); they can be grouped into two categories, that are :
 - i) the evolving formation is called a “planar yield mechanism” if the two “yield-lines” are in the same plane after the development of the yield mechanism. This kind of mechanisms are characterized by overall deformations belonging in the main bending plane of beams;

ii) the evolving formation is called a spatial yield mechanism if the two “yield-lines” are not in the same plane after the development of the yield mechanism. Differently from the previous mechanism, in this case the overall displacements occur transversally the main bending plane

The experimental evidence showed that the beam flexural collapse is characterized by the “crumplings” (buckling) of plates in compression. These “crumplings” are formed by a yield mechanism, with the plastic moments acting in the plastic hinges (peaks of waves) not constant but ever increasing due to strain-hardening. The yield mechanism performed by “crumplings” can be extended to the component plates of the beam. It is worth noting that the extension of half-wave length of buckled flange is an important parameter, because it is directly related to the rotation capacity of the beam.

Early studies (Haaijer, 1957; Lay, 1965) showed that the half-wavelength of the flange plastically buckled is in the range $(0.8-1.2)b$, being b the half-width of the flange, as shown in Figure 2a. In Figure 2b it is shown a plot giving the normalized plastic buckling length, whose mathematical equation has been derived by Lay (1965) and reported as follows:

$$\beta = \frac{l_m}{2b} = \frac{\pi}{4} \cdot \frac{t_f}{t_w} \cdot \left(\frac{A_w}{A_f} \right)^{1/4} \cdot \left(\frac{7}{3} \cdot \frac{1+\nu}{h_f} + \frac{1}{4} \right)^{1/4} \quad (9)$$

being the symbols explained in Figure 2a.

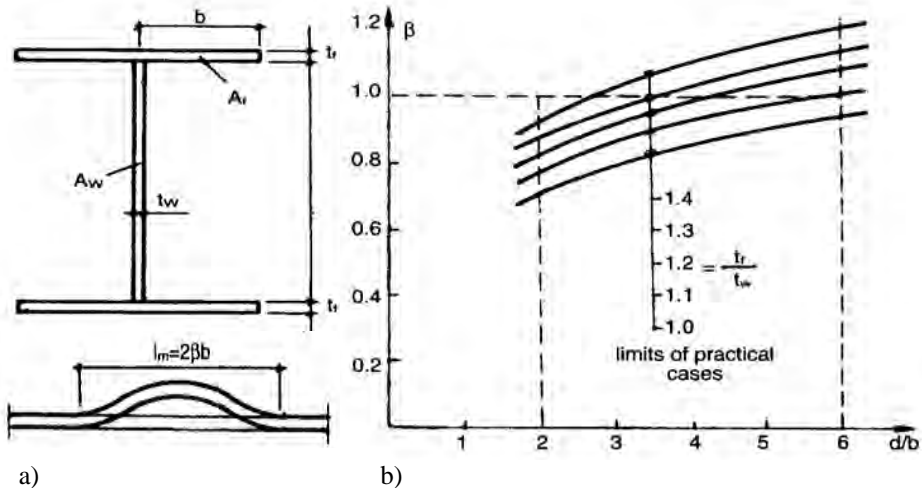


Figure 2. The half-wavelength of the flange plastically buckled (from Gioncu & Petcu, 1997).

Varying bending moment along the beam axis

The most of tests reported in the literature (Gioncu, 1995; Kuhlman, 1986; Ivanyi, 1979; Spangermaher, 1992; Climenaga & Johson, 1972; Susuki et al., 1994) have been performed on beam under monotonic moment gradient. The tests showed that the plastic deformation is localized in the zone where the plastic hinge occurred, while the remain parts of the beam behave elastically. In the plastic zone the most of deformation is concentrated and the plastic rotations can be amplified by the buckling (or crumpling) of the plates (flanges and/or web). In particular, the buckling of flanges and web can form a local plastic mechanism made of yield lines and plastic zones. The flange plastic mechanism triggered by local buckling imposes the overall shape of the failure mechanism.

Planar yield mechanisms. This kind of mechanisms are shown in Figure 3a. In particular, the in-plane plastic buckling of flanges is the principal nonlinear phenomenon, which can be symmetric or asymmetric respect to the cross-section.

Spatial yield mechanism. The out-of-plane displacements are generated by lateral-torsional buckling triggered by the flange crumpling and they could be symmetric or asymmetric as respect to the middle of the beam, as illustrated in Figure 3b.

Tests showed that in most cases the final failure mechanism is a combination of in-plane and out-of plane buckling. Indeed, the latter is caused by the loss of lateral stiffness as a consequence of the former yielding.

Constant bending moment along the beam axis

As in the previous case, for beam under constant bending, which can be experimentally obtained by four point bending tests, the collapse mechanisms can occur in-plane or out-of-plane of acting bending moment.

Planar yield mechanism. This mechanism is shown in Figure 4a, where a rotation θ develops as an effect of M , furthermore the compressed flanges buckle symmetrically to the major axis.

Spatial yield mechanism. In this case the yield mechanism is characterized by the buckling of compressed flanges leading to the lateral buckling of the beams, which could be symmetric or asymmetric respect to the middle span, as shown in Figure 4b,c.

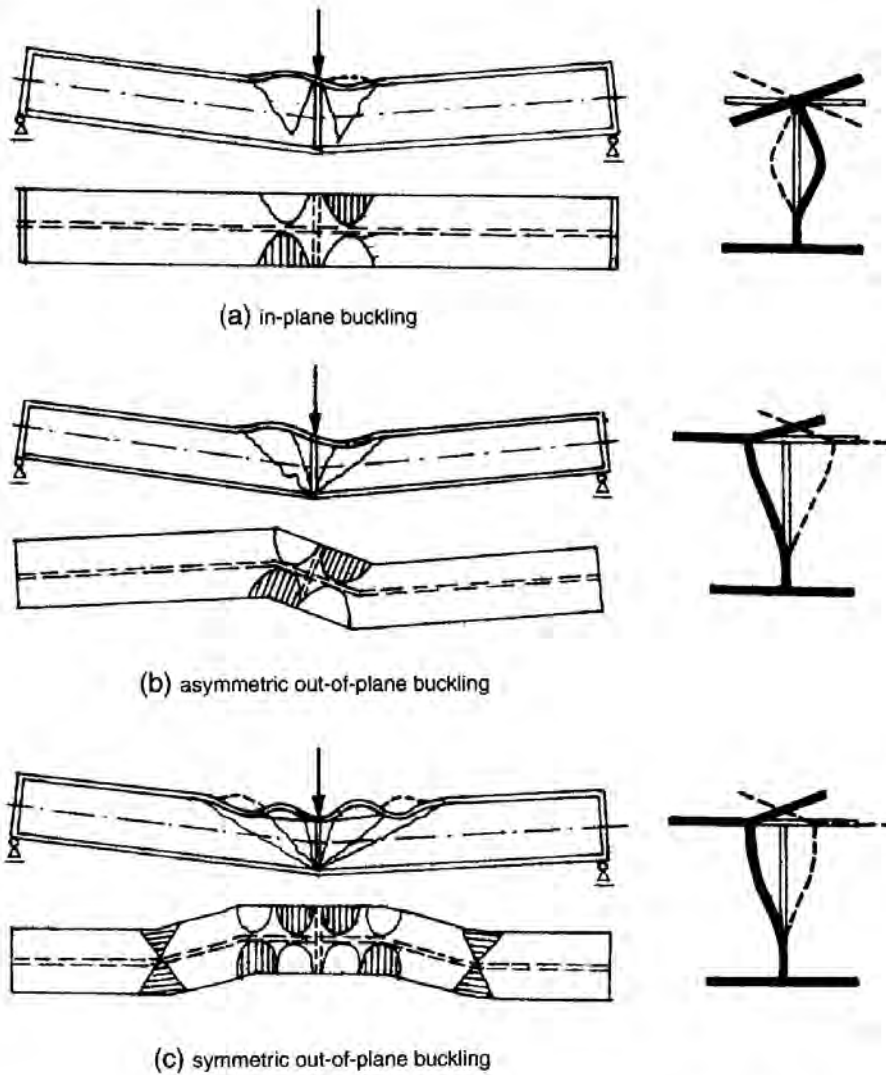
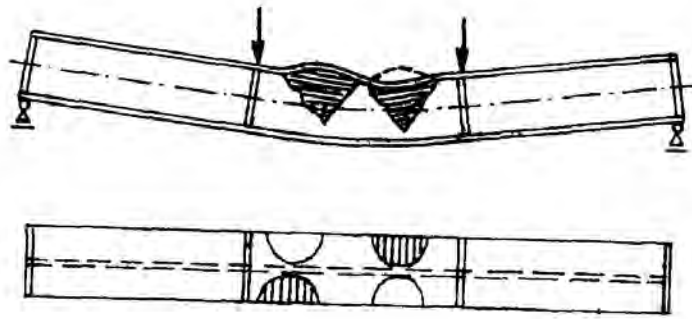
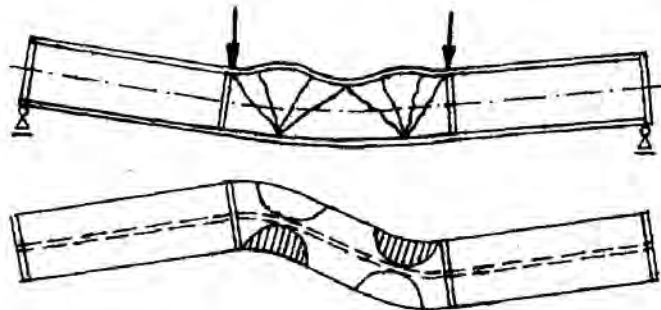


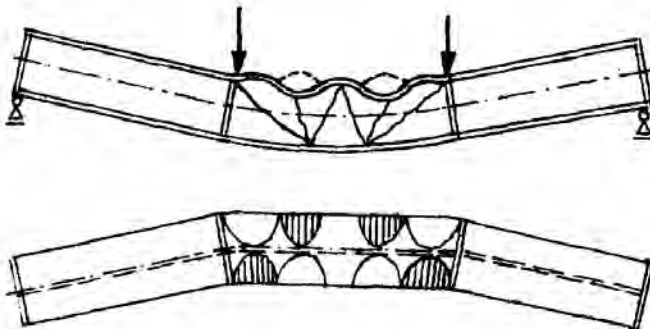
Figure 3. Planar a) and spatial b,c) yield mechanism of an I-beam with varying bending moment along the member axis (from Gioncu & Petcu, 1997).



(a) in-plane buckling



(b) asymmetric out-of-plane buckling



(c) symmetric out-of-plane buckling

Figure 4. In-plane a) and out-of-plane b) yield mechanisms of an I beam with constant bending moment along the member axis (from Gioncu & Petcu, 1997).

5. SEISMIC CLASSIFICATION CRITERIA OF STEEL MEMBERS

Generality

The seismic classification of steel members allow to know the provided cross-section ductility on the basis of geometric data, thus giving an idea of the potential ductility of the structure.

In the past, in addition to the cross-section classification, different criteria have been formulated to assess the ductility of structural systems. In particular, two approach can be recognized, that are based on:

- member ductility, when the properties of members are considered;
- structural ductility, which consider the overall behaviour of the structure.

The former has been proposed by Galambos & Lay (1965) and illustrated in Figure 5. According to this criterion, three ductility level are identified:

- ductility class HD (high ductility) corresponds to a member for which the design, dimensioning and detailing provisions are such that they ensure the development of large plastic rotations;
- ductility class MD (medium ductility) corresponds to a member designed, dimensioned and detailed to assure moderate plastic rotations;
- ductility class LD (low ductility) corresponds to a member designed and dimensioned according to general code rules which assures low plastic rotations only.

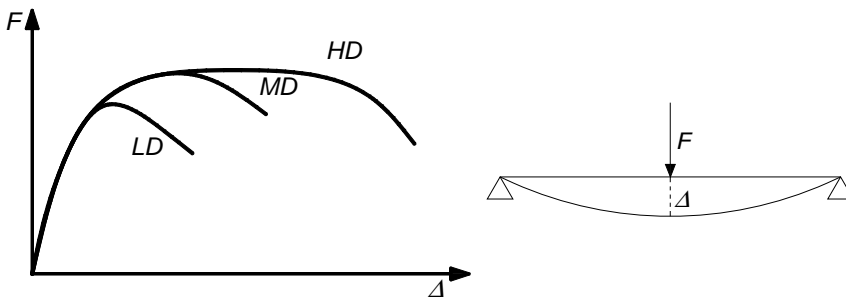


Figure 5. Member ductility classification criterion (Galambos & Lay, 1965).

The classification at the level of a frame has been proposed by Ivanyi (1992) and illustrated in Figure 6. According to this criterion, four ductility level are identified:

- ductility class 1: full support corresponds to a frame for which the design, dimensioning and detailing provisions are such that they ensure the development of the plastic carrying capacity with large plastic rotations;
- ductility class 2: adequate support that ensures the development of the plastic carrying capacity without plastic rotations;

- ductility class 3: sufficient support, which ensures the development of the elastic carrying capacity;
- ductility class 4: poor lateral support under the elastic carrying capacity.

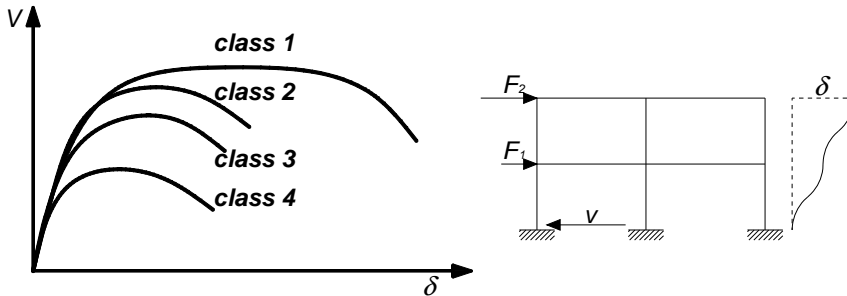


Figure 6. Frame ductility classification criterion (Ivanyi, 1992).

Eurocode 8 classification criterion

The Eurocode 8 adopts the classification criterion proposed by the Eurocode 3, illustrated in Figure 7, which subdivides the cross-sections into four classes:

- class 1 (plastic sections): sections belonging to class 1 are characterized by the capability to develop a plastic hinge with high rotation capacity;
- class 2 (compact sections): these sections are able to provide their maximum plastic flexural strength, but they have a limited rotation capacity, due to some local effects;
- class 3 (semi-compact sections): sections fall into this class when the bending moment capacity for the first yielding can be achieved without reaching the plastic moment;
- class 4 (slender sections): sections belonging to this class are not able to develop their total flexural resistance due to the premature occurrence of local buckling in the compressed parts.

Evidently, only the first two classes have sufficient ductility to assure the plastic redistribution of moments. This classification is limited to the cross-section level only, so it has many deficiencies.

The definition of the cross-section class is based on the local slenderness of flanges and web. The web and the flange are considered independent, neglecting their mutual interaction. Depending on the structural ductility class and on the behavioural factor q , the requirements regarding the cross-sectional classes of the dissipative elements are reported in Table 2.

According to EC8, the cross-section class is the only parameter that influences the global ductility of the structure, but it does not influence the application of the capacity design neither at local nor at global level.

Table 2. EC8 cross-section requirements for dissipative elements depending on ductility class and behavioural factor.

Ductility class	Behaviour factor	Cross section class (dissipative zone)
DCM	$1.5 < q < 2$	Class 1, 2 and 3
	$2 < q < 4$	Class 1 and 2
DCH	$q > 4$	Class 1

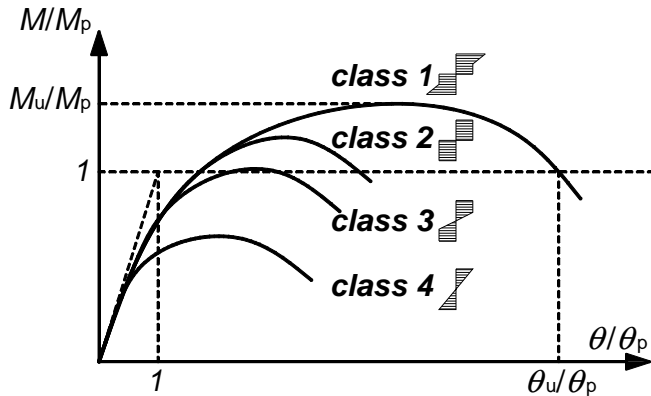


Figure 7. EC3 classification of cross sections.

OPCM 3274 classification criterion

This code implemented the concept of member behavioural classes (Mazzolani & Piluso, 1993). It provided a classification criterion which subdivides members into three categories:

- *Ductile*: the local buckling of the compressed parts of the section develops in plastic range without significant reduction of the load carrying capacity, after the member exhibits large plastic hardening deformations;
- *Plastic*: the local buckling of the compressed parts of the section develops in plastic range, allowing significant plastic rotations;
- *Slender*: the local buckling of the compressed parts of the section occurs in the elastic range.

The classification criterion adopted by the late Italian code OPCM 3274 is based on the evaluation of the overstrength factor s , as defined by Eq. (3) or Eq. (4). A simplified representation is shown in Figure 8.

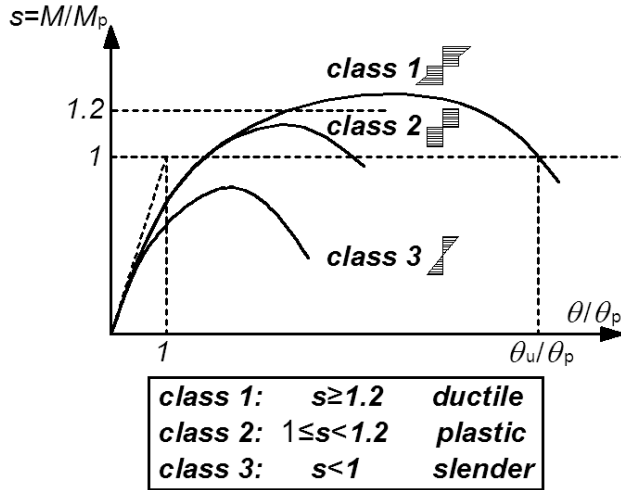


Figure 8. OPCM 3274 classification of members.

About the influence of the cross-section classification on the seismic design, it is important to underline, the explicit relationship between the value assumed by the s factor for the beams which contain plastic hinges and the behavioural factor. Indeed, the latter is expressed, for each steel structural type, such as moment resisting frames, concentric and eccentric braced frames, by the following relationship:

$$q = q_0 K_D K_R \quad (9)$$

in which:

q_0 is the reference value of the q -factor, as a function of both the structural typology and the ductility category of the structure;

K_D is a factor related to the local ductility resources of the dissipative zone by s factor;

K_R is the coefficient of structural regularity, which takes into account the elevation and the in-plane regularity characteristics of the building;

The limit values of the s parameter, which identify the ductility categories of members, are given in Table 3, where the corresponding K_D values assumed for the determination of the design q factor are indicated too.

Table 3. Classification of members in terms of ductility.

Member categories	s	K_D
Ductile	$s \geq 1.2$	1
Plastic	$1 \leq s < 1.2$	0.75
Slender	$s < 1$	0.5

Italian code NTC '08

In the new Italian code NTC '08 the classification criterion for steel members is analogous to EC8 approach. Indeed, four classes are considered according to EC3 prescriptions, but providing limit values of rotation capacity (R) as explained in the following:

- *class 1* : the section is able to develop a plastic hinge having the rotation capacity required for the structural analysis with the plastic method without strength reductions. These sections are characterized by rotational capacity of $R \geq 3$
- *class 2* : the section is able to develop its plastic moment, but with limited rotation capacity. These sections are characterized by rotational capacity of $1.5 \leq R < 3$
- *class 3* : the stresses in the external compressed fibres of the section can reach the yielding stress, but local instability prevents the development of the plastic moment ($M_y < M_u < M_{pl}$)
- *class 4* : to define the bending, shear or normal strength it is necessary to take into account the effects of the local instability in elastic range in the compressed parts of the section ($M_u < M_y$). In this case in the evaluation of the strength, the actual geometric section can be replaced of with an effective one.

From the conceptual point of view this classification criterion is consistent with the one adopted by the EC3, even there are some substantial differences:

- the performance level in terms of rotation capacity, that differentiates sections of first and second class, is made explicit
- no one specific prescription is provided respect to the evaluation models of R , leaving such choice exclusively to the designer.

For the design in seismic zone, or rather for what concerns to the consequences of such classification in terms of global ductility and capacity design, no difference can be recognized between NTC 2008 and EC8.

Classification criteria vs. experimental results

In this section, the examined classification criteria are compared in order to individuate the most reliable one. Such comparison is exclusively conducted with reference to the I sections, which are the most used in the seismic design.

First of all, a database of available experimental tests, regarding I sections, has been set up (Table 4). Subsequently the classification of the relevant cross-sections and members, and the evaluation of the experimental overstrength factors ($s_{\text{exp}} = M_{u,\text{exp}}/M_{pl}$) and rotation capacities have been done.

Table 4. Experimental tests on I section beams.

Tests number	Author	Profiles typology
24	Kuhlmann	I section welded
23	Spangemacher	I section hot rolled
4	Kemp	I section hot rolled
5	Boeraeve-Lognard	I section hot rolled
12	Lukey-Adams	I section hot rolled

From Figure 9 to 11 the experimental results are compared to those given by each classification criterion. In particular, the EC3 class has been assigned evaluating the ratios between web and flanges slenderness, while the experimental class calculating the rotation capacity values ($R > 3$ for class 1; $R < 3$ and $M_{ult} > M_{pl}$ for class 2). The OPCM 3274 class has been assigned evaluating the overstrength factor s , through the already defined Eq. (3), while the experimental class calculating the value of the ratio $s_{exp} = M_{u,exp} / M_{pl}$.

As it can be observed both the examined classification criteria do not represent the actual behaviour of the steel members in terms of rotation capacity and overstrength. In addition they often provide results in disagreement among them. Indeed, by applying the EC3 provisions, despite 63 sections showed an experimental rotation capacity greater than 3, only 23 of them belong to the theoretical class 1, with reliability (coincidence between experimental and theoretical results) of about 37%. In the case of the OPCM 3274, 38 members had $s_{exp} > 1.2$ so they were experimentally "ductile", 17 of them are also theoretically ductile, so the level of reliability is about 45%.

The second consideration is that most of the examined tests has an experimental overstrength greater than $1.1\gamma_{ov}$ (EC8 assumed value), with a maximum value $s = 1.48$ and an average value $s = 1.21$.

In conclusion, for ductile members the classification criterion based on the evaluation of the overstrength factor fits better the experimental results. In any case both criteria are not able to describe the actual behaviour of the steel members in post-critical field, because of the difficulties to model the local instability phenomena.

The Eurocode 3 classification criterion, does not allow to establish a correspondence between the theoretical class of the section and its rotation capacity. In fact, different values of R for similar values of slenderness λ_f and λ_w occur. This means that, in the codified approaches these two slenderness must be combined for defining the cross-section class. In Figures 12 and 13, the values of the rotational capacity are plotted as function of slenderness of web and flange respectively.

For members in bending, the flange is largely interested by phenomena of local buckling, while the web contributes however, with its stiffness, to stabilize it. The Eurocode 3 takes into account the interaction between web and flange by assigning the higher class to the section (less favourable) among the

web and flange ones. An interpretation of the results reached using this approach is emphasized in the Figure 14, where slenderness are combined according to EC3.

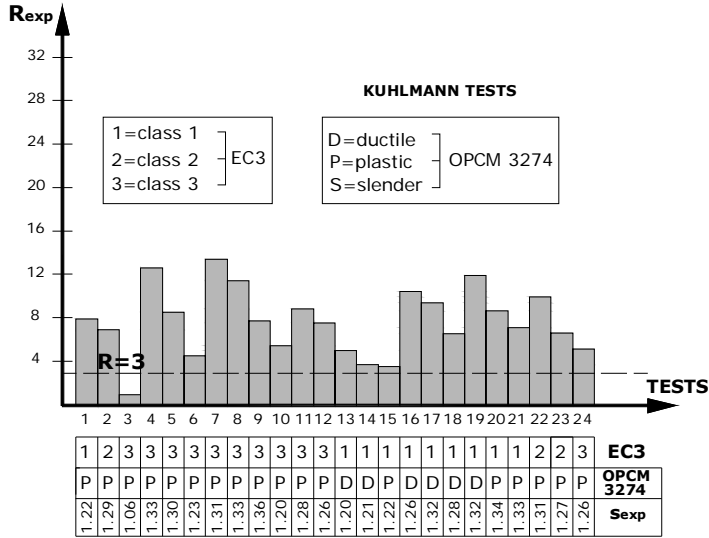


Figure 9. Rotation capacity according to EC3 and OPCM 3274 vs. experimental values (Kuhlmann tests).

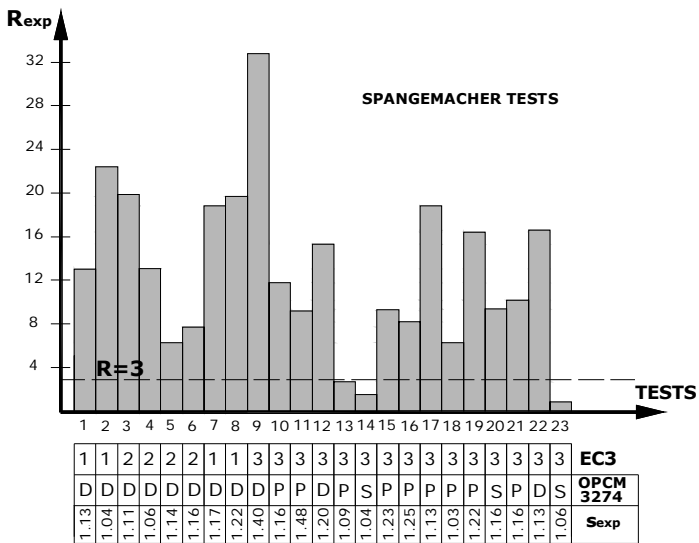


Figure 10. Rotation capacity according to EC3 and OPCM 3274 vs. experimental values (Spangemacher tests).

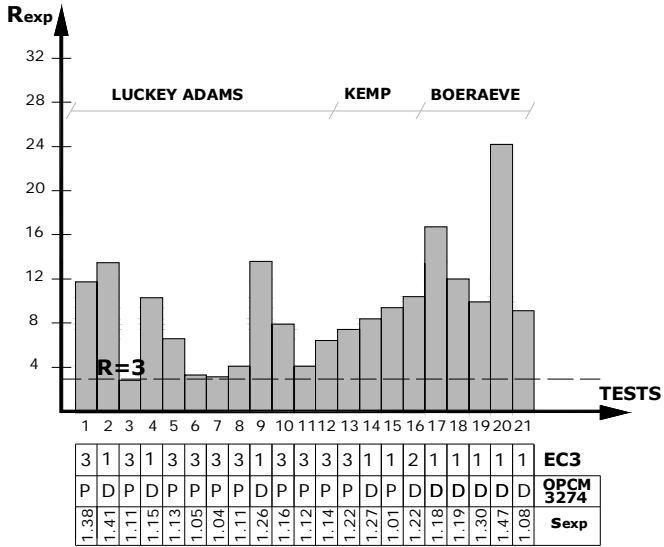


Figure 11. Rotation capacity according to EC3 and OPCM 3274 vs. experimental values (Luckey-Adams, Kemp and Boeraeve tests).

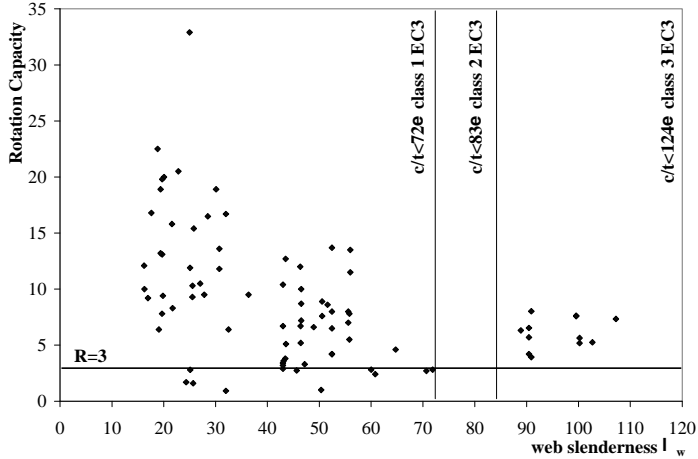


Figure 12. Rotation capacity vs. web slenderness.

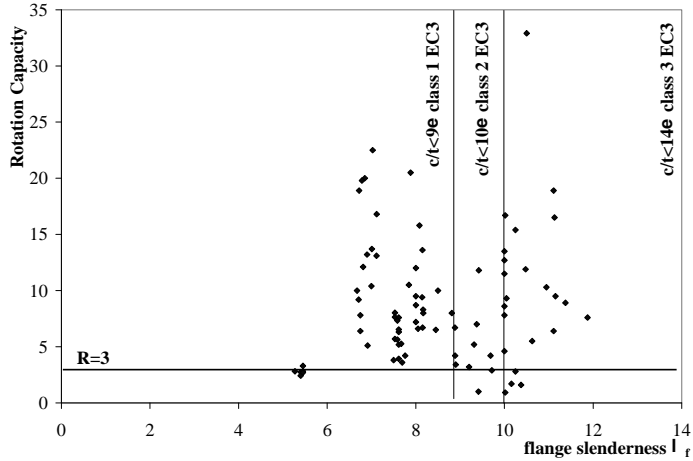


Figure 13. Rotation capacity vs. flange slenderness.

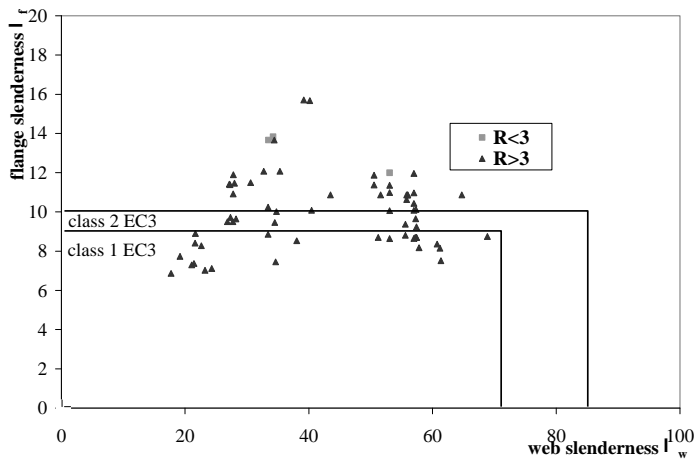


Figure 14. Rotation capacity vs. flange and web slenderness combinations.

6. EXPERIMENTAL ACTIVITY

Research framework

In order to refine the classification criterion of steel beams and to quantify and predict the flexural capacity of steel members an experimental activity was carried out. Tests have been performed in collaboration to the University of Salerno in the framework of Reluis project.

A comprehensive full-scale laboratory testing programme on a wide range of cross section typologies (I sections, Square and Rectangular Hollow sections) was conducted and the influence of geometrical and mechanical parame-

ters were analyzed. Aiming to obtain new information on the energy dissipation capacity of steel members, special attention has been paid to the parameters governing local buckling and, as a consequence, strength deterioration under cyclic actions.

Three different typologies of cross-section have been investigated: a) I sections; b) Rectangular hollow sections (RHS); c) Square hollow sections (SHS). The profiles to be tested have been selected to analyze geometrical parameters poorly investigated in the existing literature, as illustrated from Figure 15 to 19. The final selection is reported in Table 5.

The test programme comprised a total of 9 monotonic and 9 cyclic in-plane bending tests. In addition, standard coupon tests have been carried out to obtain the mechanical properties of the material by means of the corresponding stress-strain curve. Standard tensile coupon tests have been performed taking specimens both from flanges and webs.

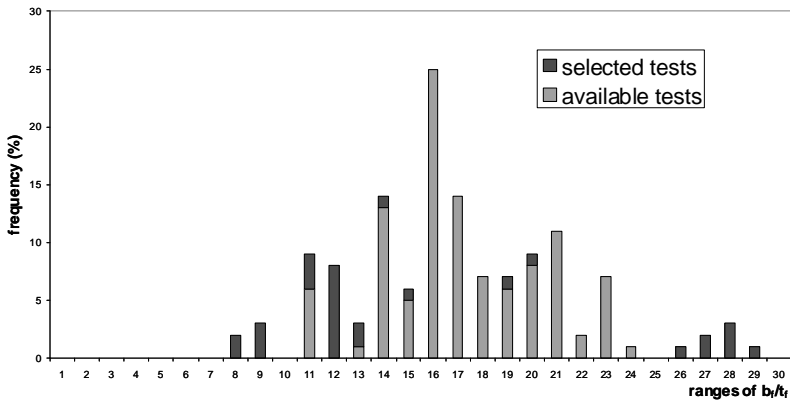


Figure 15. Variability range of the parameter b_f/t_f .

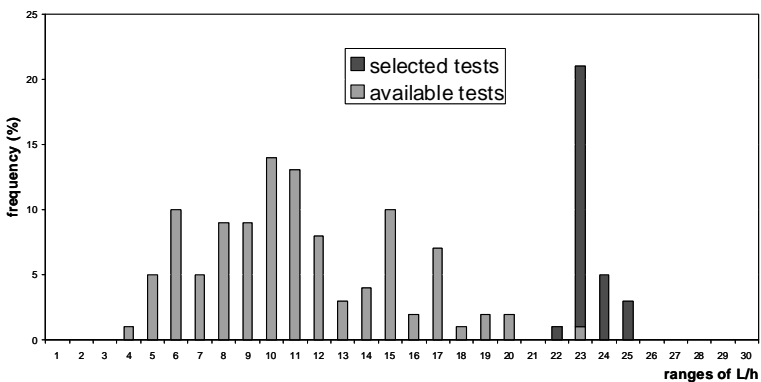


Figure 16. Variability range of the parameter L/h .

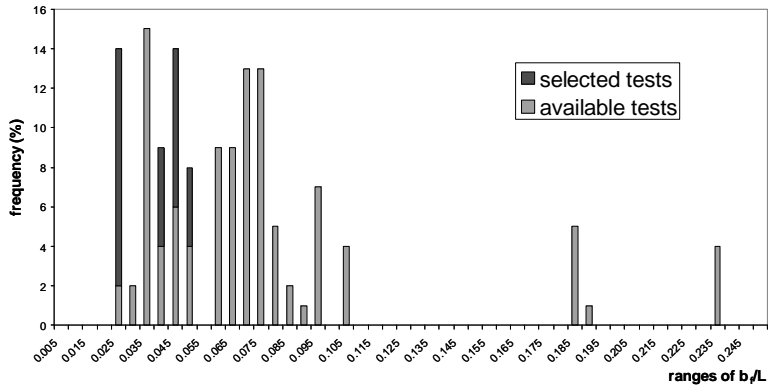


Figure 17. Variability range of the parameter b_f/L .

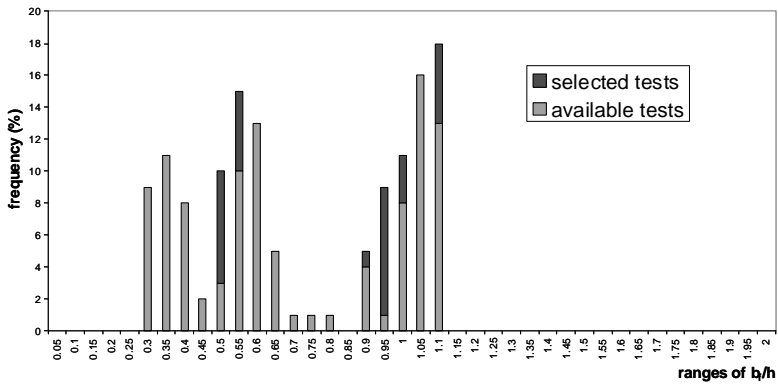


Figure 18. Variability range of the parameter b_f/h .

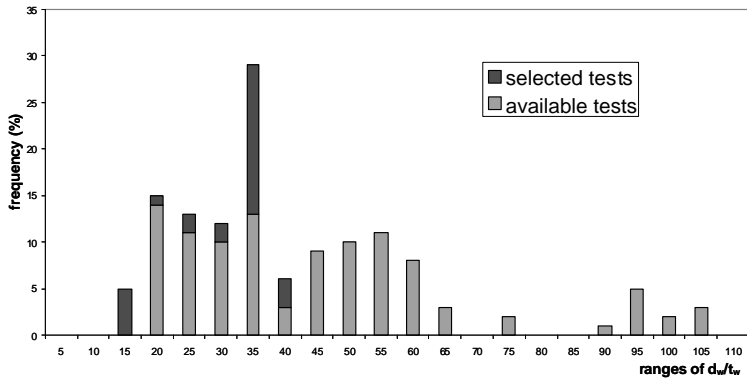


Figure 19. Variability range of the parameter d_w/t_w .

Table 5. List of experimental specimens.

Profile	L/h	c/t_f	d/t_w
HEA160	26.32	8.88	22.33
HEB240	16.67	7.05	20.60
IPE300	13.33	7.00	39.23
150x100x5	26.67	18.51	35.50
160x80x4	25.00	19.75	30.00
250x100x10	16.00	10.00	23.00
160x160x6.3	25.00	25.64	23.40
200x200x10	20.00	20.40	18.00
250x250x8	16.00	31.25	29.25

Test setup

The bending tests have been carried out on a cantilever beam, which reproduced the behaviour of beams in actual frames subjected to seismic actions.

The test setup is shown in Figure 20. Each experimental specimen is bolted to the top flange of an horizontal steel base girder connected to the RC slab (Fig. 21). In particular, each specimen has been arranged in such a way that one end could be tested monotonically and the other end cyclically. Indeed, setting the actuator in the middle of the specimen, during the test the outer part is undeformed. Once the monotonic test on one end is concluded the beam can be dismantled, then turned and fixed to the basement, ready for the cyclic test. The net length of the experimental cantilever is equal to 1875 mm.

The reaction wall is a braced steel frame connected by means of DYWIDAG steel bars to the reinforced concrete (RC) slab of the laboratory.

A hydraulic actuator (MTS 243) is used to apply a displacement history. The actuator is pin-mounted to the reaction wall and to the specimen by means of cylindrical clevis (Fig. 22). This swivel joint is attached at the head of the actuator to permit free motion of beam in its flexural plane.

Moreover, an horizontal steel frame is adopted to restrain the flexural-torsional buckling of specimens (Fig. 23).

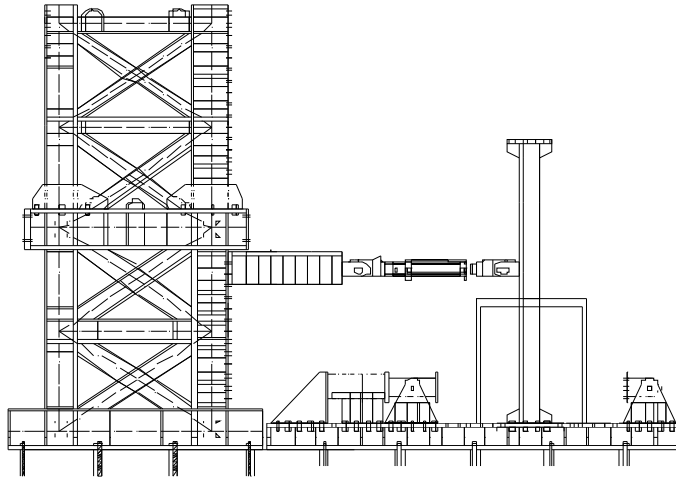


Figure 20. General layout of test setup: reacting wall and actuator system



a)

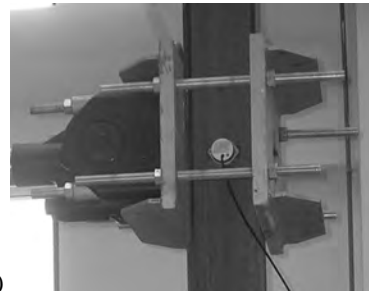


b)

Figure 21. Specimen-to-basement connection.



a)



b)

Figure 22. Connection of actuator to the specimen.

In order to measure the deformation parameters a set of LVDTs (Linear Variable Displacement Transducers) have been positioned as shown in Figure 24. In particular, one LVDT is used to monitor the displacement at the middle

of the half-wave length of buckled flange, which is equal to $1.2b_f$ according to Eq. (9). Other two LVDTs are positioned at the end of the half-wave length of buckled flange. Two LVDTs are used to measure the web deformations. In addition, other two transducers are positioned to measure the relative deformation between the end beam and the basement.

In order to measure reliably the beam rotation, a set of three inclinometers is used. In particular, one is positioned at the point where load is applied, the second at the middle of the experimental length of the beam (namely $\frac{1}{4}$ of the specimen length) and the third at the fixed end of the beam. Figures 23 and 24 clearly show this arrangement.

Finally, the standard coupon tests are carried out by means of an universal testing machine, Schenck Hydropulos S56, with maximum load capacity equal to 630 kN and piston stroke equal to ± 125 mm equipped with an extensometer for strain measures.



Figure 23. Experimental layout.

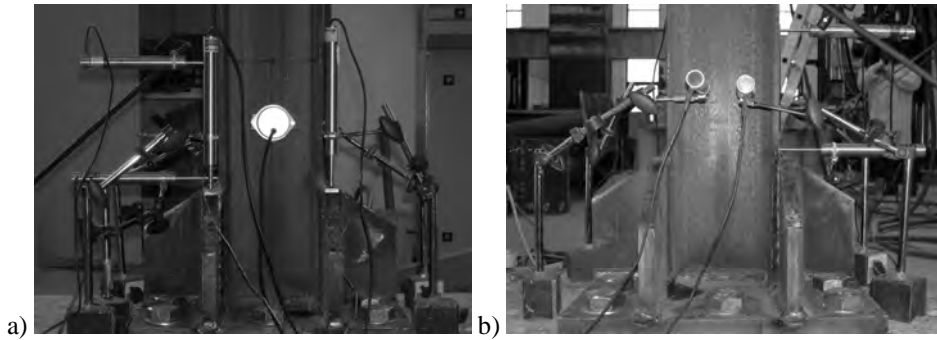


Figure 24. Positioning of LVDTs.

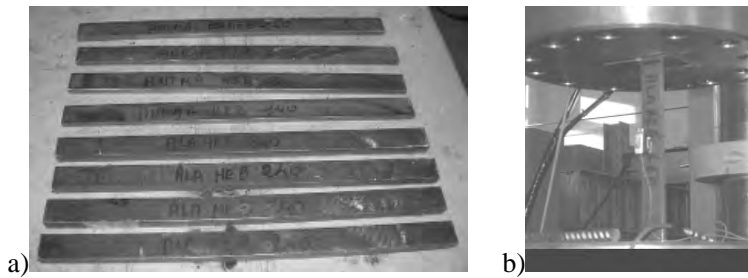


Figure 25. Coupon specimens sampled from beams (a); tensile test (b).

Loading protocol

In case of monotonic tests the applied load rate is equal to 0.25mm/s.

In cyclic tests the AISC2005 loading protocol is used. This procedure is characterized by the following steps:

- 6 cycles with $\theta = 0,00375$ rad
- 6 cycles with $\theta = 0,005$ rad
- 6 cycles with $\theta = 0,0075$ rad
- 4 cycles with $\theta = 0,01$ rad
- 2 cycles with $\theta = 0,015$ rad
- 2 cycles with $\theta = 0,02$ rad
- 2 cycles with $\theta = 0,03$ rad
- 2 cycles with $\theta = 0,04$ rad

being θ the chord rotation. If failure does not occur, the test continues increasing the displacement amplitude of 0.01rad for 2 successive cycles up to collapse.

Tensile coupon tests

Material tensile coupon tests were performed to determine the engineering stress–strain response of the material for each of the tested section sizes to be

used in the analysis of the bending test results. The resulting material properties are summarised in Table 6.

Table 6. Steel properties of tested beams.

Section	Sampling position	f_y	f_u
HEA 160	Web	338	475
	Upper Flange	328	456
	Lower Flange	346	463
HEB 240	Web	318	351
	Upper Flange	389	491
	Lower Flange	295	433
IPE 300	Web	273	448
	Upper Flange	353	447
	Lower Flange	345	460
RHS 150X100X5	Upper Flange	314	438
	Lower Flange	317	440
RHS 160X80X4	Flange	342	377
	Web	365	397
RHS 250X100X10	Flange	315	346
	Web	333	376
SHS 160X160X6.3	Flange	415	500
	Web	420	511
SHS 200X200X10	Flange	420	466
	Web	444	451
SHS 250X250X8	Flange	450	522
	Web	455	506
SHS 250X250X8	Flange	482	525
	Web	479	522

Bending tests

Tests showed the importance of the loading history on the beam flexural response. Indeed, all specimens under cyclic exhibited a lower rotation capacity than those under monotonic loading. Conversely, the flexural overstrength did not exhibit an analogous trend. In case of H and I profiles, the specimens under cyclic loading showed higher overstrength. This depended on the isotropic hardening and Bauschinger effect, which was not impaired by local buckling phenomena due to the cumulated plastic deformation. In case of hollow sections the local buckling was dominant and the hardening effects had not significant influence.

In general, the specimens experienced different flexural performance depending on the type of failure mechanism.

The H and I specimens showed a coupled mechanism made of a combination of in-plane and out-of plane buckling, as showed from Figure 26 to Figure 31. Indeed, the flange buckling occurred first and then the asymmetric-torsional buckling was triggered involving the web panel. It is very interesting to note that the height of the web plastic mechanism increased increasing flange width, and this increase is associated with a reduction of rotation capacity.

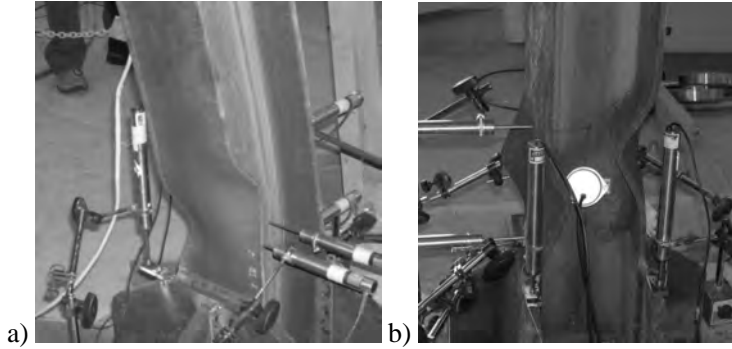


Figure 26. Failure mechanism of HEA 160 specimen under monotonic (a) and cyclic (b) loading.

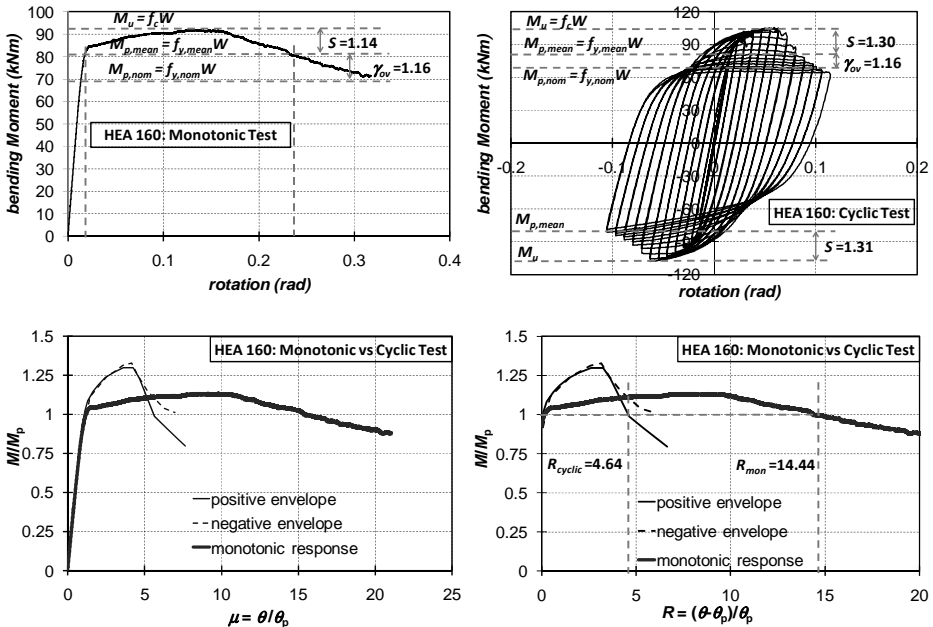


Figure 27. Flexural performance of HEA160 specimen.

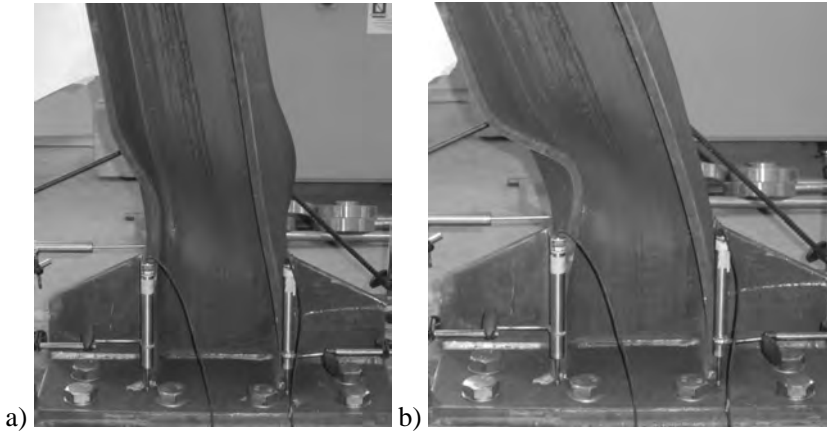


Figure 28. Failure mechanism of HEB 240 specimen under monotonic (a) and cyclic (b) loading.

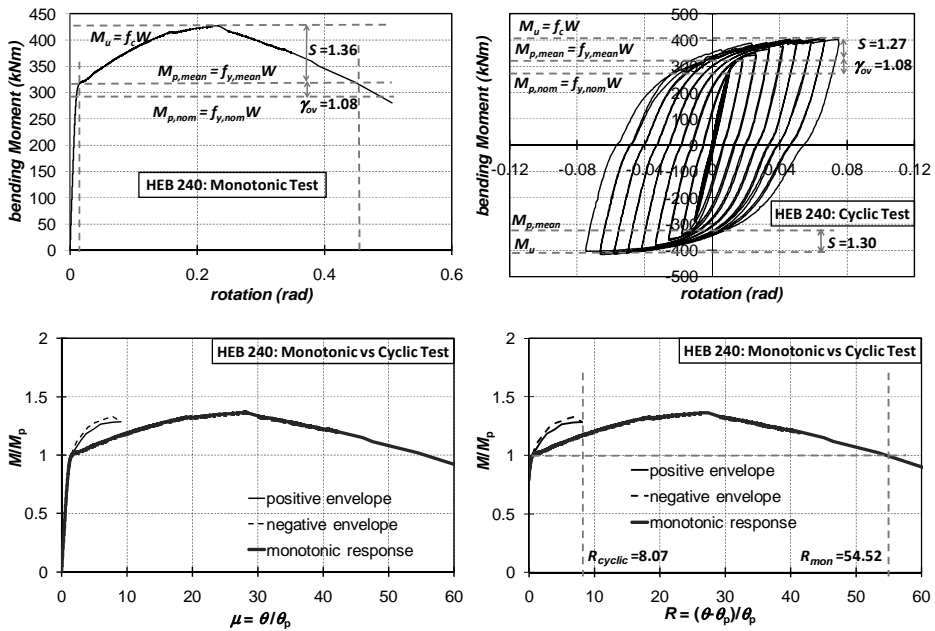


Figure 29. Flexural performance of HEB 240 specimen.

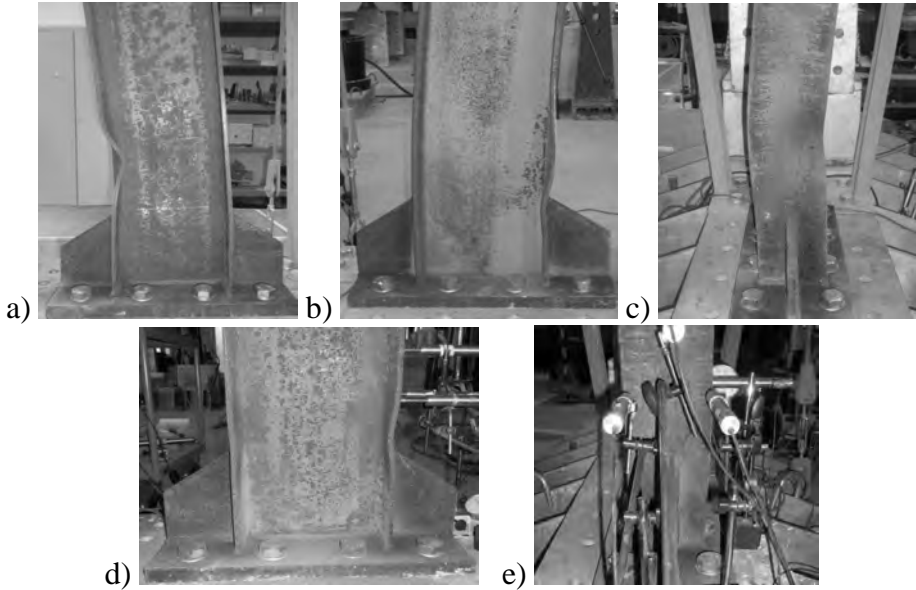


Figure 30. Failure mechanism of IPE 300 specimen under monotonic (a,b,c) and cyclic (d,e) loading.

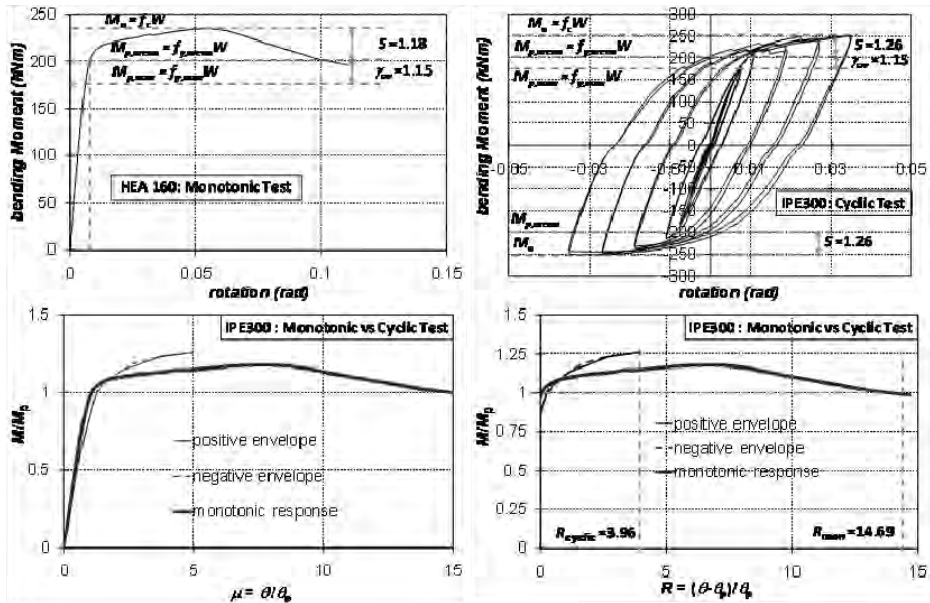


Figure 31. Flexural performance of IPE 300 specimen.

The flexural performance of Hollow cold-formed specimens is summarized from Figure 32 to Figure 43. Hollow profiles experienced web local buckling which produced a rapid shedding of load with increased deflection. Each web

buckled and compatibility of rotation at the corner caused deformation of the flange. In all cases, the buckle formed adjacent to one of the loading plates. This phenomenon was more significant for specimens having the higher local slenderness (e.g. SHS160x160x6.3, 250x250x8, SHS 160x80x4). In any case no specimen behaved as a slender section. The failure mechanisms were characterized by the so-called elephant foot shape that is the bulging of the compressed plates at the base of the specimen. This particular failure shape was due to the concentration of deformation in the compressed plates. In monotonic tests a transverse crack was observed in the tensile part at the base of the specimens. In cyclic tests it was recognized the initiation of cracks the reversal deformation in the tensile zone early bulged in compression. Cracks developed at the web-to-flange corners.



Figure 32. Failure mechanism of SHS160x160x6.3 specimen under cyclic loading.

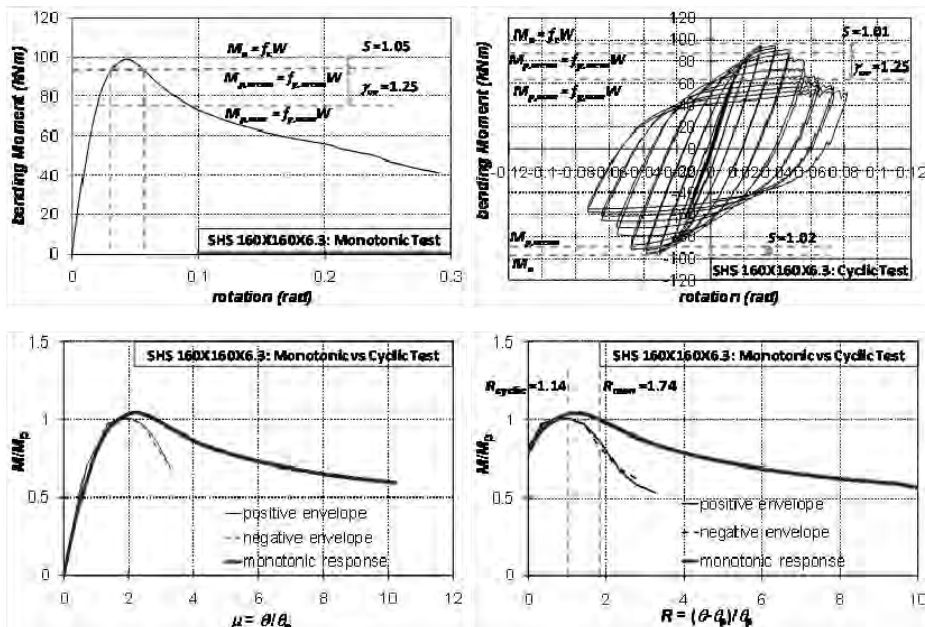


Figure 33. Flexural performance of SHS 160x160x6.3 specimen.

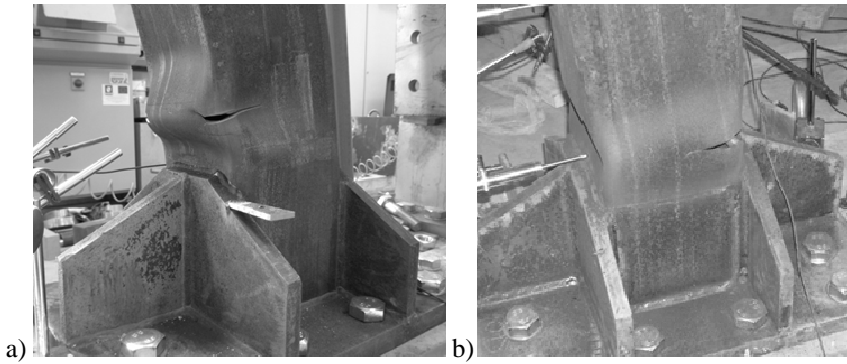


Figure 34. Failure mechanism of SHS 200x200x10 specimen under monotonic (a) and cyclic (b) loading.

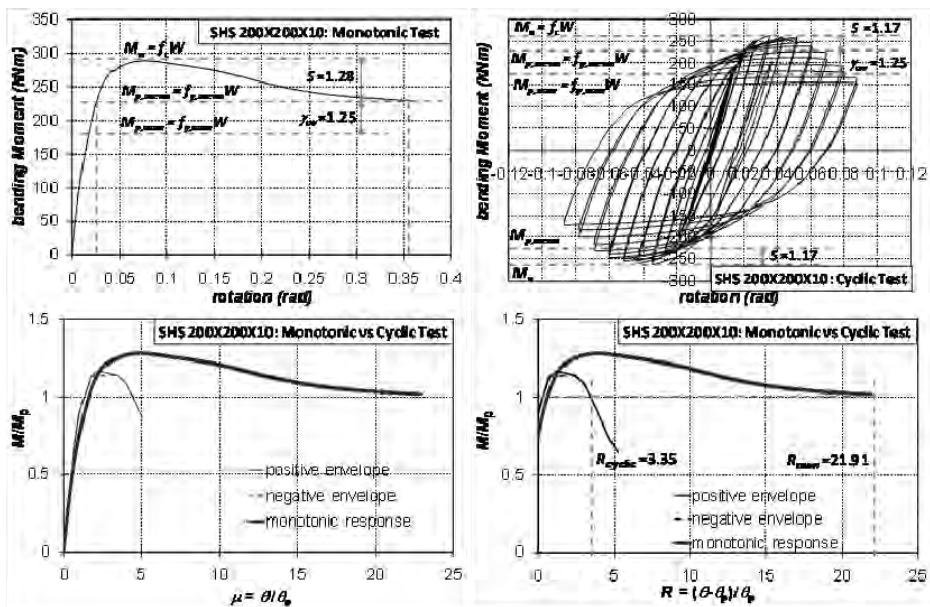


Figure 35. Flexural performance of SHS 200x200x10 specimen.

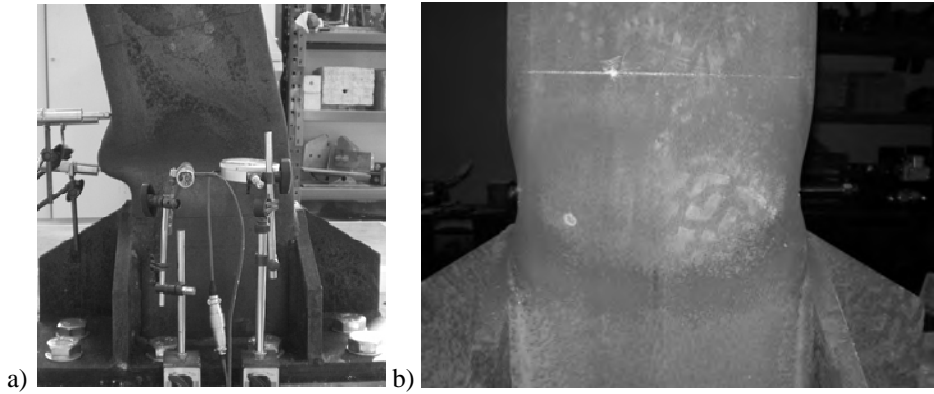


Figure 36. Failure mechanism of SHS 250x250x8 specimen under monotonic (a) and cyclic (b) loading.

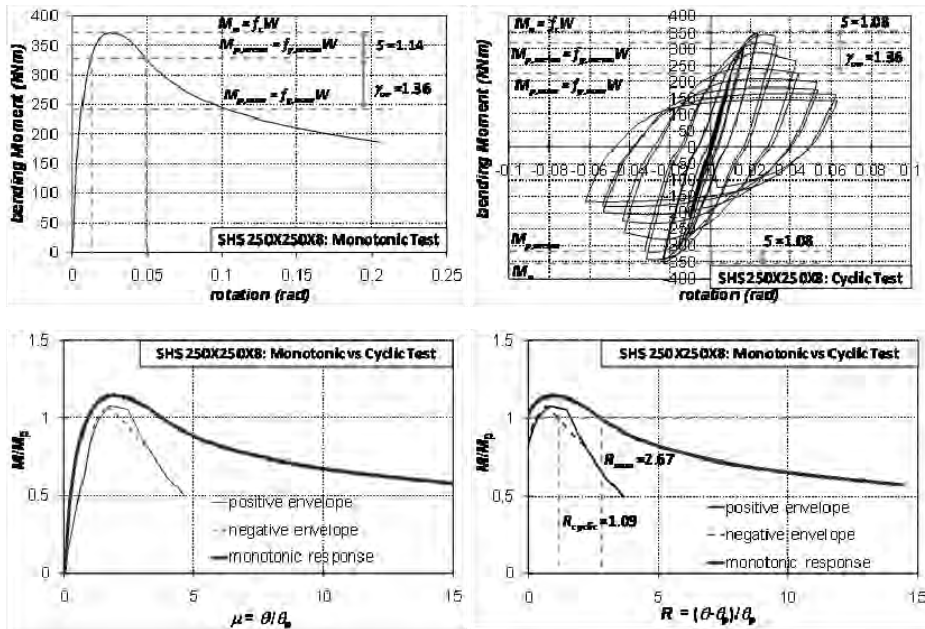


Figure 37. Flexural performance of SHS 250x250x8 specimen.

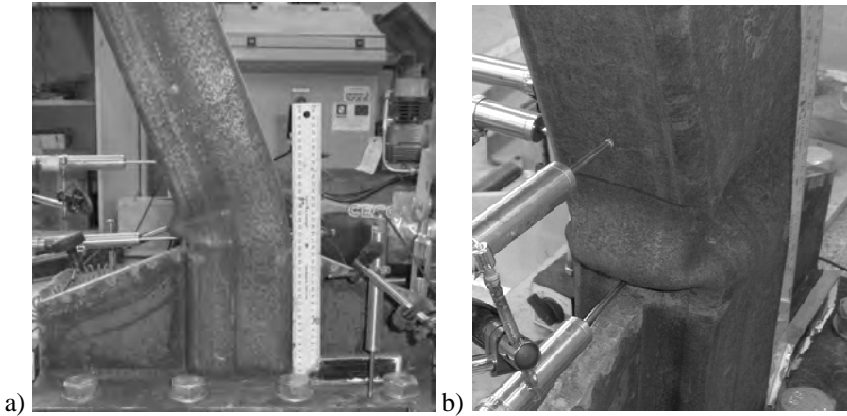


Figure 38. Failure mechanism of RHS 150x100x5 specimen under monotonic (a) and cyclic (b) loading.

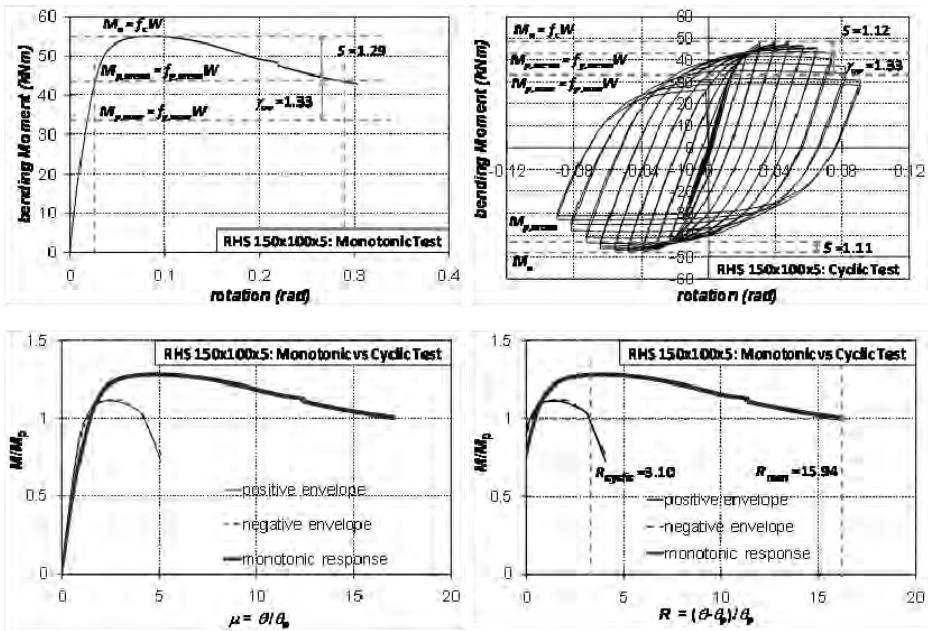


Figure 39. Flexural performance of SHS 150x100x5 specimen.

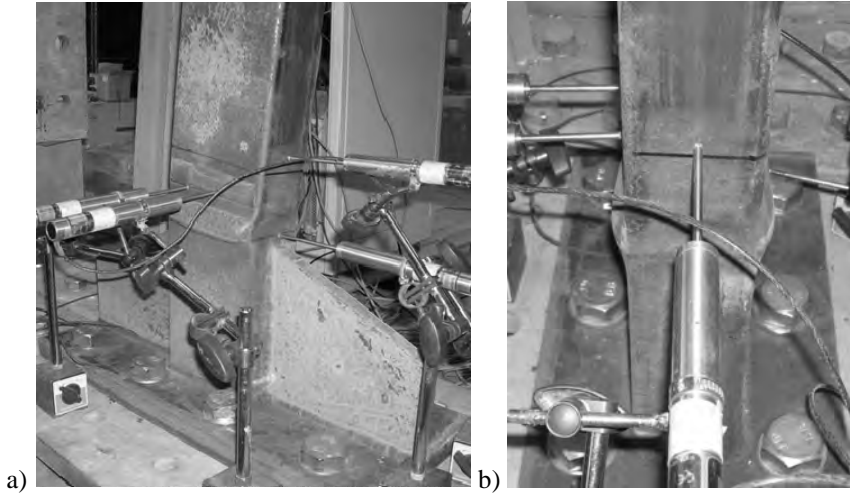


Figure 40. Failure mechanism of RHS 160x80x4 specimen under monotonic (a) and cyclic (b) loading.

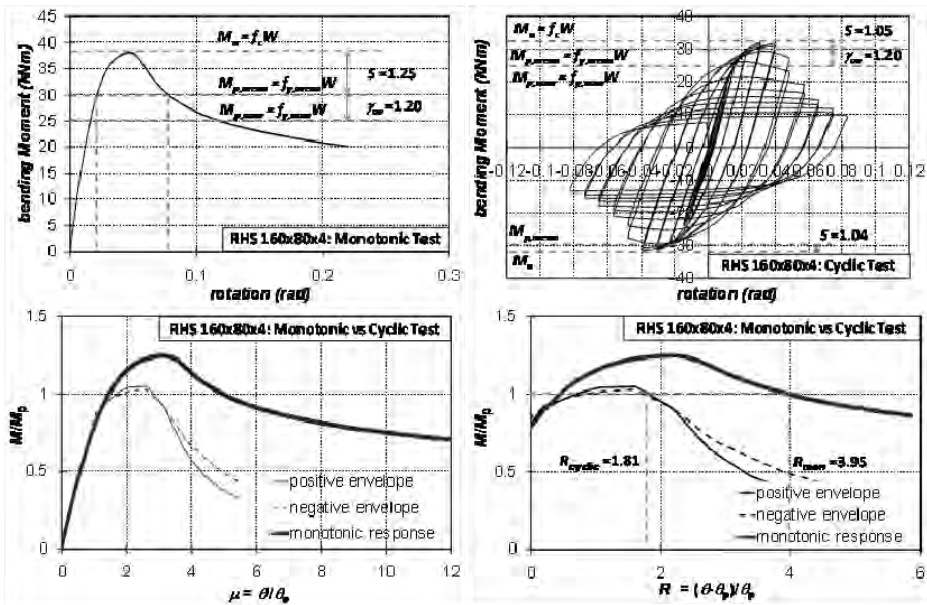


Figure 41. Flexural performance of SHS 160x80x4 specimen.

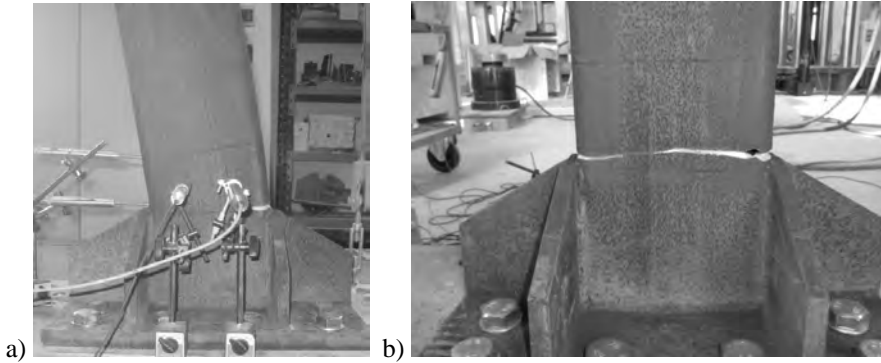


Figure 42. Failure mechanism of RHS 250x100x10 specimen under monotonic (a) and cyclic (b) loading.

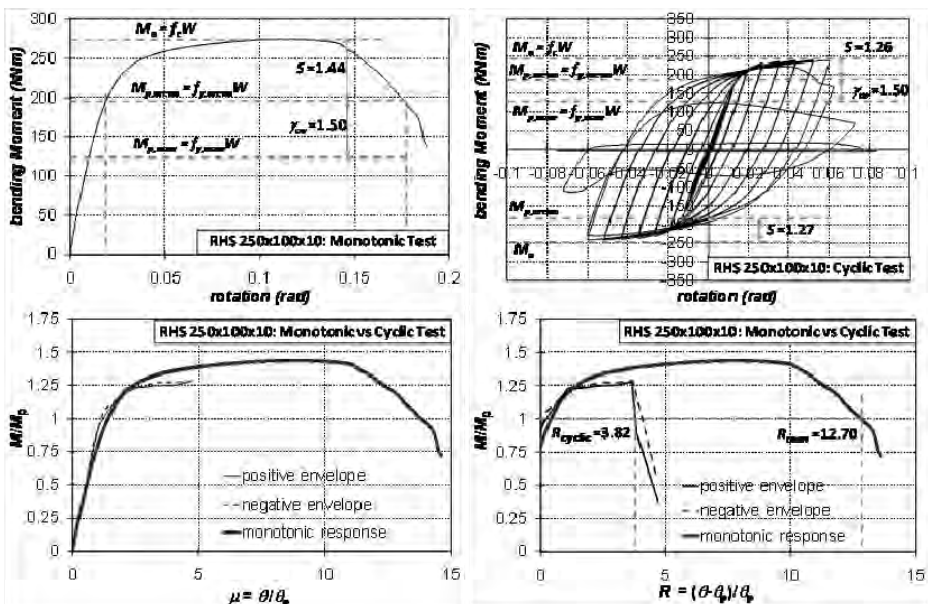


Figure 43. Flexural performance of SHS 250x100x10 specimen.

Analysis of test results

The experimental performance of tested beams has been compared to those predicted by the examined codes, namely according to EC3, NTC '08 and OPCM 3274. This comparison is reported in Table 7, where it can be noted that in case of hollow sections the codes provide different classification by different criteria.

In particular, for wide flange profiles all codes are conservative. In particular, the NTC'08 classification does not provide a reliable prediction of the rota-

tion capacity of beam, underestimating it for wide flange but being unconservative for hollow profiles. Although conservative in terms of rotation capacity, the OPCM 3274 criterion underestimates the overstrength, especially for hollow sections.

This results confirm the necessity of a classification criterion which takes into account the characteristics of the whole member and not of only cross-section and takes into account simultaneously rotation capacity and overstrength parameters.

Table 7. Flexural performance and classification of tested beams.

Profile	R_{mon}	R_{cyclic}	s_{mon}	s_{cyclic}	Beam classification criterion		
					EC3	NTC'08	OPCM3274
HEA160	14.44	4.64	1.14	1.31	2	2	2
HEB240	54.52	8.07	1.36	1.30	1	1	1
IPE300	14.69	3.96	1.18	1.26	1	1	1
150x100x5	15.94	3.10	1.29	1.12	2	2	2
160x80x4	3.95	1.81	1.25	1.05	2	2	2
250x100x10	12.70	3.82	1.44	1.27	2	2	1
160x160x6.3	1.74	1.14	1.05	1.02	2	2	3
200x200x10	21.91	3.35	1.28	1.17	2	2	2
250x250x8	2.67	1.09	1.14	1.08	2	2	3

7. NEW EXPRESSIONS OF R AND s PARAMETERS

Novel expressions of monotonic R and s factors are proposed on the basis of empirical models, which have been obtained by the multiple regression of existing experimental data summarized in Table 8.

Owing to the fact that both the rotation capacity R and overstrength parameter s are affected by the same mechanical and geometrical parameters a generalized formulation has been proposed, whose expressions are the following:

$$R = C_1^R + C_2^R \lambda_f^2 + C_3^R \lambda_w^2 + C_4^R \frac{b_f}{L^*} + C_5^R \frac{E}{E_h} + C_6^R \frac{\varepsilon_h}{\varepsilon_y} \quad (10)$$

$$1/s = C_1^s + C_2^s \lambda_f^2 + C_3^s \lambda_w^2 + C_4^s \frac{b_f}{L^*} + C_5^s \frac{E}{E_h} + C_6^s \frac{\varepsilon_h}{\varepsilon_y} \quad (11)$$

being E = the elastic modulus, E_h = the hardening modulus, ε_y = the yielding deformation and ε_h = the hardening deformation. The meaning of the symbols is better illustrated in Figure 44. In addition, the influence of the moment gradient is considered in the term b_f/L^* , where b_f is flange width and L^* is the beam shear length.

The C_i^R and C_i^s coefficients have been obtained by the multiple regression. In detail, Table 9 and Table 10 list the calibrated values of these coefficients for R and s factor, respectively.

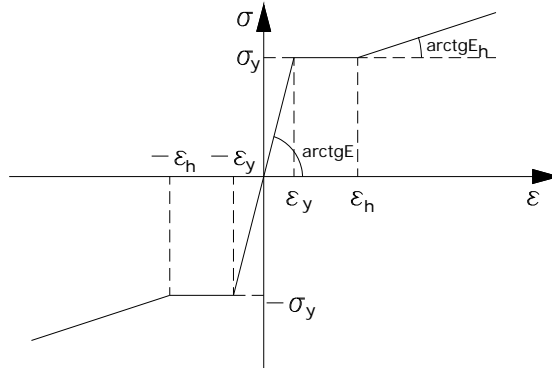


Figure 44. Elasto-plastic-hardening constitutive model of the material.

Table 8. Experimental data used for recalibration of R and s factors.

Tests	Author	Profiles type
3	Landolfo et al. (2010)	I and H hot-rolled profiles
3	Landolfo et al. (2010)	Rectangular hollow section cold-formed
3	Landolfo et al. (2010)	Square hollow section cold-formed
24	Kuhlmann (1989)	I and H hot-rolled profiles
35	Spangemacher (1992)	I and H hot-rolled profiles
4	Kemp (1985)	I and H hot-rolled profiles
5	Boeraeve-Lognard (1993)	I and H hot-rolled profiles
12	Lukey-Adams (1969)	I and H hot-rolled profiles
44	Wilkinson (1999)	Rectangular hollow section cold-formed
15	Zhou-Young (2005)	Rectangular hollow section cold-formed

Table 9. C_i coefficients in the expression of R factor.

	C_1^R	C_2^R	C_3^R	C_4^R	C_5^R	C_6^R
I	-18.268	-44.494	-1.780	56.942	-0.075	2.871
□	42.555	-20.387	-4.651	30.713	-0.697	0.000

Table 10. Ci coefficients in the expression of s factor.

	C_1^s	C_2^s	C_3^s	C_4^s	C_5^s	C_6^s
I	1.647	0.204	0.005	-0.147	-0.006	-0.050
□	-0.243	0.499	0.047	-0.914	0.023	0.000

Statistical evaluation

A statistical analysis was performed in order to verify the proposed R and s functions and to determine also the appropriate value of partial factor γ_M ensuring that the adequate reliability index is met.

The guidance for such type of analysis is given in EN 1990, Annex D, where the partial factor γ_M is defined as the ratio between the characteristic and the design value.

The procedure for the assessment of a characteristic and design value is based on the following assumptions:

- the resistance is a function of a number of independent variables X_i ;
- a sufficient number of tests is available;
- all relevant geometrical and material properties are measured;
- there is no correlation (statistical dependence) between the variables in the resistance function;
- all variables follow either a normal or a log-normal distribution.

The procedure is organized in the following steps: 1. development of the design model; 2. comparison of experimental and theoretical values; 3. estimation of the mean value of correction factor; 4. estimation of the coefficient of variation of the errors; 5. determination of the coefficients of variation of the basic variables; 6. determination of the characteristic value of the resistance.

In particular, the first step of the analysis consists in the development of the theoretical resistance model of the experimental results. In this study the proposed resistance models are given by Eq. (10) for rotation capacity and Eq. (11) for flexural overstrength.

The examined theoretical resistances r_t are assumed as functions of a number of independent variables X as the following:

$$r_t = g_r(X) \quad (12)$$

For the evaluation of these functions, the measured values of the mechanical characteristics and geometry are used.

The second step is the comparison of experimental and theoretical values. The experimental resistances are expressed by the vector r_{e1} for rotation capacity and r_{e2} for flexural overstrength. In Figure 45a,b test results $r_{e1,i}$ and $r_{e2,i}$ for

I and H profiles are plotted versus the theoretical resistance $r_{t1,i}$ and $r_{t2,i}$, respectively. Analogously, in Figure 46a,b the experimental vs theoretical expressions are plotted for RHS and HSS beams.

If the resistance function was exact and complete, all points (r_{ti}, r_{ei}) would lie on the bisector of the first quadrant. In the examined case, the points (r_{ti}, r_{ei}) show little dispersion which may be attributed to the scatter in material properties and errors in geometry.

The third step is the estimate of the mean value correction factor b , which is calculated using the least square method.

$$b = \frac{\sum_i r_{ei} r_{ti}}{\sum_i r_{ti}^2} \quad (13)$$

The next step is the estimate of the coefficient of variation of the errors. The estimated error δ_i of each experimental result is determined from:

$$\delta_i = \frac{r_{ei}}{b r_{ti}} \quad (14)$$

The mean values of theoretical resistances r_m are calculated by the mean values of basic variables X_m :

$$r_m = b r_t(X_m) \delta = b g r_t(X_m) \delta \quad (15)$$

The mean values of the geometry are adopted as nominal values for the calculation of the rivets and net cross-sections. The mean values of material properties are equal to the measured ones. The material properties are equal for all specimens because all specimens were extracted from the same steel plate.

On the basis of the estimated error δ_i , the estimator of variation coefficients for scatter V_d is determined by:

$$\Delta_i = \ln(\delta_i) \quad (16)$$

$$\bar{\Delta} = \frac{1}{n} \sum_{i=1}^n \Delta_i \quad (17)$$

$$s_\Delta^2 = \frac{1}{n-1} \sum_{i=1}^n (\Delta_i - \bar{\Delta})^2 \quad (18)$$

where n is the number of tests.

Finally:

$$V_\delta = \sqrt{\exp(s_\Delta^2) - 1} \quad (19)$$

The further step is to determine the coefficients of variation V_{X_i} of the basic variables. Indeed, to include the uncertainty of the steel grade and the fabrication of elements, the standard deviation is increased by the coefficients of

variation V_{X_i} which are determined on the basis of prior knowledge. The coefficients of variations of steel constituting the specimen is obtained from performed material tests. In particular, the following variations were used:

$V_{fy} = 0.075$ variation coefficient for tensile strength of plates;

$V_t = 0.05$ variation coefficient for plate thickness;

$V_w = 0.005$ variation coefficient for width;

For small values V_{d2} and $V_{X_{i2}}$ it is possible to determine V_r in the simplified way shown in the following:

$$V_r^2 = V_\delta^2 + V_{rt}^2, \text{ being } V_{rt}^2 = \sum_{i=1}^j V_{X_i}^2 \quad (20)$$

where j is the number of different variations.

For the calculation of the characteristic and the design resistances, the following standard deviations and coefficients are obtained from:

$$Q_{rt} = \sigma_{\ln(rt)} = \sqrt{\ln(V_{rt}^2 + 1)} \quad (21)$$

$$Q_\delta = \sigma_{\ln(\delta)} = \sqrt{\ln(V_\delta^2 + 1)} \quad (22)$$

$$Q_r = \sigma_{\ln(r)} = \sqrt{\ln(V_r^2 + 1)} \quad (23)$$

$$\alpha_{rt} = \frac{Q_{rt}}{Q} \quad (24)$$

$$\alpha_\delta = \frac{Q_\delta}{Q} \quad (25)$$

The characteristic value for a limited number of tests is given by the following expression:

$$r_k = bgr_t(X_m) \exp(-k_\infty \alpha_{rt} Q_{rt} - k_n \alpha_\delta Q_\delta - 0.5 Q_2) = bgr_t(X_m) R_k \quad (26)$$

where the appropriate values of fractile factors k_n , $k_{d,n}$, k_∞ and $k_{d,\infty}$ are provided by EN 1990.

Similarly, the design value for a limited number of tests is obtained as:

$$r_d = bgr_t(X_m) \exp(-k_{d,\infty} \alpha_{rt} Q_{rt} - k_{d,n} \alpha_\delta Q_\delta - 0.5 Q_2) = bgr_t(X_m) R_d \quad (27)$$

The estimate for the partial factor γ_M is defined as the ratio between the characteristic and the design value.

$$\gamma_M = \frac{r_k}{r_d} = \frac{\exp(-k_\infty \alpha_{rt} Q_{rt} - k_n \alpha_\delta Q_\delta - 0.5 Q_2)}{\exp(-k_{d,\infty} \alpha_{rt} Q_{rt} - k_{d,n} \alpha_\delta Q_\delta - 0.5 Q_2)} = \frac{R_k}{R_d} \quad (28)$$

The results of the statistical analysis are presented in Table 11. The difference in the value of the partial factor γ_M for the two proposed verification formulas is negligible.

Both proposed resistance models are characterized by a correction factor b close to 1 and a relatively small scatter (see Table 11 and Figures 45 and 46). Therefore, they appropriately describe the rotation capacity R (resistance model 1) and the flexural overstrength s (resistance model 2).

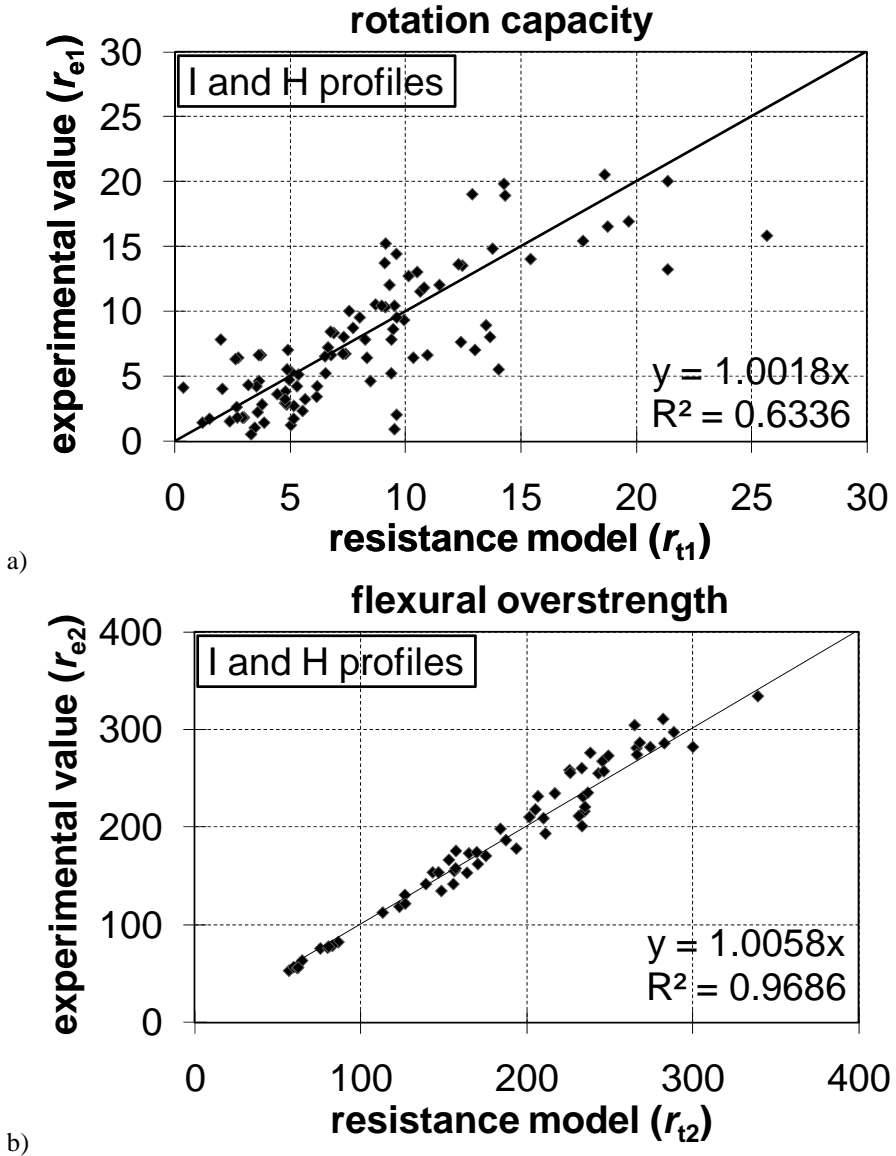


Figure 45. Experimental vs theoretical R (a) and s (b) for I and H beams.

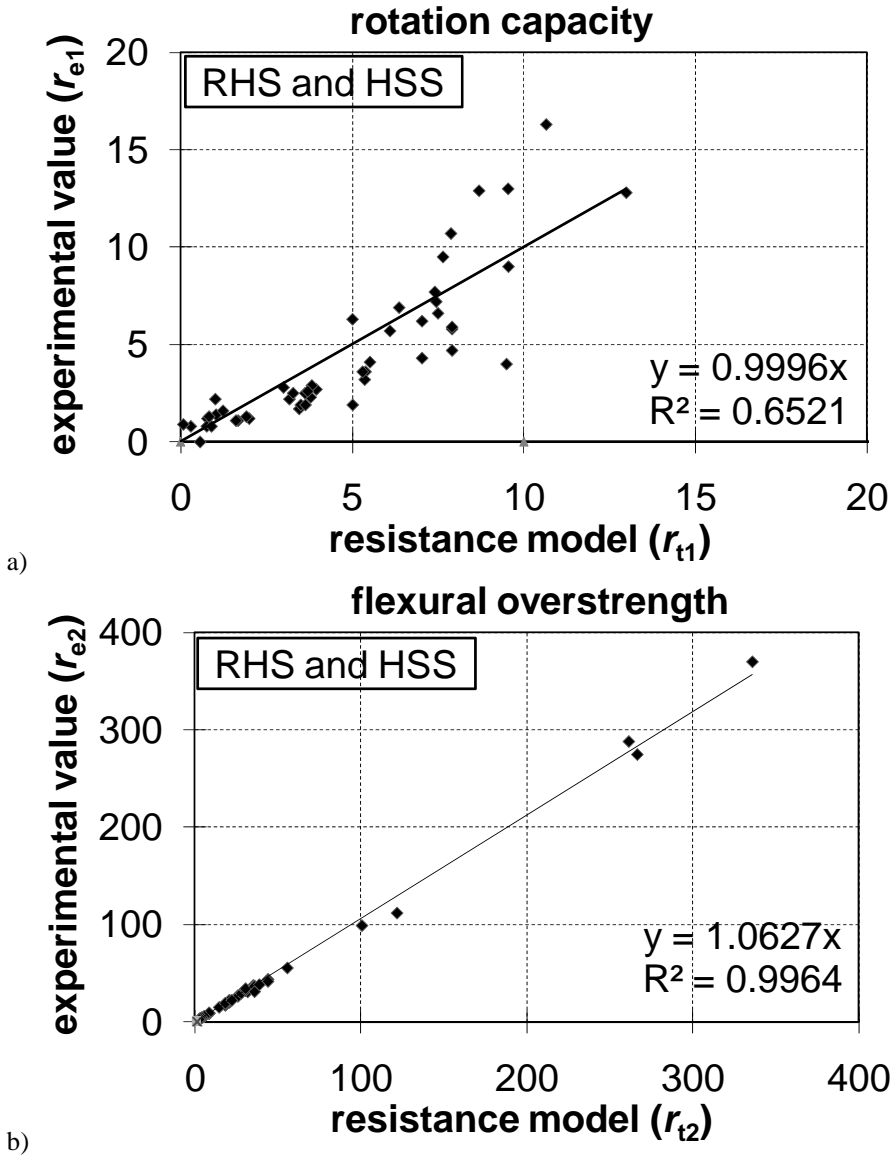






Figure 46. Experimental vs theoretical R (a) and s (b) for RHS and SHS beams.

Table 11. Results of statistic analysis.

Resistance model	beam type	N. results	b	V_d	$\gamma_{M,req}$
R		83	1.0018	0.6767	1.159
		65	0.9996	0.7998	1.220
s		83	1.0058	0.0720	1.167
		65	1.0627	0.0045	1.218

8. CONCLUSION

A review of current criteria used to classify the flexural behaviour of steel beams in steel building structures has been presented. An interaction between web and compression flange slenderness in limiting the rotation capacity of flexural members was observed in previous test results. This interaction can lead to reduced inelastic deformation capacity, measured as rotation capacity, when either the web or the compression flange slenderness is too large.

The experimental results indicated that the loading condition has a significant influence on rotation capacity. The rotation capacity R decreased when the loading is monotonic moment gradient as compared to cyclic moment gradient. On the other hand, the cyclic flexural overstrength s could be larger than the one observed in monotonic tests thanks to the steel isotropic hardening.

It was observed that the extrapolation of current compactness criteria by Eurocode 3 and NTC'08 does not appear to produce the rotation capacity and the overstrength that could be expected.

On the basis of performed tests and the experimental outcomes reported by scientific literature, two novel empirical expressions of R and s are proposed. In addition the validity of these formula has been statistically checked according to EN1990 procedure.

The current study highlighted the need of further research to determine the rotation demand of flexural members (both beams and beam-columns) under non-seismic and seismic conditions. This should include analytical investigations, along with experimental verification. The variables for investigation should include: structural system configuration; member web and flange slenderness; member unbraced length; and, material characteristics (yield-to-tensile strength, strain hardening modulus, strain at ultimate stress, strain at onset of strain hardening, yield strength).

Further research is also needed to establish criteria for web and compression flange slenderness, as well as the unbraced length, in order that beams can be

properly proportioned to ensure adequate rotation capacity under cyclic loading.

ACKNOWLEDGEMENTS

The financial support of the Italian Emergency Management Association (Protezione Civile Italiana): ReLUIIS Project – Task 5 “Development of innovative approaches to design steel and composite steel-concrete structures” is gratefully acknowledged

REFERENCES

- AISC [2005] Specification for structural steel buildings. American Institute of Steel Construction.
- AISC [2005] Commentary on the specification for structural steel buildings. American Institute of Steel Construction.
- Akiyama H. [1980]. Earthquake Resistant Limit State Design for Buildings, University of Tokio Press.
- ASCE [1971]. Plastic design in steel: A guide and commentary. Manual and report on engineering practice, no.41. Welding Research Council and ASCE.
- Bild S., Roik K, Sedlacek G, Stutzki Ch, Spangemacher R. [1989]. Background document for chapter 5 of Eurocode 3 – The b/t-ratios controlling the applicability of analysis models in Eurocode 3. Draft. Aachen.
- Brescia M. Rotation capacity and steel members classification criteria in seismic areas, Pollack Periodica vol. 2, n.2, pagg. 63-73 ISSN 1788-1994
- Brescia M., Mammana O., Landolfo R. [2007] On the classification of steel members in seismic areas, Proceedings of the Eleventh International Conference on Civil, Structural and Environmental Engineering Computing, Ed. Topping Publisher (Civil-Comp Press), Stirling, United Kingdom, ISBN 978-1-905088-15-7.
- Brescia M., Mammana O., Landolfo R. [2007] Classificazione delle membrature in acciaio: ricalibrazione e generalizzazione del fattore di sovrarresistenza s, Atti workshop Reluis: Materiali ed approcci innovativi per il progetto in zona sismica e la mitigazione della vulnerabilità sismica delle strutture”, Università di Salerno.
- Brescia M., Iannone F., Landolfo R., Mammana O., Piluso V., Rizzano G. [2009] Preliminary results of an experimental program on the cyclic response and rotation capacity of steel members, Atti convegno Stessa '09
- Brescia M. [2009]. Rotation Capacity and Overstrength of steel members for seismic design PhD Thesis.
- CEN (European Communities for Standardization), Final draft, EN 1993-1: 2004. Eurocode 3: Design of steel structures-Part 1: General rules and rules for buildings.
- Climenhaga J.J. Johnson R.P. [1972] Moment-rotation curves for locally buckling beams, in Journal of the Structural Division, Vol.98, ST6, 1239-1254.
- D.M. [2008], Nuove Norme Tecniche per le Costruzioni.

- Driscoll G.C.[1958]. Rotation capacity requirements for beams and portal frames. Ph.D. thesis. Lehigh University.
- Driscoll G.C. [1958]. 'Rotation capacity requirements for single-span frames', Fritz Engineering Laboratory Report N0.268.5, Lehigh University, September, 1958
- Driscoll G.C. [1957]. 'Rotation capacity of a 3-span continuous beam', Fritz Engineering Laboratory Report N0.268.2, Lehigh University, June.
- Fardis M.N., Carvalho E., Elnashai A., Faccioli E., Pinto P. and Plumier A. [2005]. "Designer's Guide to EN 1998-1 and EN 1998-5. Eurocode 8: Design of structures for earthquake resistance. General rules, seismic actions, design rules for buildings, foundations and retaining structures". Thomas Telford, London.
- Fukuchi Y. [1969]. Flange buckling and ultimate load of beams under moment gradient. Trans. of A.I.J., n. 166. (in Japanese).
- Galampos T.V., Lay M.G. [1965]. Studies of the ductility of steel structures, J. of the Structural Division, ASCE, Vol. 91. No. ST4. pp. 125–151.
- Gioncu V., Mateescu G., Iuhas A. [1994] Contributions to the study of plastic rotational capacity of I steel sections in Proceedings of STESSA '94, Timisoara.
- Gioncu V., Mazzolani F.M. [1995]. Alternative methods for assessing local ductility. In: Mazzolani FM, Gioncu V, editors. Behaviour of steel structures in seismic areas, STESSA'94. London: E&FN Spon, p. 182–90.
- Gioncu V., Mazzolani F.M. [2002]. Ductility of seismic resistant steel structures. London, Spon Press.
- Haaijer G. [1957]. Plate buckling in the strain-hardening range. Journal of the Engineering Mechanics Division. ASCE, 83(EM2), 1-47.
- Hasan S.W, Hancock G.J. [1989]. Plastic bending tests of cold-formed rectangular hollow sections. Steel Construction, Journal of Australian Institute of Steel Construction, 23(4):2–19.
- Hibbit, Karlsson, Soresen, [2004], Inc., ABAQUS/Standard version 6.7, Patwucket, U.S.A.
- Ivanyi M. [1979] Moment rotation characteristics of locally buckling beams, in Technical University Budapest, Vol.23, 217-230.
- Ivanyi M. [1992]. Steel frame stability, CISM Course No. 323; Eds. Ivanyi M., Skaloud M. Stability problems of steel structures, Springer–Verlag, Wien–New York.
- Kato B. Akiyama H. [1973]. Theoretical prediction of the load-deflection relationship of steel members and frames. Proc. of IABSE symposium, Lisbon.
- Kato B., Akiyama H. [1981]. Ductility of Members and Frames subject to Buckling, ASCE convention, May 11-15
- Kato B. [1988]. Rotation capacity of steel members subject to local buckling, 9th World Conference on Earthquake Engineering, Vol. 4, paper 6-2-3, Tokyo Kyoto.
- Kato B. [1989]. Rotation Capacity of H-section members as determined by local buckling, in Journal of Construction Steel Research, Vol.13, 95-109.
- Kato B. [1989] Rotation Capacity of H section members as determined by local buckling, Journal of Conctructional Steel Research, 95-109.
- Kato B., [1990], deformation capacity of steel structures, in Journal of Construction Steel Reseach, Vol.17, 33-94.

- Kemp A. [1985] Interaction of Plastic Local and Lateral Buckling, *Journal of Structural Engineering ASCE*, vol.111.
- Kemp A. [1985]. Commentary on SABS 0162-1984: Code of Practice for the use of structural steel: Chapter 12: Plastic design, South African Institute of Steel Construction. Kemp A.R., [1985]. Interaction of plastic local and lateral buckling, in *Structural Engineering*, Vol.111, n.10, 2181-2196.
- Kerfoot R.P.[1965]. Rotation capacity of beams. Report 297.14. Fritz Engineering Laboratory, Lehigh University.
- Korol R.M., Hudoba J. [1972]. Plastic behavior of hollow structural sections. *Journal of the Structural Division, ASCE*, 98(5):1007–23.
- Kuhlman U. [1986]. Rotations kapazität biegebeanspruchter I-Profil unter Berücksichtigung des plastischen Beulens, in *Technical Reports Institute für Konstruktion Ingenieurbau Ruhr-Universität Bochum*, Mit. 86-5.
- Kuhlman U. [1989]. Definition of flange slenderness limits on the basis of rotation capacity values, in *Journal of Construction Steel Research*, Vol.14, 21-40.
- Landolfo R., Brescia M., Mammana O. [2007] Capacità rotazionale e criteri di classificazione delle membrature in zona sismica, *Atti convegno Anidis: L'ingegneria sismica in Italia*, Pisa.
- Lay M.G. [1965]. Flange Local Buckling in Wide Flange Shape, *Journal of Structural Division ASCE*, Vol. 91
- Lay M.G., Galambos T.V. [1965]. Inelastic Beams Under Uniform Moment, *Journal of Structural Division ASCE*, vol.91.
- Lay M.G. [1965]. Flange local buckling in wide-flange shapes. *Journal of the Structural Division. ASCE*, 91(ST6), 95-116.
- Lay M.G., Galambos T.V. [1967]. Inelastic Beams Under Uniform Moment, *Journal of Structural Division ASCE*, vol.93
- Lukey A.F., Adams P.F. [1969]. Rotation capacity of beams under moment gradient, in *Journal of the Structural Division*, Vol.95, ST6, 1173- 1188.
- Mazzolani F.M., Piluso V. [1992]. Evaluation of the rotation capacity of steel beams and beam-columns, in *Proceedings of 1st State of the Art Workshop COST C1, Strasbourg*.
- Mazzolani F.M., Piluso V. [1992]. "Member behavioural classes of steel beams and beam-columns", In: *Proc. of First State of the Art Workshop, COSTI, Strasbourg*. p. 517–29.
- Mazzolani F.M. Piluso V. [1993]. Member behavioural classes of steel beams and beam-columns. *Proc. XIV CTA conference, Viareggio (Italy)*, 24-27 October.
- Mitani I., Makino M. [1980]. Post Local Buckling and Plastic Rotation Capacity of Steel Beam-Columns, *7th World Conference on Earthquake Engineering, Istanbul*.
- Nakamura T. [1988]. Strength and Deformability of H Shaped Steel Beams and Lateral Bracing Requirements, *Journal of Constructional Steel Research*, N.9, 217-228.
- OPCM 3274, [2003], First elements in the matter of general criteria for seismic classification of the national territory and of technical codes for structures in seismic zones, *Official Gazette of the Italian Republic, Rome*, and further modifications
- Piluso V. [1992] Il comportamento inelastico dei telai sismo resistenti in acciaio (Phd Thesis).

- Rasmussen K.J & Hancock G.J. [1998]. Buckling analysis of thin-walled structures: analytical developments and applications. *Progress in Structural Engineering and Materials* 1(3): 316–322.
- Roik K., Kuhlman U. [1987]. Rechnerische Ermittlung der Rotationskapazität biegebeanspruchter I-profile, in *Stahlbau*, Heft 11, 321- 327
- Rondal J, Boeraeve Ph, Sedlacek G, Strangh"oner N, Langenberg P. [1995]. Rotation capacity of hollow beam sections. CIDECT.
- Schleich, J.B.; Chantrain, P.; Chabrolin, B.; Galéa, Y.; Bureau, A.; Anza, J. & Espiga, F. [1998]. "Promotion of plastic design for steel and composite cross sections: new required conditions in Eurocodes 3 and 4, practical tools for designers". European commission.
- Sedlacek, G.; Dahl, W.; Stranghöner, N. & Kalinowski, B. [1998]. "Investigation of the rotation behaviour of hollow section beams". EUR 17994 EN. Final report of project No 7210-SA/-119.
- Sedlacek G, Feldmann M. [1995]. Background document 5.09 for chapter 5 of Eurocode 3 Part 1.1 – The b/t ratios controlling the applicability of analysis models in Eurocode 3 Part 1.1. Aachen.
- Stranghoner N, Sedlacek G, Boeraeve Ph. [1994]. Rotation requirement and rotation capacity of rectangular, square and circular hollow section beams. *Proceedings of the 6th international symposium on tubular structures*.
- Suzuki H., Kato B., Akiyama H. [1974]. Flange buckling of H-section stub-columns. *Proc. of Kanto Branch of A.I.J.* (in Japanese).
- Southward R.E. [1969]. Local Buckling in Universal Sections, Internal Report, University of Cambridge, Engineering Department.
- Spangemacher R. [1991]. Zum Rotationsnachweis von Stahlkonstruktionen, die nachdemtraglastverfahren berechnet werden, Dissertation, Technischen Hochschule Aachen.
- Spangemacher R., Sedlacek G. [1992]. On the Development of a Computer Simulator for Test of Steel Structures, in *Proceedings of the First World Conference on Constructional Steel Design*, Acapulco, Mexico, 6-9 december.
- Vayas, I., Psycharis I.N. [1990]. Behaviour of thin-walled steel elements under monotonic and cyclic loading, in *Structural Dynamic*, (eds. Kratzig et al.), Balkema, Rotterdam, 579-583.
- Yura J. A., Galambos T. V., Ravindra M. K. [1978]. 'The bending resistance of steel beams', *Journal of the Structural Division, ASCE*, 104, No. ST9, Proc. Paper no. 14015, September, pp.1355-1370
- Wilkinson, T. & Hancock, G. [1998]. "Tests to Examine Compact Web Slenderness of Cold-Formed RHS". *J. Structural Engineering*, vol. 124, issue 10, pp.1166-1174.
- Zhao XL, Hancock GJ. [1991]. Tests to determine plate slenderness limits for cold-formed rectangular hollow sections of grade C450. *Steel Construction, Journal of Australian Institute of Steel Construction*, 25(4):2–16.

METAL SHEAR PANELS FOR IMPROVING THE SEISMIC BEHAVIOUR OF FRAMED BUILDINGS

Gianfranco De Matteis¹, Giuseppe Brando¹, Antonio Formisano²,
Federico M. Mazzolani²

¹ *Department of Engineering, University "G. d'Annunzio" of Chieti-Pescara, Pescara, Italy*

² *Department of Structural Engineering, University of Naples Federico II, Naples, Italy*

Abstract. The manuscript is focused on the research activity carried at the University of Chieti-Pescara within the Reluis-DPC research Project 2005-2008. This has been addressed to the evaluation of the structural performances of both steel and aluminium shear panels for the seismic improvement of new and existing buildings. The described research products are basically articulated in three tasks.

The first one is related to the experimental-theoretical-numerical study of thin metal shear panels for the seismic protection of existing reinforced concrete buildings. A retrofitting design procedure of the used panel, developed on the basis of a preliminary evaluation of the load-carrying capacity of the bare structure, as well as of the performance levels to be attained for the retrofitted structure, is set-up according to the methodology proposed by the ATC-40 code. Then, appropriate finite element models are provided in order to verify that the selected devices respect the required increase of strength and stiffness for retrofitting operations. Finally, a significant case study is analysed.

The second task concerns an experimental-numerical study carried out on compact and semi-compact stiffened shear panels made of pure aluminium, according to both a "full bay" and a "bracing type" configuration. The cyclic behaviour offered by these devices is carefully analysed and the main performance parameters, such as stiffness, ductility, hardening ratio and dissipated energy, are assessed. The principal experimental evidences are presented in order to highlight the most important resisting mechanism which can be strongly affected by buckling phenomena. In addition, suitable numerical models, developed on the basis of experimental results, are used with the aim of detecting the stress levels attained for different shear strain demands

The third task is lastly devoted to assess the behaviour of steel and aluminium shear panels characterised by different thicknesses and aspect ratios (obtained also by stiffening the base plate) under theoretical and numerical ways, in order to provide useful design provisions.

Keywords: Metal Shear Walls, passive protection of buildings, retrofitting of existing structures, stiffened or un-stiffened panels, pure aluminium, full-scale experimental tests, FEM numerical models, parametric analyses, design procedures, code provisions.

1. INTRODUCTION

The objectives of the current research are related to the study of the contribution of structural Metal Plate Shear Walls (MPSWs) on the behaviour of framed buildings when these are equipped with stiffening or dissipative shear panels.

A MPSW is a lateral load resisting system composed by metal plates connected to columns and girders of a primary surrounding structure. The connection between the steel plates and the two lateral boundary columns qualitatively behaves as a vertical cantilever girder supported by foundation (Schumacher et al., 1997; Berman and Bruneau, 2004) able to resist to horizontal story shear and overturning moment due to lateral actions. The plates act as the web of the resulting girder, the columns form its flanges and the horizontal floor beams act as transverse stiffeners (Astaneh, 2001). The plates can be arranged in one or more bays along the height of the primary structure, which, in case a steel structure is of concern, can be simply pin-jointed or moment resisting (Fig. 1). In the first case the system is defined as “Standard Structural System” (SSS), while in the latter as “Dual Structural Systems” (DSS).

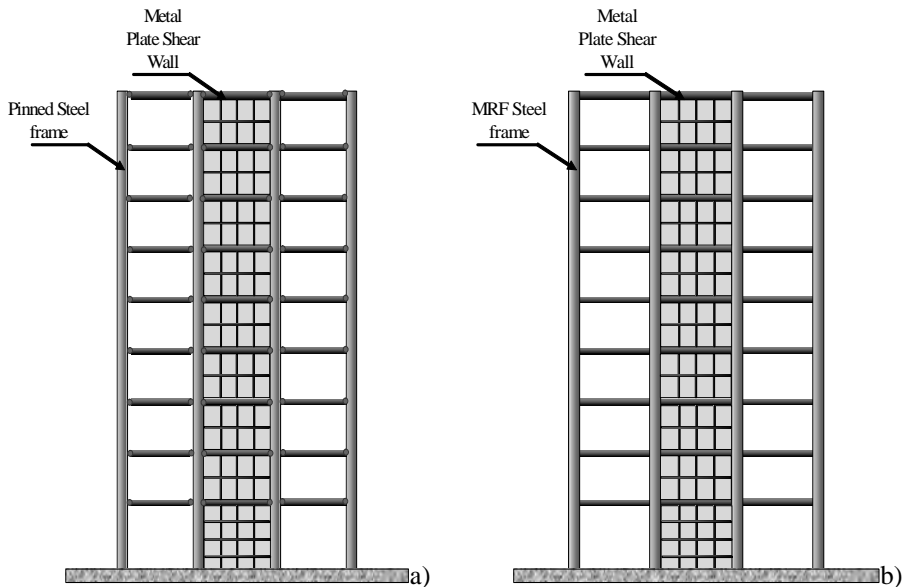


Figure 1. Typical steel structural system with metal plate shear walls: (a) Standard Structural System (SSS); (b) Dual Structural System (DSS).

Structures endowed with MPSWs provide a significant performance for different limit state requirements, which, differently from the most traditional braced systems employed for the stabilization of steel structures against lateral

loads (Table 1), can be achieved by means of simple tricks regarding the arrangement of the applied ribs on each plate or the disposal of the panels into the primary structure.

Table 1. Performances of the most popular braced systems compared to MPSWs.

	STIFFNESS	DUCTILITY	STRENGTH
MRF	poor	excellent	good
CBF	excellent	poor	good
EBF	good	good	good
SMPSWs	excellent	excellent	good
DMPSWs	good	excellent	excellent

In particular, shear walls realized with metal plates can be subdivided into two main typologies:

- 1) Walls able to improve both strength and stiffness characteristics of the primary structure (SMPSWs);
- 2) Systems able to dissipate the energy introduced by the horizontal actions in the primary structure (DMPSWs).

Both these typologies of MPSW systems can be also characterized in terms of geographical areas where they have been mainly studied and developed in the past. Thus, while SMPSWs have been principally adopted in USA and Canada, DMPSWs have been mainly proposed in Japan. In addition, the possibility of employing lightweight cladding panels for seismic purpose has been largely investigated in Europe, as a development of the well known stressed skin design approach which was mainly addressed to corrugated sheeting used as roofing of industrial buildings (Davies and Bryan, 1982).

The research carried at the University of Chieti-Pescara within the Reluis-DPC research Project 2005-2008 has been articulated in the following three main tasks:

- 1) Experimental-theoretical-numerical study on thin metal shear panels for seismic protection of existing reinforced concrete buildings.
- 2) Experimental-numerical analyses on both compact and semi-compact stiffened shear panels made of pure aluminium;
- 3) Theoretical and numerical models for evaluating the performance of metal shear panels in order to provide reliable design criteria;

In the following the main outcomes of the above activities are described. The manuscript is oriented to the description of mechanical and numerical models of the above two types of panels, calibrated on the basis of data re-

trieved from both literature and experimental tests purposely carried out. Results of analyses carried out by using these models are finally provided.

2. BACKGROUND AND MOTIVATION

In the last thirty years many studies on the performance of MPSWs have been undertaken due to the introduction of new design criteria which have been based on the assumption that shear plates can offer a suitable post-buckling strength. Such studies highlighted the advantages that such a type of lateral load resisting system can provide with respect to the traditional ones. In particular, it has been clearly pointed out that the assessment of security of buildings equipped with shear plates must not be carried out considering a design ultimate limit state simply corresponding to the out-of-plane buckling of the infill panels. Otherwise, an adequate performance of a structure with not buckled MPSWs would require heavily stiffened thick plates.

The unfounded conviction of designing shear plate without buckling also for ultimate strain demands has entailed that for long time the use of MPSWs has been considered not economically competitive with respect to other seismic strategies, such as the most employed reinforced concrete shear walls (Bruneau et al., 2005). Besides, the common practice of not taking into account the post buckling resources of steel shear plates led many engineers involved into the design of steel buildings with light-gauge panels, i.e. cladding sandwich panels, to neglect also their contributing effect on the dynamic response of the whole building, unavoidably overestimating the fundamental period of the structure and undervaluing the actual stiffening and strength capacity. However the need of a suitable theory for interpreting the post-buckling behaviour of steel plates was felt even previously. On this purpose one of the most significant conclusion of the VIII Congress AIPC in New York during the 60's states (Ballio and Mazzolani, 1987):.

“The linear theory of the instability is not an adequate base for designing structures with thin plates and it has to be surrogated with a non linear theory taking into account the post-buckling resources of the same plates. It is necessary to consider the maximum in plane tensions and deformations sustainable by the plates after that buckling phenomena occurred There is a lack of mathematical approaches which allow to establish a calculation method which keep into accounts all the decisive parameters.... A new series of experimental and numerical analyses which include the post-buckling behaviour has to be carried out...”.

Only since the 80's many experimental and numerical studies on the post-buckling behaviour of MPSWs have been carried out in order to provide useful rules and design criteria to be adopted in national and international standards. They were based on the assumption that shear plates forming shear walls can provide to a building an effective initial stiffness, thus limiting inter-story drifts

values under low seismic actions, it being also able to develop a tension field resisting mechanism, once that buckling phenomena are triggered off, behaving in a very ductile way (Fig. 2), with a significant amount of energy dissipated under cyclic loads.

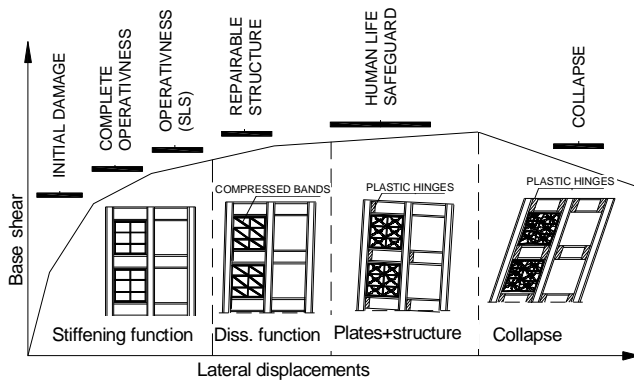


Figure 2. Non linear behaviour of a DSS equipped with MPSWs and its performance levels

In particular, the stiffening and the dissipative function of structures equipped with MPSWs, under both static and dynamic actions, have been deeply investigated, also comparing their performances with the ones offered by different seismic devices. In addition, accurate finite element models have been implemented, in order to identify the principal behavioural phenomena acting in a shear panel. Moreover, various metal materials and geometrical configuration, i.e. characterized by different arrangements of applied stiffeners or by holes wisely made on the base plate, have been considered as well.

The advancements in the research field entailed remarkable novelties in the practical applications which were based on the development of new construction technologies.

Beyond the above structural aspects, MPSWs are characterized by the following peculiarities compared to the more common reinforced concrete shear walls:

- No concrete jets are necessary, with both a significant speeding up in the erection processes and a reduction of cost of construction. Moreover, the use of controlled metals derived from industrial processes allows a major quality control and, thus, inferior safety levels to be adopted in the design phase;
- The structural lightness determines minor stresses on both columns and foundations, a reduction of the input seismic load, as well as less occupancy of space, with evident advantages from the architectural point of view;

- Inspection of the resisting structural elements, which can be necessary after a significant seismic event, is easier;
- MPSWs can be applied also in environmental conditions in which reinforced concrete shear walls may not be economical, i.e. in very cold regions of the world;
- Compared to reinforced concrete shear walls, metal plate shear walls can be much easier and faster to construct when they are used in seismic retrofitting of existing building.

MPSWs initiated therefore to be considered economically convenient also in the belief of both designer and contractors. From this point of view, it is very worthy of note what happened in 1978 for a 53-storey high rise building erected in Tokio. As referred in (Astaneh, 2001), the structure was initially designed using reinforced concrete shear walls. However, according to Engineering News Record (1978), due to patent problem, the reinforced concrete walls were converted to steel shear walls. According to ENR article (ENR, 1978):

“the contractor rejected a steel braced building core as too expensive compared to steel shear walls”.

For these and further significant reasons, a significant number of steel middle-high tall building have been built using MPSWs to accomplish the designer seismic strategy. On the other hand, many of these buildings have been subjected to strong earthquakes, showing a very good seismic response.

On the basis of the above remarks, it is possible to affirm that MPSWs are considered nowadays one of the most interesting seismic system being very effective in limiting the inter-storey drift of framed buildings and resulting also efficient from the dissipative point of view.

3. RESEARCH ACTIVITY

Tests and analysis on thin shear panels for seismic protection of existing reinforced concrete buildings

The first task of the research concerned the numerical-experimental study on metal (steel and pure aluminium) shear panels for the seismic retrofitting of existing RC buildings. The study has been developed into two main phases. In the first phase, a reliable methodology for seismic retrofitting purpose of RC buildings was given, exploiting the outcomes of both numerically and experimentally analysis on an existing two-story 3D RC frame (De Matteis et al., 2009). In the second phase, the above outcomes have been extended to an irregular multi-story RC building, whose effectiveness in being retrofitted with steel shear panels has been demonstrated by numerical way (Formisano et al., 2009).

In the first stage of this first task, the availability of a real RC building located in the Bagnoli district of Naples, where the ex steel mill of ILVA (or Ital-

sider) was located (Mazzolani, 2006), provided the occasion to exploit the potentiality of metal shear panels as retrofitting system of RC buildings. The building under investigation, which was realised in 70's to serve as an office building, is a RC framed structure designed to resist gravity loads only (Fig. 3a). The construction develops on two storeys with rectangular floors, presenting a single bay in the transversal direction, where the lateral strength is supplied by 30x30 cm columns, and twelve bays in the longitudinal one, where transversal beams having cross-section of 30x50 cm are located. Floors are made of RC and hollow tiles mixed slabs, 24 cm and 20 cm high at the first and second floor, respectively. The building, which is based on direct foundations with inverse T-cross section beams located along its perimeter, is completed with external walls made of three different layers of tile blocks filling up the space among columns. Aiming at increasing the potential number of structures to be tested with different upgrading solutions, the original building was divided into six smaller and similar sub-structures, herein called as structural modules. Firstly, demolition of external and partition walls was done, then slabs were cut at both floor levels (Fig. 3b) in order to apply the upgrading techniques reported in Figure 4.



Figure 3. The building under investigation (a) and division in sub-structures (b).

The selected module where intervention based on the use of metal shear panels is foreseen is the n.5, where concentric braces made of shape memory alloys (SMAs) were preliminarily tested in transversal direction in order to evaluate the strong self-centering capacity of these devices. The sub-structure under study is characterised by a rectangular plan with dimensions of 6.30 m x 5.90 m and two floors with heights on the ground of 3.55 m and 6.81 m, respectively. Slabs at both levels have a middle transversal floor beam and are supported along the longitudinal direction at the first level by emergent rectangular beams (30 x 50 cm and 25 x 50 cm).

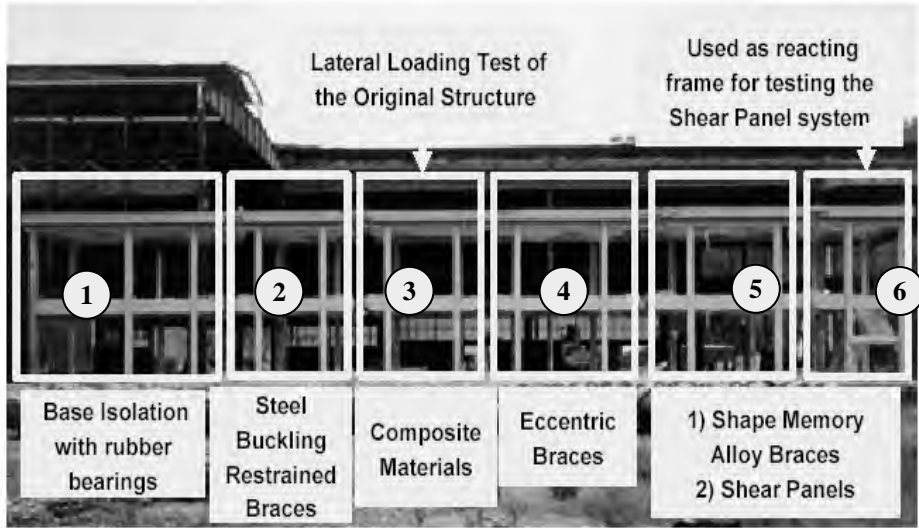


Figure 4. Different upgrading techniques considered in the experimental research program on a gravity load designed RC building (Bagnoli building).

Contrarily, at the second level, the beams have a T-cross section with the same dimensions of the first level ones. The main geometrical characteristics of the structural module, as well as some structural details, are illustrated in Figure 5.

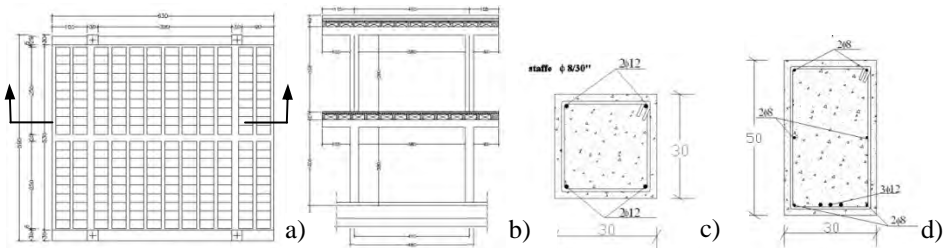


Figure 5. First floor carpentry (a), longitudinal section (b), column (c) and first floor beam (d) of the structural module n. 5.

Aiming at defining the mechanical characteristics of the base materials composing the RC structure, laboratory tests have been carried out at the Department of Structural Engineering of the University of Naples “Federico II” on specimens directly extracted from the structure. Three compression tests have provided for the concrete an average ultimate strength and Young modulus equal to 20.9 MPa and 17155 MPa, respectively. The mechanical properties of the steel bars have been obtained by performing tensile tests, which provided

an average yield stress of about 480 MPa. The obtained data have been used for implementing correctly numerical models of the RC structure.

The structural module destined to be upgraded with metal shear plates has been preliminarily tested in order to determine its performance under lateral loads in terms of both strength and stiffness. In this context it is important to observe that the experimental test performed on the same sub-structure in the transversal direction by using SMA braces caused serious damages at the ends of columns for a length of about 30 cm, where both cracking of concrete and buckling of steel bars were noticed (Fig. 6).



Figure 6. Damages in the column due to the execution of the experimental test with SMA bracings in the transversal direction of the building.

The presence of such damages, afterwards eliminated by using epoxy-resin injections, highlighted an inadequate residual flexural resistance of the columns and, therefore, required to install two steel X-bracings at the first level of the RC frame along the transversal direction (Fig. 7a) in order to avoid its torsional movements during cyclic test to be executed in the longitudinal direction, where panels had to be installed. The module n.6, where staircase is located, has been used as a reaction system for performing the experimental test. To this purpose, this sub-structure has been strengthened along the longitudinal sides by means of two steel V-bracings, made of coupled UPN 140 profiles, which have been connected to both first level beams and foundation beams.

Such a reinforcing system has allowed for the insertion of two hydraulic jacks for testing, they having a total load capacity of 300 kN (Fig. 7b).

The envelope curve of the experimental cyclic test allowed to know the level of both strength (30 kN) and initial stiffness (4010 kNm^{-1}) offered by the base RC structure under lateral loads (Fig. 8). Such values are of a fundamental importance in determining the performances that the retrofitted structure should provide. It is known that the choice of an appropriate seismic consolidation strategy depends on the determination of specific performance targets to be assured for buildings, as well as on the individuation of some deficiencies which correspond to a prefixed damage state.

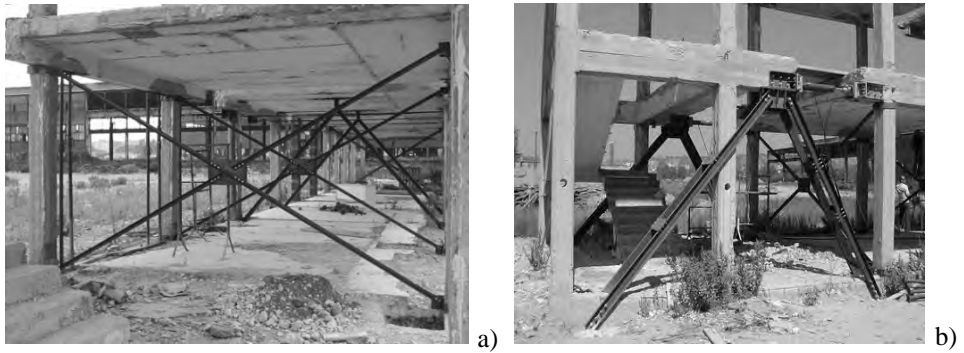


Figure 7. Installation of X (a) and V (b) bracings to perform the experimental test on the bare RC structure in the longitudinal direction.

Once defined such deficiencies, after evaluating if the selected intervention strategies are effectively able to mitigate them, a preliminary retrofitting design based on both the dimensioning and the localization of opportune devices, such as steel bracings, shear walls, isolators, etc., can be done (ATC 40, 1996).

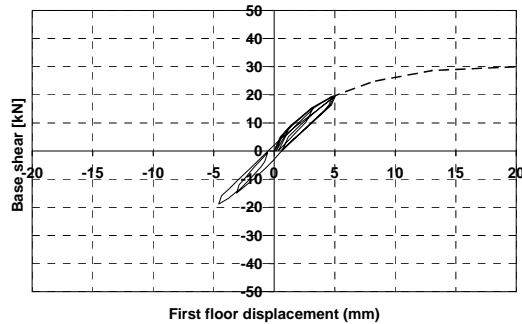


Figure 8. Envelope curve of the cyclic lateral response of the bare RC structural module.

In particular, in order to develop a preliminary design method for structures retrofitted with metal shear panels, it is important to understand in which way these panels improve the seismic performance of existing structures. Such devices are able to increase both the stiffness and the load capacity of the base structure and are also effective in improving its damping properties. Therefore, two steps must be performed in order to make a reliable design intervention:

- 1) Evaluation of the target spectral displacement for the retrofitted structure
- 2) Determination of the steel panel features that will shift the performance point toward this spectral displacement

In the current framework, procedures to be followed for seismic retrofitting design are provided by FEMA 273 (1997) and ATC 40 (1996) guidelines. The ATC 40 American guidelines emphasizes the use of non-linear static procedure focusing the interest mainly in the Capacity Spectrum Method, which provides a graphical representation of the global force-displacement capacity curve of the base structure and then compares it to the response spectra representation of the earthquake demand. Such a method provides an immediate and clear picture on the impact that the selected retrofit strategy has on the performance of the building under earthquake attacks. Based on the mentioned guidelines and according to the retrofitting methodology explained in detail in (Mistakidis et al., 2007), the design of the intervention has been done. After the determination of a performance objective for the original building, the target displacement for the retrofitted structure has been set equal to that displacement. Then, based on the “equal displacements” simplified assumption, the initial stiffness for the retrofitted structure is defined starting from the knowledge of the corresponding period, leading to the following relationship:

$$K_{ret} = K_{ini} \left(\frac{T_{ini}}{T_{ret}} \right)^2 \quad (1)$$

where K_{ini} and T_{ini} are the initial stiffness and the period of the initial structure, respectively and K_{ret} is the stiffness required for the retrofitted structure. Therefore, considering that the retrofitted structure will be able to provide at least the same level of damping of the initial structure, the “desired performance point” is defined and the required ultimate base shear capacity for the retrofitted structure can be obtained from the following equation:

$$V_{ret} = \frac{S_{a_{ret}}}{S_{a_{ini}}} V_{ini} \quad (2)$$

where V_{ini} is the ultimate base shear capacity of the initial structure, V_{ret} is the required ultimate shear capacity of the retrofitted structure, $S_{a_{ini}}$ and $S_{a_{ret}}$ are the ultimate spectral acceleration for the initial and retrofitted structures, respectively. Finally, once both the strength and the stiffness required by the retrofitted structure have been determined, the contribution that metal shear panels have to provide to the base structure are derived. In the case under analysis, the application of the proposed procedure, considering that the construction was located within a soil type B and by making appropriate assumptions about both the target objective and the damping properties for the retrofitted structure (Formisano et al., 2006), the capacity curve of the retrofitting intervention has been defined, as shown in Figure 9, it being characterised by a strength and a vibration period equal to 300 kN and 0.342 s, respectively. Once defined both

the strength and stiffness prerequisites which shear panels should provide for seismic retrofitting intervention, the detailed characterization of these devices has been set up, leading to their preliminary dimensioning through both the eq.(3), related to the stiffness,

$$K = \frac{E \cdot b \cdot t}{4 \cdot d} \quad (3)$$

and the following simplified theoretical relationship, related to the strength (Sabouri-Ghomi et al., 2003):

$$V = \frac{1}{2} f_y t b \sin 2\alpha \quad (4)$$

where:

- b and t are width and thickness of the plate, respectively;
- f_y is the yielding stress of the base material;
- α is the inclination angle of the tension field mechanism.

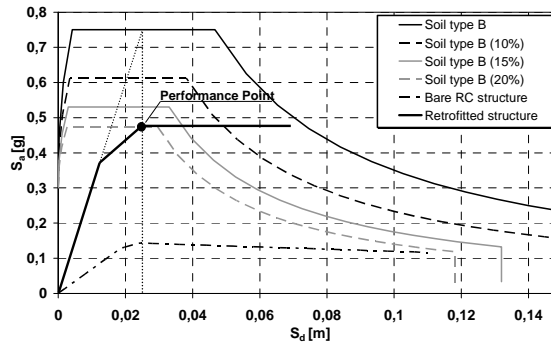


Figure 9. The design curve representative of the retrofitting intervention.

Therefore, two different metallic materials have been selected for shear panels (Fig. 10):

- DX56D steel, characterised by yield and ultimate stress equal to 300 and 340 MPa, respectively, and an ultimate strain greater than 30%, which is used for sheeting and cold-formed profiles according to the provisions of the UNI EN 10142 Italian code (1992);
- EN AW 1050 aluminium alloy, known as pure aluminium, which is characterised by a high percentage of aluminium (about 99.50%) and a limited conventional yield stress $f_{0.2}$, other than a significant ultimate elongation. Thanks to appropriate heat treatment processes both a further reduction of the yielding strength (up to 17 MPa) and an increase of the ultimate strain (about 40%) of the base material is achieved, allowing for the application of

devices made of this material to be used as an alternative to systems realised with low-yield steel in the passive seismic control of structures.

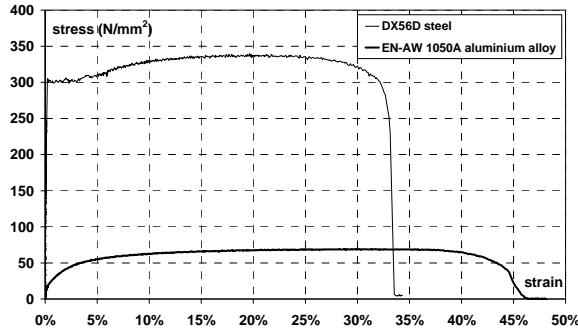


Figure 10. Comparison between curves of metallic materials used for shear panels.

On the basis of the above formulations and considering the use of the two selected metallic materials, the panel dimensions have been determined as $b=600$ mm and $d=2400$ mm, with a thickness t equal to 1.15 and 5 mm for steel and aluminium panels, respectively. It is important to observe that, since panels have a b/d ratio less than 0.8, which is the lower bound below which the development of a full tension field mechanism within the entire plate surface is not guaranteed (CSA, 2001), the insertion of appropriate stiffeners has been foreseen. In particular open rectangular shaped stiffeners having height of 100 mm and thickness of 4 mm have been located along the whole base of the panel on both its sides. As a consequence, the panel has been subdivided into six sub-elements with $b = 600$ mm and $d = 400$ mm. The single sub-panels have been connected among them and with the external frame by means of 8.8 steel grade M14 bolts having pitch of 50 mm and distance from the plate edges equal to 25 mm.

In a subsequent study phase, aiming at evaluating correctly all the main parameters conditioning the systems performance, a sophisticated FEM model through the ABAQUS non linear calculation software (Hibbitt et al., 2004) has been implemented. The thin plates, which have been modelled with shell elements having four nodes and reduced integration (type S4R) have been collocated within a supporting steel frame composed of three beams (upper, intermediate and lower) and two columns made of coupled channel profiles having height of 200 mm and made of S275 steel. In the numerical model the stiffening effect provided by intermediate ribs has been taken into account by assigning a corresponding increase of the panel thickness in the contact zones, where the thickness of stiffeners has been summed to the plate one. The panel-to-frame connections have been modelled by considering that no slip among parts occurs. This has been implemented in the program by using the internal constraint type TIE. Then, on the basis of preliminary mesh sensibility studies, fi-

nite elements with squared shape and side length of 20 mm have been used. In this way the best compromise between elaboration time and accuracy of obtained results has been achieved. On the basis of previous numerical studies, the effect of geometrical imperfections has been considered in the FEM model by assuming an initial configuration of the panel according to the deformed shape corresponding to the first eigenvalue. The amplitude of such an out-of-plane deformed configuration has been conventionally assumed to 1/1000 of the total panel height, equal to 2.4 mm. The lateral load has been applied to the top beam of the supporting steel frame and the system response has been directly obtained by means of the modified Riks algorithm.

Test results in terms of both deformed shape and stress state change related to the more significant displacement levels attained during the performed analyses have been represented in Figures 11 and 12 for steel and pure aluminium shear panels, respectively. In these figures the effective constraining action exerted by stiffeners is visible, they being able to confine buckling phenomena within single sub-panels.

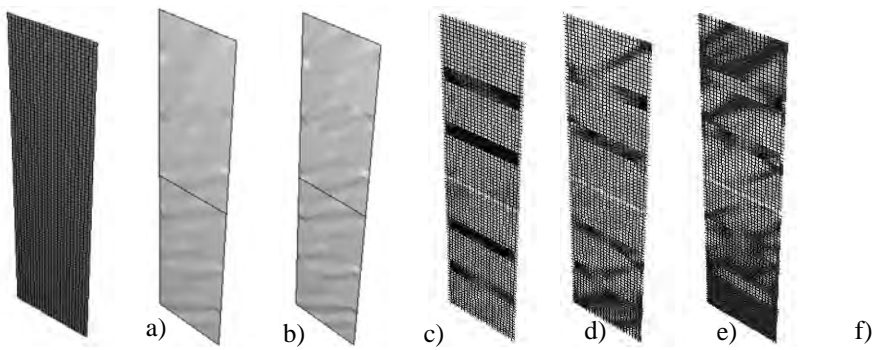


Figure 11. Meshed model (a), deformed shape at $\Delta=80$ mm (b) and $\Delta=150$ mm (c) and stress state corresponding to 30% (d), 65% (e) and 85% (f) of the maximum strength of the steel shear panel.

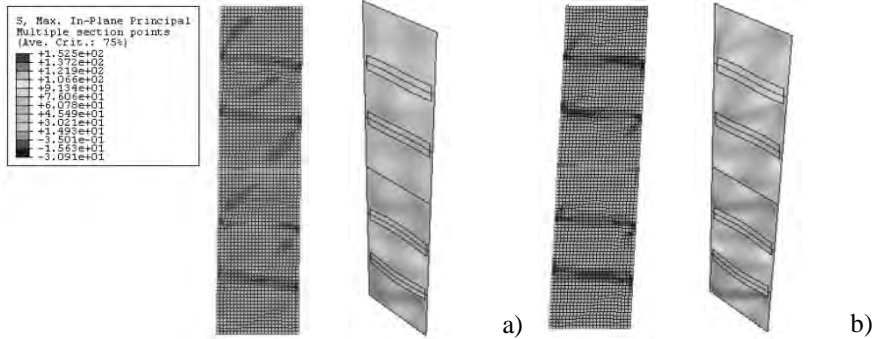


Figure 12. Stress state and deformed shape corresponding to the attainment of 73% (amplification factor = 5) (a) and of 92% (amplification factor = 1) (b) of the maximum pure aluminium shear panel strength.

The numerical response of analysed shear panels is illustrated in Figure 13 in the lateral force (F) – applied displacement (s) plane.

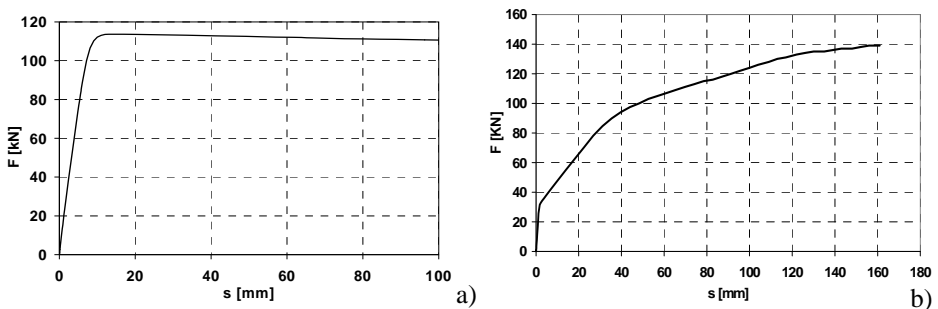


Figure 13. Numerical response of steel (a) and pure aluminium (b) shear panels.

For the sake of comparison, in Figure 14 the numerical response of steel shear panels under lateral loads is combined with the one of the original RC structure, which has been deduced under experimental way, in the spectral acceleration – spectral displacement plane and then compared with the design capacity curve of the retrofitted structure.

From the comparison it is apparent that a good agreement among curves is detected. In particular, the same level of spectral acceleration is detected, whereas a slight difference in terms of fundamental period is noticed. Such a discrepancy is due to the slip between added devices and the RC frame, which has not been considered in the performed numerical analyses and that can be taken into account by implementing a global numerical model of the retrofitted structure.

In order to confirm the validity of the proposed design solution, as well as for evaluating the possible problems related to the interaction between the seismic devices and the base module, the global analysis of the upgraded RC structure has been performed by means of the SAP2000 analysis software (CSI, Inc., 2004) (Fig. 15a).

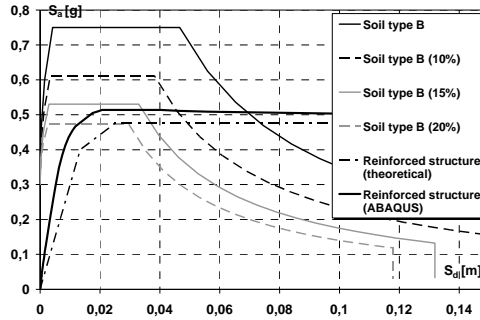


Figure 14. Comparison between numerical and theoretical design curves for the RC structure upgraded with steel shear panels.

Subsequently, metal shear panels have been directly inserted within an external steel frame on both sides of the structure at the first floor. Frame members, which have been designed in order to remain elastic under the maximum loads generated by the tension field mechanism developed into plates, have been represented with beam elements, whereas shear panels have been modelled according to the strip model theory, considering for each shear wall field ten trusses connected to the frame members through pinned joints and inclined of 45° in the same direction of the main tensile stresses (Fig. 15b).

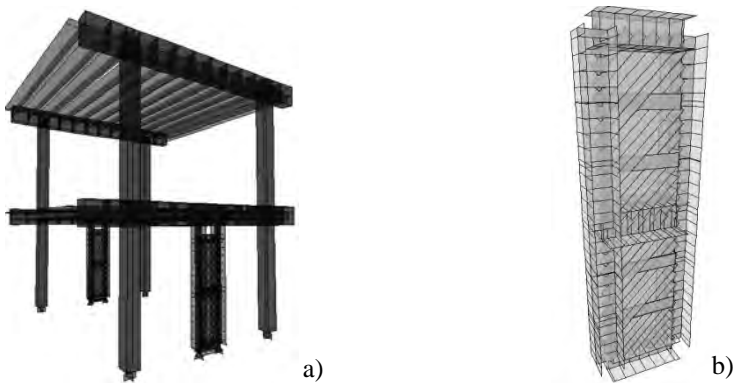


Figure 15. Global numerical model of the retrofitted RC structure (a) and modelling of the metal shear wall (b).

Moreover, analogously to the previous analysis, aiming at guaranteeing the correctness of the aspect ratio b/d of the panels, an intermediate beam has been inserted in the shear wall system, it being represented by UPN240 coupled profiles pin-joined to the frame columns.

The response of the bare RC structure, which has been preventively determined on the basis of the preliminary experimental cyclic test, has been numerically reproduced by introducing reductive coefficients of both the flexural and shear capacity of the RC members accounting for their damaging effects due to the execution of the experimental test based on the use of SMAs bracings. In particular, a modification of the reductive coefficients given by the new seismic Italian code (M. D., 2008) for deteriorated RC columns (from 0.5 to 0.4) has been done. The effectiveness of this approach has been confirmed by a very well correspondence between the experimental dynamic behaviour of the building and the numerical one, as it is reported in (Formisano, 2007).

Subsequently, the capacity curve of the upgraded structure has been achieved, as reported in Figure 16, where the response based on the use of steel panels has been represented, it being more close to the theoretical curve drawn from the application of the seismic retrofitting methodology than the ABAQUS one.

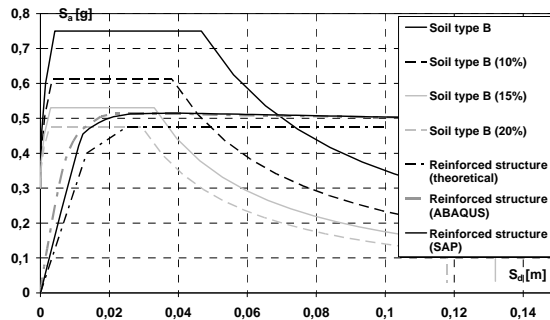


Figure 16. Comparison between the theoretical design curve and the numerical ones (SAP 2000 and ABAQUS) for RC structure equipped with steel shear walls.

In Figure 17 the design of the proposed final solution is reported. The frame columns have been connected directly to the foundation beam by means of M16 threaded bars and UPN 220 profiles, which have been opportunely stiffened through steel plates.

In addition, in order to allow for the transfer of the forces absorbed by the panels (significantly larger than the resistance of the original structure) to the first level RC beam, its jacketing by means of two coupled UPN200 profiles and threaded bars has been carried out.

The illustration of the retrofitting interventions has been reported in Figure 18, where both steel and pure aluminium shear panels have been inserted within the supporting steel frame.

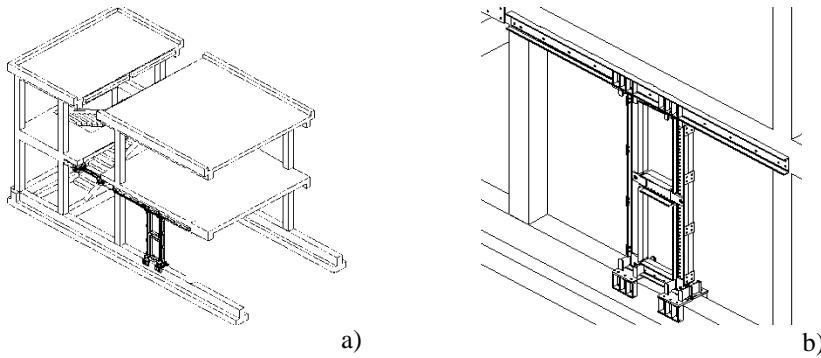


Figure 17. Global view of the upgraded structure (a) and zoom of the proposed intervention (b).

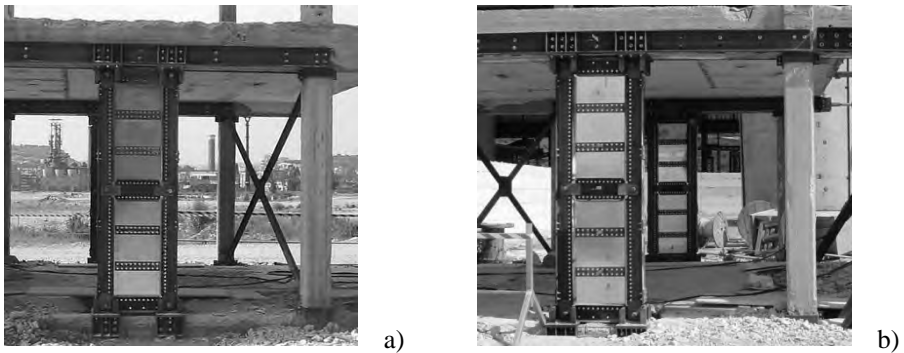


Figure 18. Global view of the structure retrofitted by means of steel (a) and aluminium (b) shear panels.

Once the insertion of the metal shear panels within the base structure has been done, two experimental cyclic tests have been performed. In both cases a cyclic loading history under quasi-static conditions has been applied (Fig. 19).

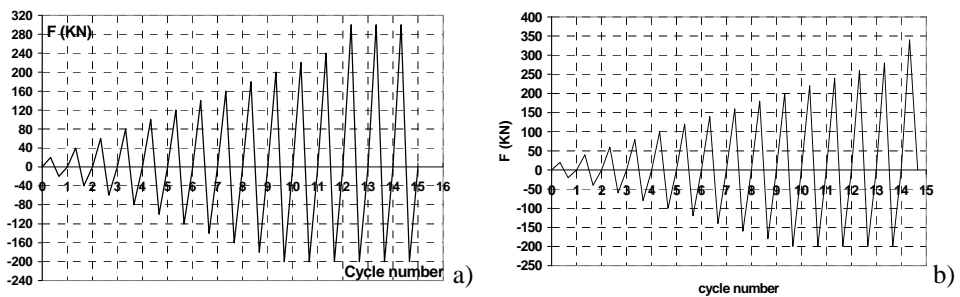


Figure 19. Cyclic loading protocol used in the test based on the use of steel (a) and aluminium (b) shear panels.

The result of the experimental tests in terms of applied force versus the first level displacement envelope curve is depicted in Figure 20a, where the comparison between the behaviour of the structure retrofitted with steel and aluminium shear panels with respect to the bare one is done. The response of the retrofitted structures is significantly improved, showing an increase of both initial stiffness (about two times) and ultimate strength (10 and 11.5 times with steel and aluminium panels, respectively). Also the deformation capacity of the structure appears to be very large, without the involvement of any brittle collapse mode up to a deformation amplitude corresponding to an inter-storey drift greater than 3.5% and 6.5% when steel and aluminium panels have been used, respectively. However it is evident as in both cases a combined dissipative mechanism between plastic hinges in the beam-to-column joint of the RC frame and plastic deformation of tensile diagonals of the applied shear panels occurs. A global view of the deformed shape of tested devices at the end of the loading process is shown in Figures 20b and c.

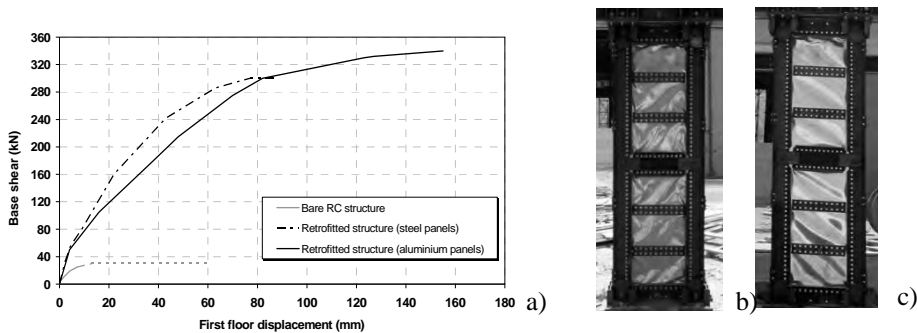


Figure 20. Comparison among envelope curves (a) and final deformed shape of tested steel (b) and aluminium (c) shear panels.

On the other hand, from the comparison between shear panels in terms of cyclic behaviour (Fig. 21), it can be noted that, while the maximum strength of the two systems is very similar, the hysteretic cycles obtained using aluminium panels are decidedly larger than the ones related to steel plates, the former evidencing a better dissipative behaviour.

Such a condition occurs for two main reasons:

- 1) for the same applied load the displacement of the structure strengthened with aluminium panels is greater in comparison to the one of the structure endowed with steel plates.
- 2) the slenderness of shear panels is smaller in case of aluminium.

In conclusion, it should be observed that the dissipation capacity of the structure retrofitted with aluminium shear panels is more satisfactory than the one endowed with steel plates, due to the excellent hysteretic characteristics of the used aluminium alloy. For this reason, steel shear panels can be considered

as strengthening and stiffening devices of existing structures, whereas the pure aluminium ones are also able to improve their ductile behaviour.

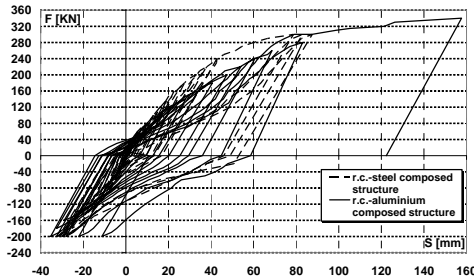


Figure 21. Comparison between experimental test results in terms of cyclic behaviour.

In the second stage of the third task, on the basis of the results obtained from the ILVA-IDEM research project, the design of the seismic retrofitting with steel shear panels of an existing irregular Greek building has been carried out.

The building under study, which is known as Koletti building, is located in Athens and is used by the National Telecommunications Organization for telecommunication network operations. It was erected in 1979 and was conceived as a strategic building, which should remain in the elastic range under strong seismic events, according to the Greek seismic code in force at that time (Vayas et al., 2006).

The building was realised with reinforced concrete frames located in two plane directions and developed on two storeys below ground floor, having a total height of 8.25 m, and six levels above ground floor, with a total height of 26.50 m. In addition, a 20 m high steel tower was positioned on the top of the building. A global view of the building is shown in Figure 22-a. The structure is shaped according to a rectangular layout of about 41 x 33 m, which is not the same above the third floor, so producing the structural irregularities shown in Figure 22-b and 22-c.

The constructional material was a concrete C16/20 with reinforcing steel bars having yield stress of 420 MPa; only for the members of the tower the S235JR steel was used.

The finite element model of the building has been implemented by the SAP2000 Advanced Version 9.0.3 analysis software (CSI, Inc., 2004). Beam elements were used to represent beams, columns and the tower members, whereas slabs and walls of the basements were modelled with shell elements.

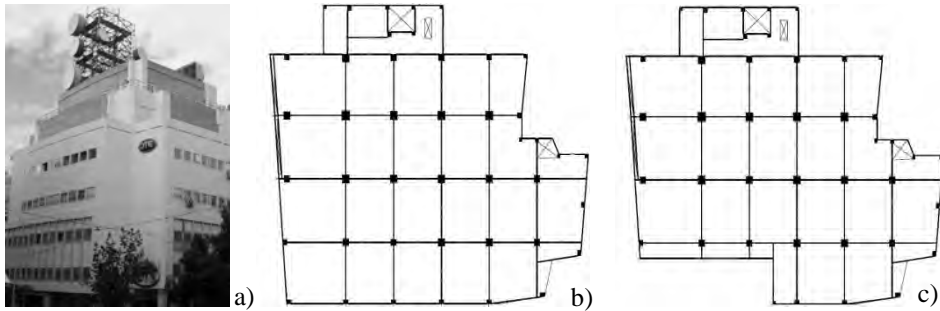


Figure 22. The Koletti building in Athens: external view of the building (a), plan view of the 1st and 2nd (b) and the 4th (c) floor.

Firstly, both the tower and the underground levels were included in the structural model (Fig. 23a). Then, since it was proved that the tower did not affect the dynamic behaviour of the structure and the underground floors were significantly rigid compared to the rest of the structure, for the sake of simplicity these two parts were excluded by the final structural model (Fig. 23b).

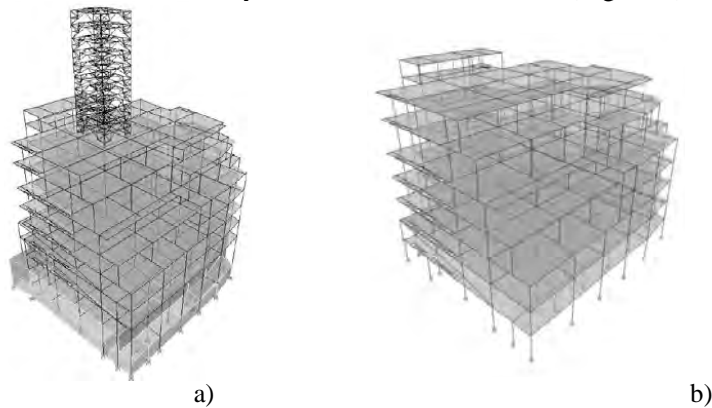


Figure 23. Complete (a) and simplified (b) FEM model of the Koletti building.

Materials properties have been considered according to the above mentioned values and the permanent and live loads applied at each storey are reported in (Vayas et al., 2006). The seismic actions have been computed according to EC8 and Greek seismic regulations. In particular, lateral forces have been applied in both plane directions proportionally to the first vibration mode. Plastic hinges assigned to beam elements have been defined according to the ATC-40 provisions (ATC 40, 1996). In the modal analysis of the structure seismic masses have been concentrated at each node starting from the applied vertical loads. The modal analysis has provided a first vibration mode with a period of 1.53 sec, it resulting greater than 0.90 sec, which is the period obtained from applying the relationship given by Eurocode 8 for regular struc-

tures (EN 1998-1-1, 2005). The effect of the structural irregularities is evident when analysing the sum of the modal participating mass ratio, both of translational and rotational type. From the achieved results, it is apparent that for the selected building, 8 modes are necessary to activate about the 85% of the structural masses. The deformed shape of the building related to the first and the second vibration mode, respectively, is depicted in Figure 24. In particular, for the first vibration mode, the displacements about Y direction are predominant, whereas for the second one the structure basically moves about the X direction. However, in both cases, as the rotational participating mass related to the second mode is higher than the one of the third mode, a coupling in terms of displacements and rotations is visible.

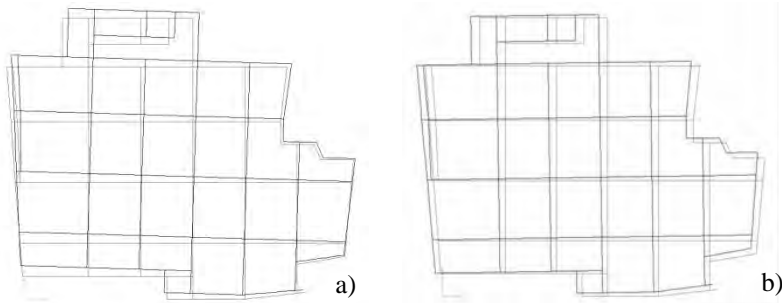


Figure 24. First (a) and second (b) vibration mode of the bare building.

Aiming at assessing the behaviour of the building under horizontal forces, preliminary nonlinear static analyses have been carried out on the bare RC structure. In particular, since the building is irregular, four different analyses (+X, -X, +Y, -Y) were developed. The relevant results are represented in the shear – displacement plane, providing the global structural response (Fig. 25).

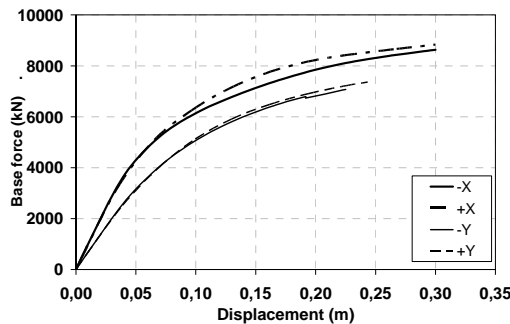


Figure 25. Pushover analyses on the bare RC building.

In the analysis about the X direction, the collapse occurred due to the formation of plastic hinges corresponding to the Life Safety (LS) level in the upper

storeys columns (Fig. 26-a). Conversely, about Y direction, the Collapse Prevention (CP) level, corresponding to the maximum plastic hinge rotation type D, is attained (Fig. 26-b).

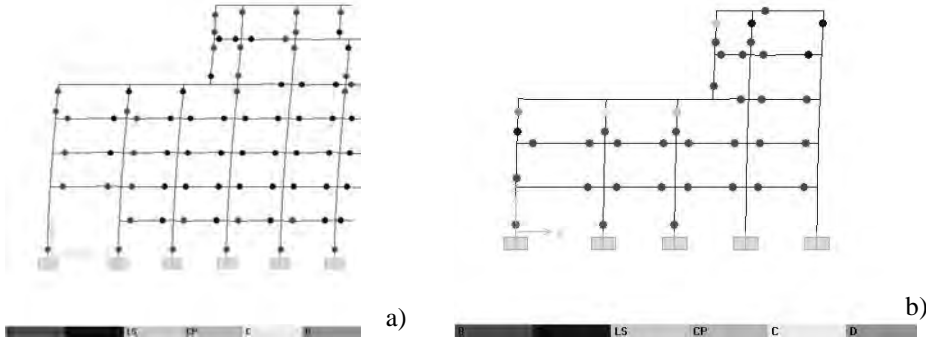


Figure 26. Pushover analyses on the bare RC building: collapse mode about direction X (a) and Y (b).

In order to define the target displacement for the retrofitted structure, the displacement corresponding to the attainment of the first plastic hinge at the IO-LS level has been determined for every analysis. Therefore, the procedure reported for the Bagnoli building has been herein extended aiming at plotting the design curves for the retrofitted structure. For the sake of example, the retrofitting design curves, which are obtained by fixing a target displacement corresponding to the Life Safety (LS) level, equal to about 7 cm in both plane directions, are illustrated in Figure 27 with reference to directions +X and +Y. The maximum values of the shear panel strength V_p and stiffness K_p derived from the four performed analyses are $V_p = 3708$ kN and 3497 kN and $K_p = 167$ kN/m and 110 kN/m in direction X and Y, respectively.

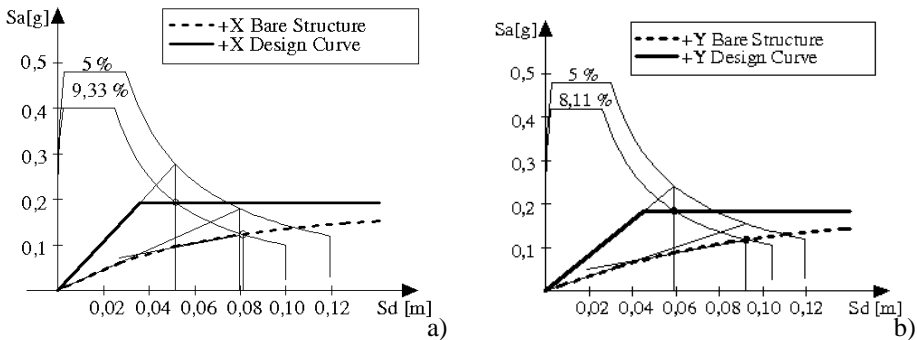


Figure 27. Retrofitting design curves for +X (a) and +Y (b) direction.

In order to define the panel geometry at each structure floor, it can be assumed that the base shear contribution required to shear panels can be distributed along the building depth according to the first vibration mode shape.

Once the requests from retrofitting are known, the design of devices has been done according to strength and stiffness, on the basis of eq. (3) and (4). It has been observed that, considering that the panel strength and stiffness depend on both the thickness and the width of the plate, for the case under study, the panel design is conditioned by the stiffness requirement rather than by the strength one. Also, it has been observed that the best distribution of panels within the building is obtained when their width is fixed and the thickness is calculated accordingly. In fact, in this way, 10 shear panels in both plane directions can be applied in order to partially fill, due to architectural requirements, a remarkable number of bays of the building. In particular, by using the S235JR mild steel and by fixing a total panel width of 16.50 m (ten panels having width of 1.65 m) and 13.00 m (ten panels having width of 1.30 m), respectively, considering also that the total depth of steel shear panels (d) is defined at each floor by subtracting the RC beam depth to the whole inter-story height, the thickness of panels has been determined at each level, leading to the values reported in Table 2.

Table 2. The panels thickness resulting from eq. (3).

Floor	d	t (dir. X)	t (dir. Y)
	(m)	(mm)	(mm)
8	2.10	3.3	3.9
7	3.20	5.0	6.0
6	4.45	7.0	8.3
5	3.20	5.0	6.0
4	3.20	5.0	6.0
3	3.20	5.0	6.0
2	3.20	5.0	6.0
1	3.20	5.0	6.0

Hence, the shape ratios (b/d) of each panel have been calculated in order to check if these values are comprised between the lower (0.8) and the upper (2.5) limits established by the Canadian code (CSA, 2001). When this ratio was lower than 0.8, an intermediate beams has been introduced in the steel frame used to contain the plates, according to previous studies (Formisano et al., 2007). So, each panel field has been subdivided into two parts, except than at the sixth floor, where the shear panels have been configured as three different sub-parts. Consequently, in the developed numerical model (CSI, Inc., 2004), the steel plates, which are modelled by trusses inclined of 45° as the main tensile stresses, are connected to UPN300 profiles of the external steel frame pro-

portioned to remain elastic under the maximum loads of the developed tension field mechanism. Some views of the retrofitted building are given in Figure 28.

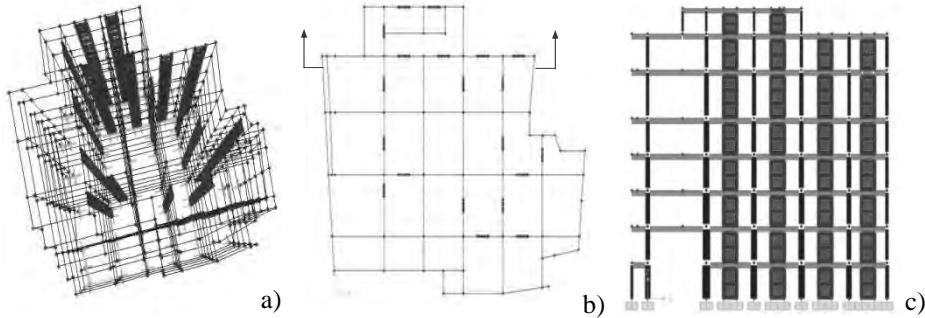


Figure 28. 3D bird view (a), plane lay-out at + 15 m (b) and vertical section (c) of the structure retrofitted with steel shear panels.

The modal analysis performed on the RC structure retrofitted with steel shear panels provided a first vibration period equal to 1.03 sec, which is a value significantly lower than the one obtained on the bare building (1.53 sec) and very close to the period (0.91 sec) achieved from EC8 for regular RC structures (EN 1998-1-1, 2005). It is worth noticing that, instead of the eight modes considered for the bare building, for the retrofitted structure only six modes are necessary to activate the 85% of the building mass. Also, the first three vibration modes are completely decoupled, confirming the structural regularity of the building.

Pushover tests on the retrofitted structure have been therefore performed both in the positive and negative X and Y directions. For the sake of example, the obtained retrofitted curves about the +X and +Y directions are reported in Figure 29.

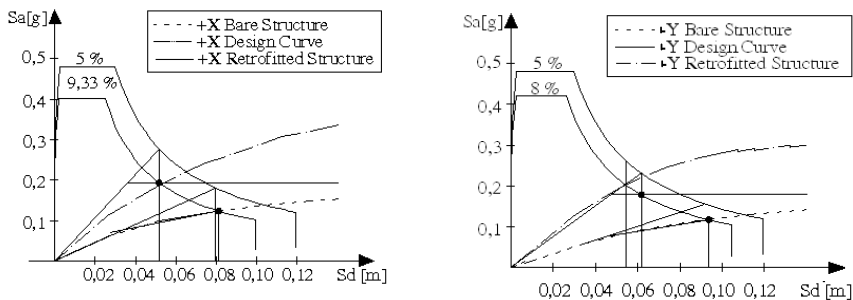


Figure 29. Results of the numerical pushover analyses on the retrofitted building.

It is apparent that, about the X direction, the retrofitted structure is perfectly able to fit the design spectral acceleration corresponding to the performance

point. In addition, the initial stiffness is the same required in the design phase. Instead, for large displacements, due to the panel over-strength, the structural capacity is greater than the design requirements.

In the whole, the obtained results are very satisfactory, proving the effectiveness of the proposed intervention as well as of the applied design methodology.

Tests and analysis on dissipative pure aluminium shear panels

General

The main purpose of this study consisted in the investigation of the structural response of dissipative pure aluminium shear panels, proposed in both a “Full bay” and a “Bracing Type” configuration. The proposed systems belong to the class of low yield shear panels that have been mainly used in Japan by employing a low yield steel (Nakashima et al., 1994; Nakashima, 1995; Nakashima et al., 1995; Katayama et al., 2000).

On the other hand, this type of material is not produced and commercialised in the European market and researches of alternative solutions were carried out. On this basis, the AW1050A aluminium alloy, almost a pure aluminium, has been proposed by the authors as base material. Compared to both conventional steels and other alloys (Tab. 3), this type of material is nominally characterized by both low conventional yield strength and high ductility.

Table 3. Nominal mechanical features of low yield stress point materials.

<i>Material</i>	$f_{0.2}$ [MPa]	f_u [MPa]	ϵ_u [%]	E [MPa]	$E/f_{0.2}$	$\alpha=f_u/f_{0.2}$
Standard Pure Aluminium (EN-AW 1099A)	15-20	40-50	40-50	70000	3500-4666	2.66-3.3
Almost Pure Aluminium (AW 1050)	30-70	70-100	20-40	70000	1000-2333	1.42-2.33
5xxx Aluminium	75.2	203.6	12	70000	931	2.71
LYS steel	86	254	50	210000	2442	2.95
S235 Steel grade	235	360	25-30	210000	893.61	1.53

These peculiar mechanical features allow the studied panels to behave as sacrificial elements when they are installed into a surrounding primary structure so that they can dissipate energy during an earthquake as frame elements are still in the elastic field. However, as it is very difficult to obtain by the industrial manufacturer a pure aluminium whose impurities content is zero and whose elastic mechanical features are not increased by possible hardening ef-

fects (desired or not desired!), it has been important to apply to the proposed material a proper treatment able to lowering the yielding stress and to increase the available ductility (Fig. 30).

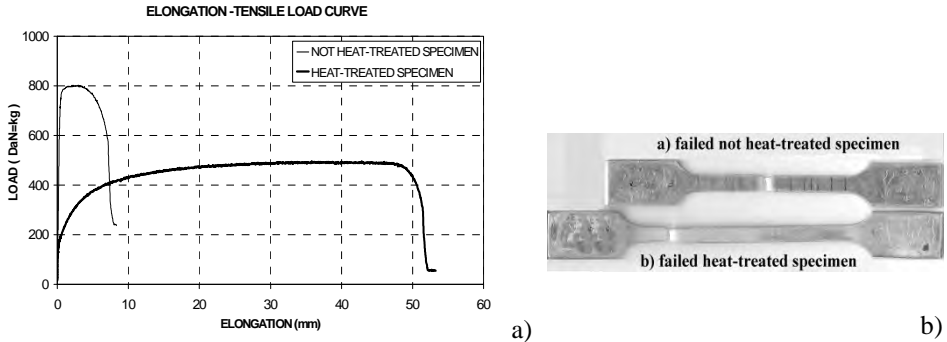


Figure 30. Comparison between heat treated and not heat treated aluminium specimens: (a) Load-elongation curves and (b) specimens aspect after failure

The employment of such a material represents one of the first applications in the civil engineering field and its properties needed to be deeply investigated (De Matteis et al., 2009). In particular, topics related to the material use under monotonic and cyclic actions, under static and dynamic forces, have been considered as worthy of being examined by experimental tests. On the basis of these tests, a careful material modelling has been implemented in order to implicate it in calibration processes of sophisticated numerical models (Brando et al., 2011).

Experimental tests

In a first stage, the research has been focused on the completion of a previous activity aimed to investigate the structural performance of pure aluminium shear panel in a full bay configuration (Panico, 2003; De Matteis et al., 2007a, 2007b, 2007c). Experimental tests were carried out on panel specimens measuring 1500 by 1000 mm and having thickness of 5 mm. They were stiffened with longitudinal and transversal ribs made with either open rectangular shaped stiffeners with a depth of 60 mm, obtained by the same sheeting used for the base shear plate, or steel channel shape. In the former case the stiffeners were connected to the base shear plate by a welding process while in the latter case bolted connections were used.

In the experimental programme, four different types of panel configurations were considered, presenting different geometry of the applied ribs (Fig. 31, where the adopted denomination for each panel is also represented). For panel type B, ribs were placed on both sides of the plate according to a square fields 500 mm of side length. Contrarily, panel configuration type F was stiffened with ribs alternatively placed on the two sides of the plate in order to obtain

square fields of 250 mm of side length. Panels with configuration type G and H were successively designed in order to overcome some drawbacks pointed out in the first four cyclic tests carried out on panels type B and F.

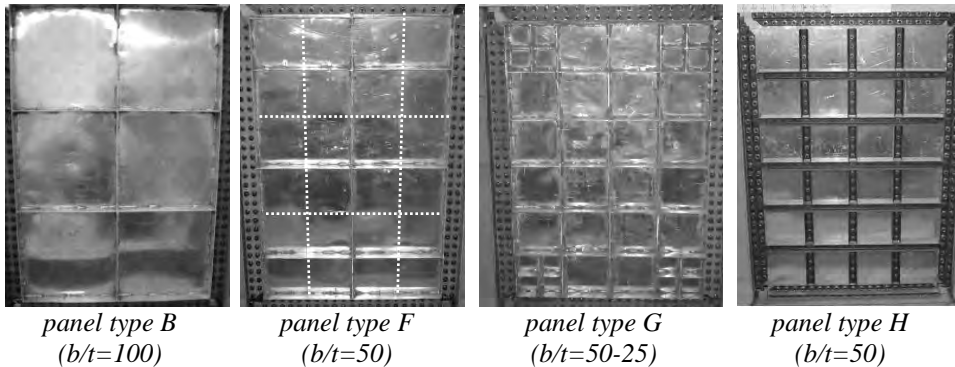


Figure 31. Tested Full Bay type pure aluminium shear panels.

As a consequence, the internal fields of the tested shear panels were characterised by different slenderness ratios, namely $b/t=100$ for panel type B and $b/t=50$ panel type F. Panel type G was characterized by $b/t=50$, but such a slenderness ratio was reduced to $b/t=25$ in the corners of the panels. Panel type H was characterized by $b/t=50$, having a configuration similar to panel type F, but it was ribbed by means of steel channel (UPN50). This choice arose from the necessity to eliminate the geometrical and mechanical imperfections induced by the welding process of stiffeners. The shear load on the panels was applied by means of an articulated steel frame composed by very rigid members and equipped with lateral out-of-plane braces (Fig. 32-a). The external load was applied at the top beam of the frame by means of a servo-hydraulic actuator (MTS System Corporation), characterised by a range of displacement of ± 250 mm and a load capacity of 500 kN in compression and 300 kN in tension. The actuator was connected to a very rigid lateral support steel frame used as reaction frame (Fig. 32-b). Testing specimens were connected to the loading steel frame by steel cover plates with friction high-strength grade 8.8 steel bolts, having a diameter of 14 mm and with a pitch of 50 mm.

The main results of the tests are represented by the relationship between the system reaction shear load and the applied lateral displacement. For each specimen such a relationship has been normalized, considering the average shear stress τ applied on the horizontal panel side, considering a nominal cross-section $A=B \cdot t=5000 \text{ mm}^2$, and the equivalent shear strain γ , evaluated as ratio between the applied displacement and the panel nominal depth $H=1500$ mm (Fig. 33).

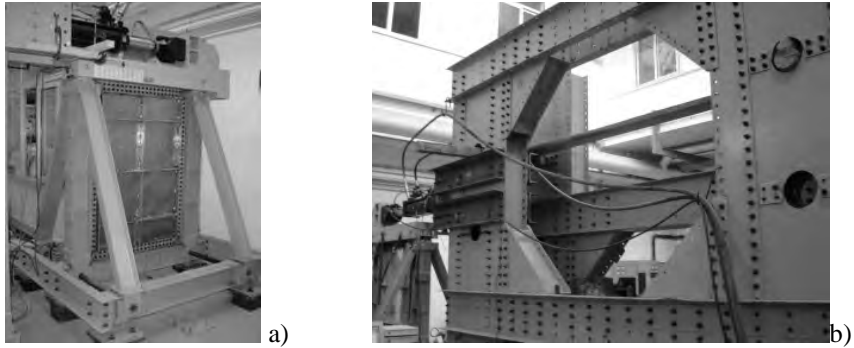


Figure 32. The testing apparatus for the Full Bay type pure aluminium shear panels

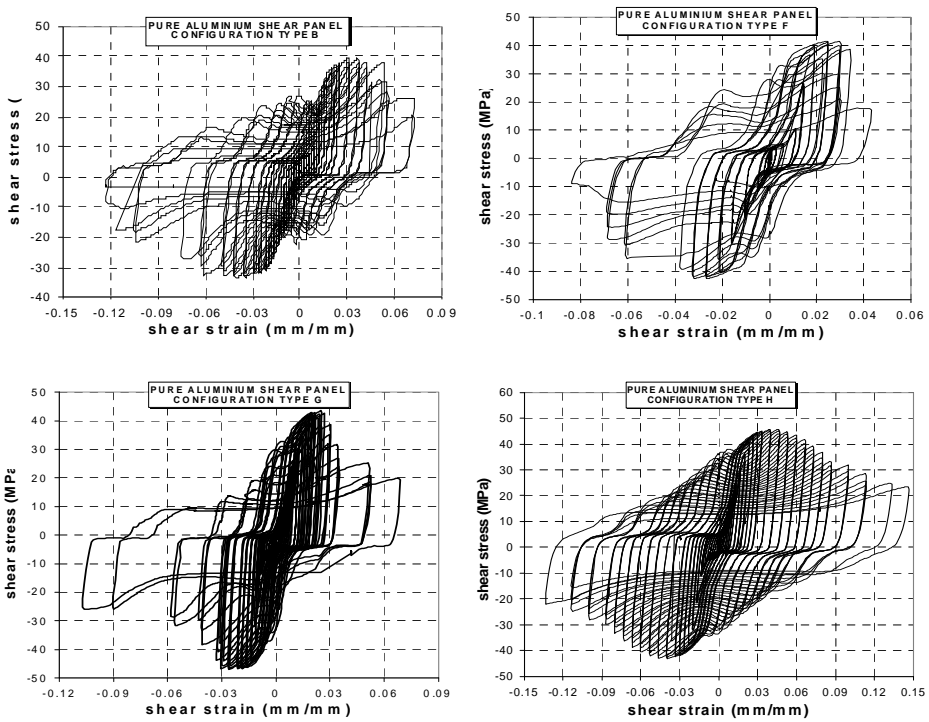


Figure 33. Hysteretic cycles provided by the tested full bay configurations.

The cyclic response of tested specimens has been also interpreted by considering three numerical parameters characterising the behaviour of the system in terms of maximum hardening ratio (τ_{\max}/τ_{02} with $\tau_{02}=f_{02}/\sqrt{3}$), secant shear stiffness (G_{sec}) and equivalent viscous damping factor (ζ_{eq}), as defined in both Figure 34 and equation (5).

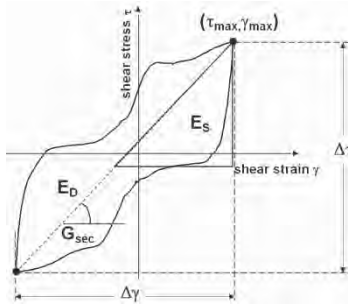


Figure 34. Definition of dissipated energy (E_d), equivalent viscous damping ratio (ζ_{eq}) and secant shear stiffness (G_{sec}).

$$E_d = \frac{1}{8} \Delta\tau \cdot \Delta\gamma$$

$$\zeta_{eq} = \frac{1}{4\pi} \frac{E_D}{E_S} \quad (5)$$

$$G_{sec} = \frac{\Delta\tau}{\Delta\gamma}$$

The experimental data were thus processed for each panel by drawing the $\tau_{max}/\tau_{02} - \Delta\gamma$, $G_{sec} - \Delta\gamma$ and $\zeta_{eq} - \Delta\gamma$ curves (Fig. 35 for panel type B and F and Fig. 36 for panel type G and H). In order to better emphasise the evolution of the system during the loading process, the cyclic behaviour of the tested panels has been furthermore divided in four different significant phases. The above phases have been characterised as in the following: phase 1: negligible buckling phenomena; phase 2: local buckling occurrence; phase 3: global buckling occurrence; phase 4: collapse phase.

A careful analysis of the hysteretic cycles provided by all the full bay type shear panels has shown that some slipping phenomena may occur for low shear strain values, thus limiting the performance of the systems. Moreover it was noted that each panel starts to exhibit its better dissipative behaviour only for high inter-story drift demands (6%:7%) with an equivalent viscous damping factor of around 30%. In order to increase the local deformation demand of shear panels for reduced inter-story drifts of the primary framed structure, exploiting the high ductility of the base material, the bracing type configuration of shear panel has been adopted (Fig. 38).

It is characterised by reduced dimensions of shear panels respect to the surrounding frame field, so to increase the ratio between the shear deformation of the panel and the developed inter-story drift.

Bracing Type Pure Aluminium Shear Panels (BTPASPs) have been therefore proposed as they may be more effectively used as passive protection device in both steel and reinforced concrete moment resisting frames (Brando, 2007; De Matteis et al., 2008a, 2008b; Brando, 2009; De Matteis et al., 2011).

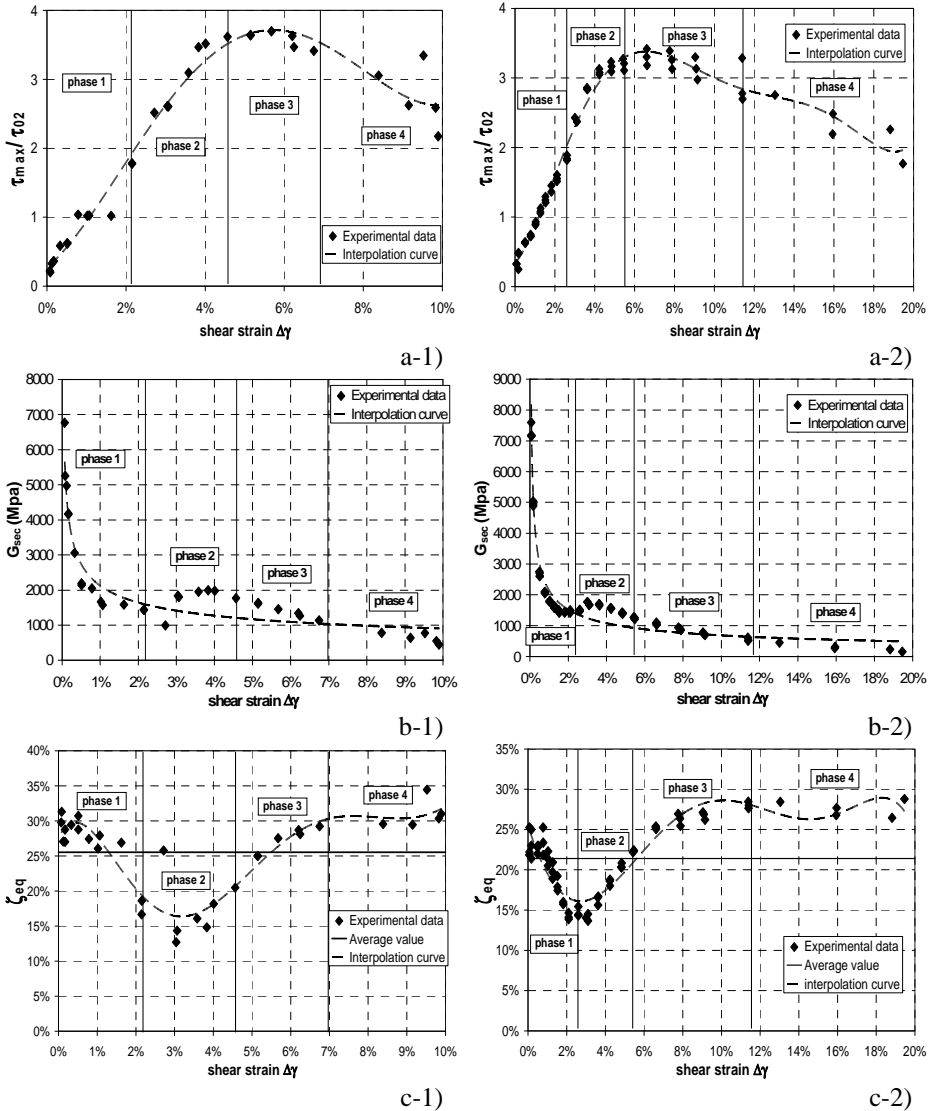
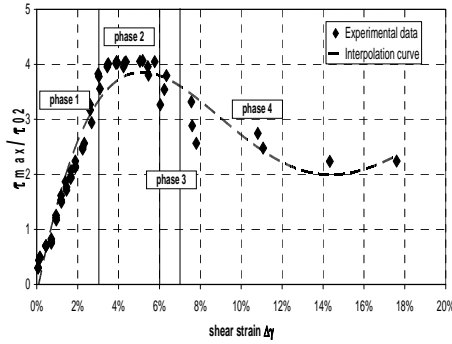


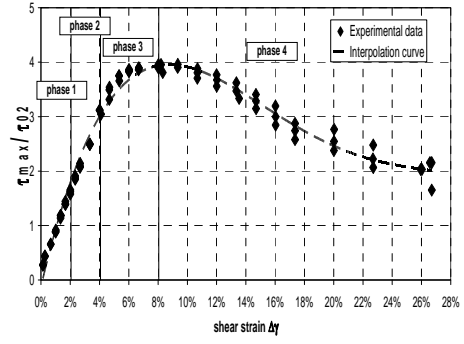
Figure 35. Cyclic performance of full bay shear panel type F (a-1, b-1, c-1) and type B (a-2, b-2, c-2)

These have been designed by fixing the spacing of the ribs according to the slenderness limit value provided by Eurocode 9 (2007) for girders with longitudinal and/or transversal web stiffeners, so that the elastic strength should not be eroded by buckling phenomena. In detail, with reference to rectangular panels whose flanges are parallel within an angle not greater than 10° , Eurocode 9 provides, for web with either rigid and non rigid transverse stiffeners at support only, the following design resistance (eq. 6):

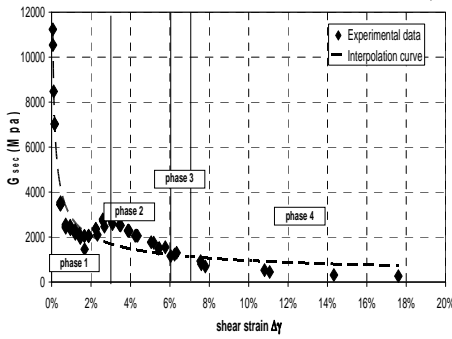
$$V_{Rd} = \rho_v \cdot t_w \cdot h_w \frac{f_0}{\sqrt{3} \cdot \gamma_{M1}} \tag{6}$$



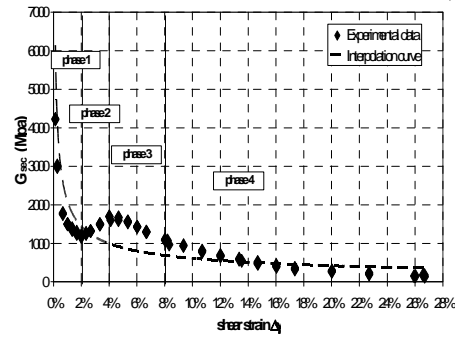
a-1)



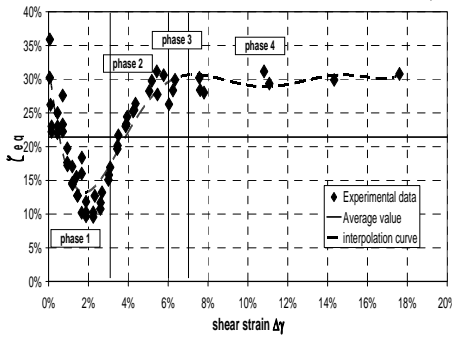
a-2)



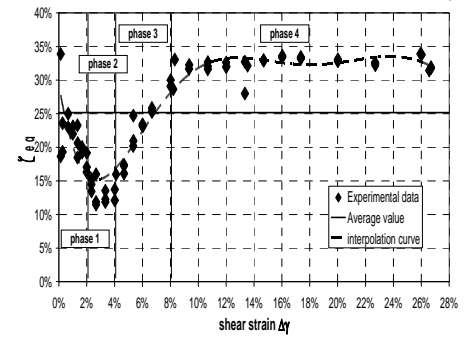
b-1)



b-2)



c-1)



c-2)

Figure 36. Cyclic performance of full bay shear panel type G (a-1, b-1, c-1) and type H (a-2, b-2, c-2).

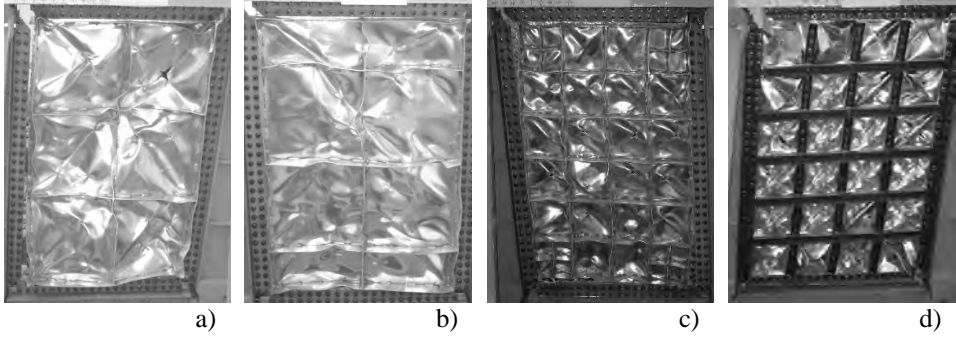


Figure 37. Collapse modes of the full bay panel “type B” (a), “type F” (b), “type G” (c) and “type H” (d).

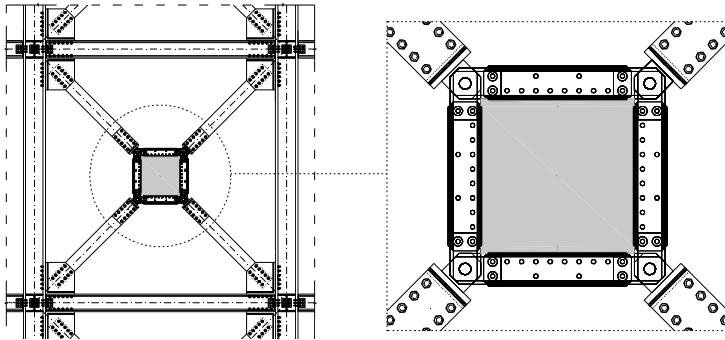


Figure 38. Bracing type shear panel configuration.

In which, according to Figure 39, t_w is the thickness of the web panel of the girder, h_w is the panel height, f_0 is the conventional yield strength, γ_{M1} is the safety factor and ρ_v is a factor for shear buckling which is obtained according to Table 4.

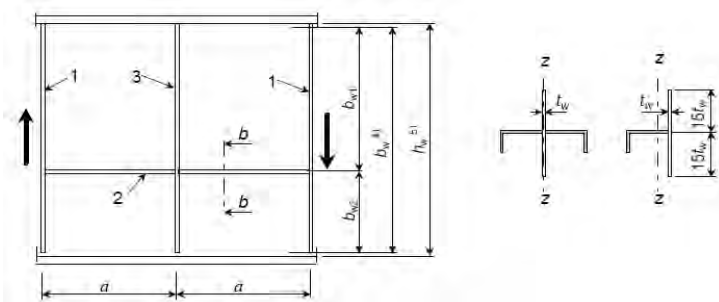


Figure 39. Web with transverse and longitudinal stiffeners (Eurocode 9, 2007).

Table 4. Factor ρ_v for shear buckling.

Ranges of λ_w	Rigid end post	Non rigid end post
$\lambda_w \leq 0.83/\eta$	η	η
$0.83/\eta < \lambda_w < 0.937$	$0.83/\lambda_w$	$0.83/\lambda_w$
$0.83/\eta < \lambda_w$	$2.3/(1.66 + \lambda_w)$	$0.83/\lambda_w$

In this table λ_w is the slenderness parameter expressed in equation (7), in which E is the modulus of elasticity of the base material, whereas the η factor, for which Eurocode 9 fixes a superior limit value of 1.2, is given as a function of the hardening ratio $\alpha = (f_{aw}/f_{ow})$ by the following expression (eq. 8):

$$\lambda_w = 0.35 \cdot \frac{b_w}{t_w} \cdot \sqrt{\frac{f_0}{E}} \quad (7)$$

$$\eta = 0.7 + 0.35 \cdot \frac{f_{aw}}{f_{ow}} \quad (8)$$

The condition that the slenderness parameter λ_w is inferior to the slenderness limit value given in equation (9) means that, in either cases of rigid and non rigid end stiffeners, no reduction of shear strength due to buckling can occur before the attainment of the elastic shear force, also taking into account a possible overstrength of the base material equal to 20%.

$$\bar{\lambda}_w = \frac{0.83}{\eta} \quad (9)$$

On the basis of the above design criteria, four shear panels to be used in a bracing type configuration have been obtained and, subsequently, tested. These, which henceforth will be indicate as “type 1”, “type 2”, “type 3” and “type 4”, are characterized by global dimensions of 500 by 500 mm and a plate thickness of 5 mm. They are equipped with welded rectangular-shaped ribs, equally placed on the two faces of the panels, whose depth is 60 mm and which are made of the same material and thickness of the basic plates (Fig. 40). The four specimens were inserted into a pin jointed steel framework and were linked to its channel elements along their edge by means of tightened steel bolts. The stiffeners arrangement has been chosen in such a way to have a slenderness ratio a_w/t_w equal to 100 (no intermediate stiffeners), 50, 33.3 and 25 for shear panel “type 1”, “type 2”, “type 3” and “type 4” respectively.

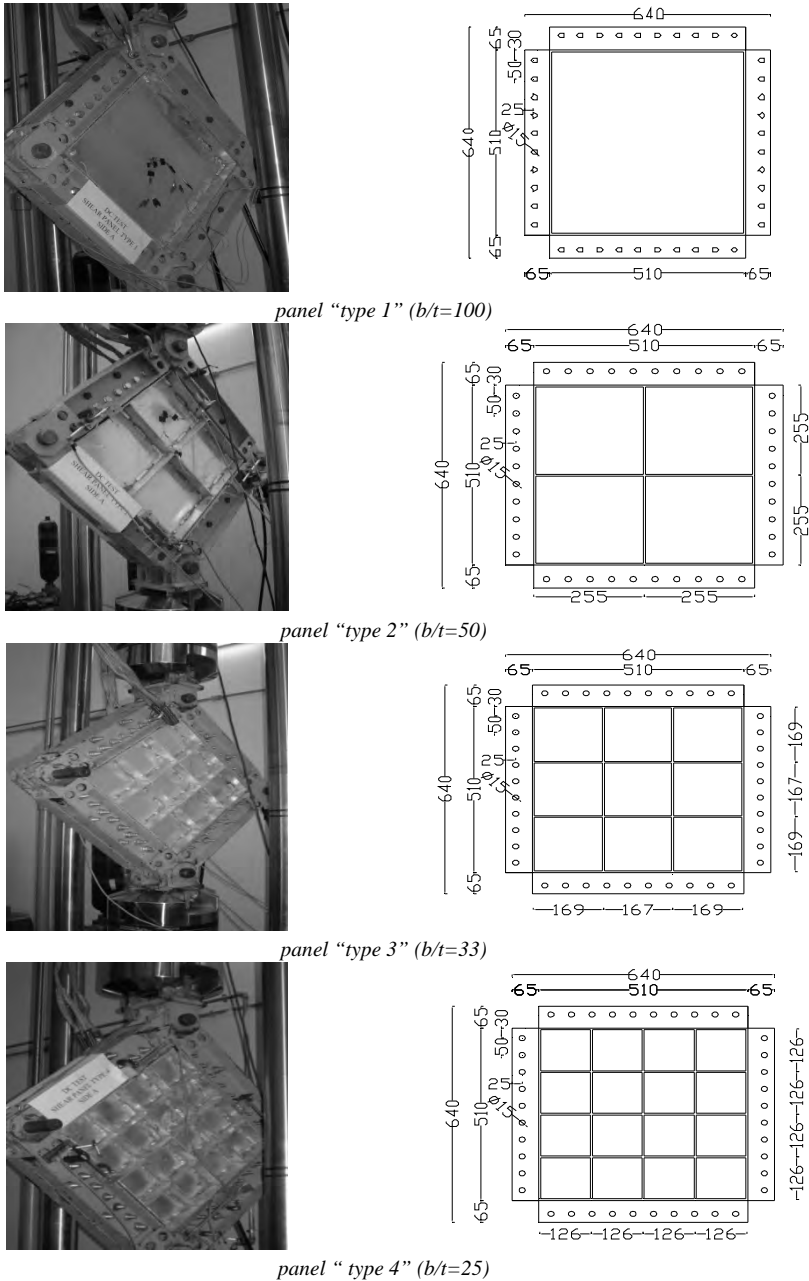


Figure 40. The tested pure aluminium bracing type shear panels configuration.

In order to evaluate the influence of the main geometrical parameters on the cyclic behaviour, four shear panel specimens characterised by different aspect ratio values have been experimentally tested at the laboratory of the University

of Naples “Federico II” by applying a diagonal cyclic loading procedure, according to the loading protocol given by ECCS-CECM (1985). On this purpose, a MTS810 universal machine, capable to carry out either load controlled ($\pm 500\text{kN}$) or displacement controlled ($\pm 75.0\text{mm}$) cyclic tests on specimens characterized by a height of almost 1.40m, has been used. When such a type of cyclic procedure is applied, test retrieves back a load history essentially based on some cycles in the elastic range and then on three cycle repetitions for progressively increasing displacement amplitudes, defined as integer multiples of v_y , which is the displacement corresponding to the attainment of yielding. In the case being, the conventional yielding tangential stress has been fixed on the basis of the conventional yielding tangential stress stated as in eq.(10).

$$\tau_y = \frac{f_{0.2}}{\sqrt{3}} = 10.39\text{MPa} \quad (10)$$

Such a stress value corresponds to a shear strain equal to $\gamma=0.04\%$. Thus, the diagonal displacement v_y corresponding to the attainment of yielding can be evaluate as about 0.5 mm. Since this value is very small, due to the intrinsic low yield of the base material, the first steps of the above procedure have been eliminated, while the other ones have been left unvaried, so that the adopted testing protocol for each panel type is the one shown in Figure 41-a, where the ordinate indicates the applied diagonal displacement on the top of the surrounding frame (Fig. 41-b).

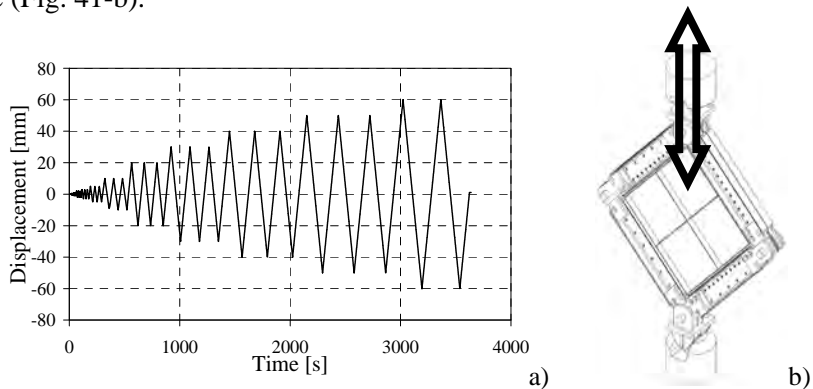


Figure 41. Applied displacement history (a) and loading scheme (b).

As a results of the performed tests, a careful analysis of the experimental evidences has been initially carried out in order to highlight the most important behavioural aspects of the tested devices. Three principal behavioural phases have been recognised. In the first any buckling phenomena did not occur and a pure shear resisting mechanism was developed. The analysis of the measurements of the strain gauges, arranged in the centre of each panel, retrieved back that the first buckling phenomena, arose for diagonal displacements v_{l-i} corre-

sponding to $v_{1-1}=\pm 2.00\text{mm}$, $v_{1-2}=\pm 5.00\text{ mm}$, $v_{1-3}=\pm 10.00\text{mm}$ and $v_{1-4}=\pm 20.00\text{mm}$ for panel “type 1”, “type 2”, “type 3” and “type 4” respectively.

These displacements can be considered as an upper limit under which panels exhibit the first behavioural phase. A detailed analysis of the initial phase of the tests gave back, in addition, information on the yielding achievement. In fact, considering a linear elastic behaviour of the base material with a Young’s modulus $E=66000\text{ MPa}$, it has been possible to fix a strain level corresponding to the attainment of the conventional yielding stress (18 Mpa) equal to (eq. 11):

$$\varepsilon_y = \frac{f_{0.2}}{E} = \frac{18}{66000} = 0.000272 \quad (11)$$

Such a strain value was achieved after that a diagonal displacement of 0.5mm was attained, this being the value of the elastic displacement (v_y) assumed to define the applied loading protocol discussed before. In Figure 42, panels configurations immediately after the attainment of v_{1-i} are shown. Initial swellings of the base plate starts to be visible along the diagonal direction, while the remaining parts of panel are not excessively distorted.

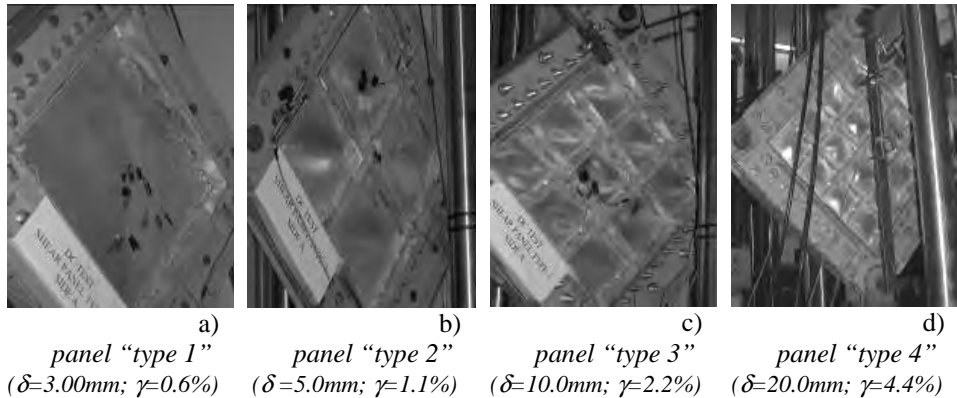


Figure 42. Experimental evidences: end of phase 1-first buckling occurring.

The second behavioural phase is characterized by the developing of tension field in each sub-panel which is determined by transversal and longitudinal stiffeners. For each panel it starts from the displacement v_{1-i} and ends when a displacement v_{2-i} , corresponding to which material failures arise, is attained. Figure 43 shows panels configuration for a diagonal displacement demand within the range $[v_{1-i}, v_{2-i}]$. Buckling waves along the diagonal directions of each sub-panel are evident and some secondary deformation modes may be also detected. For instance, it has been noted that in this phase each edge of the panel tends to move toward the opposite one, so to provoke the solicitation of the boundary connection system in the directions perpendicular to the frame members. This type of behaviour provoked a bending deformation of stiffeners

and the arising of secondary resisting mechanism such the one caused by stiffeners matching corresponding to the vertexes of the panel.

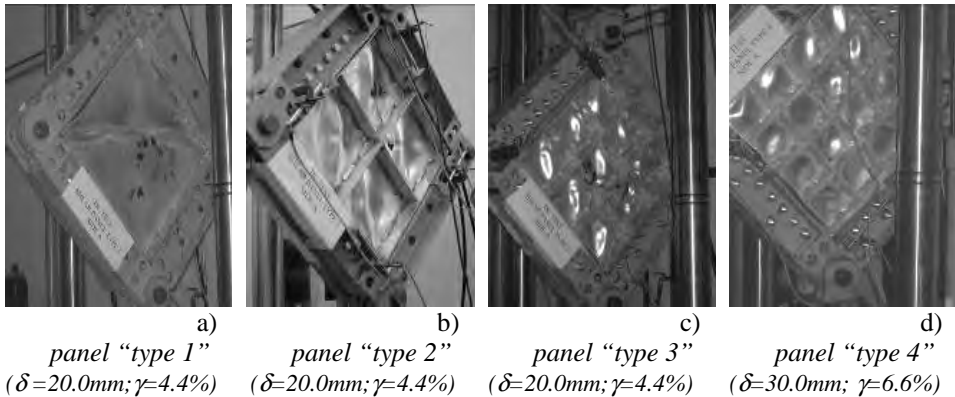


Figure 43. Experimental evidences: end of phase 2-tension field developing

For all the studied panels, it has been observed that first ruptures of material occurred corresponding to diagonal displacements equal to $v_{2-1} = v_{2-2} = v_{2-3} = v_{2-4} = 30.0$ mm. While for panel "type 1" a tearing of material was clearly revealed in the centre of the panel, at the intersection of diagonal tensile and compression bands, for panel "type 2" this rupture was less evident, but contemporarily to its arising, also boundary connections showed some crisis in terms of attaining of bearing resistance. On the other hand, panels "type 3" and "type 4" showed only failures corresponding to their connections with the external steel frame. This observation allowed to suppose that the collapse mode of the panel strongly depends on the number of transversal stiffeners, as, from one side, they increase the resisting shear area, whereas, on the other hand, they behave as an internal frame that limits the stress on the base plate by redistributing it on the external edges and therefore on the peripheral connection system.

In the third behavioural phase the above described collapse modes developed. Diagonal displacement amplitude ranged between ± 30.0 mm and ± 60.0 mm. For panels "type 1" and "type 2" large rips were concentrated on the centre of the sub-panels. Thus, a redistribution of stress toward the edge of the panel has been evidenced, with fractures placed in the perimeter of the plate corresponding to the external stiffeners system. For panel "type 3" and "type 4" breaking of the external connection system revealed to be more significant, with a detachment of the panel from the external frame that was more evident and quicker for panel "type 4" than panel "type 3". In Figure 44, the collapse mode of panels, registered for a diagonal displacement of 60 mm (shear strain equal to 11%) are shown.

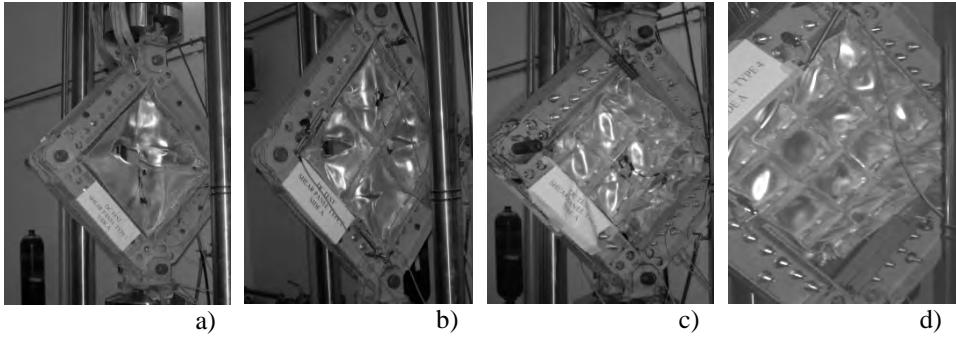


Figure 44. Collapse modes of panel “type 1” (a), “type 2” (b), “type 3” (c) and “type 4” (d).

In Figure 45 hysteretic cycles given back by tests, expressed in terms of diagonal force-diagonal displacement, are provided.

It should be noted that the four shear panels exhibited unexpected, but not so important, slipping phenomena for very small force levels which were probably due to the initial arrangement of the testing system.

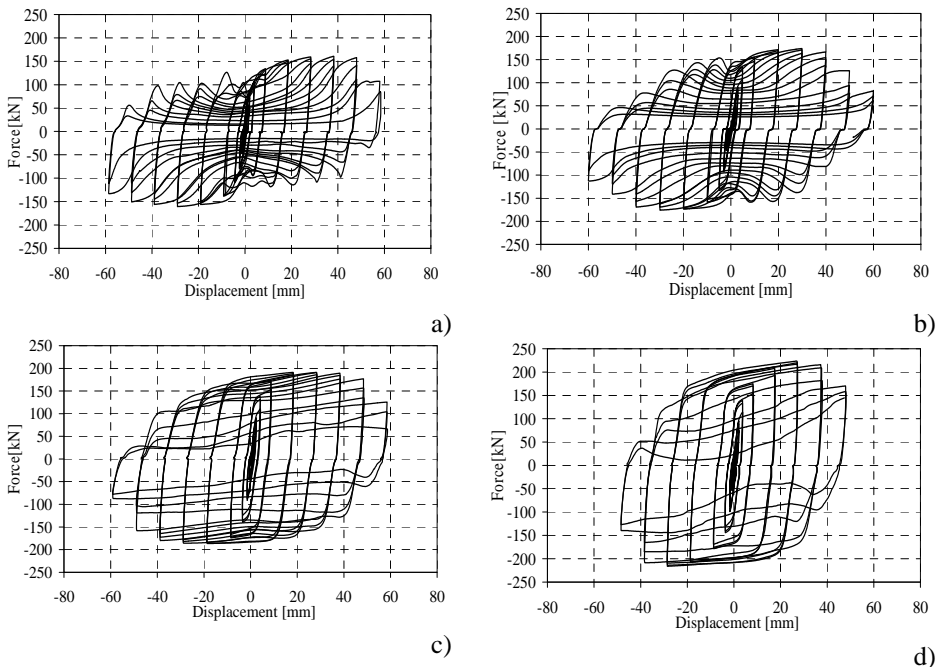


Figure 45. Hysteretic cycles: “type 1” (a), “type 2” (b), “type 3” (c) and “type 4” (d)

The registered cyclic behaviour appeared to be very attractive from the dissipative point of view due, on top of all, to the large ductility offered by the devices. However, it is evident that two different types of responses have been

obtained. The first, typical of panels usually classified as semi-compact and characterizing both shear panels “type 1” and “type 2”, returned hysteretic loops affected by pinching effects in the inelastic field. The latter, which characterized both shear panel “type 3” and “type 4”, allowed to have, despite of local buckling phenomena observed during tests, fat cycles and, therefore, the maximum dissipative capacity of the system exploited. Panels “type 3” and “type 4” can be therefore classified as compact, also in accordance with the fact that the ultimate shear strength did not result deteriorated with respect to the theoretical one offered by a pure shear resisting mechanism. Further consideration may be fruitfully obtained by the comparison of the studied panel types in terms of energy dissipation, hardening ratio, secant global stiffness and equivalent viscous damping ratio, according to the definition Figure 34. In Figure 46 and 47 these synthetic parameters, are expressed as a function of the applied shear strain value for semi-compact and compact shear panels respectively. In the same figures the interpolation curves of the above magnitudes, expressed by means of polynomial laws, are also depicted. In detail, as far as the semi-compact panels are concerned, shear panel “type 2” provided a better dissipative behaviour than panel “type 1”, due to both the larger cycles and resistant capacity, as it is detectable by the comparison carried out in terms of cumulated dissipated energy.

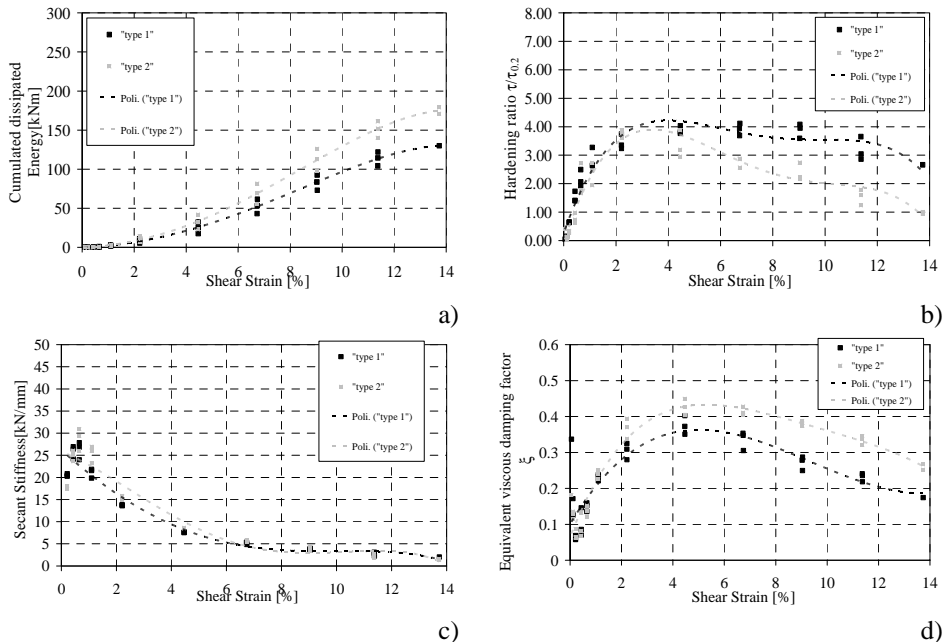


Figure 46. Results for semi-compact panels “type 1” and “type 2”: (a) cumulated dissipated energy; (b) hardening ratio; (c) secant shear stiffness and (d) equivalent viscous damping factor.

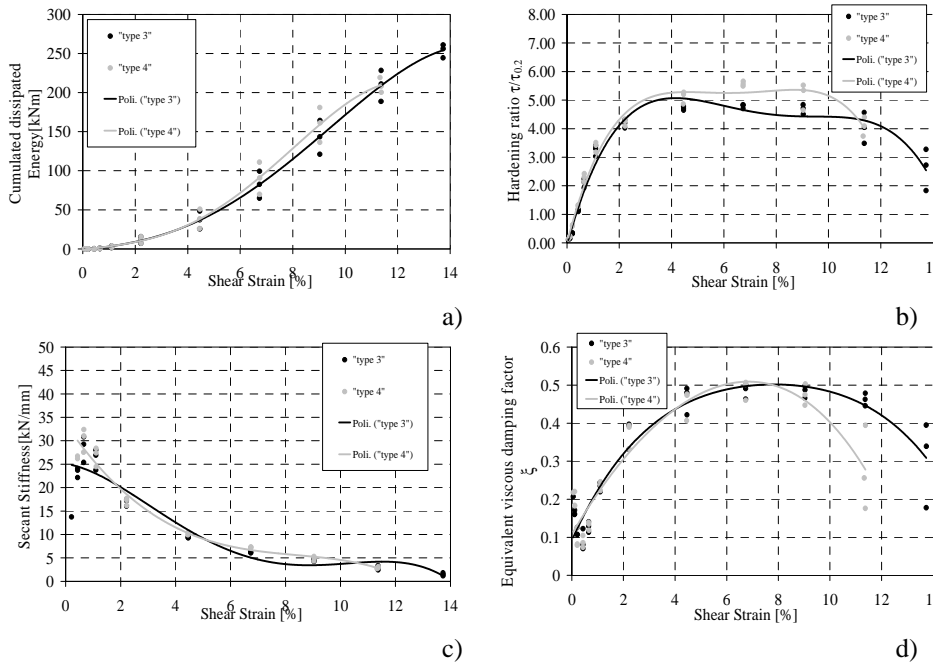


Figure 47. Results for semi-compact panels “type 3” and “type 4”: (a) cumulated dissipated energy; (b) hardening ratio; (c) secant shear stiffness and (d) equivalent viscous damping factor.

This is testified also by the higher equivalent viscous damping factor (45% versus 37%). However, panel configuration “type 1” exhibited a higher value at collapse of both the hardening ratio and the secant shear stiffness. This was mostly due to the influence provided by the perimeter connecting system. In fact, it has to be observed that panel “type 2” is characterized by higher resistant peaks of these magnitudes, which are correlated directly to the larger shear area and to a secondary resistant mechanism in which both the transversal and longitudinal intermediate ribs operate as a sort of framework axially stressed and working in parallel with the shear plate. It means that bolted connections are more stressed, anticipating their failure respect to shear panel configuration “type 1”. Obviously, a better performance of the proposed devices could be obtained by applying an improvement to the connection manufacture.

Comparison between shear panels “type 3” and “type 4” allows to state that the two panels are more or less characterized by the same type of performances in terms of cumulated dissipated energy, equivalent viscous damping factor and secant stiffness. They presented an important response from the dissipative point of view, giving back equivalent viscous damping factor equal to around 50%. Among the two panel typologies, the first results therefore the most convenient to be used as it require an inferior quantity of material to be employed.

The only differences may be observed for the comparison carried out in terms of hardening ratio which put in evidence that, due to a larger shear area, panel “type 4” presents a higher strength than panel “type 3”. This rebounds on the performances of the connecting system placed on the edges of the panels which is more stressed for panel “type 4”, this entailing a quicker decay of its strength for very high shear strength demands.

Numerical and analytical models

A detailed FEM numerical model of the studied bracing type shear panels has been implemented by means of the ABAQUS 6.5 (Hibbitt et al., 2004) non linear analysis software. The reliability of such a model has been proved by simulating the above cyclic tests and by comparing both the obtained experimental and numerical results. These models have been profitably used to check the stress states, the deformed shapes and the main resistant mechanisms of the analysed shear panel typology for different shear strain demands. Moreover, they allowed to develop the parametrical analysis carried out in third task of the current research. Details on the model, shown in Figure 48, are given in Brando et al. (2011).

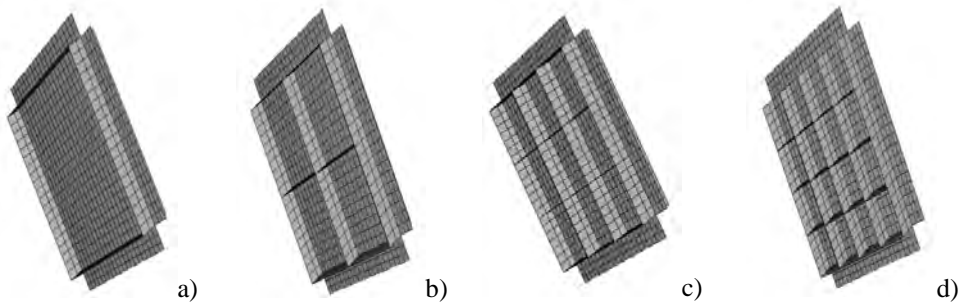


Figure 48. Geometrical model and adopted mesh: “type 1” (a), “type 2” (b), “type 3” (c) and “type 4” (d).

A preliminary mesh sensitivity study has been carried out in order to determine the optimal mesh size able to provide the best compromise between accuracy of results and analysis time.

In particular, for each panel, the results of two models, characterised by meshes with square elements of side length equal to 12.5 mm and 25 mm, respectively, have been compared in terms of corresponding cyclic curves. For the sake of example, in Figure 49 comparison is executed with reference to the shear panel model “type 2”. It is evident that the mesh characterised by 25x25 mm base elements is quite appropriate, as the slightly higher accuracy level offered by the 12.5x12.5 mm element mesh is compensated by an increment by 5 of the time of running analysis.

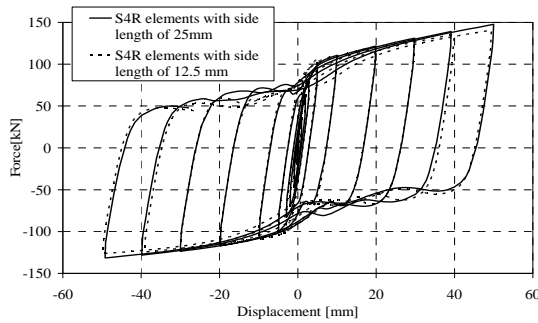


Figure 49. Mesh sensitivity study.

The reliability of the above FEM numerical model has been checked against the available experimental results. In particular, in Figure 50 the comparison in terms of global response is shown, evidencing the similarities of hysteretic cycles.

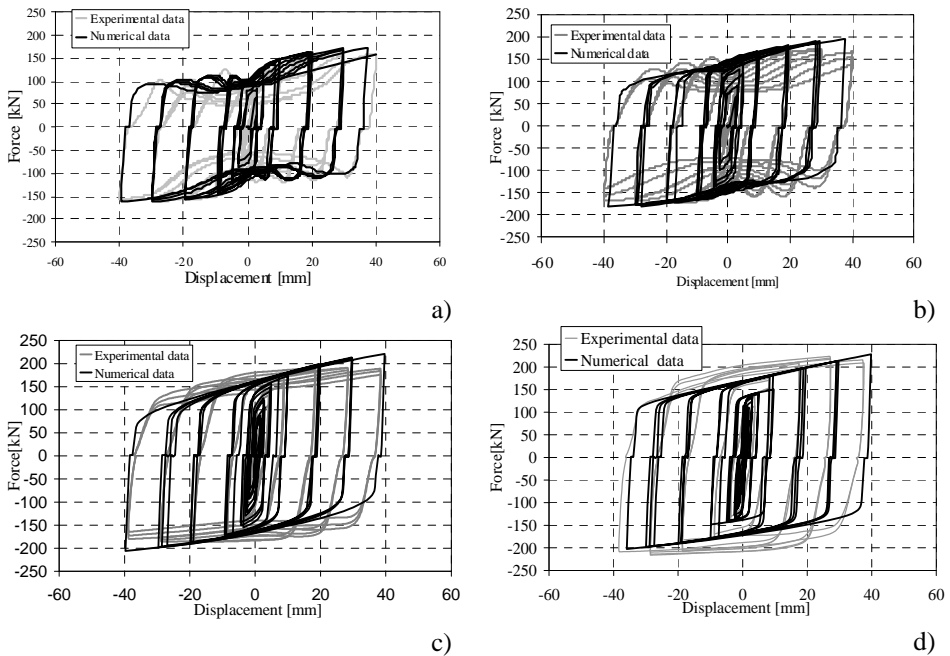


Figure 50. Comparison between numerical and experimental results in terms of hysteretic cycles: “type 1” (a), “type 2” (b), “type 3” (c) and “type 4”.

In addition in Figures 51, 52, 53 and 54, detailed comparisons in terms of dissipated energy per cycle, secant global stiffness (G_{sec}), hardening ratio and

equivalent viscous damping ratio α , according to the definition of Figure 34, are provided as a function of the applied shear strain for each panel. In such figures, the comparison is proposed only for hysteretic loops characterised by a diagonal displacement demand ranging from -40 mm to +40 mm. In fact, when larger displacements are attained, the system response is influenced by both the failure of the perimeter connection system and the fracture of the base plate, which are not contemplated in the proposed numerical models. Anyway, the obtained results testify the reliability of the numerical model, which is able to capture all the main behavioural aspects of the system, namely, the strength, the stiffness and dissipative features, including the pinching effects due to the buckling phenomena. It is also evident that the models are capable to reproduce the initial slipping phenomena, whose entity has been interpreted during the calibration process of the numerical model and which are unavoidable for the practical tolerance in every steel structure.

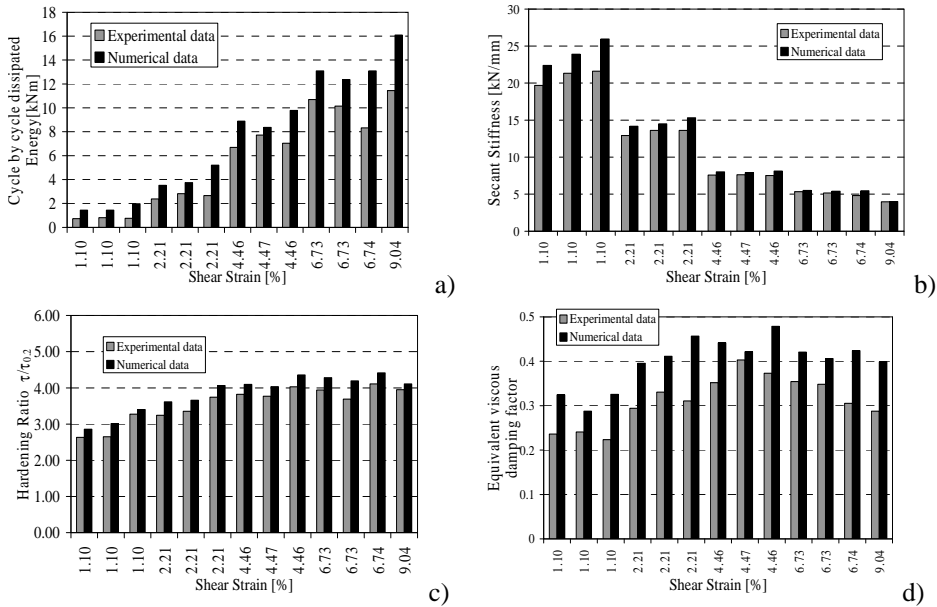


Figure 51. Comparison between numerical and experimental results for panel “type 1” in terms of (a) dissipated energy per cycle, (b) secant global stiffness, (c) hardening ratio and (d) equivalent viscous damping ratio.

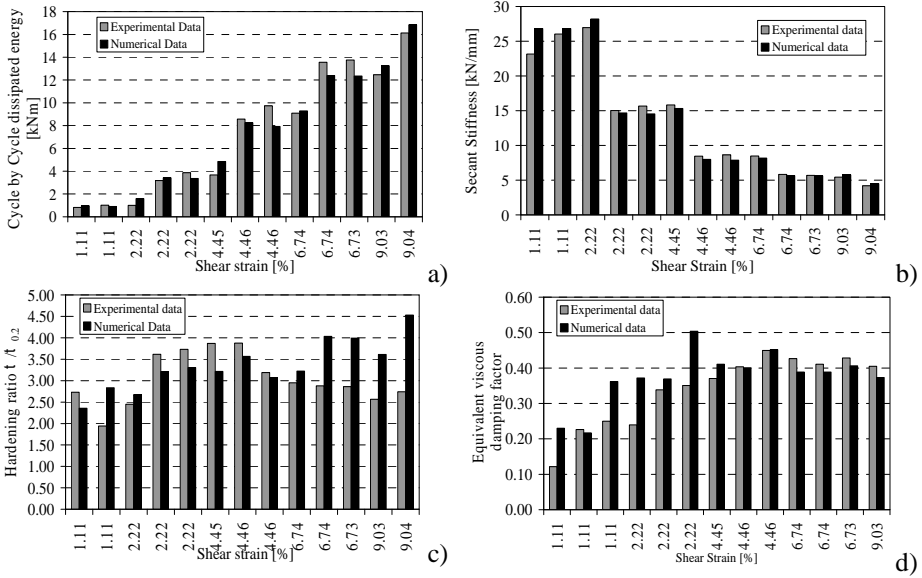


Figure 52. Comparison between numerical and experimental results for panel “type 2” in terms of (a) dissipated energy per cycle, (b) secant global stiffness, (c) hardening ratio and (d) equivalent viscous damping ratio.

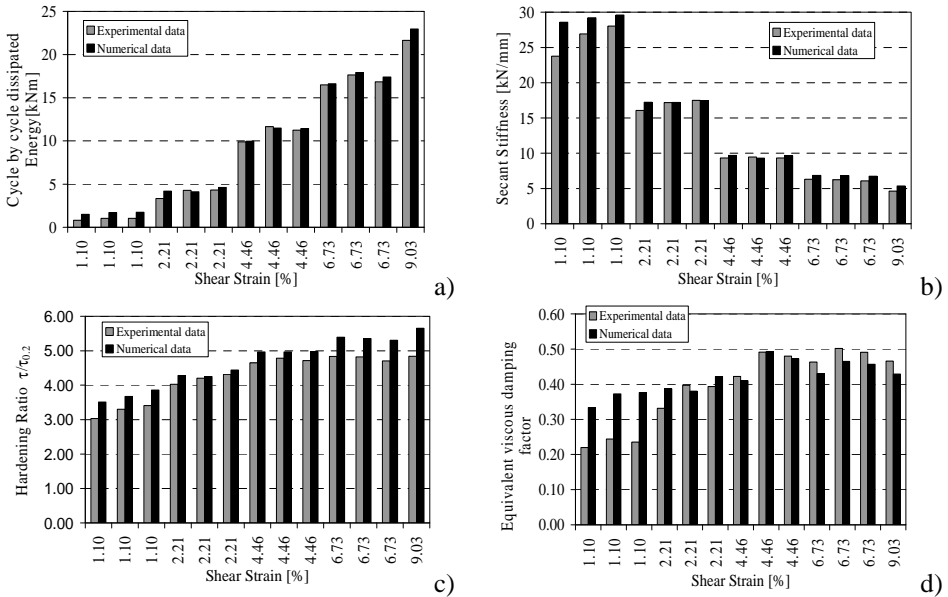


Figure 53. Comparison between numerical and experimental results for panel “type 3” in terms of (a) dissipated energy per cycle, (b) secant global stiffness, (c) hardening ratio and (d) equivalent viscous damping ratio.

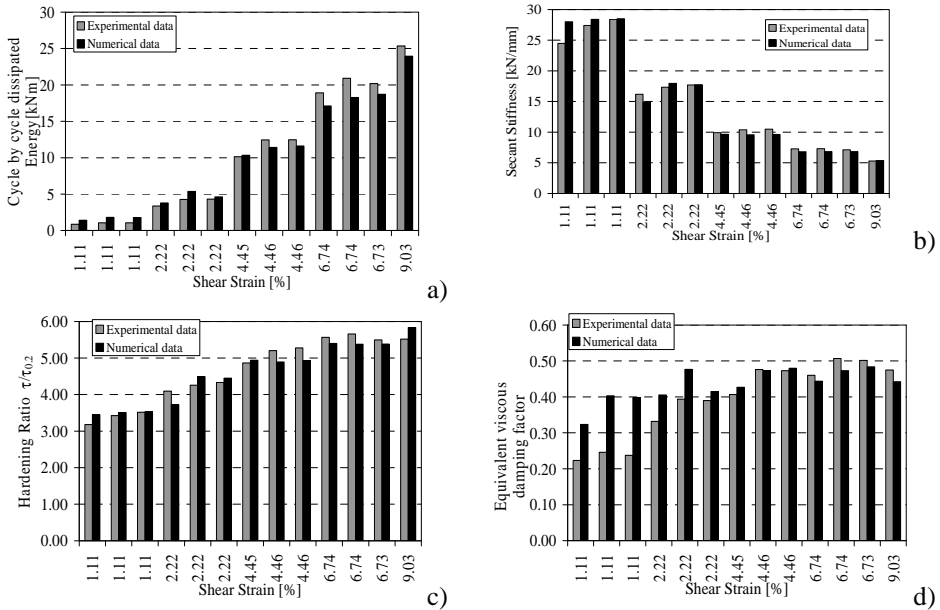


Figure 54. Comparison between numerical and experimental results for panel “type 4” in terms of (a) dissipated energy per cycle, (b) secant global stiffness, (c) hardening ratio and (d) equivalent viscous damping ratio.

It has been also proved that the proposed FE numerical model reproduces correctly all the deformed shapes and the corresponding hysteretic cycles registered during the experimental test. In particular the buckling waves exhibited for applied displacements equal to 5 mm, 10 mm, 20 mm, 30 mm and 40 mm have the same shape and extent (with a maximum out-of-plane displacement of 60 mm for panel “type 1”) of those highlighted by the experimental test. An example is depicted in Figure 55 with reference to panel “type 1”.

In addition to the above sophisticated FEM modelling, simplified analytical models for the studied compact panels have been proposed (Brando et al., 2009a). These are obtained by using element characterized by a proper generalized Ramberg-Osgood relationship which is calibrated on the basis of the same cycles obtained by the experimental analysis. This modelling approach appears to be the most adequate solution, in terms of result accuracy and time consuming, for panel modelling in numerical dynamic analyses of multi-storey frames. In fact, the use of sophisticated models based on the use of finite elements, such as the above proposed ones, could result in too much cumbersome elaborations which, in turn, could require too much difficult analysis operations. Aiming at this purpose, four non linear link elements available in the SAP2000 library (CSI, 2006) have been used for modelling the proposed shear panels (see Figure 56-a). They have been divided in two pairs. Each of them has been placed along one of the two panel diagonals. They have been characterized

only in the axial direction by a multi-linear plasticity relationship adjusted by a Ramberg-Osgood law.

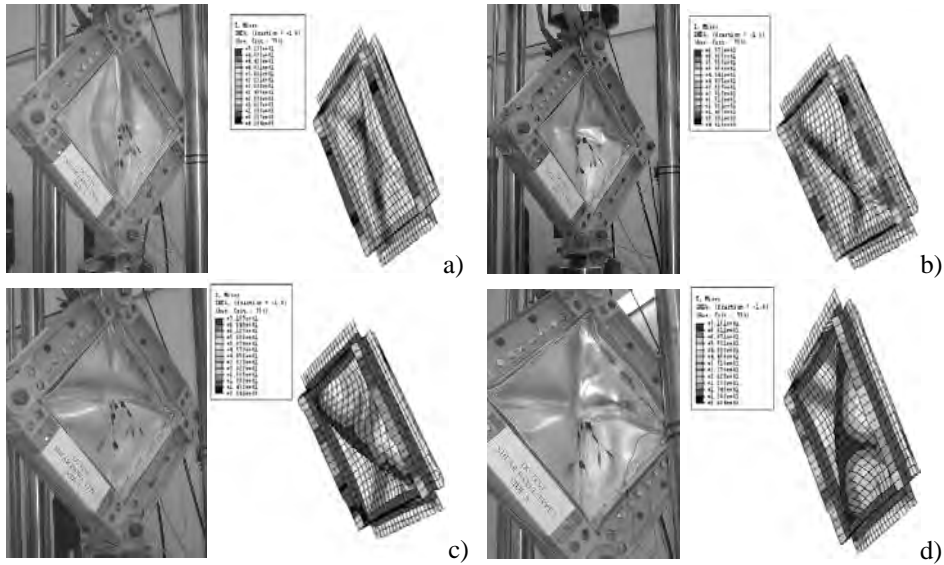


Figure 55. Comparison between deformed shapes of experimented specimen panel “type 1” and its numerical model for diagonal displacements demands of (a) 5.00 mm, (b) 10.00 mm, (c) 30.00mm and (d) 40.0 mm.

Aiming at this purpose, four non linear link elements available in the SAP2000 library (CSI, 2006) have been used for modelling the proposed shear panels (see Figure 56-a). They have been divided in two pairs. Each of them has been placed along one of the two panel diagonals. They have been characterized only in the axial direction by a multi-linear plasticity relationship adjusted by a Ramberg-Osgood law. On the contrary, the other degrees of freedom, except the in-plane rotational one (assumed equal to zero), have been left free. The proposed elements have been joined to each other at one of their edges (node “9”), whereas the other one has been linked by means of rigid elements to the ends of four pinned frame elements (nodes “2”, “3”, “4” and “5”, respectively), forming a square characterized by the same side length of the edge profiles placed on the perimeter of the shear panels. In order to reproduce the same boundary conditions realized on the proposed shear panels during the experimental tests, two of the external frame elements have been fixed to the ground at their intersection (node “5”). At the same way, the intersection of the remaining frame elements (node “7”) has been restrained about the horizontal translations. Figure 56-b shows the model deformation once a force N , corresponding to a displacement δ , is applied at the node “7” (corresponding to the upper point of the shear panel).

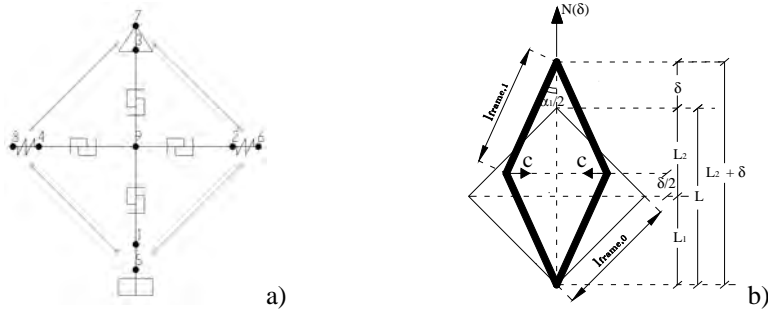


Figure 56. (a) The proposed analytical model; (b) Model deformation due to a force N applied at the “node” 7.

Assuming that the two non linear link elements representing the panel diagonal in tension are characterized by the same axial stiffness $k(\delta)$ of the ones representing the panel diagonal in compression, the four meaningful unknown parameters (the final length $l_{frame,1}$ of the edge frame elements, the angle α_1 between two frame elements, the axial force C acting on the link in compression and the stiffness $k(\delta)$) ruling the model behaviour when a diagonal displacement δ is imposed, may be obtained by solving the system of equations (12), where the first two equations are referred to the consistency of the displacements, and the others provide the equilibrium conditions of the involved forces.

$$\left\{ \begin{array}{l} l_{frame,1} \cdot \cos\left(\frac{\alpha_1}{2}\right) = L_2 + \frac{\delta}{2} \\ L_1 + L_2 - 2l_{frame,1} \cdot \sin\left(\frac{\alpha_1}{2}\right) = \frac{C}{k} \\ 2 \cdot E_s \cdot A_{frame} \cdot \frac{l_{frame,1} - l_{frame,0}}{l_{frame,0}} \cdot \sin\left(\frac{\alpha_1}{2}\right) = C \\ 2 \cdot E_s \cdot A_{frame} \cdot \frac{l_{frame,1} - l_{frame,0}}{l_{frame,0}} \cdot \cos\left(\frac{\alpha_1}{2}\right) + k \cdot \delta = N \end{array} \right. \quad (12)$$

In the above equations, E_s and A_{frame} are the base material elastic modulus and the transversal section of the edge arms of the frame where the panels are inserted, respectively, while $l_{frame,0}$ is the initial length of the same members.

Analyzing the cyclic response of tested shear panels “type 3” and “type 4”, it is possible for both panels to retrieve the total diagonal force N value corresponding to the maximum diagonal displacement δ characterizing each force-displacement loop. Using these values in equations (12), it is possible to obtain the corresponding values ($\delta_{link}=C/k$, C) that could be assigned as constitutive

multi-linear relationship to each non linear link representing the panels (see Figure 57).

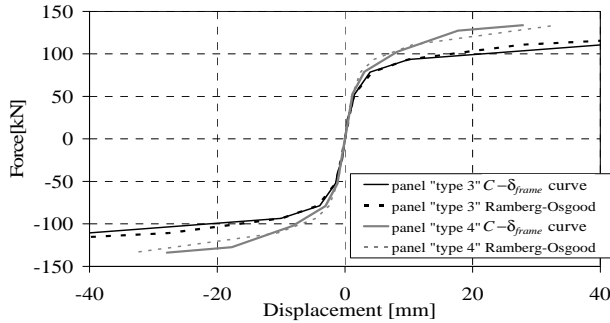


Figure 57. C - δ_{frame} curves fitting results of eq. (12) and relative Ramberg-Osgood relationship for panels “type 3” and panel “type 4”.

It is worthy of note that the obtained values of axial force $C_{panel\text{ "type4"}}$ corresponding to a general value of axial displacement δ_{link} for panel “type 4” may be obtained by the analogous values $C_{panel\text{ "type3"}}$ retrieved for panel “type 3” consistently with equation (13):

$$C_{panel\text{ "type4"}} = C_{panel\text{ "type3"}} \cdot \frac{A_4}{A_3} \quad (13)$$

where A_4 and A_3 are the shear areas of the panels which include the area of the base plate and the one of the stiffeners.

The results obtained by equation (12) in terms of force C and displacement $\delta_{link} = C/k$ may be interpolated by curve. In such a way the mechanical response of each non linear link used to model the shear panel may be represented by a predefined analytical expression. For this purpose, as mentioned above, a Ramberg-Osgood relationship has been used (Ramberg and Osgood, 1943) for the proposed panels. It has been calibrated on the basis of the experimental results obtained for panel “type 3” and has been successively extended to the case of panel “type 4”, considering that for any shear strain demand, as specified in eq. (13), the ratio between the corresponding values of the C force is equal to the ratio of the respective shear areas. The expression of the applied analytical relationship is given in eq. (14).

$$\delta_{frame} = \left(\frac{C^*}{K} \right) + \left(\frac{C^*}{B} \right)^m \quad (14)$$

where it has been assumed that:

$$C^* = C + C \cdot \left(1 - \frac{A}{A_3} \right) \quad (15)$$

In equation (14), the stiffness K , as well the two parameters related to the hardening B and m , have been determined on the basis of the value ($\delta_{ink}=C/k$, C) obtained for panel “type 3”. In particular, values of $K = 39.29$ kN/mm, $B = 70$ and $n=7$ have been fixed. In Figure 57, the curves fitting the results obtained by solving eq. (12) for panels “type 3” and “type 4”, as well as the corresponding Ramberg-Osgood relationships, are shown. It is evident that the choice of the above Ramberg-Osgood parameters is particularly appreciable as the obtained analytical relationships are able to well reproduce the panel behaviour.

The reliability of the proposed model has been proved by comparing the obtained analytical results with the experimental ones, considering the tests related to shear panels “type 3” and “type 4”, by assuming the above Ramberg-Osgood relationship for representing the mechanical response of each non linear link elements resembling the shear panel. For this purpose, a dynamic non linear analysis has been carried out for each panel by imposing a time history on the top node (node “7”) of the model described in Figure 7, according to the displacement history shown in Figure 41. The direct integration method has been used in order to solve the equation of motions. A damping coefficient equal to 99% has been imposed, so that the implemented analyses may be considered as pseudo-static because dynamic effects are negligible. Figures 58-a and 58-b show the comparison between the numerical and experimental results in terms of hysteretic cycles. Similarly, Figures 59-a and 59-b show the comparison between the experimental and numerical results in terms of cumulated dissipated energy.

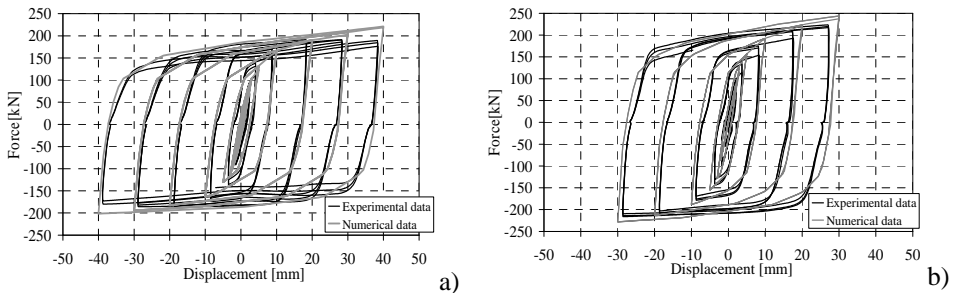


Figure 58. Comparison between experimental and numerical results in terms of hysteretic cycles for panel “type 3” (a) and panel “type 4” (b).

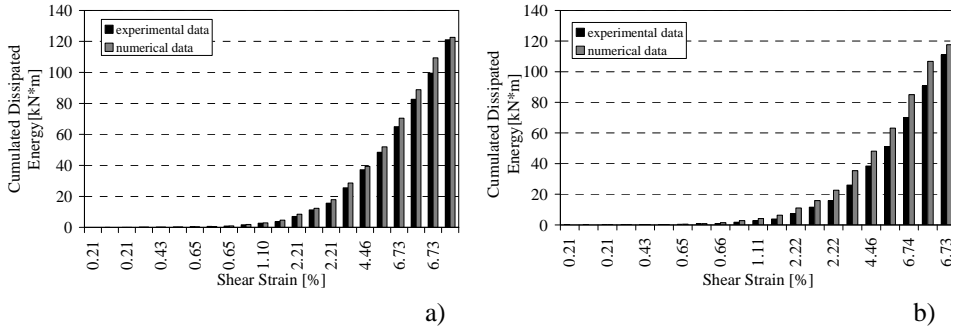


Figure 59. Comparison between experimental and numerical results in terms of cumulated energy for panel “type 3” (a) and panel “type 4” (b).

Design criteria

General

This part of the study deals with theoretical and numerical (both simplified and refined) studies on both slender, compact and semi-compact metal shear panels in order to evaluate or to set-up effective design criteria (Formisano et al., 2007; Brando et al., 2009b).

Steel panels

In the first phase, in order to evaluate the main influential parameters affecting the system stiffness, a preliminary numerical analysis of a 1000x1000x1 mm shear panel inserted within a reaction steel frame, realised with coupled UPN profiles (Fig. 60-a), has been carried out by changing the column and beam stiffness. The finite element model has been implemented by means of the ABAQUS non linear numerical analysis program (Hibbitt et al., 2004), where the shear plate and the frame members are modelled by using four nodes bi-dimensional having reduced integration (S4R type) and two-node linear (B31 type) elements, respectively. The obtained results have been compared with the theoretical ones provided by the design method known as “Plate Frame Interaction” (PFI), developed by Sabouri-Ghomi et al. (1991, 2003), and “Strip Model”, introduced by Thorburn et al. (1983).

The material used for the shear panel is a DX56D steel, which is a mild steel with limited elastic strength employed in the field of cold-formed thin walled sheeting and profiles according to the UNI EN 10142 code provisions (1992); S275 steel, characterised by an elastic-perfectly plastic behaviour, has been employed for the frame members. The material mechanical features of the panel have been preventively estimated by means of a tensile test on steel coupons, providing yield and ultimate stress values equal to 300 and 340 MPa, respectively, and ultimate strain larger than 30% . On the basis of a preliminary

sensitivity study, a mesh having square elements of 25 x 25 mm, which provides the best compromise between accuracy of results and analysis time consuming, has been used for the plate (Fig. 60-b).



Figure 60. The numerical model of a SPSW (a) and the used mesh (b).

The system response has been obtained by applying the already described modified Riks algorithm. In the numerical model, aiming at verifying the influence exerted by the columns stiffness, steel frame members having different depth have been considered, as indicated in Table 5.

Table 5. Frame members properties for the analysed shear plate configurations.

Analysed configuration	Member profile	Second moment of area [mm ⁴]
1	2 UPN 140	605 x 10 ⁴
2	2 UPN 160	925 x 10 ⁴
3	2 UPN 180	1350 x 10 ⁴
4	2 UPN 200	1910 x 10 ⁴
5	2 UPN 220	2690 x 10 ⁴

The results are provided in Figure 61 in terms of equivalent uniform shear strain τ (which is the applied shear force F divided by the shear resistant area of the plate $A = 1000 \text{ mm}^2$) versus the shear deformation γ (assumed equal to the inter-storey drift angle). The influence of the column stiffness is noticeable. In particular, it can be observed that the system stiffness tends toward the theoretical one provided by the PFI method, as the column cross section size increases. For the studied configurations, the corresponding curves of Figure 61 present a less pronounced non linear behaviour, allowing for the attainment of the panel full plastic behaviour for smaller displacement levels, which become quite close to the theoretical one.

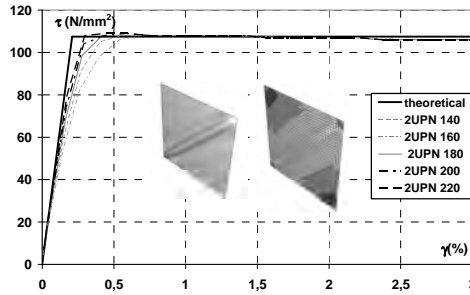


Figure 61. τ - γ curves of shear panel systems obtained by varying the frame members.

On the basis of the above described model a parametrical study has been carried out, taking into account a column sections 2UPN220. In detail, the behaviour of shear panels having a b/d aspect ratio ranging between 0.8 and 2.5 has been analysed. Such limit values are suggested by the Canadian code (CSA, 2001) in order to guarantee the development of a correct plastic mechanism (compact shear panels).

Three different aspect ratios (0.8, 1.0 and 2.0) have been analysed (Fig. 62).

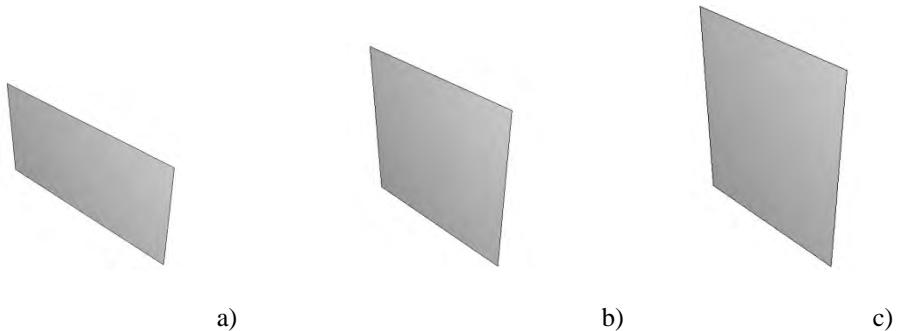


Figure 62. Geometry of analysed shear panel shapes: a) $b/d = 2.0$, b) $b/d = 1.0$, c) $b/d = 0.8$.

The results of the numerical study performed on the selected configurations have underlined as the behaviour is only slightly different from each other. In fact, the corresponding shear stress τ -shear strain γ curves do not present any difference in terms of stiffness and maximum strength, as evidenced in Figure 63.

In the same figure the theoretical behaviour of shear plates determined by the PFI method is depicted, showing as it is able to adequately interpret the behaviour of shear panels subjected to horizontal actions. This is also confirmed by the stress state developed in the panels after the occurrence of buckling phe-

nomena, which evidences an inclination angle of tensile bands close to 45° (Fig. 64).

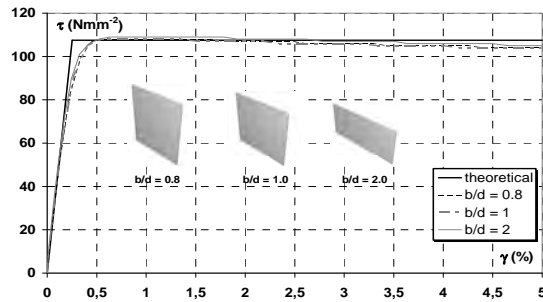


Figure 63. Numerical response of analysed shear panels for aspect ratios equal to 0.8, 1.0 and 2.0.

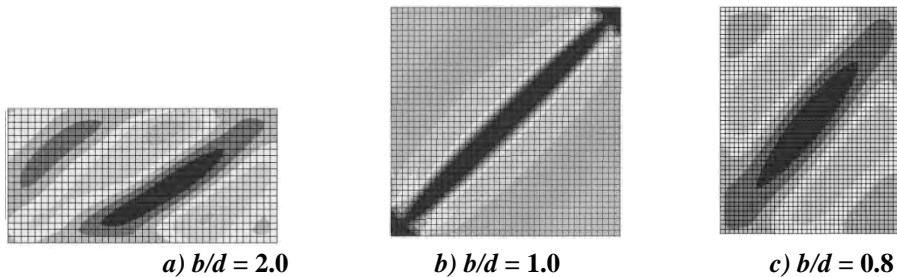


Figure 64. Tension field developed in the analysed shear panels.

Moreover, by comparing the results obtained by the application of the ABAQUS model and the ones related to the Strip Model, for the panel with $b/d = 1.0$, a very good agreement can be noticed (Fig. 65).

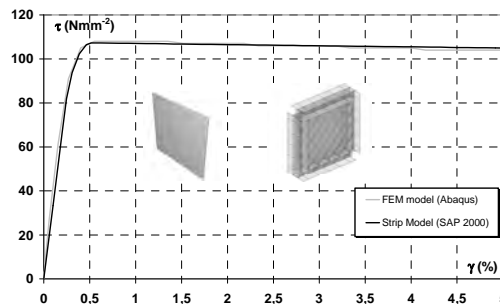


Figure 65. Numerical comparison between the numerical result (ABAQUS model) and the application of the Strip model for the panel configuration with $b/d = 1.0$.

Additional analyses have been carried out in order to establish the influence of the b/t ratio on the behaviour of panels having aspect ratios enclosed in the above range. The numerical investigation has been developed on a 1000x1000 mm panel (Fig. 66).

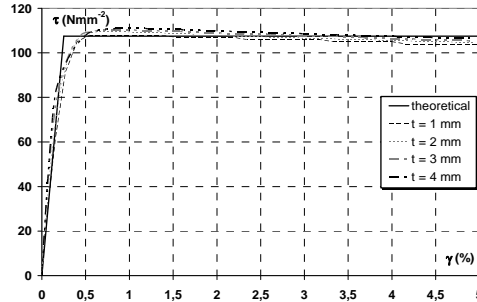


Figure 66. Results of numerical analysis carried out on panels having $b/d = 1.0$ and different thicknesses.

The comparison of the obtained results in terms of τ - γ curves shows that the normalized panel behaviour remains substantially unchanged. The only discrepancy is related to the initial stiffness. This can be explained considering that, for panels having constant shape ratio and boundary conditions, the critical load is proportional to the square thickness while the strength increases linearly with t . Therefore, the ratio between the panel critical load ($F_{cr,n}$) and its maximum strength (V) becomes more and more significant for larger plate thickness (t), as it is evident from Table 6. From Table 6 it is also evident that the numerical evaluation of the panel critical load ($F_{cr,n}$) is very close to the one obtained from the application of the Timoshenko linear theory ($F_{cr,t}$) (Timoshenko and Woinowsky-Krieger, 1959). In detail, it can be considered that the behaviour of shear panels having b/t ratio close to 200 cannot be correctly interpreted neglecting the pre-critical phase.

Table 6. Percentage scatters between the numerical critical load ($F_{cr,n}$) and the maximum strength (V) of panels.

	Thickness [mm]			
	1	2	3	4
$F_{cr,n}$ [kN]	2,65	20,70	68,90	161,30
$F_{cr,t}$ [kN]	2,71	21,69	73,21	173,5
V [kN]	107,5	219,0	331,0	444,0
C_v [%]	2,46	9,45	20,81	36,33

In addition to the above analyses, shear panels having aspect ratio $b/d < 0.8$ have been considered, in order to evaluate the effects of the non complete de-

veloping of the plastic mechanism (slender panels). In particular, two panel configurations, having aspect ratio equal to 0.67 and 0.50, have been taken into consideration by means of both finite element models and simplified models (PFI, Strip Model). In Figure 67, the results of the numerical FEM analyses are shown. In the same figure, the theoretical response predicted by the PFI method is depicted. The corresponding comparison evidences that the response of the examined systems changes significantly. In particular, when the b/d ratio decreases, the shear panel presents a more flexible behaviour, reaching the ultimate strength for large displacements only. For this reason, the PFI method, which provides a panel stiffness significantly greater than the actual one, is not able to predict the behaviour of such a system.

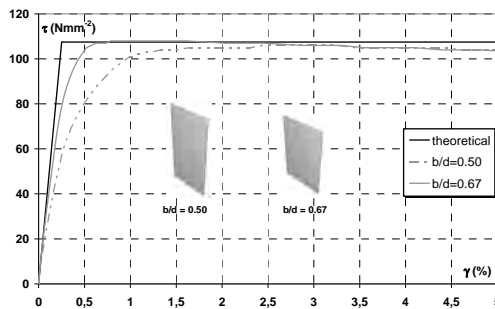


Figure 67. Structural response of analysed shear panels for aspect ratios equal to 0.8, 1.0 and 2.0.

This phenomenon is due to two different reasons, namely the tension field inclination, which is greater than 45° (Fig. 68a), and the flexibility of the surrounding columns, which are directly interested, especially in the middle panel height, by the effects due to diagonal tensile stresses. Although the tension field inclination is greater than 45° , the ultimate strength obtained by FEM analysis for large displacements is the same achieved by the application of the theoretical method due to the fact that, during the loading phase, a rotation of the tensile stress state occurs (Fig. 68b).

With reference to the panel having a b/d ratio equal to 0.50, the comparison between numerical and results obtained by the strip-model shows some discrepancies, due to the larger flexibility evidenced by the strip model curve, although both models provide the same ultimate strength which is attained at the same deformation amplitude (Fig. 69).

For the same shear panel configuration, the behaviour for different thicknesses has been evaluated. The comparison is provided in Figure 70 in terms of shear stress – shear strain curve.

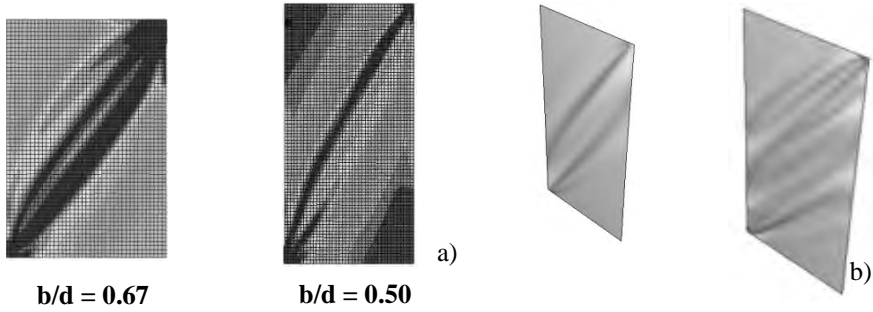


Figure 68. Tension field mechanism for the analysed panels (a) and change of the tensile bands inclination for the panel with $b/d = 0.50$ during the loading phase (b).

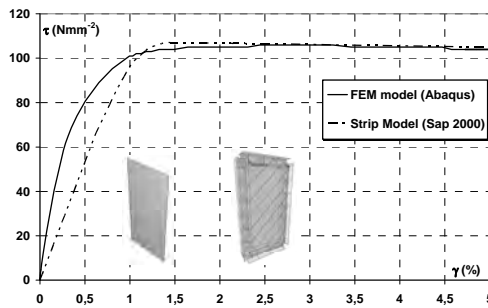


Figure 69. Comparison between numerical and theoretical curves for shear panel with $b/d = 0.50$.

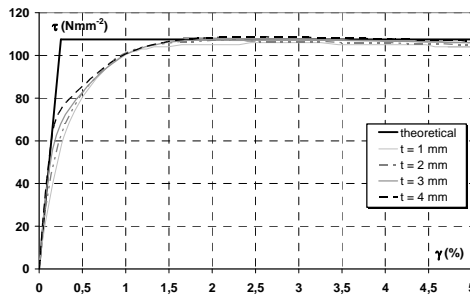


Figure 70. Numerical responses of the shear panel having $b/d = 0.50$ and different thicknesses.

It is apparent that the behaviour of the system is not significantly affected by the plate thickness, confirming the importance of the b/d ratio which, when lower than 0.8, causes a strong increase of system flexibility. The main output of the proposed study therefore consist in the confirmation of the importance of fixing the aspect ratio in the range proposed by the Canadian Codes. In order to further validate this conclusion, in the following the possibility to apply inter-

mediate horizontal stiffeners in order to control the development of the tension field mechanism is investigated. To this purpose two different methods are applied: the first approach is based on the insertion of an intermediate beam within the reaction steel frame, so to consider two different sub-panels. The second approach is instead based on the introduction of two fishplates located on both panel sides aiming at realising an intermediate stiffener. In both cases, a panel thickness of 4.00 mm has been imposed on panel characterized by initial aspect ratio of 0.5

A refined FEM model has been developed in order to determine the actual behaviour of the proposed systems (Fig. 71).

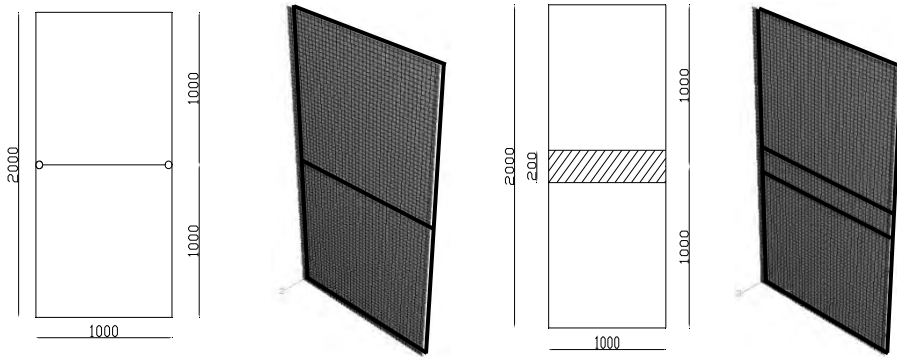


Figure 71. Geometry and numerical model of analysed slender shape shear panel endowed with an intermediate beam (a) and intermediate stiffeners (b).

The comparison shows that the numerical curves related to slender shape shear panels endowed with intermediate beam and stiffeners are characterised by a constant stiffness up to the attainment of the maximum panel strength, as it was observed for “compact” shape panels (Fig. 72). In addition, such curves appear to be very close to the theoretical one. In fact, for both shear panels the inclination angle of the tension field is about 45° , allowing for the involvement of the whole plate surface in the load resisting mechanism (Fig. 73).

Slender, semi-compact and compact pure aluminium shear panels

On the basis of the calibrated FEM numerical models on bracing type pure aluminium shear panels described in Chapter 3.2.4, a parametrical numerical study has been carried out. Models have been used for determining some instabilities curves which could be suitably used in the design process of panels. In particular, a “first instability” curve has been provided with the aim of establishing the shear force level corresponding to the first attainment of buckling.

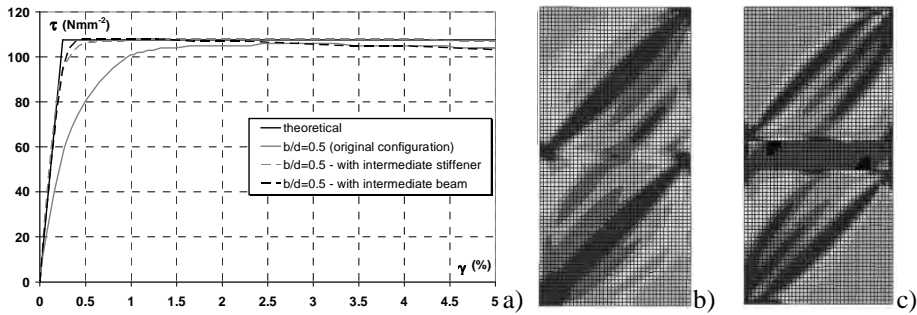


Figure 72. (a) Behaviour of slender shear panels ($b/d = 0.5$) with and without intermediate stiffeners; stress state developed in the analysed shear panel: endowed with an intermediate beam (b) and with stiffening fish plates (c).

This is very important for the design process of panels, as the retrieved force level can be taken into account as a limit for the serviceability limit state of the whole frame in which they are arranged. At the same time, curves giving back the reduction factor of the ultimate shear strength of panels, because of buckling phenomena, are proposed as a very useful tool for the ultimate state design purpose. As exposed in Section 3.2.3, this last issue is already covered by Eurocode 9, but it is developed with reference to aluminium alloys that are different by the here dealt with.

With reference to the numerical model of the un-stiffened pure aluminium panel (“type 1”), monotonic analyses have been carried out taking into account different slenderness values obtained by varying the panel thickness. An increasing shear strain demand has been imposed and the shear force (V) versus shear strain (γ) relationships have been obtained. Then, the maximum shear strength for each panel thickness has been evaluated. In Figure 73 the factor for shear buckling ρ_v , evaluated according to eq (6), as the ratio between the measured maximum shear strength and the conventional yield strength, is provided for different slenderness values λ_w , which have been defined consistently with the definitions given in equation (7). In the same figure, the factor ρ_v provided by EC9 is also shown in order to provide a direct comparison with the obtained numerical results. The large discrepancies between the two curves are mainly due to the difference of the hardening ratio between the proposed material ($f_u/f_{0.2}=97.5/21=4.65$, considering the true stress values) and the one considered for the calibration of the EC9 formulae (maximum hardening ratio $f_u/f_{0.2}=1.42$). However, assuming $\eta=4.65$, it is possible to establish the following interpolation curve, which fits correctly the measured values of ρ_v (see Figure 73):

$\lambda_w < \frac{0.48}{\eta}$	$\frac{0.48}{\eta} \leq \lambda_w < 0.95$	$0.95 \leq \lambda_w < 2.29$	$\lambda_w \geq 2.29$
$\rho_v = \eta$	$\rho_v = \frac{2.8}{\lambda_w^{0.22}}$	$\rho_v = \frac{2.8}{\lambda_w^{0.10}}$	$\rho_v = \frac{2.6}{\lambda_w^{0.01}}$

In Figure 73, the “first instability curve” has been also plotted. It represents the shear load corresponding to the occurrence of the first buckling phenomenon, normalized to the conventional elastic strength.

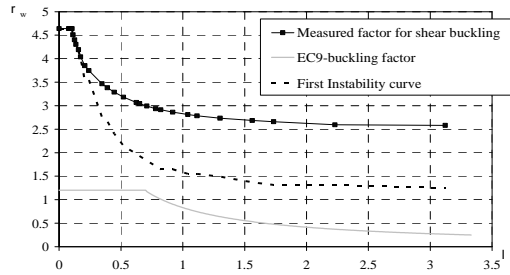


Figure 73. Shear buckling factor for a Pure aluminium plate with web stiffeners at support.

This shear force has been detected for each slenderness value by monitoring the principal stresses for an increasing shear strain demand and determining the value corresponding to a stabilization of the compressive stresses, when the tension field resisting mechanism is originated. Such a curve may represent an important design tool, allowing, for a given value of the shear strength and/or shear deformation demand, the distinction between compact (for which the response of the system is not degraded by buckling phenomena) and slender shear panels. In addition, it is possible to observe that the proposed curve always provides values bigger than 1, meaning that buckling phenomena develop after the conventional elastic strength of the material ($f_{0.2}$) has been attained.

Another problem that has been dealt with by using the proposed numerical models and which is preparatory for the extension of the curve proposed in the above equation to multi-stiffened shear panels, regards the effectiveness of the transverse stiffeners on the system response. This issue is strictly linked to the fact that several coupled buckling modes could simultaneously arise due to specific slenderness ratios of the plate and flexural stiffness of the applied stiffeners. This possibility may lead to a critical behaviour of the system, with the localisation of specific buckling patterns, which, due to the erosion of the critical bifurcation load, could provoke an unstable post-buckling behaviour (Fig. 74) characterized by large local inelastic deformation producing the plastic

folding of panel and therefore the collapse of the system due to the development of plastic mechanisms.

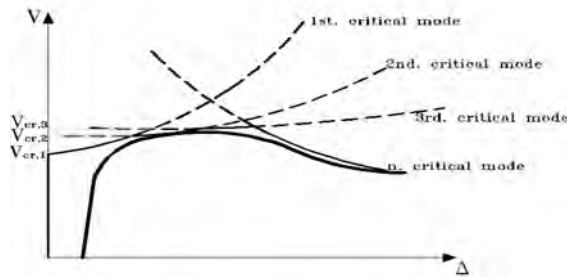


Figure 74. Shear (V) – Displacement (Δ) behaviour of a shell plate affected by several buckling modes.

The numerical model of panel “type 2” has been usefully employed for this purpose. A parametrical analysis has been carried out evaluating the hysteretic responses corresponding to a diagonal displacement demand of $\Delta = \pm 40.0$ mm. Four plate and rib thickness values (namely 5.0 mm, 4.0 mm, 3.0 mm and 2.0 mm) have been considered, as well as the rib depth (d) has been ranged from 10.0 mm to 50.0 mm. For each thickness, the hysteretic energy has been computed and normalized to the value obtained for a rib depth $d=50.0$ mm. The comparison of results (Fig. 75-a) allows to determine the actual influence of the stiffeners on the global response of the system. On this purpose, a global criterion has been considered, namely a reduction of the dissipated energy lower than 5% respect to the reference value ($d=50$ mm). In fact, upon this limit panel deformed shapes without global buckling phenomena and almost coincident hysteretic cycles have been observed. Therefore, the stiffener complying with this criterion might be defined as rigid, it being not involved in a global buckling behaviour with interaction between local and global instabilities. By way of example, in the case of plate and rib thickness equal to 5.0 mm, the stiffeners can be considered effective if their depth d is at least equal to 30 mm. This is also evident when comparing both the hysteretic cycles (Fig. 75-b) and the deformed shapes of the panels (see from Fig. 75-c to 75-f), which show a progressive change from local to coupled local-global instability when the depth d is smaller than 30.0 mm. Similarly, it is possible to state that ribs with depth d larger than 20.0 mm can be considered as rigid for panel thicknesses of 4.0 mm and 3.0 mm, whereas a depth $d=10.0$ mm is enough a plate thickness of 2.0 mm. On this basis, the same curves proposed for panel “type 1” in Figure 108 are also proposed for the other studied panel typologies (Fig. 76), assuming always a stiffeners depth of 60 mm which, according to the above results, can be always considered as rigid in the displacement range expected for the studied devices.

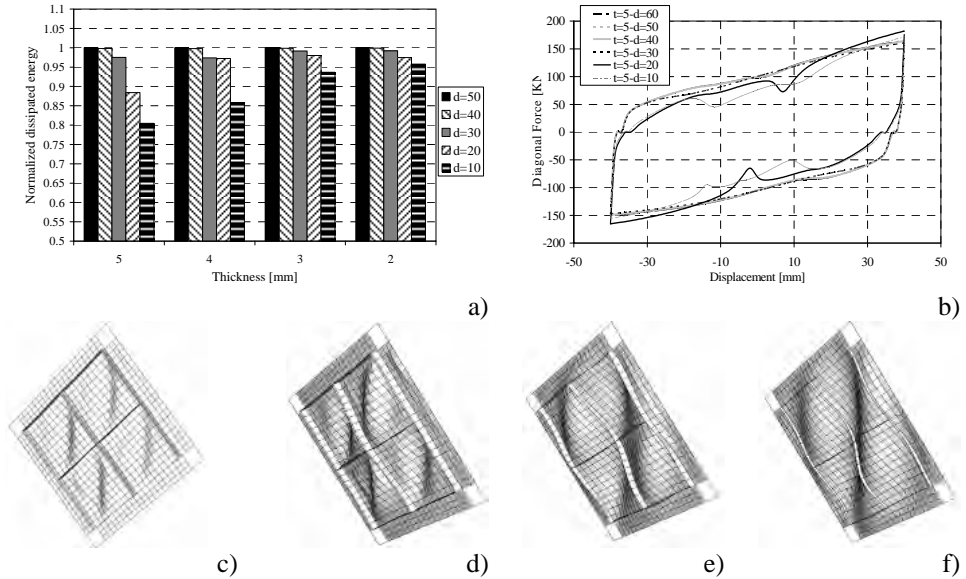


Figure 75. Effectiveness of intermediate transverse stiffeners: normalized dissipated energies (a), hysteretic response of 5.0 mm thick panels characterized by different ribs depth (b), deformed shapes of 5.0 mm thick plates with ribs depths of d=40 mm (c), d=30 mm (d), d=20 mm (e) and d=10 mm (f).

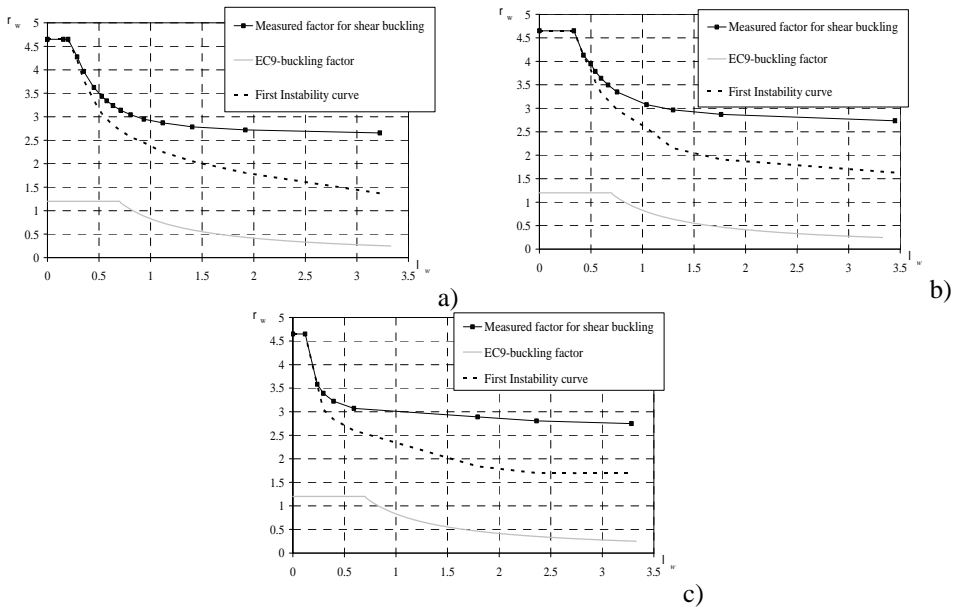


Figure 76. Shear buckling reduction factor for bracing type pure aluminium shear panels with one (a), two (b) and three (c) intermediate stiffeners.

The obtained results allow to state that the width-to-thickness ratios under which the studied panels may be classified as compact, independently by the shear strain value to which they are subjected, are $(b_w/t_w)_1=16.6$, $(b_w/t_w)_2=33.3$, $(b_w/t_w)_3=62.5$ and $(b_w/t_w)_4=100$ in the cases of panels with stiffeners at support, with one, two and three intermediate stiffeners respectively.

In addition, it is possible to observe that the proposed curves always provides values higher than 1, meaning that buckling phenomena develops after the conventional elastic strength of the material ($f_{0.2}$) has been attained.

4. CONCLUSION

The current report has dealt with the research activity carried at the University of Chieti-Pescara within the Reluis research Project. It has been articulated in the following three main tasks:

- 1) Experimental, theoretical and numerical studies on slender metal shear panels for seismic protection of existing reinforced concrete buildings.
- 2) Experimental and numerical analyses on both compact and semi-compact stiffened shear panels made of pure aluminium;
- 3) Theoretical and numerical models for evaluating the performance of metal shear panels in order to provide reliable design criteria.

As far as the first task is concerned, the use of steel and aluminium shear panels as seismic retrofitting systems of existing RC structure has been analysed with particular reference to a full-scale test carried out on a real building.

The retrofitting design, developed on the basis of a preliminary evaluation of the load-carrying capacity of the bare structure, has been set-up according to the methodology proposed by the ATC-40 code. On the basis of these results and according to simplified relationships, the shear panel geometry has been defined. Then, appropriate finite element models have been implemented in order to verify that the selected devices respected the required increase of strength and stiffness for retrofitting operations. This allowed also the evaluation of the loads transmitted to the connection systems. A case study of an existing building has been finally provided.

With reference to the second task, the cyclic behaviour of pure aluminium shear panels have been investigated from both the experimental and numerical points of view. Two panel typologies have been considered. The first has been based on a “full bay” configuration, while the latter, has been proposed as an improvement of the previous system, according to a “bracing type” solution.

The experimental tests have been pursued considering different stiffener arrangements in order to detect their influence on the overall dissipative behaviour of the system. Moreover, a careful analysis of the experimental evidences has been carried out, in order to detect the performance of the proposed shear panels for different shear strain demands. The obtained experimental results put

in evidence that the proposed devices can be profitably adopted as a protection device of new and existing buildings, they being characterized by a fair stiffness, able to reduce the lateral story drift of the frame in which they must be arranged, and by an excellent dissipative capacity, as it has been testified by the values obtained for the equivalent viscous damping ratio which ranged between 35% and 50%, depending on the adopted stiffeners configuration. On the basis of the above tests, reliable numerical models have been therefore set up.

As a third task of the study, the behaviour of steel and aluminium shear panels characterised by different thicknesses and aspect ratios (obtained also by stiffening the base plate) has been investigated under theoretical and numerical ways, in order to provide useful design provisions.

REFERENCES

- Astaneh-Asl, A., [2001], "Seismic Behavior and Design of Steel Shear Walls", Steel Tip Report, Structural Steel Educational Council, CA, January.
- ATC 40 [1996]. "Seismic evaluation and retrofit of concrete buildings", *Report No. SSC 96-01*, Vol.1.
- Ballio, G., Mazzolani, F.M., [1987], "Strutture in acciaio", Hoepli ed., ISBN 8820315505.
- Berman, J., Bruneau, M., [2004], "Steel Plate Shear Wall Are Not Plate Girder", *AISC Engineering Journal*, Third Quarter, pp. 95-106
- Berman J., Bruneau M. [2005]. "Experimental Investigation of Light-Gauge Steel Plate Shear Walls", *Journal of Structural Engineering*, ASCE, Vol. 131, No.2, pp. 259-267.
- Brando G., [2007] "Experimental analyses on stiffened bracing type pure aluminium shear panels BTPASPs", POLLACK PERIODICA- An International Journal for Engineering, Amalia Ivanyi and Miklos Ivanyi (editors-in-chief) and Information Sciences, Vol. 2 No. 3.
- Brando G. [2009]. Experimental and Numerical Assessment of Bracing Type Pure Aluminium Shear Panels Hysteretic Behaviour, PhD Thesis in Design, Analysis and Experimentation of Structures , University of Chieti-Pescara "G.d' Annunzio".
- Brando, G., De Matteis, G., Mazzolani F.M. [2009a]. "Simplified analytical models of compact pure aluminium shear panels", in "Behaviour of Steel Structures in Seismic Areas" (STESSA 2009), F. M. Mazzolani and J. Ricles editors, Taylor and Francis/Balkema publisher, London, ISBN-13: 978-0-415-56326-0, pagg 829-834.
- Brando, G., De Matteis, G , Mazzolani F.M. [2009b]. "Design of Multi-stiffened Pure Aluminium Shear Panels for Passive Control devices", in Proceedings of the International Conference on "Protection of Historical Buildings" (Prohitech 2009), Rome, Italy, 21-24 June, F. M. Mazzolani editor, Taylor and Francis/Balkema publisher, London, ISBN-13: 978-0-415-55803-7, Vol. 1 pagg 663-668.
- Brando, G., De Matteis, G., Mazzolani, F.M. [2011] "Experimental and Numerical Analysis of a Multi-Stiffened Pure Aluminium Shear Panel", in *Thin Walled Structures*, ELSEVIER ed. (accepted for publication) DOI: 10.1016/j.tws.2011.05.007
- Canadian Standards Association (CSA). [2001]. *Limit States design of steel structures*, CAN/CSA S16-01, Willowdale, Ontario, Canada.
- Computer and Structures, Inc. [2004]. *SAP 2000 Non linear, version 9.03*. Berkeley, California, USA.
- Davies, J.M., Bryan, E.R., [1982], "Manual on stressed skin diaphragm design", Granada Publishing Ltd., London, 1982.

- De Matteis G., Formisano A., Mazzolani F.M. [2009]. "Seismic retrofitting methodology of existing R.C. buildings based on metal shear panels", in *Earthquake Engineering and Structural Dynamics*, ISSN: 1096-9845, John Wiley & Sons Ltd, The Atrium, Southern Gate, Chichester, England, Wiley InterScience, Volume 38, Issue 1, January 2009, pp. 61-78, DOI: 10.1002/eqe.841.
- De Matteis, G., Formisano, A., Panico, S. and Mazzolani, F. M., [2007a] "Numerical and experimental analysis of pure aluminium shear panels with welded stiffeners", in *Computer and Structures*, ISSN: 0045-7949, Pergamon-Elsevier Science Ltd, Oxford, England, doi: 10.1016/j.compstruc, 2007.05.027, Vol 86/6 pp 545-555.
- De Matteis, G., Mazzolani, F.M. and Panico, S., [2007b], "Pure aluminium shear panels as dissipative devices in moment-resisting steel frames", in *Earthquake Engineering and Structural Dynamics*, ISSN: 0098-8847, John Wiley & Sons Ltd, The Atrium, Southern Gate, Chichester, England, Wiley InterScience, DOI: 10.21002/eqe, vol. 36: 841-859.
- De Matteis, G., Panico, S., Mazzolani, F.M., [2007c], "Experimental tests on pure aluminium shear panels with welded stiffeners", in *Engineering Structures*, ISSN 0141-0296, printed by Krips b.v., Meppel, The Netherlands, Elsevier, Volume 30, Issue 6, June 2008, Pages 1734-1744, DOI: 10.1016/j.engstruct.2007.11.015.
- De Matteis, G., Brando, G., Panico, S., Mazzolani, F.M., [2008a], "Bracing type pure aluminium stiffened shear panels: an experimental study", in *International Journal of Advanced Steel Construction (IJASC)*, S.L. Chan, W.F. Chen and R. Zandonini (editors-in-chief), ISSN 1816-112X, Vol. 5, No. 2, pp. 106-119 (2009).
- De Matteis, G., Brando, G., Panico, S., Mazzolani F.M., [2008b] "Cyclic behaviour of Bracing Type Pure Aluminium Shear Panels (BTPASPs): Experimental and Numerical Analysis", *Proceeding of the 14th. World Conference on Earthquake Engineering (14th WCEE)*, Beijing, China, 12-17 October, 2008. Paper ID: 05-06-0144 (Published on DVD).
- De Matteis, G., Brando, G., Mazzolani F.M. [2009a]. "Pure Aluminium, as Innovative Material for seismic Protection Devices", in *Proceedings of the International Conference on "Protection of Historical Buildings"* (Prohitech 2009), Rome, Italy, 21-24 June, F. M. Mazzolani editor, Taylor and Francis/Balkema publisher, London, ISBN-13: 978-0-415-55803-7, Vol. 2 pagg 1003-1008.
- De Matteis G., Formisano A., Mazzolani F.M. [2009b]. "Seismic retrofitting methodology of existing R.C. buildings based on metal shear panels", in *Earthquake Engineering and Structural Dynamics*, ISSN: 1096:9845, John Wiley & Sons Ltd, The Atrium, Southern Gate, Chichester, England, Wiley InterScience, Volume 38, Issue 1, January, pp. 61-78, DOI: 10.1002/eqe.841.
- De Matteis, G. Brando, G., Mazzolani, F.M. [2011]. "Hysteretic Behaviour of Bracing Type Pure Aluminium Shear Panels by Experimental Tests", in *Journal of Earthquake Engineering and Structural Dynamics*, Vol.40, Issue 8, 10 July 2011.
- ECCS-CECM, [1985], "Recommended testing procedure for assessing the behaviour of structural steel elements under cyclic loads".
- EN1999-1-1 [2007] EUROCODE 9, "Design of Aluminium structures", 2007.
- Engineering News Record, [1978], "Patent Problems, Challenge Spawn Steel Seismic Walls", McGraw Hill, January 26, 1978, p. 17.
- Federal Emergency Management Agency (FEMA) 273. [1997]. *NEHRP - Guidelines for the seismic rehabilitation of buildings*, Washington (DC), 1997.
- Formisano A. [2007]. Seismic upgrading of existing RC buildings by means of metal shear panels: design models and full-scale tests, PhD Thesis in Construction Engineering, University of Naples "Federico II".
- Formisano A., Mazzolani F.M., De Matteis G. [2007]. "Numerical Analysis of Slender Steel Shear Panels for Assessing Design Formulas". *International Journal of Structural Stability and Dynamics*, Vol. 7, No. 2, June, pp. 273-294.

- Formisano A., De Matteis G., Mazzolani F. M. [2008] "Numerical and experimental behaviour of a full-scale RC structure upgraded with steel and aluminium shear panels", in *Computer and Structures*, ISSN: 0045-7949, Pergamon-Elsevier Science Ltd, Oxford, England, doi: 10.1016/j.compstruc.2008.09.010
- Formisano A., Mazzolani F.M., De Matteis G. [2009]. "Seismic vulnerability of RC structures integrated with metal shear panels: a study case". *Proc. of the 6th International Conference on the "Behaviour of Steel Structures in Seismic Areas" (STESSA '09)*, Philadelphia, August 16-20, pp. 237-243.
- Hibbitt, Karlsson, Sorensen, Inc. [2004]. *ABAQUS/Standard, version 6.4*, Patwucket, RI, U.S.A..
- Katayama, T., Ito, S., Kamura, H., Ueki, T., Okamoto, H., [2000], "Experimental study on hysteretic damper with low yield strength steel under dynamic loading", Proceedings of the 12th WCEE.
- Mazzolani F.M. (co-ordinator & editor) [2006]. *Seismic upgrading of RC buildings by advanced techniques – The ILVA-IDEM Research Project*, Polimetrica International Scientific Publisher, Monza.
- Ministerial Decree of Public Works (M. D.) [2008]. *New technical codes for constructions*. Official Gazette of the Italian Republic published on January 14th.
- Mistakidis E. S., De Matteis G., Formisano A. [2007]. Low yield metal shear panels as an alternative for the seismic upgrading of concrete structures. *Advances in Engineering Software*, 38, pp. 626-636.
- Nakashima, M., Iwai, S., Iwata, M., Takeuchi, T., Konomi, S., Akazawa, T., Sabouri, K. [1994], "Energy dissipation behaviour of shear panels made of low yield steel. Earthquake Engineering and Structural Dynamics", Vol. 23, 1299-1313.
- Nakashima, M., [1995], "Strain-hardening behaviour of shear panel made of low yield steel. I: test", *ASCE Journal of Structural Engineering*, 1742-1749.
- Nakashima, M., Akazawa, T., Tsuji, B. [1995], "Strain-hardening behaviour of shear panel made of low yield steel. II: model", *ASCE Journal of Structural Engineering*, 1750-1757.
- Panico, S., [2003] "Aluminium shear panels for seismic protection, numerical analysis and experimental tests", Ph.D thesis, Department of Structural Engineering (DIST), University of Naples "Federico II", Naples, Italy.
- Ramberg, W. and Osgood, W.R., [1943], "Description of stress-strain curves by three parameters", *NACA Techn. No.902*.
- Sabouri-Ghomi S., Roberts T. M. [1991]. "Nonlinear Dynamic Analysis of Thin Steel Plate Shear Walls", *Computers & Structures*, Vol. 39., No. 1/2, pp. 121-127.
- Sabouri-Ghomi S., Ventura C., Kharrazi M.H.K. [2003]. "Shear analysis and design of ductile steel plate walls", *Proc. of the 4th Int. Conference on "Behaviour of Steel Structures in Seismic Areas" (STESSA 2003)*, Naples, Italy, June 9-12.
- Schumacher, A., Grondin, G. Y., Kulak G. L., [1997], "Connection of infill panels in steel plate shear walls". *Structural Engineering Report No. 217*, University of Alberta, Canada.
- Thorburn L.J., Kulak G.L., Montgomery C.J. [1983]. "Analysis of Steel Plate Shear Walls", *Structural Engineering Report No. 107*, Department of Civil Engineering, Universtiy of Alberta, Edmonton, Alberta, Canada.
- Timoshenko S., Woinowsky-Krieger S. [1959]. *Theory of Plates and Shells, Second Edition*, McGraw- Hill, New York, NY.
- Vayas I. et al. [2006]. "Feasibility study "Koletti building"". Report within the PROHITECH "Protection of Historical Buildings by Reversible Mixed Technologies" Research Project.

SEISMIC PERFORMANCE EVALUATION OF STEEL MOMENT RESISTING FRAMES USING ADAPTIVE PUSHOVER

Massimiliano Ferraioli, Angelo Lavino, Alberto Maria Avossa,
Alberto Mandara

Department of Civil Engineering, Second University of Naples, Aversa (CE), Italy

Abstract. The primary focus of this study is on the development of a detailed assessment of the inelastic seismic behaviour, response, and performance of typical ductile steel moment resisting frame structures. At this aim, a multi-objective and multi-criteria performance evaluation of steel moment-frame buildings was realized with a combination of the performance criteria both for structural members and for non-structural components at the different limit state. Analytical models of various complexities are evaluated using nonlinear static pushover analysis and incremental dynamic analysis, to evaluate the potential for collapse in flexible steel moment resisting frame structures due to P-delta effect. In particular, as an alternative to incremental response history analysis, an incremental non-iterative nonlinear static procedure based on adaptive capacity spectra method was used for displacement-based seismic assessment.

Keywords: steel frames, adaptive capacity spectrum method, seismic performance.

1. INTRODUCTION

The estimation of lateral displacement demands is of primary importance in performance-based earthquake-resistant design, especially, when damage control is the main quantity of interest. In particular, the steel moment resisting frames (SMRFs) are expected to be able to sustain large plastic deformations in bending and shear. However, so that the dissipative capacity of the structure can be completely activated, it is necessary to optimize the energy dissipation and guarantee the formation of a global plastic mechanism of collapse. Such objectives are persecuted not directly through nonlinear response history analysis, but indirectly through design procedures essentially based on capacity design criteria. These traditional design provisions may be not effective to obtain a global plastic mechanism and to avoid that interruption or damage may far outweigh the cost of the structural system. It is, rather necessary a multi-level and multi-objective design procedure based on the estimation of the global behavior of the structure in terms of lateral displacement. The validity and appli-

cability of the static pushover analysis have been extensively studied in literature. In particular, many researchers have compared the pushover curves with idealized envelopes obtained from incremental dynamic pushover analyses of structures subjected to artificial and natural input ground motions. Furthermore, the effectiveness of the Capacity Spectrum Method (CSM) has been validated by comparison with experimental results from pseudo-dynamic, cyclic and pushover tests. The Capacity Spectrum Method - by means of a graphical procedure - compares the capacity of the structure to resist lateral forces to the demands of earthquake response spectra. Different Nonlinear Static Procedures (NSPs) based on the CSM have been introduced in pre-standards reports and guidelines. Some of them were incorporated in the new generation of seismic codes to determine the deformation demand imposed on a building expected to behave inelastically. This study develops a simplified seismic demand estimation procedure in which the spectral characteristics of the ground motion are related to the inelastic deformation capacity for the structure.

2. DESIGN OF SEISMIC RESISTANT STEEL FRAMES

The aim of the conventional design approach is to satisfy the two requirements that a structural system must meet: a) under ordinary actions the structure must be stiff in order to minimize structural and non-structural damage; b) under severe earthquakes the structure must be safe from collapse even if some structural damage may be tolerable. The serviceability limit state (SLS) and the ultimate limit state (ULS) are checked with a linear elastic analysis. Undesirable brittle failure mechanisms are usually avoided using local ductility requirements and capacity design rule. Finally, full-strength connections concur to avoid the failure of beam-column joints. In modern seismic codes the problem of the reduction of the available ductility due to undesirable collapse mechanisms is faced by providing design criteria which are aimed at guaranteeing the complete exploitation of the plastic reserves of the structural scheme. The structural damage and collapses during recent earthquakes have evidenced some critical aspects in the seismic behaviour of steel structures even when designed according to the current design codes. The main limit of traditional design provisions is that the performance cannot be predicted because the seismic behaviour of the structure is governed by phenomena which are not adequately captured in the simple design process. In particular, the formation of local plastic mechanism could not be avoided and the safety factor could change with the design level. Three different approaches are generally used to apply the capacity design rule: 1) amplification of the acting moment in the seismic design situation (ECCS, 1988; New Italian Code, 2008); 2) check of hierarchy criterion after analysis (EC8, 2003; UBC, 1997; AISC, 1997; Lee, 1996); 3) Plastic design (Mazzolani & Piluso, 1997) based on the application of the kinematic theorem of plastic collapse.

Italian Code 2008 – EC8 2003

The aim of capacity design approach is to avoid collapse mechanisms characterized by poor energy dissipation capacity, such as soft-storey mechanisms. In particular, it is usually required that plastic hinges develop in beams rather than in columns. The first step in the seismic design of dissipative structures is the selection of a suitable location of dissipative zones, i.e. a suitable collapse mechanism. Non-dissipative parts of dissipative seismic resistant structures and their connections to the dissipative ones have to be designed with sufficient overstrength to allow the cyclic yielding of the dissipative parts. This means that non-dissipative parts have to be designed in order to remain in the elastic range and, therefore, they have to be proportioned on the basis of the maximum internal actions that the dissipative zones are able to transmit. Conversely, the dissipative zones have to be proportioned on the basis of internal actions arising from the design seismic forces. For plastic hinges at the ends of the beams it should be verified that the full plastic moment of resistance and rotation capacity are not decreased by compression and shear forces. For sections belonging to cross sectional classes 1 and 2:

$$\begin{aligned}
 M_{Ed} &\leq M_{pl,Rd} \\
 N_{Ed} &\leq 0.15 \cdot N_{pl,Rd} \\
 V_{Ed} = V_{G,Ed} + V_{M,Ed} &\leq 0.5 \cdot V_{pl,Rd}
 \end{aligned}
 \tag{1}$$

where:

- M_{Ed} , N_{Ed} , V_{Ed} are the design bending moment, axial force and shear force, respectively;
- $M_{pl,Rd}$, $N_{pl,Rd}$, $V_{pl,Rd}$ are the design resistances;
- $V_{G,Ed}$ is the shear force due to the non seismic loads;
- $V_{M,Ed}$ is the shear force due to the application of the plastic moments with opposite signs at the end sections A and B of the beam;

The columns shall be verified in compression considering the most unfavourable combination of the axial force and bending moments. The design action effects should be computed as:

$$\begin{aligned}
 M_{Ed} &= M_{Ed,G} + 1.1\gamma_{Rd}\Omega M_{Ed,E} \\
 N_{Ed} &= N_{Ed,G} + 1.1\gamma_{Rd}\Omega \cdot N_{Ed,E} \\
 V_{Ed} &= V_{Ed,G} + 1.1\gamma_{Rd}\Omega V_{Ed,E}
 \end{aligned}
 \tag{2}$$

- $M_{Ed,G}$, $N_{Ed,G}$, $V_{Ed,G}$ are the bending moment, axial force and shear force in the column due to the non-seismic actions;
- γ_{Rd} is the overstrength factor;
- Ω is the minimum value of $\Omega_i = M_{pl,Rd,i}/M_{Ed,i}$ for all the beams in which dissipative zones are located. $M_{Ed,i}$ is the design value of the bending moment in i^{th} beam in the seismic design situation and $M_{pl,Rd,i}$ is the corresponding plastic moment.

The following condition should be satisfied at all joints of beams with primary seismic columns:

$$\sum M_{c,Rd,rid} \geq \gamma_{RD} M_{b,pl,Rd,i} \quad (3)$$

- $\sum M_{c,Rd,rid}$ is the sum of design values of the moments of resistance of the columns framing into the joint;
- $\sum M_{b,pl,Rd,i}$ is the sum of design values of the moments of resistance of the beams framing into the joint;
- γ_{RD} is equal to 1,3 for structures of ductility class High (CDA) and equal to 1,1 for structures of ductility class Low (CDB).

Plastic Design (Mazzolani & Piluso, 1997)

The collapse mechanism plays a very important role in the seismic design of structures, because it influences the value of the available global ductility and the energy dissipation capacity of the structure. The method proposed by Mazzolani and Piluso (1997) is used to design moment resisting steel frames able to guarantee a global collapse mechanism under seismic actions. In particular, this design goal is attained by the application of the kinematic theorem of plastic collapse and on second order plastic analysis. It is based on the observation that the collapse mechanisms of frames under horizontal forces can be considered as belonging to three main types (Fig. 1). The collapse mechanism of the global type is a particular case of type-2 mechanism. The control of the failure mode can be performed through the analysis of $3n_s$ mechanisms (where n_s is the number of storeys).

It is assumed that the beam sections are already designed to resist vertical loads. Therefore, the values of the plastic section modulus of columns only have to be defined so that the kinematically admissible multiplier of the horizontal forces corresponding to the global mechanism is less than those corresponding to the other $(3n_s-1)$ kinematically admissible mechanisms. The mechanism equilibrium curve method is used for an approximate estimate of the collapse multiplier. The linearized mechanism equilibrium curve can be expressed as:

$$\alpha_c = \alpha - \gamma\delta \tag{4}$$

- α is the kinematically admissible multiplier of horizontal forces;
- γ is the slope of the mechanism equilibrium curve;
- δ is the top sway displacement given by $H_o \cdot \sin\theta$ (where H_o is the sum of the interstorey heights of the storeys involved by the generic mechanism) and θ is the angle of rotation of the plastic hinges.

To design frames failing in a global mode, the cross-sections of columns have to be dimensioned so that, according to the upper bound theorem, the kinematically admissible horizontal force multiplier corresponding to the global-type mechanism is the minimum among all kinematically admissible multipliers. From the practical point of view, is necessary to impose that the mechanism equilibrium curve corresponding to the global mechanism has to lie below those corresponding to all other mechanisms. The only one parameter to be selected is the ultimate top displacement, that must be compatible with plastic rotation capacity of members due to $H \cdot \theta_p$ (Fig. 2). The plastic rotation supply θ_p is variable in a range of 0.02 and 0.04 radian.

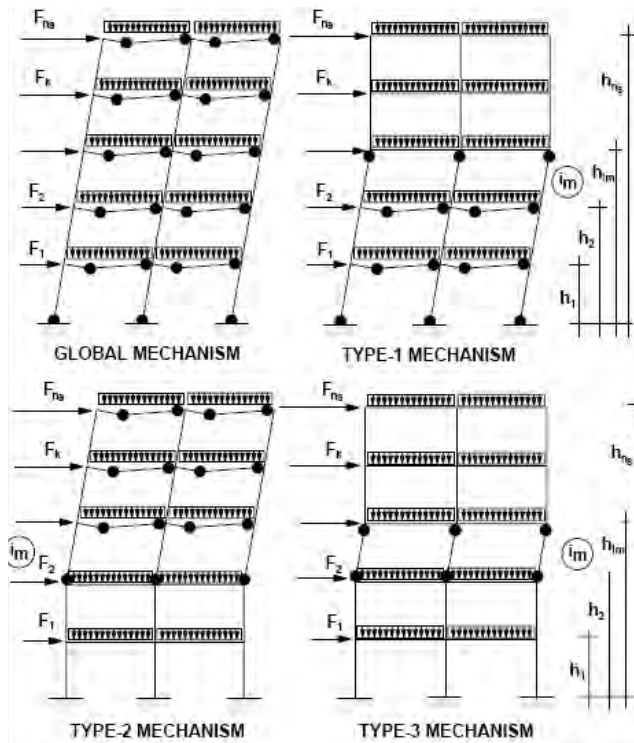


Figure 1. Analysed collapse mechanism typologies (Mazzolani & Piluso, 1997).

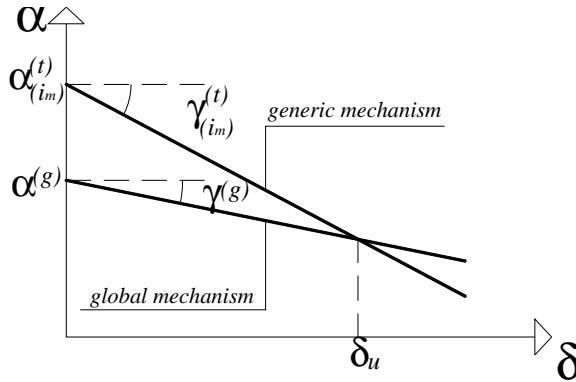


Figure 2. Design conditions.

The following design conditions have to be imposed:

$$\alpha^{(g)} - \gamma^{(g)}\delta_u \leq \alpha_{i_m}^{(t)} - \gamma_{i_m}^{(t)}\delta_u \quad i_m = 1,2,3,\dots,n_s \quad t = 1,2,3 \quad (5)$$

- i_m mechanism index;
- t mechanism type;

This means that there are $3n_s$ design conditions to be satisfied in the case of a frame having n_s storeys, which derive directly from the extension of the upper bound theorem to the mechanism equilibrium curves. These conditions are integrated by conditions related to technological limitations, allowing reducing the sections of the columns over height.

The design procedures based on the second order plastic analysis proved to be effective to ensure a global plastic mechanism, but require a great overstrength of steel members. Furthermore, the design strength of the structure is independent by the intensity level of the earthquake ground motion. Finally, the ultimate limit state verification is not sufficient to ensure the verification at the other limit states. For this reason, the plastic design method is modified increasing the design ultimate displacement (and, therefore, the ultimate plastic rotation capacity of the beams) till to satisfy the SLS verification of Italian Code (interstorey drift $d_{lim} \leq 0.005h$).

Study cases

Three different steel frames are considered in the analyses (Tab. 1). The frames are designed according to four different design provisions: 1) New Italian Code - IC08 (2008); 2) Eurocode 8 - EC8 (2003); 3) Plastic Design – PD (Mazzolani et al., 1997); 4) Plastic Design with SLS Verification - PD-SLS. In the last approach the design ultimate displacement is increased till to satisfy the SLS verification of Italian Code (interstorey drift ratio=5‰). The design seismic action

is defined with soil class A, damping ratio $\xi=5\%$, peak ground acceleration $PGA=0.25g$, behavior factor $q=6.5$. Steel members are made from Italian S275 ($f_y=275$ MPa). The interstorey height is 3.5m for the first floor and 3.0m for the other floors. The bay length is 5.00 m. EC8 and IC08 gives very similar results. On the contrary, PD gives a great overstrength of the steel members.

Table 1. Study cases: Steel moment resisting frames designed.

Design	ELEMENT	3 STOREYS – 3 BAYS									
IC08	Level	1°	2°	3°							
	Beams	IPE270	IPE270	IPE270							
	Columns	Ext.	HE400B	HE400B							HE400B
		Int.	HE400B	HE400B							HE400B
PD	Level	1°	2°	3°							
	Beams	IPE300	IPE300	IPE300							
	Columns	Ext.	HE300B	HE280B							HE260B
		Int.	HE280B	HE260B							HE240B
PD-SLS	Level	1°	2°	3°							
	Beams	IPE300	IPE300	IPE300							
	Columns	Ext.	HE450B	HE340B	HE300B						
		Int.	HE400B	HE300B	HE260B						
EC8	Level	1°	2°	3°							
	Beams	IPE300	IPE300	IPE300							
	Columns	Ext.	HE400B	HE400B	HE400B						
		Int.	HE400B	HE400B	HE400						
7 STOREYS – 3 BAYS											
IC08	Level	1°	2°	3°	4°	5°	6°	7°	8°	9°	
	Beams	IPE270	IPE270	IPE270	IPE270	IPE270	IPE270	IPE270	-	-	
	Columns	Ext.	HE220B	HE220B	HE220B	HE220B	HE220B	HE220B	HE220B	-	-
		Int.	HE280B	HE280B	HE280B	HE280B	HE280B	HE280B	HE280B	-	-
PD-SLS	Level	1°	2°	3°	4°	5°	6°	7°	8°	9°	
	Beams	IPE270	IPE270	IPE270	IPE270	IPE270	IPE270	IPE270	-	-	
	Columns	Ext.	HE550B	HE450B	HE400B	HE400B	HE360B	HE320B	HE260B	-	-
		Int.	HE500B	HE450B	HE360B	HE360B	HE340B	HE300B	HE240B	-	-
EC8	Level	1°	2°	3°	4°	5°	6°	7°	8°	9°	
	Beams	IPE270	IPE270	IPE270	IPE270	IPE270	IPE270	IPE270	-	-	
	Columns	Ext.	HE160B	HE160B	HE160B	HE160B	HE160B	HE160B	HE160B	-	-
		Int.	HE240B	HE240B	HE240B	HE240B	HE240B	HE240B	HE240B	-	-
9 STOREYS – 3 BAYS											
IC08	Level	1°	2°	3°	4°	5°	6°	7°	8°	9°	
	Beams	IPE270	IPE270	IPE270	IPE270	IPE270	IPE270	IPE270	IPE270	IPE270	
	Columns	Ext.	HE220B	HE220B	HE220B	HE220B	HE220B	HE220B	HE220B	HE220B	HE220B
		Int.	HE280B	HE280B	HE280B	HE280B	HE280B	HE280B	HE280B	HE280B	HE280B
PD-SLS	Level	1°	2°	3°	4°	5°	6°	7°	8°	9°	
	Beams	IPE270	IPE270	IPE270	IPE270	IPE270	IPE270	IPE270	IPE270	IPE270	
	Columns	Ext.	HE500B	HE450B	HE450B	HE450B	HE400B	HE400B	HE400B	HE320B	HE260B
		Int.	HE500B	HE400B	HE400B	HE400B	HE400B	HE400B	HE360B	HE340B	HE300B

3. DISPLACEMENT-BASED SEISMIC ASSESSMENT

The building codes generally use strength as the main design criterion and they consider the lateral force procedure at the base of the earthquake resistant design. The displacement control usually plays a secondary role, and the deformation demand is generally checked at the end of the design process for the serviceability limit state. However, recent earthquakes have shown that struc-

tures may suffer irreparable or too costly to repair damages. Furthermore, inelastic behavior, indicating damage, is observed even during smaller earthquakes. As a consequence, the modern seismic design requires the application of performance-based concepts. In this way, multi-level objectives may be pursued and structures that perform appropriately for all earthquakes may be obtained. In this context, building codes in the United States and Japan are rapidly moving towards the adoption of performance based design procedures for earthquake resistance. The displacement-based design (DBD) and the performance-based design (PBD) seem to be more promising than the traditional force-based design (FBD). As a consequence, the fundamental design parameters are the displacements and the ductility demands, and the most suitable approach in modern seismic design is to ensure that these parameters will not be exceeded under the design-level earthquake ground motion. The defined level of damage during a specified earthquake ground motion should be ensured by performance-based criteria. These criteria should be selected such that at the specified levels of ground motion and with defined levels of reliability, the structure will not be damaged beyond certain limiting states.

In this paper the displacement-based assessment is carried out for three different levels of performance (Immediate Occupancy - IO, Life Safety – LS, Collapse Prevention – CP). Two control parameters are monitored to check the attainment of the different performance levels of the building (acceptance criteria): 1) interstorey drift damage index (IDI); 2) plastic rotations in columns and beams as a function of yield chord rotation. The plastic rotations are defined by Table 5.6 of FEMA 356. The limit values for the interstorey drift damage index are shown in Table 2.

Table 2. Performance levels and acceptance criteria.

Performance Level	IDI	Plastic rotation			
		Beams		Columns $0.20 < P/P_{CL} < 0.50$	
		$\frac{b_f}{2t_f} \leq \frac{52}{\sqrt{F_{ye}}}$ $\frac{h}{t_w} \leq \frac{418}{\sqrt{F_{ye}}}$	$\frac{b_f}{2t_f} \geq \frac{65}{\sqrt{F_{ye}}}$ $\frac{h}{t_w} \geq \frac{640}{\sqrt{F_{ye}}}$	$\frac{b_f}{2t_f} \leq \frac{52}{\sqrt{F_{ye}}}$ $\frac{h}{t_w} \leq \frac{260}{\sqrt{F_{ye}}}$	$\frac{h}{t_w} \geq \frac{400}{\sqrt{F_{ye}}}$ $\frac{h}{t_w} \geq \frac{400}{\sqrt{F_{ye}}}$
Immediate occupancy	0.01	θ_y	$0.25 \theta_y$	$0.25 \theta_y$	$0.25 \theta_y$
Life safety	0.02	$6 \theta_y$	$2 \theta_y$	$8 (1-1.7 P/P_{cl})\theta_y$	$0.50 \theta_y$
Collapse prevention	0.04	$8 \theta_y$	$3 \theta_y$	$11 (1-1.7 P/P_{cl})\theta_y$	$0.80 \theta_y$

4. PUSHOVER ANALYSIS

Nonlinear modelling

The Performance-Based Design approach requires the use of nonlinear analysis. In this paper, both distributed plasticity-fiber element model and plastic hinge model implemented, respectively, in Seismostruct (SeismoSoft, 2009) and SAP2000 nonlinear computer programs are considered in the analyses. The model takes into account geometrical nonlinearity and material inelasticity. Sources of geometrical nonlinearity considered are both local (beam-column effect) and global (large displacement/rotation effects). The distributed plasticity fiber element model accounts for the spread of plasticity along the element and inside the cross section and so it allows for the accurate estimation of structural damage distribution. The sectional stress-strain state or beam-column elements is obtained through the integration of the nonlinear uniaxial stress-strain response of the fibers in which the section has been subdivided. A bilinear model with kinematic strain-hardening of 0.5% is used for steel. The spread of plasticity along the element derives from an inelastic cubic formulation with two Gauss points to use for numerical integration of the equilibrium equations. Relatively short elements (four per structural member) are considered in the inelastic model. In this way, the numeric accuracy problems derived from the constant generalized axial strain shape function are avoided. The empirical method of Kato-Akiyama is used for the determination of local ductility in plastic hinge model. According to this method the rotational capacity of the members is described by means of a trilinear moment-rotation curve with parameters calculated taking into account the axial load of the member, the slenderness of the web and the flange, the flexural-buckling phenomena. The values of plastic rotation and residual strength are defined by FEMA 356 as a function of geometric and mechanical characteristics of steel members (Tab. 3).

Table 3. Modeling parameters and acceptance criteria for nonlinear procedures

	Beams		Columns $0.20 < P/P_{CL} < 0.50$	
	$\frac{b_f}{2t_f} \leq \frac{52}{\sqrt{F_{ye}}}$ $e \frac{h}{t_w} \leq \frac{418}{\sqrt{F_{ye}}}$	$\frac{b_f}{2t_f} \geq \frac{65}{\sqrt{F_{ye}}}$ $o \frac{h}{t_w} \geq \frac{640}{\sqrt{F_{ye}}}$	$\frac{b_f}{2t_f} \leq \frac{52}{\sqrt{F_{ye}}}$ $e \frac{h}{t_w} \leq \frac{260}{\sqrt{F_{ye}}}$	$\frac{b_f}{2t_f} \geq \frac{65}{\sqrt{F_{ye}}}$ $o \frac{h}{t_w} \geq \frac{400}{\sqrt{F_{ye}}}$
Plastic Rotation angle a (radians)	$6\theta_y$	$4\theta_y$	$11(1-1.7 P/P_{cl})\theta_y$	θ_y
Plastic Rotation angle b (radians)	$11\theta_y$	$6\theta_y$	$17(1-1.7 P/P_{cl})\theta_y$	$1.5 \theta_y$
Residual Strength ratio c	0.60	0.60	0.20	0.20

According to FEMA 356 the modeling of nodal panel is avoided in the hypothesis that: 1) the expected shear strength of panel zones exceeds the flexural strength of the beams at a beam-column connection; 2) the stiffness of the panel zone is at least 10 times larger than the flexural stiffness of the beam. First of all a comparative evaluation of design procedures considering both building code provisions both innovative methods based on the limit analysis or on the second order plastic analysis was carried out. In the case of steel frames designed with the capacity design rule both plastic hinge formation in columns and undesirable story mechanism are not completely avoided. In Figure 3 the comparison of capacity curves obtained with distributed plasticity fiber element model and plastic hinge model under the first mode distribution of lateral load is reported. Results show that the plastic hinge model generally underestimates the lateral strength. However, the results obtained with the two models are very similar.

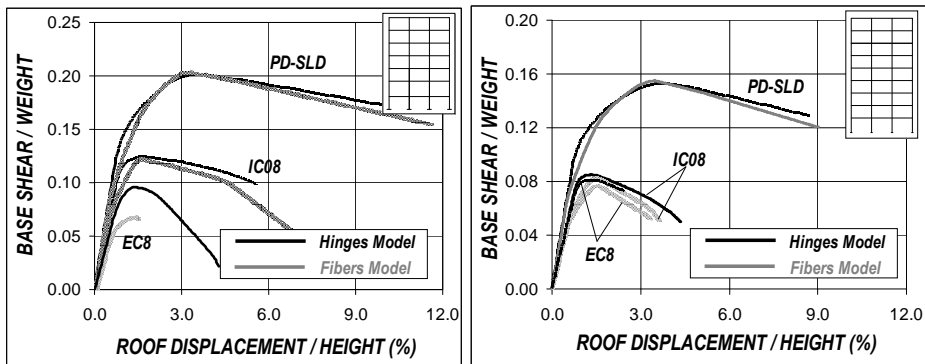


Figure 3. Base shear versus roof displacement – Influence of modelling.

Lateral load pattern effect

The shear forces vs. story drift relationship may be very sensitive to the applied load pattern, especially for structures in which local plastic mechanism occurs. The lateral load pattern effects are investigated using six distributions: 1) Uniform Distribution (UD). The lateral load distribution is proportional to the floor masses m_i . 2) First Mode Distribution (FMD). The vertical distribution is proportional to the floor masses and the shape of the fundamental mode. 3) Equivalent First Mode Distribution (EFMD). The lateral force distribution is proportional to an equivalent first mode defined from SRSS combination of sufficient modes to capture at least 90% of the total mass. 4) SRSS Distribution. The vertical distribution is proportional to the story shear distribution calculated by combining modal responses. 5) Force-based adaptive pushover (FAP); 6) Displacement-based adaptive pushover (DAP). In Figure 4 the comparison of capacity curves is reported. The 9-storey frame designed according to EC8

or to Italian Code shows very little variation with the lateral load pattern. On the contrary, the steel frames designed with plastic design are very sensitive to the lateral load pattern. Particularly, DAP tends to overestimate the lateral strength if compared to other pushover analyses. This result derives from the higher mode contribution that in DAP analysis gives a reduction of the axial force in the external column of the first floor. Consequently, P-delta effects decrease and the plastic bending moment consequently increases.

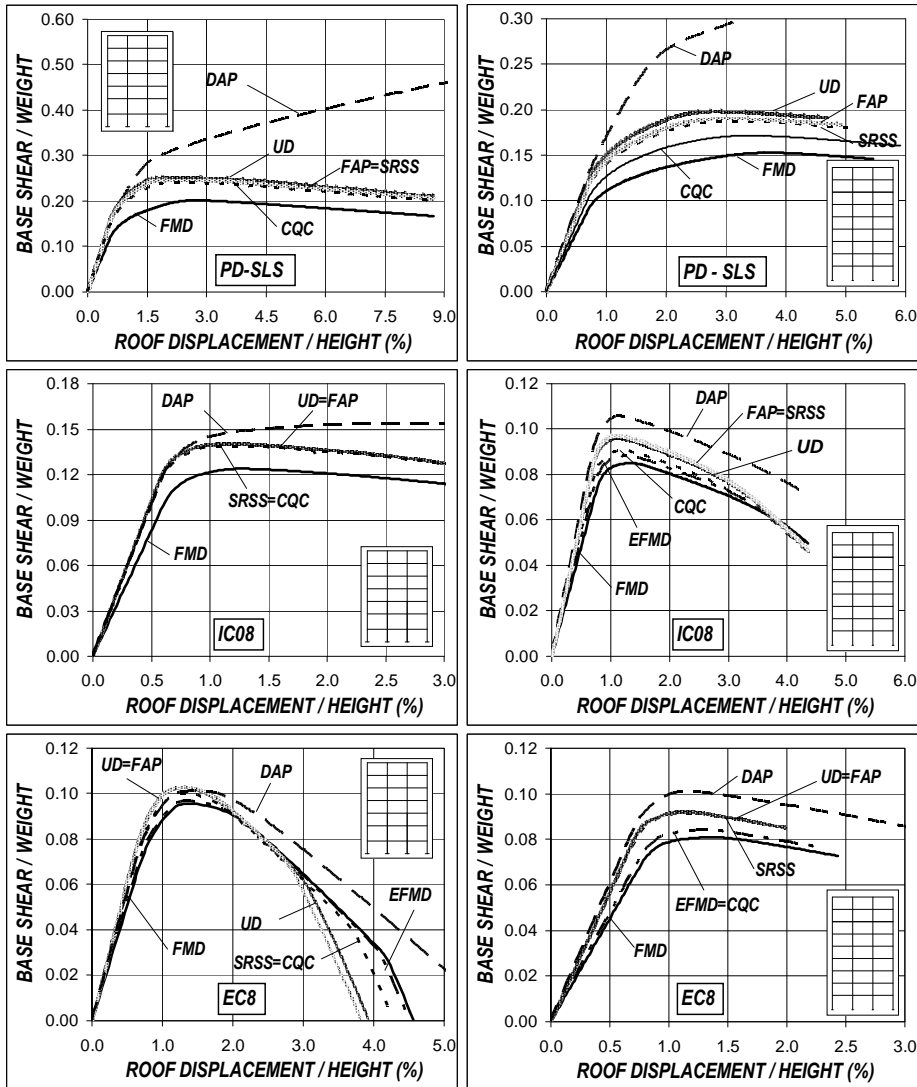


Figure 4. Base shear versus roof displacement. Pushover Analysis.

Static versus dynamic pushover analysis

Sensitivity analysis of SMRFs loaded into the plastic response range is more complicated and computationally intensive because the state of internal forces depends on the loading history. In order to verify the accuracy of nonlinear static procedures and the sensitivity to input ground motion a series of FAP, DAP and conventional pushover analyses are compared with the predictions of inelastic dynamic analysis, employing a set of artificial earthquakes. Particularly, a set of 10 input ground motions is generated to be consistent to 5%-damped EC8 elastic spectrum for soil class A. In Figure 5 the comparison between pushover analyses and Incremental Dynamic Analyses (IDA) is shown. For the 9-storey frame designed with Italian Code (IC08) the static pushover seems to be conservative since it underestimates the capacity. On the contrary, for the frame designed with plastic design and SLS verification DAP analysis gives much greater lateral strength.

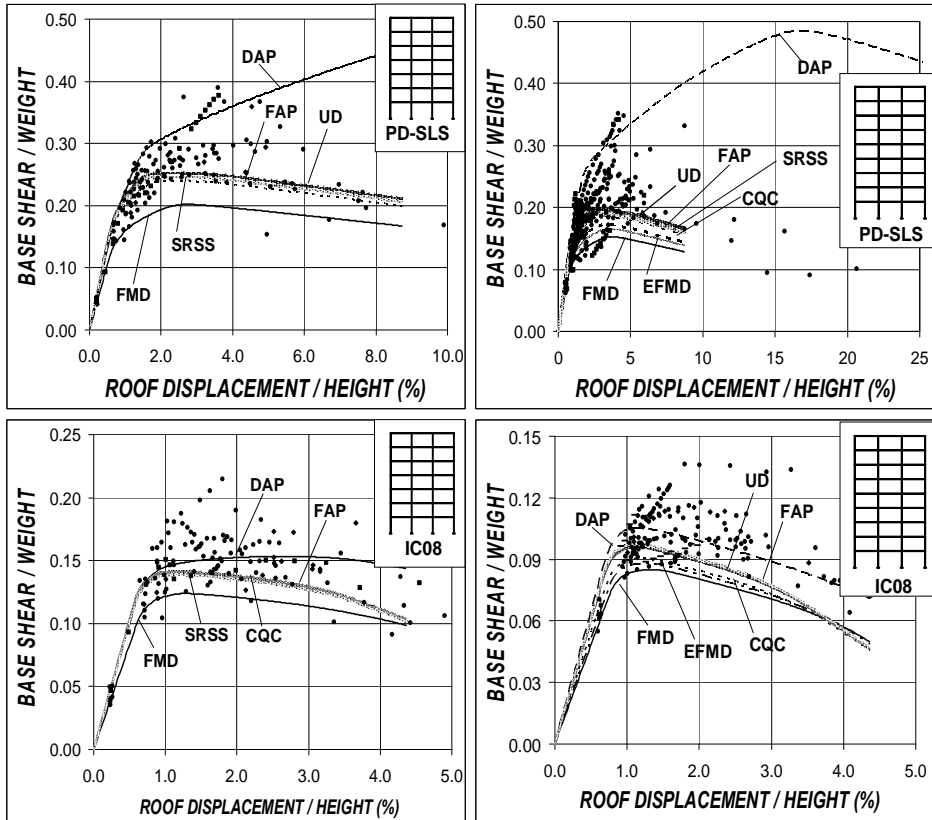


Figure 5. Base shear versus roof displacement. Pushover Analysis.

The distribution of localized demands in the MDOF system can differ from those associated with the equivalent SDOF system, and the importance of this so-called “MDOF Effects” increases with the amount of inelasticity in the structure and with the occurrence of local plastic mechanism.

In order to investigate these effects the interstorey drift profiles obtained from pushover analyses are compared to the drift profiles from nonlinear time-history analysis (Fig. 6). The drift profile from pushover analysis is referred to the CP limit state. The drift profile from dynamic analysis is referred to the input ground motion corresponding to the maximum total drift ratio. The earthquake is scaled to have the same roof displacement obtained from pushover analysis at the collapse prevention limit state.

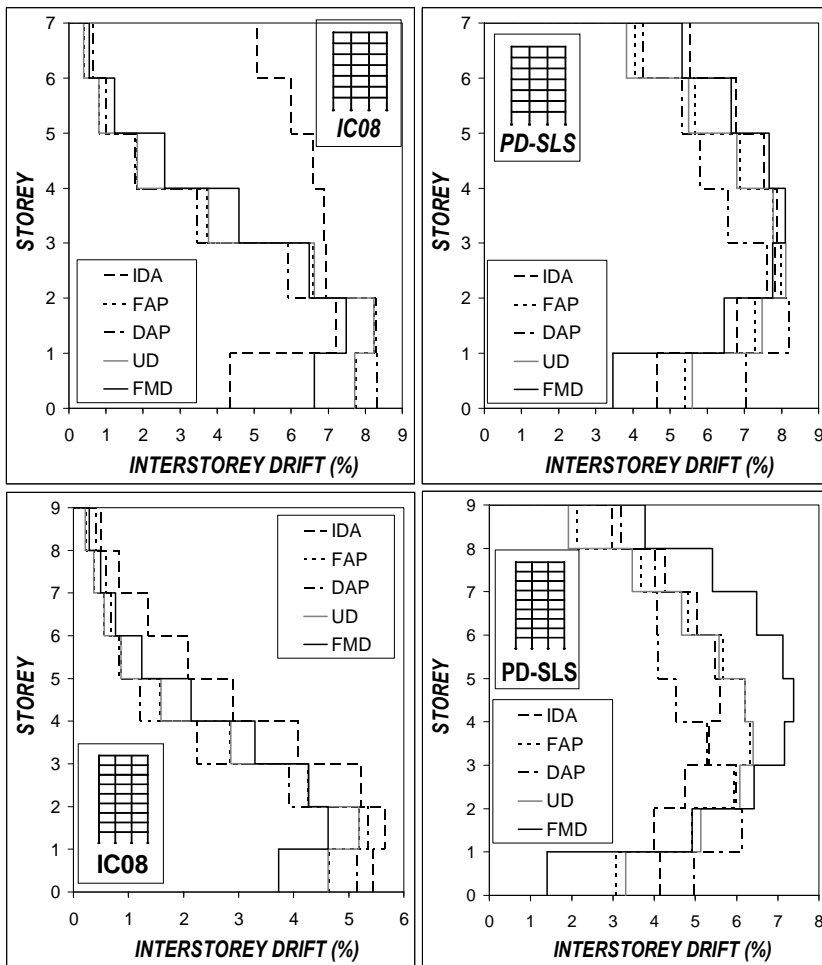


Figure 6. Base shear versus roof displacement. Pushover Analysis.

The results obtained show that the DAP analysis systematically underestimates the interstorey drifts if compared to dynamic analysis, while the FMD distribution seems to be more effective. All the nonlinear static procedures underestimates the interstorey drifts of the 7-storey frame designed with the Italian Code. This result derives from the high strength required to the roof columns by the capacity design criteria

5. NONLINEAR STATIC PROCEDURES (NSPS) IN PERFORMANCE-BASED SEISMIC ASSESSMENT

A simplified procedure based on the pushover analysis and on the strength reduction factor was introduced in Eurocode 8 (2003). Static Displacement-Based Procedures were developed by the Federal Emergency Management Agency (FEMA). The Coefficient Method (CM) of FEMA-356 (2000) is based on a displacement modification procedure in which several empirically derived factors are used to modify the response of a linearly-elastic single-degree-of-freedom (SDOF) model of the structure. In other words, the CM is a form of equivalent linearization. Empirically derived relationships, that gives the effective period and damping as a function of ductility, are used to estimate the response of an equivalent nonlinear SDOF system.

ATC-40 Report (ATC-40, 1997) proposes three nonlinear static procedures (A,B,C) based on the Capacity Spectrum Method and on the High Damping Elastic Response Spectra (HEDRS) with an equivalent viscous damping accounting for the energy dissipation due to yielding. However several deficiencies were found by some authors. In particular, no physical principle justifies the existence of a stable relationship between the hysteretic energy dissipation and equivalent viscous damping, particularly for highly inelastic systems, and so the convergence of ATC iterative procedures is not assured. Moreover, the ATC-40 procedures require the calculation of the characteristic periods of earthquake spectrum which often are not easy to be estimated.

The N2 method proposed by Fajfar (2001) combines together the visual representation of the CSM and the superior physical basis of Inelastic Demand Response Spectra (IDRS) which are expected to be more accurate than HEDRS, especially in the short period range and in the case of high ductility factors. Both CM and CSM were found to provide substantially different estimates of target displacement for the same ground motion and the same building (Aschheim et al., 1998; Akkar and Metin, 2007; Chopra and Goel, 2000; Goel, 2007; Miranda and Luiz-Garcia, 2002) and have proposed improved procedures for estimating the target displacement. Recently, FEMA-440 document (ATC-55, 2003) re-examined the existing NSPs and proposed improvements to both the CM and CSM. Recommendations in the FEMA-440 document have been adopted in the ASCE/SEI 41-06 standard (ASCE, 2007). The nonlinear static procedures (FEMA-356, ATC-40, FEMA-440, ASCE/SEI 41-06, CSM-N2)

usually require the pushover analysis. The structure is pushed statically to a target displacement at the control node to check for the acceptable structural performance. Different height-wise distributions of lateral loads are usually considered. In fact, the shear forces vs. story drift relationship may be very sensitive to the applied load pattern. Generally, different distributions of lateral load are considered. 1) Equivalent lateral force distribution (ELFD). The seismic forces at each floor level of the building are distributed according to the distribution of floor mass m_i and to the height h_i above the base. 2) Fundamental Mode Distribution (FMD). The vertical distribution is proportional to the floor masses and the fundamental mode shape. 3) Response Spectral Analysis distribution (RSA): the vector of lateral forces is proportional to the story shear distribution calculated by combining the modal responses of sufficient modes to capture at least 90% of the total mass. 4) Uniform Distribution (UD). The lateral load distribution is proportional to the floor masses m_i . FEMA-356 requires development of the pushover curve for two height-wise distributions of lateral forces: UD and one selected from ELFD, FMD and RSA. ATC-40, FEMA-440, and ASCE/SEI 41-06 require only the fundamental mode distribution.

FEMA-356 - Coefficient Method

The Coefficient Method of FEMA 356 (ASCE, 2000) is based on an equivalent linearization. In particular, the maximum inelastic displacement (target displacement) is obtained from the linear elastic response of the equivalent SDOF system, as follows:

$$\delta_t = C_0 C_1 C_2 C_3 S_a \frac{T_e^2}{4\pi^2} g \quad (6)$$

S_a is the response spectrum acceleration at the effective fundamental vibration period and damping ratio of the building under consideration. g is the acceleration due to gravity. T_e is the effective fundamental period of the building in the direction under consideration, computed as follows:

$$T_e = T_i \sqrt{K_i/K_e} \quad (7)$$

where T_i is the fundamental vibration period defined from elastic eigenvalue analysis; K_i is the elastic stiffness of the building; K_e is the effective stiffness of the building obtained by idealizing the pushover curve as a bilinear relationship. The coefficient C_0 is the modification factor that relates the elastic response of a SDOF system to the elastic displacement of the MDOF building. The control node of the building may be defined from the first mode participation factor PF or selected from tabulated values in FEMA-356. C_1 is the modi-

fication factor that relates the maximum inelastic and elastic displacement of the SDOF system computed from:

$$C_1 = \begin{cases} 1.0; & T_e \geq T_s \\ (1.0 + (R-1) T_s / T_e) / R; & T_e < T_s \\ 1.5; & T_e < 0.1 s \end{cases} \quad (8)$$

where R is the ratio of elastic and yield strengths and T_s is the corner period where the response spectrum transitions from constant pseudo-acceleration to constant pseudo-velocity. The modification factor C_2 represents the effects of pinched hysteretic shape, stiffness degradation, and strength deterioration. $C_2=1$ for nonlinear analysis and tabulated as a function of framing system and performance level otherwise.

The modification factor C_3 accounts for the in-cresed displacement due to P-delta effects, as follows:

$$C_3 = \begin{cases} 1.0; & \alpha \geq 0 \\ (1.0 + |\alpha| (R-1)^{3/2} / T_e); & \alpha < 0 \end{cases} \quad (9)$$

where α is the ratio of the post-yield stiffness to effective elastic stiffness.

ATC-40 - Capacity Spectrum Method

The ATC-40 procedures are based on CSM Method. The basic assumption is the equivalent linearization by which the maximum inelastic deformation of a nonlinear SDOF system (target displacement) is approximated from the maximum deformation of a linear elastic SDOF system with equivalent period T_{eq} and equivalent damping ratio ξ_{eq} , expressed as follows:

$$T_{eq} = T_0 \sqrt{\frac{\mu}{1 + \alpha\mu - \alpha}}; \quad \xi_{eq} = \xi_0 + \kappa \frac{1}{\pi} \frac{(\mu-1)(1-\alpha)}{\mu(1 + \alpha\mu - \alpha)} \quad (10)$$

where T_0 is the initial period of vibration of the nonlinear system; α is the post-yield stiffness ratio; μ is the maximum displacement ductility ratio; κ is the adjustment factor to approximately account for changes in hysteretic behavior. In particular, the ATC-40 document defines three types of hysteretic behaviors: Type A with stable, reasonably full hysteretic loops. Type C with severely pinched and/or degraded loops. Type B between Types A and C. The equivalent linearization procedure requires prior knowledge of the displacement ductility ratio. ATC-40 provides three iterative procedures: (A, B, C). The procedures A and B are the most transparent and convenient for programming, whereas the Procedure C is purely a graphical method that is not suitable for programming.

FEMA-440 - Coefficient Method

FEMA 440 introduces some improvements in Coefficient Method of FEMA-356. In particular, the coefficient C_1 is given by

$$C_1 = \begin{cases} 1.0 + \frac{R-1}{0.04a}; & T_e < 0.2s \\ 1.0; & T_e > 1.0s \\ 1.0 + \frac{R-1}{aT_e^2}; & 0.2s < T_e < 1.0s \end{cases} \quad (11)$$

where $\alpha=130$ for site class A and B, 90 for site class C, $a=60$ for site classes D, E, and F. The coefficient C_2 is given by

$$C_2 = \begin{cases} 1.0; & T_e > 0.7s \\ 1.0 + \frac{1}{800} \left(\frac{R-1}{T_e} \right)^2; & T_e \leq 0.7s \end{cases} \quad (12)$$

Finally, the coefficient C_3 is eliminated and substituted by a limitation on strength to avoid dynamic instability. This limitation on strength is specified by imposing a maximum limit on R given by

$$R_{max} = \frac{\Delta_d}{\Delta_y} + \frac{|\alpha_e|^{-h}}{4}; \quad h=1.0+0.15 \ln(T_e) \quad (13)$$

In eq.8 Δ_d is the deformation corresponding to peak strength, Δ_y is the yield deformation, and α_e is the effective negative post-yield slope given by

$$\alpha_e = \alpha_{P-\Delta} + \lambda(\alpha_2 - \alpha_{P-\Delta}) \quad (14)$$

Where α_2 is the negative post-yield slope ratio; $\alpha_{P-\Delta}$ is the negative slope ratio caused by $P-\Delta$ effects; λ is the near-field effect given: $\lambda=0.8$ for $S_I \geq 0.6$ and $\lambda=0.2$ for $S_I < 0.6$ (S_I is defined as the 1-second spectral acceleration for the Maximum Considered Earthquake). The α_2 slope includes $P-\Delta$ effects, in-cycle degradation, and cyclic degradation.

FEMA-440 - Capacity Spectrum Method

The improved FEMA-440 CSM includes new expressions to determine the effective period and effective damping developed by Guyader and Iwan (2006). Consistent with the original ATC-40 procedure, three iterative procedures for estimating the target displacement are also outlined. Finally, a limitation on the

strength is imposed to avoid dynamic instability. Improved formulas for the effective period and viscous damping are proposed as a function of several coefficients tabulated in Table 6-1 and Table 6-2 of FEMA-440 document. The equivalent linearization procedures applied in practice normally require the use of spectral reduction factors to adjust an initial response spectrum to the appropriate level of effective damping β_{eff} . This factor $B(\beta_{eff})$ is a function of the effective damping and is used to adjust the spectral acceleration ordinates as follows:

$$(S_a)_\beta = (S_a)_{5\%} / B(\beta_{eff}) \quad (15)$$

where the damping coefficient $B(\beta_{eff})$ is given by:

$$B = \frac{4}{5.6 - \ln \beta_{eff}} \quad (16)$$

Capacity Spectrum Method –N2

The CSM-N2 procedure is based on the Capacity Spectrum Method and the Inelastic Demand Spectra. The inelastic seismic demand is not represented by High Damping Elastic Response Spectra (HDEERS), but it is represented by means of the Inelastic Demand Response Spectra (IDRS). The IDRS is not directly obtained through the nonlinear time-history analysis of the equivalent bilinear SDOF system, but it is indirectly computed scaling the Elastic Demand Response Spectra (EDRS). The IDRS is obtained by scaling the EDRS (with viscous damping ratio $\xi=5$ per cent) by means a ductility reduction factor R_μ . In particular, the inelastic pseudo-acceleration S_a and displacement S_d - which represents the coordinates of the IDRS in ADRS format - are characterized from the coordinates $[S_{de}; S_{ae}]$ of the EDRS ($\xi=5$ per cent) as follows:

$$S_a = \frac{S_{ae}}{R_\mu} \quad S_d = \frac{\mu \cdot S_{de}}{R_\mu} \quad (17)$$

In eq.17 μ is the ductility ratio and the ductility reduction factor R_μ is defined by the following expressions derived from statistical data analysis (Vidic et al., 1994):

$$R_\mu = (\mu - 1)T/T_0 + 1 \quad \text{for } T \leq T_0 \quad (18)$$

$$R_\mu = \mu \quad \text{for } T \leq T_0 \quad \text{with } T_0 = 0.65\mu^{0.3} \cdot T_c \leq T_c \quad (19)$$

where T_c is the corner period of the earthquake ground motion between the constant acceleration region and the constant velocity region of Newmark- Hall response spectrum.

6. AN ADAPTIVE CAPACITY SPECTRUM METHOD

Adaptive modal combination procedure for nonlinear static analysis

Static pushover analysis is usually employed to determine the deformation demands with acceptable accuracy without the intensive modeling and computational effort of a dynamic analysis. The lateral force distribution should be defined to reproduce the inertia forces deriving from the earthquake ground motion. As the damage progresses, the inertia forces are redistributed, the vibration properties of the structure change and local plastic mechanism may occur. As a consequence, also the original participation and dynamic amplification of the mode shapes changes, and higher mode effects may be significantly increased. Therefore, multimodal and adaptive pushover analyses may be required to improve the accuracy of the deformation estimates. Several researchers have proposed adaptive force distributions that attempt to follow more closely the time-variant distributions of inertia forces. These approaches can give better estimations of the inelastic response, but they are conceptually complicated and computationally demanding for application in structural engineering practice. The Modal Pushover Analysis (MPA) (Chopra and Goel, 2002) allows for the change in load distribution due to damage of the structure without resorting to an adaptive load pattern. Target displacement values are computed by applying equivalent nonlinear procedures with a SDOF system representative of each modal load pattern and, finally, response quantities are combined with the SRSS method. Other authors (Antoniou and Pinho, 2004) proposed adaptive pushover procedures: Force-based adaptive pushover (FAP) and Displacement-based adaptive pushover (DAP). Particularly, in the force-based adaptive pushover approach (FAP), a modal analysis is performed step by step to update the force modal ratios. The lateral load distribution is continuously updated during the process according to modal properties, softening of the structure, its period elongation, and the modification of the inertial forces due to spectral amplification. The lateral load profiles of each vibration mode are then combined by using SRSS or CQC method. An incremental updating with increment of load calculated according to the spectrum scaling is applied at each analysis step. Despite its apparent conceptual superiority, the results obtained through FAP appear to be similar to those from conventional pushover analysis. Both types of analysis may give very poor prediction of deformation patterns. In the displacement-based adaptive pushover (DAP), the modal shape is directly imposed to the structure, using a displacement control analysis. The maximum interstorey drift values are obtained directly from modal analysis, rather than from the difference between not-necessarily simultaneous maximum floor displacement values. However, the use of SRSS or CQC rules to combine modal results lead to load vector shapes which neglect the possibility of sign change in storey displacements from different modes. Generally, the displacement-based adaptive pushover provides much improved approximation of highly ir-

regular dynamic deformation profile envelopes, even if it assumes that all the interstorey drifts are maxima at the same time, which is of course not realistic. Two shortcomings of the modal combination rules can be pointed out: the first one is that the result obtained does not fulfill equilibrium; the second limitation is that signs are lost during the combination process eliminating the contribution of negative quantities. In other words, an “always-additive” inclusion of higher modes contribution is considered.

Adaptive capacity spectrum method

The result of the analysis is the pushover curve, which plot a deformation index (typically roof displacement δ_{TOP}) against a force index (typically base shear V). This capacity curve (CC) is the starting point for all the NSP_s based on Capacity Spectrum Method. In the case of adaptive pushover, the lateral load pattern is updated during pushover analysis according to variation in modal properties as the stiffness of the structure changes. This leads to variation in lateral displacement pattern and in lateral force pattern. Therefore, also the equivalent SDOF system, which is representative of MDOF three-dimensional model of the building in the Capacity Spectrum Method, changes during pushover analysis. In order to consider such effect, an adaptive version of the Capacity Spectrum Method (ACSM) is considered in the analyses. At each step of the pushover analysis a different equivalent SDOF system is defined as a function of the actual lateral displacement pattern. Particularly, the mass M_{eq} and the stiffness K_{eq} of the equivalent SDOF system at the i^{th} step of pushover analysis can be expressed as a function of the j^{th} storey displacement, as follows:

$$M_{eq}^i = \frac{\left(\sum_{j=1}^N m_j \cdot \delta_j^i \right)^2}{\sum_{j=1}^N m_j \cdot \delta_j^{i2}} \quad K_{eq}^i = \frac{\left(\sum_{j=1}^N m_j \cdot \delta_j^i \right)^2}{\left(\sum_{j=1}^N m_j \cdot \delta_j^{i2} \right)^2} \sum_{j=1}^N F_j^i \cdot \delta_j^i \quad (20)$$

where F_j^i is the j^{th} storey force at the i^{th} step. The transformation from Capacity Curve (CC) to Capacity Spectrum (CS) in ADRS format (Acceleration-Displacement Response Spectra) is carried out considering the following variation of the spectral coordinates to every step of pushover analysis:

$$\Delta S_a^i = \Delta V^i \cdot \frac{\sum_{j=1}^N m_j \cdot \delta_j^{i2}}{\left(\sum_{j=1}^N m_j \cdot \delta_j^i \right)^2} \quad (21)$$

$$\Delta S_d^i = \Delta d_{TOP}^i \frac{1}{\delta_N^i} \frac{\sum_{j=1}^N m_j \cdot \delta_j^{i2}}{\sum_{j=1}^N m_j \cdot \delta_j^i} \quad (22)$$

Finally, the CS is approximated with an elastic-perfect-plastic equivalent model (Bilinear Capacity Spectra – BCS). In particular, the elastic stiffness and the yielding displacement S_{dy} are defined from the point of the CS correspondent to 60% of the yielding acceleration S_{ay} . The seismic demand is generally represented by means of the Inelastic Demand Response Spectra (IDRS). In this paper the IDRS are computed scaling the 5%-damped Elastic Demand Response Spectra (EDRS – S_{de} versus S_{ae}) using eqs.12. A reduction factor depending on velocity and displacement elastic spectra is adopted (Ordaz et al., 1998).

$$R_\mu = 1 + \left(\frac{S_v(T)}{PGV} \right)^{\alpha(\mu)} \cdot \left(\frac{S_d(T)}{PGD} \right)^{\beta(\mu)} \cdot (\mu - 1) \quad (23)$$

where PGV is the peak ground velocity; PGD is the peak ground displacement; $S_d(T)$ is the elastic spectral displacement; $S_v(T)$ is the elastic spectral velocity; $\alpha(\mu)$ and $\beta(\mu)$ are functions obtained with a statistical data analysis on spectrum compatible earthquakes. For seismic inputs consistent to Eurocode 8 type 1 elastic response spectrum for firm soil (class A) a very good fitting was found for the following functions (Ferraioli et al., 2004):

$$\alpha(\mu) = -0.1967 \cdot \log(\mu) + 0.454 \quad \beta(\mu) = 0.2314 \cdot \log(\mu) - 0.0071 \quad (24)$$

R_μ depends from the ductility μ and, therefore, from the lateral displacement of the equivalent SDOF system. Consequently, an iterative procedure is usually required in order to estimate the intersection between IDRS and BCS. Applied for the displacement-based assessment the capacity spectrum method may become non-iterative. In fact, the performance-based assessment is displacement-based since the performance parameters used in the acceptance criteria are the plastic rotations and the interstorey drift damage index (IDI). As a consequence, the performance levels may be associated to the displacement demand of the structure. Then, the equivalence between MDOF and SDOF system gives the lateral displacement of the SDOF system ($S_{d,O}$ $S_{d,LS}$ $S_{d,CP}$) at each performance level. Consequently, the position of the performance point (PP) on capacity spectrum in ADRS format is defined (Fig. 7). This greatly simplifies the estimation of the intensity levels of the earthquake ground motion. In fact, the position of the PP gives the ductility ratio μ and ductility reduction factor R_μ without any iterative procedure. So the PGA may be increased until IDRS intersects BCS in PP. As a consequence, the problems in convergence and accuracy of the iterative graphical procedures based on the Capacity Spectrum Method are avoided.

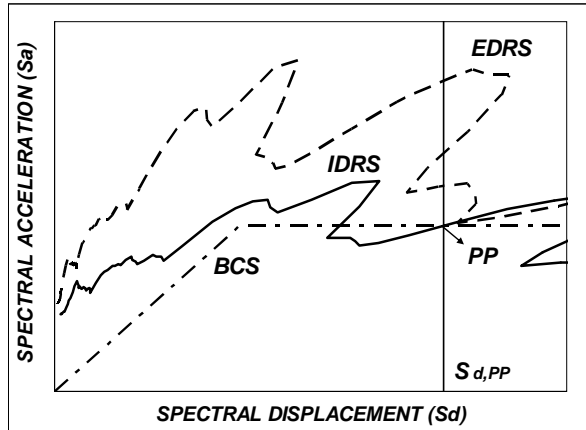


Figure 7. Incremental non-iterative capacity spectrum method

7. VALIDATION OF ACSM BY COMPARISON WITH NSP AND IDA

9-storey steel frames designed according to the Italian Code (2008) and Plastic Design (Mazzolani et al., 1997) are considered in the analyses. The design seismic action is defined with soil class A, damping ratio $\xi=5\%$, peak ground acceleration $PGA=0.25g$, behavior factor $q=6.5$. Steel members are made from Italian S275 steel ($f_y=275$ MPa). The interstorey height is 3.50 m for the first floor and 3.00 m for the other floors. The bay length is 5.00 m. The design sections of the two steel frames are reported in Table 1. A distributed plasticity-fiber element model implemented in Seismostruct (SeismoSoft, 2009) is considered in the analyses. Sources of geometrical nonlinearity considered are both local and global. The spread of plasticity along the element derives from an inelastic cubic formulation with two Gauss points to use for numerical integration of the equilibrium equations. A bilinear model with kinematic strain-hardening of 0.5% is used for steel. The plastic rotation and the residual strength are defined according to FEMA 356. The following current nonlinear static procedures are considered in the analysis: 1) ATC 40 under first mode distribution (FMD); 2) ATC 40 under uniform distribution (UD); 3) FEMA 356 Coefficient Method (CM); 4) FEMA 440 Coefficient Method (CM); 5) Capacity Spectrum Method (CSM-N2) under first mode distribution; 6) Capacity Spectrum Method (CSM-N2) under uniform distribution; 7) FEMA 440 (CSM) under first mode distribution; 8) FEMA 440 (CSM) under uniform distribution. The NSPs are applied for the performance-based assessment of IC08 and PD-SLS steel frames. Three different levels of performance are considered: Immediate Occupancy – IO; Life Safety – LS; Collapse Prevention – CP. The acceptance criteria are based on the following performance parameters: 1) in-

terstorey drift damage index (IDI); 2) plastic rotations in columns and beams. (defined by Tab. 5.6 of FEMA 356).

The limit values for the interstorey drift damage index are: 1) IDI=0.01 for IO limit state; 2) IDI=0.02 for LS limit state; 3) IDI=0.04 for CP limit state. The assessment of current nonlinear static procedures is carried out by comparison against dynamic analysis. At this aim, six ground motions are selected to be consistent to EC8 elastic spectra for different soil classes (Tab. 4). In Figure 8 the envelope values of the spectral acceleration are compared to EC8 elastic response spectra. In Figures 9 and 10 the roof displacement for the limit states (Immediate Occupancy – IO; Life Safety for non-structural elements LS_{ns} ; Life Safety for structural members LS_s , Collapse Prevention - CP) are related to the corresponding peak ground acceleration levels (PGA).

Table 4. Earthquake ground motion characteristics.

<i>N.</i>	<i>Input</i>	<i>Date</i>	<i>Dir.</i>	<i>Ms</i>	<i>PGA/g</i>	<i>t_R</i>	<i>T_C(s)</i>
1	Bevagna	1997	NS	5.50	0.034	46.1	0.700
2	Sturno	1980	EW	6.87	0.323	71.9	0.932
3	Gubbio	1997	NS	5.90	0.099	106.03	0.652
4	Izmit	1999	EW	7.80	0.161	51.98	0.621
5	Calitri	1980	NS	6.87	0.156	86.05	0.912
6	Gebze T.	1999	EW	7.60	0.135	47.63	0.514

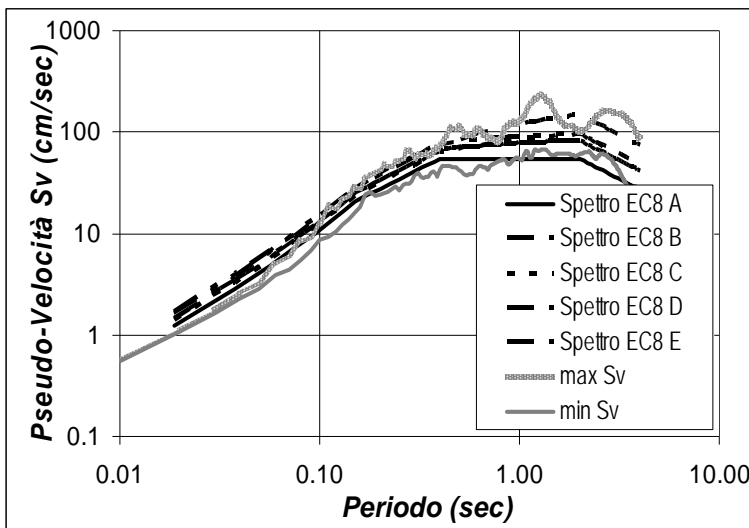


Figure 8. Envelope of ground motion response spectra and comparison with elastic response spectra of Eurocode 8.

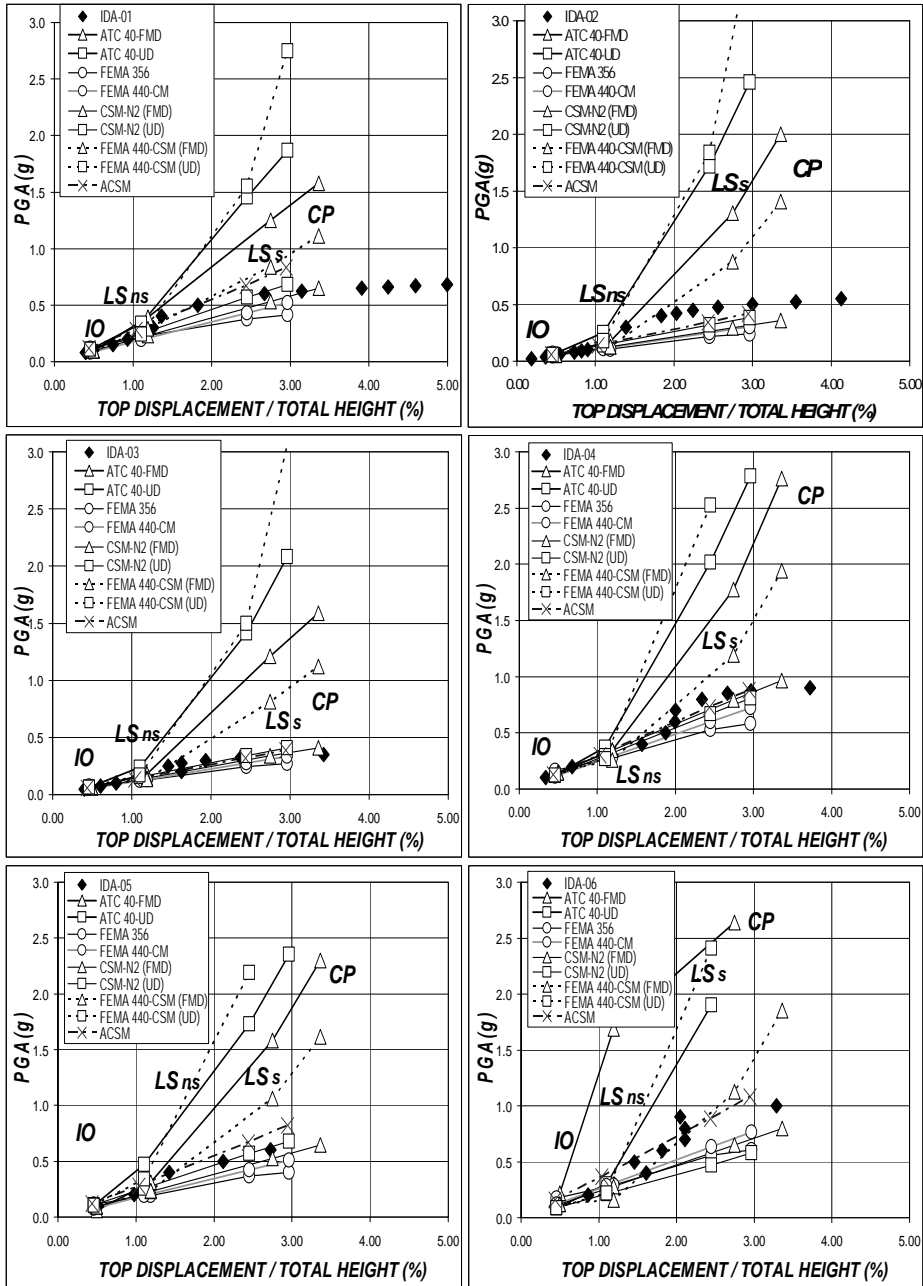


Figure 9. Peak ground acceleration versus roof displacement – Nonlinear Static Procedures and Incremental Dynamic Analysis (IC08 design).

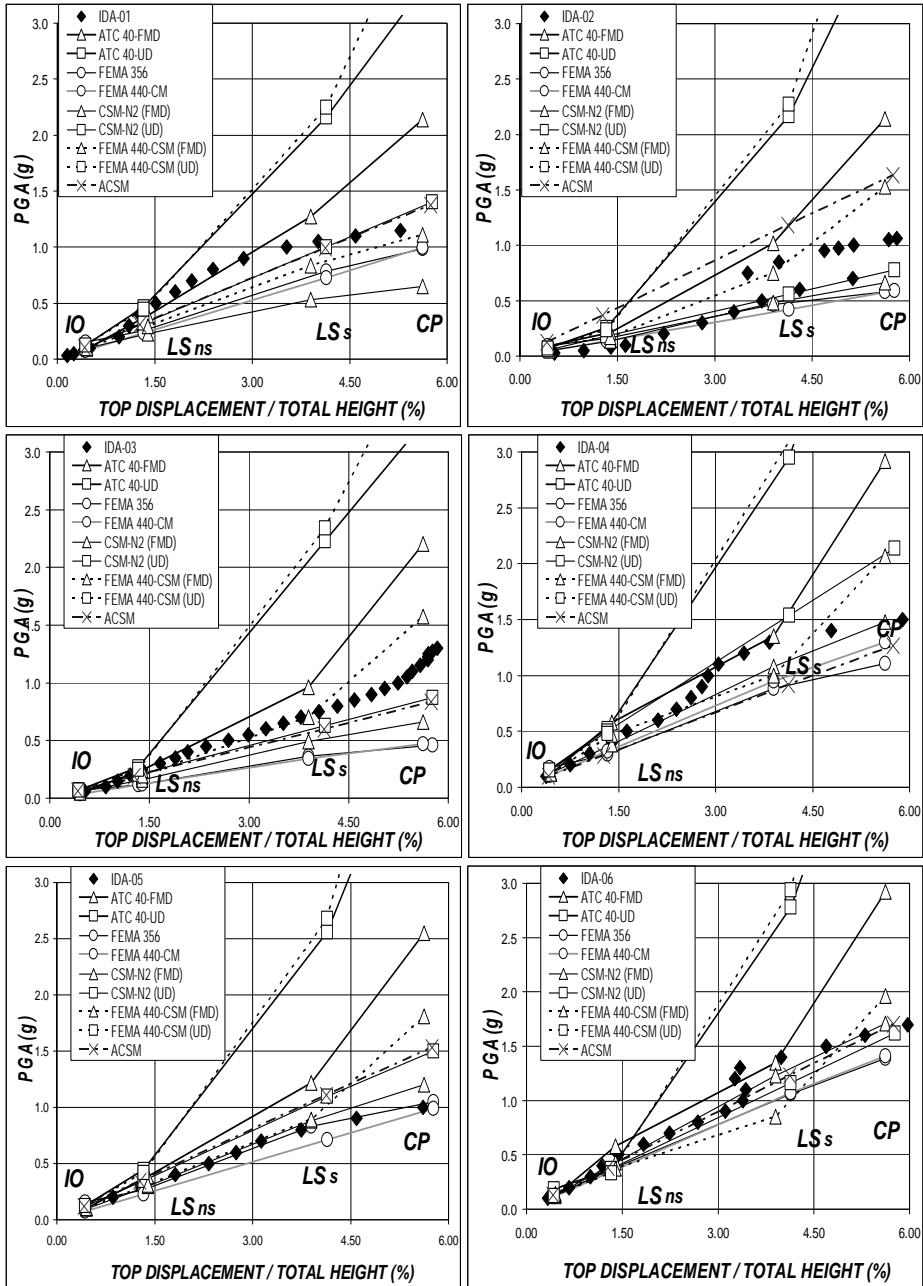


Figure 10. Peak ground acceleration versus roof displacement – Nonlinear Static Procedures and Incremental Dynamic Analysis (PD-SLS design).

Furthermore, also the peak roof displacement obtained from the incremental dynamic analysis is reported. FEMA 356 and FEMA 440 (Coefficient Method) give very similar performance points. This result derives from the value of the coefficient C_3 that is approximately equal to 1.0 in both cases.

The procedures based on the High Damping Elastic Demand Response Spectra (HEDRS) such as ATC 40 and FEMA 440 (ATC 55) give higher peak ground accelerations when compared to the other NSPs. Furthermore, the results are more sensitive to the lateral force distribution of the load pattern. In particular, the uniform distribution may give a non-conservative overestimation of PGA. This result derives from the differences between HEDRS and IDRS used to represent the seismic demand. In order to show this effect in Figure 11 the collapse HEDRS and IDRS spectra are compared. The PGA intersecting the demand and the capacity spectrum in the performance point at collapse is 2.14 for HEDRS and 1.2 for IDRS.

In Figures 12 and 13 the lateral displacement patterns obtained with different nonlinear static procedures and with incremental dynamic analysis are shown. The displacement demand is calculated by scaling the selected ground motion time histories with the peak ground acceleration $PGA=0.50$ g. The accuracy of NSPs is evaluated introducing the following error function:

$$\frac{\|D_S - D_D\|}{\|D_D\|} \quad (25)$$

where D_S is the lateral displacement vector from nonlinear static analysis and D_D is the vector defined by the peak lateral displacements from nonlinear dynamic analysis. The results reported in Table 5 give evidence to the effectiveness of the adaptive capacity spectrum method if compared to other NSPs available in literature.

Finally in Table 6 are reported some parameters synthesizing the seismic response of moment steel frames. The estimation of these parameters may be very important to evaluate the effectiveness of the design process. In particular, q is the design behaviour factor; α_1 is the value by which the horizontal seismic design action is multiplied in order to first reach the flexural resistance; α_u is the value by which the horizontal seismic design action is multiplied, in order to form plastic hinges in a number of sections sufficient for the development of overall structural instability; μ_{GLOB} is the global ductility ratio. The PGA risk indices are defined as the ratio between capacity (PGA^C) and demand (PGA^D) at different limit states: Operational limit state (SLO); Damage limit state (SLD); Life Safety limit state (SLV) and Collapse limit state (SLC). Values of α_u/α_1 higher than those specified in Italian Code ($\alpha_u/\alpha_1=1.30$) are obtained with nonlinear static analysis. In particular, for the moment resisting frames designed with plastic design and SLS verification the values of α_u/α_1 is 2 times the code value or more. In the same way, the ratio between capacity and de-

mand at SLV limit state and SLC limit state is greater than 4 for PD-SLS design and it is greater than 2 for IC08 design. In other words, the seismic safety is very high if compared to other structural types. However, the safety factors for the other limit states are very lower, especially for Immediate Occupancy limit state.

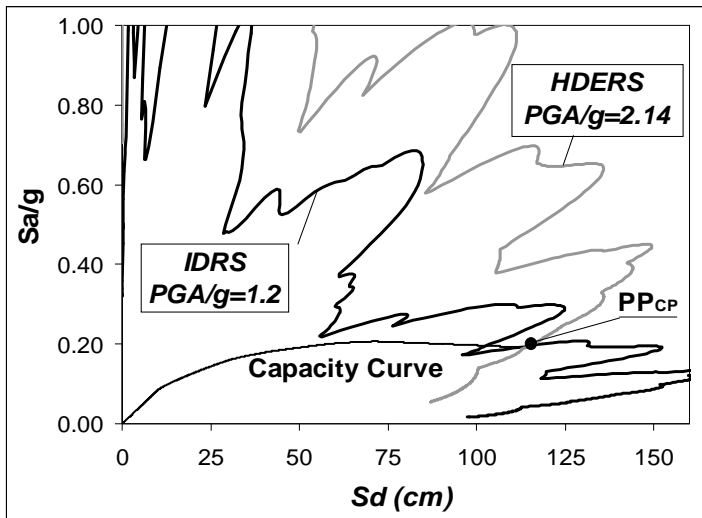


Figure 11. Comparison between ATC40 High Damping Elastic Demand Response Spectrum (HDEERS) and CSM-N2 Inelastic Demand Response Spectrum at collapse. PD-SLS frame.

Table 5. Error on lateral displacement pattern (%).

	ACSM	ATC-40 (CSM)	FEMA 440 (CSM)	FEMA 273 (CM)	FEMA 440 (CM)	CSM-N2
9 storey – IC08	18.45	24.72	92.35	27.72	63.79	34.59
9 storey – PD-SLS	21.58	20.52	53.81	28.00	41.87	42.43

Table 6. Error on lateral displacement pattern (%).

	q	α_{it}/α_1	μ_{GLOB}	$\frac{PGA_{SLO}^C}{PGA_{SLO}^D}$	$\frac{PGA_{SLD}^C}{PGA_{SLD}^D}$	$\frac{PGA_{SLV}^C}{PGA_{SLV}^D}$	$\frac{PGA_{SLC}^C}{PGA_{SLC}^D}$
7 storey IC08	6.50	1.726	6.745	1.297	2.211	2.434	2.253
7 storey PD-SLS	-	2.611	12.14	1.324	3.160	4.096	4.320
9 storey IC08	6.50	1.836	8.209	1.216	2.266	2.660	2.558
9 storey PD-SLS	-	2.611	12.85	1.216	3.170	4.320	4.593

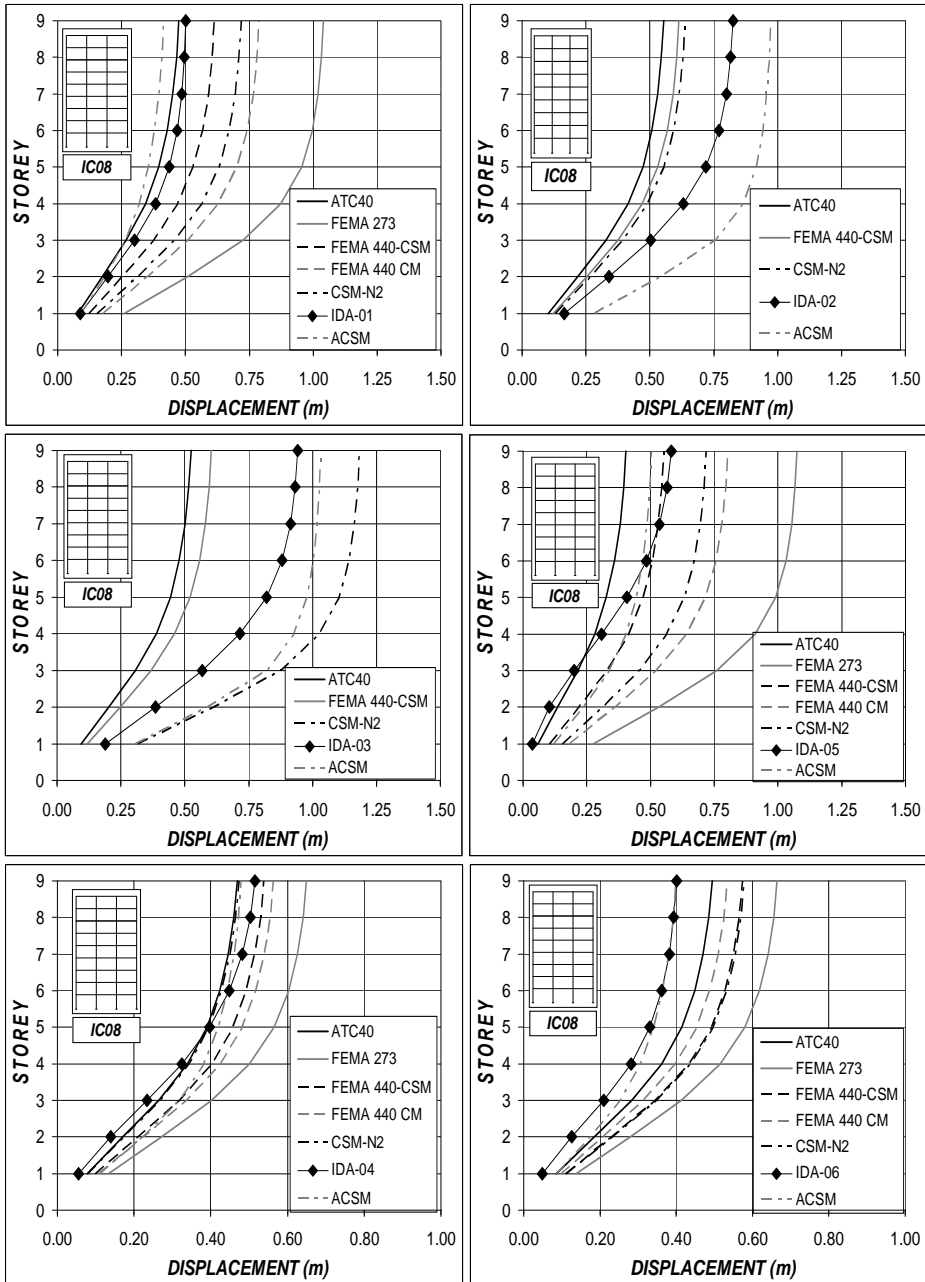


Figure 12. Lateral displacement pattern – Nonlinear Static Procedures and Incremental Dynamic Analysis (IC08 design - PGA = 0.50 g).

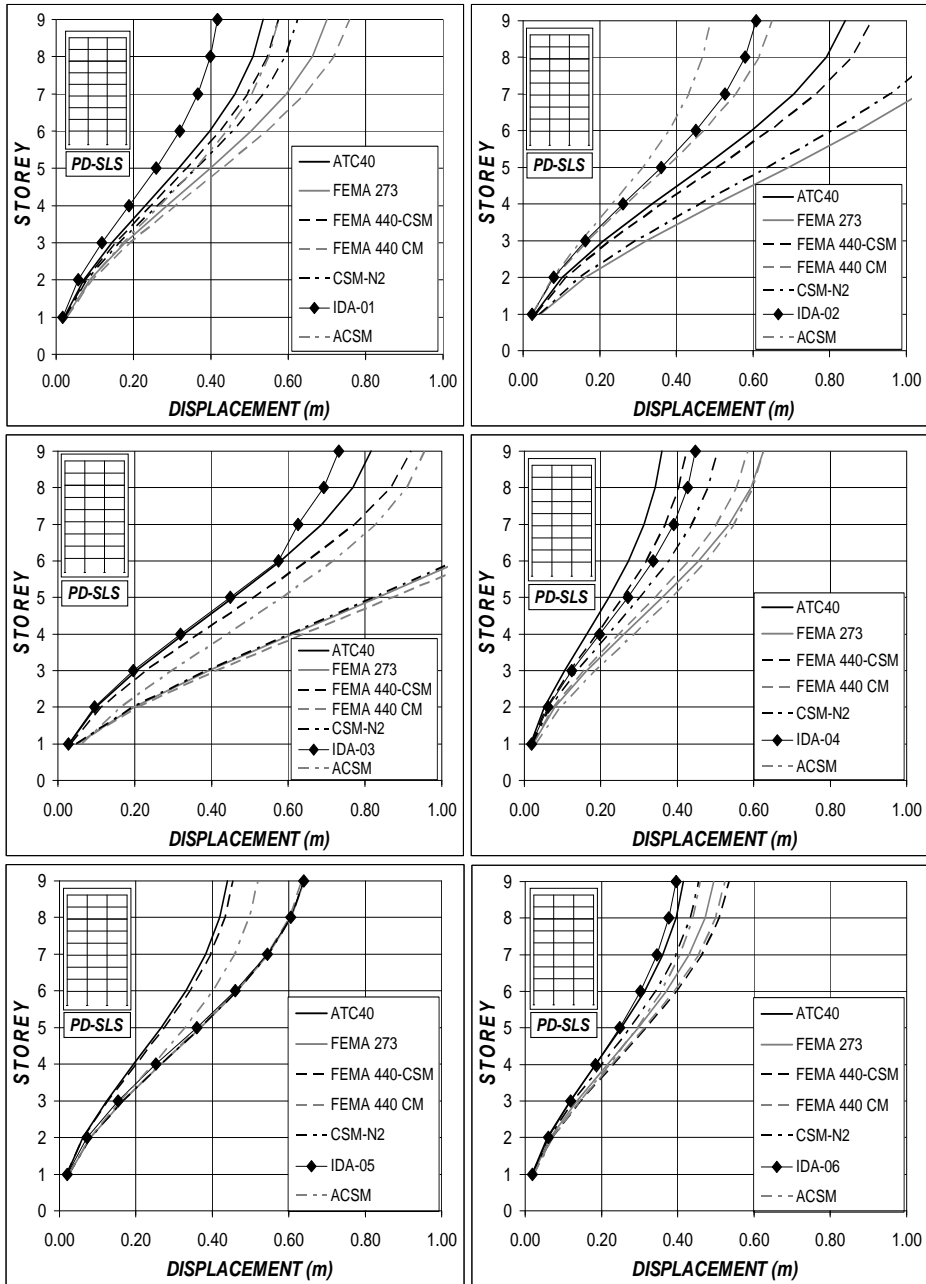


Figure 13. Lateral displacement pattern – Nonlinear Static Procedures and Incremental Dynamic Analysis (PD-SLS design - PGA = 0.50 g).

8. CONCLUSIONS

The comparative evaluation of design procedures confirmed that also recent codes based on the local ductility condition and the capacity design rule are not able to assure the suitable plastic mechanism. On the other side, the results demonstrated the effectiveness of the plastic design in governing the collapse mechanism. The design procedure based on the control both of collapse mechanism and of lateral displacement requires an iterative design process to avoid that the increase of structural overstrength produced by the damage limit state provisions leads to undesired collapse mechanisms. Furthermore, their cost is often an uncontrollable overstrength of the structure. However, the same safety factor for the other limit states (Immediate Occupancy and Life Safety) is not guaranteed. Finally, the overstrength generally increases the seismic demand and so reduces the benefits deriving from the control of collapse mechanism and lateral displacement.

An incremental non-iterative nonlinear static procedure based on adaptive capacity spectra method was used for performance assessment. The results obtained were compared with incremental time-history response and with nonlinear static procedures available in literature. The procedures based on the Capacity Spectrum Method and on the High Damping Elastic Response Spectra (ATC-40, FEMA 440) give deformation much different than the nonlinear response history analysis. On the contrary, the superior physical basis of adaptive pushover and inelastic demand response spectra and proved to give more accurate estimation of the seismic performance, especially in the case of steel framed structures that usually exhibit high ductility factors.

REFERENCES

- Antoniou, S., Pinho, R. [2004] "Advantages and Limitations of Adaptive and Non-Adaptive Force-Based Pushover Procedures" *Journal of Earthquake Engineering* 8:4. 497–522.
- Antoniou, S., Pinho, R. [2004] "Development and Verification of a Displacement-Based Adaptive Pushover Procedure" *Journal of Earthquake Engineering* 8:5. 643–661.
- ASCE [2000] Prestandard and Commentary for the Seismic Rehabilitation of Buildings. Report No. FEMA-356, Building Seismic Safety Council, Federal Emergency Management Agency, Washington, D.C.
- ASCE [2007] *Seismic Rehabilitation and Evaluation of Existing Buildings*, ASCE Standard No. ASCE/SEI 41–06, American Society of Civil Engineers, Reston, VA.
- Akbar, S., Metin, A. [2007] "Assessment of Improved Nonlinear Static Procedures in FEMA-440" *Journal of Structural Engineering* 133(9): 1237–1246.
- Aschheim, M.A., Maffei, J., Black, E. [1998] "Nonlinear Static Procedures and Earthquake Displacement Demands" *Proceedings of 6th U.S. National Conference on Earthquake Engineering*, Earthquake Engineering Research Institute, Seattle, WA.
- ATC-40 [1997] *Seismic Evaluation and Retrofit of Concrete Buildings*. Report No. ATC-40, Applied Technology Council, Redwood City, CA.

- ATC-55 [2003] *Improvement of Inelastic Seismic Analysis Procedures*. Report No. FEMA-440, Applied Technology Council, Redwood City, CA.
- CEN [2003] *Eurocode 8. Design of structures for earthquake resistance*. European Committee for Standardization.
- Chopra, A.K., Goel, R.K. [2000] "Evaluation of NSP to Estimate Seismic Deformation: SDF Systems" *Journal of Structural Engineering* 126(4): 482–490.
- Chopra, A.K., Goel, R.K. [2002] "A modal Pushover analysis procedure for estimating seismic demands for buildings" *Earthquake Engineering and Structural Dynamics* 31:3, 561–582.
- ECCS [1988]. *European recommendations for steel structures in seismic zones*. Publication No. 54.
- Faggiano, B., De Matteis, G., Landolfo, R. [2000]. "Comparative study on seismic design procedures for steel MR frames according to the force-based approach". Third Int. Conf. STESSA 2000, Montreal, Balkema, Rotterdam.
- FEMA 356, [2000] *Prestandard and Commentary for the Seismic Rehabilitation of Buildings*, prepared by the American Society of Civil Engineers for the Federal Emergency Management Agency. Washington, D.C.
- Ferraioli, M., Avossa, A.M., Malangone, P. [2004] "Approximate method for evaluation of seismic damage of rc buildings". *Proc. of the 13th World Conference on Earthquake Engineering* August 1–6, Vancouver. B.C., Canada.
- Ferraioli, M., Lavino, A., Avossa, A.M., Mandara, A. [2008] "Displacement-based seismic assessment of steel moment resisting frame structures" *14th World Conference on Earthquake Engineering*. October 12–17. Beijing, China.
- Goel, R.K. [2005] "Evaluation of Modal and FEMA Pushover Procedures Using Strong-Motion Records of Buildings" *Earthquake Spectra* 21(3): 653–684.
- Goel, R.K., Chadwell, C. [2007] "Evaluation of Current Nonlinear Static Procedures for Concrete Buildings Using Recorded Strong-Motion Data", Final Report, California Strong Motion Instrumentation Program, CDMG, Sacramento, CA.
- Guyader, A.C., Iwan, W.D. [2006] "Determining Equivalent Linear Parameters for Use in a Capacity Spectrum Method" *Journal of Structural Engineering* 132(1): 59–67.
- Italian Code. 2008. D.M. 14.01.08, G.U. No.9 – 04.02.08.
- Landolfo, R., Mazzolani, F.M. [1990] "The consequence of design criteria on the seismic behavior of steel frames" *Proc. of IX Intern. European Conference on Earthquake Engineering ECEE*, Moscow.
- Mazzolani, F.M., Piluso, V. [1997] "Plastic Design of Seismic Resistant Steel Frames" *Earthquake Engineering and Structural Dynamics* 26:2, 167–191.
- Miranda, E., Ruiz-Garcia, J. [2002] "Evaluation of Approximate Methods to Estimate Maximum Inelastic Displacement Demands" *Earthquake Engineering and Structural Dynamics* 31(3): 539–560.
- Ordaz, M., Pérez-Rocha, L.E. [1998] "Estimation of strength-reduction factors for elastoplastic systems: New approach" *Earthquake Engineering and Structural Dynamics* 27:9, 889–901.
- SeismoSoft [2009] SeismoStruct. A computer program for static and dynamic analysis for framed structures. (online) available from URL:www.seimosoft.com.

ULTIMATE BEHAVIOUR OF STEEL-CONCRETE COMPOSITE BRIDGE PIERS

Fabio Iannone, Luigi Mastrandrea, Rosario Montuori, Vincenzo Piluso,
Gianvittorio Rizzano

Department of Civil Engineering, University of Salerno, Salerno, Italy

Abstract. The seismic response of a bridge structure is mainly influenced by the ultimate behaviour of the piers. Therefore, with reference to steel-concrete composite bridges, the main topic of this work is the study of seismic responses of composite piers (i.e. composite beam-columns). First, the state-of-the-art concerning this topic is dealt with. Then, an analytical procedure able to foresee the behaviour of a CFT column is illustrated. The procedure takes into account all the parameters influencing the response of a composite member: the confinement of concrete, the biaxial stress state in the steel tube, the local buckling effects for the steel profile and the constitutive laws of the materials. The purpose is the evaluation of both the moment-curvature relationship of the composite section and the load-displacement curve of the member. In addition, an experimental program has been led at University of Salerno, testing CFT beam-columns in Square Hollow Section, both under monotonic and cyclic loading conditions. The experimental results have been useful to evaluate the accuracy of the numerical results.

Keywords: composite bridges, steel-concrete composite beam-columns, concrete confinement, steel tube, local buckling, three point bending tests.

1. INTRODUCTION

Within the research project ReLUIS supported by the Italian Department of Civil Protection, the Research Unit coordinated by Prof. Vincenzo Piluso has been devoted to the study of the ultimate behaviour of steel-concrete composite bridge piers. This activity has been carried out within the framework of the overall research line, dealing with innovative studies on steel and composite structures aiming to the improvement of Italian Seismic Code OPCM 3274.

The topic of composite structures has gained increasing research interest, since during last years such structural typology has been widely investigated, pointing out its capacity of leading to excellent performances in terms of stiffness, resistance and ductility, provided that appropriate design and detailing rules are applied. Therefore, researchers are more and more focusing their at-

tention on the design issues concerning the behaviour of such structural typology not only in case of building structures, but also in case of bridges and, in particular, for the bridge substructure.

In fact in case of bridge structures a lot of applications of steel-concrete composite constructional systems can be found worldwide since 1930s, but the combination of steel and concrete acting as a composite system is limited to the deck in most cases. Typically, the use of steel girders with a collaborating reinforced concrete slab located on the top flange of girders is adopted. Conversely, the substructure is usually made by means of traditional systems, by using reinforced concrete for the bridge piers, the abutments and the foundations. Only in few cases bridge piers are made of bare steel, when more simple erection procedures, reduction of the time required for execution and saving of working space in urban environment constitute critical design restraints. In the same framework, the use of steel-concrete composite bridge piers has been sometimes preferred, mainly in Japan, where also the use of partially filled composite columns has been proposed. This typology is characterised by the fact that a steel hollow profile is used for the pier by filling it with concrete only in the lower part, where the bending moment due to seismic forces is predominant and the development of a plastic hinge is expected.

Modern international seismic codes suggest to design bridge structures according to the principles of capacity design. Therefore, dissipative zones have to be designed to resist the internal actions due to the design load combinations provided by the codes, including the seismic load combination with the other actions, while non dissipative zones have to be dimensioned on the basis of the maximum internal actions that dissipative zones, in their ultimate limit state, are able to transmit to the non dissipative ones. Eurocode 8 and Italian code are in agreement with this approach. In particular, the base sections of bridge piers are recognised as dissipative zones, so that under severe earthquakes the seismic input energy has to be dissipated by means of their plastic excursions, while all the other parts of the bridge, i.e. the bridge deck, the bearing devices, the abutments and the foundations have to remain in elastic range.

Under this point of view, referring to the seismic behaviour of bridges, steel-concrete composite bridges can be considered as those bridges whose piers are made of a steel-concrete composite solution, while constructional technologies adopted for the bridge deck are not relevant. Two typologies can be adopted for steel-concrete composite bridge piers: Concrete Filled steel Tubular columns (CFT) and Concrete Encased steel Composite columns (CEC). In the first case a steel tube made of a rectangular or circular hollow section is filled with concrete, while in the second one a steel profile is encased into a reinforced concrete column. However, several reasons suggest to prefer the first typology with respect to the second one, as described in the following Sections. For this reason, the main topic of the planned research activity is represented by the investigation of the ultimate behaviour of CFT-columns under both

monotonic and cyclic actions, since they are more suitable as bridge piers from both the structural and the technological point of view.

The issues concerning the behaviour of steel-concrete composite members are nowadays worldwide investigated. In fact, during last years the use of composite structures is widely increased due to their performance in terms of stiffness, resistance and ductility. A lot of researchers have focused their attention on several issues concerning this topic, such as the interaction between steel and concrete (Mander et al., 1988; Shams and Saadeghvaziri, 1999, Susantha et al., 2002), the axial load carrying capacity (Shams and Saadeghvaziri, 1997), the response under cyclic flexural loads (Gourley et al., 2001; Han et al., 2005), in some cases providing models for the prediction of the behaviour at collapse. Nevertheless, only in few cases the proposed models exhibit well defined theoretical bases, while in most cases they are obtained by means of numerical calibrations requiring regression analyses of available experimental results. Conversely, the final purpose of the research activity carried out by the Research Unit of Salerno University is the development of theoretical models able to predict the ultimate response of CFT-columns, i.e. steel-concrete composite bridge piers, on the bases of well recognised theoretical formulations describing all the effects influencing the ultimate behaviour of composite members. The developed fiber models is strictly related to the theoretical interpretation of the phenomena affecting the ultimate behaviour of CFT bridge piers. In particular, the fiber model is preliminarily devoted to the determination of the moment-curvature relationship and, successively, to the evaluation of the force-displacement response of such members, leading to the complete knowledge of the ultimate behaviour. Moreover, the behaviour factor to be adopted in the seismic design of steel-concrete composite bridge is strictly related to the piers behaviours under cyclic actions, so that reliable non linear dynamic analyses are needed to provide specific design provisions for such pier typology which, nowadays, is not covered by seismic codes. Therefore, the developed fiber model has to be considered as the background for the setting up of an analytical model for predicting the cyclic response of CFT-members which will be the goal of the forthcoming research activity.

In the proposed fiber model, all the issues concerning the interaction between steel and concrete are accounted for: the confinement of concrete, the biaxial stress state in the steel tube and the local buckling effects for the steel profile. All these effects are accurately treated in next Sections, with particular reference to the analytical formulations adopted in the development of the proposed fiber model.

Furthermore, within the research project, experimental tests have been led on CFT members subjected to non-uniform bending at the *Materials and Structures Laboratory* of the *Department of Civil Engineering of Salerno University*. The comparison between the obtained experimental results and those resulting

from numerical predictions provides a preliminary validation of the proposed fiber model.

2. STEEL-CONCRETE COMPOSITE COLUMNS

Preliminary remarks

As already underlined, steel-concrete composite bridge piers can be realised according to two constructional systems: Concrete Filled steel Tubular (CFT) and Concrete Encased steel Composite (CEC) columns.

For several reasons, the CFT typology seems to be preferable. In fact, no other reinforcement is needed, because the tube itself acts as longitudinal and lateral reinforcement for the concrete core. In addition, the location of longitudinal steel at the perimeter of the section constitutes the most efficient use of steel, because it provides the best contribution to the inertia moment and to the flexural resistance of the section. Moreover, the continuous confinement provided to the concrete core by the steel tube enhances the core strength and ductility and prevents the concrete spalling. The concrete core gives a great contribution to the load bearing capacity under axial loads and delays the local buckling of the steel tube by preventing inward buckling. Finally, drying shrinkage and creep of concrete are smaller than those occurring in ordinary reinforced concrete structures and in CEC members.

In addition, the use of CFT system is advantageous also from the technological point of view. In fact, the steel profile represents the form for concrete casting, leading to more simple erection procedures reducing both the construction costs and the time required for execution. In addition, the concrete core implicitly provides the stiffening of the panel zone between the pier and the cap beam.

Conversely, some difficulties in properly compacting the concrete core may lead to a gap between concrete and steel. In order to avoid the occurrence of such drawback and to ensure compactness of the member, it is suggested the use of high-quality concrete with low water-content and super plasticizers to improve the workability during the cast. On the other hand the main advantage of CEC typology is that encasing concrete protects the steel profile from atmosphere corrosion. Some studies have also shown that the concrete core improves the fire resistance of the steel tube so that the fire resistance of axially loaded CFT members is greater than that occurring in the case of the steel tube only (Kodur & Lie, 1995), but such advantage obviously is of concern in the case of columns for building structures, rather than in the case of bridge piers.

With reference to CFT typology, the collaboration between the steel profile and the concrete core is due to the bond between the two materials. Therefore, under this point of view, CFT columns can be distinguished in Bonded Concrete Filled steel Tubular (BCFT) columns and Unbonded Concrete Filled

steel Tubular (UCFT) columns. The first typology is the most usual, and is characterised by the collaboration between the two materials. In the second case, an anti-friction fluid is adopted on the inner steel walls before concrete casting, so that the role of the steel profile is limited to the confinement effect, while its contribution to the axial load carrying capacity is negligible.

The effect of the bond is related to load transmission between steel and concrete, which arises due to the friction at the interface. In particular, if the axial load is applied to the entire section, the contributions of steel and concrete remain constant along the height and they are independent of the bond at the interface. Conversely, when the axial load is applied only to the steel or only to the concrete, the axial load must be transmitted by means of the contact surface between the two materials. Therefore, the bond strength between the concrete core and the steel tube influences the distribution of the axial force within the section, and, in addition, influences the structural behaviour and the axial load resistance of the CFT column. Friction develops between the concrete core and the steel tube due to the normal contact pressure generated by the lateral expansion of the concrete core when subjected to compressive loading. The magnitude of the friction force depends on the rigidity of the tube walls against pressure perpendicular to their plane.

As it has been discussed, several reasons suggest the adoption of CFT solution rather than CEC one. In particular, with reference to bridge piers, due to the relevant dimensions of the cross section, the axial load values are quite low compared to the squash load, so that the flexural capacity of the member constitutes the governing design parameter. Consequently, the choice of maximising the flexural capacity of the section by locating the steel material at the perimeter constitutes the most effective structural choice. For this reason, the research activity has been focused on CFT bridge piers.

In particular, the interaction between the concrete core and the steel profile in a CFT column is due to the fact that, increasing the axial stress, the Poisson ratio of concrete becomes, due to plasticity, even greater than that of steel. As a consequence, the lateral expansion of concrete is restrained by the steel tube, so that a radial stress state arises at the interface between the two materials, the concrete being subjected to compression stresses and the steel tube walls to tensile stresses. In particular, due to the relatively small thickness of the steel tube, the compression radial stresses are balanced by means of tensile stresses which arise along the circumference, whose value σ_{θ} can be considered uniform within the thickness.

Therefore, the stress state acting in the plane of the section is responsible of two effects which influence the behaviour of concrete and steel, respectively. In fact, the solid stress state of the concrete benefits of the confinement effect and the bi-axial stress state of the steel modifies the yield stress available in the axial direction of the member (Shams and Saadeghvaziri, 1999; Elremaily and Azizinamini, 2002).

In addition, due to the presence of the concrete core, the inward deformations of the steel tube walls are prevented. This issue is particularly important with reference to the buckling modes. In fact, local buckling of an empty steel tube is characterised by the combination of inward and outward deformations of the plates. In case of SHS (square hollow sections) and RHS (rectangular hollow sections) members, such deformations are related each other through the rotations at the corners due to compatibility requirements. Conversely, in the case of a CFT column, both inward displacements and inward corner rotations are prevented so that only outward local buckling of plates can be activated affecting the buckling factor of the plate elements constituting the member section.

In the following Sections, the issues concerning concrete confinement, stress state actually affecting the steel profile and local buckling effects are detailly examined.

The confinement of concrete

The behaviour of structural concrete is usually described by means of mono-axial compressive tests, i.e. by means of the relationship between the mono-axial stress and the corresponding strain. Nevertheless, in most cases concrete is actually subjected to tri-axial stress state. If stresses occurring in transversal directions are negligible, the mono-axial state is representative of the stress condition and the mono-axial resistance in compression is reliable; conversely, when transversal lateral stresses are significant, the behaviour of concrete changes significantly, both in terms of resistance and ductility.

In particular, concrete confinement is defined as the condition in which the concrete is subjected to significant transversal compressive stresses. These stresses can arise internally due to the deformations of the cross section (passive confinement), as in the case of a steel tube filled by concrete, or can be applied and controlled externally (active confinement). In the first case, lateral stresses are not uniform into the cross section, depending on the lateral deformation of the concrete core and on the stress-strain law of the confining steel. However, the behaviour of confined concrete is the same despite of the confinement typology (Attard and Setung, 1996).

In the case of confined concrete significant increases of resistance, stiffness and ductility are observed with respect to unconfined concrete. In fact, it is well known that unconfined concrete (i.e. concrete without lateral reinforcement), exhibits a brittle behaviour due to micro fractures arising from tensile transversal stresses. These micro fractures increase as far as the load increases, so that a progressive worsening of the behaviour of the cross section occurs. Conversely, when lateral reinforcements are adopted, micro fractures are avoided and the material benefits of greater load carrying capacity.

With reference to confinement, several analytical formulations have been proposed in the technical literature in order to obtain an appropriate constitu-

tive law (Elremaily and Azizinamini, 2002; Mander et al., 1988; Susantha et al., 2002; Han et al., 2003). Mander et al. (1988) model is probably the most accredited one. The method was originally developed with reference to reinforced concrete columns, i.e. with reference to the case of circular columns confined by means of spirals or circular hoops and, successively, with reference to the case of rectangular sections confined by means of stirrups and ties leading to different arrangements of the steel adopted as transverse reinforcement. However, by means of the correct definition of the lateral confining stress, the approach can be easily extended to the case of concrete filled tubes.

In particular, in the case of spirals or circular hoops, the confined compressive strength f_{cc} is given by:

$$f_{cc} = f_c \left(2.254 \sqrt{1 + \frac{7.94 f_l}{f_c}} - 2 \frac{f_l}{f_c} - 1.254 \right) \tag{1}$$

being f_c the unconfined concrete compressive strength and f_l the effective lateral confining stress. Eq. (1) can be adopted also in the case of a confining circular tube by means of an appropriate definitions of the lateral confining stress f_l . In particular, accounting for the hoop stress σ_θ arising in the steel tube walls (Fig. 1), the equilibrium equation of the stress distribution acting on half section provides the following formula:

$$f_l = \frac{2 \sigma_\theta t}{D} \tag{2}$$

where the meaning of symbols is clarified in Figure 1.

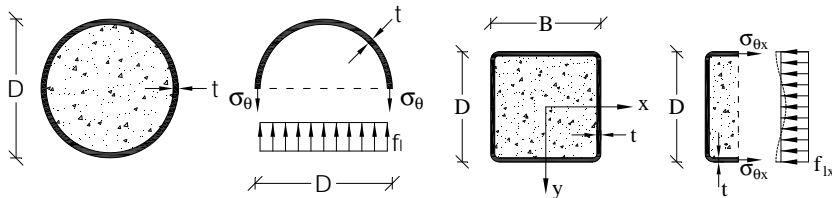


Figure 1. Lateral confining stresses for CHS and RHS CFT columns.

Mander et al. have provided the solution also in the case of rectangular sections. In Figure 2 the ratio f_{cc}/f_c between the confined strength and the unconfined one is depicted depending on the lateral confining stresses f_{l1} and f_{l2} , which are determined according to the following relationships:

$$f_{l1} = \min(f_{lx}, f_{ly}) \quad f_{l2} = \max(f_{lx}, f_{ly}) \tag{3}$$

being f_{lx} and f_{ly} the lateral confining stresses in the x and y directions of the cross section, respectively. With reference to Figure 1, by approximately assuming a uniform distribution of the lateral confining stresses on the concrete core, the equilibrium equations provide the following relationships:

$$f_{lx} = \frac{2 \sigma_{\theta x} t}{D} \quad f_{ly} = \frac{2 \sigma_{\theta y} t}{B} \quad (4)$$

Eqs. (2) and (4) require the knowledge of the hoop stresses ($\sigma_{\theta x}$ and $\sigma_{\theta y}$). Nevertheless, hoop stresses depend on the interaction between the steel profile and the concrete core, as discussed in next Sections.

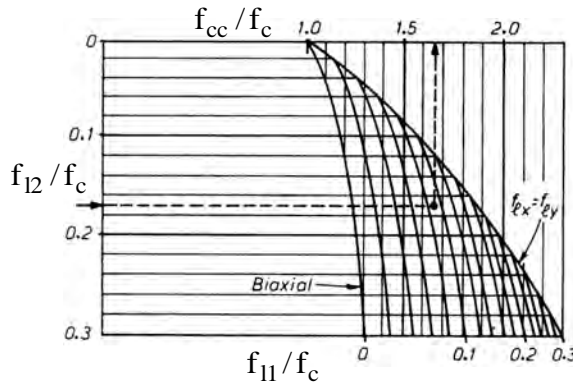


Figure 2. Confined strength ratio for rectangular sections.

Starting from the value of f_{cc} , Mander et al. model is based on the relationship proposed by Popovics (1973). In particular, for slow (quasi-static) strain rate and monotonic loading, the longitudinal compressive concrete stress σ_c is provided by the following relationships:

$$\sigma_c = \frac{f_{cc} x r}{r - 1 + x^r} \quad (5)$$

$$x = \frac{\varepsilon_c}{\varepsilon_{cc}} \quad \varepsilon_{cc} = 0.002 [1 + 5(f_{cc}/f_c - 1)] \quad \varepsilon_{cu} = 0.004 + 1.4\rho \frac{\varepsilon_{su}}{f_c} \quad (6)$$

$$r = \frac{E_c}{E_c - E_{sec}} \quad E_{sec} = \frac{f_{cc}}{\varepsilon_{cc}} \quad E_c = 5000\sqrt{f_c} \text{ (MPa)} \quad \rho = \frac{2t_w}{B - 2t_w} + \frac{2t_w}{D - 2t_w} \quad (7)$$

being ε_c the longitudinal compressive strain of confined concrete, ε_{cc} the strain value corresponding to the achievement of the peak stress f_{cc} , ε_{su} the ultimate steel strain, ρ the volumetric ratio of confining steel, E_c and E_{sec} the tangent

modulus and the secant modulus of concrete, respectively. Eq. (5) describes the stress-strain constitutive law for the confined concrete also in the softening branch, until the ultimate concrete deformation ϵ_{cu} is reached. Therefore, the method allows the complete description of the confined concrete behaviour.

The bi-axial stress state in the steel tube

As underlined, due to the lateral expansion of compressed concrete, the steel tube of a CFT column is characterised by the simultaneous occurrence of hoop stresses σ_θ and longitudinal stress σ_v , due to the applied loads, which are responsible of a bi-axial stress state of the steel plate elements constituting hollow profile (Elremaily and Azizinamini, 2002; Shams and Saadeghvaziri, 1999; Tao et al., 2001). Steel tubes under bi-axial state of stress exhibit a lower yield stress in compression in the longitudinal direction. In case of short columns, the level of such decrease depends on the D/t ratio (the decrease is more significant in columns with higher D/t values) and on the cross sectional shape (the maximum hoop stress in circular columns is higher than in square columns, Shams and Saadeghvaziri, 1999).

From a theoretical point of view, Von Mises criterion is herein adopted. Due to the hoop stresses, it results that yielding stresses in compression and tension become different, i.e. the elastic-perfectly plastic constitutive law of the material in tension becomes different from the one in compression. In particular, the yield stress in compression f_{yc} is less than the mono-axial value f_y , while the yield stress in tension f_{yt} is greater than f_y . This result is easily obtained by means of the yield surface corresponding to Von Mises criterion, which is provided by the following relationship (Fig. 3):

$$\sigma_v^2 - \sigma_\theta \sigma_v + \sigma_\theta^2 = f_y^2 \quad (8)$$

being σ_v the longitudinal stress, and σ_θ the tension hoop stress (in positive value).

Therefore, the determination of the yield stress values requires a preliminary estimation of the hoop stress. This is possible by means of an iterative process (Elremaily and Azizinamini, 2002). In particular, several σ_θ attempt values can be assumed ($\sigma_\theta = \sigma_{\theta x} = \sigma_{\theta y}$ for SHS columns), varying between 0 and f_y . For each value, the corresponding yield longitudinal stresses f_{yc} and f_{yt} can be determined by solving Eq. (8) with respect to σ_v , so that the constitutive laws of steel in tension and in compression, for the longitudinal direction, can be obtained. Moreover, by means of Eqs. (4)-(7) the corresponding confined concrete stress-strain relationship is established. As a consequence, for each value of the hoop stress σ_θ , an analytical value of the moment capacity can be determined by means of a moment-curvature analysis. If experimental results are available, the actual hoop stress can be obtained as the value of σ_θ leading to

the match between analytical moment capacity and the flexural resistance obtained from experimental evidence.

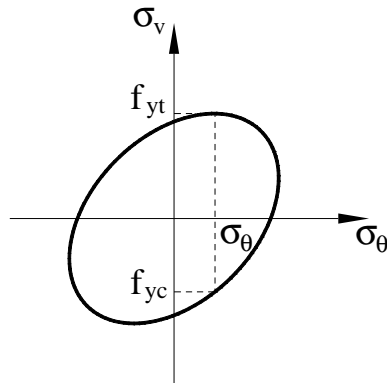


Figure 3. Von Mises criterion.

Following this approach, on the basis of an experimental campaign and the use of Mander et al. (1988) constitutive law of confined concrete, Elremaily and Azizinamini (2002) suggest an average value of $\sigma_\theta = 0.1 f_y$ with reference to CHS columns, regardless of the slenderness of the steel profile and of the concrete strength. As a consequence, by means of Eq. (8) the values $f_{yt} = 1.046 f_y$ and $f_{yc} = -0.946 f_y$ are obtained for the longitudinal yield stress in tension and in compression, respectively.

Local buckling

It is well known that the behaviour of steel thin tubes is strongly influenced by the occurrence of local buckling of the plate elements constituting the cross section. In particular, local buckling can be responsible of a significant decrease of resistance, and gives rise to a softening branch of the load versus displacement curve characterising the ultimate behaviour of the profile.

In the case of concrete filled tubes the effect of local buckling is delayed by the presence of the concrete core. In fact, in case of CFT columns the inward deformations of the thin plate walls are prevented, so that only the outward buckling is possible. The presence of the concrete core prevents the plate rotation at the corners, so that in the case of box columns (both SHS and RHS) the buckling of each plate requires the development of yield lines at both edges. Therefore, the number of yield lines needed to develop the kinematic mechanism describing the post local buckling behaviour of the hollow profile is greater than that needed in the case of an empty profile. This means that the internal work engaged in the development of the kinematic mechanism is also increased, so that local buckling is delayed, even though not completely avoided.

A similar phenomenon develops in the case of CHS columns, where the circular section changes in an oval one after deformation due to buckling (Saiho et al., 2004).

It can be observed that the ratio D/t has a significant influence on the local buckling of steel tubes. In particular, for high values of D/t , i.e. for slender steel sections, local buckling is anticipated, so that the bond between steel and concrete at the interface is lost, and the outward instability of the plate prematurely occurs. The concrete maintains its compressive capacity until the separation is completed; thereafter, the behaviour of the member is affected by cracking and spalling phenomena. In these conditions, CFT columns cannot sustain higher loads, but they are able to maintain an high percentage of the maximum load carrying capacity, showing a ductile behaviour despite of local buckling. In particular, circular columns show a more ductile behaviour (Shanmugam and Lakshmi, 2001).

A useful approach to account for the influence of local buckling of compressed plates of box columns (both SHS and RHS) is the effective width approach. This method is based on the study of the buckling behaviour of steel plates in plastic range. In particular, starting from the formula of the elastic critical stress:

$$\sigma_{cr.e} = k \frac{\pi^2 E}{12(1-\nu^2)(b/t)^2} \quad (9)$$

being k a buckling coefficient depending on the boundary conditions and the plate geometry and E the steel modulus of elasticity, the critical stress in plastic range and the corresponding critical strain are given by:

$$\sigma_{cr.p} = \eta \sigma_{cr.e} \quad \varepsilon_{cr.p} = \eta \frac{1}{E_s} \frac{k \pi^2 E}{12(1-\nu^2)(b/t)^2} \quad (10)$$

being E_s the steel secant modulus of elasticity. The non dimensional factor η depends on the shape of the stress-strain curve of the material, and several proposals are provided in the technical literature (Gherzi and Landolfo, 1995).

In particular, the accuracy of the available formulations has been investigated by comparing the results of numerical analyses with those obtained from experimental evidence. The different available formulations are herein listed:

- T1) secant modulus theory: $\eta = \frac{E_s}{E}$ (11)

- T2) tangent modulus theory: $\eta = \frac{E_t}{E}$ (12)

- T3) Perason (1950), Bleich (1952) and Vol'Mir (1965): $\eta = \sqrt{\frac{E_t}{E}}$ (13)

- T4) Radhakrishnan (1956): $\eta = \sqrt{\frac{E_t}{E_s}}$ (14)

- T5) Gerard (1957, 1962): $\eta = \frac{\sqrt{E_t E_s}}{E}$ (15)

- T6) Weingarten et al. (1960): $\eta = \frac{E_s}{E} \sqrt{\frac{E_t}{E}}$ (16)

- T7) Stowell (1948) and Bijlaard (1949):

$$\eta = \frac{E_s}{E} \left(0.33 + 0.67 \sqrt{0.25 + 0.75 \frac{E_t}{E_s}} \right)$$
 (17)

- T8) Li and Reid (1992): $\eta = \frac{E_s}{E} \left(0.50 + 0.50 \sqrt{0.25 + 0.75 \frac{E_t}{E_s}} \right)$ (18)

where E_t is the tangent modulus.

In the postbuckling phase, the in-plane stress distribution becomes non uniform. Stress concentrations occur close to the restrained edges, while the stress decreases as far as the distance from the edge increases. Due to this redistribution, the maximum stress σ_{max} reached at the edges is higher than $\sigma_{cr.p}$. Nevertheless, by means of the effective width method the determination of the actual non uniform stress distribution is not necessary. In fact, it is substituted by an equivalent constant stress distribution $\sigma = \sigma_{max}$ extending for a reduced width, namely effective width b_{eff} , which is defined as that corresponding to the condition $\varepsilon = \varepsilon_{cr.p}$. Therefore, by combining Eqs. (9) and (10) with $b = b_{eff}$, the following relationship is determined between the effective width and the strain level ε :

$$b_{eff} = t \sqrt{\eta \frac{k \pi^2 E}{12 (1 - \nu^2) E_s \varepsilon}} \quad (19)$$

Eq. (19) provides the effective width in the postbuckling phase of the steel plate as a function of the strain level ε . It also means that the central portion of the plate, having a width equal to $b - b_{eff}$, has to be neglected (i.e. $\sigma = 0$) in the computation of axial resistance and moment capacity of the cross section.

3. NUMERICAL PROCEDURES

Objectives

The final goal of the research activity is the development of a fiber model for the analysis of the ultimate behaviour of CFT beam-columns. To this scope, the main analytical aspect to be faced is constituted by the evaluation of the moment-curvature relationship which is the primary tool of non-linear structural analysis. In fact, the moment-curvature relationship completely describes the non-linear behaviour of the cross section, accounting for the section geometry, the material mechanical properties, the confining effect, the bi-axial state of stress of steel and the occurrence of local buckling. Starting from the knowledge of the moment versus curvature relationship, which depends on the level of the simultaneous axial load, non linear structural analyses can be carried out aiming at the evaluation of force-displacement curve describing the global response of the bridge pier, subjected to any external action, depending on the geometrical scheme and the boundary conditions.

By means of these tools, the whole prediction of the ultimate behaviour of CFT bridge piers is attained. This analytical issue has a primary importance in the design process, because the response of CFT members is affected by complex phenomena concerning the interaction between steel and concrete, as described above.

The validation of the developed fiber model has been carried out with reference to test results obtained from an experimental campaign led by the authors at the *Materials and Structures Laboratory* of the Department of Civil Engineering, at the University of Salerno. The experimental campaign has been focused on CFT-SHS beam-columns, and it is described in the following Sections.

Evaluation of the moment-curvature relationship

The moment-curvature relationship is the primary analytical tool to describe the non-linear structural behaviour of the cross section. Moreover, the complete knowledge of such relationship allows to correctly estimate the ultimate strength and ductility supply at the section level. In order to evaluate the moment-curvature relationship a fiber model has been developed. The cross section is subdivided in several elementary areas, each one characterised by the corresponding constitutive law of the material. In particular, the elementary areas are distinguished between confined concrete and steel. Regarding confined concrete, the stress-strain constitutive law proposed by Mander et al. (1988) has been adopted (Section 2.1) by assuming that the lateral confining stress as corresponding to an hoop circumferential stress in the steel tube equal to $0.10 f_y$. Concerning the steel, the stress-strain constitutive law (Section 4.2) has been assumed according to the classical Ramberg-Osgood relationship by adopting

different yield stress values in tension and in compression to account for the bi-axial stress state in the steel tube (Section 2.2), according to Von Mises yield criterion.

Moreover, the influence of local buckling is taken into account by means of the effective width approach previously described.

For an assigned value of the axial force, the moment-curvature relationship is obtained step-by-step by means of an iterative process. In particular, at each step the value of the curvature χ is fixed, and the actual strain distribution is obtained iteratively by imposing the fulfilment of the translational equilibrium equation. As soon as the strain diagram is known, i.e. the stress level of each elementary area is determined, the bending moment of the section is obtained.

The procedure stops when one of the following conditions occurs:

- one of the concrete elementary areas reaches the ultimate strain;
- one of the tensile steel areas reaches the ultimate strain;
- the ratio between b_{eff} and the actual width of the plate under compression is less than the 5% (Chen, 1993).

Under the combination of axial force and bending moment, one of the plates perpendicular to the bending plane (flange plates) is completely under compression, while the two plates lying in the bending plane (web plates) are partially compressed.

In particular, with reference to the buckling modes, the compressed flange behaves as an isolated plate fully restrained at its edges. The plate is subdivided into elementary areas, whose strain level ε governs local buckling. If the condition $\varepsilon \geq \varepsilon_{cr,p}$ occurs, the plate is subjected to local buckling in plastic range and the effective width method can be applied. Therefore, Eq. (19) provides the width b_{eff} to be considered, depending on the strain level, by assuming the value 6.97 for the buckling factor k , being the plate edges clamped.

Conversely, the web plates are subjected to a linear strain distribution. Therefore, Eq. (10) can be applied by assuming $b = y_c$, i.e. with reference to the compressed part of the web. When $\varepsilon_{max} > \varepsilon_{cr,p}$, the compressed portion of the web plates is subdivided into two parts: one where $\varepsilon \leq \varepsilon_{cr,p}$, with length equal to $l_e = \varepsilon_{cr,p}/\chi$ and one where $\varepsilon \geq \varepsilon_{cr,p}$, with length equal to $l_b = y_c - l_e$, being y_c the distance between the neutral axis and the top edge of the plate in compression (Fig. 4). Therefore, only the l_b portion is characterised by buckling in plastic range.

In order to identify the effective part of the compressed web portion, Eq. (19) is applied with $\varepsilon = \varepsilon_{max}$. The non effective width $y_c - b_{eff}$ is assumed to be located in the central part of the l_b segment as depicted in Figure 4. If the elementary area belongs to the non-effective width its contribution is neglected. Regarding the edge conditions of the web plate in compression, it is observed that the top edge at the corner is practically clamped because inward deforma-

tions are prevented and, similarly, the same assumption can be made for the lower edge of the compressed zone due to the restraining action exerted by the part in tension below the neutral axis. Therefore, the value 6.97 can be assumed for the buckling factor k of the web plates too.

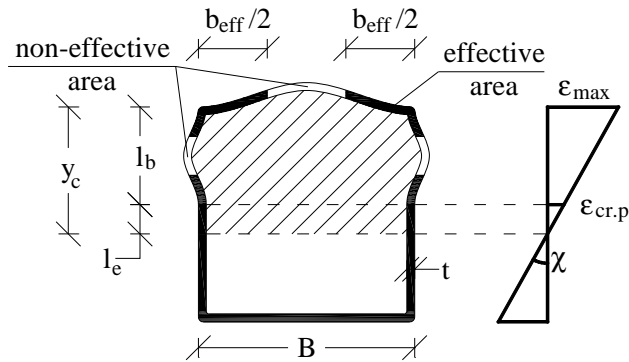


Figure 4. Outward buckling of steel plates.

It is useful to point out that, for increasing values of the curvature, local buckling provides a reduction of the effective width of the plates in compression. This is responsible, in pair with the softening branch provided by Eq. (5), of the decrease of the bending capacity of the cross section, so that the moment-curvature relationship is characterised by a softening branch.

Evaluation of the force-displacement curve

Starting from the knowledge of the moment-curvature relationship, a procedure able to provide the force-displacement curve of CFT bridge piers has been implemented. The reference scheme is represented by a cantilever beam-column (which also corresponds to the behaviour of one half of a simply supported member subjected to a three-point bending test). However, the implemented procedure has a general relevance, because it can be applied to any 2D structural system. Monotonic loading conditions have been considered.

The member is subdivided in several finite elements, each one characterised by means of the actual moment-curvature relationship of the cross section. In this way, the procedure is independent of the constructional system of the member provided that an appropriately developed subroutine is implemented to compute the moment-curvature relationship. The elements are connected by means of nodes, one of which is identified as the control node.

The force-displacement curve is obtained by means of an iterative non-linear step-by-step procedure, led under displacement control. In particular, at each step the displacement of the control node is assigned and the displacements of all the other nodes are proportionally assumed. With this attempt

shape of the displacement vector, by calculating secant stiffness matrix of the whole structural system, the internal actions are computed for each frame element. In particular, at each step the secant stiffness matrix of the whole structural system is updated considering, for each element, the internal actions computed by means of the stiffness matrix resulting from the previous step. In fact, by means of the moment-curvature relationship, as soon as the bending moments acting on the frame elements are known, the secant stiffness of each element can be determined, so that the secant stiffness matrix of the whole structural system can be updated. Therefore, the actual displacements are calculated for each node and the corresponding displacement vector is compared with the previous one. The iterations terminate when the differences between two vectors obtained in two successive steps are close within the assigned tolerance. In this case (i.e. at convergence), a displacement increment is assigned to the control node, and the procedure is repeated to obtain another point of the force-displacement curve.

In the calculation procedure, particular care has to be devoted to the unloading process. In fact, even if a monotonic displacement control is performed, when the most loaded element reaches the peak of the moment-curvature relationship the corresponding moment capacity starts to decrease. As a consequence, the external load decreases, and the internal actions acting on each frame element are reduced. This means that the frame elements are subjected to unloading conditions, so that the branch to be followed of the moment-curvature relationship is now the elastic unloading branch, while the critical zone is subjected to increasing curvature.

4. EXPERIMENTAL PROGRAM

Specimens and testing procedure

An experimental program concerning CFT members has been developed at the *Materials and Structures Laboratory* of the *Department of Civil Engineering of Salerno University*. The tests are devoted to analyse the response of SHS columns filled with concrete, both in monotonic and cyclic loading conditions. In the following Sections all the structural details of specimens, the testing devices and the experimental results are summarised.

According to the planned experimental activity, eight CFT columns made of SHS steel members have been tested. The main difference among the tested specimens is represented by the width-to-thickness ratio D/t . The measured geometrical properties and the main material properties of tested specimens are provided in Table 1.

Each specimen was manufactured from a rolled steel sheet, folded and welded along one longitudinal side. At the ends of the specimen, steel square plates (20 mm thick) were welded, being one of them holed to allow concrete

filling. The specimens were placed upright and filled with concrete, then waiting for its complete cure. Concrete class C30/35 has been used. In order to recover the small longitudinal shrinkage at the top of the column, high strength epoxy was used to fill the gap and let the end surface be uniform between concrete and steel. The length of specimens is equal to 2400 mm.

Table 1. Geometrical and mechanical properties of tested specimens.

<i>Specimen</i>	$D \times t$ [mm]	D/t	f_{su} [N/mm ²]	f_{cu} [N/mm ²]	F_u [kN]
S1	300 × 7.7	38.96	564	36.46	895
S2	300 × 6.1	49.18	595	36.46	851
S3	300 × 7.7	38.96	579	36.46	955
S4	300 × 6.1	49.18	570	36.46	733
S5	220 × 7.8	28.20	567	36.46	507
S6	220 × 4.9	44.89	460	36.46	233
S7	220 × 4.9	44.90	472	36.46	272
S8	220 × 7.8	28.21	559	36.46	504

Regarding material properties, three coupon specimens have been prepared for each steel tube. Coupon tests have been carried out to evaluate the average maximum tensile strength f_{su} , given in Table 1, and the actual stress-strain relationship, depicted in Figures 5 to 12 for all the specimens. From these figures, it can be recognised that the shape of the stress-strain relationship is significantly different from a bi-linear one, being of round house type. For this reason, in order to better describe the actual characteristics of steel of such hollow profiles, it is convenient to refer to Ramberg-Osgood (1943) formulation. Therefore, the stress-strain constitutive law of steel has been expressed by means of the following formula:

$$\varepsilon = \frac{\sigma}{E} + \alpha \left(\frac{\sigma}{f_0} \right)^n \quad (20)$$

where σ and ε are the actual stress and strain, respectively, the term σ/E represents the elastic part of the strain, the parameters α and n describe the hardening behaviour of the material, and f_0 is the conventional value of the yield stress. For each specimen, the parameters α , n and f_0 have been calibrated by means of a curve fitting technique with reference to the experimental curve. The adopted values are reported in Table 2.

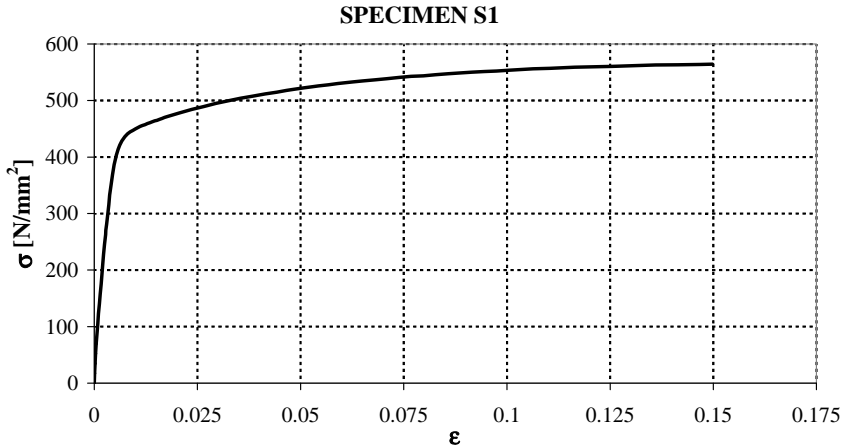


Figure 5. Steel stress-strain diagram for specimen S1.

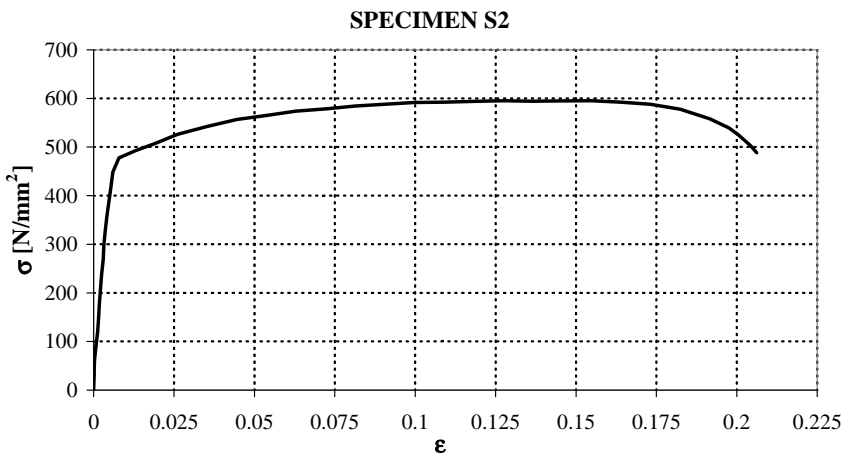


Figure 6. Steel stress-strain diagram for specimen S2.

Regarding the concrete strength, all the steel tubes were filled with the same concrete cast. Therefore, some 150 mm concrete cubes have been taken from the cast and subjected to compression tests, after 28 days, which revealed a satisfactory agreement, being the scatter quite small. In addition, some cubes have been tested at the same date of the main tests on CFT members, revealing, obviously, a small variation of the compressive strength of concrete due to aging. For this reason, considering that due to the confinement effect a small variation of the unconfined concrete strength leads to negligible effects on the load carrying capacity of CFT members, the same unconfined concrete strength has been assumed for all the specimens. In detail, the corresponding value of the unconfined concrete strength has been obtained as the average compression

strength results from tested cubes and it is given in Table 1 with reference to the corresponding cylindrical value.

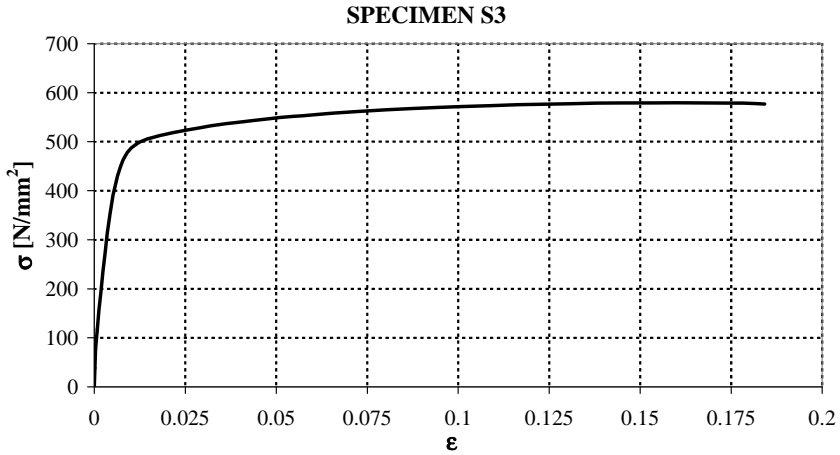


Figure 7. Steel stress-strain diagram for specimen S3.

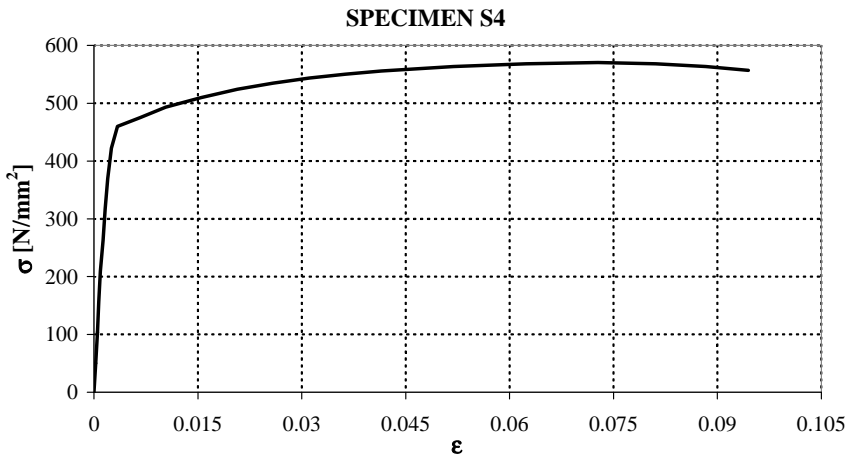


Figure 8. Steel stress-strain diagram for specimen S4.

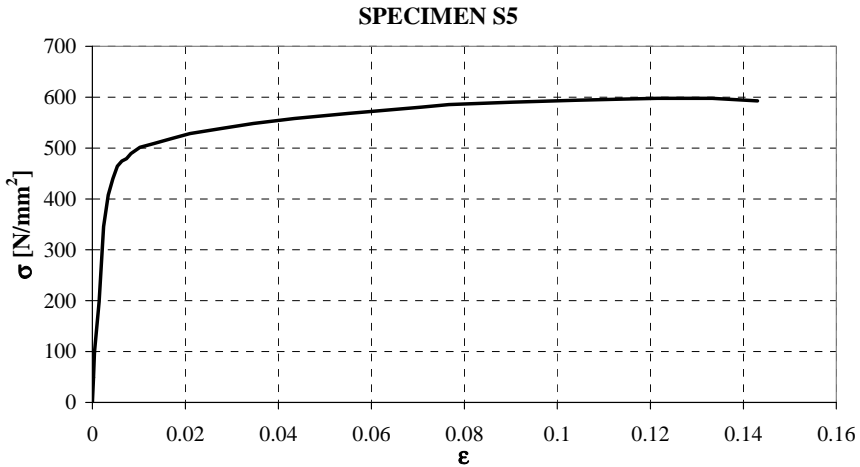


Figure 9. Steel stress-strain diagram for specimen S5.

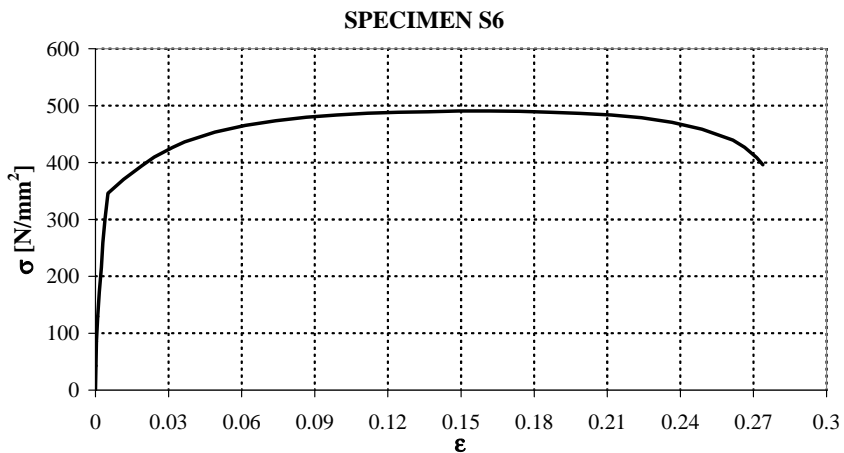


Figure 10. Steel stress-strain diagram for specimen S6.

Regarding the tests on CFT members, three point bending tests under cyclic loading conditions have been performed. No axial load was applied to the specimens, because the experimental program is focused on the response of composite bridge piers. In fact, the axial load acting on bridge piers is a small part of the squash load (usually about 0.10 times the squash load). This means that the flexural behaviour governs the response of such structural members, while the axial load is not particularly significant.

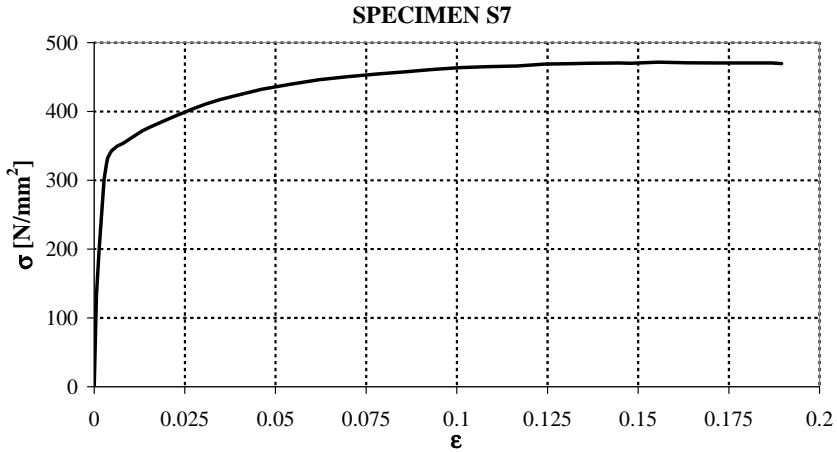


Figure 11. Steel stress-strain diagram for specimen S7.

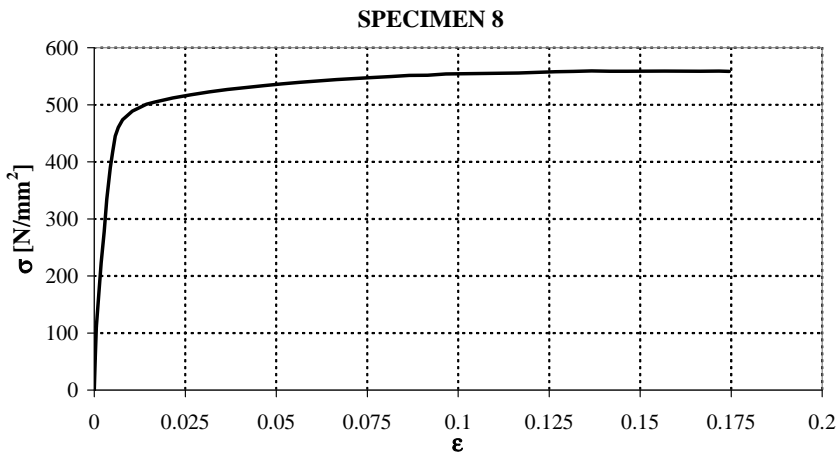


Figure 12. Steel stress-strain diagram for specimen S8.

Figure 13 provides a schematic view of the test setup. The ends of the specimen are free to rotate in-plane due to the connection to pin jointed hinges. Therefore, a simply supported scheme is adopted to test the beam-column. The distance between the two pins, i.e. the actual length of specimens, is equal to 3000 mm. However, the results can be easily extended to a cantilever beam-column scheme (which is relevant for bridge piers) by considering an half member. One of the two end hinges is equipped with slotted hole, in order to allow free sliding of the specimen in the longitudinal direction.

Table 2. Stress-strain relationship parameters.

<i>Specimen</i>	α	n	f_0 [N/mm ²]
S1	0.01500	13.00	48.00
S2	0.00419	19.54	50.85
S3	0.00948	18.23	50.14
S4	0.00310	20.00	48.00
S5	0.01800	13.00	49.00
S6	0.00320	11.00	33.00
S7	0.02060	10.71	40.05
S8	0.00720	21.40	49.00

The flexural loading has been applied, in the middle of the member, by means of an hydraulic actuator having 2500 kN capacity in tension and 3000 kN in compression. The connection between the specimen and the actuator is constituted by means of a rigid stub located in the middle of the specimen. The stub is realised by means of two rigid plates on the horizontal sides of the specimen, joined by means of steel bars. Therefore, loads both in tension and in compression can be applied to the specimen. The length of the rigid stub is equal to 460 mm.

Several measuring devices have been adopted to record displacements and deformations. The measure of the displacement at force location has been carried out by means of the LVDT of the hydraulic actuator and also by means of additional displacement transducers. Additional displacement transducers have been also located along the length of the specimen to measure its deflected shape. Moreover, strain-gauges have been applied on the vertical lateral sides of the steel box, in two control sections, one on the right side and one on the left side of the rigid stub. These sections are those characterised by the occurrence of the maximum value of the bending moment. They are placed at 1250 mm distance from the center of rotation of each hinge. In particular, longitudinal strain-gauges were applied on the webs at 55 mm distance from the top and the bottom flanges of the tube, respectively. In this way, deformations close to the maximum values are measured. Finally, in order to evaluate transversal deformations, two strain gauges have been applied also transversally, one for each control section.

All the experimental tests have been continued until either the specimen fails due to the fracture of the steel tube at the corners with concrete leakage, or at least a 50% loss of the lateral load resistance is observed.

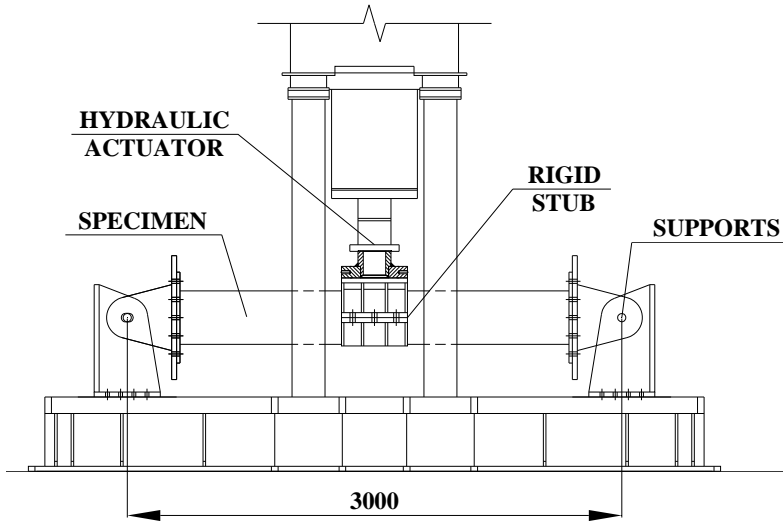


Figure 13. Test setup.

Test results and discussion

All the specimens have shown a ductile response. The results are herein summarised by means of force-displacement curves and moment-curvature relationships.

In particular, force-displacement curves represent the relationships between the lateral load and the deflection at the middle of the specimens. They are directly provided by the actuator data.

Instead, moment-curvature relationships are obtained by means of deformations measured through the strain gauges, so that they are referred to the sections adjacent to the rigid stub. Since four measures are available (two control sections and two webs for each one), the moment-curvature relationships have been obtained considering the average values of the deformations. However, the moment-curvature relationship has been evaluated only for the first loading branch, because due to large deformations, strain-gauges went off-scale.

In Figures 14 to 21 the force-displacement curves for each specimen are shown, while in Figures 22 to 29 the experimental moment-curvature relationships are depicted, respectively. The maximum lateral loads achieved at the midspan of all specimens are reported in Table 1 (F_u).

As shown by the force-displacement curves, specimens S5 and S8 having the smallest D/t ratio (equal to 28.2) have exhibited the most stable cyclic response with low strength degradation as far as the number of cycles increases, so that many cycles are needed before the occurrence of tube flange fracture and concrete leakage.

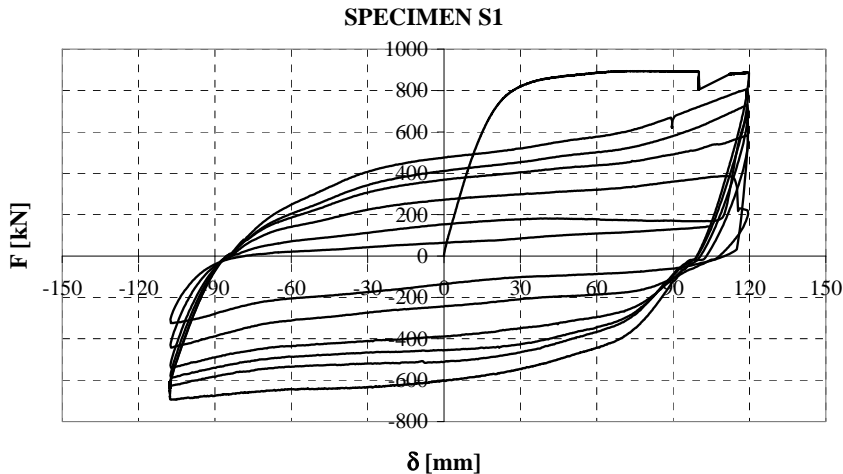


Figure 14. Lateral load-deflection curve for specimen S1.

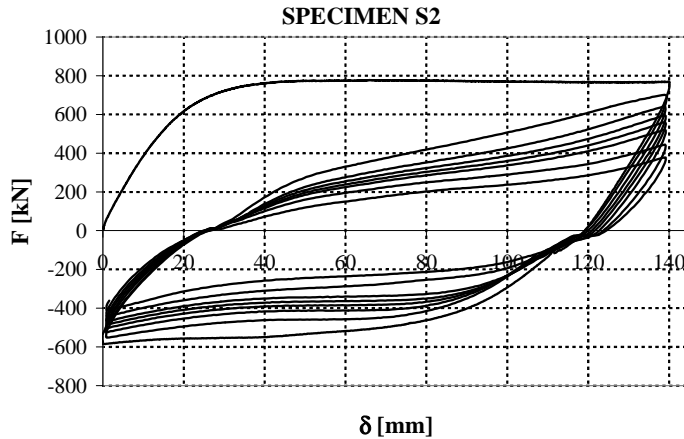


Figure 15. Lateral load-deflection curve for specimen S2.

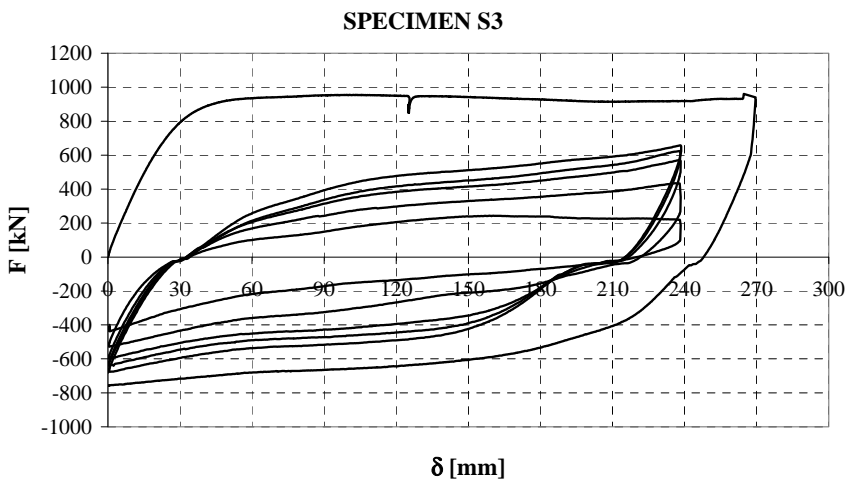


Figure 16. Lateral load-deflection curve for specimen S3.

It can be recognised that the amount of strength degradation and, as a consequence, of reduction in energy dissipation capacity at any cycle is affected both by D/t ratio, governing the occurrence of local buckling, and the applied displacement history. In fact, the cyclic response of specimen S1 is characterised by strength degradation and energy dissipation capacity degradation at any cycle greater than those occurring in case of specimens S6 and S7, despite of the D/t ratio of specimen S1 is equal to 38.96, while specimens S6 and S7 are characterised by a D/t ratio equal to 44.9 (i.e. greater than specimen S1).

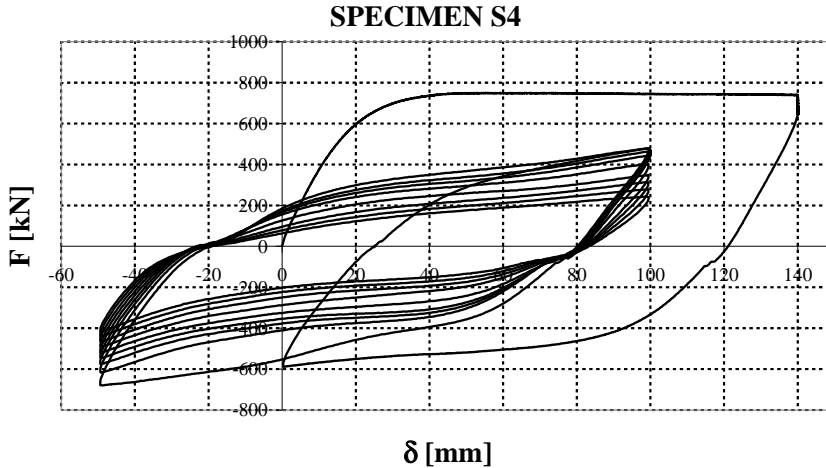


Figure 17. Lateral load-deflection curve for specimen S4.

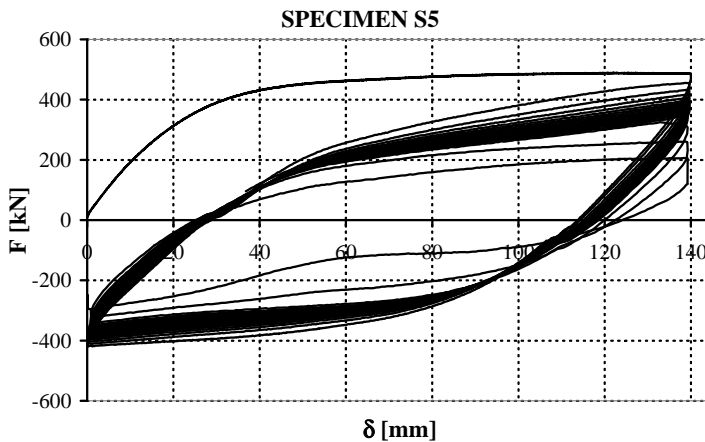


Figure 18. Lateral load-deflection curve for specimen S5.

Obviously, the more important degradation phenomena occurring in case of specimen S1, compared to S6 and S7, is due to the whole amplitude of the applied cyclic displacement history. In fact, such amplitude is equal to 140 mm (i.e. cycling from 0 to +140 mm) in case of specimens S6 and S7 and equal to almost 240 mm in case of specimen S1 (i.e. cycling from -120 mm to +120 mm). Moreover, it is also useful to note that the influence of the displacement history is essentially related to the whole displacement amplitude rather than to the features of the applied history. In fact, even though specimens S1 and S3, having the same D/t ratio are subjected to displacement histories having different features (symmetrical history for specimen S1 and unsymmetrical history

for specimen S3), with the same whole displacement amplitude, the number of cycles to fracture is almost the same.

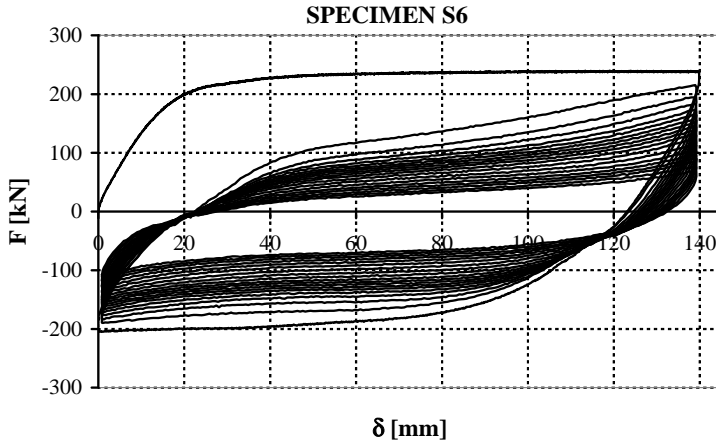


Figure 19. Lateral load-deflection curve for specimen S6.

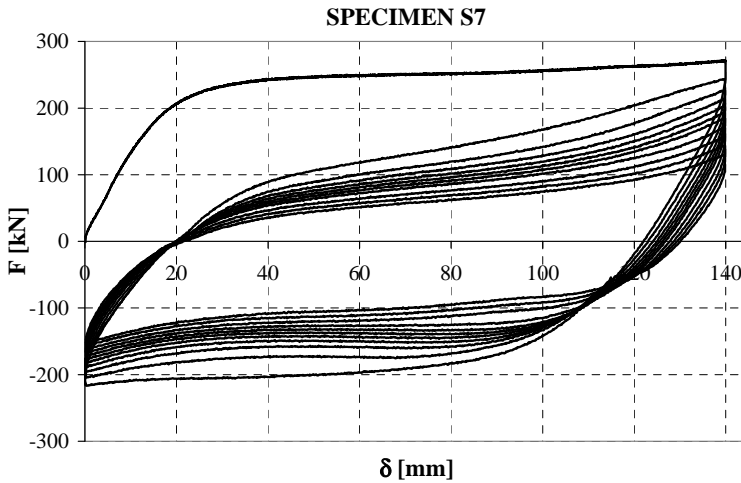


Figure 20. Lateral load-deflection curve for specimen S7.

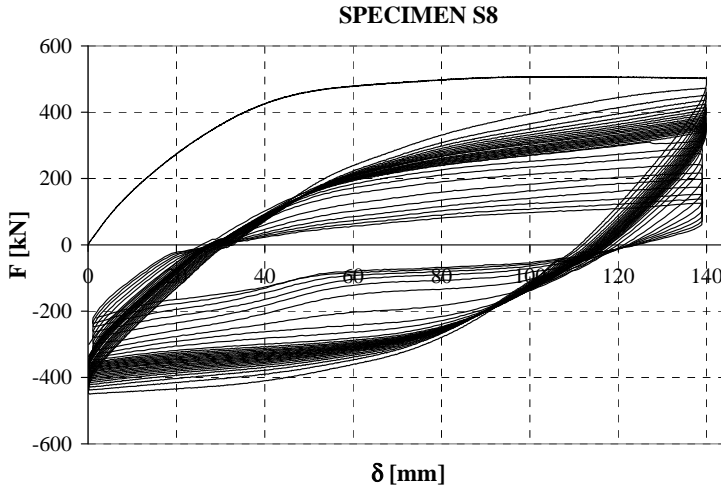


Figure 21. Lateral load-deflection curve for specimen S8.

A further increase of the D/t ratio gives rise to a further worsening of the energy dissipation capacity due to the increase of strength degradation, as it is testified by the comparison between specimen S2 (having $D/t = 49.2$) and specimen S6 (having $D/t = 44.9$) which are subjected to unsymmetrical cyclic displacement histories having the same displacement amplitude. Moreover, comparison between specimen S2 and specimen S4 points out the influence of the displacement history.

In all the cases, bulges formed at both top and bottom flanges of steel tubes, close to the rigid stub, where the bending moment assumed the maximum value. Since the first displacement ramp was downward the first bulge always formed on the top flange, i.e. the steel plate in compression. Then, the bulge formed also on the other flange when the lateral displacement was reversed. Regarding the small slips occurring in some cases at load reversal points (Figs. 14 to 21), they are probably due to the settlement of the connecting system of the rigid stub embracing the specimen.

Referring to the first loading branch corresponding to the initial ramp which has been carried out to investigate the monotonic behaviour up to a displacement range compatible with the actuator stroke, the maximum lateral load is almost sustained without any loss of strength. This means that CFT bridge piers can exhibit high global ductility with reduced loss of strength due to delayed local buckling phenomena.

With reference to transversal strain-gauges, applied on the upper part of the webs to evaluate the deformations due to the interaction between the steel tube and the concrete core, even if the corresponding longitudinal stress field was in compression, they measured tensile deformations. This agrees with the phenomenon described in Section 2.2. It means that, due to the interaction between

the steel tube and the confined concrete, a bi-axial stress state arises in the steel plate elements, being hoop stresses in tension.

Finally, Figures 22 to 29 show the moment versus curvature relationship derived from experimental evidence by means of the strain gauges located on the web plates of the steel profile. Such results will be compared in next Section with the numerical results coming from the application of the proposed fiber model.

The moment versus curvature relationships provided in the figures, with respect to the rough experimental data, are evaluated accounting for the influence of friction at the base of the supporting end hinges which gives rise to an unavoidable horizontal component of reaction at the supports. Therefore, second order effects develop during the loading process. Such second order effects have been evaluated considering a friction coefficient equal to 0.78, according to literature, and accounting for the force applied by the actuator and the weight of both the specimen and the testing equipment.

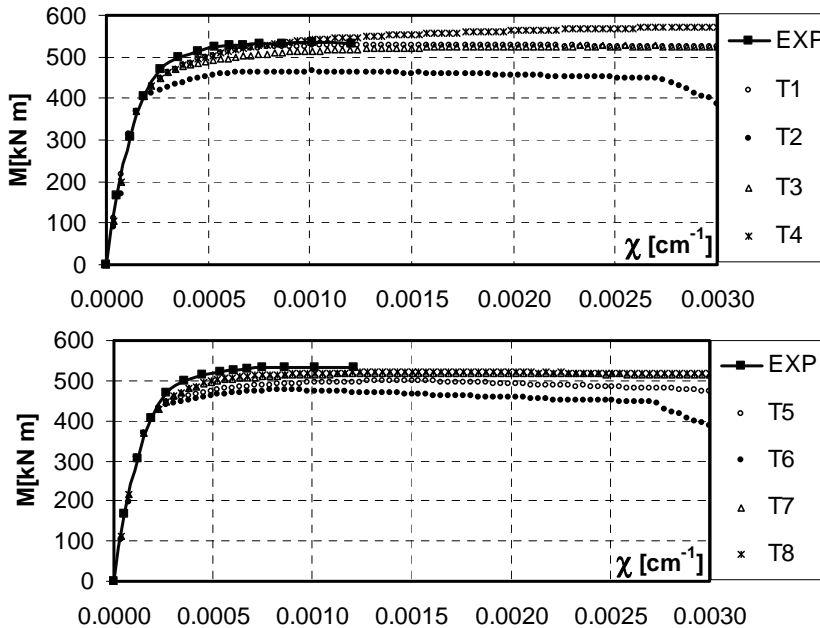


Figure 22. Experimental vs analytical moment-curvature relationships for sp. S1.

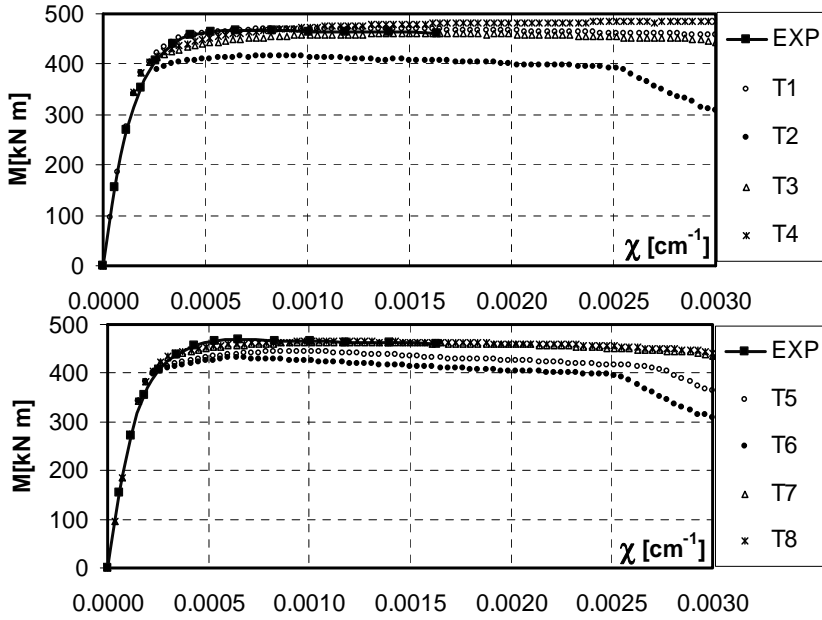


Figure 23. Experimental vs analytical moment-curvature relationships for sp. S2.

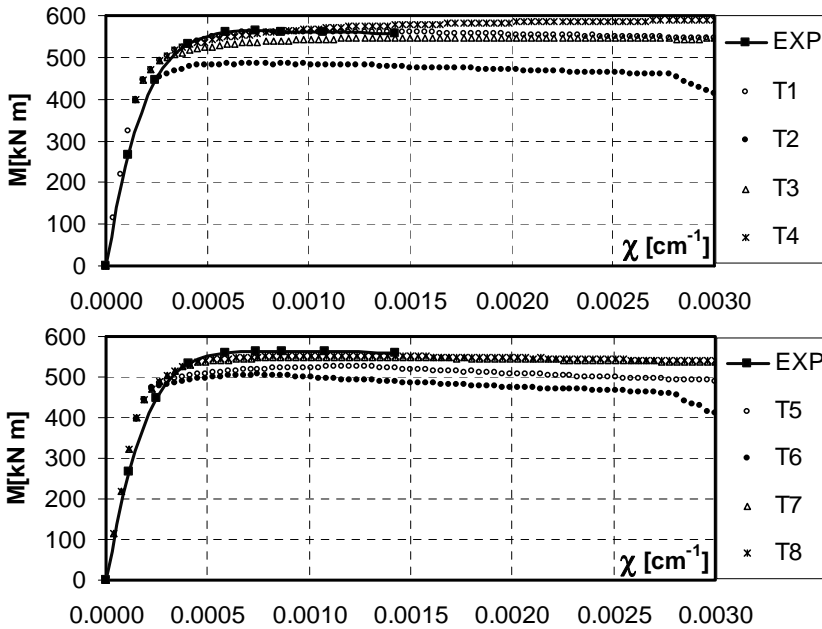


Figure 24. Experimental vs analytical moment-curvature relationships for sp. S3.

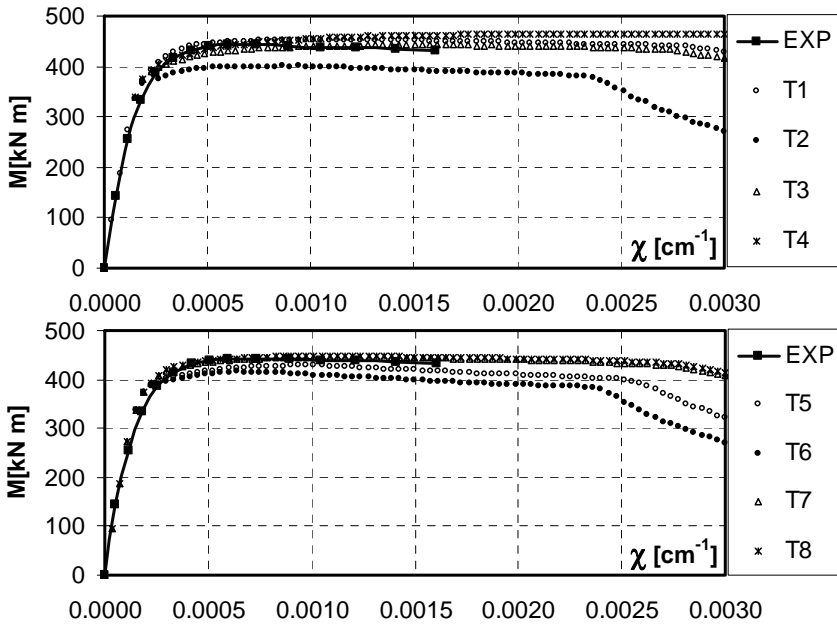


Figure 25. Experimental vs analytical moment-curvature relationships for sp. S4.

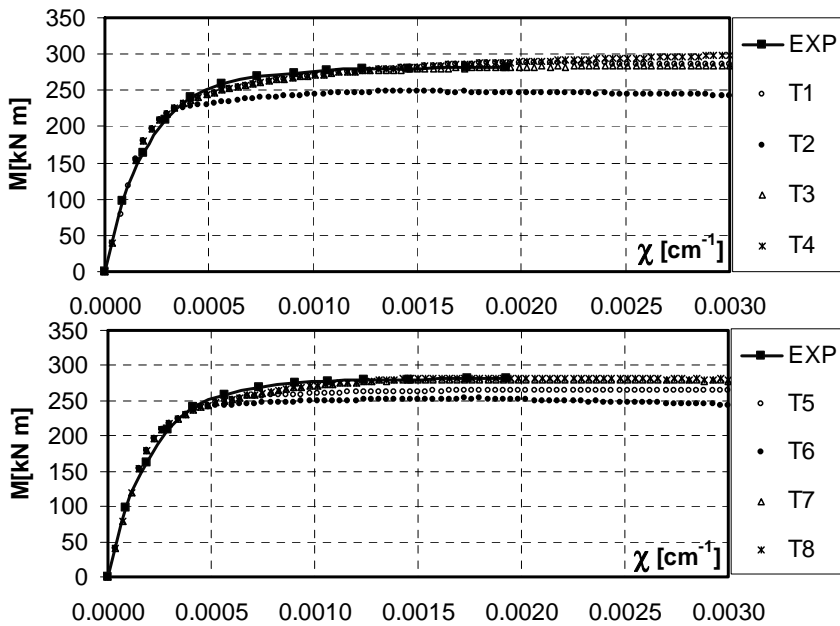


Figure 26. Experimental vs analytical moment-curvature relationships for sp. S5.

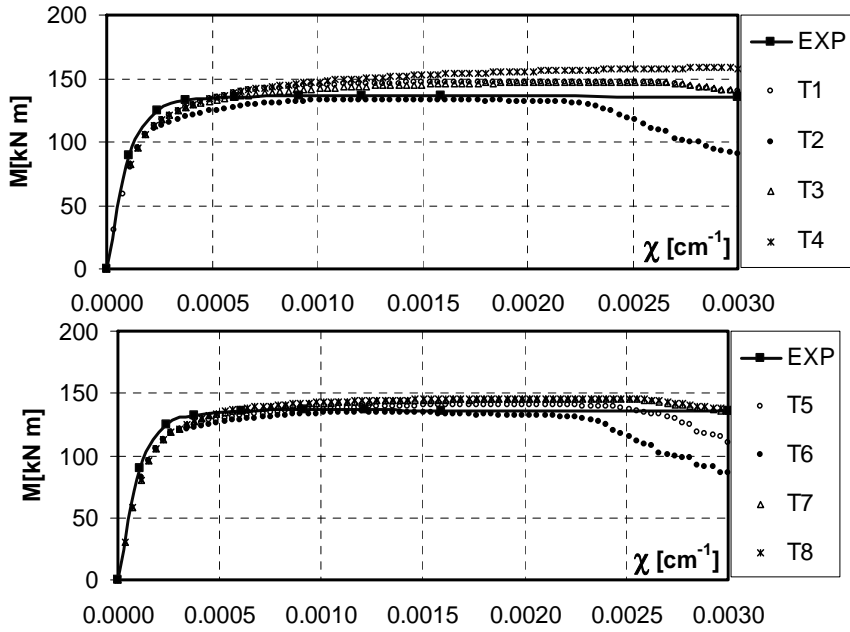


Figure 27. Experimental vs analytical moment-curvature relationships for sp. S6.

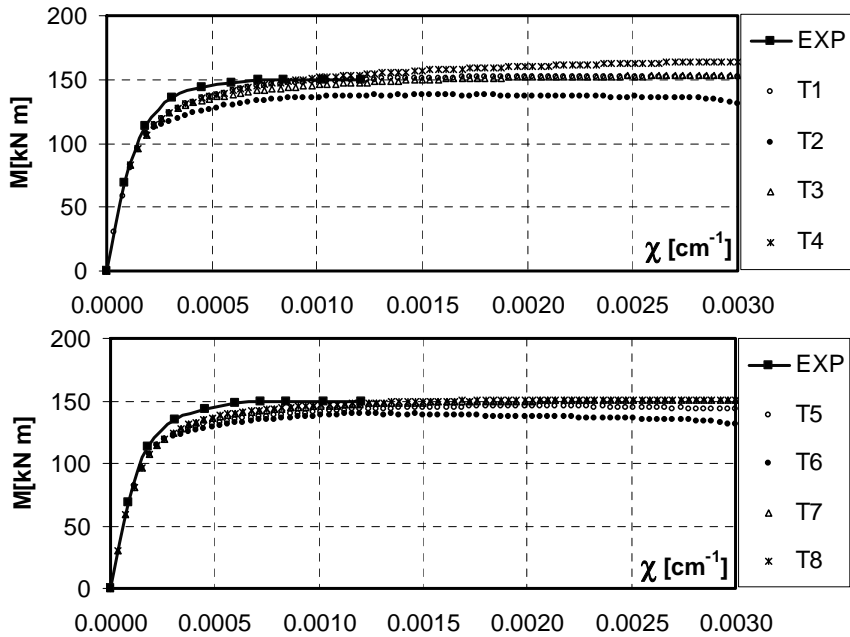


Figure 28. Experimental vs analytical moment-curvature relationships for sp. S7.

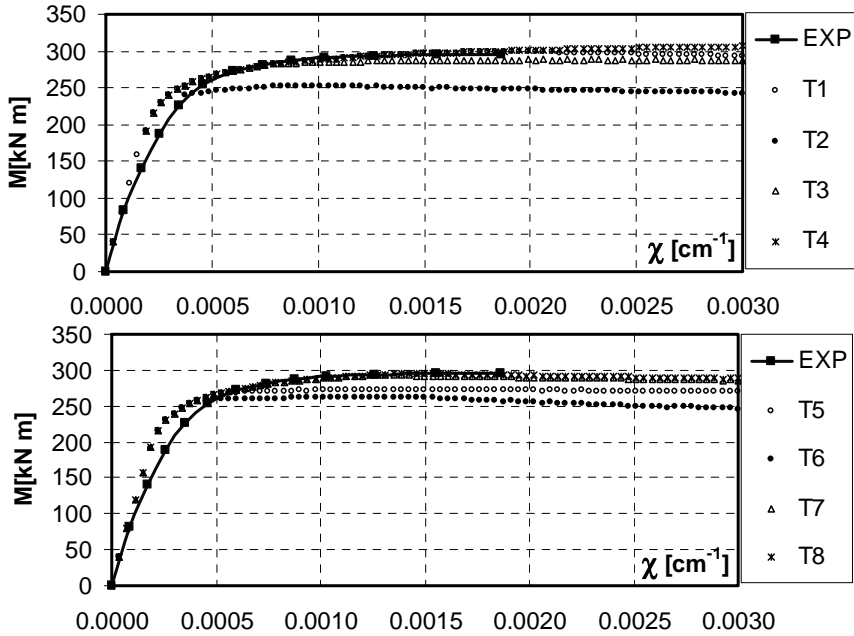


Figure 29. Experimental vs analytical moment-curvature relationships for sp. S8.

Table 3. Ratio between the maximum theoretical and maximum experimental moment in the range of measured curvatures.

η	Specimen								Mean
	S1	S2	S3	S4	S5	S6	S7	S8	
T1	0.989	1.007	0.999	1.024	1.018	1.079	0.999	1.017	1.016
T2	0.871	0.889	0.861	0.905	0.880	0.975	0.916	0.858	0.894
T3	0.970	0.984	0.972	1.000	0.999	1.079	0.985	0.976	0.996
T4	1.024	1.027	1.026	1.043	1.022	1.159	1.026	1.017	1.043
T5	0.932	0.953	0.935	0.969	0.937	1.031	0.954	0.924	0.954
T6	0.895	0.922	0.900	0.940	0.897	0.989	0.929	0.889	0.920
T7	0.969	0.990	0.976	1.006	0.991	1.062	0.983	0.994	0.996
T8	0.975	0.995	0.983	1.011	0.999	1.067	0.987	1.000	1.002

Table 4. Ratio between theoretical and experimental values of the area below moment versus curvature diagram in the range of measured curvatures.

η	<i>Specimen</i>								<i>Mean</i>
	S1	S2	S3	S4	S5	S6	S7	S8	
T1	1.011	1.025	1.048	1.038	1.011	1.052	0.996	1.036	1.027
T2	0.911	0.910	0.921	0.923	0.918	0.919	0.927	0.915	0.918
T3	0.990	0.994	1.014	1.006	1.005	1.044	0.980	1.018	1.006
T4	1.021	1.022	1.051	1.035	1.011	1.097	1.003	1.035	1.034
T5	0.961	0.965	0.985	0.978	0.969	0.992	0.959	0.982	0.974
T6	0.934	0.934	0.950	0.948	0.937	0.923	0.941	0.951	0.940
T7	0.997	1.008	1.031	1.022	1.004	1.036	0.985	1.029	1.014
T8	1.002	1.013	1.036	1.026	1.007	1.040	0.988	1.032	1.018

5. VALIDATION OF THE PROPOSED FIBER MODEL

The experimental results presented in the previous Sections can be used in order to investigate the accuracy of the proposed fiber model. In particular, the moment versus curvature relationship obtained by means of the proposed fiber model is compared, for each tested specimen, with the one coming from experimental evidence. Aiming to analyse the influence of the different formulations, available in the technical literature, to account for the occurrence of local buckling, either in elastic range or in plastic range, depending on the width-to-thickness ration of the plate elements constituting the steel tube profile, the theoretical prediction of the moment-curvature relationship has been carried out, for each specimen, with reference to the eight formulations, namely T1 to T8, i.e. Eq. (11-18), presented in Section 2.4.

The comparison between the results coming from experimental evidence and those obtained by application of the proposed fiber model is given in Figures 22 to 29, with reference to specimens S1 to S8, respectively. The top part of each figure provides the comparison between the experimental curve and the moment-curvature relationship obtained by means of the fiber model adopting the formulations T1, T2, T3 and T4 for the η factor governing the occurrence of local buckling. Similarly, the bottom part of each figure deals with the same comparison, but referring to formulations T5, T6, T7 and T8 for local buckling prediction. From a qualitative point of view, these figures show that a good agreement between experimental results and the predictions provided by the fiber model is obtained in case of formulations T1, T3, T7 and T8. Conversely, the use of formulations T2, T5 and T6 leads to an underestimation of the ultimate flexural resistance and, in addition, to the premature development of a

softening branch related to local buckling. Moreover, it can be noted that the use of formulation T4 always provides an overestimation of the ultimate flexural resistance and, in addition, the obtained curve is always increasing without exhibiting any significant influence of local buckling.

In order to provide a quantitative comparison among the different available formulations to account for local buckling, two parameters have been considered.

The first parameter is the ratio between the maximum flexural resistance evaluated with the fiber model, for any given theoretical formulation of the η factor, and the experimental value. To this scope reference has been made to the maximum flexural resistance occurring in the experimentally investigated curvature range, i.e. the curvature range before the failure of strain gauges. With reference to the same curvature range, the second parameter is the ratio between the area below the theoretical moment-curvature diagram and the same area evaluated with reference to the experimental curve.

The obtained results are given in Table 3 with reference to the first parameter which provides a measure of the fiber model accuracy in terms of flexural resistance. In particular, last column provides the mean value of the above parameter showing that a very good agreement between experimental evidence and fiber model predictions is obtained in case of T3, T7 and T8 formulations, leading to a mean scatter less than 1%.

Regarding the second parameter, the obtained values are given in Table 4 providing the fiber model accuracy in terms of absorbed energy. Last column, again, provides the mean value of the investigated accuracy parameter outlining that T3, T7 and T8 formulations provide a very good agreement with experimental evidence, being the mean scatter less than 2%.

Therefore, as a conclusion of the above comparisons, it is confirmed the importance of local buckling and of its prediction in the modelling of the ultimate behaviour of CFT members. The theoretical formulations, accounting for local buckling either in elastic range or in plastic range, providing the greatest accuracy are those herein namely T3, T7 and T8. Under this point of view, it is interesting to note that formulation T8, due to Li and Reid (1992), is able to provide a very good agreement with experimental evidence even in the case of SHS and RHS aluminium hollow members (empty), subjected to the local buckling under uniform compression (Faella et al., 2000; Laugseth and Hopperstad, 1995).

Finally, a preliminary comparison has been performed in terms of force-displacement curves. Theoretical force-displacement curves have been numerically computed starting from moment-curvature relationships evaluated by means of the proposed fiber model. The reference scheme is a cantilever beam-column (see Section 3.3) of 1250 mm length, which is the length of the specimen portion included between the end pin and the rigid stub at midspan. In

Figure 30, as an example, the comparison between numerical simulation and experimental results is shown with reference to specimen S7.

In particular, the depicted experimental displacements are those obtained as the difference between the deflection at midspan and the displacement measured by the first transducer, which is located at a distance equal to 550 mm distance from the pin of the end hinge. In this way, the measured relative displacement is independent of the deformabilities of the testing equipment which are concentrated at the support, i.e. the displacements due to the connection between the specimen and the hinge device and the displacements due to the deformability of the hinge device. Similarly, in order to compare homogeneous displacements, theoretical displacements of Figure 30 are obtained as the difference between the numerical values computed at the end of the equivalent cantilever scheme and the ones evaluated at a distance equal to 550 mm from the pin centre of rotation.

The theoretical curve seems to fit the experimental one with good agreement both in elastic and plastic range. Similar results have been obtained for all the other specimens.

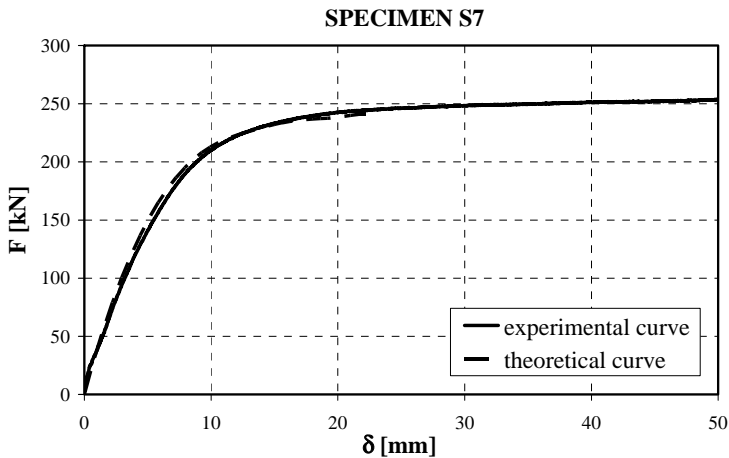


Figure 30. Experimental versus numerical force-displacement curve for sp. S7.

6. CONCLUSIONS

The main goal of the presented research activity is the study of the seismic response of steel-concrete bridges. As the base sections of bridge piers are recognised as dissipative zones, in terms of seismic behaviour a bridge can be considered made of a steel-concrete composite structure provided that the bridge piers are made of a composite solution, while constructional technologies adopted for the bridge deck are not relevant. Starting from this point of view,

the attention has been focused on the topic of the ultimate behaviour of concrete filled tubes subjected to non-uniform bending. A fiber model for predicting the moment-curvature relationship of such composite members has been developed allowing the evaluation of both the ultimate strength and the ductility of bridge piers detailed according to such technology.

An experimental program has been developed in order to study the response of steel tubes filled with concrete, both in monotonic and cyclic loading conditions. The results have confirmed the attitude of such structural typology to the absorption of the seismic input energy, being both strength and ductility suitable and satisfactory for the role of dissipative zones.

The accuracy of the proposed fiber model has been tested comparing numerical results with the ones provided by the experimental evidence. The theoretical approach has shown a very good agreement with experimental results, by correctly predicting both resistance and ductility of CFT beam-columns provided that concrete confinement, bi-axial stress state of steel and local buckling phenomena are properly accounted for. Therefore, the developed fiber model can constitute a useful tool for designing such structural members, including steel-concrete composite bridge piers.

ACKNOWLEDGEMENTS

This work has been supported by Italian research grant DPC ReLUIS 2005-2008.

REFERENCES

- Attard M.M., Setung S. [1996]. "Stress-strain relationship of confined and unconfined concrete", *ACI Materials Journal*, title 93-M49: 432-442.
- Bijlaard P.P. [1949]. "Theory and tests on the plastic stability of plates and shells", *Journal of the Aeronautical Sciences*, September: 529-543.
- Bleich F. [1952]. "Buckling Strength of Metal Structures", McGraw Hill Book Co., Inc., New York: 343-355.
- CEN/TC 250 [2005]. EN 1998-2:2005: "Eurocode 8 - Design of Structures for Earthquake Resistance. Part 2: Bridges", Comité Européen de Normalisation.
- Chen W.F. [1993]. "Advanced analysis of steel frames", Crc Press Llc.
- Consiglio Superiore dei Lavori Pubblici [2008]. D.M. 14/01/2008: "Nuove Norme Tecniche per le Costruzioni", *Gazzetta Ufficiale della Repubblica Italiana*, G.U. 29/2008, February.
- Elremaily A., Azizinamini A. [2002]. "Behaviour and strength of circular concrete-filled tube columns", *Journal of Constructional Steel Research*, 58: 1567-1591.
- Faella C., Mazzolani F.M., Piluso V., Rizzano G. [2000]. "Local buckling of aluminum members: testing and classification", *Journal of Structural Engineering*: 353-360.

- Gerard G. [1957]. "Plastic stability theory of thin shells", *Journal of the Aeronautical Sciences*.
- Gerard G. [1962]. "Plastic stability theory of orthotropic plates and shells", *Journal of the Aeronautical Sciences*.
- Gherzi A., Landolfo R. [1995]. "Thin-walled sections in round-house type material: a simulation model", Proc. of XV Italian Conference on Steel Construction, Riva del Garda, Italy, October 15-17.
- Gourley B.C., Tort C., Hajjar J.F., Schiller P.H. [2001]. "A synopsis of studies of the monotonic and cyclic behavior of concrete-filled steel tube beam-columns", *Structural Engineering Report*, N.ST-01-4.
- Han L.H., Yang Y.F. [2005]. "Cyclic performance of concrete-filled steel CHS columns under flexural loading", *Journal of Constructional Steel Research*, 61: 423-452.
- Han L.H., Yang Y.F., Tao Z. [2003]. "Concrete-filled thin-walled steel SHS and RHS beam-columns subjected to cyclic loading", *Thin-Walled Structures*, 41: 801-833.
- Iannone F., Mastrandrea L., Montuori R., Piluso V. [2008]. "Experimental analysis of the cyclic response of CFT-SHS members", *Proc. of Stessa 2009, 6th International Conference on Behaviour of Steel Structures in Seismic Areas*, Philadelphia, U.S.A., 16-20 August.
- Kodur V.K.R., Lie T.T. [1995]. "Fire Performance of Concrete-Filled Hollow Steel Columns", *Journal of Fire Protection Engineering*, 7(3): 89-98.
- Lanseth, M. and Hopperstad, O.S. [1995]. "Local buckling of square thin-walled aluminium extrusions." *Proc. of 3rd International Conference on Steel and Aluminium Structures*, Istanbul, Turkey: 147-154.
- Li S., Reid S.R. [1992]. "The plastic buckling of axially compressed square tubes", *Journal of Applied Mechanics*, 59.
- Mander J.B., Priestley M.J.N., Park R. [1988]. "Theoretical stress-strain model for confined concrete", *Journal of Structural Engineering*, 114(8): 1804-1826.
- Mastrandrea L., Montuori R., Piluso V. [2008^o]. "Numerical model of the ultimate behaviour of SHS-CFT columns", *Proc. of Eurosteel 2008, Conference on Steel and Composite Structures*, Graz, Austria, 3-5 September.
- Mastrandrea L., Montuori R., Piluso V. [2008b]. "Experimental analysis of the cyclic flexural response of CFT members", *Proc. of 7th Italian Workshop on Composite Structures*, Benevento, Italy, 23-24 October.
- Mastrandrea L., Piluso V. [2007]. "Modellazione del Comportamento Ultimo di Pile da Ponte del Tipo CFT", *Proc. of Workshop "Materiali ed approcci innovativi per il progetto in zona sismica e la mitigazione della vulnerabilità delle strutture"*, Salerno, C. Faella, G. Manfredi, V. Piluso, R. Realfonzo editors, Polimetrica International Scientific Publisher, Monza, Italy, 12-13 February.
- OPCM 3274, Presidenza del Consiglio dei Ministri [2003]. "Primi elementi in materia di criteri generali per la classificazione sismica del territorio nazionale e di normative tecniche per le costruzioni in zona sismica". *Gazzetta Ufficiale della Repubblica Italiana*, G.U. 105/2003, May.
- OPCM 3431, Presidenza del Consiglio dei Ministri [2005]. "Ulteriori modifiche ed integrazioni all'ordinanza del Presidente del Consiglio dei Ministri n.3274 del 20 marzo 2003, recante "Primi elementi in materia di criteri generali per la classificazione

- sismica del territorio nazionale e di normative tecniche per le costruzioni in zona sismica””. Gazzetta Ufficiale della Repubblica Italiana, G.U. 107/2005, May.
- Pearson C.E. [1950]. “Bifurcation criterion and plastic buckling of plates and shells”, *Journal of the Aeronautical Sciences*.
- Popovics S. [1973]. “A numerical approach to the complete strain stress-strain curves for concrete”, *Cement and Concr. Res.*, 3(5): 583-599.
- Radhakrishnan S. [1956]. “Plastic buckling of circular cylinders”, *Journal of the Aeronautical Sciences*.
- Ramberg W., Osgood W.R. [1943]. “Description of stress-strain curves by three parameters”, Technical Note No.902, National Advisory Committee For Aeronautics, Washington D.C..
- Saisho M., Kato M., Gao S. [2004]. “Local buckling of CFT-column under seismic load”, Proc. of 13th World Conference on Earthquake Engineering, Vancouver, B.C., Canada, 1-6 August.
- Shams M., Saadeghvaziri M.A. [1997]. “State-of-the-Art of Concrete-Filled Steel Tubular Columns”, *ACI Structural Journal*, 94(5): 558-571.
- Shams M., Saadeghvaziri M.A. [1999]. “Nonlinear Response of Concrete Filled Steel Tubular Columns under Axial Loading”, *ACI Structural Journal*, 96(6): 1009-1019.
- Shanmugam N.E., Lakshmi B. [2001]. “State of the art report on steel-concrete composite columns”, *Journal of Constructional Steel Research*, 57: 1041-1080.
- Stowell E.Z. [1948]. “A unified theory of plastic buckling of columns and plates”, Technical Note 1556, *Natl. Advisory Committee for Aeronautics* (presently NASA), Washington, D.C..
- Susantha K.A.S., Ge H., Usami T. [2002]. “Cyclic analysis and capacity prediction of concrete-filled steel box columns”, *Earthquake Engineering and Structural Dynamics*, 31: 195-216.
- Tao Z., Han L.H., Zhao X.L. [2001]. “Hysteretic behaviors of concrete filled steel tubular beam-columns with square section”, Proc. of *The First International Conference on Steel & Composite Structures*, Pusan, Korea, 14-16 June: 1717-1724.
- Vol’Mir A.S. [1965]. “Stability of Elastic Systems”, Foreign Technology Division, Wright Patterson Air Force Base, Ohio.
- Wingarten V.I., Morgan E.J., Seide P. [1960]. “Final Report of Design Criteria for Elastic Stability of Thin Shell Structures”, Space Tech. Labs.

SEISMIC BEHAVIOR AND DESIGN RULES FOR STEEL BRIDGES

Giuseppe Chellini, Francesco Vittorio Lippi, Walter Salvatore

Department of Civil Engineering, University of Pisa, Pisa, Italy

Abstract. Steel bridges constitute a fundamental element for the realization of the infrastructures since a long time ago, especially in the railway sector. In the past such structures were designed and built on the basis of statically determined structural schemes, design loads were constituted by the proper weights of railway convoys and generally the seismic effects were neglected. In the last years the evolution of methods for structural analysis allowed to analyze and to develop new constructive solutions, actually facilitating structural design and allowing to consider, in an easy way, the effects of the seismic action too. These new methods are essentially based on the use of finite element analysis, whose numerical answer strongly depends on the chosen finite element type. It appears therefore necessary to fully understand abilities and limits of the numerical calculation in order to avoid the incorrect evaluation of the structural behavior. In the present work the results of some comparative investigations on the adoption of different modeling strategies are illustrated. These results underlined merits and defects of each technique and allowed the development of guidelines for a correct structural modeling of bridges.

Keywords: bridges, steel-concrete composite, numerical modeling, seismic behavior.

1. INTRODUCTION

In the construction of road and railway networks, for a long time designers faced the realization of bridge's and viaduct's decks adopting primarily prefabricated and prestressed concrete solutions, with the addition of a concrete slab, cast in the field.

In the recent years, however, steel and composite steel-concrete solutions were more and more used with good results. Many factors underlie this change: the use of new high yield thermo-mechanical steels; the use of high thick plates with a consequent reduction in the connecting joints, resulting in an overall improved behavior with regard to fatigue; new possibilities offered by methods of structural analysis and new design rules; the reduction of maintenance costs through the use of new treatments for steel and new products for the painting; the increase in transport capacity and assembly; the improvement of welding

technologies¹. Different structural solutions were adopted generally on the basis of the span length to be overcome: for small spans (30-40 m) parallel girders solution is adopted, for medium spans (40/80 m) single or double box section solutions are used, while for large spans bow-string solutions are preferred.

From the seismic point of view, in the current literature many studies exist on the behavior of prestressed concrete girder bridges, while much less attention was paid so far to steel and composite steel-concrete solutions².

In the design of new bridges generally superstructures, designed to support design loads in the elastic domain, are expected to remain in the elastic domain also during earthquakes.

Substructures and bearings can react to seismic actions by remaining in the elastic domain or by entering into plastic domain. It is also possible to include ductile elements capable to dissipate seismic energy, generally located near to the piers or to the end cross-frames³. Moreover superstructure insulation systems⁴ or semi-active control devices⁵ can be foreseen and designed

From the analysis of damages induced by several earthquakes in different countries, in fact it was clear that the major damages are typically present in bearings (metal or elastomeric) and substructures (piers and abutments). Nevertheless once triggered, those "primary" damages lead to the occurrence of "secondary" damages of various typologies on the superstructure, with a significant incidence of instability phenomena caused by the redistribution of internal forces⁶.

It is so clear that seismic design and testing of bridges demands a proper evaluation of dynamic characteristics of the structure, both for resistance analysis of superstructure, and for estimation of design forces transferred to the substructure (bearings, piers and abutments). This assessment is usually performed by numerical analysis of finite element models, for which in current regulations the modeling rules and the values of mechanical parameters such as materials mass, stiffness and damping properties are rather uncertain. Depending on structural typology and modeling technique, the numerical dynamic characteristics and the estimation of seismic actions can be strongly dependent on the values assigned to these parameters⁷.

In the case of existing structures, it is possible to evaluate the seismic behavior through the use of modern experimental dynamical tests and updating procedures of mechanical model ("model updating"), capable of providing an ac-

¹ Hoorpah et al., 2004.

² Dicleli et al., 1995; MCEER, 2001; NHCPR, 2002.

³ Maleki, 2006.

⁴ Uang et al., 2000.

⁵ Erkus et al. [2002]

⁶ Moehle et al., 2000.

⁷ Dicleli et al., 1995.

curate estimate of resistant scheme and current values of mechanical parameters.

In the design of new structures, instead at present it is clearly necessary to develop a technical knowledge specifically aimed at identifying the best modeling techniques for the analysis of bridge's typical structures, as the lack of reliable criteria makes the evaluation of seismic actions extremely variable, to the detriment of structural safety in the case of an understatement and of an unreasonable burden in the case of an overestimation.

In this chapter the results of a study on currently available modeling techniques for the analysis of steel and composite steel-concrete bridges are reported. Particularly some study cases representative of the usual typologies adopted in road and railway bridges were analyzed, also making reference to the results of experimental tests aiming at the dynamic characterization of structures. Results allowed the development of some general modeling rules, which can conduct the designer to a better estimation of seismic forces.

2. MODELING TECHNIQUES

In the last years, thanks to the development of computer power and speed, a large range of programs for the numerical structural analysis based on the finite element method were realized. Such programs easily furnish an accessible tool to the designers and permit to obtain all useful results in a very short time. Nevertheless the incorrect use of finite element numerical models can conduct to macroscopic errors, especially in the case the designer hasn't familiarity with structural modeling techniques.

In the design of composite steel-concrete bridges, many different approaches for the realization of numerical models describing properly bridge characteristics, as planimetric disposition, structural typology, bearings scheme, piers and abutments position, are available.

For instance it is possible to consider the case of a composite steel-concrete girder bridge. The most simple and direct modeling approach consists in representing concrete slab through SHELL elements and main girders through BEAM elements, positioned eccentrically in comparison with slab elements (Fig. 1 - Model A). The nodes of BEAM elements (girders) and SHELL elements (slab) are connected by internal restraints (rigid link) to restore the actual structural connection. It is also possible to represent girders in more complex ways: using SHELL elements for flanges and webs (Fig. 1 - Model B), BEAM elements for flanges and SHELL elements for webs (Fig. 1 - Model C), or SHELL elements for flanges and BEAM elements for webs (Fig. 1 - Model D)⁸.

⁸ Chung et al., 2006.

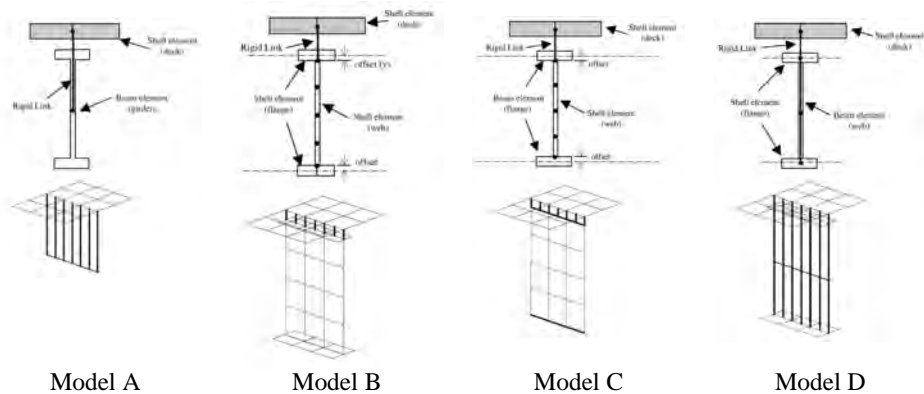


Figure 1. Modeling techniques for composite steel-concrete girder bridges.

Another modeling approach, characterized by a high complexity level, consists in representing concrete slab through SOLID elements and girders flanges and webs through SHELL elements. In this case the nodes of upper flanges elements are merged with the nodes of slab elements, realizing the structural connection directly without using internal restraints. This technique requires an elevated time for model realization and an elevated computational power in comparison to simpler approaches because of the high number of nodal degrees of freedom.⁹

In conclusion many different modeling approaches of composite decks conducting often to numerical results very different are available, so that the evaluation of structural seismic behavior can depend on the adopted modeling technique.

3. ROAD STEEL-CONCRETE COMPOSITE VIADUCT

In the sector of road viaducts with small and medium spans, designers have frequently adopted the composite steel-concrete girders solution. In order to understand merits and defects of modeling techniques for this structural typology, a road steel-concrete composite bridge realized by a continuous beam on four intermediate supports has been analyzed¹⁰. The deck has a total length equal to 130 m (40 m + 50 m + 40 m) and is composed of two parallel girders with intermediate cross beams connected with the upper concrete slab, for a total width of 12 m (Fig. 2).

⁹ Mabsout et al., 1997.

¹⁰ Dezi et al., 2006.

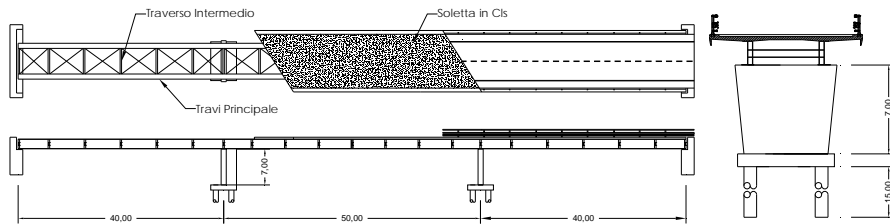


Figure 2. Plan view, lateral view and cross section of bridge.

The dynamic behavior of viaduct has been studied from the numerical point of view using different modeling strategies, by means of FE software ANSYS.

Basing on available modeling techniques, a three-dimensional FE model (SHELL/3DS model) was developed. It was characterized by a high level of refinement in the representation of structural parts: steel parts are represented by SHELL elements, while the concrete slab is modeled with SOLID type elements¹¹ (Figs. 3a and 3b). This modeling technique is the most reliable for evaluation of structural dynamic behavior, as it allows a detailed representation of structural masses and stiffness distribution. Furthermore, the SHELL/3DS model accurately describes the global structural behavior and the local effects at critical details, even if it takes long modeling time and high computational power.

Two further FE simplified models were also developed. In these models concrete slab is represented by SHELL elements, while girders are modeled through BEAM elements (Figs. 3c and 3d). The connection between structural steel and concrete slab is restored through the use of internal constraints between BEAM and SHELL elements, which can be full fixed (BEAM / SHELL A model) or cylindrical hinge (BEAMS / SHELL B model). Such models are able to describe the global behavior of the structure while can't capture local effects. Moreover, they are especially suitable to evaluate internal forces in the form usually adopted by designers, that is direct force, shear force and bending moment.

Described models not only differ in the representation of structural parts and in the type of used numerical elements, and they were also characterized by different dynamic properties. SHELL/3DS model was used as a reference for the evaluation of simplified models ability to describe the structural dynamic properties. Performing the modal analysis on the three models, it was possible to notice that the dynamic characteristics were in good accordance, the model with cylindrical hinge internal constraint (BEAM / SHELL B) in particular showed dynamic behavior closer to those obtained for the complete model (SHELL/3DS) than to the ones characterizing the model with full fixed internal

¹¹ Chellini et al., 2007a.

constraint (BEAM / SHELL A), in terms of both frequencies and modal participation factors (MPF)¹² (Tab. 1).

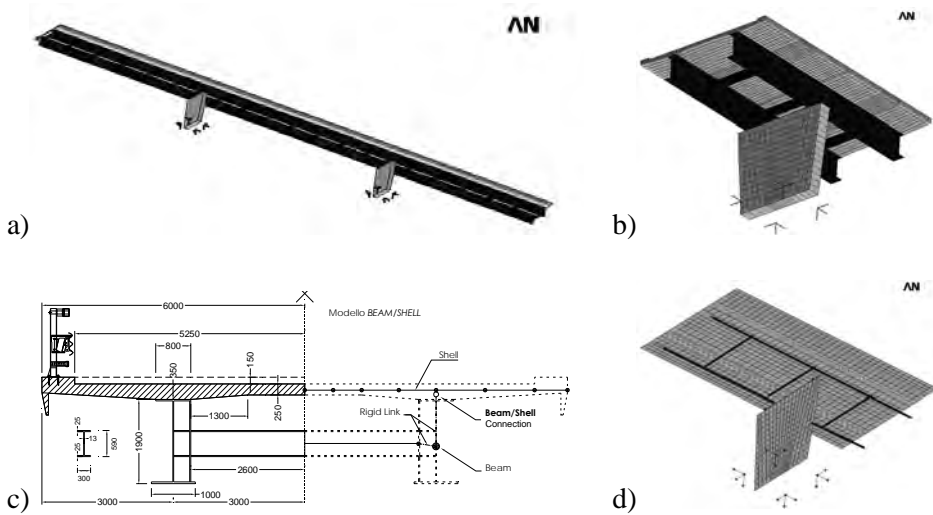


Figure 3. General view (a) and particular view (b) of SHELL/3DS model; modeling scheme (c) and particular view of simplified models.

Table 1. Dynamical properties of FE models.

Mode	SHELL/3DS		BEAM/SHELL A			BEAM/SHELL B		
	Frequency [Hz]	MPF [%]	Frequency [Hz]	Δf (%)	MPF [%]	Frequency [Hz]	Δf (%)	MPF [%]
1	1.783	0.44	1.713	3.89	0.05	1.710	4.05	0.22
2	1.950	1.76	1.857	4.75	0.07	1.852	4.99	0.25
3	1.972	86.50	2.231	-13.12	62.53	1.975	-0.14	86.02
4	2.368	90.21	2.411	-1.82	83.28	2.370	-0.06	89.15
5	2.689	90.21	2.679	0.36	83.28	2.668	0.77	89.15
6	2.781	90.22	3.101	-11.51	88.20	2.928	-5.28	89.20

The transverse elastic response spectrum seismic analysis, adopting the Italian OPCM 3431 rules for soil type B and hazard level 2 (PGA equal to 0.25g), was performed on all models. The comparison between numerical results showed that simplified models provide good results in terms of structural glob-

¹² Chellini et al., 2007.

al behavior, while they are more approximate in the evaluation of internal forces. In particular forces acting on one of the two pier cross beams (Fig. 4a) were compared. The full fixed constraint model led to an underestimation of internal forces, on the contrary the model with cylindrical hinge constraint overestimated the internal forces (Tab. 2). Analyzing the deformed configuration of the cross section at the pier, it was also possible to observe that it is necessary to take into account the transverse deformation of main girders for a correct evaluation of seismic action (Fig. 4b).

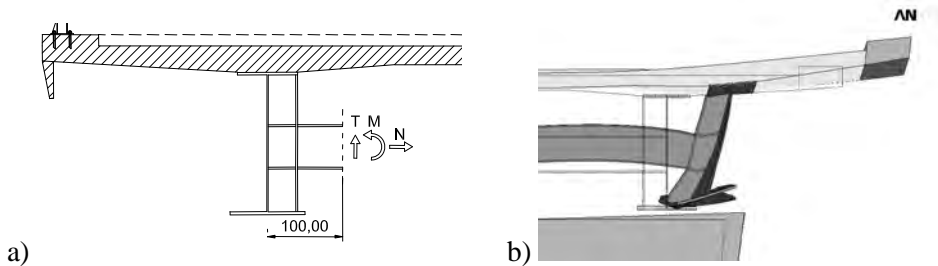


Figure 4. Internal forces (a) and deformed configuration (b) of pier cross beam.

Table 2. Comparison between internal forces obtained by seismic analysis for the considered FE models.

<i>Model</i>	<i>Pier Cross Beam</i>			
	M [kN·m]	T [kN]	N [kN]	Δ [m]
SHELL/3DS	1868	713	3795	$5.48 \cdot 10^{-2}$
BEAM/SHELL A	2790	1268	4358	$5.84 \cdot 10^{-2}$
Error %	+49	+78	+15	+7
BEAM/SHELL B	1125	465	3240	$3.38 \cdot 10^{-2}$
Error %	-40	-35	-15	-38

The study of modeling techniques for the considered structural solution showed how different models, with dynamic behavior in good accordance, can lead to different evaluations of seismic response. Therefore it appears to be necessary to adopt proper safety factors that can protect from these uncertainties, as in practice it is uncommon to develop sophisticated structural models. In order to validate design assumptions and model calculations, experimental dynamic tests can be an extremely useful tool, as shown in the following section.

3. THE RAILWAY VIADUCT ON ELVO RIVER

Composite steel-concrete decks assumed in the recent years a role of increasing importance also in the railway sector. The two girders composite solution became a standard in French high-speed railway network¹³. Composite solutions were also often chosen for the realization of bridges and viaducts in the new high speed / high capacity Italian railways.

In this section it is illustrated a modeling study realized on the new steel-concrete composite railway viaduct on Elvo river, placed along the high speed line Torino - Milano. The viaduct is composed of 11 spans of length equal to 33.7 m, for a total length of 370 m as shown in the Figures 5a and 5b. Each deck is composed of four steel girders with a collaborating concrete slab. Main girders are connected by reticular intermediate torsional diaphragms. Three different cross-sections are present along deck axis: at the mid-span, where the main girders are connected with bracings; at the quarters cross-section, where only the two pairs of external main girders are connected with bracings; at end cross-sections, where torsional K-shape diaphragms with stiffening plates are present (see Fig. 6).

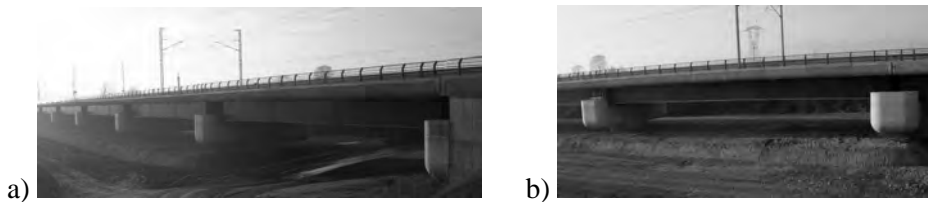


Figure 5. General view (a) and single span view (b) of Elvo viaduct.

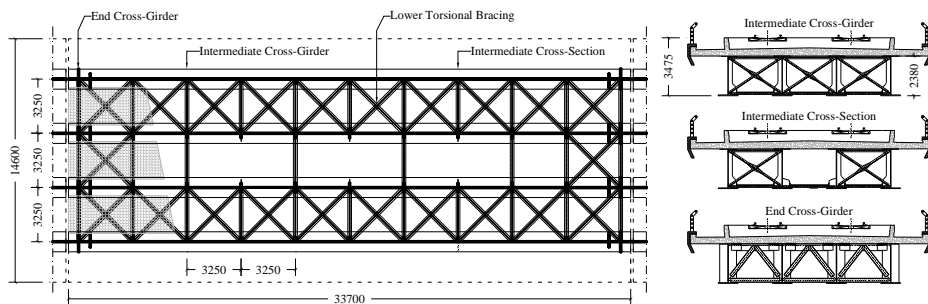


Figure 6. Plan view and cross-sections of Elvo viaduct.

¹³ Hoorpah, 2004.

The structure was experimentally analyzed in the framework of the European research project DETAILS (Design for optimal performance of high-speed railway bridges by enhanced monitoring systems), funded by the European Commission. Experimental dynamic analysis was realized, using the experimental modal analysis technique, now widely diffused and used¹⁴. The purpose of the EMA was the analysis of the dynamic behavior of the overall structure, with particular attention to flexural, torsional and distortional modes of vibration. Instruments (accelerometers) were installed on the structure mainly in vertical position, so to analyze the dynamical behavior of the deck under the passage of vehicles. It was so possible to identify modal shapes and frequencies of the structure, together with damping values corresponding to each mode. Figure 7 shows the experimental results for the first two identified modes.

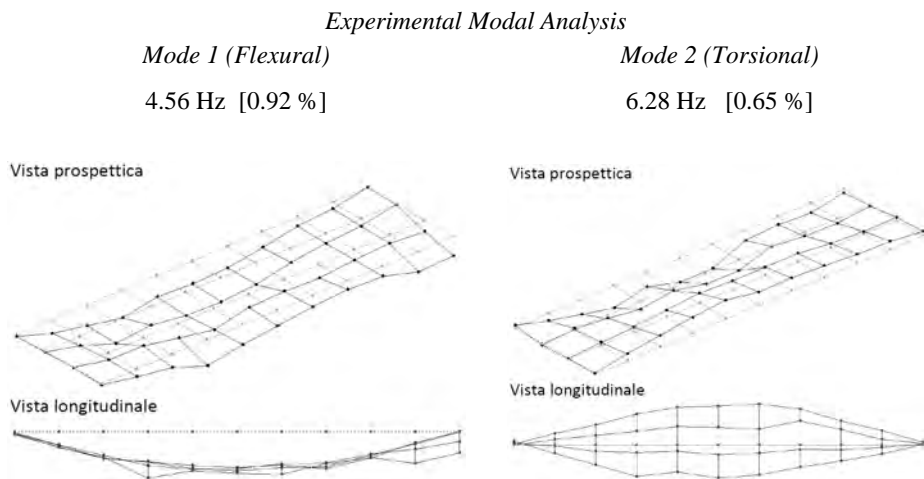


Figure 7. Experimental modal shapes of Elvo viaduct.

The structural behavior of the single span was analyzed using a three-dimensional finite element model, characterized by a high level of refinement in the representation of structural parts, realized with the structural software ANSYS. SHELL elements were used for steel parts of main girders, together with SOLID elements for concrete slab and ballast, and with BEAM elements for bracing members (Fig. 8). The structural contribution of rails was also considered, using SHELL elements positioned on the upper surface of ballast elements. External restraints were imposed on nodes of end shell elements representing main girder lower flanges, in order to model the single span actual

¹⁴ Chellini, 2007.

supporting scheme. Two longitudinal and one transverse spring elements were introduced at the end faces of the model to take into account the interaction between adjacent decks, that are linked together through ballast and tracks (Fig. 9a). Stiffness values of springs were firstly estimated as the inverse of deck deformability, obtained by imposing an exploratory unit load in the acting direction of each spring (Fig. 9b).

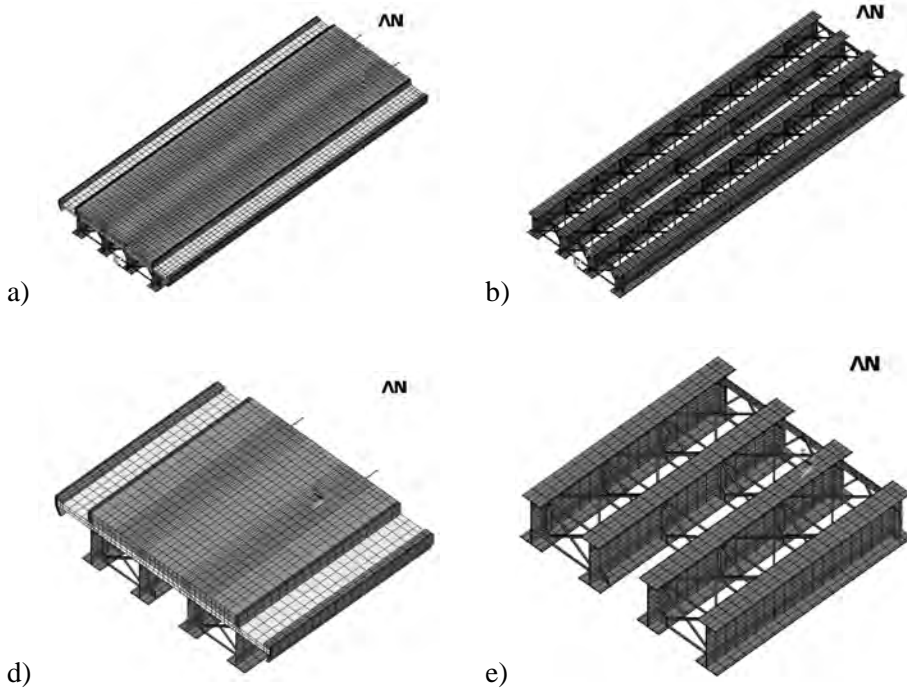


Figure 8. FE model of Elvo viaduct: General view (a), steel girders elements (b), detailed view of the entire model (c), detailed view of steel girders elements (d).

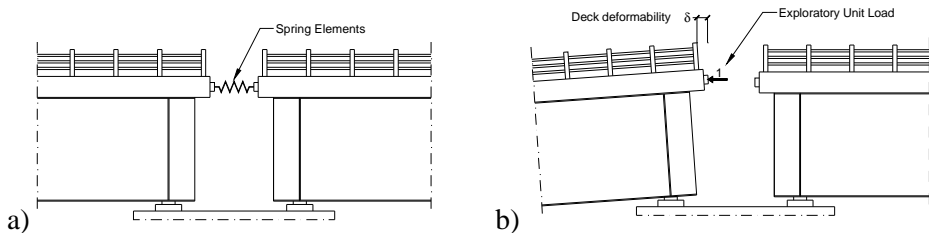


Figure 9. Interaction of adjacent spans modeling scheme: a) spring elements b) evaluation of spring stiffness values.

The availability of experimental data permitted a detailed assessment of the actual capability of model to describe the real structural behavior. The model was subjected to an updating process in order to optimize the dynamical characteristics in comparison with experimental data¹⁵. This procedure consists in studying the variation of numerical response varying significant mechanical parameters as elastic modulus, specific weight of concrete and ballast, and stiffness values of end springs. In Table 3 the initial and final values of mechanical parameters considered in the updating process are reported.

Table 3. Elvo viaduct: Initial and final values of updated mechanical parameters.

<i>Name</i>	<i>Definition</i>	<i>Initial Value</i>	<i>Final Value</i>	<i>Unit</i>
E_C	Concrete elastic modulus	$3.500 \cdot 10^{10}$	$3.026 \cdot 10^{10}$	N/m ²
E_B	Ballast elastic modulus	$2.200 \cdot 10^9$	$2.443 \cdot 10^9$	N/m ²
D_B	Ballast density	1800	1752	Kg/m ³
A_C	Cross area of intermediate torsional diaphragm beams	0.0025	0.0043	m ²
A_T	Cross area of end torsional diaphragm beams	0.013	0.0051	m ²
K_P	Stiffness of longitudinal spring elements	$1.800 \cdot 10^9$	$2.622 \cdot 10^8$	N/m
K_S	Stiffness of transverse spring elements	$5.360 \cdot 10^8$	$5.36 \cdot 10^8$	N/m

The updated model was able to provide an estimate of the structural dynamic behavior in good accordance with experimental data (Tab. 4). Updated model was then supposed to evaluate the seismic action with a high degree of reliability. This study showed the great potential of experimental analysis coupled with updating processes for the study of existing structures, in order to obtain a correct evaluation of the resistant mechanisms and of mechanical parameters.

In the case of Elvo viaduct, the results of experimental and numerical analysis showed that the overall dynamic behavior of the deck doesn't depend on the mechanical behavior of the substructures, that weren't represented into the finite element models, that is substructures were particularly stiff. This result is not always valid; in the next section the results of a modeling study on another railway viaduct are reported; in this case the overall dynamic behavior was clearly also dependent on the dynamic response of piers and foundations.

¹⁵ Chellini, 2007.

Table 4. Comparison between numerical and experimental modal frequency of Elvo viaduct.

<i>Mode #</i>	<i>Numerical Frequency (Hz)</i>	<i>Experimental Frequency (Hz)</i>	<i>Error (%)</i>
1	4.61	4.56	1.09
2	6.49	6.28	6.07
3	14.87	14.16	5.01
4	16.88	15.84	6.56
5	21.57	20.90	3.20
6	28.85	26.62	8.37
7	29.36	28.47	3.12

4. THE RAILWAY VIADUCT ON SESIA RIVER

Sesia viaduct is part of the new high speed / high capacity Torino – Milano line, and it is composed of 7 composite steel-concrete decks of length equal to 46 m for a total length of 322 m as shown in Figure 10.

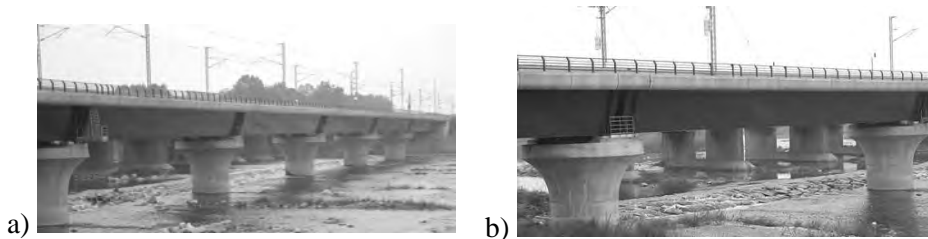


Figure 10. General view (a) and single span view (b) of Sesia viaduct.

Each deck was realized by a composite double box steel section with collaborating concrete slab (Fig. 11). Intermediate torsional diaphragms are composed by two diagonal members and a cross beam, realizing a V shape resistant scheme. At support sections, torsional diaphragms are composed by diagonal members connected to vertical web stiffeners and to lower box plates¹⁶.

A campaign of experimental modal analysis was realized on the viaduct, in order to obtain the dynamic characteristics of the single span (frequency, damping and modal shapes), using the suitable experimental modal analysis tech-

¹⁶ FIATENGINEERING, 2002.

nique¹⁷. Figure 12 shows experimental results for the first two identified modes.

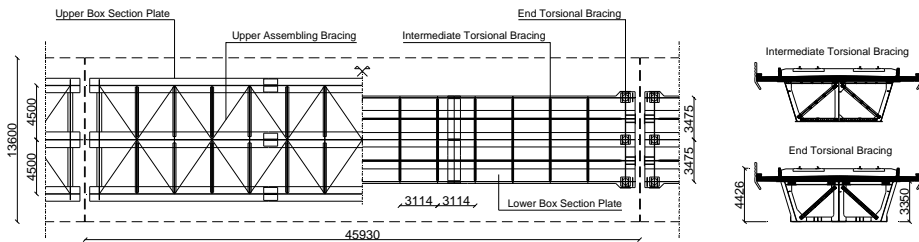


Figure 11. Plan view and deck cross-sections of Sesia viaduct.

Experimental Modal Analysis

Mode 1 (Lateral)

3.07 Hz [10.35 %]

Mode 2 (Flexural)

3.62 Hz [2.13 %]

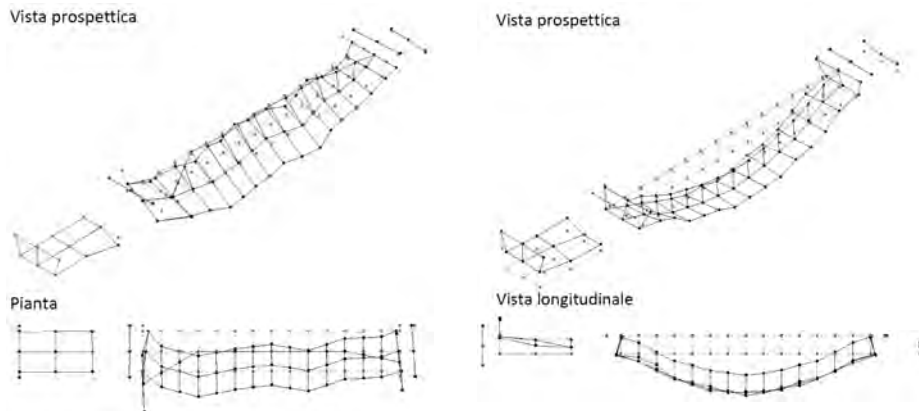


Figure 12. Experimental modal shapes of Sesia viaduct.

The structure was studied from the numerical point of view, through the development of finite element models, created with the structural software ANSYS. Many modeling techniques, based on different representation of structural elements, are again available for this type of structure. These techniques can lead to different evaluations of dynamic characteristics, resulting then in a different estimation of seismic actions too.

On the basis of numerical analysis, it was possible to highlight merits and defects of each technique, taking the dynamic experimental data as a reference

¹⁷ Chellini, 2007.

point for the correct evaluation of the structural behavior. Modeling techniques of the deck were analyzed, together with techniques that represent the entire structure composed by decks, piers and foundations. Additionally, the effects of these techniques on the evaluation of seismic actions in the critical details were evaluated, with particular regard on seismic shear on piers and on internal forces acting on end torsional diaphragms.

Deck Models: 3D Complete Model

3D Complete Model (Fig. 12) is composed by SHELL / BEAM elements for steel parts, and of SOLID elements for concrete slab and ballast. Flanges and webs of main girders were modeled using SHELL elements; torsional bracing members were represented through BEAM elements; SOLID elements were adopted for concrete slab and ballast. To consider the dynamic interaction between neighbouring spans, one longitudinal and one transverse spring elements connected with full fixed constraints to concrete slab and ballast end elements were introduced into the model, adopting the same interaction modeling scheme used for dynamic analysis of Elvo viaduct (Fig. 13).

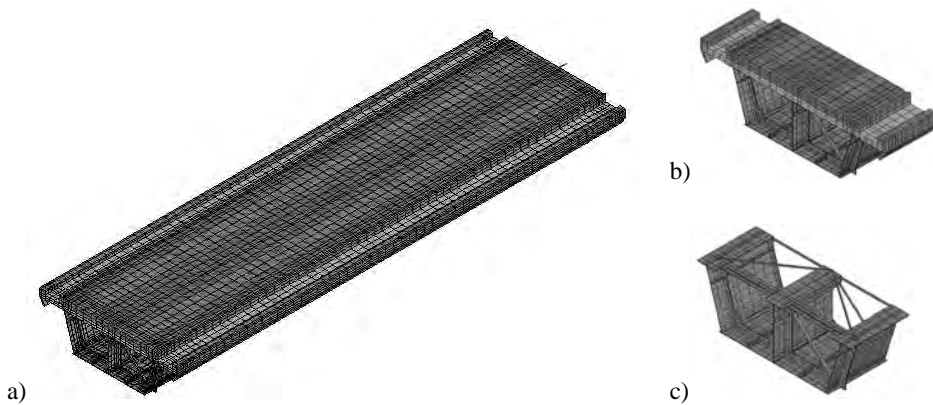


Figure 13. 3D Model Sesia viaduct: General view (a), model detail view (b), steel elements detailed view (c).

Elements representing different structural parts are connected together directly at common nodes. External constraints were imposed on the basis of the real supports scheme. This model, which is particularly complex and characterized by a high level of refinement in the representation of structural elements, has the defect of requiring a high realization time and a large computational power.

Deck Models: Multi-Beam Model

Multi-beam Model (Fig. 14) is composed of BEAM / SHELL elements for steel parts and SHELL elements for concrete slab. Three main girders were identified into the steel double box cross section. These girders are composed by upper plates, webs and directly connected parts of lower plates, and they were modeled by BEAM elements. Intermediate lower box plates were represented by SHELL elements. The concrete slab was modeled using SHELL elements positioned along the middle plane, while the contribution of structural ballast was neglected. To represent structural connection between concrete slab, girders, and intermediate lower box plates, full fixed constraints between the nodes of elements representing these structural parts were introduced. The full fixed constraints of cross sections are independent with each other and from those of adjacent girders. Nodes of the ends of main girders were connected with full fixed constraints to MASS elements located at the position of external support, to which constraints corresponding to the real bearing conditions were imposed.

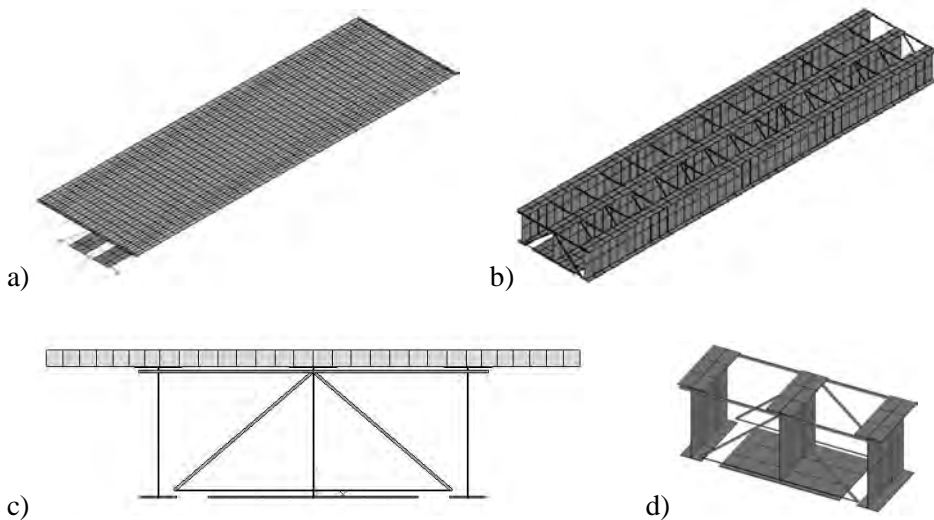


Figure 14. Multi-Beam Model of Sesia viaduct: general view (a), steel girders elements (b), model cross-section (c), steel elements detailed view (d).

Deck Models: Single-Beam Model

Single-beam Model (Fig. 15) consists of a single BEAM element representing the entire deck. The adopted element (BEAM188) allows to calculate the overall inertia of the cross section by defining the geometry and the position of different components, taking into account the proper mechanical properties of ma-

materials (steel, concrete, ballast). In this model external constraints were imposed to the two end nodes of the BEAM element representing the total effect of pier bearings.

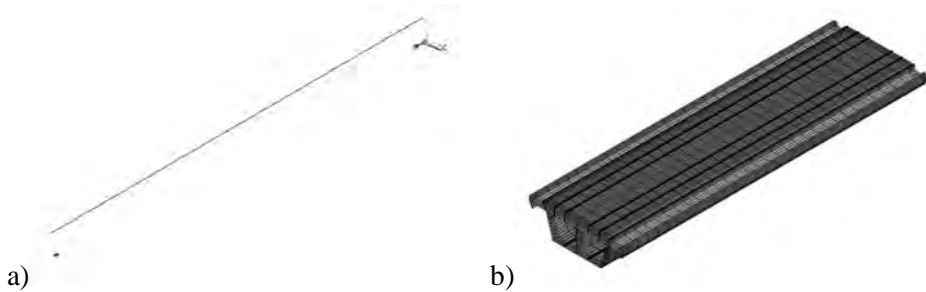


Figure 15. Single-Beam Model of Sesia viaduct: general view (a), general view with extruded representation of elements (b).

Dynamic Characteristics of Deck Models

3D Complete Model was optimized through the updating process in order to obtain numerical modal frequencies and shapes as near as possible to experimental values¹⁸. Stiffness values of springs were calibrated during the updating procedure, together with other significant mechanical parameters. In Table 5 the initial and final values of updating parameters are reported.

Table 5. Sesia viaduct: Initial and final values of updated mechanical parameters.

<i>Name</i>	<i>Definition</i>	<i>Initial Value</i>	<i>Final Value</i>	<i>Unit</i>
E_C	Concrete elastic modulus	$3.500 \cdot 10^{10}$	$3.141 \cdot 10^{10}$	N/m ²
E_B	Ballast elastic modulus	$2.200 \cdot 10^9$	$1.588 \cdot 10^9$	N/m ²
D_B	Ballast density	1800	1750	Kg/m ³
A_C	Cross area of intermediate torsional diaphragm beams	0.00464	0.0043	m ²
K_P	Stiffness of longitudinal spring elements	$4.000 \cdot 10^9$	$1.450 \cdot 10^8$	N/m
K_S	Stiffness of transverse spring elements	$5.360 \cdot 10^8$	$5.36 \cdot 10^8$	N/m

¹⁸ Chellini, 2007.

From this study, it was possible to highlight the influence that neighbouring spans have on the dynamic properties of each single span, particularly on the modal frequencies of vertical and torsional vibrations.

In Single-Beam Model the horizontal rotation, parallel to deck axis, was firstly fixed at external supports. This condition, however, imposed to the model a full fixed distortional restraint due to the infinite in-plane stiffness of BEAM element cross-section, resulting in a significant increase of the first transverse modal frequency, which in this type of modeling coincides with the first torsional mode. Torsional springs were then introduced at external supports, whose stiffness value $K_t = 8.08 \cdot 10^9 \text{ N}\cdot\text{m}/\text{rad}$ was evaluated in order to obtain a frequency of the first transverse mode equal to that of Multi-Beam Model (Fig. 16).

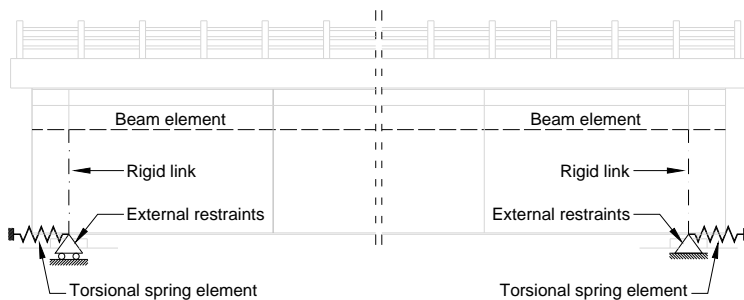


Figure 16. Single-Beam Deck Model: modeling scheme of deck and bearings.

Table 6 shows the comparisons between the values of the frequencies of the three models. The three models have very similar dynamic properties and show frequency values of flexural modes close to experimental data, while are not able to properly describe the transverse dynamic behavior of the structure, since the first experimental transverse frequency is around 3.07 Hz¹⁹.

Table 6. Frequency modal values of deck models.

Type	3D	Multi-Beam		Single-Beam	
	Complete (Hz)	(Hz)	Δ %	(Hz)	Δ %
1° flexural	3.58	3.30	- 8	3.28	- 8
1° lateral	4.42	5.40	+ 22	5.40	+ 22
1° torsional	9.72	10.41	+ 8	---	---
2° flexural	9.92	9.40	- 5	10.02	+ 1

¹⁹ Chellini, 2007.

Numerical Modeling of Piers

Piers of Sesia viaduct consist of a variable circular cross-section pillar, whose diameter is equal to 5 m at the base and, enlarging on the upper, to 8.76 m at pulvino surface. Pillar is connected to a circular basement, whose diameter is equal to 13.8 m and whose thickness is equal to 2.5 m. This basement constitutes the upper head of a pile group foundation²⁰ (Fig. 17a).

Pillar was modeled using a BEAM element (with axial, flexural and torsional stiffness) defined between two nodes, the first on basement upper surface and the other on deck supporting surface. Basement was modeled by a MASS element positioned in its geometric center and characterized by a concentrated mass equal to basement total mass. Between the lower node of pillar BEAM element and the central node of basement MASS element an internal full fixed restraint was introduced to take into account the real monolithic connection (Fig. 17b).

The MASS element central node was also connected by an internal full fixed restraint to the central node of another MASS element, defined at basement bottom face and properly connected to external supports in order to represent the dynamic characteristics of the pile group.

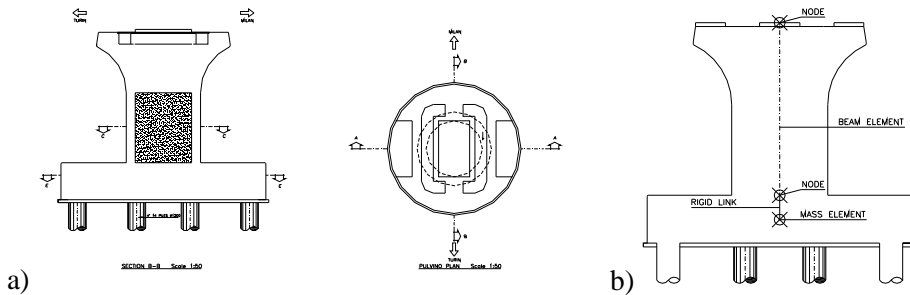


Figure 17. Sesia viaduct: vertical and horizontal pier sections (a), FE modeling scheme (b).

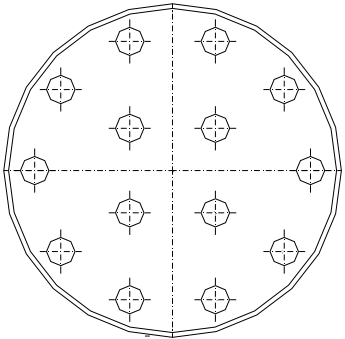
Dynamic Characterization of Foundations

Basement lower surface is founded on a layer of saturated sand and gravel that extends in depth over the length of the pile group, which consists of 14 piles arranged according to the plan scheme and geometrical characteristics reported in Table 7²¹.

²⁰ FIATENGINEERING, 2002.

²¹ FIATENGINEERING, 2002.

Table 7. Sesia Viaduct: Plan view and general characteristics of pile group foundation.

	<i>Pile Diameter</i>	<i>Pile Length</i>	<i>Concrete Elastic Modulus</i>	<i>Pile number</i>
	120 cm	3500 cm	31220 MPa	14
<i>Basement Diameter</i>		<i>Pile to Pile Distances</i>		
1380 cm		min 3.34 m max 11.66 m		

In foundation analysis, the soil was considered as a uniform homogeneous layer, with constant mechanical properties to increase depth and with damping capability. The values of mechanical parameters used in the analysis (Tab. 8) were derived from the design technical documentation²² and from literature information²³.

Table 8. Foundation soil mechanical properties.

<i>Soil Type</i>	<i>Density</i>	<i>Young's Modulus</i>	<i>Poisson's Coefficient</i>	<i>Damping Coefficient</i>	<i>Shear Wave Velocity</i>
Saturated sand and gravel	2000 kg/m ³	237 MPa	0.4	5%	205635 m/s

The dynamic characteristics of pile group foundation were evaluated using the analytical model proposed by Dobry and Gazetas²⁴, which allows to study the dynamic behavior of circular pile groups subjected to a generic harmonic force. In the model, piles are considered as beams in a uniform soil layer, represented by a linear hysteretic material, and they are connected at the heads by a rigid cap. Each pile is subjected to a vibration state and induces mechanical cylindrical waves into the ground if excited by an external force action. These waves propagate until they reach the outer surface of contiguous piles and impose them a vibration state in addition to their own, by releasing part of their mechanical energy. Each pile then influences the vibration state of others and is influenced in turn.

²² FIATENGINEERING, 2002.

²³ Whitman & Richart, 1967.

²⁴ Dobry & Gazetas, 1988.

Considering the case of vertical vibration, it is possible to define the dynamic impedance of the single pile with the complex relationship:

$$K_z(\omega) = \bar{K}_z(\omega) + i \cdot a_0 \cdot C_z(\omega) \quad (1)$$

where $\bar{K}_z(\omega)$ and $C_z(\omega)$ are the pile's stiffness and damping, expressed as a function of frequency (ω).

Consider a foundation composed of two identical piles p and q at distance S. It is assumed that vibration of pile p influences the response of pile q by emanating mechanical cylindrical waves into the soil. The effect of this interaction can be expressed by the function $\alpha_z(\omega)$, that is the ratio between the additional displacement of pile q caused by the pile p and the own displacement of pile q. The function $\alpha_z(\omega)$ is expressed by the following relationship:

$$\alpha_z(\omega) = \left(\frac{S}{r_0} \right)^{-1/2} \cdot e^{-\beta \cdot \omega S / V_s} \cdot e^{-i \omega S / V_s} \quad (2)$$

where S is the axis-to-axis distance, r_0 is the pile radius, β is the soil damping coefficient, V_s is the shear-wave velocity²⁵.

Consider the foundation composed of the two piles p and q subjected to a vertical external force equal to 2F. External action is shared equally in the two piles due to loading and structure symmetry, with the result that the total vertical displacements of the two piles are identical each other. The total vertical displacement w_q of the pile q is the sum of the displacement w_{qq} , caused to the force F directly applied to the pile, and the displacement w_{pq} , induced by the other pile p. The total value w_q is expressed as:

$$w_q = w_{qq} + w_{pq} = \frac{F_q}{K_z(\omega)} + \alpha_z(\omega) \cdot \frac{F_q}{K_z(\omega)} = \frac{F}{K_z(\omega)} \cdot [1 + \alpha_z(\omega)] \quad (3)$$

while the group global vertical impedance $K_z^G(\omega)$ is expressed as:

$$K_z^G(\omega) = \frac{2 \cdot F}{w_q} = \frac{2 \cdot K_z(\omega)}{1 + \alpha_z(\omega)} \quad (4)$$

In the case of pile groups with more than two piles, it is assumed that each pile independent influences the others, and the total effect on every pile is given by the sum of the effects of all the different possible pairs of interaction.

The assumption of rigid cap allows to impose kinematic constraints between the movements of pile heads in vertical, horizontal and rotational direction. In this way, the group total impedance for each degree of freedom is equal to the

²⁵ Dobry & Gazetas, 1988.

sum of piles reaction, calculated with basement centre of gravity as point of reference, that are obtained imposing unit displacements to the basement.

Vertical Impedance

Imposing a vertical displacement w_{gz} to the rigid cap, the total displacements (w_{1z} , w_{2z} , ... w_{iz}) of piles are related to the acting forces (F_{1z} , F_{2z} , ... F_{iz}) by the following relationship:

$$\begin{aligned} w_{1z}(\omega) &= \alpha_{11z}(\omega) \cdot \frac{F_{1z}(\omega)}{K_z(\omega)} + \alpha_{12z}(\omega) \cdot \frac{F_{2z}(\omega)}{K_z(\omega)} + \dots + \alpha_{1iz}(\omega) \cdot \frac{F_{iz}(\omega)}{K_z(\omega)} \\ &\vdots \\ w_{iz}(\omega) &= \alpha_{i1z}(\omega) \cdot \frac{F_{1z}(\omega)}{K_z(\omega)} + \alpha_{i2z}(\omega) \cdot \frac{F_{2z}(\omega)}{K_z(\omega)} + \dots + \alpha_{iiz}(\omega) \cdot \frac{F_{iz}(\omega)}{K_z(\omega)} \end{aligned}$$

that can also be expressed as:

$$\begin{aligned} \frac{w_{1z}(\omega)}{\alpha_{11z}(\omega) + \alpha_{12z}(\omega) + \dots + \alpha_{1iz}(\omega)} &= \frac{F_{1z}(\omega)}{K_z(\omega)} \\ &\vdots \\ \frac{w_{iz}(\omega)}{\alpha_{i1z}(\omega) + \alpha_{i2z}(\omega) + \dots + \alpha_{iiz}(\omega)} &= \frac{F_{iz}(\omega)}{K_z(\omega)} \end{aligned} \quad (5)$$

Equation (5) can be conveniently expressed in the matrix way:

$$K_z(\omega) \cdot \begin{bmatrix} w_{1z}(\omega) & 0 & 0 & 0 \\ 0 & w_{2z}(\omega) & 0 & 0 \\ 0 & 0 & \ddots & \vdots \\ 0 & 0 & \dots & w_{iz}(\omega) \end{bmatrix} \cdot \begin{bmatrix} 1 \\ \alpha_{11z}(\omega) + \alpha_{12z}(\omega) + \dots + \alpha_{1iz}(\omega) \\ \vdots \\ 1 \\ \alpha_{i1z}(\omega) + \alpha_{i2z}(\omega) + \dots + \alpha_{iiz}(\omega) \end{bmatrix} = \{F_z(\omega)\}$$

that, synthetically, is:

$$K_z(\omega) \cdot [W_z(\omega)] \cdot \{\alpha_z(\omega)\} = \{F_z(\omega)\} \quad (6)$$

where $[W_z(\omega)]$ is the displacement matrix, $\{\alpha_z(\omega)\}$ is the interaction vector, $\{F_z(\omega)\}$ is the force vector.

As the vertical displacement w_{gz} is imposed, the displacements w_{1z} , w_{2z} , ... w_{iz} have all the same value w_{gz} , and are represented by the following relationship:

$$\begin{aligned} w_{1z}(\omega) &= w_{2z}(\omega) = \dots = w_{iz}(\omega) = w_{gz} \\ [W_z(\omega)] &= w_{gz} \cdot [I] \end{aligned} \quad (7)$$

The total sum of pile forces is equal to the total stiffness $K_{Gz}(\omega)$ multiplied by the vertical displacement w_{gz} . After all the total impedance $K_{Gz}(\omega)$ is expressed by the following relationship:

$$K_{Gz}(\omega) \cdot w_{gz} = \text{Tr}(\{F_z(\omega)\}) = \text{Tr}(K_z(\omega) \cdot w_{gz} \cdot [1] \cdot \{\alpha_z(\omega)\}) \quad (8)$$

$$K_{Gz}(\omega) = \text{Tr}(K_z(\omega) \cdot [1] \cdot \{\alpha_z(\omega)\})$$

where $K_z(\omega)$ is the single pile vertical impedance.

Transverse Impedance

Imposing a lateral displacement w_{gh} to the basement, transverse pile displacements (w_{1h} , w_{2h} , ... w_{ih}) are related to the acting forces (F_{1h} , F_{2h} , ... F_{ih}) by a relationship formally identical to the previous obtained for the vertical impedance:

$$w_{1h}(\omega) = \alpha_{11h}(\omega) \cdot \frac{F_{1h}(\omega)}{K_h(\omega)} + \alpha_{12h}(\omega) \cdot \frac{F_{2h}(\omega)}{K_h(\omega)} + \dots + \alpha_{1ih}(\omega) \cdot \frac{F_{ih}(\omega)}{K_h(\omega)}$$

$$\vdots$$

$$w_{ih}(\omega) = \alpha_{i1h}(\omega) \cdot \frac{F_{1h}(\omega)}{K_h(\omega)} + \alpha_{i2h}(\omega) \cdot \frac{F_{2h}(\omega)}{K_h(\omega)} + \dots + \alpha_{iih}(\omega) \cdot \frac{F_{ih}(\omega)}{K_h(\omega)} \quad (9)$$

Proceeding in the same way as for vertical impedance, the total transverse impedance $K_{Gh}(\omega)$ is expressed by the following relationship:

$$K_{Gh}(\omega) = \text{Tr}(K_h(\omega) \cdot [1] \cdot \{\alpha_h(\omega)\}) \quad (10)$$

where $\{\alpha_h(\omega)\}$ is the vector of horizontal interaction coefficients and $K_h(\omega)$ is the transverse impedance of the single pile.

Horizontal Rotation Impedance

Imposing to the basement a rotation θ around one of the two pile group axis of symmetry, each pile is subjected to a rotation θ and to a vertical displacement w_{iz} equal to:

$$w_{iz}(\omega) = \theta \cdot x_i \quad (11)$$

where x_i is the distance between pile axis and rotation axis.

The relationship (11) can also be expressed in the following matrix way:

$$[W_z(\omega)] = \theta \cdot [X] \quad (12)$$

where $[W_z(\omega)]$ is the diagonal matrix of vertical displacements $[X]$ is the diagonal matrix of distances between pile axis and rotation axis.

Each pile is subjected to a moment $m_i(\omega)$, caused by the rotation θ , and to a vertical force $F_{iz}(\omega)$, caused by the vertical displacement w_{iz} . Pile vertical displacements ($w_{1z}, w_{2z}, \dots w_{iz}$) are related to acting forces ($F_{1z}, F_{2z}, \dots F_{iz}$) by the same relationship adopted for vertical impedance (5), while the moment $m_i(\omega)$ is expressed by:

$$m_i(\omega) = \theta \cdot K_{\text{rot}}(\omega) \quad (13)$$

where $K_{\text{rot}}(\omega)$ is the rotational impedance of the single pile.

The sum of vertical force moments, calculated adopting the rotation axis as reference axis, and of moments $m_i(\omega)$ is equal to the total impedance $K_{\text{Grot}}(\omega)$ multiplied by rotation θ . After all, total impedance $K_{\text{Grot}}(\omega)$ can be expressed by:

$$\begin{aligned} \{F_z(\omega)\} &= K_z(\omega) \cdot [W_z(\omega)] \cdot \{\alpha_z(\omega)\} \\ K_{\text{Grot}}(\omega) \cdot \theta &= 14 \cdot K_{\text{rot}}(\omega) \cdot \theta + \text{Tr}\left([X] \cdot \{K_z(\omega) \cdot \theta \cdot [X] \cdot \{\alpha_z(\omega)\}\}\right) \\ K_{\text{Grot}}(\omega) &= 14 \cdot K_{\text{rot}}(\omega) + \text{Tr}\left(K_z(\omega) \cdot [X]^2 \cdot \{\alpha_z(\omega)\}\right) \end{aligned} \quad (14)$$

Vertical Rotation Impedance

Concerning with rotation around the vertical axis, foundation is considered as an ideal one by assuming the condition of full fixed restraint.

After all, the model proposed by Dobry and Gazetas gives the analytical complex expressions of dynamic impedance for vertical, horizontal and rotational vibrations, depending on soil mechanical properties (Tab. 7), geometry, on pile mechanical characteristics, on foundation layout (Tab. 8), and on proper dynamic impedance characteristics of the single pile^{26 27}.

Foundation FE Modeling

Foundations were modeled by an MASS element connected to external supports through five elastic springs with damping properties, one for each nodal degree of freedom except for the vertical rotation, and characterized by variable mass values depending on the nodal degree of freedom considered (Fig. 18). The full fixed restraint on the vertical rotation degree of freedom was imposed.

²⁶ Dente, 2000.

²⁷ Lancellotta, 1993.

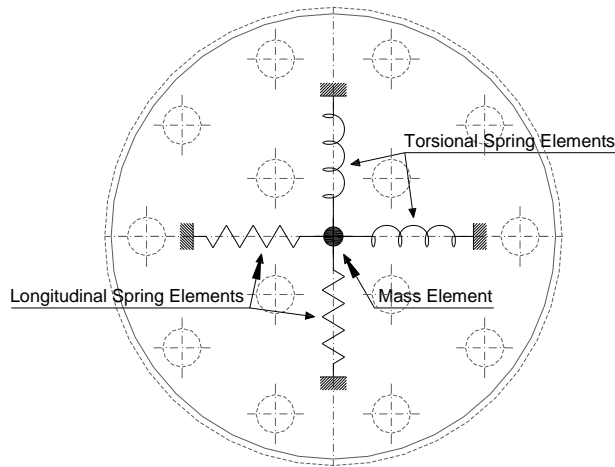


Figure 18. Plan view of foundation FE modeling scheme.

Each spring, acting along his own j -th degree of freedom on the corresponding mass value, creates a complex impedance $Z_j(\omega)$ that can be expressed by:

$$Z_j(\omega) = (K_j - \omega^2 \cdot M_j) + i \cdot \omega \cdot C_j \quad (20)$$

where K_j and C_j are the spring stiffness and damping, M_j is the mass value of the MASS element.

The values of K_j , C_j and M_j (Tab. 9) were calibrated on vertical, horizontal and rotational impedance functions of pile group, calculated with the model proposed by Dobry and Gazetas, in order to approximate the analytical solution in the frequency range 0-10 Hz²⁸.

Figure 19 shows the analytical (solid line) and approximate (dashed line) fluctuations of the real and imaginary parts of the dynamic impedances, that are in good accordance in the frequency range 0-10 Hz.

Table 9. FE coefficients of foundation springs.

<i>Vertical Dof</i>	<i>Horizontal Dof</i>	<i>Horizontal Rotation Dof</i>
$K = 1.364 \cdot 10^7$ [kN/m]	$K = 2.198 \cdot 10^6$ [kN/m]	$K = 1.830 \cdot 10^8$ [kN·m/rad]
$C = 4.546 \cdot 10^8$ [kg/s]	$C = 5.860 \cdot 10^7$ [kg/s]	$C = 6.558 \cdot 10^9$ [kg·m ² /rad·s]
$M = 3.337 \cdot 10^6$ [kg]	$M = 2.745 \cdot 10^5$ [kg]	$M = 4.855 \cdot 10^7$ [kg·m ² /rad]

²⁸ Dezi et al., 2007.

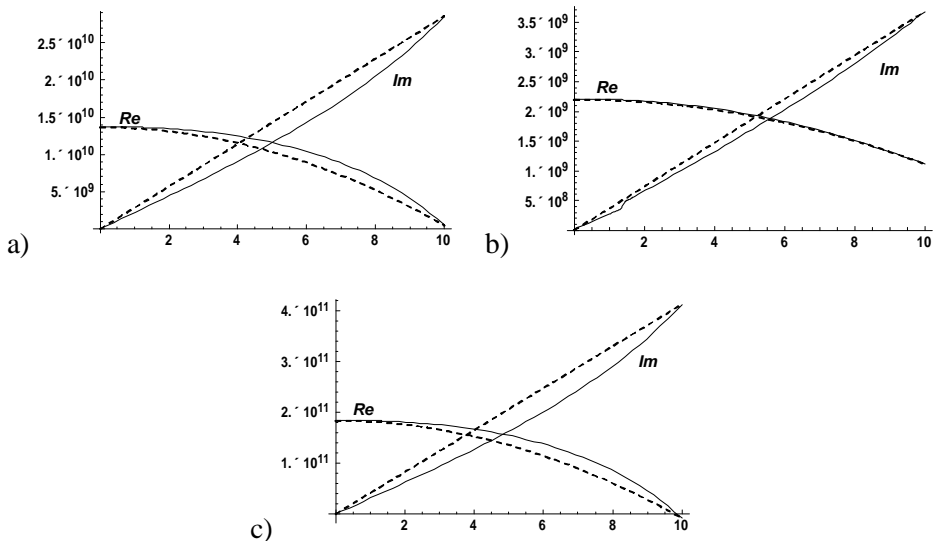


Figure 19. Analytical (solid line) and approximate (dashed line) fluctuations of impedance functions: Vertical Dof (a), Horizontal Dof (b), Horizontal Rotation Dof (c).

Complete Single Span FE Models

Once the modeling approach of foundations and piers was defined, it was possible to model a complete single span of viaduct Sesia, by removing the external perfect and elastic constraints at the ends of deck elements. This analysis was realized on Single-Beam and Multi-Beam models only, because of the great computational slenderness and the reliability from the dynamical point of view. Table 10 shows the comparisons between the frequency values obtained by the two deck models and by the two complete single span models.

Small variations of the first flexural vibration mode frequency are present between the models, while there is a clear change in the first transverse frequency. This result points out the substantial difference between deck only models, with perfect end supports, and complete single span models, in which deck, piers and foundations are represented. There are also small frequency variations of the first torsional mode and of the second flexural mode of vibration.

Table 10. Deck Models and Complete Single Span Models: modal frequencies.

<i>Type</i>	<i>Multi-Beam Deck Model</i>	<i>Multi-Beam Complete Model</i>	Δ %	<i>Single-Beam Deck Model</i>	<i>Single-Beam Complete Model</i>	Δ %
	(Hz)	(Hz)		(Hz)	(Hz)	
1° flexural	3.30	3.40	+ 3	3.28	3.63	+ 11
1° lateral	5.40	3.03	- 44	5.40	3.13	- 42
1° torsional	10.41	9.25	- 11	---	---	---
2° flexural	9.40	12.09	+ 29	10.02	10.98	+ 10

The modal analysis was realized also with the full fixed restraint to the nodes of basement MASS elements, in order to evaluate the actual influence of foundation impedance on dynamical behavior of complete models. Table 11 shows the comparisons between the frequency values of the two complete single span models with fixed basements (FB) and with free basements, while in parentheses the corresponding frequencies of deck only models are reported.

The condition of fixed basement brings the first transverse modal frequency to a value close to that obtained with the deck model. Fixing basements practically cancels the influence of foundation impedance on the transverse dynamic characteristics of the structure.

Table 11. Complete Single Span Models with Fixed Basements (F.B.) and free basements: modal frequencies (*Modal frequencies of Deck Models*).

<i>Type</i>	<i>Multi-Beam Complete</i>	<i>Multi-Beam Complete F.B.</i>	<i>Single-Beam Complete</i>	<i>Single-Beam Complete F.B.</i>
	(Hz)	(Hz)	(Hz)	(Hz)
1° flexural	3.40	3.37 (3.30)	3.63	3.36 (3.28)
1° lateral	3.03	4.98 (5.40)	3.13	5.87 (5.40)
1° torsional	9.25	9.53 (10.41)	---	---
2° flexural	12.09	11.94 (9.40)	10.98	11.12 (10.02)

In summary we can say that:

- the introduction in the models of elements representing piers leads to a change in the numerical response with regard to the first transverse mode of vibration, but has little influence on the other modes
- the introduction of elements representing the impedance of the foundations influences the dynamic response of the models with respect to the first lat-

eral vibration mode, while it has less influence on the first flexural, the first torsional and second flexural vibration modes.

Complete Multi-Span FE Models

The last step in the study of modeling techniques focused on the influence of interaction between adjacent spans on the dynamic response of the structure, through the development of complete Multi-Span models adopting the Single-Beam and the Multi-Beam modeling techniques. Adjacent spans on same piers were connected by SHELL elements (Multi-Beam Models) or by BEAM element (Single-Beam Models), representing the structural contribution of ballast actually present along the decks. The Complete Three Spans Multi-Beam Model and Complete Three Spans Single-Beam Model are shown in the Figures 20a and 20b.

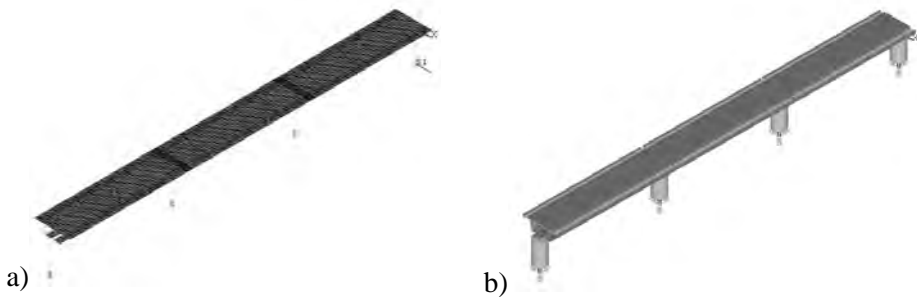


Figure 20. Complete Three Spans Models: Multi-Beam (a), Single-Beam (b).

Observing numerical results, it is evident that the Multi-Spans models have "families" of vibration modes, which consist of modal shapes of the same type with frequencies close between each other (e.g. bending) but that differ in the displacements (symmetric or antisymmetric) of the adjacent spans. Figure 21 show two modal shapes from the "family" of the first flexural mode of the Complete Three Spans Multi-Beam Model, for which the frequencies are in the range 3.35-3.45 Hz.

Modeling of several adjacent spans leads to a change in the numerical response with regard to the first transverse vibration mode, giving a lower value of frequency to increase the number of modeled spans.

The Single-Beam Model was further developed, passing from three to seven spans represented. The number of vibration modes belonging to bending "families" increased, maintaining the frequencies in the same range of variation of the Three Spans Model, while the frequency of the transverse mode was essentially unchanged. Table 12 shows the values of experimental data compared with the numerical results of Complete Single Span Models and of Three and

Seven Spans Models, for which the "family" range of modal frequencies were only reported.

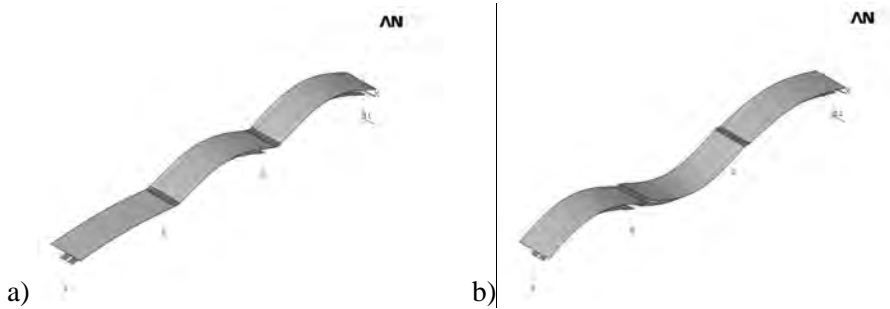


Figure 21. Modal shapes of the first flexural mode "family": 3.35 Hz (a), 3.45 Hz (b).

Table 12. Experimental data and numerical values obtained from Complete Multi-Beam (MLB) and Single-Beam (MoB) Models.

Type	Exp. Data. (Hz)	Complete MLB (Hz)	Complete 3 Spans MLB (Hz)	Complete MoB (Hz)	Complete 3 Spans MoB (Hz)	Complete 7 Spans MoB (Hz)
1° flex.	3.62 - 4.14	3.40	3.35 - 3.45	3.63	3.41 - 3.60	3.41 - 3.94
1° lat.	3.07	3.01	2.56	3.13	2.43	2.37
1° tors.	8.32 - 9.05	9.24	9.38 - 9.40	---	---	---
2° flex.	9.94 - 10.53	12.09	11.97 - 13.02	10.97	11.22 - 13.70	11.05 - 13.92

In summary, with respect of Multi-Spans Models, it was verified that:

- complete Multi-Span Models show a multiplication of modes of the same type with frequencies next one to each other, because of the possible combinations of symmetric and/or antisymmetric displacements of adjacent spans.
- the frequency of the first transverse vibration mode lowers increasing the number of spans modeled, becoming stable when representing three or more spans.

Evaluation of Seismic Action

During earthquakes, structural elements of end torsional diaphragms play a crucial role by transferring the horizontal load to the external fixed supports. In the case of the Sesia viaduct, end diaphragms are constituted by diagonal beams made by pairs of double L120x10, and they transfer the seismic action on piers through the fixed bearings (Figs. 22a, 22b).

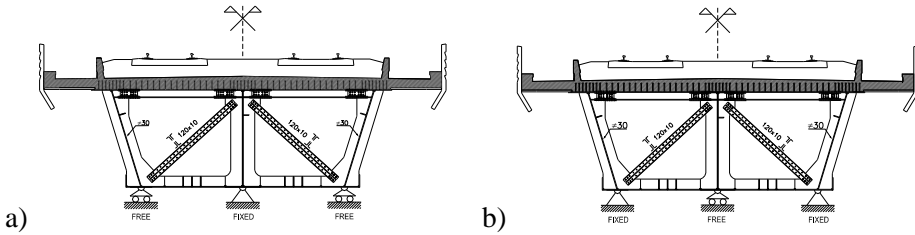


Figure 22. End cross-sections with one central fixed bearing (a) and with two lateral fixed bearings (b).

The transverse elastic response spectrum seismic analysis, adopting the Italian OPCM 3431 rules for soil type B and hazard level 2 (PGA equal to 0.25g), was performed on the 3D Complete Model of the deck, in order to evaluate how the horizontal seismic action is distributed inside the end torsional diaphragms and on piers. The total seismic shear is divided equally between the two piers, and about 90% of the action is transferred to the fixed support only trough the end diaphragm diagonal beams, which are subjected to equal forces of opposite sign. In piers type "A", with central fixed bearing, load passes from the diagonal beams trough the lower box plates, which are then in tension on one side and compressed on the other, up to the bearing (Fig. 23a). In piers type "B", with two lateral fixed bearings, the seismic action passes directly from the diagonal beams to the external supports, with lower box plates substantially unloaded (Fig. 23b).

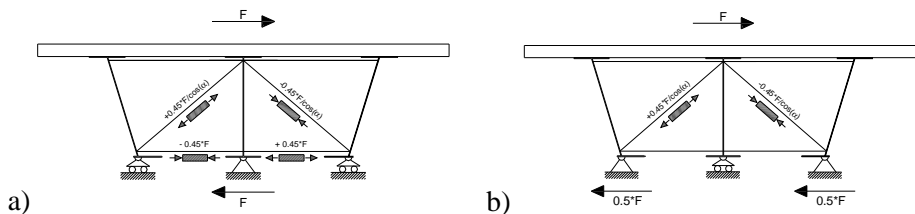


Figure 23. Distribution of seismic shear on piers type "A" (a) and type "B" (b).

The elastic response spectrum seismic analysis was realized on all the models developed for the study of Sesia viaduct (Deck, Complete Single-Span, Complete Multi-Span). Table 13 shows the values of the total seismic shear on the span piers.

For Deck Models seismic shears were calculated as the sum of external constraint reactions, for Single-Span Models they were considered as the sum of shears on lateral piers, for Multi-Span Models the actions on central piers of the model were evaluated. Figure 24 shows the seismic shears on piers for all analyzed models, with regard to the position along the viaduct axis. For Deck Models, Complete Single Span Model and Complete Three-Spans Models it was assumed that they represent the central part of the viaduct.

Numerical results of the elastic response spectrum seismic analysis pointed out how much the intensity of seismic action on piers changes depending on the modeling technique. Deck Models showed seismic shear values similar each other, with a maximum difference of about 15%. The results of Complete Single Span Models were also quite close each other, with a maximum difference of 7% in comparison to the lowest value. Finally, Complete Three-Span and Seven Span Models showed seismic action of similar intensity, with differences up to 20% in comparison to the lowest value.

Table 13. Seismic shear on piers; Single-Beam Models (MoB), Multi-Beam Models (MLB).

<i>Seismic Shear [kN]</i>	<i>Deck Models</i>			<i>Complete Single-Span Models</i>		<i>Complete Multi-Span Models</i>		
	<i>3D</i>	<i>MLB</i>	<i>MoB</i>	<i>MLB</i>	<i>MoB</i>	<i>MLB 3 Spans</i>	<i>MoB 3 Spans</i>	<i>MoB 7 Spans</i>
Pier A	3630	3609	3542	6608	7575	---	---	---
Pier B	4361	5107	5695	7519	7575	---	---	---
Total	7991	8716	9237	14127	15150	12925	14053	16000

A non-uniform distribution of shear action on piers along the viaduct (Fig. 24) was also highlighted by the analysis. This result was obtained in Multi-Span Models realized with Multi-Beam and Single-Beam modeling technique. This phenomenon is probably due to the shape of the first transverse vibration mode of the viaduct (Fig. 25), which has a sinusoidal shape, with a non-uniform distribution of displacements along the deck.

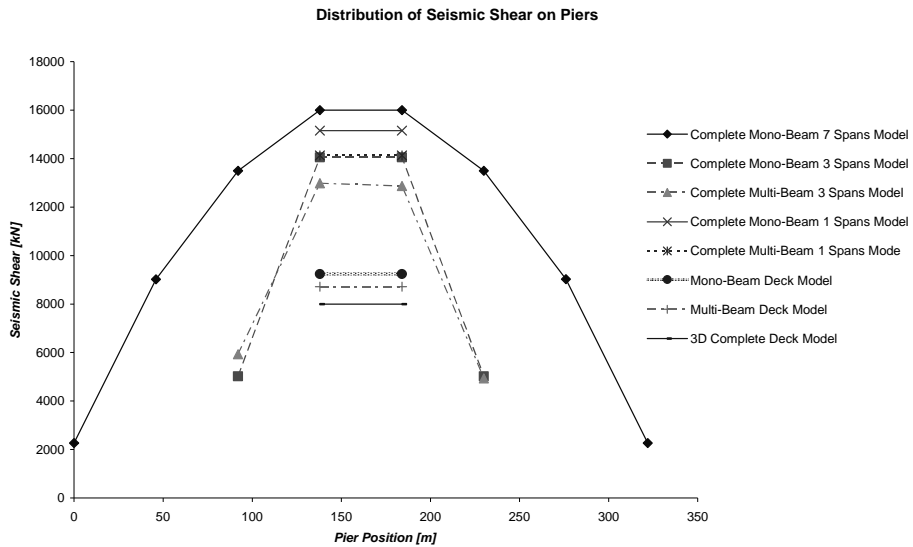


Figure 24. Seismic shear action on piers along the viaduct.

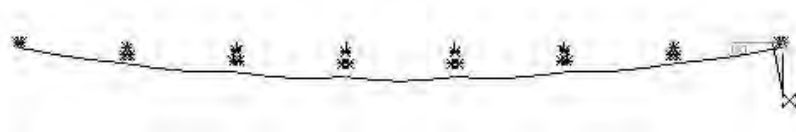


Figure 25. Plan view of the first transverse vibration mode shape of viaduct, obtained from Complete 7 Spans Single-Beam Model.

5. GUIDELINES FOR THE NUMERICAL ANALYSIS OF BRIDGES

The results of the modeling analysis described in the previous paragraphs made possible to understand merits and defects of various modeling techniques, with respect to the dynamic behavior of bridge decks and to the subsequent evaluation of seismic actions. These tests also allowed the development of some basic guidelines for proper modeling of this specific structural type, which can be summarized in the following aspects:

- 3D Complete models are the best approach to the numerical analysis of bridge structures, because they describe in detail the actual distribution of mass and stiffness. However they require high computational efforts.

- Among simplified approaches, the Multi-Beam modeling technique is an ideal compromise for the current design practice, as it allows to represent in sufficient detail the distribution of mass and stiffness, and at the same time, it allows to obtain quickly the forces acting in structural parts expressed in the form normally used by designers.
- The modeling of piers, simplified as well, is very important for the correct evaluation of seismic actions into structure and on heads of piers themselves.
- It is possible to take into account the impedance characteristics of foundations by introducing into numerical models spring elements, properly calibrated using typical approaches of geotechnical analysis, in order to evaluate more correctly the dynamic characteristics of the structure.
- Complete modeling of viaducts allows a more precautionary evaluation of forces on pier heads, taking into account the amplification of seismic shear on central piers due to the sinusoidal shape of the first transverse mode of vibration.
- For the seismic analysis of existing structures, the experimental modal analysis techniques coupled with the updating procedures permits a proper dynamic analysis and modeling of the structure.

REFERENCES

- Chellini, G. [2007] *Identificazione strutturale e Modellazione di Ponti Ferroviari in struttura composta acciaio-calcestruzzo per le nuove linee per l'Alta Velocità*, Tesi di Dottorato in Ingegneria delle Strutture, Università di Pisa, 2007.
- Chellini, G., Salvatore W. and Squarcini, B. [2007] *Valutazione della risposta sismica di ponti a travata in struttura composta acciaio-calcestruzzo*, in proceedings of Workshop "Materiali ed Approcci Innovativi per il Progetto in Zona Sismica e la Mitigazione della Vulnerabilità delle Strutture", Fisciano, 12-13 Febbraio 2007.
- Chung, W., Sotelino, E. D. [2006] *Three-dimensional finite element modeling of composite girder bridges*, Engineering Structures, Vol. 28, pp. 63–71.
- Dente, G. [2000] *La risposta sismica dei pali di fondazione*, Hevelius, 2000.
- Dezi, L., Formica, M. [2006] *Impalcato bitrave continuo a sezione composta. Verifica secondo gli eurocodici*, in Strutture Composte, Nuove Costruzioni – Recupero – Ponti, Monografie CISM, Udine.
- Dezi, F., Dall'Asta, A., Leoni, G., Scarpelli, G. [2007] *Dynamic spatial response of structures considering soil-foundation-structure interaction: application to a railway bridge*, in proceedings of XII ANIDIS Congresso Nazionale "L'ingegneria Sismica in Italia", Pisa, 10-14 Giugno 2007.
- Dicleli, M., Bruneau, M. [1995] *Seismic performance of multispan simply supported slab-on-girder steel highway bridges*, Engineering Structures, Vol. 17, No.1, pp. 4-14.

- Dobry, R., Gazetas, G. [1988] *Simple method for dynamic stiffness and camping of floating pile groups*, Geotechnique 38, No. 4, 557-574.
- Erkus B., Abe´ M. and Fujino Y. [2002] *Investigation of semi-active control for seismic protection of elevated highway bridges*, Engineering Structures, Vol. 24, pp. 281–293.
- FIATENGINEERING [2002] *Progetto Costruttivo – Linea AC:Torino-Venezia, Tratta: Torino-Milano – Viadotto ValSesia*
- Hoorpah, W., Montens S. and Ramondenc P. [2004] *Steel and composite bridges for high speed railways - The French know-how*, In Bridges for High-Speed Railways, Porto, Portugal, June 3-4.
- Lancellotta, R. [1993] *Geotecnica*, Zanichelli, 2005.
- Mabsout, M. E., Tarhini, K. M., Frederick, G.R., Tayar C.T., *Finite-Element Analysis of Steel Girder Highway Bridges*, Journal of Bridge Engineering, August 1997, 83-87.
- Maleki, S. [2006] *Seismic energy dissipation with shear connectors for bridges*, Engineering Structures, Vol. 28, pp. 134–142.
- MCEER Multidisciplinary Center For Earthquake Engineering Research [2001] *Recommended LRFD Guidelines for the Seismic Design of Highway Bridges*, Technical report prepared under the MCEER Highway Project 094, Task F3-1.
- Moehle, J.P., Eberhard, M.O. [2000] *Earthquake Damage to Bridges*, Bridge Engineering Handbook. Ed. Wai-Fah Chen and Lian Duan. Boca Raton: CRC Press, 2000.
- NCHRP Report 472 [2002] *Comprehensive Specification for the Seismic Design of Bridges*, Project C12-49 FY'98, ISBN 0-309-06753-7, Library of Congress Control Number 2002104275, Transportation Research Board.
- Uang, C., Tsai, K., Bruneau, M. [2000] *Seismic Design of Steel Bridges*, Bridge Engineering Handbook. Ed. Wai-Fah Chen and Lian Duan. Boca Raton: CRC Press, 2000.
- Whitman, R. V., Richart, F. E. [1967] *Design procedures for dynamically loaded foundations*, Journal of the Soil Mechanics and Foundations Division – Proceedings of the American Society of Civil Engineers, November 1967, 169-193.

ANALYSIS PROCEDURES OF THE LOW CYCLE FATIGUE BEHAVIOUR FOR STRUCTURAL ELEMENTS AND CONNECTIONS

Carlo A. Castiglioni, Alberto Drei

Structural Engineering Department, Politecnico di Milano, Milano, Italy

Abstract. A state-of-the-art research was performed in the scientific literature to assess the experimental procedures generally adopted by the scientific community for quasi-static testing of structural elements and connection. The main and widely used recommended protocols, particularly ECCS and ATC-24 recommendations, to which refers the large part of the researches performed on this topic, are described and analyzed. In order to overcome some limitations of the existing testing procedures, particularly in what regards the description of the unsymmetrical displacement histories experienced by real structural elements when subjected to an earthquake motion, acting simultaneously to vertical loads, a new testing procedure is proposed. Moreover some results of an experimental campaign on steel rack structural systems, carried out adopting the loading protocols of this new procedure, are presented.

Keywords: low cycle fatigue, loading histories, testing recommendations, seismic bearing capacity.

1. INTRODUCTION

The testing procedures used for the assessment of low cycle fatigue of steel building elements and details, in order to assess their resistance to seismic action, are summarized in this paper.

For this purpose a state of the art research was carried out, in the scientific literature, considering also the different national norms and recommendations on testing procedures.

In order to take into account some disadvantage and incompleteness of the test recommendations applied in Europe and United States, a new testing procedure is proposed, and the results of an experimental campaign validating this new proposal are described.

2. TYPES OF CYCLE TESTING

The performance of a *Monotonic Test* to qualify or to model a structural element is meaningful only for the elements for which the expected load is always increasing until the collapse.

In this test the control parameter can be indifferently the load or the displacement if the elastic behavior is to be investigated, the displacement if the behavior until collapse is investigated.

For structures or structural details for which the expected load condition is characterized by a cyclic loading history with known or unknown amplitude, as, for instance, for a structure in seismic area, a *Cyclic Test* is necessary.

Cyclic Tests can be classified on the basis of the velocity by which the load/displacement control parameter is applied; we have:

- *Dynamic Tests* – characterized by the high velocity of application of the control parameter. In this case shaking machines or shaking tables are usually used to simulate the dynamic loads. This kind of test is very expensive, and the specimens are generally in reduced scale.
- *Pseudo-Dynamic Tests* – characterized by the application of variable step-by-step static forces in order to simulate the dynamic behavior. This method provides a realistic seismic simulation using an equipment considerably less expensive than the shaking table. In the *Pseudo-Dynamic Tests*, time domain analytical procedures are combined with experimentally measured parameters. The equations of motion for a discrete parameter model of the tested structural system are solved on line using a step-by-step numerical integration method. This test is generally applied to structures that can be easily modeled with few degrees of freedom (cantilevers, one or two-three storey frames, etc.). This limitation is due to the characteristics of the method, which requires an actuator for each degree of freedom. The tested elements are mainly steel or reinforced concrete structures.
- *Quasi-Static Cyclic Test* – characterized by the application of forces by means of electro-hydraulic actuators with very low velocity. This kind of test is less suitable than dynamic and pseudo-dynamic tests to simulate dynamic or seismic load conditions; but it is generally less expensive. The test apparatus is the most common in research laboratories. Quasi-static tests are generally very simple, but a rational planning of the loading process is needed; the choice of a proper loading history (load/displacement) depends on the aims of the research.

The quasi-static loading histories generally used are *linear type*, characterized by an uniform increase Δx of the control parameter x for each cycle, or *step type*, with two cycle repetitions, or *ECCS type* with three cycle repetitions for each increment Δx .

Other loading history commonly adopted are: the *low cycle fatigue type*, characterized by a fixed imposed value of the control parameter x repeated until

failure, which allows the assessment of a linear cumulative damage, or the *accumulation type*, which presents i steps of load/displacement x_i with n_i repetitions. Sometimes a *random type* loading history is adopted, applying a generic history $x(t)$ of the control parameter.

Cyclic Tests can be classified in three groups regarding their aim: *comparison tests*, *qualification tests* and *modeling tests*.

The *comparison tests* compare the experimental behavior of different structural elements; the *qualification tests* aim at evaluating if an element is adequate to resist to expected real cyclic events; the *modeling tests* are used for the complete characterization of the cyclic behavior of the specimen.

The dynamic and the pseudo-dynamic tests are, by common practice, qualification tests. Their results are not generally very suitable for developing analytical models, due particularly to analytical difficulties (i.e. non linear system identification).

The quasi-static tests have the advantage of an easy employment, but the quality and the utility of the results are strictly related with a good choice of the loading patterns.

3. LOW CYCLE FATIGUE: STATE OF THE ART

In order to assess the state of the art on low cycle fatigue testing of structural elements, a research was done through the Internet and the Scopus search engine (a web-based abstract and citation database provided by Elsevier in cooperation with university and research libraries). Also the journals related to the topic were searched (e. g. *Earthquake Engineering and Structural Dynamics*, *International Journal of Steel Structures*, *Journal of Earthquake Engineering*, *Journal of Structural Engineering*, etc.) The research was limited to about the last 20 years.

Another research through the proceedings of the World Conferences on Earthquake Engineering and other major and minor Conferences was done; from the *IX World Conference on Earthquake Engineering (Tokyo, Japan - 1988)*, to the

XIII World Conference on Earthquake Engineering (Vancouver, Canada - 2004) and the available Proceedings of the *STESSA Conferences (Behaviour of Steel Structures in Seismic Areas)* where thoroughly searched, particularly those of the last ten years.

The research performed is neither exhaustive nor complete. As the topic in study is very specific, the results found were not many but enough to get an idea of the available material, resulting in about 150 articles/papers, and a few PhD thesis.

In addition, there are the following Research Project Reports:

- INCO-Copernicus (2000)- European Union research project - *Moment Resistant Connections of Steel Frames in Seismic Areas*.

- F. M. Mazzolani (editor), Taylor & Francis, 2000 “*Moment resistant connections of steel frames in seismic areas: design and reliability*”
- STEELQUAKE (1997) – *A European Research Program to improve the Assessment of Steel Buildings Behaviour during Earthquakes*
A. Castellani, C.A. Castiglioni, C. Chesi, A. Plumier, P. Panzeri, P. Pezzoli, P. Negro, F. Taucer, P. Carydis *Final report, Contract ENV4-CT96-0278*.
 - SEISRACKS (2007) - *Storage racks in seismic areas*, Research Programme of the Research Fund of Coal and Steel, *Final Report, Report no. 5*

Particularly important, the North-American SAC Project, for the extensive research carried out. SAC is a joint venture partnership funded by FEMA (*Federal Emergency Management Agency*), made from SEAOC (*Structural Engineers Association of California*), ATC (*Applied Technology Council*) and CU-REE (*California Universities for Research in Earthquake Engineering*) to determine the causes of the large damages of the Northridge earthquake of January, 17 1994 and to provide solutions to these damages for new and existing buildings.

The majority of the papers found are from European or North American universities. As a result, the scientific community follows mainly two official testing protocols, the European ECCS and the North-American ATC-24, apart from some recent North-American papers which explicitly cite the AISC-341-05 appendix S. Nevertheless many papers, mainly from Japanese authors, don't indicate explicitly an official procedure, but apply loading histories defined in the paper, which are generally similar to the ECCS or ATC-24 protocols.

The structural elements tested are generally beam-to-column connections, a critical point in steel structures subjected to a cyclic action. The other elements tested are very heterogeneous, with particular relevance to the testing of composite columns and to the cyclic behavior of braces.

4. GEOMETRY OF SPECIMENS

To achieve an adequate knowledge of the cyclic structural behavior of a steel structure by means of quasi static testing, the first step is to define the “minimum sub assemblage” that should be tested. For a framed steel structure, the minimum sub-assemblage is a two storey spatial frame, made with two bays and two naves, with concrete slabs at each floor level. This specimen contains beams, columns, two, three and four ways beam-to-column joints and can be loaded vertically, to simulate gravity loads and horizontally, to simulate earthquake loading (Fig. 1). The specimen is complete, but it can be tested only in special circumstances, due to its dimensions, the cost and the complication of the procedure.

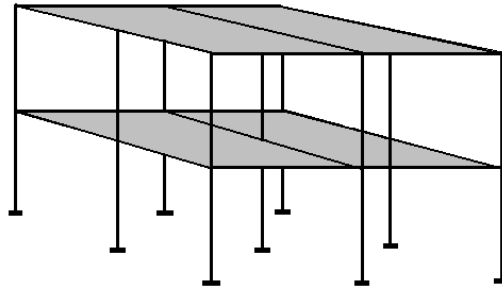


Figure 1. Spatial frame sub-assembly of the structure.

A first simplification can be the testing of part of the sub-assembly, that is only one plane frame (two bays, two storeys). The specimen becomes less complete, because the interaction between the frames due to the transversal effect of the slabs cannot be taken into account, but both the gravity and the seismic loads can still be considered (Fig. 2).

Also this type of sub-assembly remains complicated and expensive, even in the case of a further reduction to a single storey portal frame.

As the most critical details to be investigated are usually the beam-to-column joints, the next step is to consider a single node of the plane frame, made with part of a column and part of a beam. This test setup is simple and is the less expensive, but it is the less complete. The test configuration can be a horizontal T, with vertical column and horizontal beam, or an inverted T, with horizontal column and vertical beam (Fig. 3).

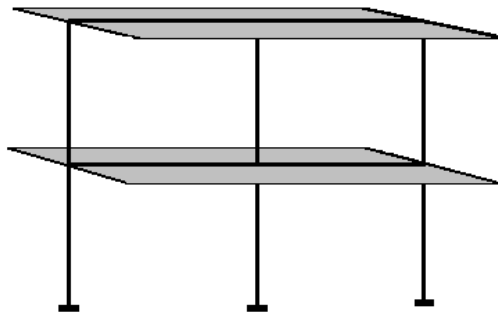


Figure 2. Plane frame sub-assembly of the structure.

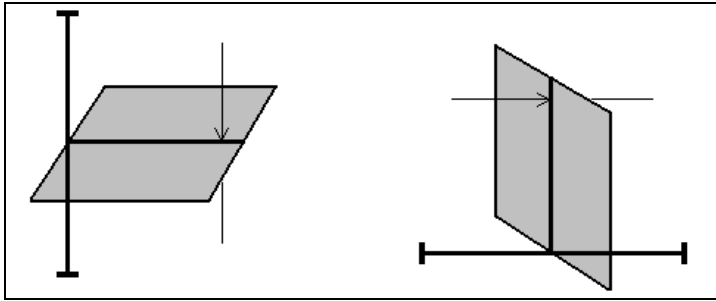


Figure 3. Testing setup outline for Horizontal T and inverted T specimens.

The main problem is that the effects of the vertical loads acting in the real structure, in the usual testing procedure are generally neglected. A cyclic load applied in this testing configuration, following ECCS or ATC-24, gives information on the moment-rotation characteristics of the node, but it is not sufficiently representative of the cyclic behavior of the real node in the structure.

A real node is subjected, in addition to the cyclic load, also to a shear force and to a bending moment due to gravity loads. Positioning an additional constant transversal force close to the node, corresponding to the acting shear, can improve the experimental test behavior, obtaining more realistic results, but it is not possible, in this way to catch the influence of the initial node rotation due to the gravity load, only shear is taken into account.

When there are deformable nodes, in presence of elements with thin flanges, the real behavior is influenced by the initial bending moment, and shows a cumulative deformation in one direction. A proper approach to this problem is proposed in detail in the following, by means of a modification of the present procedures.

5. LOADING HISTORIES

In the following the testing procedures ECCS, ATC-24, AISC-341-05 and interim FEMA 461, will be briefly described. For beam-to-column connections, AISC-341-05 and FEMA 461, as discussed in the following, can be considered an upgrading of ATC-24 procedures, to be applied in special and intermediate moment frames.

Moreover, a new proposed test loading history will be illustrated. It was developed because in certain circumstances, both ECCS and ATC-24 and subsequent ATC and FEMA recommendations fail to address the unsymmetrical displacement histories experienced by beam-to-column connections, as well as the governing phenomena.

ECCS-45 Recommendations

ECCS (*European Convention for Constructional Steelwork*) is the federation of the national associations of steelwork industries and covers a worldwide network of Industrial Companies, Universities and Research Institutes. The Full Members of ECCS are the national associations representing the steel construction industry in twenty European countries. There are also Associate Members and International Members from non-European countries.

In the area of seismic design and testing the ECCS published in 1986 the “*Recommended Testing Procedure for Assessing the Behavior of Structural Elements under Cyclic Loads*”(ECCS-45). No update followed that first edition.

This protocol considers two different procedures: the Complete Testing Procedure, which includes preliminary monotonic displacement tests, and the Short Testing Procedure, which disregards them.

ECCS-45 Complete testing procedure

The recommended testing procedure is composed by three tests. The first and the second test are performed imposing monotonically increasing displacements up to failure. Aim of these tests is the assessment of the yielding load F_y^+ and of the yielding displacement e_y^+ in one direction, and in the opposite direction (F_y^- and e_y^-). They are defined, in each direction, by the intersection of the tangent to the F - e curve at the origin, with the tangent to the F - e curve which has a slope $1/10$ of the previous value.

Nevertheless ECCS points out that there are many possible definitions of a conventional limit of the elastic range F_y .

The third test is a cyclic test with increasing imposed displacement.

The positive and negative cycle amplitudes, after six cycles in the elastic range and one at the yield displacement, are based upon the series of three cycles in the $(2+2n) e_y^+ \div (2+2n) e_y^-$ interval with $n = 0, 1, 2, 3, \dots$ up to the end of the test.

The parameters of interpretation of the results for one cycle, for every group of three cycles, and for the whole test are then defined by the recommendations.

ECCS-45 Short testing procedure

In this case, the first and second tests of the complete testing procedure are not executed. The third test is executed alone but F_y^+ , F_y^- , e_y^+ and e_y^- are not known at the beginning of the test, so the procedure is as follows:

The test should be performed with steps of displacement sufficiently small to ensure that at least 4 levels of displacement are reached before e_y^+ and e_y^- .

The tangent modulus at the origin $tg \alpha_y^+$ and $tg \alpha_y^-$ are evaluated from the first cycle curve.

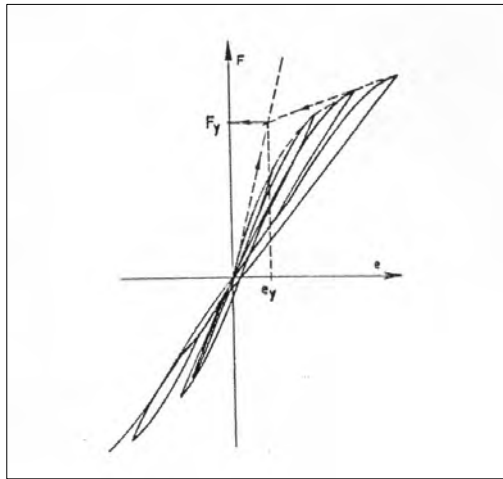


Figure 4. Short testing procedure: conventional elastic range.

As in the complete procedure, F_y^+ and F_y^- are defined by the intersection of two tangent lines or by any other justified definition.

In the first case, one tangent is evaluated in the origin (slope $tg\alpha_y^+$); the other one, with a $0.1 \cdot tg\alpha_y^+$ slope, is now the tangent not to a single curve, but to the envelope curve of the cycles (Fig. 4). Similar definitions are used on the negative side for F_y^- and e_y^- .

As soon as these F_y^+ , F_y^- , e_y^+ , and e_y^- are defined, the testing procedure becomes the same as the third test of the complete testing procedure.

ECCS-45 Combination of loads

The combination of seismic action with long duration actions which have no reversal in sign (e. g. gravity loads) may bring unsymmetrical demand on structural elements. ECCS-45 suggests that in this case the tests can be performed with a partial reversal of displacement. This partial reversal can be of various forms and must be properly justified. No other indication on this item is reported.

Failure criterion for ECCS-45

There is not any definition of collapse in the ECCS-45 recommendations. In paragraph 5, regarding the end of the test, it is only specified that the test may be stopped at any level of displacement decided with regard to specific code or research requirements.

In an experimental investigation a comparison of the capacity of the specimens may be required, so the adoption of a conventional collapse definition is

needed. Different approaches concerning this subject presently circulate. When applying the ECCS recommendations, there is not a consensual definition of failure, considering also that collapse, generally speaking, depends on the type of elements tested. The fact of not having a conventional definition is considered one of the main disadvantages of the ECCS procedure.

ATC-24 Recommendations

The ATC (*Applied Technology Council*) is a nonprofit, tax-exempt corporation established in 1971 through the efforts of the SEAOC (*Structural Engineers Association of California*). The purpose of ATC is to assist the design practitioners in structural engineering and related design specialty fields in the task of keeping abreast of and effectively using technological developments. One of the primary purposes of Applied Technology Council is to develop resource documents that translate and summarize useful information to practicing engineers. This includes the development of guidelines, manuals and research recommendations. ATC is not a code development organization, although several of the ATC project reports serves as resource documents for the development of codes, standards and specification.

In 1992 it was published the ATC-24: “*Guidelines for Seismic Testing of Components of Steel Structures*”, result of a project commenced in 1988, promoted jointly by the AISI (*American Iron and Steel Institute*), the AISC (*American Institute of Steel Construction*), the NCEER (*National Center for Earthquake Engineering Research*), and the NSF (*National Science Foundation*).

The report provides guidance for most cyclic experiments on components of steel structures, for the purpose of consistency in experimental procedures and test evaluation. It contains recommendations and companion commentary concerning loading histories, presentation of the test results, and other aspects of the experimentation. The recommendations are written specifically for experiments with slow cyclic load application.

Differently from the ECCS 45 recommendations, ATC-24 encompasses different types of testing programs.

ATC Single-Specimen testing program

This is the basic testing program that can be performed if only one specimen is available, provided the monotonic load-deformation response (or at least the yield strength) can be predicted with good confidence, the rate of strength deterioration is slow, and analytical cumulative damage modeling is not part of the investigation. This testing program should not be used if the rate of strength deterioration is rapid and the level at which deterioration occurs may exhibit considerable scatter.

The control parameter is generally the displacement; in some parts can be the force. The recommended loading (displacement) history to be applied in this testing program consists of stepwise increasing displacement cycles (*Mul-*

iple Step Tests). In this history the cycles should be symmetric in peak displacements, unless good reasons exist to do otherwise.

The loading history is defined by the parameters:

General recommendations on the number of cycles and peak displacements at each step are:

- The number of cycles n_0 with a peak displacement less than δ_y should be at least six; δ_y is the yield displacement.
- The number of cycles n_1 with peak displacement δ_1 equal to δ_y should be at least three.

The number of cycles n_2 with peak displacement $\delta_2 = \delta_y + \Delta$ should be at least three, unless a lower number can be justified.

Δ is the increment in peak displacement between two consecutive steps.

- The number of cycles n_3 with peak displacement $\delta_3 = \delta_y + 2\Delta$ should be at least three, unless a lower number can be justified.
- The number of cycles n_4 to n_m with peak displacement $\delta_4 = \delta_y + 3\Delta$ to $\delta_m = \delta_y + (m-1)\Delta$ should be at least two, unless a lower number can be justified.

Elastic cycles should be performed with force control. At least three of the elastic cycles should be carried out using the force amplitude of $0,75Q_y$. (Q_y is the yield force). The cycles with $\delta = \delta_y$ and all the cycles with larger peak displacement should be performed with displacement control.

More cycles per step than those specified should be applied if:

- There is anticipation that in a severe earthquake the component, as part of a structure, would experience a cumulative plastic displacement larger than that simulated in the test at the maximum displacement level, or:
- Deterioration occurs during a load step and it is deemed appropriate to evaluate the rate of deterioration through additional cycles with the same load step amplitude.

The ATC-24 loading history, quite similar to that proposed by ECCS-45, is illustrated in Figure 5.

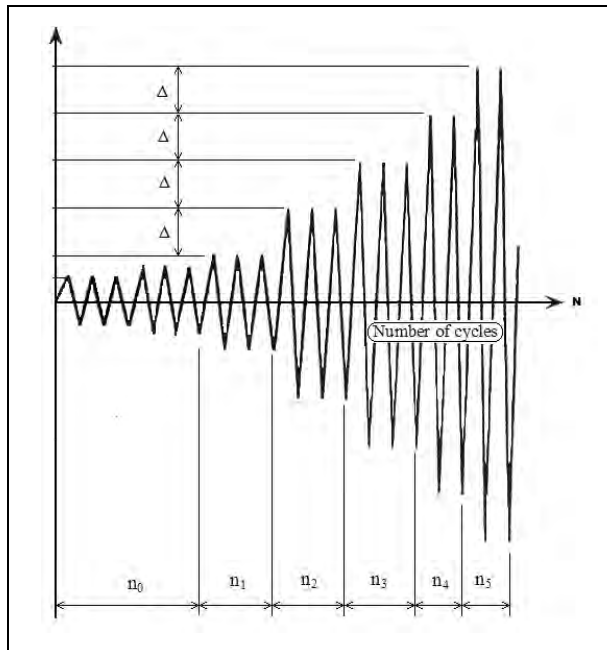


Figure 5. ATC-24 loading history.

According to ATC-24, it is often advisable to interrupt the recommended loading history with small cycles in order to evaluate intermittent stiffness degradation. It is suggested to perform these cycles with force control, using a peak value of approximately $0,75Q_y$.

In all load steps with a peak displacement greater than δ_y , the increment Δ of the peak displacement should be constant. This increment should be equal to δ_y , if the displacement control parameter and the storey drift in the real structure are linearly related.

It is recommended to continue the loading history in the established pattern until severe strength deterioration is evident, even if the attained displacement level is unlikely to be exceeded by the component in the maximum expected earthquake. If the force or displacement limit of the test setup is approached before deterioration occurs, the test should be continued cycling the specimen at that reached maximum level.

ATC-24 gives, with respect to ECCS-45, more detailed indications on the parameters characterizing the test, and has a specific chapter on the presentation of the documentation and of the experimental results, with a table example.

In what regards the conventional yielding values of the specimens, an evaluation of Q_y and δ_y can be obtained by a specific preliminary test or, in case of a single specimen test, by an evaluation from analytical models and the me-

chanical characteristics of the material. There is no conventional definition suggested for these parameters, it is only specified that “*judgment is needed to determine these values, and it is understood that these parameters are for test control only and that different values may be more useful for test interpretation*”.

While ECCS-45 indicates only the recommended testing procedure, ATC-24 provides an additional commentary with general considerations justifying the proposed loading histories in term of seismic demand and seismic capacity of components.

ATC-24 suggests the inter-storey drift in structures as the most suitable parameter to represent the demand imposed by earthquakes to structural components and their global capacity, considering also that this parameter can usually be related to component deformation. As a consequence of this point of view, ATC-24 suggests that the increment Δ in peak deformation between load steps for the specimen should correspond to the deformation at an increase in storey drift equal to the yield displacement of the storey.

As the deformation demand in single degree of freedom systems can often be used to estimate inter-storey drift, the basis for the recommended loading histories are statistical studies on the seismic behavior of bilinear and stiff-degrading SDOF (single degree of freedom) systems, subjected to a set of 15 ground motions, with magnitude from 5.7 to 7.7, from western American earthquakes.

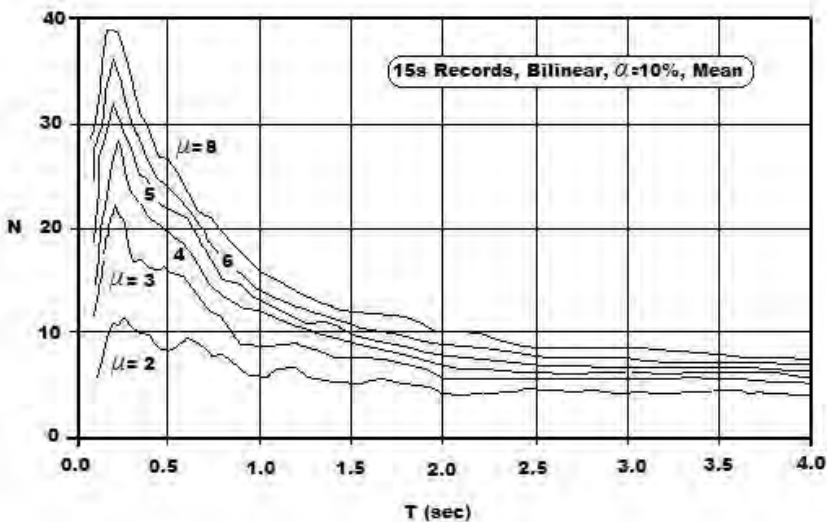


Figure 6. Dependence of mean number N of inelastic excursion on Natural Period T and Ductility Ratio μ .

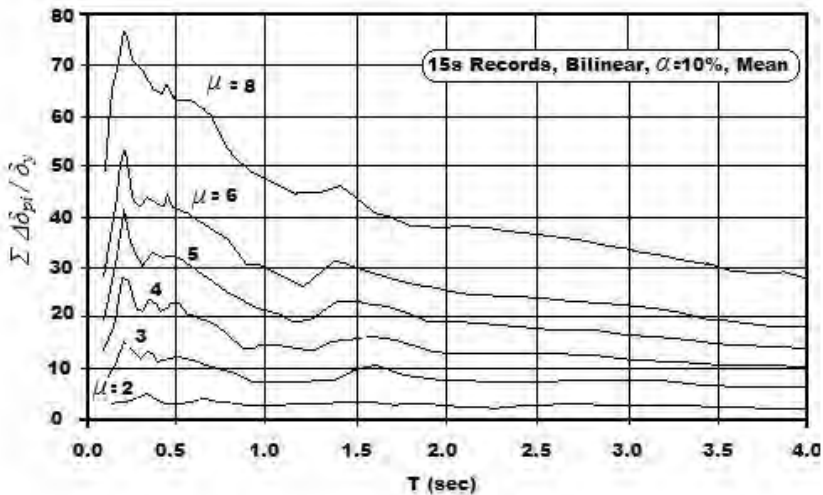


Figure 7. Dependence of the mean of the sum ($\Sigma \Delta \delta_{pi} / \delta_y$) of normalized plastic deformation ranges on natural period T and ductility ratio μ .

Some of the obtained results are summarized in the two Figures 6 and 7 (Nassar and Krawinkler, 1991, from ATC-24) which report respectively the number N (mean values) of plastic excursions and the sum $\Sigma \Delta \delta_{pi} / \delta_y$ of the normalized plastic deformation range (mean values) depending on the natural period and on the ductility factor of the SDOF systems. $\Delta \delta_{pi}$ is the permanent deformation at the i cycle between the beginning and the end of a loading excursion, from zero to zero load, and δ_y is the yield displacement. This parameter can be assumed as a cumulative damage indicator; for bilinear systems it is equal to the dissipated hysteretic energy, normalized by $F_y \delta_y$.

The recommended loading history, whose experimental application should yield indications on the specimen capacity to correspond with an acceptable security margin to the seismic demand previously considered, is based on the following concepts:

- The seismic demand for the inter-storey drift can be represented by the response of bilinear SDOF systems.
- The loading history should represent a “reasonable and generally conservative” demand on N , $\Delta \delta_{pi}$, and $\Sigma \Delta \delta_{pi} / \delta_y$ for the full range of practical storey drift ductility ratios. Since these parameters depend strongly on the period of the structure to which the component belongs, the demand should be established for short period structures, 0.2 and 0.5 seconds, for which the demands are high (Figs. 6 and 7).

ATC-24 reports in the Table 1 a comparison between predicted demands for periods of 0.2, 0.5 and 2.0 seconds in SDOF systems and experimentally executed demands applying the recommended loading history.

Table 1. Predicted and Experimentally executed Demands.

<i>Period</i>	<i>Ductility</i>	<i>N</i>			$\Sigma\Delta\delta_{pi}/\delta_y$		
		<i>mean</i>	<i>mean+σ</i>	<i>experiment</i>	<i>mean</i>	<i>mean+σ</i>	<i>experiment</i>
0.2	2	12	19	6	4	7	11
	4	28	42	16	28	41	57
	6	36	55	24	54	76	127
	8	39	59	32	78	109	229
0.5	2	8	12	6	3	5	11
	4	19	30	16	23	36	57
	6	24	35	24	41	64	127
	8	26	38	32	64	97	229
2.0	2	4	7	6	3	4	11
	4	7	10	16	13	20	57
	6	9	12	24	25	36	127
	8	10	14	32	38	52	229

Table 1 shows that the loading history is very conservative in what regards $\Sigma\Delta\delta_{pi}/\delta_y$, but for the smaller periods, the number of inelastic excursions is smaller than the predicted mean values.

The reason is attributed to the fact that during earthquakes short period structures generally experience a large number of small inelastic excursions, and a small number of large inelastic excursions, whereas in the recommended loading history the magnitude of inelastic excursions are distributed more uniformly. Many small excursions due to the earthquake are replaced by a few larger excursions in the test; as a consequence the number of cycles to be performed in the experiment is reduced. Nevertheless the cumulative damage effect, represented by $\Sigma\Delta\delta_{pi}/\delta_y$, is still simulated conservatively. The fact that, generally speaking, the number of cycles with smaller amplitude predicted from seismic demand studies is larger than in the Multiple Step Test, is in part compensated executing more than one cycle with larger amplitude in the loading history. If necessary, in order to simulate more accurately the expected number of inelastic excursions, the loading history can be modified by the experimentalist.

It should be pointed out that the indicated seismic demand characteristics come from a group of only 15 seismic records on stiff soil, therefore in case of earthquakes with large magnitude and with long strong motion duration, or in case of sites on soft soil, the requested performance of components in terms of number of inelastic cycles and total plastic deformation range can be larger.

ATC-24 Multi-specimen testing program

The necessity of testing more than one identical specimen may occur if:

- The monotonic behavior cannot be predicted with reasonable confidence, either analytically or from the results of a single specimen test. In this case,

it is recommended to perform one or two monotonic tests (in the positive and negative direction) until severe strength deterioration occurs.

- The strength deterioration is rapid and the level at which deterioration occurs may exhibit considerable scatter (e.g. crack propagation and fracture at welds, which is affected by workmanship).
- A cumulative damage model needs to be developed. In this case a *Cumulative damage testing program* is appropriate.

The loading history for the additional tests remains the same. A minimum of three specimens should be tested and the performance evaluation should be based on the test with the smallest cumulative measured plastic displacement range, unless a sufficient number of specimens are tested to permit a statistical evaluation of the results.

Cumulative damage testing program

A special testing program is needed to develop a cumulative damage model for assessing the seismic performance of the component under random loading histories. A cumulative damage model can be used to evaluate the cumulative effect of inelastic cycles on an accepted limit state.

The limit state may be associated with excessive strength deterioration or other measures of damage tolerance. A cumulative damage hypothesis may include several structural performance parameters. The validity of the hypothesis and the values of the performance parameters have to be determined experimentally. This requires a multi-specimen testing program whose details depend on the type of damage model and of the failure mode to be investigated.

In order to perform this testing program, assuming Manson-Coffin relationship and Miner's rule as cumulative damage model, at least three constant amplitude tests on identical specimens are necessary. For ductile elements, suggested values for the three deformation amplitudes are $3\delta_y$, $6\delta_y$ and $9\delta_y$.

Failure for ATC-24

ATC presents the same problem as ECCS in defining failure. There is not a conventional definition of this phenomenon, nevertheless the parameter Q_{min} , required strength before failure is specifically considered. It is defined as the minimum force at peak deformation that must be resisted according to a stipulated performance criterion.

This force may be expressed as $Q_{min} = \alpha Q_y$ where Q_y is the measured or the predicted yield strength. The parameter α , according to ATC-24, is a matter of judgment and should depend on the rate of strength and stiffness deterioration close to failure. If the rates of deterioration are high, it is recommended to take α close to unity or maybe somewhat larger, otherwise α value can be less than unity. ATC-24 points out that the maximum ductility ratio determined by the experiment, in case of gradual strength deterioration is greatly affected by the value assigned to Q_{min} , while in the opposite case it is insensitive to its value.

AISC-341-05 and FEMA-461 Recommendations

In AISC (*American Institute of Steel Construction*) “Seismic Provisions for Structural Steel Buildings”, the recommendations for testing procedures are contained in Appendix S “Qualifying Cyclic Tests of Beam-to-Column and Link-to-Column Connections”. They are expressly for special (SMF) and intermediate moment frames (IMF), and for eccentrically braced frames (EBF).

The 2005 edition of the “Seismic Provisions for Structural Steel Buildings” supersedes the previous editions of 2002 and 1997. They are based on the results of the 1997 FEMA-SAC project, established by FEMA, after the 1994 Northridge earthquake. These advances were incorporated in various FEMA recommendations. Among them, FEMA-350 “Recommended Seismic design Criteria for New Steel Moment Frame Buildings” edited in 2000, contains a protocol for cyclic testing procedures based on SAC results, e. g. SAC/BD/00/10 “Loading Histories for Seismic Performance Testing of SMRF (*Steel Moment Resisting Frames*) Components and Assemblies” by H. Kra-vinkler, A. Gupta, R. Medina and N. Luco, edited in 2000.

The most recent recommendations on testing procedures based on the previous achievements of the FEMA-SAC project are contained in AISC-341-05.

The testing protocol is considered mainly a qualification oriented procedure; the most important changing in it with respect to ATC-24 is in the definition of the applied loading history. In ATC-24 there was the indication that the value of the increment Δ in peak deformation between load steps for the specimen should correspond to the deformation at an increase in storey drift equal to the inter-storey yield displacement. Now for beam-to-column connections the inter-storey drift angle θ (*inter-storey displacement divided by the storey height*) is directly assumed as the control parameter and defined in values imposed to the test specimen as specified below:

- 1) 6 cycles respectively at $\theta = 0.00375 \text{ rad}$, $\theta = 0.005 \text{ rad}$, $\theta = 0.0075 \text{ rad}$
- 2) 4 cycles at $\theta = 0.01 \text{ rad}$
- 3) Then steps of 2 cycles with increments of 0.005 rad up to $\theta = 0.05 \text{ rad}$, continuing with increments of $\theta = 0.01 \text{ rad}$.

As this experimental tests are qualifying tests, the provisions specify requirements for strength and inter-storey drift angle θ . As an example, for SMF “*the connection shall be capable of sustaining an inter-storey drift angle of at least 0.04 radian*” (*paragraph 9.2a.*) Moreover, the test specimen must sustain the required values for at least one complete loading cycle.

FEMA 461 (June 2007) *Interim Testing Protocols for Determining the Seismic Performance Characteristics of Structural and Non-structural Components* – limiting our interest only to Quasi-Static test loading carried out with displacement control – looks as a further recent upgrading of previous protocols, with more detailed and explicative considerations on the recommended loading histories for Quasi-Static test loading (see FEMA 461 paragraph 2.9 *Loading Histories*)

6. PROPOSED INNOVATIVE PROCEDURE

The previous state of the art analysis, conducted mainly on ECCS-45 and ATC-24 recommended testing procedures, shows some limitations of both. Although commonly accepted, these documents suffer for aging: ECCS-45, a pioneering document on this topic, is nearly 25 years old.

Recent AISC-341-05 can be considered an enhancement, qualification oriented, of ATC-24. The same ATC-24, published nearly five years later than ECCS-45, based on knowledge of the previous European experiences, can be considered an enhancement of ECCS-45.

In any case, 25 years of experience in cyclic testing and extensive exchange of information among researchers all over the world indicated the need for a possible review of the existing cyclic testing procedures, as carried out in the SAC joint venture project, but other significant improvements or different points of view can be developed.

A preliminary observation is that both ECCS-45 and ATC-24, but almost all the procedures found in literature, encompass only displacement controlled conditions, and fail to describe the unsymmetrical displacement histories experienced by real beam-to-column connections when subjected to earthquake motion, that acts simultaneously to vertical (live and dead) loads.

This is particularly evident when testing is performed in the inverted-T configuration, with the beam standing vertically and the column horizontally. The obtained parameters, in presence of a cyclic action, tend to cycle around the zero value, while the actual behavior of beam-to-column connections, when subjected to vertical and horizontal effects, is different.

In order to overcome the discussed limitations of the existing testing procedures, a new procedure is proposed hereafter.

This new procedure takes into account the effect of the gravity loads in the real structure applying a load to the beam of the specimen. To simulate an experimental condition similar to the real behavior of the node element in the structure, the load, corresponding to the shear force at the node, should be positioned at a distance L_s from the node, in order to produce both the same node shear force and the same node rotation determined in reality by the vertical loads.

As an example, in case of distributed load q on a slab, to have the proper shear force the load applied should be $qLb/2$, where L is the beam length and b is the width of the influence area of the slab pertinent to the beam.

The distance L_s is obtained by equalizing the rotation of the node of the specimen and the rotation of the node in the portal frame configuration.

Vertical load: L_S parameter

Let us consider a beam with length L , connected to two columns by joints with rotational stiffness respectively K_1 and K_2 . Let the beam be subjected to a uniform linear load p .

This uniform load will cause an elastic rotation θ_1 on the left edge and an elastic rotation θ_2 on the right edge, and a bending moment $M_1 = \frac{pL^2}{12}$ at the left and $M_2 = -\frac{pL^2}{12}$ at the connection on the right.

Hence the equilibrium equation on each joint will be:

$$\begin{aligned} \text{Joint 1: } & \frac{4EI}{L}\theta_1 + \frac{2EI}{L}\theta_2 + K_1\theta_1 = \frac{pL^2}{12} \\ \text{Joint 2: } & \frac{4EI}{L}\theta_2 + \frac{2EI}{L}\theta_1 + K_2\theta_2 = -\frac{pL^2}{12} \end{aligned}$$

Introducing the stiffness of the beam $K_b = \frac{EI}{L}$ these equations are now:

$$\begin{aligned} \text{Joint 1: } & (4K_b + K_1)\theta_1 + 2K_b\theta_2 = \frac{pL^2}{12} \\ \text{Joint 2 } & 2K_b\theta_1 + \theta_2(4K_b + K_2) = -\frac{pL^2}{12} \end{aligned}$$

Solving with respect to the node rotations, we obtain:

$$\begin{aligned} \theta_1 &= \frac{pL^2}{12} \frac{(6K_b + K_2)}{(4K_b + K_1)(4K_b + K_2) - 4K_b^2} \\ \theta_2 &= -\frac{pL^2}{12} \frac{(6K_b + K_1)}{(4K_b + K_1)(4K_b + K_2) - 4K_b^2} \end{aligned}$$

To represent the situation of a T specimen subjected to a discrete load F on its extremity, let us have a cantilever of length L_S with a rotational elastic stiffness K_1 at its connection.

It is:

$$F = \frac{K_1\theta_1}{L_S}$$

Comparing the node rotations θ_i of the previous beam configuration and of the inverted T cantilever configuration (Fig. 8) we obtain:

$$\frac{FL_s}{K_1} = \frac{pL^2}{12} \frac{(6K_b + K_2)}{(4K_b + K_1)(4K_b + K_2) - 4K_b^2}$$

F represents the force applied on the cantilever at a distance L_s , which causes the same rotation of the joint as in the beam configuration, whose length is L .

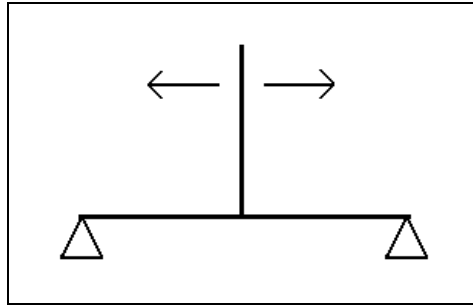


Figure 8. Experimental configuration: inverted T cantilever.

The shear force at each connection of the beam with a distributed load p , is $F = \frac{pL}{2}$; hence it is $L_s = \frac{L}{6} \frac{K_1(6K_b + K_2)}{(4K_b + K_1)(4K_b + K_2) - 4K_b^2}$

Generally the stiffness of the joints in the real structure is approximately the same: $K_1 = K_2 = K$, therefore $L_s = \frac{L}{6} \frac{K(6K_b + K)}{(4K_b + K)^2 - 4K_b^2}$

That can be simplified as

$$L_s = \frac{L}{6} \frac{K}{(2K_b + K)}$$

Substituting for the beam stiffness $K_b = \frac{EI}{L}$

$$L_s = \frac{L}{6} \frac{KL}{(2EI + KL)}$$

And inverting this relation
$$L = 3L_S + \sqrt{9L_S^2 + 12 \frac{EI}{K} L_S}$$

For a distributed load, L_S ranges from $L_S = 0$ for a supported beam ($K = 0$), to the limit value $L_S = \frac{L}{6}$ for a perfectly rigid joint ($K = \infty$).

The values of L_S are generally small, for a beam length $L = 6.0$ m, the maximum value is $L_S = 1.0$ m, for a rigid joint. Considering the joint stiffness with respect to the beam stiffness, for values $K = K_b$, $K = 2K_b$, $K = 4K_b$ and $K = 6K_b$, L_S is respectively about 5% L , 8% L , 11% L and 12.5% L that is, for a 6m real beam, about 30 cm, 48 cm, 67 cm and 75 cm.

These considerations can be a limit to the application of the procedure in some loading situations, due to the characteristics of the experimental setup.

Loading history of the proposed innovative procedure

The procedure is referred to cyclic tests, performed after two monotonic tests which identify yielding forces (F_y^+ ; F_y^-) and yielding displacements (d_y^+ ; d_y^-) in the two opposite directions of loading. The yielding values can be assessed preferably according to ECCS-45. Other conventional definitions, if properly justified can be adopted.

These tests are generally necessary, because this new procedure is particularly suitable for elements and details with unsymmetrical behavior.

The cyclic test now is composed by a sequence of reversed cycles (repeated when in the post-elastic range) in which each cycle has an initial force-controlled part and a final displacement-controlled part. Gravitational load effects are expressed through F_g , which can be expressed as a fraction of the yielding force F_y . In what follows, the gravity force is considered to be positive. As a consequence of this conventional choice, the “positive” bending moments are those associated with “hogging” bending.

A typical positive cycle is composed of two parts (Fig. 9):

- Application of the force correspondent to vertical (gravitational) load effects F_g on the beam-to-column connection (force-controlled part of the cycle). The values of F_g can be assumed for example as 25%, 50%, 66% or 75% of the yield force F_y .
- Starting from the displacement at the end of the force-controlled part of the cycle the displacement controlled part of the cycle is imposed. The applied displacement amplitude is a multiple of the yielding displacement. Also the following negative cycle is composed by two different parts:
 - Force-controlled unloading until the attainment of the Force F_g associated with the presence of the vertical (gravity) loads alone
 - Starting from the displacement Δd_n^- reached at the end of the force-controlled part of the cycle, the displacement-controlled part of the cycle is

imposed to the specimen, until the intended displacement amplitude is reached.

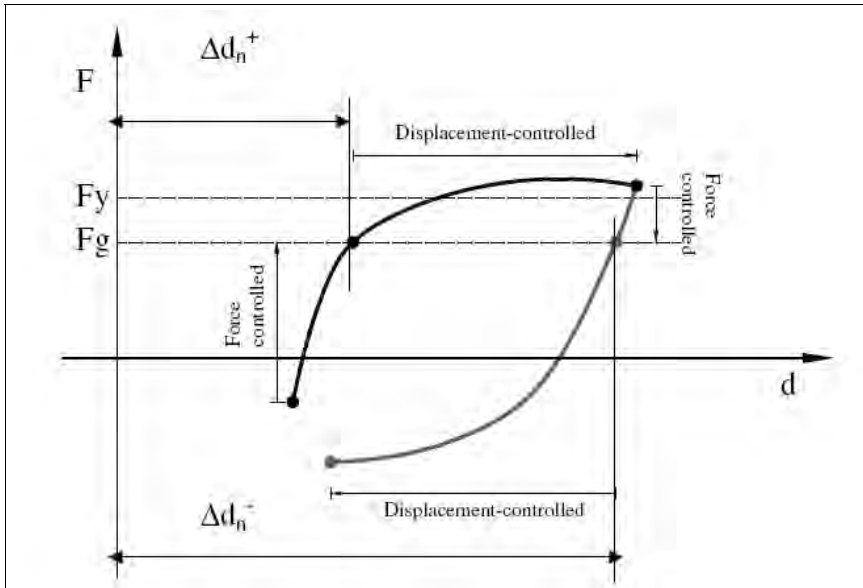


Figure 9. The two phases of the proposed new procedure.

The positive and negative cycle displacements (in the post-elastic range) are derived from the following relation:

$$[(2 + n)d_y^+ + \Delta d_n^+] \div [(2 + n)d_y^- + \Delta d_n^-] \quad (n = 0, 1, 2, 3..)$$

Failure for the proposed procedure

Failure is identified when in any of the positive or negative cycles one of the following situations occurs:

- I. When the specimen fails to develop the force correspondent to gravitational loads F_g in the force-controlled part of the positive cycle (Fig. 10)
- II. When the restoring force decreases to values below those corresponding to gravitational loads F_g in the displacement-controlled part of the positive cycle (Fig. 11).

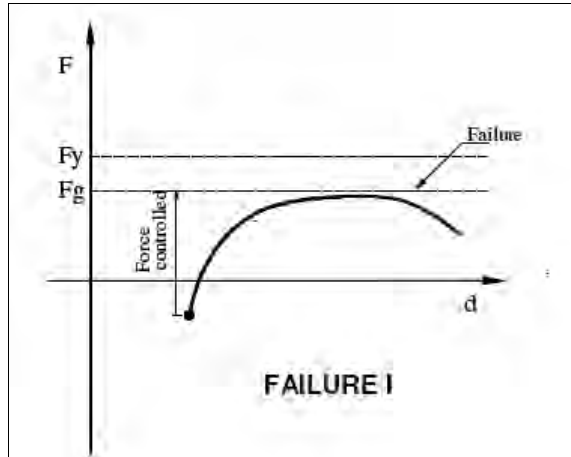


Figure 10. Type I failure.

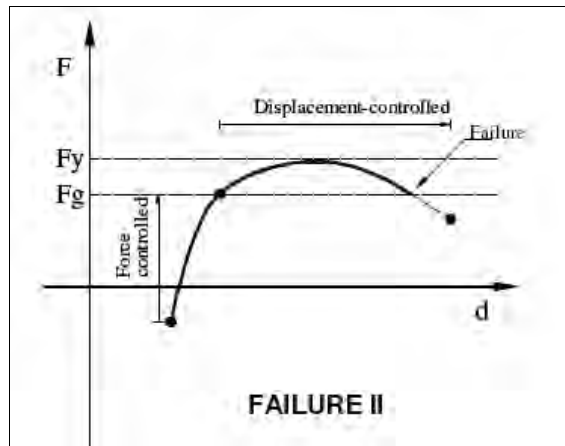


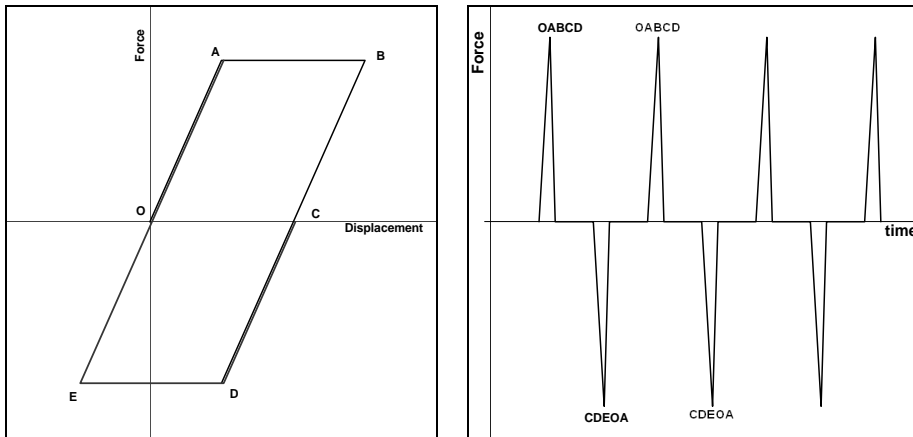
Figure 11. Type II failure.

Using this procedure for a qualifying test, the acceptance criteria can be, as in recent procedures, the inter-storey drift angle, which now is strongly influenced by the cumulative displacement simulated during the test. The limit drift angle must be reached without the collapse, defined as specified previously, of the structural element. The number of cycles at every step can be defined according to the considerations developed in the previous protocols.

Seismic bearing capacity representation

The effectiveness of the new testing procedure in representing the seismic bearing capacity of a structural element, can be suggested also by the following qualitative considerations.

For an elastic–perfectly plastic Single-Degree-of-Freedom element, subjected to an impulsive force large enough to cause a plastic excursion, the displacement behavior can be represented by the line OABCD in Figure 12.



Figures 12 and 13. Time spaced opposite impulsive forces.

The absorbed energy exceeding the elastic energy that can be accumulated in the element, is dissipated by the plastic deformation (AB), then the element oscillates between the positions B and D. The amplitude of these oscillations decrease in time due to the damping of the system. Neglecting this dynamic effect, it is possible to consider the cycle represented in Figure 12 as the result of two consecutive opposite impulsive forces, spaced in time, as in Figure 13. The second impulsive force determines the force-displacement relation of line CDEOA, with final damped oscillations between points A and E.

From this point of view, an usual quasi-static testing cycle, performed between two opposite values of the displacement, as points B and F in Figure 14, can be considered as the result of four consecutive impulsive forces, spaced in time, inverting their sign at every two impulses (Fig. 15).

Increasing plastic cycles, imposed in traditional quasi-static tests, can be obtained from the effect of larger impulsive loads, spaced in time, as represented in Figure 16, with the same sign properties.

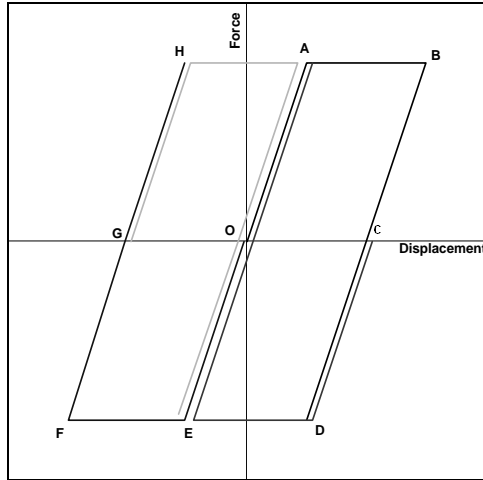
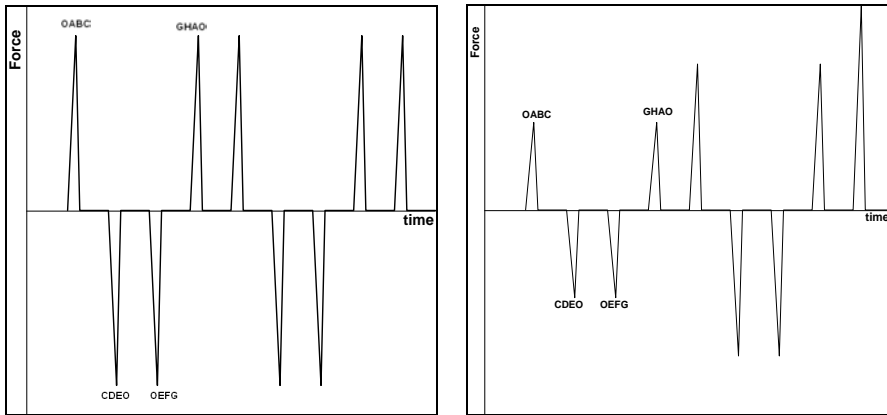


Figure 14. Equal displacement cycle obtained by four time spaced impulsive forces.



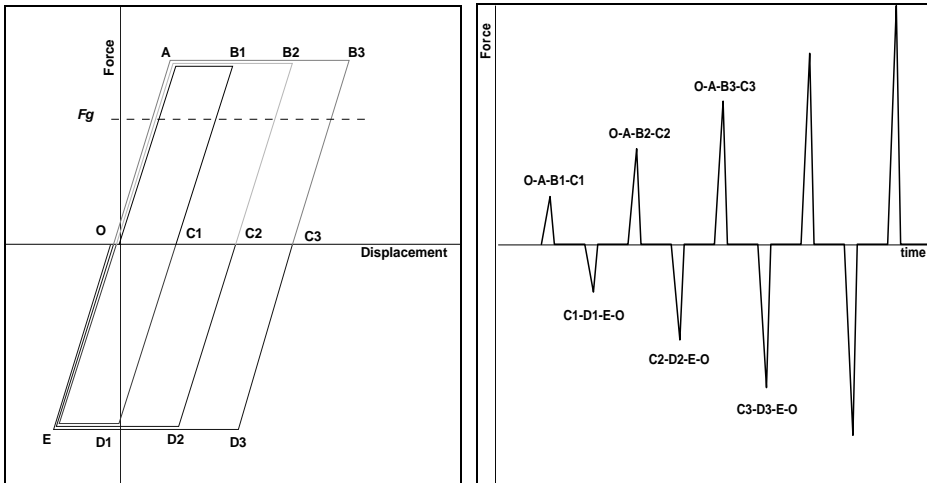
Figures 15 and 16. Impulsive forces for constant and for increasing equal displacement cycles.

As a seismic load can be seen as the application of a series of alternate impulsive forces, the seismic carrying capacity of a structural element may be represented by a quasi-static simulation of the effect of a group of alternate increasing impulsive forces spaced in time, as respectively in Figures 17 and 18.

The first impulse in plastic range can be considered to cause a total displacement of $2 e_y$ (point B1) transferring the total energy $1.5 F_y e_y$. The second impulse is equal to the previous one, but in the opposite direction, so the maximum displacement corresponds to point E. The third impulse can be set to cause a total displacement of $3e_y$ (point B2) transferring the total energy $2.5 F_y e_y$, followed by an opposite similar impulse, reaching again point E. Subsequent

couples of opposite impulses will cause total displacements of $4e_y$, $5e_y$, and so on, involving the energy $3.5 F_y e_y$, $4.5 F_y e_y$. Of course the cycles can be repeated. The result is a global behavior of the specimen with cumulated displacement in one direction.

The loading cycles obtained (Fig. 17) are similar to the new proposed testing procedure with no permanent loading, with displacement accumulation in one direction. Applying the new procedure, in the first cycle the force is applied with displacement control from point O up to the required displacement in point B1, then with force control the specimen is unloaded until point C1.

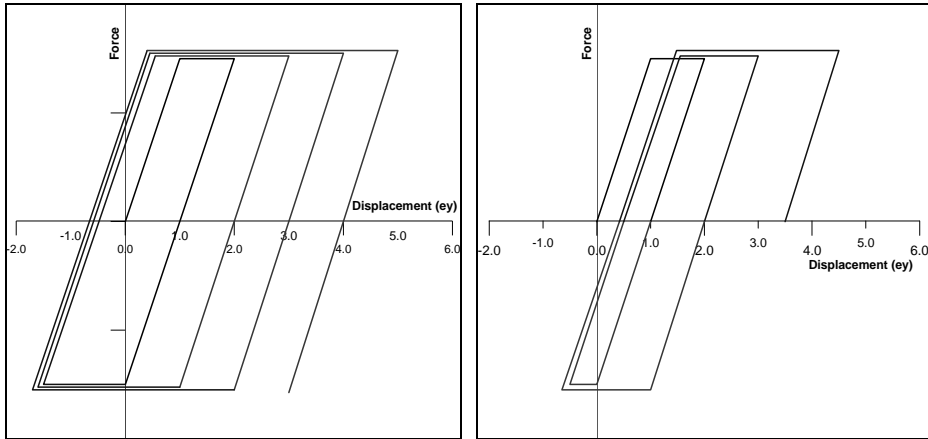


Figures 17 and 18. Force-displacement cycles from time spaced increasing impulsive forces.

The reverse load is applied with displacement control from C1 up to point E, imposing a displacement equal to OB1, and with force control the specimen is unloaded to point O. The subsequent cycle is performed with the same steps but a larger required displacement, corresponding to point B2, and so on.

To take into account the presence of permanent vertical loading, signifies only to limit the force control loading and unloading to the considered load F_g .

Moreover it can be observed that, even if an impulsive force is applied before the completion of the effect of the previous one, that is during the elastic oscillation after the plastic displacement, the global aspect of the cycles obtained is similar. The energy of the subsequent impulse, depending on the direction of the oscillation, can be added to the elastic energy $0.5 F_y e_y$ of the specimen or can cancel it or only a part of it. The cycles obtained in these situations are presented in Figures 19 and 20, with different cumulative displacement.



Figures 19 and 20. Cycles with and without complete addition of energy.

Comments on the new testing procedure

This new procedure gives a significant improvement to the commonly adopted recommendations for low cycle fatigue testing. The global performance of the specimen is clearly defined with explicit reference to its requested carrying capacity F_g in usual service conditions, therefore in this sense the new experimental tests may be considered “complete”: the performance of the specimen subjected to reversal loads is investigated as far as it can resist the design permanent (dead and live) loads or a previously assigned multiplier of them. The failure to resist these loads represents the collapse of the specimen.

Accepting this point of view, the proposed new testing procedure could be the basis for new Low Cycle Fatigue testing recommendations, or for a new edition of ECCS recommendations, which takes into account the experiences accumulated in the last 25 years on this item.

Applying the new proposed procedure, the Single Specimen Test and the Multiple Specimen Test may be carried out in the same frame of ECCS-45 and ATC-24 recommendations. Moreover, the new testing procedure can be applied also in cumulative damage assessment, performing cyclic tests with constant amplitude of different values on an adequate number of specimens. The governing deformation parameter Δ can be assumed as in ATC-24, or according to other damage models.

Comments on the application of vertical loads

If the effect of vertical loads is neglected, as generally made up to now, the test is executed following ECCS-45 or ATC-24 recommendations, and the new loading procedure is not suitable. The end of the test, therefore, depends on a commonly accepted collapse definition or a performance required value. As previously discussed, ATC-24 considers the parameter $Q_{min} = \alpha Q_y$ minimum

force to be resisted at peak deformation. On the other hand, other authors consider energy based parameters. As an example, for cyclic loading of constant amplitude on steel components, Calado and Castiglioni, proposed the condition: $W_f \leq \alpha_f W_0$ as failure criterion, where W_f is the absorbed energy at the considered cycle (i.e., the cycle during which failure occurs), W_0 represents the absorbed energy at the first cycle in the plastic range, and α_f is a coefficient for which the value of 0.5 was recommended, specifying that the value $\alpha_f = 0.5$ is conservative only for ductile fracture phenomena.

If the effect of the design vertical loads is essential to the assessment of the specimen capacity, the new procedure takes it explicitly into account, defining the collapse when the specimen loses the design bearing capacity.

In all the situations where, due to the experimental setup characteristics it is not possible to apply the hybrid procedure, as an example when the parameter L_s results quite small, the simplest procedure to obviate the small value of L_s , is to apply independently the gravity load F_g at the distance L_s and then performing the testing procedure with the variable force applied to a suitable distance. Nevertheless the distance L_s should be large enough in order to allow considering the stress distribution and node rotation caused by the applied load at L_s distance similar to those given by the real shear force and bending moment.

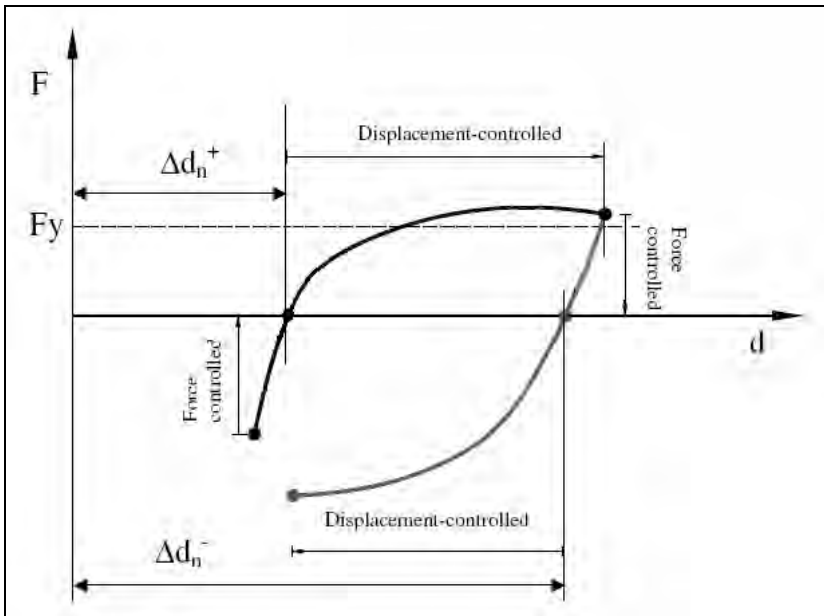
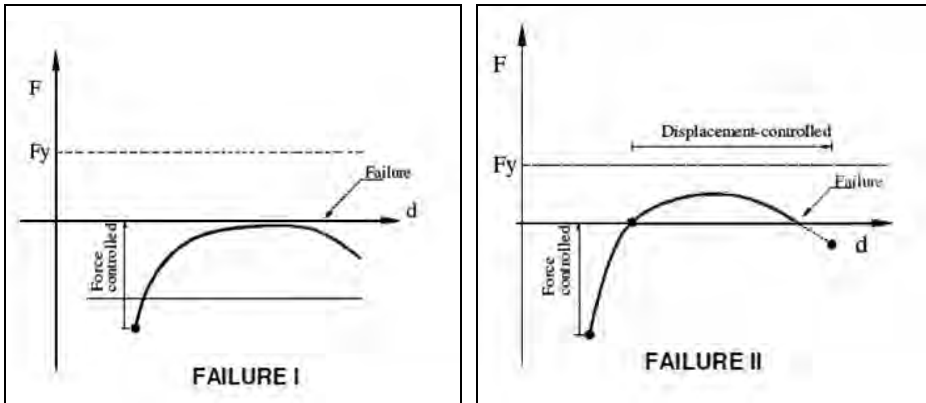


Figure 21. Vertical load directly applied: the two phases of the proposed new procedure.

In this case the test begins with the displacement controlled part, considering that the origin of the load-displacement diagram now corresponds to a pre-

loaded an pre-deformed condition (Fig. 21). The collapse conditions are the same previously defined (Figs. 22 and 23) paying attention that now F_g is zero.



Figures 22 and 23. Vertical loads directly applied: type I and type II failure.

Alternatively, when the parameter L_s is too small, in order to obtain the correct initial moment and initial node rotation, and a stress distribution due to the applied shear similar as possible to the real one, a portion of the proper vertical load can be applied directly on the specimen, close to the node, determining part of the shear force and a negligible bending moment, and the remaining part at a suitable distance, permitted by the testing setup, giving the correct initial bending moment and node rotation. In this situation the new testing procedure is now performed considering a reduced collapse load F_g .

Nevertheless the new hybrid procedure can be performed directly, without applying an independent shear load, considering only partially the global effect of the vertical load, as an example applying to a distance generally larger than L_s , depending on the characteristics of the experimental setup, the load producing the same node rotation of the real vertical load. In this case the shear force is only a fraction of its effective value; and the experiment is not completely representative of the field conditions.

Up to now, the new hybrid procedure has been successfully applied only to T and inverted T elements. Its application to more representative structural specimens may be objective of further research.

7. EXPERIMENTAL PROGRAM

An experimental testing campaign on beam-to-upright connections of racking systems, applying the loading histories of the new proposed testing procedure, was performed by L. Calado at the Instituto Superior Técnico of Lisbon, in November 2005 and January 2006. The tests allow the characterization of the behavior of the joints, as well as a correct interpretation of full scale tests afterwards performed. Moreover, the results were compared to those of the ECCS procedure, applied on some specimens.

The aim of the testing campaign was:

- The assessment of the moment-rotation curves.
- The assessment of the collapse modes for monotonic and cyclic loading.

Beam-to-upright connections

Both components considered, beam and upright, are thin walled section elements.

Their connections are all non symmetric, at the base-to-ground joints of the uprights and in the beam-to-upright connections. The base-to-ground joint is non symmetric in one direction due to the asymmetry of the upright section (Fig. 24b), to the eccentric position of the upright on the base-plate, and to the asymmetrical disposition of two fixing bolts only (Fig. 25b).

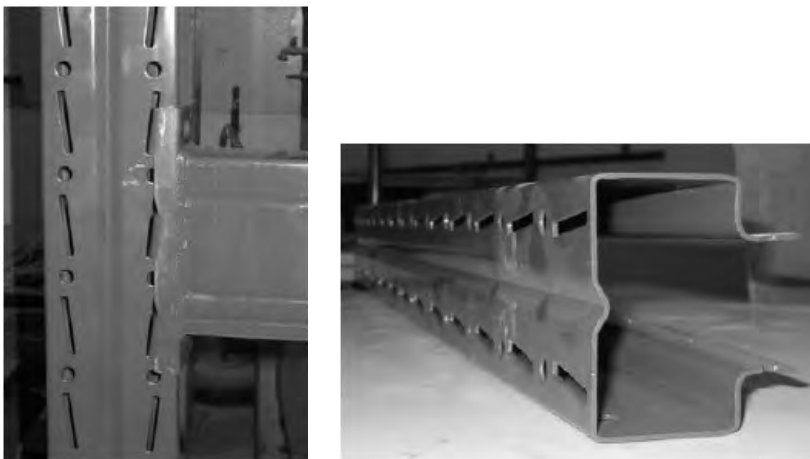


Figure 24. a) Beam-to-upright connection. b) Upright (100/20b type).

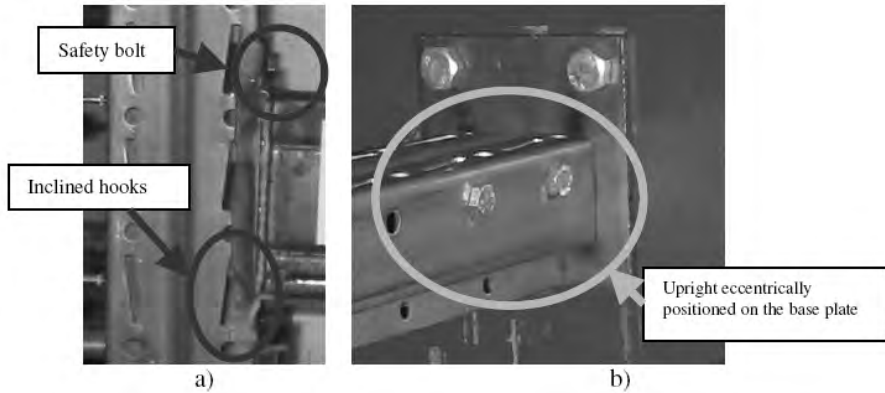


Figure 25. Asymmetry of the connections: a) beam-to-upright b) Upright-ground connection.

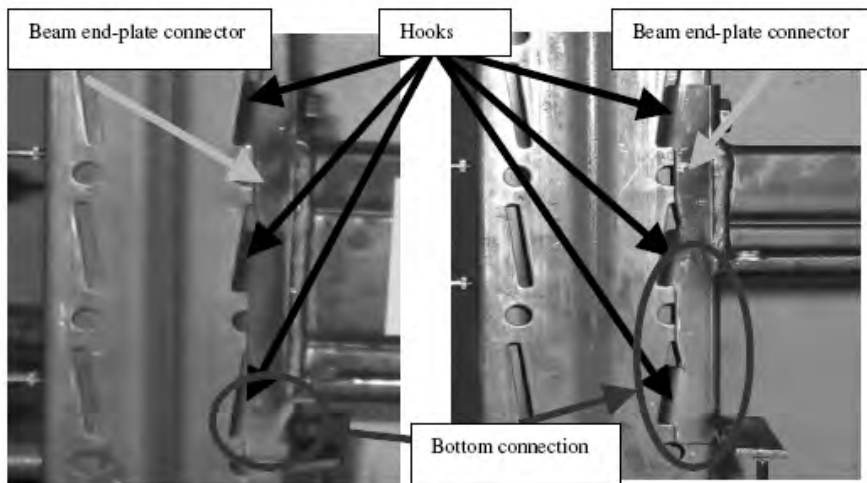


Figure 26. Beam-to-column connection tested.

On the other hand, the beam-to-upright connection, that is a proprietary moment joint typical for beam-to-upright connections of steel pallet storage racks, is strongly non-symmetric in both vertical and horizontal direction. The junctions to the upright (Figs. 24-26) are made by means of hooked end plate connectors, fillet-welded to the beam at both ends, but only at three sides of the beam rectangular section, leaving the lower flange un-welded. The connection is attained by introducing the hooks in special inclined openings on the uprights, and by adding only one safety bolt between the upper part of the end-plate and the upright (Figs. 25 and 26). This fact, and the three sides fillet-

welding of the end plates give the vertical non-symmetry. In the horizontal direction, non-symmetry is due to the shape of the end-plate connector that has hooks at one side only (Fig. 25a). Due to these geometric characteristics, a non-symmetric response is expected under hogging and sagging bending.

Material characteristics

Two different cross-sections of the beams, G70×45×1.5mm and TG130×45×1.5mm (*height*×*width*×*plate thickness*) were considered [Fig. 27, connected to the same type of upright (100/20b type) shown in Fig. 24b]. Table 2 reports their geometrical properties.

The material of the beams and of the upright is S275 steel, its yield and ultimate stresses and the ultimate deformation are reported in Table 3.

Table 2. Geometrical properties of the upright and of the beams.

Member	Properties	Gross section	Net section
100/20b	A [mm ²]	588.8	525.7
	t [mm]	2.0	2.0
	J _x [mm ⁴]	436020	406100
	J _y [mm ⁴]	812280	694680
	W _x [mm ³]	8543	8330
	W _y [mm ³]	16747	14323
TG 70x45x1.5 mm	A [mm ²]	514.06	514.06
	t [mm]	1.5	1.5
	J _x [mm ⁴]	407500	407500
	J _y [mm ⁴]	136272	136272
	W _x [mm ³]	11754	11754
	W _y [mm ³]	4764	4764
TG 130x45x1.5 mm	A [mm ²]	697.66	697.66
	t [mm]	1.5	1.5
	J _x [mm ⁴]	1742220	1742220
	J _y [mm ⁴]	168662	168662
	W _x [mm ³]	26792	26792
	W _y [mm ³]	5171	5171

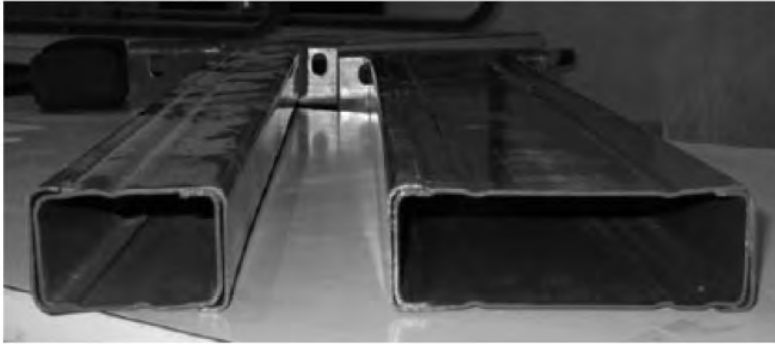


Figure 27. Type of beam (70×45×1.5mm and 130×45×1.5mm).

Table 3. Material characteristics.

Member	f_y [MPa]	f_u [MPa]	ϵ_u (%)
Beam 70x45x1.5	353.6	446.1	26.90
Beam 130x45x1.5	357.0	458.0	27.00
Upright 100x82x2.0	348.0	493.0	25.50
Beam end connector	263.0	385.0	41.10

Test-set-up

The test set-up is shown in Figures 28 and 29. Specimen size, configuration and instrumentation (Figs. 28 and 29) were adopted according to CEN (2002) and FEM 10.2.02-2001 (*The design of static steel pallet racks*) specifications, containing instructions for testing procedures.

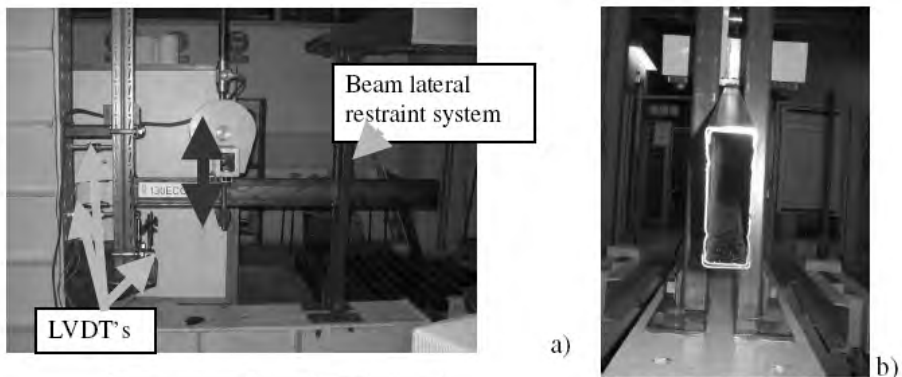


Figure 28. a) Test set-up. b) Lateral restraint system.

The load was applied through an electric actuator placed in vertical position. The out of plane movement of the beam was constrained by two vertical guides connected to the inferior girder of the reaction frame (Figs. 28 and 29).

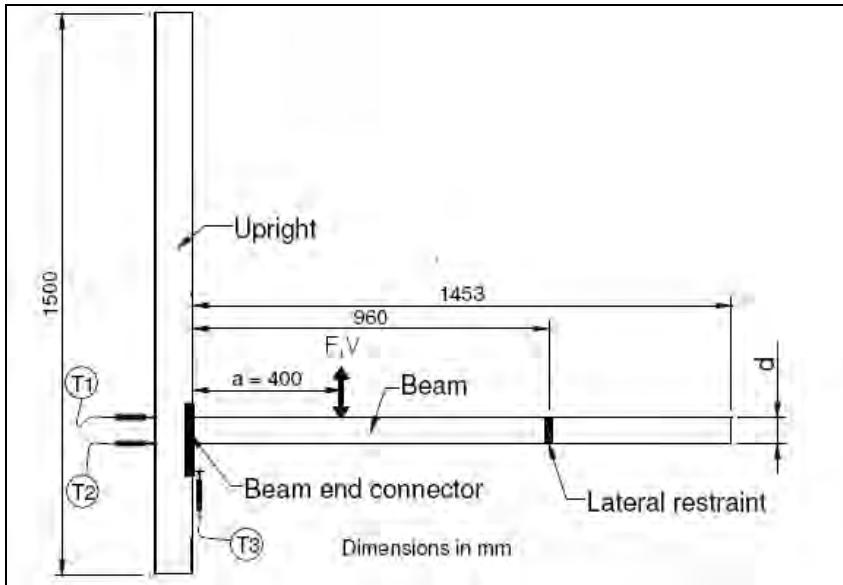


Figure 29. Specimen dimensions and instrumentation.

Controlling load and displacement were measured respectively by a double-action load cell and a displacement transducer. Other displacement transducers were assembled on the tested sub-assembly to measure the upright rotation and the vertical slip between the upright and the beam end connector.

For each test the moment-rotation curves were plotted. The bending moment was defined as $M = F \cdot a$ and the rotation of the connection as:

$$\varphi = \frac{V}{a} - \left(\frac{\delta_1 - \delta_2}{d} \right) \text{ where (Fig. 29):}$$

V = displacement due to load F ;

a = lever arm for the load F ;

δ_1 = deflection measured by transducer T1;

δ_2 = deflection measured by transducer T2;

d = beam height.

Following the proposed new cyclic testing procedure, the cyclic tests were carried out applying different levels of vertical load (namely 0%, corresponding to the ECCS procedure, 25%, 50%, 66% and 75% of the yield load F_y of the connection) at a constant distance $a = 40 \text{ cm}$, in order to simulate the presence of a service gravity load on the beam.

Considering the mean stiffness K of the node obtained from hogging monotonic tests on $70 \times 45 \times 1.5$ mm and on $130 \times 45 \times 1.5$ mm beams, and the mean stiffness K_b of these beam, the assumed distance $L_s = 40$ cm corresponds to a beam length in the real structure respectively about 3 m ($70 \times 45 \times 1.5$ mm beam) and 4.2 m ($130 \times 45 \times 1.5$ mm beam).

The yield strength F_y , as well as other relevant parameters, such as the yield displacement V_y , the ultimate strength F_u , the ultimate displacement V_u and the initial elastic stiffness $S_{j,ini}$ were conventionally defined according to ECCS (1986), with reference to the results of a monotonic test.

8. EXPERIMENTAL RESULTS

Monotonic tests on beam $70 \times 45 \times 1.5$ mm

Table 4 reports the values of the yield (M_y) and ultimate (M_u) bending moment, of the yield (ϕ_y) and ultimate (ϕ_u) rotation and of the initial node elastic stiffness ($S_{j,ini}$) measured for each test, as well as the mean values of the same parameters.

Table 4. Monotonic tests on beam-to-upright connections with $70 \times 45 \times 1.5$ mm beam.

Loading	Specimen	M_y [kNm]	ϕ_y [mrad]	$S_{j,ini}$ [kNm/rad]	M_u [kNm]	ϕ_u [mrad]
Hogging bending	70MB-1	1.30	34.7	42.7	1.58	143
	70MB-3	1.22	26.0	48.7	1.68	191
	70MB-4	1.18	22.7	52.4	1.53	202
	Average	1.23	27.8	47.9	1.60	178.7
Sagging bending	70MT-3	1.27	27.3	46.0	1.44	86
	70MT-5	1.20	24.0	49.4	1.37	76
	70MT-6	1.26	26.7	51.3	1.44	71
	Average	1.24	26.0	48.9	1.42	77.7

Figure 30 compares the moment-rotation curves for hogging (MB tag) and sagging (MT tag) bending. The specimens under hogging bending (negative moment, cantilever down) show a slightly larger ultimate strength than the specimens under sagging bending moment (positive moment, cantilever up), but about the same yield strength.

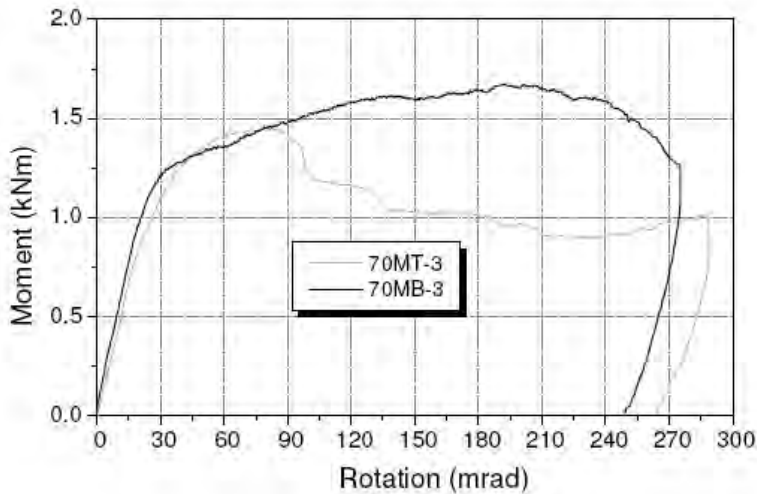


Figure 30. Moment-rotation curves for beams 70×45×1.5mm.

The obtained ductile behavior is quite different: while the initial elastic stiffness is similar, the average ultimate rotation of the specimens under hogging bending is larger than that under sagging bending. This can be explained by the unsymmetrical beam-to-upright connection and by the safety bolt only on the upper side of the beam.

The failure mode of MB specimens, subjected to hogging bending, consisted of large deformations in the top zone of the beam end connector, leading to the loosening of the hooked connection, with the hooks exiting from the holes in the upright.

The failure mode of MT specimens subjected to sagging bending was the fracture of the beam close to the weld between the beam and the end connector. For all tests the connection behavior was not influenced by the deformation of the safety bolt, while large deformations occurred in the plate, and in the plate hole for the bolt.

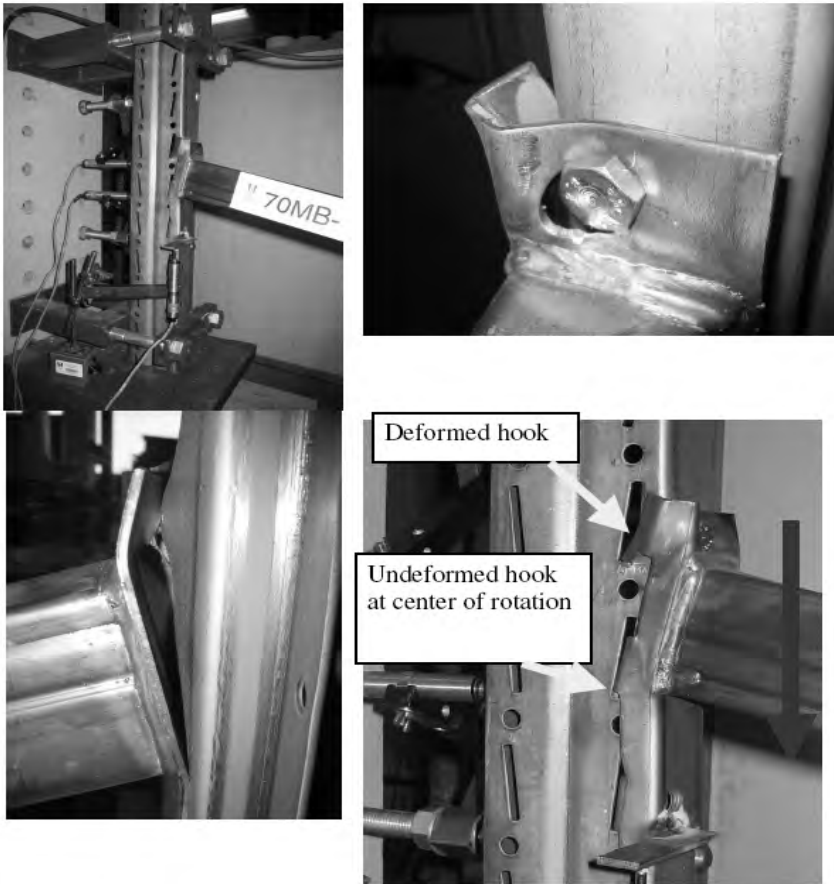


Figure 31. Monotonic tests on beam-to-upright connections with 70×45×1mm beam. Typical collapse mode under hogging bending moments.

Monotonic tests on beam 130×45×1.5mm

Figure 32 compares the moment-rotation curves for hogging (MB tag) and sagging (MT tag) bending. The specimens under hogging bending show larger ultimate moment (M_u) and ultimate rotation (φ_u), but lower initial elastic stiffness ($S_{j,ini}$) than the specimens under sagging bending moments.

The failure of both specimens subjected to hogging and sagging bending was due to large deformations in the beam end connector, resulting respectively in the top and bottom hooks coming out of the holes in the upright.

Under hogging bending the safety bolt is in tension. The presence of the bolt restrains the deformation of the upper part of the end-plate, until it is completely thrown out through the hole in the end-plate connector, but only the upper hook comes out of the opening.

On the other hand, under sagging bending, the collapse mechanism is governed by the failure of the hooks in the lower part of the end-plate connector. As the openings in the upright are inclined, for the sagging bending there is a different hook-opening interaction than in hogging situation. In fact, in sagging, failure is attained with cracks on the hooks, due their large deformation.

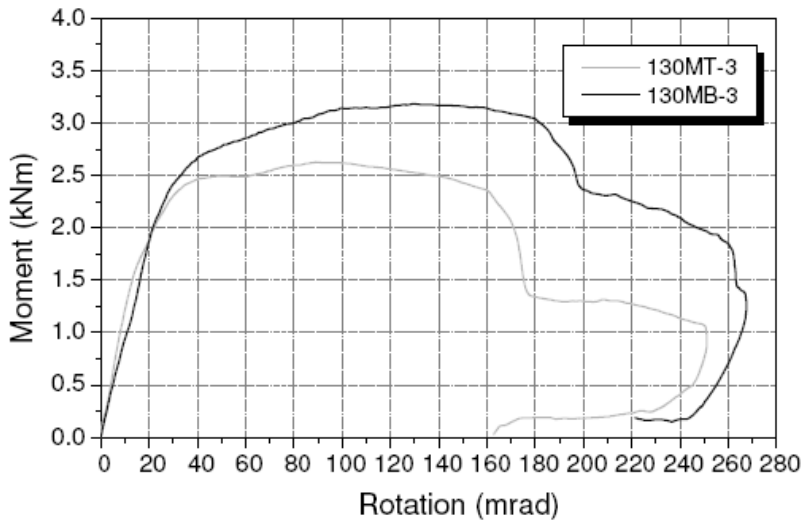


Figure 32. Comparison of the moment-rotation curves for beams $130 \times 45 \times 1.5$ mm.

Cyclic tests on beam $70 \times 45 \times 1.5$ mm

Figure 33 shows the hysteretic loops in terms of moment and rotation, for the cyclic tests performed on beam-to-upright connections specimens with beam $70 \times 45 \times 1.5$ mm.

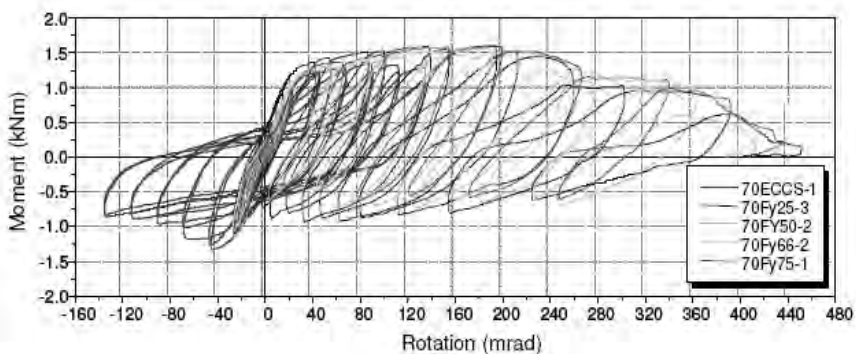
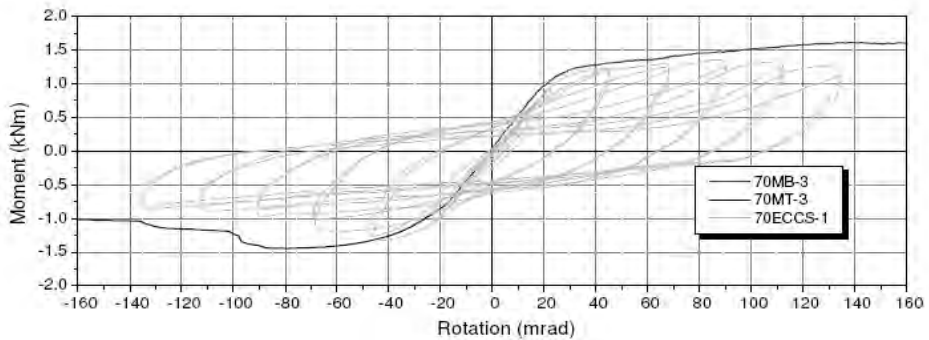


Figure 33. Cyclic tests on beam $70 \times 45 \times 1.5$ mm specimens.

Table 5. Response parameters of the cyclic tests on beam 70×45×1.5mm.

Test	$S_{j,ini}$ [kNm/rad]	M_y [kNm]	ϕ_y [mrad]	M_{u+} [kNm]	ϕ_u^+ [mrad]	M_{u-} [kNm]	ϕ_u^- [mrad]	N_c	ϕ_c [mrad]	M_c [kNm]
70ECCS-1	41.2	1.17	28.1	1.36	89.9	-1.34	-45.0	10	134.0	0.00
70ECCS-2	43.3	1.21	28.1	1.36	113.0	-1.40	-45.0	13	178.6	0.00
70Fy25-3	47.6	1.36	29.7	1.59	195.4	-0.94	65.0	11	393.1	0.30
70Fy25-4	47.7	1.22	26.0	1.55	191.2	-0.87	145.2	9	338.5	0.30
70Fy50-1	50.8	1.19	28.2	1.50	212.3	-0.81	125.1	8	427.6	0.60
70Fy50-2	50.9	1.17	28.2	1.48	197.4	-0.74	129.1	7	364.0	0.60
70Fy66-1	51.1	1.19	27.4	1.55	194.7	-0.61	74.6	6	331.5	0.79
70Fy66-2	43.8	1.20	26.4	1.57	193.0	-0.66	75.7	6	321.5	0.79
70Fy75-1	47.5	1.25	25.7	1.61	196.4	-0.64	81.7	6	342.0	0.90
<i>Average All</i>	47.1	1.22	27.5							
<i>Average ECCS</i>	42.3	1.19	28.1	1.36	101.5	-1.37	-45		156.3	
<i>Average cyclic</i>	48.5	1.23	27.4	1.55	197.2	-0.75	99.5		359.7	

**Figure 34.** Comparisons of the ECCS cyclic and monotonic tests for 70×45×1.5mm beam specimens.

In tests performed according to the innovative cyclic testing procedure, the imposed displacement history is unsymmetrical. In fact, displacements tend to systematically accumulate in the positive direction.

The response parameters for all cyclic tests are presented in Table 5 where, in addition to the elastic parameters (initial stiffness $S_{j,ini}$, yield moment M_y and rotation ϕ_y), the maximum positive (hogging) moment (M_{u+}) and correspond-

ing rotation (φ_{u+}), as well as the minimum negative (sagging) moment (M_{u-}) and corresponding rotation (φ_{u-}) are reported, together with the number of cycles to failure N_c , the failure rotation φ_c and the bending moment for gravity loads (M_g).

The cyclic tests show practically the same initial stiffness of the monotonic tests (as shown in Fig. 34, in the case of an ECCS test).

The strength of the specimens is shifted in the positive (hogging) direction for the new testing procedure, while, in the case of ECCS tests, the load carrying capacities under positive and negative bending are not excessively different, apart from the small asymmetry that may result from the unsymmetrical connection details.

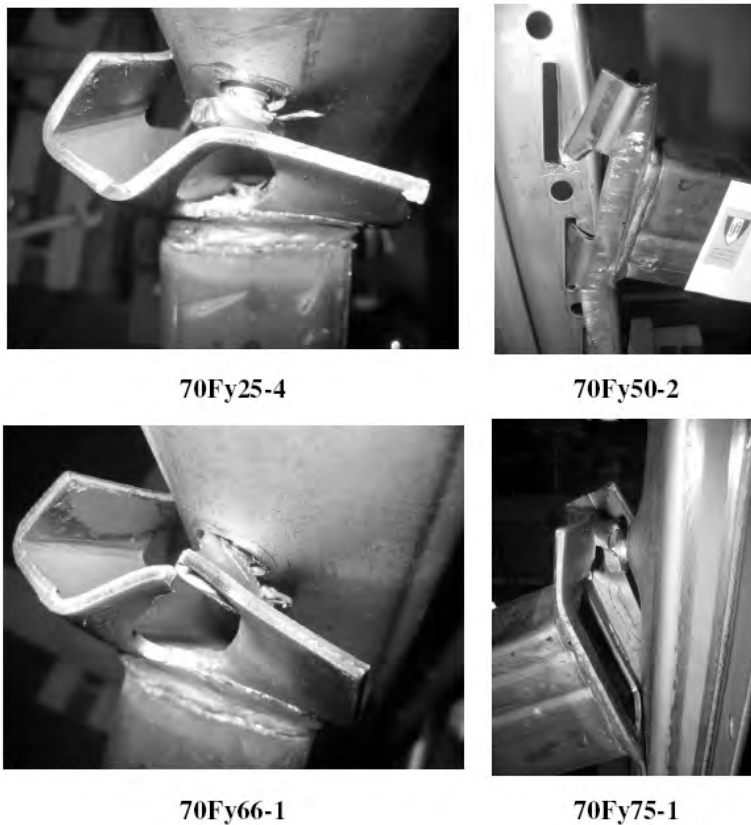


Figure 35. Cyclic tests on 70×45×1.5mm beam specimens – failure modes.

The innovative testing procedure allows a clear assessment of the detrimental effects of the magnitude of the gravitational loads, that result in a reduction of the available ductility as the magnitude of the gravitational loads increases, leading to premature collapse.

According to the previous definitions, connection 70Fy50-2 exhibited type I failure mode, while all other specimens exhibited failure mode type II. Premature collapse occurred as the magnitude of the gravity loads increased. In all cyclic tests, the observed collapse mechanisms were the same as in monotonic tests under hogging bending, but with amplified displacements. At the end of some tests with gravitational force 50%, 66% and 75% of the yield strength, fracture of the beam end-plate connector occurred around the upper hole (Fig. 35).

Cyclic tests on beam 130×45×1.5mm

Figure 36 shows the hysteretic loops in terms of moment and rotation, for the cyclic tests performed on beam-to-upright connections specimens with beam 130×45×1.5mm.

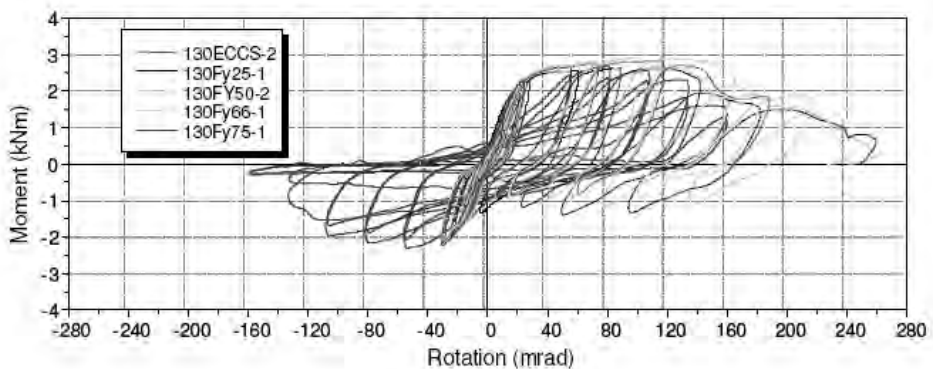


Figure 36. Cyclic tests on beam 130×45×1.5mm specimens.

The cyclic tests show practically the same initial stiffness when compared to the monotonic tests (as shown in Fig. 37, in the case of an ECCS test). The degrade of the resistance during the cyclic test (130ECCS-3) was nearly the same for both ways of loading (hogging and sagging bending).

Premature collapse as well as a reduction of the rotation capacity was observed when the magnitude of the gravity load increased. At the end of the test the beam end connector was tied to the upright only by means of the bolt, which sometimes punched through the end-plate connector. According to the previous definitions, the collapse mode for the connections part type I and part type II.

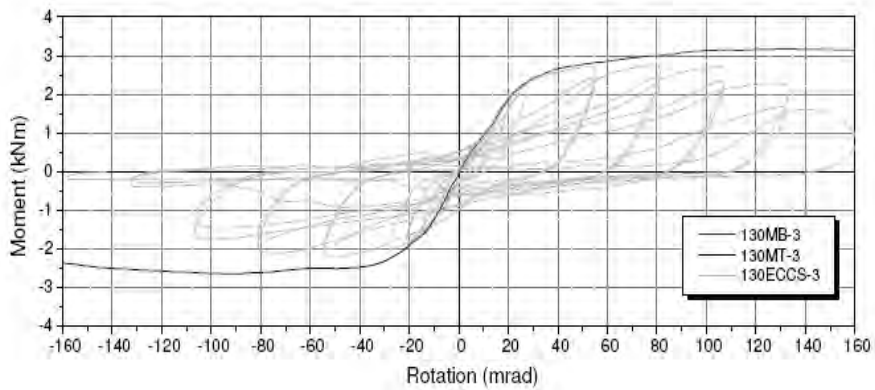


Figure 37. Comparisons of the cyclic and monotonic tests for 130×45×1.5mm beam.

Comparison of the results in terms of beam size

The effect of the beam size and of the gravity loads on the hysteretic loops is shown in Figure 38 and Figure 39, respectively with reference to ECCS and to the innovative cyclic tests, as well as in Table 6 which summarizes the mean values of the response parameters for both 70×45×1.5mm (a) and 130×45×1.5mm (b) beam, with different values of the gravity loads.

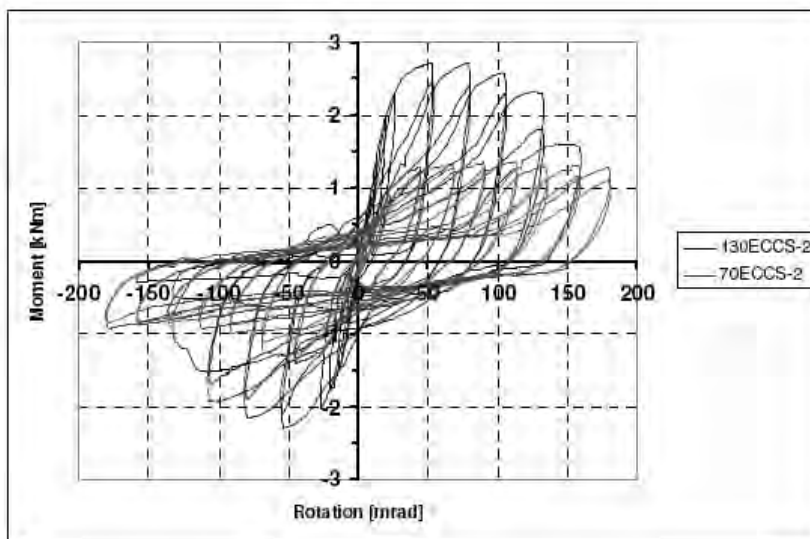


Figure 38. Effect of the beam size – ECCS cyclic tests.

Table 6, in addition to the elastic parameters (i.e. initial stiffness $S_{j,ini}$, yield moment M_y and rotation φ_y , the maximum positive –hogging - moment M_{u+} and corresponding rotation φ_{u+} , as well as the minimum negative – sagging - moment M_{u-} and corresponding rotation φ_{u-}) reports the number of cycles to failure N_c , the failure rotation φ_c and the bending moment for gravity loads M_g . It is evident that the response of the connections under symmetric cycles and in absence of gravity loads (ECCS tests, Figure 40) is very different from that of the same connections tested in presence of gravity loads (Fig. 41).

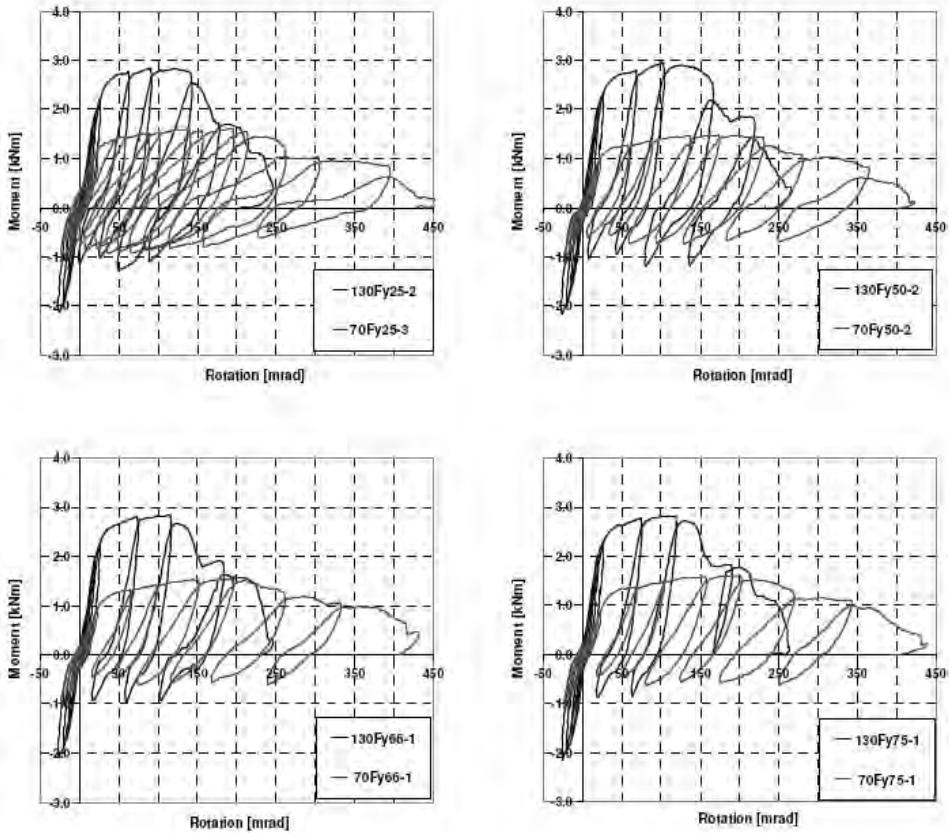


Figure 39. Effect of the beam size and of the gravity loads – cyclic tests.

In particular, the response of the specimens tested in presence of gravity loads is characterized by cyclic creep, with a progressive accumulation of plastic deformation in the same direction of the mean applied load. The measured cyclic creep rate increases with the applied gravity load.

The collapse of the connection is attained approximately under the same rotation φ_c (360 mrad for 70×45×1.5mm beams and 192 mrad for

130×45×1.5mm beams), although some dependence of φ_c on the applied gravity load can be observed, at least for large values of the gravity load (66% and 75% of the yield value). Connections of beams supporting a high gravity load collapse at a number of cycles N_c smaller than those supporting a smaller gravity load, due to the different creep rate.

Table 6. Mean values of response parameters for 70×45×1.5mm (a) and 130×45×1.5mm (b) beams.

	M_g [kNm]	$S_{j,ini}$ [kNm/rad]	M_y [kNm]	ϕ_y [mrad]	M_{u^+} [kNm]	ϕ_{u^+} [mrad]	M_{u^-} [kNm]	ϕ_{u^-} [mrad]	N_c	ϕ_c [mrad]
70-ECCS	0.00	42.25	1.19	28.10	1.36	101.45	-1.37	-45.00	11.5	156.30
70-Fy25	0.30	47.65	1.29	27.85	1.57	193.30	-0.91	105.10	10	365.80
70-Fy50	0.60	50.85	1.18	28.20	1.49	204.85	-0.78	127.10	7.5	395.80
70-Fy66	0.79	47.45	1.20	26.90	1.56	193.85	-0.64	75.15	6	326.50
70-Fy75	0.90	47.50	1.25	25.70	1.61	196.40	-0.64	81.70	6	342.00

a)

	M_g [kNm]	$S_{j,ini}$ [kNm/rad]	M_y [kNm]	ϕ_y [mrad]	M_{u^+} [kNm]	ϕ_{u^+} [mrad]	M_{u^-} [kNm]	ϕ_{u^-} [mrad]	N_c	ϕ_c [mrad]
130-ECCS	0.00	94.65	2.49	24.05	2.75	79.40	-2.27	-53.05	9.5	157.50
130-Fy25	0.63	93.65	2.45	25.00	2.74	120.50	-1.33	51.05	4.5	217.60
130-Fy50	1.26	105.35	2.58	28.95	2.93	128.55	-1.16	105.20	4	214.55
130-Fy66	1.66	88.50	2.43	22.95	2.79	113.90	-1.07	119.70	3	182.80
130-Fy75	1.89	107.00	2.47	24.20	2.83	118.70	-0.87	63.00	2	118.30

b)

The hysteretic loops are clearly non symmetric, with similar maximum values of the hogging moment M_{u^+} and of its corresponding rotation φ_{u^+} , practically independent on the applied gravity load, but with the minimum values of the sagging moment M_{u^-} and of its corresponding rotation φ_{u^-} becoming (in absolute value) smaller and smaller when the gravity load increases.

Of course, the elastic parameters (i.e. initial stiffness $S_{j,ini}$, yield moment M_y and rotation φ_y) are not influenced by the value of the applied gravity load.

In absence of gravity load (ECCS tests), the response of the specimens is nearly symmetric; a small asymmetry is due to the different response of the connection under hogging and sagging bending, already highlighted in the case of monotonic tests.

In particular, it should be noticed that under sagging bending the connections show a lower ductility than under hogging bending ($\varphi_{u^-} < \varphi_{u^+}$). The values of M_{u^+} , φ_{u^+} , M_{u^-} and φ_{u^-} are (in absolute value) smaller than those measured in monotonic tests, because obtained under cyclic loading.

Differences can also be noticed in the failure modes of the different specimens.

In absence of gravity loads (ECCS tests), the failure occurred always under sagging bending, i.e. under the loading condition for which the connection showed the lower strength and ductility in monotonic tests.

Also in the case of $130 \times 45 \times 1.5$ mm beams, the collapse mechanism for cyclic (ECCS) tests is similar to that described for monotonic tests under sagging bending.

In presence of gravity loads, on the contrary, failure occurred always under hogging bending.

No difference could be noticed in the failure mechanisms under increasing values of the gravity loads, but only a smaller number of cycles to failure.

Comparison between the cyclic procedures

A comparison between the results obtainable by means of the ECCS and of the innovative testing procedure is presented hereafter in the case of tests on $130 \times 45 \times 1.5$ mm beams, without compromising the generality of the conclusions.

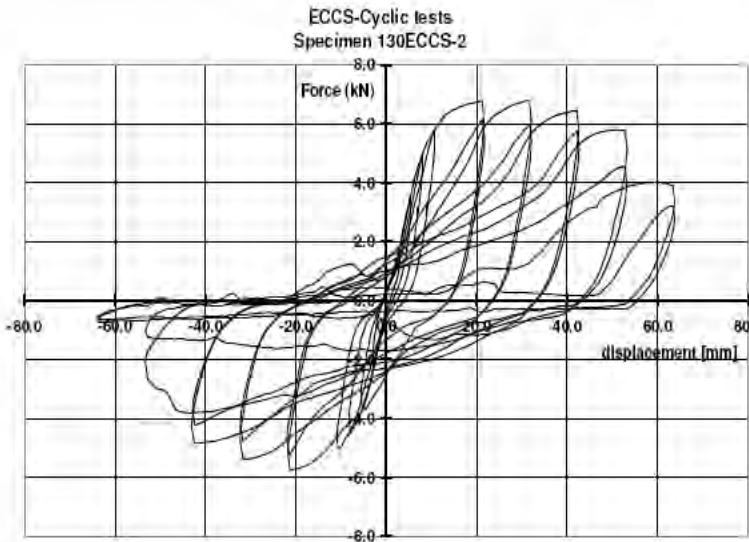


Figure 40. ECCS cyclic test results for 130mm height beam specimen.

ECCS-type cyclic test results can be exemplified in Figure 40, which shows the force-displacement graph for specimen 130ECCS-2.

The force-displacement graph is almost symmetrical with some slight differences in the positive and negative strength, which result from the unsymmetrical details of the beam-to-upright connection, as previously explained.

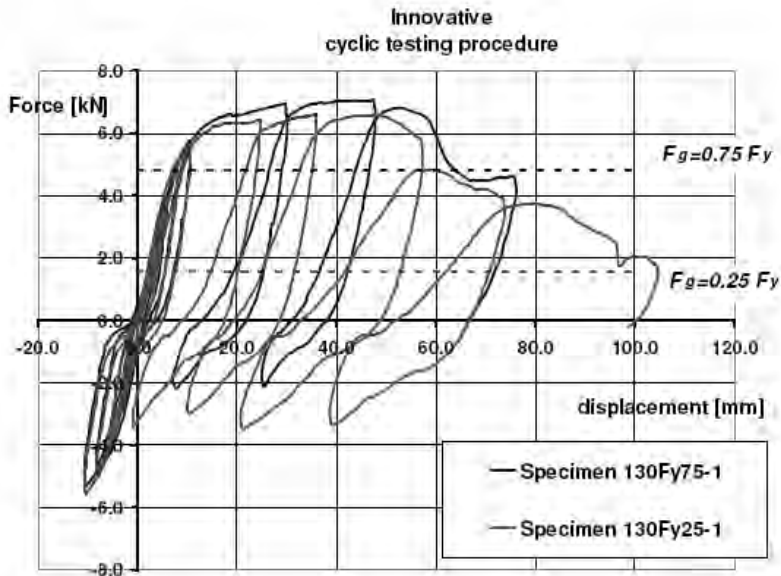


Figure 41. Innovative cyclic testing procedure results for tests 130Fy25-1 and 130Fy75-1.

Figure 41 represents the innovative cyclic testing procedure results. The first elastic cycles are similar in both types of test (ECCS and the proposed hybrid procedure), but the following cycles (as for all the remaining tests conducted with the innovative cyclic testing procedure) are fundamentally different.

Among the others, the following differences can be identified:

- Imposed displacement history is unsymmetrical in the tests performed according to the new hybrid procedure.
- Displacements tend to systematically accumulate in the positive direction.
- Imposed forces are shifted in the positive (hogging) direction for the innovative testing procedure. On the contrary, apart from the asymmetry that may result from unsymmetrical connection detailing, positive and negative force amplitudes for ECCS tests are not excessively different.

Hence, the innovative testing procedure manages to capture the detrimental effects of the gravitational loads magnitude, that can lead to premature collapse.

Moreover failure of the connection is explicitly addressed by the innovative testing procedure since failure occurs when the connection is no longer able to withstand vertical load effects.

On the other hand, application of the innovative cyclic testing procedure led to a displacement history that could not be predicted a-priori, as a consequence

of the force controlled part of the cycles. Loading histories applied in tests with different values of F_g are different, as can be observed in Figure 39.

In test 130 Fy25-1 the specimen was subjected to elastic cycles, after which it endured two cycles of $\pm 2V_y$ and $\pm 4V_y$ and failure occurred in the first positive $6V_y$ displacement cycle.

In test 130 Fy75-1 the specimen failed in the first positive cycle with $4V_y$ amplitude.

9. CONCLUSIONS

Considering the former limitations of the commonly accepted testing procedures, it has been presented a new cyclic procedure that can be interpreted as a logical development of the former ones. This innovative cyclic procedure explicitly considers the vertical load effects on the critical cross-sections. The proposed loading history consists of a sequence of force-controlled and displacement controlled parts of cycles that account for the hybrid nature of earthquake actions when acting simultaneously with other (gravitational) loads. Failure can consequently be defined objectively as the loss of capacity to withstand vertical loads, as a result of accumulated damage.

In fact, the proposed procedure clearly shows the detrimental effects that result from higher gravitational loads, conveniently expresses as a fraction of the yielding loads, on the bearing capacity of the structure subjected to reversal actions.

REFERENCES

Note:

The results of the bibliographic research performed on the state of the art on low cycle fatigue testing and the references to papers indicated in the previous text, are not reported, as they extend on many pages.

However these bibliographic data are available from the authors, who will send them by request.

TESTS AND ANALYSIS OF STRUCTURES AND JOINTS FOR STEEL-CONCRETE MOMENT-RESISTING FRAMES AND STEEL-CONCRETE BOX-GIRDER BRIDGES

Oreste S. Bursi¹, Fabio Ferrario¹, Raffaele Pucinotti², Nicola Tondini¹,
Riccardo Zandonini¹

¹ *Department of Mechanical and Structural Engineering,
University of Trento, Trento, Italy*

² *Department of Architectural and Urban Patrimony,
Mediterranean University of Reggio Calabria, Reggio Calabria, Italy*

Abstract. A multi-objective advanced design methodology is proposed in the first part of this chapter for steel-concrete composite moment-resisting frames. The research activity mainly focussed on the design of beam-to-column joints under seismic-induced fire loading together with the definition of adequate structural details for composite columns. Thermal analyses of cross sections were performed in order to obtain internal temperature distribution; structural analyses were then performed on the whole frame, to assess the global behaviour under the combined action of static and fire loadings. Besides, results of numerical analyses were used in order to derive information about the mechanical and numerical behaviour of joints. Moreover, the experimental program carried out at the Laboratory for Materials and Structures of the University of Trento on four full-scale substructures representing interior full-strength bolted beam-to-column joint specimens are described and experimental results are presented and discussed together with the outcomes of numerical simulations. Since beam-to-column joints are rigid and inelastic phenomena occurred in adjacent beams, it was justified to assume that bolted joints behaved like welded joints. As a results fire tests on welded joints, carried out on both pre-damaged and undamaged specimens at the Building Research Establishment in UK, were considered to be representative for bolted joints too. Therefore, since the scope of the project was to promote joint typologies able to survive a seismic-induced fire before being subjected to fire loadings, specimens were damaged by imposing monotonic loads equivalent to damage induced by seismic excitations. Thus, valuable information was obtained about the performance of the proposed joint typology. Experimental tests demonstrated the adequacy of both seismic and fire design and numerical simulations showed a satisfactory performance of joints under seismic-induced fire loadings.

This contribution also investigates the performance of steel-concrete composite box-girder bridges in the second part of the chapter. The first advantage of the box-girder typology lies in a high stiffness and strength for minimum weight. In addition, box-girder sections exhibit high torsional rigidity and therefore they are suitable to be used

for curved spans. As a result, this research mainly focussed on the analysis of one existing steel-concrete composite box-girder viaduct that has to be retrofitted, giving more attention to steel elements and connections that the box-girder is composed of, both with regard to static and seismic behaviour. Moreover, the assessment of the remaining life of the bridge was also performed. In detail, the finite element (FE) model of the bridge as originally designed was developed and it allowed to identify the critical details, by checking the bridge both statically and seismically through the application of the new Italian Building Code. A main issue was represented by the calibration of the FE model used for a subsequent reliability analysis. The uncertainties related to the mass, and in particular to the stiffness of the bridge were very high owing to an advanced corrosive degradation of the steel inside the box. With this regard an in-situ output-only ambient vibration dynamic identification test of the bridge was carried out. The results of the test were subsequently used to perform the FE model updating by employing the inverse eigensensitivity method. Finally by using the updated FE model, the study was completed by performing a reliability analysis in order to compute the β reliability index used to estimate the residual performance of the bridge. The reliability analysis for the midspan bending moment showed that the bridge can be deemed safe.

Keywords: composite joints, steel, concrete, moment-resisting frames, earthquake, seismic-induced fire loading, box-girder bridges, fatigue, dynamic identification tests, output-only ambient vibration tests, FE model updating.

1. INTRODUCTION

Steel-concrete composite structures are becoming increasingly popular around the world due to the favourable stiffness, strength and ductility performance of composite systems under seismic loading, and also due to the speed and ease of erection. Moreover, such structures exhibit better fire resistance characteristics compared to bare steel structures. Considering the high probability of a fire after a seismic event, the use of steel-concrete composite structures in seismic areas, potentially represents a fairly effective design solution. In fact, the adoption of such a solution is in general more efficient from both a structural and a constructional viewpoint when compared to bare steel structures. The benefit increases, if the high probability that an earthquake and a fire can occur in sequence. In current Eurocodes for structural design, seismic and fire safety are accounted for separately, and no sequence of seismic and fire loading is taken into account. In reality, the risk of loss of life increases if a fire occurs in a building after an earthquake. In the Kobe Earthquake (1995) many people died due to the collapse of buildings exposed to a fire that followed an earthquake; in fact, large sections of the city burned, greatly contributing to the loss of lives. It is obvious therefore that seismic-induced fire is a design scenario that should be properly addressed in any performance-based seismic design. In this situation the traditional single-objective design is not adequate, and a multi-objective advanced design has to be adopted. This enables a proper account of: (i) seismic safety with regard to accidental actions; (ii) fire safety with regard

to accidental actions (iii) fire safety on a structure characterized by stiffness deterioration and strength degradation due to seismic actions. As a result, the fire design applied to a structure with reduced capacity due to seismic damage will permit simultaneous fulfilment of the requirements associated with structural, seismic and fire safety, and with structural fire safety and structural seismic safety separately taken as accidental actions. In order to characterize the seismic behaviour of composite joints, a research project has been carried out by the University of Trento with the objective of developing a design procedure for composite joints under the 'combined' action of earthquake and post-earthquake fire. The research activity was mainly concerned with the design of bolted beam-to-column joints with CFT columns with circular hollow steel sections. This solution derives from a parent welded design solution developed in an European project (Bursi et al., 2008) and is aimed at ensuring easiness of assembly and avoiding the problems related with on site welding. The project achieved its objectives through a balanced combination of analytical/numerical and experimental work; for which we present: i) the frame design and the definition and the joint design for seismic and fire loadings; ii) the analysis of the mechanical and thermal behaviour of this typology by means of experimental tests; iii) results from moment resisting frames endowed with the investigated joint solution under seismic loading.

Besides the part relative to steel-concrete composite joints in buildings, a second part of the chapter aimed at studying the performance of steel-concrete composite bridges. Bridge engineering has always been a branch of civil engineering that has attracted great interest, because it deals with structures of fundamental importance for the economic framework of a region. The strategic significance of a bridge in a road network is clear, since it connects two distinctive areas allowing a fast access that otherwise would be prevented. Its characteristics should remain unaltered during its entire lifetime to guarantee full functionality, above all in cases of emergency caused by environmental hazards, like earthquakes, floodings etc. On the basis of several factors, among others, span, location, soil, aesthetics, costs, etc., the bridge can be designed according to different typologies. For instance, a box-girder section can represent an effective and economical solution when dealing with curved bridges.

In detail, the box-girder typology is commonly employed for span ranges between 30-150 m both for steel or steel-concrete composite bridges and concrete bridges, the latter usually with a prestressed deck. The first advantage of this type of section lies in a high stiffness and strength for minimum weight. This characteristic becomes more important when the span gets longer and consequently dead loads begin to be more significant. Moreover, box-girder sections exhibit high torsional rigidity and therefore they are very suitable to be used for curved spans in the horizontal plane.

On the basis of the span and material as well as of the location of the bridge, we can focus on different main aspects that characterise a bridge structure. In

steel and steel-composite structures in general, detailings are fundamental since may influence considerably their performance, both during their construction and fabrication and their service life. In addition, box-girder bridges are more sensitive to this aspect as detailings usually have a larger extent in structures conceived according to this typology.

Furthermore, particular attention should be paid to the maintenance of bridges as a general good practice, but above all to those with a low degree of redundancy as most steel bridges commonly are. In fact, steel bridges are not suitable for a frame typology since piers are usually made of concrete and a fixed connection between the steel deck and the concrete piers is extremely difficult to make, and therefore, it is not advisable. Conversely, concrete bridges do not suffer from this issue since continuity between the superstructure and the substructures is widely employed. Furthermore, the presence of many road joints, if not well maintained, is the principal source of deterioration especially in box-girder bridges with a continuous bottom plate that prevents the water containing salts and pollution to run off.

In Italy, the new building code, (NTC, 2005) now superseded by the NTC (2008), introduced, by means of the OPCM-3274 (2003) and its integration OPCM-3431 (2005), a new approach in the seismic design of structures as well as a new seismic classification of the national territory. This entailed that portions of the country that previously were not classified as seismic sensitive, suddenly changed their requirements low-seismicity zones. This implied that existing strategic structures, like bridges, schools, hospitals, etc., had to be checked against a possible seismic event. With regard to the design of new bridges the OPCM-3431 (2005) imposes that the deck remains elastic during a seismic event; and that the energy introduced by the ground motion should be dissipated by the substructures or particular seismic isolation devices. Therefore, if the bridge is not seismically designed, it does not present any particular detailing able to dissipate seismic energy, so that the deck might experience low-cycle fatigue in critical details that shall be identified. As a result, one existing steel-concrete composite box-girder viaduct that has to be retrofitted is analysed, giving more attention to steel elements and connections that the box-girder is composed of, both with regards to static and to seismic behaviour. Output-only ambient vibrations tests are carried out in order to calibrate the finite element (FE) model by employing a model updating procedure. Finally, by using the updated FE model the study is completed by performing a reliability analysis in order to identify possible different sensitive details as well as to assess the static residual performance of the bridge.

2. ANALYSIS AND DESIGN OF BEAM-TO-COLUMN JOINTS

Reference Frames: Seismic and Fire Design

A reference composite steel-concrete office building was considered, made up of three bays five storeys moment resisting frames, placed at a distance of 7.5 m each in the longitudinal direction and braced in the transverse direction. The storey height was equal to 3.5 m. Two moment resisting frames, having the same structural typology but different slab systems, were analysed: i) a composite steel-concrete slab with a structural profiled ribbed steel sheeting; ii) a concrete slab composed of electro-welded lattice girders. Since the two slab systems had different load bearing capacities, a different distance between the secondary beams was adopted for the two solutions. The distance slightly affected the frame geometry. The first solution (steel sheeting slab), is depicted in Figure 1a while the second one, with the slab on prefabricated lattice elements, is shown in Figure 1b. The elevation is shown in Figure 1c (Bursi O.S. et al., 2008).

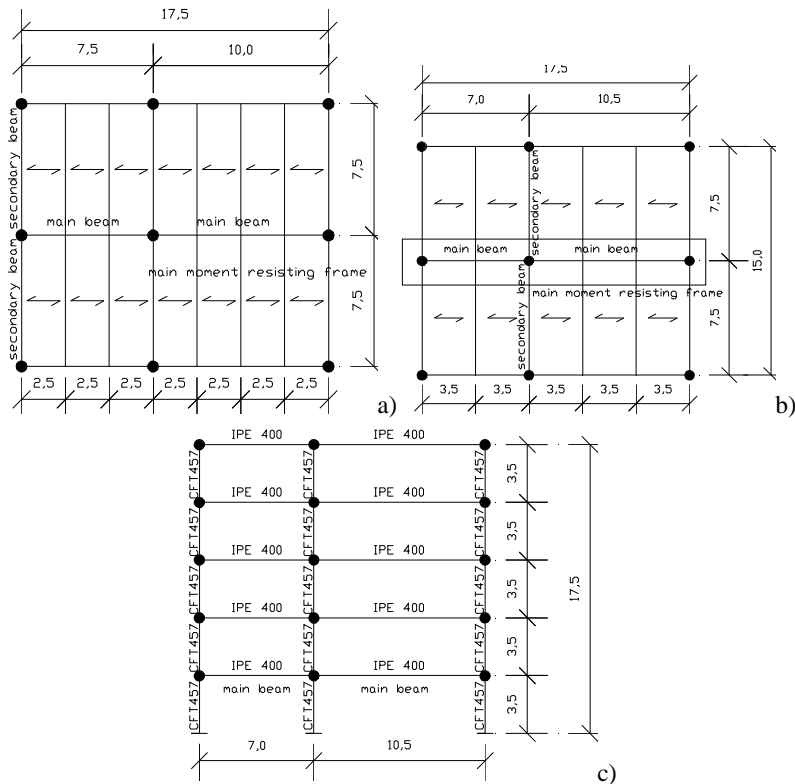


Figure 1. The configuration of building and the longitudinal five-storey MR frame; building endowed with a slab characterized by a) profiled ribbed steel sheeting; b) prefabricated lattice girder; c) frame elevation.

Two different types of composite beams were hence designed according to EC4-1 (2005); the steel section was maintained in both cases as an IPE400 of steel grade S355. The slab, 150 mm deep, was designed in accordance with the relevant specifications of Section 9 of EC4-1 (2005); moreover design procedure indicated by the producer of the prefabricated lattice elements was followed in the second case. All connections between the steel beam and the slab were made by Nelson 19 mm stud connectors made of steel with an ultimate tensile strength $f_u=450$ MPa. The frames were designed to have a dissipative structural behavior according to EC8 (2005). In detail the two following structural types were considered: Moment Resisting Frames and Concentrically braced frames (EC8, 2005). The effective width of the slab in composite beams was determined according to EC4 (2005) for static and fire analyses, and to EC8 (2005) for seismic analyses. Beam-to-column connections resulted to be rigid according to EC4-1 (2005) criterion. The design of structural elements were performed considering static and seismic design situations.

Numerical simulations on two-dimensional (2D) frames, were first performed by means of the SAFIR program (Franssen, 2005), in order to study different fire scenarios acting in the reference buildings and to evaluate the performance of different elements, i.e. composite beams, composite columns, and beam-to-column joints, under fire load for different times of exposure to fire. Five fire scenarios were considered as depicted in Figure 2.

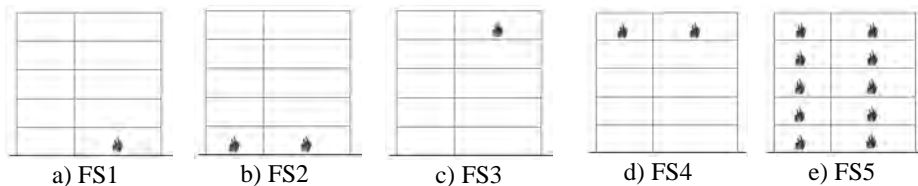


Figure 2. Fire scenarios considered in thermal analysis.

The fire load followed the ISO 834 (1999) fire law. The results of the analysis shows that the frame collapses because of the formation of a beam mechanism in the longest span involving the formation of three plastic hinges located at mid-span and at both beam ends near supports.

The beam-to-column joint design aimed at ensuring a joint overstrength with respect to the beam. The proposed bolted solution derives from a parent welded design (Bursi et al., 2008) shown in Figure 3a and it was conceived to guarantee easiness of assembly and to avoid problems related to welding on site. The joint comprised of two horizontal diaphragm plates and a vertical through-column plate attached to the tube by groove welds as indicated in Figure 3b. The flanges and the web of each beam were connected to the horizontal plates and the vertical plate by two and three rows of bolts M27 10.9, respectively. Apart from the slab type, also the joints differed due to the presence of strengthening plates with holes required by EC8 (2005) to avoid brittle fracture

in the net sections of bolted joints. Thus, specimens JB-P1 and JB-S1, see Table 1, where endowed with extra plates; whereas JB-P2 and JB-S2 had no plate being non-dissipative joints.

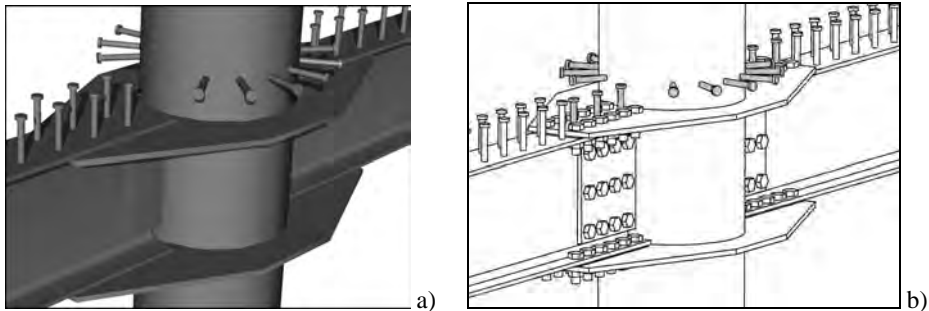


Figure 3. Steel-concrete composite joint: a) welded solution; b) bolted solution.

Beam-to-column joint design was developed using the component method (Fig. 4). The joint was simulated by a series of different components in agreement with EC3-1-8 (2005) and EC8 (2005) achieving the necessary over-strength of the joint with respect to the connected composite beams. Stiffness and strength of complex components, like top and bottom plates or concrete slab in compression, were defined by means of refined Finite Element (FE) models of the joint including friction between the slab and the column (Figs. 5 and 6).

Table 1. Major experimental data.

Name	Test Method	d [mm]	F [kN]	*M [kNm]	N	Type of Specimen
JB-P1	Cyclic	210	+655.09 -680.92	+1047.2 -747.75	22	Specimen with electro-welded lattice girders slab and Nelson connectors around the column, with reinforcement plates
JB-P2	Cyclic	210	+666.70 -657.60	+892.60 -760.23	20	Specimen with electro-welded lattice girders slab and Nelson connectors around the column, without reinforcement plates
JB-S1	Cyclic	210	+647.12 -639.66	+760.09 -537.59	20	Specimen with profiled Steel Sheeting slab and Nelson connectors around the column with reinforcement plates
JB-S2	Cyclic	175	+627.19 -634.58	+887.46 -636.37	19	Specimen with profiled Steel Sheeting slab and Nelson connectors around the column, without reinforcement plates
* + Sagging Moment; - Hogging Moment						

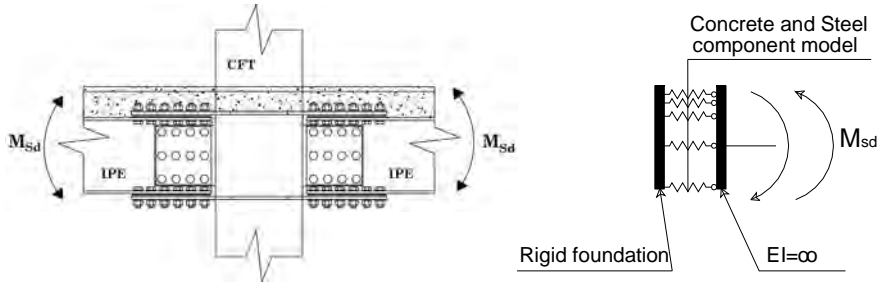


Figure 4. Mechanical model of a steel-concrete composite interior joint.

Depending on the level of friction, the distribution of the compression forces in the slab under sagging bending moment was found to be different: it is localised in front of the column for a friction coefficient equal to 0.35 as indicated in Figure 6a, while it spreads over a more extended portion of the slab due to increasing values of the friction coefficient. In detail, the diffusion angle becomes greater than 80 degrees for a friction coefficient of about 1.

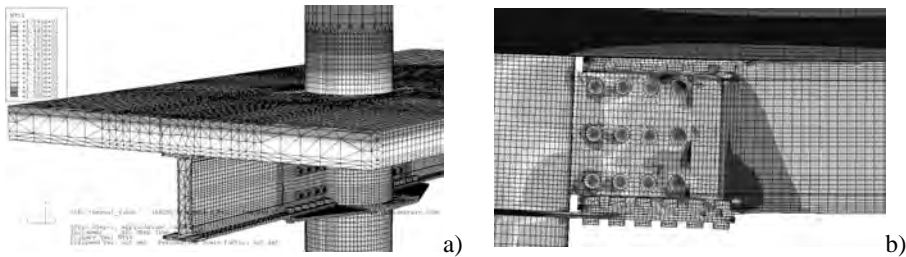


Figure 5. FE model a joint endowed with a prefabricated lattice girder slabs a) thermal analysis: temperature distribution; b) mechanical analysis: plastic hinge.

The results show that, in order to activate the transfer mechanisms proposed in EC8 (2005), i.e. Mechanism 1 front mechanism and Mechanism 2 strut and tie mechanism, as illustrated in Figure 6b, it is necessary to increase the level of friction between the concrete slab and the composite column.

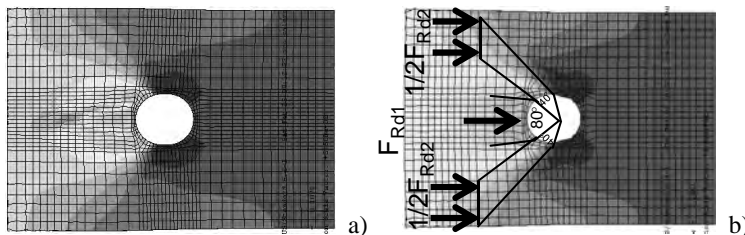


Figure 6. Distribution of compression stresses in the slab for: (a) a friction coefficient equal to 0.35; b) a friction coefficient equal to 1.

As a result, Nelson 19 mm stud connectors welded around the column were used in the tested specimens as indicated in Figure 3b. As a result, beam-to-column joints were rigid full-strength joints satisfying the relation:

$$M_{j,Rd} \geq s \cdot \gamma_{ov} \cdot M_{b,pl,Rd} \quad (1)$$

in which $M_{j,Rd}$ is the resisting moment of full-strength beam-to-column joints and $M_{b,pl,Rd}$ is the resisting moment of the composite beam (EC8, 2005). Moreover, the ductile behaviour of joints was guaranteed by the following relationships:

$$R_{d,bolt} \geq s \cdot \gamma_{ov} \cdot R_{pl,Rd,beam} \quad (2)$$

$$R_{d,bolt} \geq R_{pl,Rd,plates} \quad (3)$$

$$F_{v,Rd} \geq F_{b,Rd} \quad (4)$$

where $s = \min\{f_t/f_y; 1.25\}$, $\gamma_{ov} = 1.1$, $R_{d,bolt}$ is the design strength of bolts, $R_{pl,Rd,beam}$ is the plastic design strength of the beam, $R_{pl,Rd,plates}$ is the plastic design strength of the plates, while $F_{v,Rd}$ and $F_{b,Rd}$ are the design shear strength and design bearing resistance of bolts, respectively. The following conditions were also fulfilled for joints JB-P1 and JB-S1 to avoid brittle fracture in the net sections, i.e.:

$$\frac{0.90A_{net}f_u}{\gamma_{M2}} \geq \frac{A_f f_y}{\gamma_{M0}} \quad \text{and} \quad \frac{0.90A_{net}f_u}{\gamma_{M2}} \geq \frac{A_f f_y}{\gamma_{M0}} \quad (5)$$

where A_f is the area of the tension flange. Nevertheless, being non-dissipative joints, JB-P2 and JB-S2 did not. A 3D finite element model of the interior joint, shows in Figure 5 was implemented in the Abaqus 6.4.1 code (Hibbitt et al., 2000). Then, beam-to-column joints subjected to fire load were designed. In particular, the component approach, exclusively applied to the moment-rotation-temperature behaviour, was adopted, in the absence of axial thrust owing to the thermal expansion restraint of the beam. A simplified model was derived, which can predict the moment-rotation-temperature characteristic of the joint. As a result, at high temperatures, the joints were designed to transfer shear forces owing to vertical loads from one beam to the other. Accordingly, vertical through column plate, top horizontal plate together with Nelson stud connectors welded around the column were arranged (see Fig. 3b). In addition, two longitudinal steel rebars were added to the slab to reduce the damage produced by the seismic actions before fire (Fig. 7).

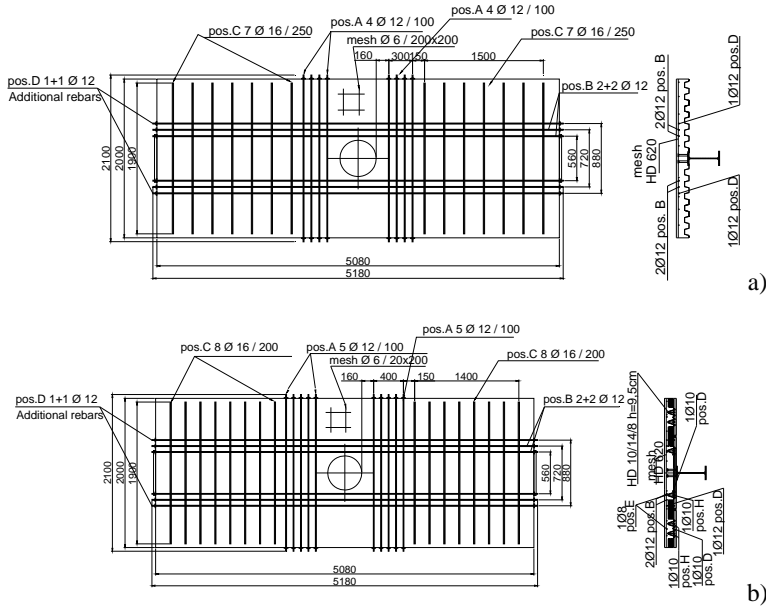


Figure 7. Slab reinforcement of a) a profiled steel sheeting slab; b) of a prefabricated lattice girder slab.

Experimental Tests Results

The experimental programme consisted of 4 tests under cyclic loading of full-scale substructures representing an interior full-strength bolted beam-to-column joint (Fig. 8). Experimental tests were carried out at the Laboratory for Materials and Structures of the University of Trento. Joint specimens were subjected to cyclic loadings up to collapse, according to the ECCS (1986) stepwise increasing amplitude loading protocol, modified with the SAC procedure (1997) by using $e_y = 0.005h = 17.5$ mm where h represents the storey height.



Figure 8. Bolted beam-to-column specimens a) slab with electro-welded lattice girders, b) slab with profiled steel sheeting.

The slab reinforcement, in the composite steel-concrete beams with steel sheeting, consisted of 2+2 ϕ 12 longitudinal steel rebars in order to carry the hogging moment, and of 4+4 ϕ 12@100 mm and 7+7 ϕ 16@250 mm transverse steel rebars, in order to enable development of the seismic slab-to-column transfer mechanism as well as the resistance to the shear force. A mesh ϕ 6@200x200 mm is also present as shown in Figure 7a. Two additional longitudinal rebars 1+1 ϕ 12 were designed to resist seismic damage, as illustrated in Figure 7a. The concrete class was C30/37 while the steel grade S450 was adopted for reinforcing steel bars. In the case of the concrete slab prefabricated R.C. elements, the slab reinforcement was made up of 2+2 ϕ 12 longitudinal steel rebars and by 5+5 ϕ 12@100 mm plus 8+8 ϕ 16@200 mm transverse steel rebars. The same mesh and the same number of additional longitudinal rebars were adopted as for the composite slab, as depicted in Figure 7b. The columns were concrete-filled columns with a circular hollow steel section with a diameter of 457 mm and a thickness of 12 mm. Steel grade is S355. The column reinforcement consisted of 8 ϕ 16 longitudinal steel rebars and of stirrups ϕ 8@150 mm (Fig. 9). The concrete class was C30/37, while the steel grade S450 was adopted for the reinforcing steel bars. Actual values better than nominal ones can be found in Bursi et al. (2008). A scheme of the test set-up is shown in Figure 10.

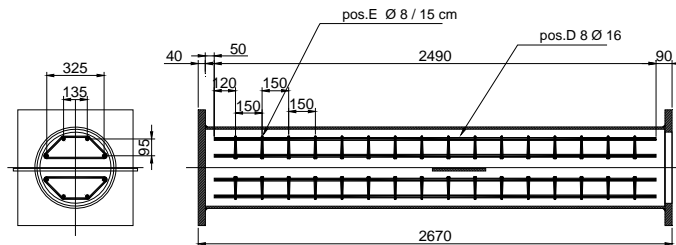


Figure 9. Column and column reinforcement.

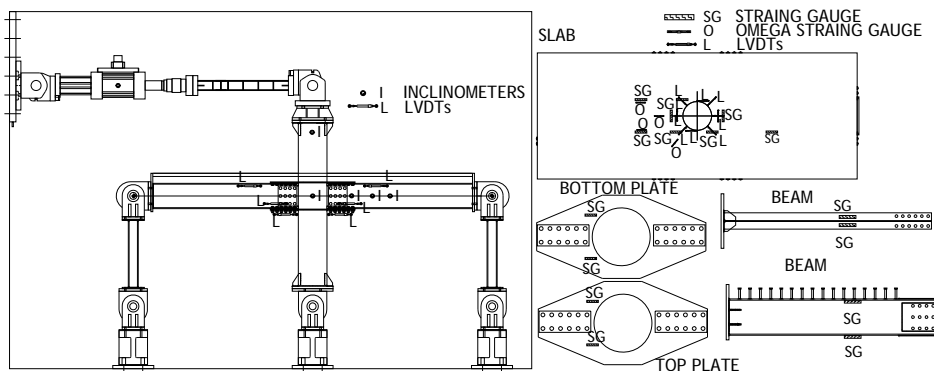


Figure 10. Lateral view of the test set-up and main instrumentation on specimens.

No vertical actuator was imposed on the column in order to be consistent with tests in other labs. In the tests, the following instrumentation was employed as illustrated in Figure 10: a) 5 inclinometers measured the inclinations: of the column at the top, of the zone adjacent to the joint, and of the beams near the connection; b) 4 LVDTs detected the interface slip between the steel beam and the concrete slab and between the bottom horizontal joint plate and the flange of beam; c) 2 LVDTs were employed in order to measure the bottom horizontal joint plate deformations; d) 10 LVDTs were utilized in order to measure concrete slab deformations in the zone around the column; e) 4 Omega-shaped strain gauges detected the deformations of the concrete slab; f) 8 strain gauges monitored axial deformations of the reinforcing bars to scrutinise the effective breadth of the reinforcing bars at each loading stage; g) 4 strain gauges monitored deformations of top and bottom horizontal plates; h) 4 strain gauges recorded flange strains in order to estimate internal forces in steel beams; i) 2 load cells were set on the top of pendula and were utilized in order to measure the horizontal and vertical components of the forces; l) 1 digital transducer (Heidenhein DT500) was used in order to measure the top column displacement. The observed response clearly indicated that all specimens exhibit a good performance in terms of resistance, stiffness, energy dissipation and local ductility. Both the overall force-interstorey drift relationship and the moment-rotation relationships relevant to plastic hinges formed in composite beams exhibited a hysteretic behaviour with large energy dissipation without evident loss of resistance and stiffness, as seen in Figures 11 and 12.

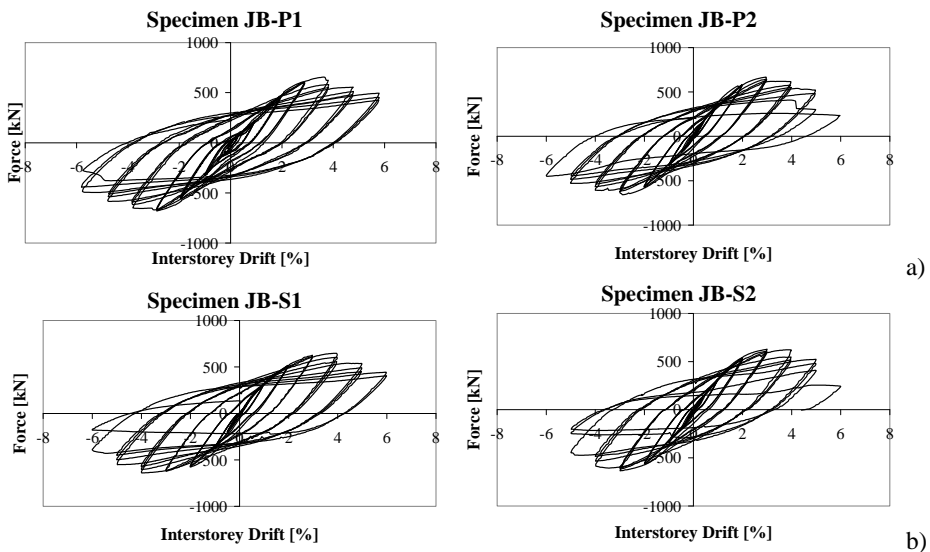


Figure 11. Force-Interstorey Drift relationship a) Specimens endowed with prefabricated girder slab; b) Specimens endowed with steel sheeting.

Hysteretic loops of moment-rotation relationship are unsymmetrical owing to the different flexural resistance of the composite beam under hogging and sagging moments as can be observed in Figure 12. It was evident that owing to local buckling effects, severe strength degradations appeared to exceed 20% of maximum strength values with rotations of about 40 mrad. The collapse of all specimens was caused by plastic buckling in compression of the bottom beam flange near the horizontal plate or fracture in tension.

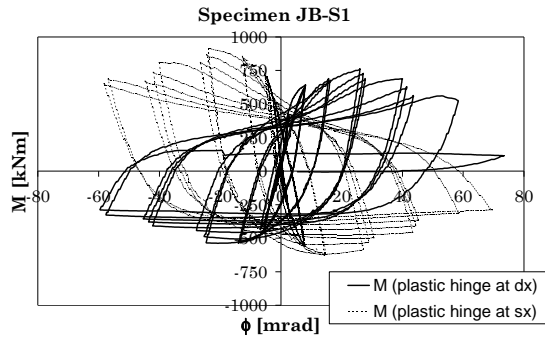


Figure 12. Moment-rotation relationship of plastic hinges for the JB-S1 specimen.

Table 1 reports some key experimental data for each test: maximum applied displacement d , maximum value F of the force, maximum values of both sagging and hogging moments M , total number N_{tot} of cycles performed during the tests. Joint behaviour is essentially symmetric in terms of force, while, for all specimens, sagging moments are about 40% larger than hogging moments. Figure 13 shows a comparison between Force-Interstorey drift curves for the specimens with and without plate strengthening of the horizontal diaphragms in both prefabricated slabs and steel sheeting slabs. These reinforcing plates were introduced in order to satisfy the relationships in (5). In this case, in which dissipative zones were located at the end of the beams, beam-to-column joints were rigid full-strength and the introduced reinforcing plates did not influence the specimen behaviour.

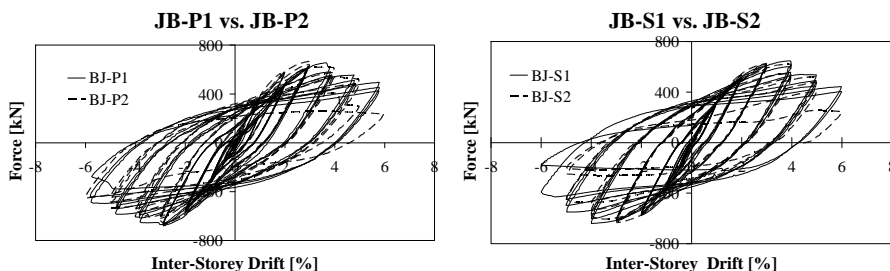


Figure 13. Comparison between Force-Interstorey drift curves.

Because beam-to-column joints are rigid and inelastic phenomena occurred in adjacent beams, it was justified to assume that bolted joints behaved like welded joints (Bursi et al., 2008). As a results fire tests on welded joints, carried out on both pre-damaged and undamaged specimens at the Building Research Establishment, UK, were considered to be representative for bolted joints too. Therefore, since the scope of the project was to promote joint typologies able to survive a seismic-induced fire before being subjected to fire loadings, specimens were damaged by imposing monotonic loads equivalent to damage induced by seismic excitations. To accurately simulate damage owing to seismic events, non-linear dynamic time histories were performed by using the IDARC-2D program (Valles et al., 1996). Experimental data of joints were used to define both hysteretic laws in IDARC-2D and damage domains according to the Chai & Romstad criterion (Chai et al., 1995). The corresponding values of damage in joints provided by IDARC-2D simulations are gathered in Table 2 where average values for joints with prefabricated slab and steel sheeting slab are provided owing to the limited number of experimental data. The trend is evident: the damage in joints was limited and repairable. Subsequently, specific deformations were prescribed on joints through monotonic vertical loading to induce the damage identified in Table 2. Hence, specimens were loaded according to the fire load combination [12] and fire tests were undertaken.

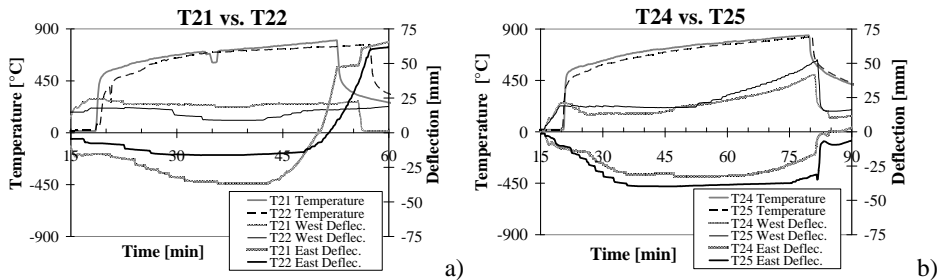
Table 2. Damage index for joints with prefabricated slabs and slabs with steel sheeting.

Joint typology	Damage index D
Exterior joint	0.43
Interior joint	0.34

Both pre-damaged and undamaged specimens were subjected to fire loading, see Table 3, and some results are presented herein. The temperature vs. time curve imposed to the specimens T21-T22 and T24-T25 is shown in Figure 14(a) and (b), respectively. Specimens T21 and T22 with profiled steel sheeting slabs exhibited failure owing to an excessive rate of deflection at approximately 40 minutes. The test on specimen T21 terminated after approximately 34 minutes owing to runaway deflection. Following the fire test, the profiled steel sheeting separated from the slab; then the slab cracked both along the surface and through the depth with extensive buckling at one hour both for the lower flange and for the web of the adjacent east beam. T24 and T25 specimens endowed with prefabricated slabs endured one hour of fire; however, in both cases specimens were very close to failure as indicated, in Figure 14b, by an increasing rate of deflections towards the end of the test.

Table 3. Specimens subjected to fire tests.

N.	Label	Test Method	Type of Specimen
1	T21	Fire	Pre-damaged Specimen endowed with steel sheeting slabs
2	T22	Fire	Undamaged Specimen endowed with steel sheeting slabs
3	T24	Fire	Pre-damaged Specimen endowed with prefabricated lattice slabs
4	T25	Fire	Undamaged Specimen endowed with prefabricated lattice slabs


Figure 14. Performance of damaged (T21/T24) and undamaged (T22/T25) specimens.

However, at this stage, there was no permanent deformation and no sign of any significant damage from fire tests. Hence, it can be underlined that: i) there was no noticeable difference in the fire performance between pre-damaged and undamaged specimens both with precast and steel sheeting slabs; this result is in agreement with damage values reported in Table 2 and with the inherent safety of composite joints (Bursi et al., 2008; EC8, 2005); ii) precast slabs performed better also in fire tests than the corresponding specimens with steel sheeting at a fire exposure in excess of the 15 minutes required; iii) all specimens exhibited favourable seismic properties by performing in a ductile manner also under fire loading.

3. PERFORMANCE BASED ANALYSIS OF STEEL-CONCRETE COMPOSITE BRIDGES

Description of the viaduct

The Montevideo viaduct, an infrastructure built in the early eighties shown in Figure 15, is located on the state road SS 45-bis Gardesana in the western outskirts of the town of Trento, a primary way in the road network of the region.

In detail, the viaduct is composed of seven simply supported spans. Each span is 75 m long.



Figure 15. The Montevideo viaduct.

Three spans are straight whereas the other four are curved in the horizontal plane, as shown in Figure 16.

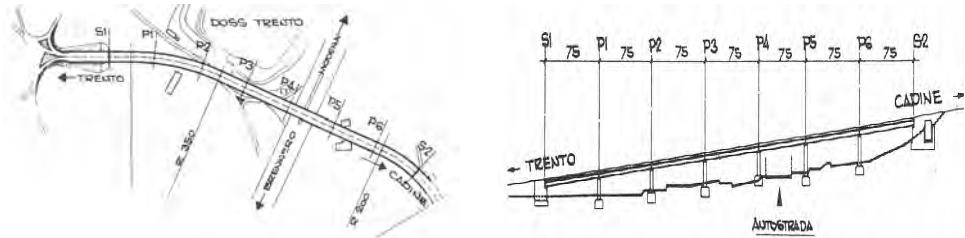


Figure 16. Plan and longitudinal section of the viaduct after Boller et al. (1984). Dimensions in m.

Travelling over the bridge, from east to west, the first three spans have radius $R=350$ m, while the 7th, the last span, has approximately $R=200$ m. The choice of a simply supported scheme was mainly determined by the high soil variability in the zone where the bridge had to be located. In this way the designers wanted to avoid possible stresses caused by differential soil settlements. Since the bridge is simply supported, we chose the span with the smallest radius, i.e. $R=200$ m also called P6-S2, to be analysed. The transverse section consists of four lanes corresponding to two carriageways and two footpaths with a total deck width of 18 m, as shown in Figure 17.

The actual state of the whole viaduct is characterised by a widespread corrosion of the steel box owing to unfavourable environment conditions, basically caused by an inefficient maintenance of the joints, as illustrated in Figure 18. Furthermore, inside the steel box the extent of rust has undermined some bolted joints, as depicted in Figure 18, and the water is able to get in and stagnate without flowing away.

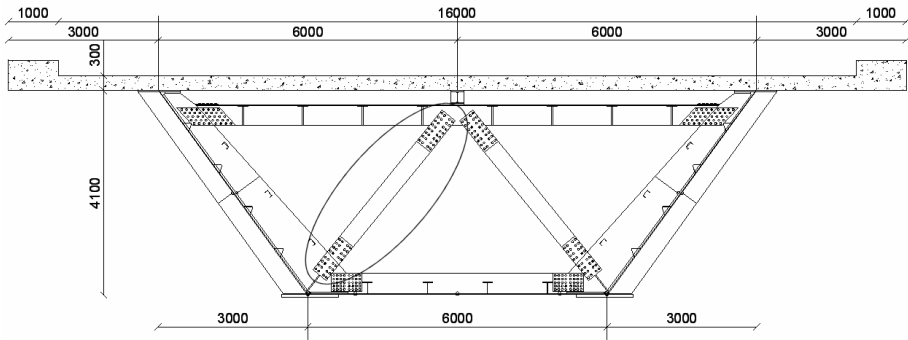


Figure 17. Transverse section at the end-diaphragms. Dimensions in mm.

A realistic estimate of the corrosion damage is about 1 mm of reduced thickness of the steel plates that form the box. Finally, the bridge was not seismically designed, so that the deck might experience low-cycle fatigue in critical details.

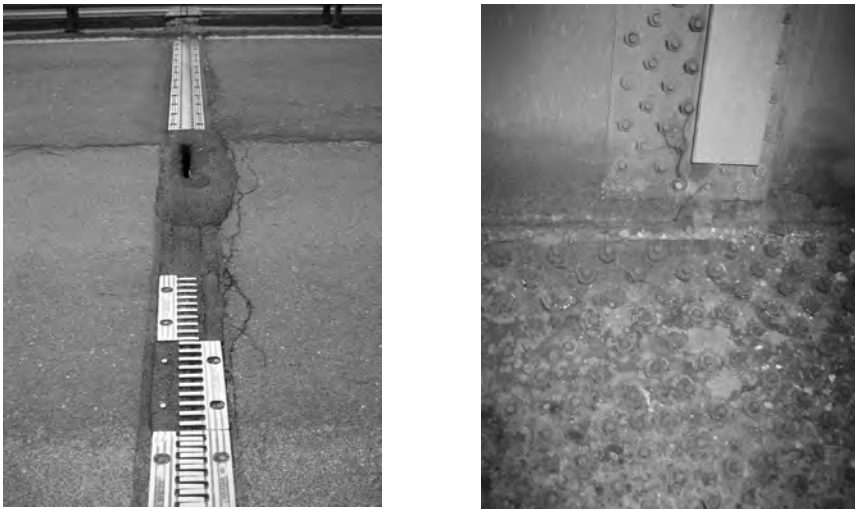


Figure 18. A deteriorated road joint and a corroded bolted connection.

FE analysis of the viaduct

Different FE models were developed by using the SAP2000 software (2004): a) a fine mesh model of the span under study for static analysis purposes; b) a coarse mesh model of the whole viaduct for dynamic analysis purposes; c) a coarse mesh model of the span under study for dynamic analysis purposes. The FE Model A allowed to investigate the local behaviour of the span owing to its

highly refined mesh and it was used for static analyses only. Due to the static scheme a single span model was sufficient. Model B was used in a preliminary phase to take into account the possible interaction among the various spans that compose the structure. Above all the interaction in the horizontal plane and the soil spatial variability were investigated. Model C was employed to check whether a single span model could be sufficient to characterise the dynamic behaviour of the span under study. From a preliminary analysis by performing the modal analysis of both model B and C, we found out that the stocky piers of the viaduct did not significantly influence the structural natural frequencies and mode shapes. For this reason, we focussed on the P6-S2 span only. A coarse mesh was implemented into the model because, in order to characterise the dynamic behaviour of a structure, it is sufficient that mass and stiffness be modelled accurately. Moreover, a fine mesh would imply computational demanding analyses with many activated local modes that are associated with low participating modal masses. Figure 19 shows the 3D FE model of the P6-S2 span. In detail, the bridge was discretized with shell elements for modelling the slab and the steel box, while frame elements were used for the truss elements of the transverse diaphragms and of the horizontal bracings. The composite action between the concrete slab and the steel box was made effective by body constraints which guarantee a full interaction as established by the European (EC4-2, 2005) and Italian rules (CNR 10016, 2000).



Figure 19. 3D FE model used for dynamic analysis purposes.

Static analysis

Since the study is part of a national project, the Italian Building Code in force at the time of the design checks, NTC (2005), was employed and, where there were deficiencies, the Italian Design Recommendations (CNR) on steel - CNR 10011 (1988) -, on steel-concrete composite - CNR 10016 (2000) - and on thin-

steel structures - CNR 10022 (1984) - were adopted. Every structural element was checked, but here only the elements that did not exhibit a satisfactory behaviour at the ultimate limit states (ULS), in detail the diagonals of the end diaphragms shown in Figure 17, are presented and summarised in Table 4. Moreover, also the midspan section did not result satisfied for the rules in force at the time of the checks, but for our purposes it will not be reported. From Table 4 it is possible to observe that the diagonal cross-section and the connection are largely underestimated for the loads given by the NTC (2005), which are, however, sensitively heavier than the ones used during the original design process dated in the early 80s.

Table 4. Diagonal design checks that did not result to be satisfied.

<i>Check</i>	σ_N [MPa]	f_d [MPa]	%
Tensile check	437	283	154
Buckling	383	283	135
Web plate connection	444	283	157
Flange top plate connection	385	283	136
Flange bottom plate connection	483	283	171

This highlights a weak point in the structure, where we expect stress concentration. This aspect should be carefully analysed during the design process, above all when we extend this analysis to the box-girder typology as a whole. Moreover, the significance of designing accurately the end diaphragms lies in the fact that they have the important function to transfer the flexural-torsional actions to the piers. These actions are basically caused by vertical loads, but can also be determined by transverse actions, like strong seismic events. For these reasons, also in a context of the bridge lifetime, they should be designed by paying particular attention to durability and structural effectiveness.

Seismic analysis

For the seismic analysis the rules included in the OPCM-3431 (2005) related to bridge structures were adopted. These rules are a revision of the ones published originally in March 2003 (OPCM-3274, 2003) which have introduced a different approach in the seismic design, that is similar to the EC8 (2005) philosophy. The seismic analysis was carried out by means of a modal response spectrum analysis, using both horizontal and vertical design spectra.

The bridge is located in a low seismicity area, i.e. Zone 3 according to the code classification. This entails a Peak Ground Acceleration (PGA) $a_g=0.15g$. The soil is very variable along the bridge site and it can be classified as A, B or C. In this respect, we decided to select the worst category, i.e. Class C, to define the seismic action; we also considered the soil spatial variability with pseudo-static displacements applied at the base of each pier as described in the

code (OPCM-3431, 2005). On the basis of the soil category it was possible to obtain the S parameter as well as the periods that characterise the horizontal and vertical elastic response spectra. The η factor, that considers the damping ratio value, was set to 1.0, hence $\xi=5\%$. Table 5 reports the parameters that define the horizontal and vertical elastic response spectra depicted in Figure 20 and Figure 21, respectively.

Table 5. Parameter values for the definition of the horizontal and vertical elastic response spectrum.

<i>Component</i>	a_g [m/s^2]	η	S	T_B [s]	T_C [s]	T_D [s]
Horizontal	0.15	1.00	1.25	0.15	0.50	2.0
Vertical	0.15	1.00	1.00	0.05	0.15	1.0

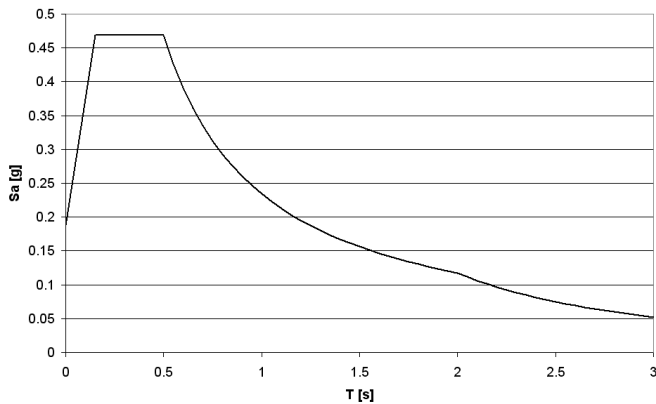


Figure 20. Horizontal elastic response spectrum.

The horizontal and vertical design spectra are obtained by dividing the respective elastic response spectra by the behaviour factor q which is set equal to 1.0 because the piers are classified as stocky. Hence, the design response spectra match the elastic ones.

As far as the structural behaviour under seismic loading is concerned, the seismic action was not strong enough to cause high stresses, and it was not significant in any deck structural checks, as conversely static actions were. For this reason, here we present the structural parts of the deck that might be critical under a severe seismic event. As mentioned previously, the end diaphragms being fundamental in transferring the flexural-torsional actions to the piers, resulted therefore to be the main stress concentration zone for seismic actions.

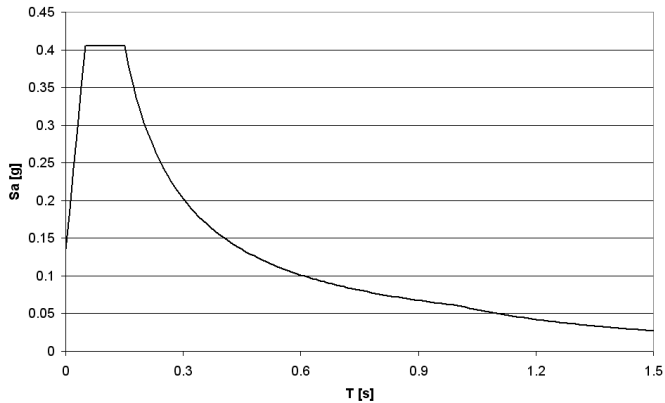


Figure 21. Vertical elastic response spectrum.

Figure 22 highlights this behaviour showing transverse shell stresses, i.e. transverse to the longitudinal axis of the bridge, in the end diaphragm and the longitudinal stresses in the steel box and concrete slab, owing to the modal response spectrum analysis with $a_g=0.15g$. One may observe that the stresses locally increase in correspondence of the end-diaphragm truss joints.

Now, increasing the PGA up to $0.35g$, i.e. Zone 1 according to (OPCM-3431, 2005), we obtained qualitatively the same stress distribution because the analysis is linear elastic. Quantitatively speaking, the increase of PGA was not enough to determine significant stresses when we considered the seismic load combination.

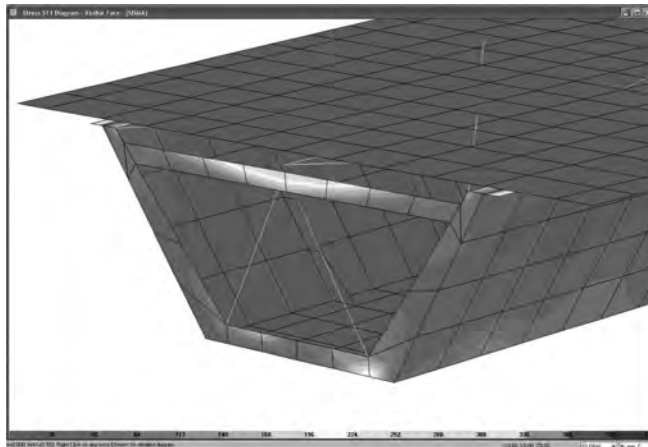


Figure 22. Transverse stresses in the end-diaphragm owing to the modal response spectrum analysis with $PGA=0.15g$.

Fatigue analysis

A structure subjected to cyclic loads can experience a damage caused by the propagation of cracks. This kind of damage is called fatigue and it translates in a loss of resistance with time. The fatigue is one of the main damage causes of steel elements along with corrosion and wear. Bridges, in particular steel and steel-concrete composite bridges, are typical structures that may be affected by fatigue since the traffic flow is a source of variable actions. Therefore, a fatigue analysis results especially significant in the performance evaluation of the examined viaduct. In fact, a fatigue failure is fragile even though the involved material like the steel is ductile, and it may occur for stresses below the yield stress. Sensitive details, like welds and shear connection studs were checked according to both the Italian Code (NTC, 2005), (CNR 10011, 1988) and the Eurocodes: EC1-2 (2003), EC2-2 (2003), EC3-2 (2005) and EC4-2 (2005) and they exhibited a satisfactory behaviour. The two codes provide different load models for fatigue. For the Eurocode, we employed Fatigue Load Model 3 and therefore the simplified method that is intended to be used for fatigue life assessment by reference to fatigue strength curves defined in EC2 to EC9. Comparing the two methods, it may be stated that the Eurocode along with the Fatigue Load Model 3 and its check procedure is stricter in terms of checks, basically owing to the correction factors that must be applied in order to obtain the damage equivalent stress range at $2 \cdot 10^6$ cycles.

Dynamic identification tests

In “Description of the viaduct” Section we described the actual state of the bridge as deteriorated owing to an advanced corrosion process. Therefore, the widespread degradation might have sensitively altered the static behaviour as well as the dynamic properties of the structure and hence the seismic response. The uncertainties in the dynamic properties caused by an aggressive environment might be related more likely to a stiffness variation rather than a change of mass. For these reasons we decided to carry out experimental output-only dynamic identification tests in order to obtain the actual dynamic characteristics of the bridge. This campaign aimed at calibrating the FE model, then used to assess the residual performance of the bridge.

Dynamic identification techniques can be classified according to the source of vibration that excites the structure. In detail, there are forced techniques that include: mechanical exciters, electromagnetic exciters or shakers and instrumented hammers. Forced vibration methods have the advantage that the level of excitation and induced vibration can be carefully controlled. In order to obtain this, no other significant forcing inputs than the one known applied to the structure during the test should be present. In this way, the input source is entirely known to compute the Frequency Response Function (FRF). However,

problems may rise when high levels of disturbance, comparable to the forced excitation, are present. For instance, it occurs when the structure is so massive that the exciters are not big enough, causing the inherent noise to have a comparable amplitude level of the response. Bridges are structures where forced techniques are not suitable. First of all, for large bridges big and expensive exciters would be needed. A second main reason lies in fact that a forced test would entail the temporary total closure of the bridge, that often is not allowed because it would cause major inconveniences to the traffic circulation. Moreover, the presence of other environmental non-controllable, and thus unknown, forcing inputs may affect the quality of a forced test, e.g. wind. To overcome these issues output-only dynamic identification tests based on ambient-induced vibrations were developed. Thus, they are suitable for large structures such as bridges, dams, tall buildings (Paultre et al., 1995), (Aktan et al., 1997), (Ventura and Schuster, 1996) and we actually performed our tests by employing output-only ambient vibration tests. They have the advantage to be less complex and to be conducted with minimum interruption to the normal operativeness of the structure. For instance considering our case, we exploited the traffic flow, along with the wind, as vibration sources. Moreover, one may note that the instrumentation should be carefully chosen since working with uncontrolled input forces may imply very low levels of vibration. Therefore, the sensitivity of sensors used for ambient vibration measurements is usually higher than that required for forced tests. In addition, it is not possible to compute the FRF, since the input is unknown; hence other techniques of modal extraction are employed. In these techniques the important assumption is that the loads acting as vibration source are approximately white noise. For natural loads this assumption is reasonably close to reality (Brincker, 2000) and this means that the spectral density function spectrum is practically flat, being therefore constant.

Test planning

We mentioned in “Description of the viaduct” Section that the bridge under study is a strategic structure in the road network of the area. For this reason, the road administrators did not allow us to close the bridge and hence, we discarded the idea to carry out forced tests and decided to employ output-only ambient vibration techniques. However due to safety issues, the two outmost lanes next to the sidewalks, where the accelerometers had been put in place, were temporary closed during the tests. This arrangement reduced the eccentricity of the traffic flow with respect to the centre line of the bridge and therefore also the excitation of torsional modes. Moreover, the traffic, as its inherent characteristic, is more likely to excite vertical - flexural and torsional - modes than transverse or longitudinal modes.

We employed piezoelectric accelerometers as acquisition devices and since we expected larger vibrations in the vertical direction rather than in the trans-

verse one, we selected the accelerometers with lower sensitivity to measure acceleration in the vertical direction, while higher sensitivity sensors were used to acquire transverse accelerations. A preliminary dynamic analysis using the 3D FE model confirmed a predominance of flexural and torsional modes, as illustrated in Figure 23 and as reported in Table 6, where the first significant global modes with high participating modal mass are shown.

Table 6. Significant modes from the modal analysis of the 3D FE model.

<i>Mode</i>	<i>Mode shape</i>	<i>f [Hz]</i>
1	1st flexural	1.35
2	1st longitudinal	1.53
3	1st torsional	2.01
4	transverse + torsional	2.95
6	2nd flexural	4.43

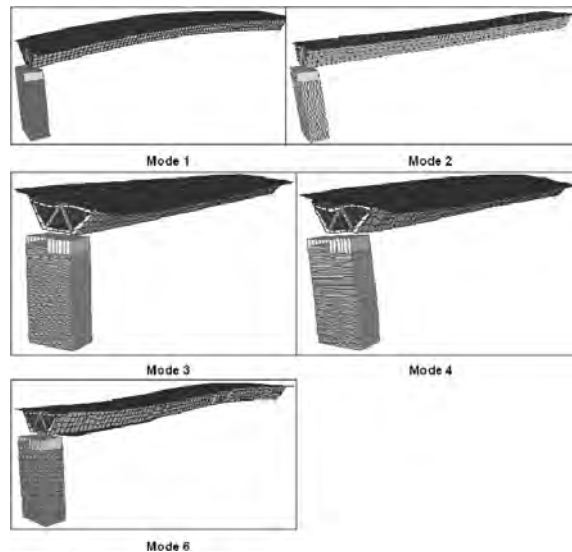


Figure 23. Significant mode shapes from the modal analysis of the 3D FE model.

The accelerometer location should be chosen so as to have a good identification of the significant modes. In this way, we guarantee the discrimination between various modes during data treatment. The mathematical tool used to discriminate mode shapes and to assess the correlation between an experimental and a numerical mode shape is the Modal Assurance Criterion (MAC)

$$MAC(A, X) = \frac{|\Psi_X^T \cdot \Psi_A|^2}{(\Psi_X^T \cdot \Psi_X)(\Psi_A^T \cdot \Psi_A)} \quad (6)$$

where Ψ_X is an experimental mode shape and Ψ_A is a numerical mode shape. It provides a measure of scatter of the points from the straight line correlation (Ewins, 2000). If two mode shapes are similar with a high degree of correlation, the MAC tends to be 1, otherwise it tends to vanish. An optimal dynamic identification would consist of obtaining a MAC matrix for all considered modes that corresponds to the identity matrix. Therefore, it becomes important both the location and the number of employed sensors. A simple method consists of looking at the mode shapes of the FE model and then of choosing the most suitable sensor locations. A little more sophisticated method is based on the MAC feature. In fact, if we compute the AutoMAC (Ewins, 2000) between the numerical mode shapes themselves by using Equation (6), but considering only the number of DOFs which are to be instrumented in the modal test, one gets a measure of the accelerometer location quality. By definition, the AutoMAC matrix is symmetric and the diagonal terms are 1, but the off-diagonal terms might not be zero mainly for two reasons: i) the orthogonality between mode shapes is only strictly true if the mass matrix is also considered, i.e. $\Psi_i^T \mathbf{M} \Psi_i = 0$; ii) if all DOFs are included in the computation. Ewins (2000) underlined that if the computation of the AutoMAC matrix for the significant modes entails off-diagonal terms greater than 70%, there will be difficulty to match pairs of test and analysis modes, at least for the modes in question. The AutoMAC matrix for the significant modes is shown in Table 7.

Table 7. Significant modes from the modal analysis of the 3D FE model.

<i>Mode</i>	1	2	3	4	6
1	1				
2	0.015	1			
3	$2.87 \cdot 10^{-5}$	0.020	1		
4	0.018	0.010	0.019	1	
6	0.024	0.009	0.003	0.007	1

We already said that the sensor location is also influenced by the available number of sensors. Since the acquisition system could acquire up to 16 channels simultaneously and owing to the length of the bridge, we reckoned to use two distinct accelerometer configurations as shown in Figure 24. From Figure 24 it is possible to observe that, firstly, we instrumented the western part of the bridge and, secondly, the eastern part moving all accelerometers, but leaving 3 of them in the same position for both acquisitions. These 3 reference accel-

ometers allowed us to unite the 2 configurations during the data elaboration so as to obtain the mode shapes for the whole bridge length.

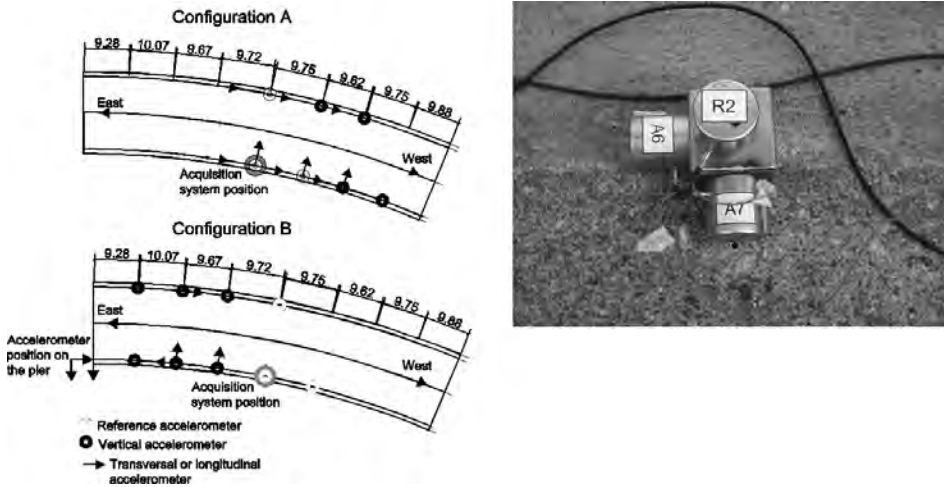


Figure 24. a) Accelerometer configurations; b) accelerometer rigid support system with 3 sensors.

Experimental tests

The dynamic identification tests were performed on 8 May 2007. After the completion of the device installation, we started to acquire the ambient vibrations generated by the traffic vehicles at a frequency rate of 100 Hz for a length of about 30 minutes. This acquisition frequency was high enough to avoid the *aliasing* phenomenon for the frequency range of interest, i.e. 1-20 Hz. In fact, it is known from the sampling theorem that to sample a continuous-time signal with a maximum frequency content of f_{max} without biasing its description in discrete time, the sampling frequency must be $f_{sampling} \geq 2f_{max}$; $f_{Nyquist} = f_{sampling}/2$ is referred to as the Nyquist frequency. Since the acquisition system contains an anti-aliasing filter with cut-off frequency equal to $f_{Nyquist}$, we sampled the continuous-time signals coming from the accelerometers having a frequency content up to 50 Hz without introducing alterations. Moreover, the sampling operation may introduce another phenomenon called *leakage*. It is related to the necessity of analysing a finite time record and to the periodicity of the signal. In fact, if the time record does not contain a finite number of periods the frequency spectrum is affected by frequency components that do not exist. The interpretation is that the energy associated to the actual spectral lines "leaks" to neighbouring frequencies, thus altering the frequency spectrum of the signal. Because our signals are not strictly periodic, to overcome this issue we applied a *windowing* process by multiplying a function to the signal that

smooths the limits of the recorded time frame to zero. 5-minute time histories of the reference accelerometers are reported in Figure 25.

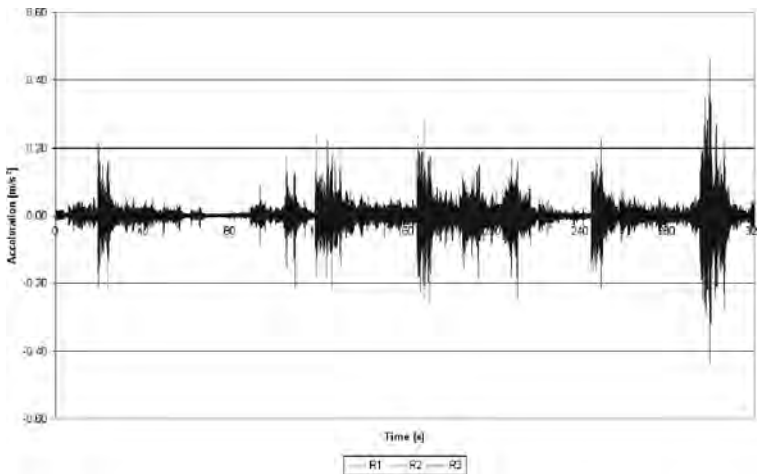


Figure 25. 5-minute time histories of the reference accelerometers. Configuration A.

Experimental data evaluation

In order to identify the bridge span dynamic characteristics, i.e. natural frequencies and mode shapes, the acquired data were elaborated by applying the Frequency Domain Decomposition (FDD) (Brincker et al., 2001). The FDD technique relies on peak picking and allows to overcome the identification issue of close modes. Moreover, it improves the physical understanding of its use by dealing directly with the Power Spectral Density (PSD) function. In addition, it provides insight into the discrimination between structural modes and harmonic components as well.

The main idea of this technique is to consider the loading as white noise, the structure lightly damped and the mode shapes orthogonal. As a result, it is possible to apply the Singular Value Decomposition (SVD) to the spectral matrix, which is decomposed into a set of auto spectral density functions, each corresponding to a SDoF system (Brincker et al., 2001).

The procedure we applied is the following. Initially, we prepared the data by removing possible linear trends and we checked the stationarity of the random signal by applying the reverse arrangement test (Bendat and Piersol, 2000). Then, we applied the FDD technique to the ambient acquisitions and we looked at the peaks that the PSD functions gave us for both configurations. Moreover, we plotted the mode shapes by means of a MatLab routine in order to see if the chosen peaks actually corresponded to structural modes. Finally, we checked

that at the same frequency what we got matched for both configurations in terms of mode shapes.

Figure 26 and Figure 27 show the PSD functions of the ambient acquisitions corresponding to Configurations A and B, respectively. The comparison between the two figures shows that the first singular values are dominant and that the energy content of the peaks at the same frequency is different, at some frequencies sensitively different between the two spectra. The reason lies in the fact that the acquisitions were carried out at different times with consequently different traffic volumes, thus entailing diverse forcing inputs.

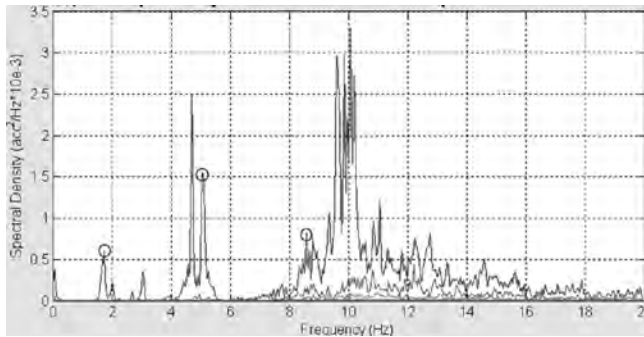


Figure 26. PSD functions of ambient acquisitions corresponding to Configuration A.

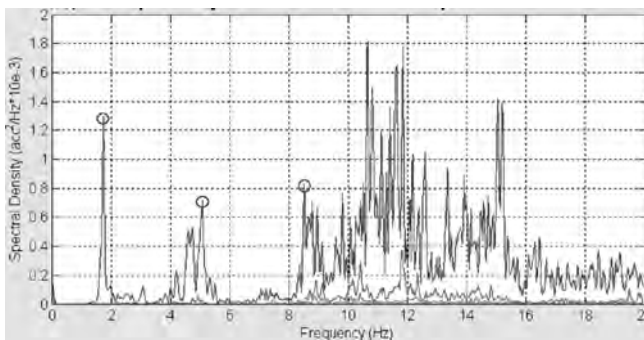


Figure 27. PSD functions of ambient acquisitions corresponding to Configuration B.

However, some peaks at low frequencies are clearly present in both spectra. In fact, the circles indicate the structural modes that were actually identified in a reliable and accurate way. In detail, no similar mode shapes were detected at other frequencies than those marked. We could do it by implementing a Mat-Lab routine capable to plot the mode shapes graphically. For higher frequencies, it was difficult to discriminate structural modes with certainty and uniqueness, mainly because the mode shapes did not exactly match in both configura-

tions, and owing to very similar shapes that repeated at different frequency values. As expected, the traffic flow could not excite sufficiently the transverse and longitudinal mode; in addition, wind was negligible on the test day, thus the identified modes were only vertical. In particular, the identified experimental structural modes are reported in Table 8, while Figure 28 shows the experimental mode shapes obtained by inserting the coordinate of the bridge and the modal displacements in the routine. From Figure 28, it is possible to observe how well mode shapes represent the first vertical mode shape of the structure and how well they match between the two configurations.

Table 8. Identified experimental structural modes.

<i>Mode</i>	<i>Mode shape</i>	<i>f</i> [Hz]
1	1st flexural	1.74
2	1st torsional	5.09
3	2nd flexural	8.55

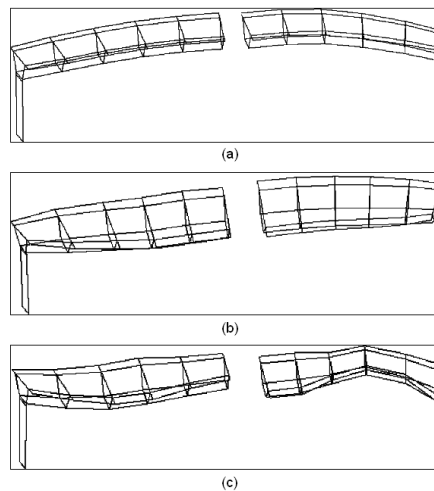


Figure 28. Experimental mode shapes: (a) 1st flexural; (b) 1st torsional and (c) 2nd flexural.

Model updating and reliability analysis

After the identification of the actual dynamic characteristics of the bridge by means of dynamic identification tests, it is possible to calibrate the FE by means of a model updating procedure, so that the numerical dynamic properties match the experimental ones. In this way, we basically change the stiffness of the model by modifying some significant parameters, thus obtaining an updated FE that represents much closer the actual structure. Therefore, we can perform

a further analysis aimed at detecting possible different critical details. We can also carry out analyses with the objective to establish the residual performance of the bridge by employing simple concepts developed in the reliability theory.

The FE model updating procedure employed in this study relies on the Inverse Eigensensitivity Method (Friswell and Mottershead, 1995), as implemented, for instance, in (Molinari et al., 2009). It is an indirect iterative method operating in the modal domain. It compares numerical with experimental eigenvalues and eigenvectors, by taking the difference component by component. Then, it seeks to minimise this difference by adjusting unknown parameters applied to some significant structural properties of the FE model. Minimization methods are applied to model updating procedures in order to provide the optimum estimation of the parameters. In order to achieve optimization through minimization we employed the Powell's Dog Leg method (DL), which is a trust region method, based on the combination of the classical Gauss-Newton (GN) method and the Steepest Descent (SD) method (Madsen et al., 2004). The objective function is approximated within a trust region of radius R , whose magnitude depends on the solution at the previous step. When an adequate approximation of the objective function is found within the trust region, the radius is increased, otherwise it is reduced. In this manner, it provides, firstly, the step size and, secondly, the step direction.

The model updating procedure is based on the variation of unknown parameters applied to significant structural properties of the FE model. It is evident that not every structural property is relevant to the model updating, that is the variation of a structural characteristic during the updating may not entail any improvement. Hence, it is necessary to carry out a preliminary identification of the significant structural properties, each to be associated with a parameter, by means of a sensitivity analysis. First of all, the choice of a limited number of possible significant structural property candidates, and hence of parameters, is needed. Basically, this first step is based on physical insight. Usually, the mass properties are kept deterministic and parameters related to stiffness are considered variable.

Since an iterative process is needed the commercial software SAP2000 is not a suitable tool to be used for model updating problems, simply because it is not conceived for this purpose. In addition, a 3D shell-beam element-based model is too complex, because of many modal inversions that occur during the updating as well as the presence of several local modes; and last but not least the high computational demand that requires. Therefore, the simplicity of a beam FE model, that may well represent the global behaviour of the structure implemented in a suitable FE software that allows iterative processes was deemed necessary. From this standpoint, the open-source FE software OpenSees (Mc Kenna and Fenves, 2000) was reckoned to be a suitable tool to reach our objective. In fact, it allows parametric and iterative procedures and its high speed elaboration in conjunction of a simple beam model guarantees a fast

process if many iterations are needed. We modelled the P6-S2 span with 7 elements, as illustrated in Figure 29. In order to simplify the model, the pier was not modelled and at the boundary conditions we inserted a set of springs that permitted the stiffness of the bearings and the stiffness of the pier-soil or abutment-soil combined system to be allowed for. The stiffness was initially set on the basis of data found in the literature by considering the type of bearings. The section properties of the frame elements were calculated on the basis of the actual sections of the bridge according to the classical elastic theory. We considered the values of the elastic moduli based on a material analysis and we reduced the thicknesses of the steel plates of 1 mm in order to try to start from an initial solution closer to the actual bridge state. Furthermore, the DOFs corresponding to the accelerometer locations were added and connected to the beam elements by means of rigid links, as depicted in Figure 29.

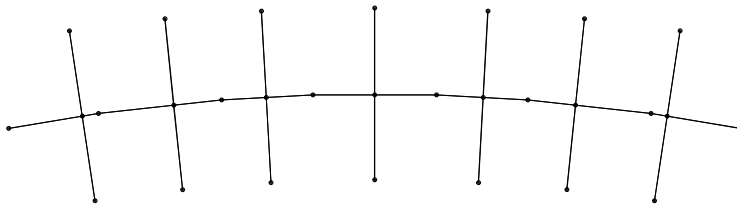


Figure 29. OpenSees FE beam model geometry.

The first step consisted of performing the modal analysis of the bridge by using the new FE beam model. The modal properties are reported in Table 9 and Figure 30 depicts the first 5 mode shapes. From Table 9, one may note that the FE model is stiffer than the actual bridge for the modes of interest, apart of the 2nd flexural mode. This agrees with what we would expect, i.e. a reduced stiffness owing to the degraded actual state of the bridge.

Table 9. Comparison between numerical f_{FE} and experimental f_{EXP} mode shapes and frequencies.

<i>Mode</i>	<i>Mode shape</i>	f_{FE} [Hz]	f_{EXP} [Hz]
1	1st flexural	1.82	1.74
2	1st transverse	4.77	-
3	1st torsional	6.62	5.09
4	2nd flexural	7.16	8.55
5	1st longitudinal	9.68	-

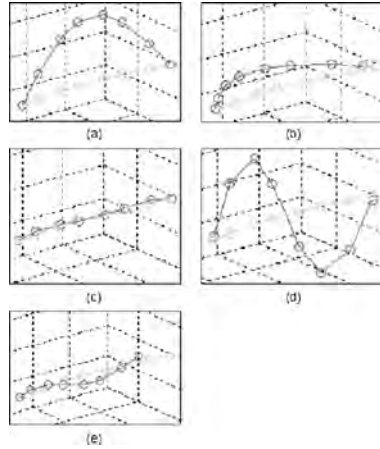


Figure 30. First 5 mode shapes of the FE OpenSees model. Static and relative mode shape: (a) 1st flexural; (b) 1st transverse; (c) 1st torsional; (d) 2nd flexural; (e) 1st longitudinal.

The sensitivity analysis was performed by considering the following parameters: the thickness of the bottom steel plate h_{plate} , the thickness of the outer curve web t_{webout} , the thickness of the inner curve web t_{webin} , the concrete elastic modulus E_c , the bearing vertical K_v , transverse K_t and torsional K_r stiffnesses. It resulted that the significant parameters were: h_{plate} , t_{webout} , t_{webin} and E_c . It is interesting to note that these parameters are important for the updating of the torsional mode, whose behaviour is governed by the Bredt formula for closed-thin sections.

Table 10. Results of the model updating.

<i>Mode</i>	<i>Mode shape</i>	f_{EXP} [Hz]	$f_{FE,0}$ [Hz]	$error_0$ [%]	$f_{FE,7}$ [Hz]	$error_7$ [%]
1	1st flexural	1.74	1.82	4.55	1.71	-1.92
2	1st torsional	5.09	6.62	30.05	5.89	15.63
3	2nd flexural	8.55	7.16	-16.24	6.72	-21.41

Table 11. Final mean parameter values.

<i>Struct. par</i>	<i>Initial mean value</i>	<i>Final mean par. value</i>	<i>Final struct. value</i>
E_c	30220 MPa	1.07	32335 MPa
h_{plate}	26 mm	0.85	22.1 mm
t_{webin}	11 mm	0.69	7.6 mm
t_{webout}	15 mm	0.74	11.1 mm

Table 12. MAC matrix.

0.971	$3.951 \cdot 10^{-4}$	$5.515 \cdot 10^{-4}$
0.016	0.939	0.047
$3.111 \cdot 10^{-4}$	0.014	0.758

The results of the FE model updating are reported in Table 10 and Table 11. The frequency outcomes after 7 iterations are presented in Table 10. As before, looking at the frequencies, it may be observed that the updating determined an overall stiffness reduction; see also

Table 11 in this respect. The 1st numerical frequency matched very well the experimental one, while for the torsional frequency a good improvement occurred: the error halved passing from 30% to 15%. The 3rd frequency match worsened, being the 2nd flexural more flexible.

Table 11 shows the amount of thickness reduction of the steel parameters as well as the small increase of the elastic modulus E_c . Furthermore, the MAC matrix, reported in

Table 12, presents a good correlation between corresponding numerical and experimental mode shapes. Finally, although we obtained an updated FE model, the fact of being based on a beam model introduces the drawback to prevent the local analysis for the identification of possible critical details, different from those found in “FE analysis of the viaduct” Section. However, a reliability analysis can be performed in order to assess the residual performance of the bridge.

Although we were not able to perform a local analysis on the updated FE model, we present an optimisation of the bolted end-diaphragm connections. As a result, the diagonal and the bottom chord joints were optimised by applying the same conceptual solution. We conceived a welded-bolted solution, of the diagonal joint shown in Figure 31.

**Figure 31.** Bolted end-diaphragm connection detail.

One part of the connection is welded and assembled in the workshop, whereas the other part remains bolted, in order to keep assembly easiness on

the construction site, as illustrated in Figure 32. Moreover, it was designed in order to satisfy the design checks presented in “FE analysis of the viaduct” Section.

In detail, the sections should be increased; the electrodes, that are used to weld, should be overmatched with regard to the steel grade being used and fillet welds with side of 15 mm and thus, effective throat thickness of about 11 mm should be considered; high-strength 10.9 M18, for the diagonals, and M20, for the bottom chord, bolts should be finally employed. The other elements that compose the end diaphragm should be adjusted to cope with the aforementioned changes.

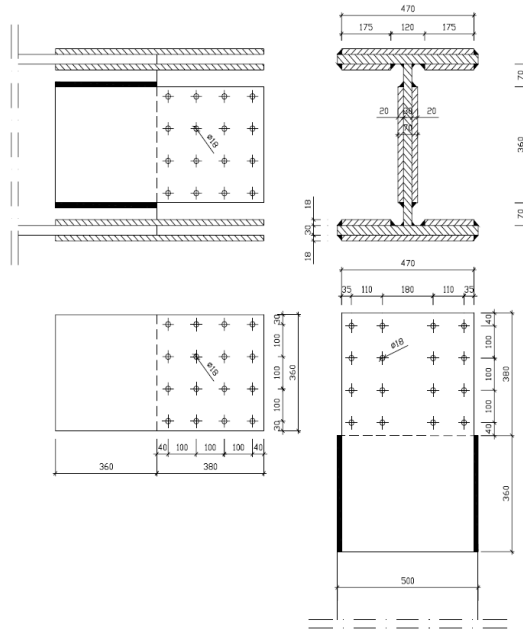


Figure 32. Optimised welded-bolted diagonal connection.

Reliability analysis

In this part, we employ the beam FE model of the bridge to perform a reliability analysis with the aim at checking the variation of the static performance of the structure during its service life. This reliability analysis was carried out with respect to the bending moment at midspan, since the bridge is simply supported. Hence, we exploited reliability concepts to carry out an analysis that provides a quantitative measure of the actual state of the bridge.

We employed the β reliability index method which is a Level 2 method (Madsen et al., 1986). A Level 2 method is based on the knowledge of 2 characteristic parameters, usually mean value and standard deviation, as well as a correlation measure between the parameters to model uncertain values. There-

fore, the choice of the quantities to be modelled by stochastic or deterministic variables assumes a fundamental role in reliability analysis. The traffic load on a bridge is generally modelled by means of a stochastic variable, whereas the span length is usually modelled as deterministic. In conjunction of the β reliability index method, a First Order Reliability Method technique (FORM) was applied. The basic idea is to build a failure function g that is linearised, and then the reliability is estimated by using the β reliability index as defined by Cornell (1966)

$$\beta = \frac{\mu_M}{\sigma_M} \quad (7)$$

where μ_M is the mean value, defined as the linear combination of the mean values of the single basic stochastic variables and σ_M is the standard deviation, defined as the square root of the sum of the squared standard deviations of the single basic stochastic variables. If the reliability index $\beta > 3.5$ (AASHTO, 1994), the structure can be considered as safe. The failure surface g is defined as a surface in the n -dimensional basic variable space that separates safe states from unsafe states of the structure, e.g. we can define $g(s,p)=s-p$ where s is the strength variable and p is the load variable. Therefore, $g > 0$ corresponds to a safe state, conversely $g < 0$ indicates a failure state. For the estimate of the reliability with a linear failure function, the quantities that we decided to model with basic stochastic variables were: the steel yield strength f_y , the car or light traffic load Q_{car} and the truck or heavy traffic load Q_{truck} . We assumed independent normally distributed stochastic variables. With regard to traffic loads, the heavy traffic load Q_{truck} is the 6% of the average daily traffic on the bridge according to a survey carried out by the provincial transportation agency (PAT-BMS, 2006) and the heavy traffic spectrum was obtained by the CNR 178 (1995). The mean values and the standard deviations are collected in Table 13.

Table 13. Mean values and standard deviations of the stochastic variables.

<i>Stochastic variable</i>	<i>Mean value</i>	<i>Standard deviation</i>
f_y	433.4 MPa	47.68 MPa
Q_{car}	170.5 kN	110.90 kN
Q_{truck}	16.0 kN	4.95 kN

We supposed the most unfavourable load case, i.e. congested traffic. As a result, the bridge was fully loaded considering the average traffic composition. We performed the reliability analysis by computing the β reliability index for two cases:

1. Structural characteristics from the original project,
2. Structural characteristics after the model updating procedure.

The results are shown in Table 14 and they show a decrease of β from Case 1 to Case 2. This was expected since the cases follow the chronological life of the bridge and a deterioration process is a natural part of a structure life. Note that $\beta > 3.5$ for both cases.

Table 14. β reliability index for midspan bending moment.

	<i>Case 1</i>	<i>Case 2</i>
β	4.88	4.03

In sum, the reliability analysis provided useful structural safety indications about the bridge. The evaluation of the β reliability index for the midspan bending moment showed that the structure has experienced a degradation process; nonetheless it can be still deemed safe according to the AASHTO (1994) code. Moreover, it may be concluded that a major retrofit might be avoided at this stage from a midspan bending moment viewpoint. A more complete reliability analysis with the aim to assess the shear and seismic reliability should provide a more comprehensive picture.

4. CONCLUSIONS

On the basis of the seismic and fire analyses carried out on steel-concrete composite moment resisting frames, and the performance-based analysis of an existing steel-concrete composite box-girder bridge the main conclusions are drawn herein.

With regard to steel-concrete composite moment-resisting frames the following key aspects can be highlighted.

- Experimental and numerical results showed how joint details influence beam-column sub-assembly responses. All sub-assemblages exhibited a rigid behaviour and a favourable performance in terms of resistance, stiffness, energy dissipation and local ductility.
- As expected plastic hinges developed in beams as a consequence of the capacity design methodology. Moreover, a behaviour factor of about 4 was obtained in other studies for the composite frames investigated. As a result, these joints can be used for Ductility Class M structures according to EC8.
- There was no noticeable difference in the fire performance between pre-damaged and undamaged specimens both with precast and steel-sheeting slab. This result appears to be in agreement with the inherent safety of composite joints.
- Precast slab performed better also in fire tests with respect to the corresponding specimens with steel sheeting at a fire exposure in excess of the 15

minutes required. In addition, all specimens exhibited favourable seismic properties by performing in a ductile manner also under fire loading.

- The fire design applied to a structure with reduced capacity owing to seismic actions has provided structural, seismic and fire safety. These objectives were achieved through a balanced combination of analytical/numerical and experimental work.

As regards the part relative to the study on the performance of an existing steel-concrete composite bridge major conclusions follow.

- The seismic action is not strong enough to cause high stresses in the bridge examined and it is not significant in any deck structural checks. However, the end diaphragms being fundamental in transferring the flexural-torsional actions to the piers, result to be the critical zone for seismic actions.
- High-cycle fatigue is not an issue for both Italian code and Eurocode. However, we observed that the Fatigue Load Model 3 suggested by the Eurocode, together with its check procedure results to be stricter in terms of checks owing to correction factors applied in order to evaluate the damage equivalent stress range related to $2 \cdot 10^6$ cycles.
- The dynamic identification tests allow to accurately identify only vertical modes owing to the peculiar characteristics of the vibration source, i.e. the traffic flow. In particular, 3 structural modes are found: i) the 1st flexural one; ii) the 1st torsional one and iii) the 2nd flexural one.
- The model updating carried out by using the OpenSees beam FE model provides good results in matching the first two experimental modes, while the improvement is basically null for the third one.
- The use of a beam FE model prevents the identification of possible different critical details; however, it allows a reliability analysis to be performed, based on the computation of the β reliability index. Both the results before and after the updating result to be satisfactory, i.e. $\beta > 3.5$ as provided by the AASHTO (1994) code. Hence, results suggest that a major retrofit might be avoided.

REFERENCES

- AASHTO. [1994] *LFRD Bridge Design Specifications*, American Association of State Highway and Transportation Officials, Washington, D.C.
- Aktan, A. M., Farhey, D. N., Helmicki A. J., Brown D. L., Hunt V. J., Lee, K. and Levi A. [1997] "Structural Identification for Condition Assessment: Experimental Arts" *Journal of Structural Engineering* 123: 1674-1684.
- Bendat, J. S. and Piersol, A. G. [2000] *Random Data. Analysis and measurements procedures*, John Wiley & Sons, Inc, New York.

- Boller, W., Dalla Torre, A., De Miranda, M. and Gnecci Ruscone, E. [1984] "Il viadotto Vela a Trento" *Costruzioni Metalliche*. Rivista bimensile dei tecnici dell'acciaio 36(2): 83-91.
- Brincker, R. [2000] "Introduction to Random Processes" in *Lecture notes for the course: Modal identification of output-only systems*, Universidad Politecnica de Madrid, 5-6 June.
- Brincker, R., Zhang, L. and Andersen, P. [2001] "Modal identification of output-only systems using frequency domain decomposition" *Smart materials and structures* 10: 441-445;
- Bursi O.S., et al. Editors, [2008] Final Report PRECIOUS Project Contr. N. RFSCR-03034, 2008. Prefabricated Composite Beam-to-Concrete Filled Tube or Partially Reinforced-Concrete-Encased Column Connections for Severe Seismic and Fire Loadings;
- Chai Y.H., Romstad K.M., Bird S.M. [1995], "Energy-based linear damage model for high-intensity seismic loading", *Journal of Structural Engineering*, ASCE, 121(5), 857-864.
- CNR 178. [1995]. *Catalogo delle pavimentazioni stradali*, Consiglio Nazionale delle Ricerche, Roma.
- CNR 10011. [1988]. *Costruzioni in acciaio. Istruzioni per il calcolo, l'esecuzione, il collaudo e la manutenzione*, Consiglio Nazionale delle Ricerche, Roma.
- CNR 10016. [2000]. *Strutture composte di acciaio e calcestruzzo. Istruzioni per l'impiego nelle costruzioni*, Consiglio Nazionale delle Ricerche, Roma.
- CNR 10022. [1984]. *Profili di acciaio formati a freddo. Istruzioni per l'impiego nelle costruzioni*, Consiglio Nazionale delle Ricerche, Roma.
- Cornell, C. A. [1966] "A probability-based structural code" *ACI Journal* 66: 974-985.
- EC1-2. [2003] *Eurocode 1. Actions on structures. Part 2: Traffic loads on bridges*, CEN, Brussels.
- EC2-2. [2005] *Eurocode 2. Design of concrete structures. Part 2: Concrete bridges - Design and detailing rules*, CEN, Brussels.
- EC3-1-1. [2005] *Eurocode 3. Design of steel structures. Part 1: General rules and rules for buildings*, CEN, Brussels.
- EC3-1-8. [2005] *Eurocode 3. Design of steel structures. Part 8: Design of joints*, CEN, Brussels.
- EC3-1-9. [2005] *Eurocode 3. Design of steel structures. Part 9: Fatigue*, CEN, Brussels.
- EC3-2. [2005] *Eurocode 3. Design of steel structures. Part 2: Steel bridges*, CEN, Brussels.
- EC4-1 [2005] *Eurocode 4. Design of composite steel and concrete structures. Part.1.1: General rules and rules for buildings*, CEN, Brussels.
- EC4-2. [2005] *Eurocode 4. Design of composite steel and concrete structures. Part 2: General rules and rules for bridges*, CEN, Brussels.
- EC8. [2005] *Eurocode 8. Design of structures for earthquake resistance*, CEN, Brussels.
- ECCS 1986. Recommended Testing Procedure for Assessing the Behaviour of Structural Steel Elements under Cyclic Loads. ECCS Publication n° 45;
- Ewins, D. J. [2000] *Modal testing: theory, practice and application*, Research Studies Press LTD, Baldock, UK.
- Franssen J.-M. 2000. "SAFIR; Non linear software for fire de-sign". Univ. of Liege;

- Friswell, M.I. and Mottershead, J.E. [1995] *Finite element model updating in structural dynamics*, Kluwer Academic Publishers, Dordrecht, The Netherlands.
- Hibbitt, Karlsson and Sorensen [2000]. "ABAQUS User's manuals". 1080 Main Street, Pawtucket, R.I. 02860
- ISO 834-1 [1999]. Fire-resistance tests - Elements of building construction - Part 1: General requirements.
- Madsen, H. O., Krenk, S. and Lind, N. C. [1986] *Methods of structural safety*, Prentice-Hall, 1986.
- Madsen, K., Nielsen, H. B. and Tingleff O. [2004] Methods for non-linear least square problems. Informatics and mathematical modelling, Technical University of Denmark.
- McKenna, F. and Fenves, G. L. [2000] "An object-oriented software design for parallel structural analysis" in *Proceedings of the Advanced Technology in Structural Engineering, Structures Congress 2000*, ASCE, Washington, D.C.
- Molinari, M. and Savadkoohi, A. T. and Bursi, O. S. and Friswell, M. I. and Zonta, D. [2009] "Damage identification of a 3D full scale steel-concrete composite structure with partial-strength joints at different pseudo-dynamic load levels" *Earthquake Engineering and Structural Dynamics* 38(10): 1219-1236.
- NTC. [2005] *Decreto Ministeriale. Norme Tecniche per le Costruzioni 14/9/2005*, Ministero delle Infrastrutture e dei Trasporti, Roma.
- NTC. [2008] *Decreto Ministeriale. Norme Tecniche per le Costruzioni 14/1/2008*, Ministero delle Infrastrutture e dei Trasporti, Roma.
- OPCM-3274. [2003] *Primi elementi in materia di criteri generali per la classificazione sismica del territorio nazionale e di normative tecniche per le costruzioni in zona sismica - Allegato 3*, Dipartimento della Protezione Civile, Roma.
- OPCM-3431. [2005] *Primi elementi in materia di criteri generali per la classificazione sismica del territorio nazionale e di normative tecniche per le costruzioni in zona sismica - Allegato 3*, Dipartimento della Protezione Civile, Roma.
- PAT-BMS. [2006] *Il sistema di gestione delle opere stradali della PAT*, DIMS, Draft Whitepaper Version: 1.0.
- Paultre, P., Proulx, J. and Talbot, M. [1995] "Dynamic testing procedures for highway bridges using traffic loads" *Journal of Structural Engineering*, 121(2): 362-376.
- SAC 1997, Protocol for Fabrication, Inspection, Testing, and Documentation of Beam-Column Connection Tests and Other Experimental Specimens, report n. SAC /BD-97/02;
- SAP2000 Wilson, E. L. [2004] *SAP2000 Users Manual*, Berkeley, CA, USA.
- Valles R.E., Reinhorn A.M., Kunnath S.K., Li C., Madan A. [1996], IDARC2D Version 4.0: A Program for the Inelastic Damage Analysis of Buildings, Tech. Report NCEER-96-0010, 1-8.
- Ventura, C. E. and Schuster, N. D. [1996] "Structural dynamic properties of a reinforced concrete high-rise building during construction" *Canadian Journal of Civil Engineering* 23: 950-972.

ROTATION CAPACITY AND CLASSIFICATION CRITERIA FOR COMPOSITE MEMBERS

Marisa Pecce, Francesca Ceroni, Luigi Di Sarno

Department of Engineering, University of Sannio, Benevento, Italy

Abstract. The evaluation of rotation ductility of composite steel and concrete structural members is a complex topic requiring further experimental tests and numerical models. In this paper non-linear behaviour of partially encased columns and composite beams is discussed in a detailed fashion. The results of bond experimental tests on partially encased columns are presented; such tests are aimed to estimate the efficiency of stress transfer at steel-concrete interface especially at beam-column joints. A special set-up was designed and constructed to apply compression and tension to concrete and measure the slip and the shear stress at the interface with steel. The bond strength estimated experimentally is compared to threshold values implemented in codes of practice. An innovative type of base column connection was studied and a finite element model implemented and calibrated on the basis of the experimental test results. The design and results of experimental tests on composite beams subjected to hogging moment are also presented. The tests were carried out in order to evaluate the plastic rotation capacity. It was found that premature buckling occurred limiting the plastic deformations. Preliminary analyses point out that the plastic bending moments are not reached; further numerical simulations are still ongoing using a refined.

Keywords: composite structures, beam, column, rotation capacity, base-column, bond.

1. INTRODUCTION

Composite steel and concrete structural systems possess adequate seismic performance because of their stiffness, strength and ductility, and have been found to be cost-effective especially for multi-storey buildings (e.g. Ricles and Paboojian, 1994; Broderick and Elnashai, 1996; Lee and Pan, 2001; among many others). Composite systems for buildings often include steel moment resisting frames, consisting of steel beams (acting compositely with a metal deck reinforced slab or solid concrete slab through shear studs) and encased composite columns, or braced frame with steel-concrete composite columns (Cosenza and Zandonini, 1997). Consequently, lateral drifts, both interstorey and roof drifts, under horizontal forces (wind and/or earthquakes) are lowered. Under severe earthquake loading concrete encasement cracks and reduces the flexural stiffness of composite beam-columns but the steel core acts as a back-

up system in providing the shear strength and increase especially if suitable connectors between concrete and steel are used (Elnashai and Elghazouli, 1993; EC8, 2004). The assessment of structural response of composite steel and concrete columns is thus of paramount importance, especially in the earthquake design of framed systems (e.g. Fabbrocino et al., 2001; Thermou et al., 2004; Bursi et al., 2004, among many others).

The present research deals with the post-elastic deformability of composite steel and concrete beams and columns. The targets of the project are: 1) the definition of the transfer mechanism (bond) at the concrete – steel interface in composite columns type partially encased; 2) the study of the base connections of partially encased columns, 3) the evaluation of the rotational capacity of composite beams under hogging bending moment.

For each items a state of the art was initially compiled. Then experimental tests have been designed and full scale specimens constructed. Furthermore available experimental results were analysed in order to develop a refined finite element model. The outcomes of the present research may be implemented in the forthcoming provisions of the national code of practice.

2. COMPOSITE COLUMNS

The inelastic response of composite columns is significantly affected by beam-column joints (Shanmugam and Lakshmi, 2001) and column base connections.

It was deemed necessary to carry out experimental and theoretical studies in order to enhance the existing knowledge; it was focused on the partially encased columns and the following two specific problems were analysed in details: the transfer mechanism at steel concrete interface and the behaviour of an innovative base column connection.

Bond behaviour in partially encased columns

Steel-concrete bond plays an important role in the beam-to-column joints; it has to warrant the stress transfer from an element to another. Such transfer should be guaranteed in a short length.

The bond behaviour between steel profile and concrete is usually completely neglected in beams made of a steel profile and a concrete slab, where the stress transfer is due to mechanical devices (connectors). On the contrary in columns the contribution of bond at steel-concrete interface can be introduced in design approach since the contact surface is wider and concrete is completely or partially encased in the steel profile with a beneficial confinement effect.

The large extension of the interface usually may give rise to low values of bond strength, but allows to reach the total interaction of the two material and the plastic moment for the composite section, particularly for sections where the centroid of concrete and steel section coincide.

The bond mechanism in composite columns is complex and depends on many geometrical and mechanical parameters (Cosenza and Zandonini, 1997, Viridi and Bowling, 1980; Hamdan and Hunaiti, 1991; Hunaiti, 1994). Values of bond strength are suggested by international standards, such as Eurocode 4 (2004) and AISC (2005), and Italian recommendations, e.g. CNR 10016 (1999) and more recently the latest version of the NTC (DM, 2008).

The bond capacity is important for transferring stresses in the zones where structural elements are connected; the composite joints can be realized with various systems, but it is essential to transfer the stresses from one element to another loading both the materials to achieve the composite action. This result is based on a sufficient bond capacity able to guarantee short transfer lengths or on the use of mechanical connectors.

The threshold values of bond strength suggested by codes are based on experimental results of monotonic tests on composite columns concrete filled (Khalil, 1993; Hunaiti, 1994; Kilpatrick and Rangan, 1999; Johansson and Gylltoft, 2002; Mouli and Khelafi, 2007). Under seismic actions, significant degradation of strength and stiffness should be accounted for.

In order to study the bond behaviour of composite columns partially encased, experimental tests (Pecce and Ceroni, 2008a; Pecce and Ceroni, 2009) were designed and carried out at the Laboratory of University of Sannio (Benevento, Italy). The specimens are made of HEB profiles partially encased with concrete with and without longitudinal and transversal steel rebars. The influence of the interface roughness was tested by spreading the interface with oil in some cases; furthermore the effects of cyclic loads were considered.

In the following the experimental results are presented; some comparisons with code limits and with the results of similar studies on concrete filled columns are also developed

The tested specimens consist of steel profiles HEB 180 (flange thickness $t_f = 14$ mm, web thickness $t_w = 8.5$ mm, width and height of the section $H = B = 180$ mm) 630 mm length with a bond length of 450 mm. The experimental program includes specimens with and without steel reinforcement in concrete, oil at the interface before casting, monotonic and cyclic loading histories in compression and tension.

In Table 1 a list of specimens with their characteristics is provided: the type of load, the presence of steel reinforcement or oil along the interfaces, the mean strength of concrete in compression, R_{cm} , evaluated on three cubic specimens (side 150mm) for each casting. The structural steel members are made of steel type S275 and the internal re-bars are Fe430; in these tests the mechanical characteristics of steel are not significant since stresses are very low and far from yielding.

To allow the stress transfer between the two materials, each specimen was designed and constructed with the concrete part staggered from the steel one in longitudinal direction of 50 mm at both ends (Fig. 1a). The tests were carried

out placing the specimens in a universal electro-mechanic machine with capacity of 300kN (Fig. 1). For tests in compression only in one case (specimen C5) the load was applied on the steel profile turning over the specimen. In all cases the stress transfer to steel profile was measured and analysed.

In Figures 2a and b the specimens before casting with and without oil at the interfaces are displayed; in Figures 2c and 2d the specimens for the tensile tests with and without internal reinforcement are provided.

Table 1. Data of specimens for bond tests.

specimen	Stress	Load	Internal steel	Oil	R_{cm} [MPa]
C1	Compression	Monotonic	-	-	22
C2	Compression	Monotonic	-	-	22
C3	Compression	Monotonic	-	-	35
C4	Compression	Monotonic	-	-	35
C5	Compression (on steel)	Monotonic	-	-	35
Ca1	Compression	Monotonic	Yes	-	22
Co1	Compression	Monotonic	-	Yes	22
T1	Tension	Monotonic	-	-	22
T2	Tension	Monotonic	-	-	22
Ta1	Tension	Monotonic	Yes	-	22
To1	Tension	Monotonic	-	Yes	22
CYC1	Compression-Tension	Cyclic	-	-	35
CYCa1	Tension-Compression	Cyclic	Yes	-	35
CYCo1	Tension-Compression	Cyclic	-	Yes	35

Three displacement transducers were applied: one was placed vertically to measure the slip between concrete and steel, the other two were positioned horizontally on the two opposite sides to check eventual effects of load accidental eccentricity (Fig. 1).

In Figures 3a-b the experimental curves load versus slip obtained by the monotonic tests in compression are plotted; the slip is given by measures of the vertical transducer.

The elements signed C1 to C4 are characterized by two different castings of concrete with different compressive strength (22 MPa for casting 1, 35 MPa for casting 2), the element C5 (casting 2) was tested applying the compressive load on the steel profile.

The bond-slip relations of specimens C1 and C2 (casting 1, Fig. 3a) show three branches; the beginning of the curves shows a rigid behaviour without slip up to a peak value of bond strength, then there is a steep descending branch and finally a stable, practically horizontal, branch as far as great slips with a residual strength of about 40% of the peak one.

The experimental curves of elements C3 and C4 (casting 2, Fig. 3a) have a different shape; small slips occur from the beginning, there is not a peak, the

maximum load is reserved for the horizontal branch (mean value = 50kN) and is greater than the residual strength of specimens C1 and C2 (mean value = 30kN) of about 24%. For the specimens of the same casting but loaded applying compression on the steel profile, the result is similar with slips from the beginning and an equal value of the residual load (50kN).

In Figure 3b the reference specimen C1 is compared with the specimens Co1 and Ca1, from the same casting, having, respectively, oil at the interface and internal steel reinforcement. The surface treated with oil eliminates the effect of initial adhesion, the horizontal branch is reached without a peak and the maximum load is about 25% of the one of the specimen without oil.

A negative effect of internal reinforcement appears with a load reduction both at the peak and the residual strength, being the latter about 15% lower of the standard specimen.

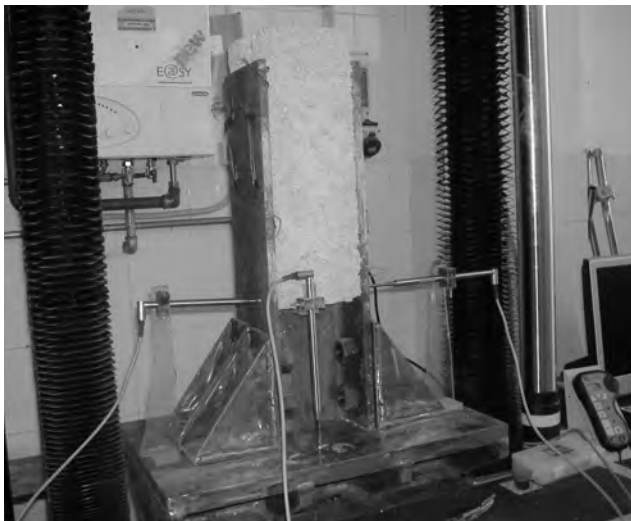


Figure 1. Set-up for bond tests on composite elements.

The experimental results suggest the shape of the curve varies with the quality of concrete in terms of casting and hardening conditions or the use of internal reinforcement; these conditions could influence shrinkage and subsequently reduce the adhesion and friction phenomena at the beginning.

Therefore the effective bond shear strength can be identified as the load corresponding to the horizontal branch after the peak, if it exists. This strength is less sensitive to concrete strength (when compressive strength increases of 50%, the bond strength increases of 24%), but depends heavily on the surface roughness, because it becomes less than 50% when the steel surfaces are impregnated with oil.

Similar results were obtained for tensile tests: the peak shape was not

always evident, the oil strongly reduced the bond strength, the reinforcement gave a slow reduction of bond strength. The residual bond, previously identified as the effective bond strength is about the same than in compression tests.

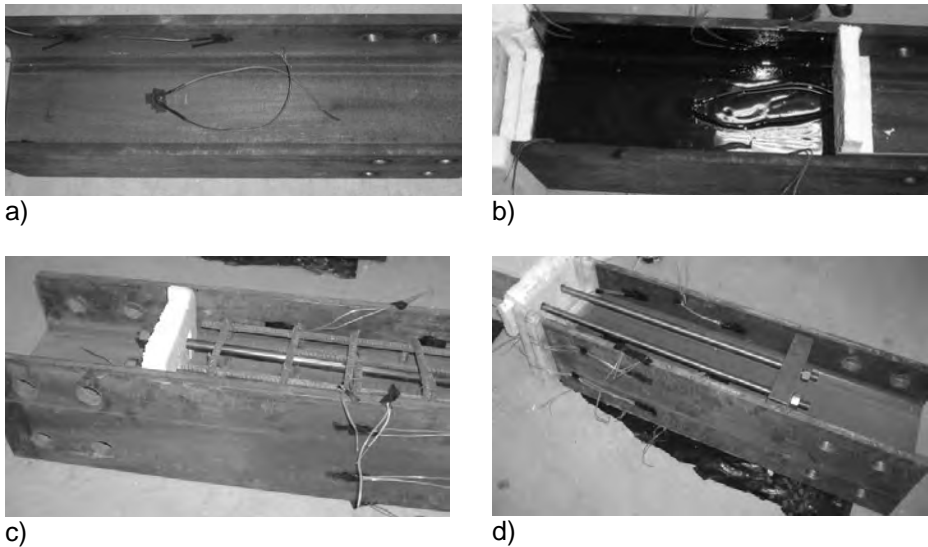


Figure 2. a) Specimen for test in compression; b) Specimen with oil for test in compression; c) Specimen with internal re-bars and reinforcement for tensile tests; d) Specimen with re-bars for tensile tests.

Three cyclic tests were performed. The first one (CYC1, casting 2) was carried out at beginning of the load history in compression, then 5 cycles were made between +20 kN and -20kN, a monotonic compression was applied up to a slip of 17 mm and finally the load was reversed to achieve a zero slip (Fig. 4).

It is worth to notice that during the 5 cycles at a load of about 40% of the monotonic strength (specimens C3 and C4 belonging to the same casting), when the load becomes zero, the slip is not recovered and higher values of slip need for reaching again the same load.

An evident phenomenon of pinching happens and the load is gained again only when concrete contrasts with steel profile at the interface zones where the friction is not yet exceeded.

The comparison of the cyclic curves with the monotonic one of a similar specimen of the same casting (C3) show the residual strength after 5 cycles is about 50% of the monotonic one. In the last branch in tension the cyclic curve shows an higher reduction respect to the monotonic one, that is referred to a specimen T1 (casting 1) with a concrete strength (22 MPa) lower than the one (casting 2, 35 MPa) used for cyclic tests.

The other cyclic tests confirm the observations previously noticed; when the specimen is oiled, degradation is negligible since friction have been already removed.

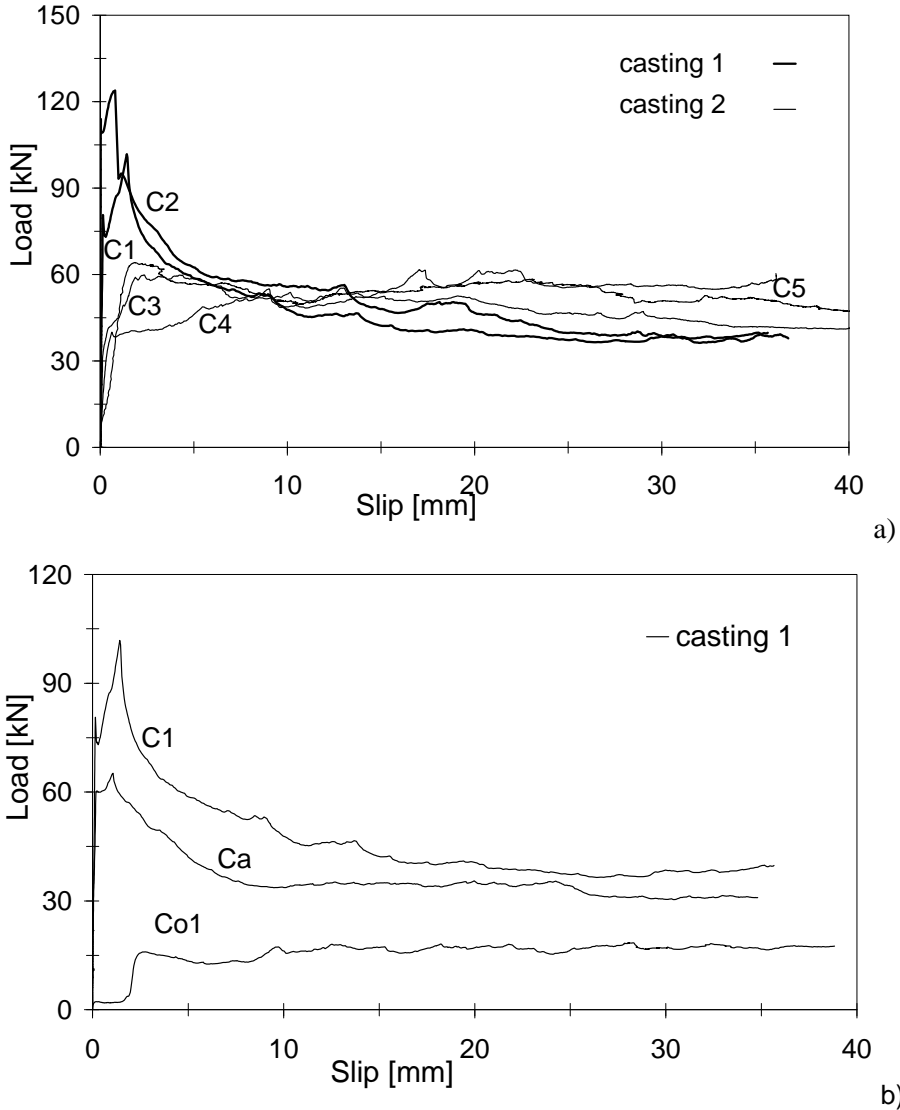


Figure 3. Load-slip relationship for specimens in compression: a) standard specimens; b) specimens with oil and internal reinforcement.

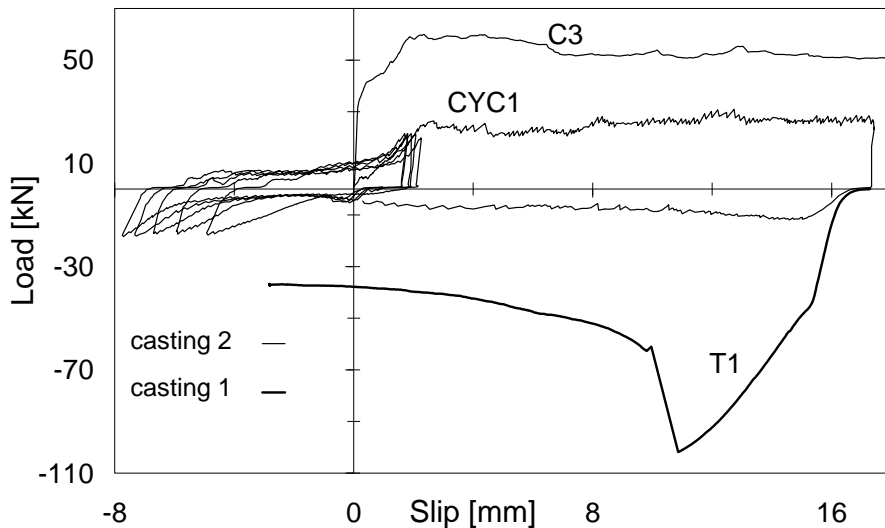


Figure 4. Load-slip relationship for cyclic tests of specimen CyC1.

The Italian code (NTC, 2008) gives the following values of bond strength to be assumed for design composite columns, according to the type of element:

- fully encased: 0.30 MPa
- circular concrete filled: 0.55 MPa
- rectangular concrete filled: 0.40 MPa
- for the flanges of partially encased: 0.20 MPa
- for the web of partially encased: 0.00 MPa

If these limits are exceeded, the entire load has to be transferred by connectors. These same limits are suggested also by Eurocode 4 (EC4, 2004), and similar values were provided in the previous edition of Eurocode 4 and in the Italian guidelines devoted to composite elements (CNR 10016, 1999); in these instructions it was clearly affirmed that in the joints between elements the transfer length has to be not greater than twice the smallest dimension of the cross section. The American recommendations (AISC, 2005) gives similar values for the concrete filled columns (0.40 MPa) and suggestions about the transfer length at joints, but recommends to neglect bond for partially encased columns.

The Italian code (NTC, 2008) for structures under seismic actions suggests (par. 7.6.5) that in the cases the transfer of shear stresses by bond mechanism is not sufficient mechanical connectors have to be introduced to guarantee the composite action. In the European code for seismic constructions (Eurocode 8, 2003) the values of bond stresses are not indicated, but constructive details and geometrical limits are suggested in order to assume an active collaboration between materials and to develop the ductility required. In columns partially encased with double T profiles, the concrete between flanges have to be

connected to web with stirrups or re-bars in order to form a clear mechanism of transferring between the concrete and the steel web.

The mean values of the experimental shear stresses could be evaluated dividing the applied load (in tension or in compression) by the entire interface area of the profile ($\tau=N/A_p$ with $A_p = 29.9 \cdot 10^4 \text{ mm}^2$).

However, in order to compare the experimental results with the code limits, it seems more correct to take into account only the interfaces of flanges since codes neglect the web contribution. Therefore the shear stress is calculated dividing the applied load to the only interface area of flanges ($\tau=N/A_{fl}$ with $A_{fl} = 16.2 \cdot 10^4 \text{ mm}^2$).

In Figure 5 the values of stresses are depicted versus slips. All compressive tests, except the specimen treated with oil, had a residual strength greater than 0.2 MPa; for tensile tests the specimens with oil and internal reinforcement gave values lower than this limit.

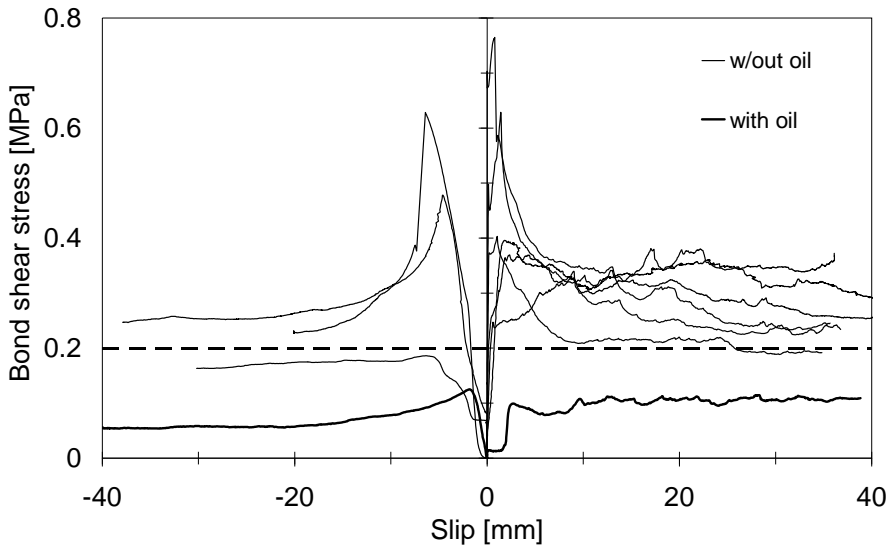


Figure 5. Bond stress-slip relationship of all monotonic tests assuming adherent only the flanges.

The bond tests planned and carried out to study the bond behaviour at the steel-concrete interface in composite columns partially encased have highlighted many information that are yet not available in the literature. The first part of the bond-slip relationship is strongly influenced by adhesion phenomena, that can result in an initial very stiff branch until a peak followed by a sharp descending branch and a last horizontal branch characterized by a constant residual bond stress. In other cases, depending on the casting of concrete, the behaviour at beginning is more deformable and the horizontal

branch occurs without reaching a peak before. It is clear that the bond strength is defined by the horizontal line that allows great values of slip develop.

Application of compressive or tensile loads does not change the residual value of bond strength, which remains constant if load is applied to concrete or steel, even if this aspect has been analyzed in only one test.

The compressive strength of concrete controls the bond strength according to a dependence much lower than proportional, therefore the concrete strength does not appear a relevant parameter, as already assumed in Italian (NTC, 2008) and European codes (Eurocode 4, 2004) that give both a limit value of bond strength depending only on the type of column.

The specimens with oil at the interfaces showed a reduction of bond strength lower than 50% of the reference ones confirming the importance of friction phenomena related to the roughness of the contact surfaces. A reduction of bond strength of about 10-20% is also due to the presence of internal steel reinforcement made of longitudinal re-bars and stirrups.

The experimental values of bond strength are always higher than the limit given by the codes, if the web contribution is neglected and the entire transfer is attributed to the flanges.

The comparison of the results obtained in the presented experimental program confirms that the values of the bond strength suggested by the Italian code is too high for columns partially encased; moreover the friction is very important in this type of columns, so that the reduction of roughness, by using oil treatment of surfaces, causes a large decreasing of bond strength.

Finally, the few tests performed according to cyclic load histories show a strong degradation of stiffness and strength in the bond-slip relationship, due to the fundamental role of friction.

In conclusion the limits of European and Italian codes need to be reviewed in order to be reduced and probably details relative to the surface conditions have to be introduced. Furthermore in seismic constructions the bond contribute has to be neglected and suitable connectors have to be applied to guarantee strength and stiffness under cyclic actions, as already suggested in Eurocode 8.

Base joint type socket

The ductility of base column connections depends on the type of column and connection system. It is noteworthy that, to date, analytical and experimental research are focusing on the effects of the base connection layout on the performance of beam-columns, either partially or fully encased, is lacking (Spacone and El-Tawil, 2004). Few results are available and were derived chiefly from the steel structures; their applicability within the capacity-design framework should be further investigated (Hajjar, 2002; Mazzolani, 2003). The composite action, may, however, affect the failure modes thus endangering the

inelastic performance of the structural member (e.g. Di Sarno and Elnashai, 2002).

Experimental tests (Di Sarno et al., 2007) have shown that an innovative base-column joint is the socket-type system, derived from precast reinforced concrete structures that leads to large energy dissipation. However a few experimental data and numerical models (Pertold et al. 2000a, 2000b) are still available, furthermore the codes do not give provisions for the design, therefore more studies need about this innovative joint.

A finite element model was developed for a partially encased column tested during another research program (Di Sarno et al., 2007); the connection system at the base used for the test is an innovative one type socket. In Figure 6 the scheme of the connection is shown together with the section of one of the composite column. Three-dimensional finite elements were used for column and foundation block; the constitutive relationship was assumed elastic-plastic for steel, bilinear for concrete in tension and multilinear in compression. In Figure 7 the mesh of the model is shown; since the element is symmetric, only half of it has been modelled.

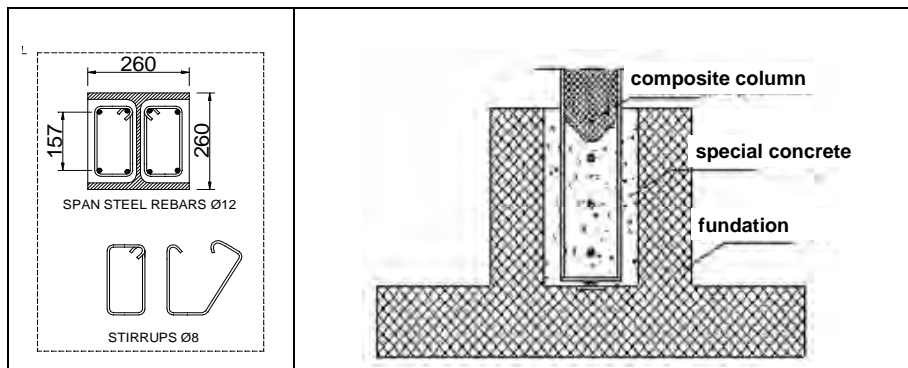


Figure 6. The section of the composite column (left), the type of connection at the base (right).

The numerical model for this innovative base connection was assembled in order to grow a parametric analysis; the numerical analysis and the experimental results would allow to develop guide lines and provisions for evaluating ductility.

The finite element model shows a good agreement with the experimental test; in Figure 8a the comparison with the experimental test on a column (Fig. 6) with the socket type connection at the base is reported in terms of force-displacement curve. Besides the model allows to analyse the stress and strain distribution in the foundation block; the extension of the transfer zone in the block increases enhancing the post-elastic displacement.

The numerical simulations have been carried out up to the maximum displacement reached during the tests; at such condition the maximum strains attained in the materials by the FE model are about equal to 0.08 and are quite the same in steel and concrete due to the perfect bond hypothesis assumed for the two materials. These high values of strains in the concrete, at the displacement actually reached during the test, confirm the effective confinement action of the steel profile on the filling concrete, which thus results more ductile.

In Figure 8b the strain distribution is plotted along the columns both in the part above the foundation block and inside it: the ends lines indicate the yielded zone, the intermediate line corresponds to the beginning of the part of the column embedded in the socket. The strain distribution shows that the yielding zone of the column, i.e. the part of column in which strains exceed the yielding limit (about 0.0016 for flanges), extends to about 500 mm along the height outward from the foundation block (about 0.3 times the total height), while in the part of column inside the block, a small part of about 50 mm is involved (each finite element has an height of 5 mm).

Further analyses are in progress to use the model for defining the role of mechanical and geometrical properties on the rotational capacity at the base of the column using this type of connection. In particular the variation of concrete strength and steel yielding stress, the column length embedded in the foundation block have been identified as the most important variables.

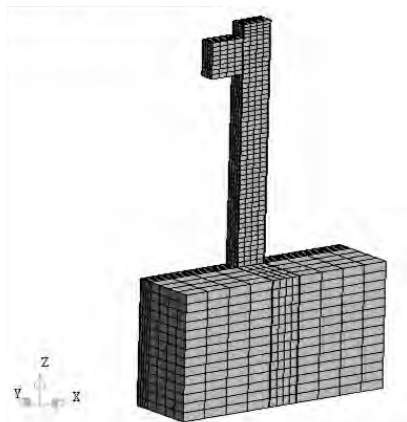


Figure 7. Mesh of the column and foundation.

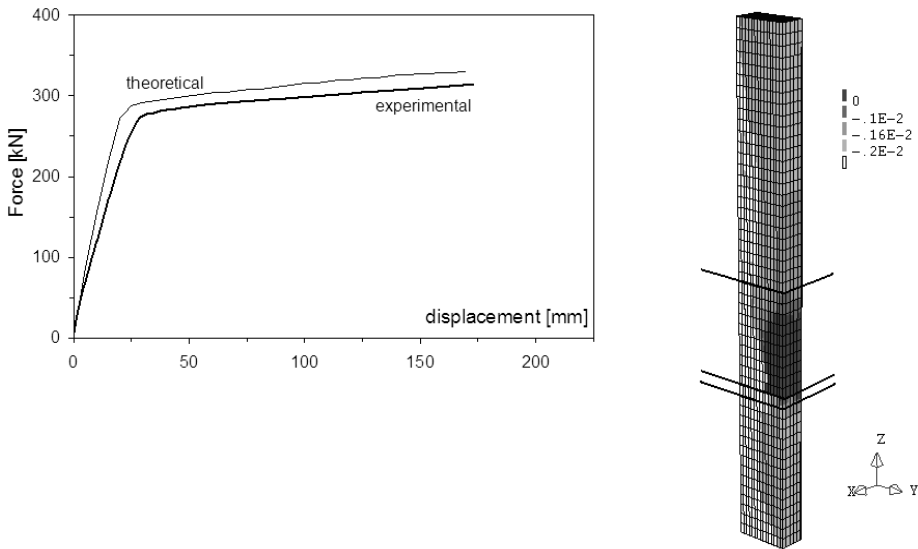


Figure 8. Comparison between numerical model and experimental results (left).
Theoretical strain distribution along the column.

3. COMPOSITE BEAMS

As far as the deformation capacity in post-elastic field of composite beams is concerned, the behaviour under hogging bending moment is particularly interesting, since it is the most probable stress condition at the column joint due to vertical load effect and is an unfavourable working condition of a composite beam. For evaluating the ultimate rotation of a plastic hinge assessed formulations are available for reinforced concrete elements (OPCM-3431/2005, Eurocode 8, 2004); on the contrary for composite elements the behaviour of steel elements is sometimes assumed as reference neglecting the effect of steel concrete interaction.

The problem solution could be very complex since the rotational capacity of composite beams depends on many parameters: the concrete slab and its reinforcing rebars, the type of steel profile, the beam-column connection and the shear connectors. Also for this topic further experimental results need to analyze the influence of the various features.

The classification of composite beams for local buckling depends hardly on the extension of the compressed part of the web, especially if it is larger than 50% of the entire web; furthermore other parameters influence the rotational capacity: percentage of slab reinforcement, connection degree and connectors distribution, semi-rigid joint to column .

A state of the art has been considered of the experimental results of composite beams under hogging bending moment. The focus is to evaluate rotational capacity and organize the data according the most important issues.

State of the art

A thorough assessment of the parameters that may influence the rotation capacity of the structural member was carried by considering the available experimental tests (Loh et al., 2004; Kemp et al., 2001; Fabbrocino et al., 2001; Amadio et al., 2004). The tests were carried out on simply supported beams under hogging moments; the plastic rotation is thus measured through the rotation at the supports. The main parameters affecting the stiffness and strength of composite steel and concrete beams are as follows:

- the ratio $M_{pl} / M_{pl,steel}$ expressing the overstrength, given by the ultimate bending moment of the composite section and the moment of the steel beam;
- the ratio $(A \cdot f_y)_{rebar} / (A \cdot f_y)_{profile}$ correlating the strength of the longitudinal steel rebars to the strength of the structural steel beam. This parameter is essential to estimate the position of the neutral axis and to determine whether or not the buckling erodes the rotational capacity of the beam;
- the ratio L' / H_{tot} expresses the distance of the point of application of the force from the support and the section depth;
- the steel reinforcement overstrength $(f_u / f_y)_{rebars}$;
- the shear stud interaction ratio N / N_f ;
- the factor ρ expressing the ratio of the steel reinforcement in the slab and the slab cross section area;
- the ductility $(\varepsilon_u / \varepsilon_y)_{rebars}$ of the steel reinforcement.

Table 2 summarises the results of the experimental tests assessed and shows the effects on the plastic rotations at the support ϑ_{pl} .

Table 2. Values of plastic rotation ϑ_{pl} and the parameters influencing the rotation capacity of the composite beams.

paper	beam	ϑ_{pl}	$\frac{M_{pl}}{M_{pl,steel}}$	$\frac{(A \cdot f_y)_{rebar}}{(A \cdot f_y)_{profil}}$	$\frac{L'}{H_{tot}}$	$\left(\frac{f_u}{f_y}\right)_{rebars}$	$\frac{N}{N_f}$	ρ (%)	$\left(\frac{\epsilon_u}{\epsilon_y}\right)_{rebars}$
Fabbrocino et al. (2001)	A1	164.00	1.54	0.09	2.03	1.16	1.00	0.64	51.90
	B1	144.60	1.44	0.09	2.03	1.16	1.00	0.64	51.90
Kemp et al. (1995)	MR2	3.20	2.28	0.12	3.98	-	1.00	0.31	10.00
	LR2	25.50	1.79	0.12	3.44	-	1.00	0.31	10.00
	SR	21.00	1.96	0.12	4.50	-	1.00	0.31	13.40
	LSR	49.00	1.98	0.24	3.56	-	1.00	0.50	4.20
	SSR	59.90	2.17	0.20	4.50	-	1.00	0.50	4.20
Loh et al. (2004)	CB1	30.90	4.50	0.37	6.79	1.27	0.83	1.95	95.00
	CB2	157.80	3.86	0.37	6.79	1.27	0.50	1.95	95.00
	CB3	152.20	4.17	0.37	6.79	1.27	0.33	1.95	95.00
	CB4	10.60	4.34	0.37	6.79	1.27	0.83	1.95	95.00
	CB5	64.10	4.06	0.37	6.79	1.27	0.50	1.95	95.00
	CB6	92.00	4.23	0.37	6.79	1.27	0.33	1.95	95.00
	CB7	165.80	3.53	0.18	6.79	1.27	1.00	0.98	95.00
	CB8	28.20	4.75	0.55	6.79	1.27	0.88	2.93	95.00
Amadio et al. (2004)	B1	86.80	1.94	0.17	2.67	1.29	1.00	1.00	10.00
	B2	110.50	2.00	0.17	2.67	1.29	1.00	1.00	10.00

The values expressed in Table 2 show that any single parameter assessed in the performed tests does not significantly influence the plastic rotation. However, it can be argued that:

- the increase of $(A \cdot f_y)_{rebar} / (A \cdot f_y)_{profil}$ lowers the plastic rotation;
- the value of ϑ_{pl} increases by enhancing the slenderness of the beam L' / H_{tot} . However slender beams could be affected by the member buckling limiting the plastic rotation;
- the material overstrength $(f_u / f_y)_{rebars}$ does not influence significantly the rotation capacity of beams under hogging bending moments;
- the lower the percentage ρ of longitudinal rebars the higher the plastic rotation;
- the plastic rotation increases as the degree of shear interaction N / N_f decreases;

- the material ductility $(\varepsilon_u / \varepsilon_y)_{rebars}$ augments the plastic rotation of the composite beams;

The effect of $M_{pl} / M_{pl,steel}$ is not significant on the member plastic rotation. Further results are aimed to provide a reliable relationship for the available plastic rotation depending on the parameters introduced above.

Experimental tests

Experimental tests were designed and carried out on four composite beams under hogging moment. The length of the beams is 4 m, that could be significant of a continuous beam about 8m long in a frame; the loading pattern of three point bending test was used loading the beam upside-down (the slab below). The profile is an IPE360 and the steel is S275; for the rebars the steel is Feb 44k (equivalent to B450C). Two different distributions of connectors (uniform and not uniform) and two types of RC slabs have been realized; the slab is solid or with profiled sheeting, the thickness is always 13cm and two widths are considered (Fig. 9).

The beams were designed assuming class 1 sections for the specimen 1, 2 and 3 and class 2 sections for the specimen 4.

The shear studs consists of 19mm diameter Nelson type connectors; they can be assumed ductile in compliance with the code specifications. The resistance of the studs is estimated through the provisions implemented in EC4 (2004). The computed values are 65.1kN for the specimen with solid slabs and 26.2kN for the beams with steel deck. The concrete cubic strength is $f_{ck}=25\text{MPa}$.

The number of shear studs to achieve full interaction is computed obtaining: 10 for beam #1 and #2, 23 for beam #3, 36 for beam #4.

The degree of shear interaction N / N_f is 0.9 for beam #1 and greater than 1 for beams #2,3,4.

A number of tests were carried out on the material of construction used for the specimens. For the structural steel, tensile tests were carried out in compliance with UNI 10002/92. The following mean values were derived for the coupon extracted from the flanges and webs of the steel members:

$$f_y=401 \text{ MPa} \quad f_t=588 \text{ MPa} \quad \varepsilon_u=17.5 \%$$

with a standard deviation of 8.4 MPa, 8.8 MPa and 1.5 %, respectively. The nominal characteristic yield strength of the steel is thus $f_{yk}=369 \text{ MPa}$.

Three tensile tests were carried out on the steel longitudinal reinforcement; the results are as follows:

$$f_y=455 \text{ MPa} \quad f_t=577 \text{ MPa} \quad \varepsilon_u=20,5 \%$$

with a standard deviation of 6.6 MPa, 3.6 MPa and 4.1 % respectively. It may be thus assumed that the nominal characteristic value of the grade is 430 MPa

Crushing tests were carried out on 3 concrete cubic specimens; the width of the specimen is 150mm; the mean value of the strength is 37.6MPa.

It is observed that the reinforcement steel have a negligible overstrength with respect to the nominal value included in the standards; conversely, a value of overstrength equal to 1.34 was found for the structural steel. The latter figure exceeds the limit provided in the recent NTC 2008, i.e. 1.20.

The degree of shear connections does not change significantly utilizing the actual values of the steel grades computed experimentally.

The steel and composite cross sections were re-assessed on the basis on the actual mechanical properties estimated experimentally. It follows:

$$\frac{c}{t_f} = \frac{85}{12.7} = 6.7 < 10 \cdot \varepsilon = 10 \cdot \sqrt{235 / f_y} = 10 \sqrt{235 / 401} = 10 \cdot 0.77 = 7.7 \quad \text{and the}$$

section class is 1.

Beams # 1, 2 and 3

Neutral axis (compression zone depth) $x = 236 \text{ mm}$

$$\alpha = \frac{x - (t_f + r)}{d} = \frac{236.00 - (12.70 + 18.00)}{360.00 - 2 \cdot (12.70 + 18.00)} = \frac{205.3}{298.6} = 0.69$$

hence $\frac{d}{t_w} = 37.32 < \frac{393\varepsilon}{13\alpha - 1} \approx 38.18$ and the cross section belongs to class 2.

$$\frac{d}{t_w} = 37.32 < \frac{456\varepsilon}{13\alpha - 1} \approx 40.08 \Rightarrow \text{class section 2}$$

Beam # 4

Neutral axis (compression zone depth) $x = 268 \text{ mm}$

$$\alpha = \frac{x - (t_f + r)}{d} = \frac{268.00 - (12.70 + 18.00)}{360.00 - 2 \cdot (12.70 + 18.00)} = \frac{237.3}{298.6} = 0.80$$

thus $\frac{d}{t_w} = 37.32 < \frac{456\varepsilon}{13\alpha - 1} = 37.39$

and the class section is 2, at the border with class 3.

In Table 4 the properties of the four specimens are summarized. In Figure 10 the distribution of connectors along the beam span is shown for each specimen, and in Figure 11 the preparation of specimens is shown.

Table 4. Properties of the sample beams.

BEAM	CONNECTION	TYPE OF SLAB	SLAB WIDTH
beam #1	Partial	Solid	100 cm
beam #2	Full	Solid	100 cm
beam #3	Full	profiled sheet	100 cm
beam #4	Full	profiled sheet	160 cm

The tests were conducted in displacement control and many global (deflection) and local measurements (strains of the profile, rebars in the slab, slip between slab and profile) were performed. The aim was to have information, for adding to the knowledge of the technical literature, of the rotational plastic capacity and assess in a detailed fashion the role of the various parameters that establishes its threshold and in case review the code classification.

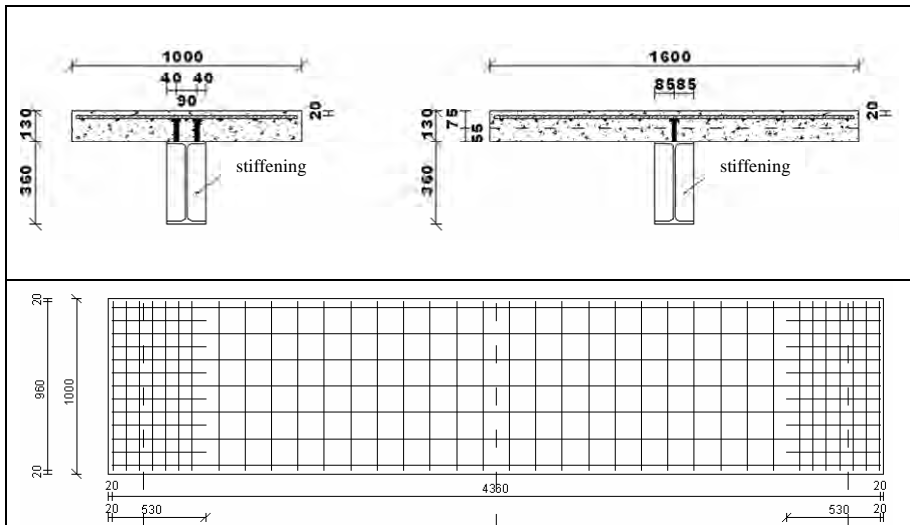


Figure 9. Beam layout: steel reinforcement of the slab with 100cm width.

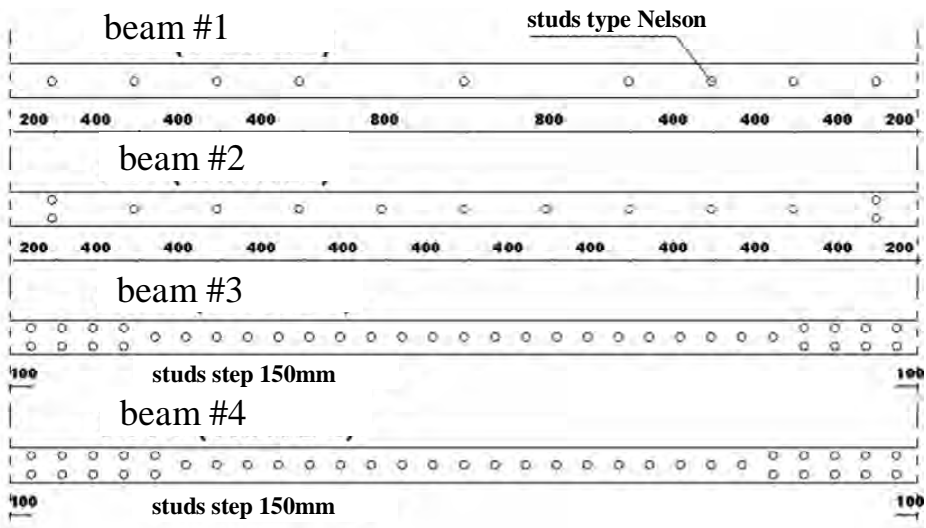


Figure 10. Distribution of the studs in the sample beams.

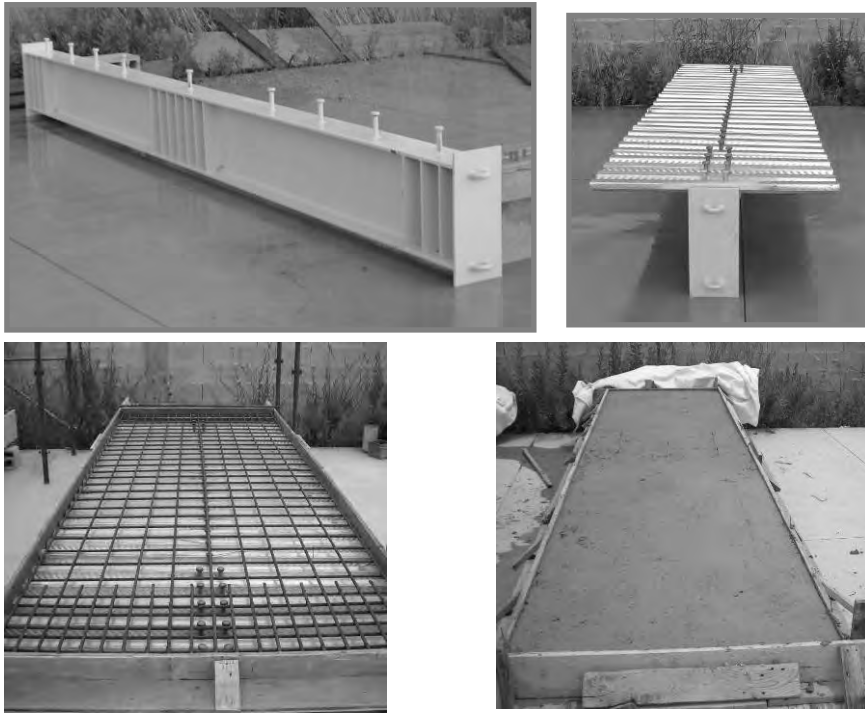


Figure 11. The beams before and during concrete casting.

Experimental results

The experimental tests gave results disagreeing from the predictions of the project. The beams were designed with the steel profile of class 1 or 2 to have great plastic rotations, but global and local buckling occurred limiting the plastic rotation of all the 4 beams. In Figures 12 and 13 global and local buckling are shown for one beam; in Figure 14 the cracking pattern of the slab at the end of the test is shown. In Figure 15 the force-displacement curve is depicted for all the specimens.

The shape of the plots shows that the specimens behave initially in a similar manner; however the response differs as the inelastic deformations increase. The beam with the larger slab exhibits the higher strength.

All the tests were terminated at the onset of either global or local buckling. The post-elastic branch is limited; as a result the rotation ductility is eroded because of the occurrence of the premature buckling.

In Figure 16 the force-slip relation measured with the transducers located at 400mm from the support of beam #1 is depicted. It is the position of the first stud from the support and the measure was carried out on both sides of the

beam; the clear difference of slip in the post elastic field is due to the torsion deformation of the beam after global buckling.



Figure 12. Global buckling

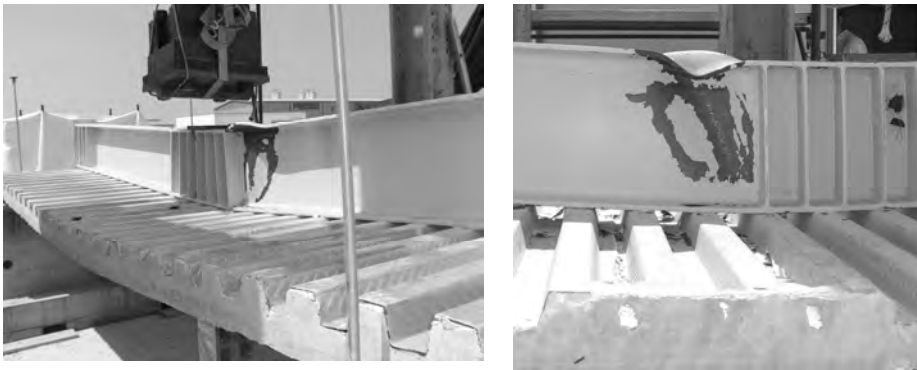


Figure 13. Local buckling of a beam tested.

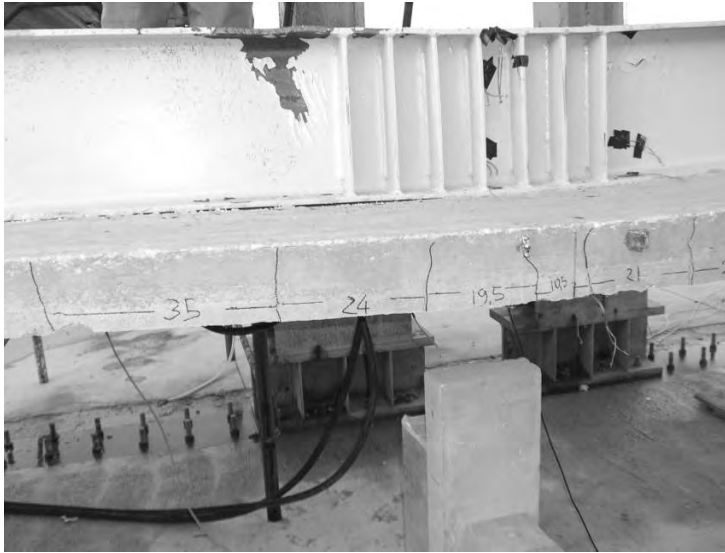


Figure 14. Cracking of the slab.

The bending plastic moments due to the steel rebars and structural steel cross section were evaluated, using the actual strength of the two steel grades, and neglecting concrete in tension. The results are in Table 3; they are compared with the maximum bending moment determined through the experimental test.

For all the beams the experimental plastic moment is lower than the theoretical counterpart but is higher than the steel one, that is 408 kNm. The buckling prevented the onset of the bending plastic moment.

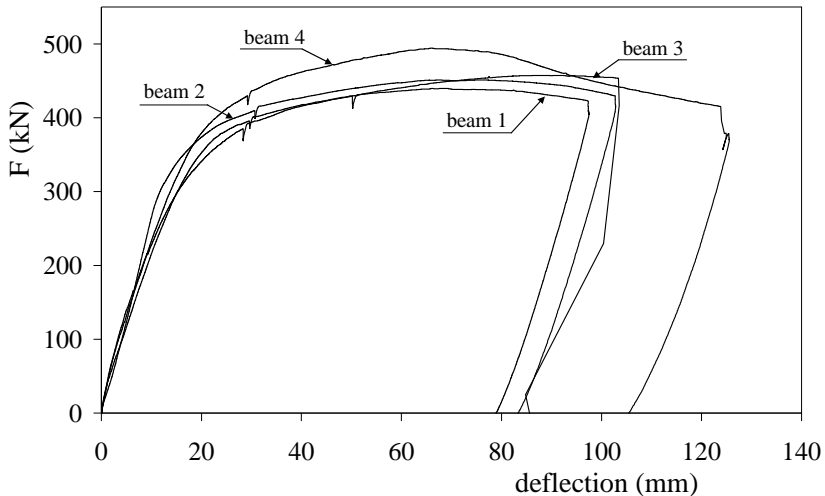


Figure 15. Force-displacement relation for the four beams tested.

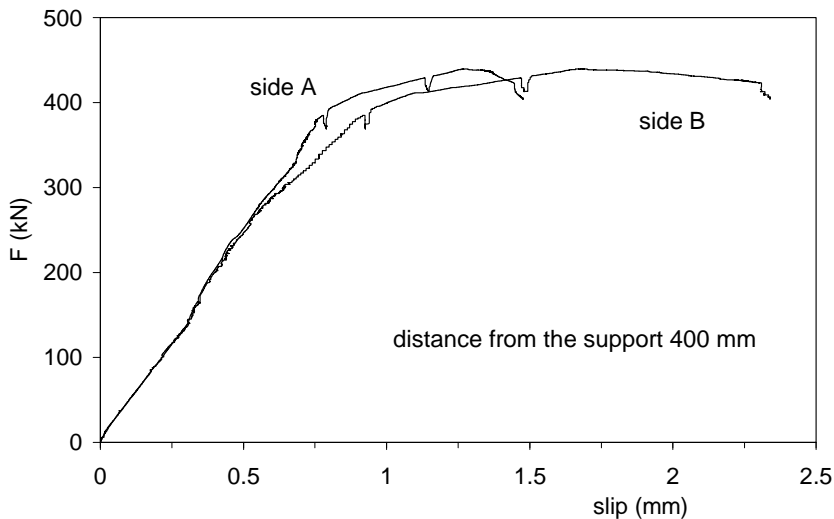


Figure 16. Force slip at one end of beam 1.

Table 3. Experimental and theoretical plastic moments.

beam	$M_{pl, test}$ (kNm)	$M_{pl, num}$ (kNm)
1	440	483
2	450	483
3	457	483
4	493	534

Final remarks

The experimental tests carried out in the present research led to unexpected results. The restraints applied to elements were probably not effective to avoid global buckling for this shape of steel profile. Furthermore the yield strength of the steel member, much higher than that employed in the design, caused the onset of the local buckling and in turn prevented the attainment of the full plastic capacity of the sample members.

The implementation of a refined finite element model is still in progress; such model is being calibrated in such a way to simulate accurately the onset of buckling phenomena. The outcomes of the present research are interesting for future similar experimental tests because they highlighted the needs to perform more accurate checks for local and global buckling occurrence and to re-assess the existing cross-section classification for steel and composite structural members.

REFERENCES

- Amadio, C., Fedrigo, C., Fragiaco, M. and Macorini, L., [2004] "Experimental evaluation of effective width in steel-concrete composite beams", *Journal of Constructional Steel Research*, 60, 2, pp. 199-220.
- American Institute of Steel Construction [2005]. "Specification for Structural Steel Buildings", *ANSI/AISC*, 360-05, Illinois, Chicago.
- Broderick, B.M and Elnashai, A.S. [1996]. "Seismic response of composite frames-I. Response criteria and input motion", *Engineering Structures*, 18(9), 696-706.
- Bursi, O.S., Caramelli, S., Fabbrocino, G., Molina, J., Salvatore, W., Taucer, F., [2004]. "3D Full-scale seismic testing of a steel-concrete composite building at ELSA", *Contr. No. HPR-CT-1999-00059*, European Community.
- CNR 10016 [1999]. "Strutture composte di acciaio e calcestruzzo istruzioni per l'impiego nelle costruzioni", *CNR Bollettino Ufficiale n. 194 – Norme tecniche, parte IV*, Roma. In Italian.
- Cosenza, E and Zandonini, R. [1997]. "Composite Construction, in Handbook of Structural Engineering", *W.F. Chen Editor, CRC, Boca Raton, USA*.
- Di Sarno, L. and Elnashai, A.S. [2002]. "Seismic Retrofitting of Steel and Composite Building Structures", *Mid-America Earthquake Center Report, CD Release 02-01*, University of Illinois at Urbana-Champaign, IL, USA
- Eurocode 4 [2004]. "Design of composite steel and concrete structures - Part 1.1: General rules and rules for buildings", *European Committee for Standardization*, Brussels, Belgium.
- Eurocode 8, [2004] "Design provisions for earthquake resistance of structures. Part 1.3: General rules. Specific rules for various materials and elements", *European Committee for Standardization*, Brussels, Belgium.
- Fabbrocino, G., Manfredi, G. and Cosenza, E., [2001] "Ductility of composite beams under negative bending: an equivalence index for reinforcing steel classification", *Journal of Constructional Steel Research*, 57, 2, pp. 185-202.
- Fabbrocino, G., Manfredi, G., Cosenza, E. and Pecce, M. R. [2001]. "Some remarks on deformation capacity of composite frames in seismic areas", *Proc. of the 1st International Conference on Steel and composite Structures*, ICSCS '01, Pusan, Korea.
- Hajjar, J.F. [2002]. "Composite Steel and Concrete Structural Systems for Seismic Engineering", *Journal of Constructional Steel Research*, 58(5-8), 702-723.
- Hamdam, H. and Hunaiti, Y. [1991]. "Factors affecting bond strength in composite columns", *Proceedings of the 3rd International Conference on Steel-Concrete Composite Structures*, Fukuoka, Japan, 213-218.
- Hunaiti, Y.M. [1994]. "Aging effect on bond strength in composite sections", *Journal of Materials in Civil Engineering*, 6 (4), 469-473.
- Johansson, M. and Gylltoft, K. [2002]. "Mechanical Behavior of Circular Steel-Concrete Composite Stub Columns", *Journal of Structural Engineering*, 128(8), 1073-1080.
- Kemp, A.R. and Nethercot, D.A., [2001] "Required and available rotations in composite beams with semi-rigid connections", *Journal of Constructional Steel Research*, 57, 4, pp. 375-400.

- Kemp, A.R., Dekker, N.W. and Trincherò, E., [1995] "Differences in inelastic properties of steel and composite beams", *Journal of Constructional Steel Research*, 34, 2-3, pp. 161-185.
- Khalil, H.S. [1993]. "Push-out strength of concrete-filled steel hollow sections", *The Structural Engineer*, 71(13), 230-233.
- Kilpatrick, A. E., and Rangan, B. V. [1999]. „Influence of interfacial shear transfer on behavior of concrete-filled steel tubular columns", *ACI Structural Journal*, 96(S72), 642–648.
- Lee, T.K.L. and Pan, A.D.E. [2001]. "Analysis of composite beam-columns under lateral cyclic loading", *Journal of Structural Engineering*, ASCE, 127(2), 186-193.
- Loh, H.Y., Uy, B. and Bradford, M.A., [2004] "The effects of partial shear connection in the hogging moment regions of composite beams, Part I – Experimental study", *Journal of Constructional Steel Research*, 60, 6, pp. 897-919
- Mazzolani, F.M. [2003]. "Steel and composite structures in European seismic areas: research, codification, design and applications", *Earthquake Spectra*, 19(2), 415-452.
- Min.LL.PP, DM 14 gennaio [2008]. "Norme Tecniche per le Costruzioni (NTC)", *Gazzetta Ufficiale della Repubblica Italiana*, 29.
- Mouli M., Khelafi H., [2007]. "Strength of short composite rectangular hollow section columns filled with lightweight aggregate concrete", *Engineering structures*, 29(8), 1791-1797.
- OPCM [2003]. "General Criteria for New Seismic Zonation in Italy and Seismic Standards", *Department of National Emergency Agency*, Rome, Italy (*in Italian*).
- Pertold J., Xiao R;Y., Wald F. [2000a]. "Embedded steel column bases – I. Experiments and numerical simulation", *Journal of Constructional Steel Research* 56, pp. 253–270.
- Pertold J., Xiao R;Y., Wald F. [2000b]. "Embedded steel column bases – II. Design model proposal", *Journal of Constructional Steel Research* 56, pp. 271–286
- Ricles, J.M. and Paboojian, S.D. [1994]. "Seismic performance of steel-encased composite columns", *Journal of Structural Engineering*, ASCE, 120(8), 2474-2494.
- Shanmugam, N.E. and Lakshmi, B. [2001]. "State of Art Report on Steel-Concrete Composite Columns". *Journal of Constructional Steel Research*, 57(10), 1041-1080.
- Spacone, E. and El-Tawil, S. [2004]. "Nonlinear analysis of steel-concrete composite structures: State of the art", *Journal of Structural Engineering*, ASCE, 130(2), 159-168.
- Thermou, G.E., Elnashai, A.S., Plumier, A. and Doneux, C. [2004]. "Seismic design and performance of composite frames", *Journal of Constructional Steel Research*, 60(1), 31-57.
- Virdi, K.S. and Dowling, P.J. [1980]. "Bond strength in concrete filled steel tubes", *Proc. of the IABSE Periodica*, 125-130.
- Di Sarno L., Pecce M.R. [2007]: Capacità rotazionale di travi composte acciaio-calcestruzzo, *Atti del XX congresso CTA*, Catania, Italy.
- Di Sarno L., Pecce M.R., Fabbrocino G. [2007]: "Inelastic response of composite base column connections", *Journal of Constructional Steel Research*, 63(3), 819-832.
- Pecce M, Ceroni F. Bibbò F., Rossi F. [2008] "Comportamento sperimentale di travi composte soggette a momento negativo", *Atti del VII Workshop italiano sulle strutture*

- composte*, Benevento, pp. 9-22, Dicembre 2009, Aesse Stampa – Benevento, ISBN 9788890275234.
- Pecce M., Ceroni F. [2008a] “Prove di aderenza in colonne composte partially encased”, *Atti del VII Workshop italiano sulle strutture composte*, Benevento, pp. 229-240, Dicembre 2009, Aesse Stampa – Benevento, ISBN 9788890275234.
- Pecce M., Ceroni F. [2008b] “Modellazione del collegamento alla base per colonne composte partially encased”, *Atti del VII Workshop italiano sulle strutture composte*, Benevento, pp. 263-274, Dicembre 2009, Aesse Stampa – Benevento, ISBN 9788890275234.
- Pecce M., Ceroni F., Bibbò F.A., Rossi F. [2010], Experimental results on steel-concrete composite beams under hogging moment, *Proceedings of 4th International Conference on Steel & Composite Structures*, 21–23 July 2010, Sydney, Australia, CD ROM
- Ceroni F., Garofano A., Pecce M. [2010] “Numerical model of a base connection for partially encased columns” *Proceeding of 14th European Earthquake Conference*, 28 August-2 September 2010, Ohrid, Macedonia, CD ROM.
- Pecce M., Ceroni F. [2010] “Bond tests of partially encased composite columns”, *International Journal of Advanced Steel Construction (IJASC)*, Vol. 6, No. 4, December 2010, 1001-1018.
- Pecce M., Ceroni F., Bibbò F., Rossi F. [2011] “Experimental behavior of composite beams under hogging bending moment” submitted to *Steel & Composite Structures*, under review.

STEEL BRACED FRAMES WITH VISCOELASTIC OR ELASTOPLASTIC STRUCTURAL DAMPERS

Andrea Dall'Asta¹, Luigino Dezi², Graziano Leoni¹, Laura Ragni²,
Alessandro Zona¹

¹ *Dipartimento di Progettazione e Costruzione dell'Ambiente,
Università di Camerino, Ascoli Piceno, Italy*

² *Dipartimento di Architettura Costruzioni e Strutture,
Università Politecnica delle Marche, Ancona, Italy*

Abstract. Experimental and numerical investigations on steel structures equipped with dissipative braces based on elastoplastic and elastomeric devices are illustrated. The experimental campaign involved a steel-concrete composite mock-up with semi-rigid joints equipped with two kind of braces: dissipative diagonals made of Bulking Restrained Braces (BRBs) devices placed in series with elastic braces, and chevron-type braces equipped with High Damping Rubber (HDR) dampers. Quasi-static displacement-controlled cyclic tests were carried out on the first case, whereas free vibration tests, followed by force-controlled and displacement-controlled cyclic tests were performed in the second case. Afterward, numerical models developed for the dissipative braces and relevant design methods are illustrated. Specifically, a Displacement-Based-Design (DBD) procedure for dissipative steel braced frames with pinned joints, valid for both elastoplastic and elastomeric (viscoelastic) dampers is presented.

Keywords: steel braced frames; viscoelastic dampers; elastomeric dampers; elastoplastic dampers; buckling restrained braces; displacement-based design.

1. INTRODUCTION

Concentrically braced steel or steel-concrete composite frames present some advantages as compared to other seismic resistant systems, such as moment resisting frames [1]. To begin with, they are simple structural systems, especially if pinned beam-column connections are used, offering high lateral stiffness for drift control. In addition, the earthquake-induced energy is dissipated by the diagonal bracing members only, not part of the gravity framing system. However, conventional steel braces present several problems under strong earthquakes. First of all, braces can dissipate a reduced amount of seismic energy because of compression buckling, leading to oversized bracing members and foundations. In addition, conventional steel braces often fracture prematurely due to low cycle fatigue, as

documented in [2]. Finally, due to the limited capacity of braces to redistribute the seismic demand over the building height, the inelastic deformations tend to concentrate in few stories and significant residual lateral deformations at the end of a seismic event may occur [3]. In order to overcome these disadvantages, dissipative devices can be used to obtain innovative highly dissipative braces. Supplemental dampers may be classified into three categories: hysteretic, velocity-dependent and others. Examples of hysteretic (displacement-dependent) dampers include devices based on friction and yielding of metals. Examples of velocity-dependent systems include dampers consisting of viscoelastic solid materials, dampers operating by forcing fluid through an orifice, e.g., viscous fluid dampers. Other systems have characteristics that cannot be classified by one of the basic types, such as dampers made of shape memory alloys. A complete state-of-the-art and state-of-the-practice on energy dissipation devices may be found in [4][5][6][7]. In the present work attention is focused on concentric steel braced frames with pinned joints (or semi-rigid joints) in which the dissipative bracing system is the only (or the main) seismic resistant component. Thus only dissipative devices with adequate stiffness and damping are considered, such as elastoplastic (metallic) and viscoelastic devices.

A great number of configurations of metallic devices exists. Among them, Buckling-Restrained-Braces (BRBs) have been extensively used for seismic applications in the last years all around the world. The concept of BRBs was originally developed in Japan: the yielding steel element either sandwiched between precast concrete panels or encased in concrete-filled steel sections to avoid buckling. Afterwards various developments on BRBs with a steel core confined by a steel casing filled with mortar or only by an hollow structural section were made in different countries since the 1980s and different proprietary BRBs have been developed [8]. Suitable features of yielding dampers are: their stable hysteretic behaviour, their long term reliability, their insensitivity to load rate and to the environmental temperature. The only inconvenience in the application of these devices is that they are prone to damage concentration at certain stories and to residual deformations [8][9].

Viscoelastic materials have been used for many decades to reduce vibrations caused by wind. Only in this last decade they have been used in seismic applications. Viscoelastic dampers are usually obtained from viscoelastic materials (copolymers or glassy substances) bonded to steel plates attached to the structure by means of elastic braces [4]. An alternative form of viscoelastic dampers are elastomeric dampers that employ High Damping Rubber (HDR), usually found in seismic isolators [6]. Compared with typical viscoelastic materials, HDR is less sensitive to frequency and ambient temperature and has adequate damping capacity for seismic applications [10][11][12][13]. Moreover, even if the constitutive behaviour of HDR is quite complex [12], simplified linear models can be used for the design [10][14]. Viscoelastic devices generally provide lower energy dissipation with respect to elastic-plastic dampers, however

they may be preferred as not sensitive to response concentration in a limited number of storeys due to their elastic stiffness regardless of the stress level. In addition, they can withstand a large number of cycles without permanent deformations and they can dissipate energy even for small lateral displacements, as in the case of low intensity earthquakes or wind.

Some design indications for structures equipped with energy dissipation systems are available in the recent technical literature. FEMA guidelines [15] present some basic design concepts addressed to all types of dissipating systems and based on a large numbers of background studies, as reported in [6] and [7]. The most important aspect of these guidelines is that all proposed linear or nonlinear analysis methods are displacement-based, in the sense that they all, directly or indirectly, make use of displacement-related information for component verification. However, FEMA guidelines [15] are mainly centred on Seismic-Force-Resistant-Systems (SFRS) that are able to provide a complete lateral load path without the damping system, i.e., dissipative bracings are only introduced to improve seismic performances. Displacements, directly related to structural and non structural damages, have assumed an increasing role in structural seismic design and a number of detailed Displacement-Based Design (DBD) procedures were developed for different structural systems [16][17][18][19].

In this research project experimental and numerical investigations were carried out on steel structures equipped with dissipative braces based on elastoplastic and HDR-based devices. In the first part of this research project, an experimental campaign involved a steel-concrete composite mock-up with semi-rigid joints equipped with two kind of braces: dissipative diagonal braces made of BRB devices placed in series with elastic braces, and chevron-type braces equipped with HDR-based dampers. Experimental tests aimed at studying the dynamic response of the resulting frame-braces coupled systems. The objective was to investigate the effectiveness of dissipative braces in increasing the stiffness and dissipation capacity of the frame, and to highlight the aspects related to their non linear behaviour. Quasi-static displacement-controlled cyclic tests were performed on the steel-concrete composite mock-up with dissipative diagonal braces made of BRB devices, whereas free vibration tests, followed by force-controlled and displacement-controlled cyclic tests were performed on the steel-concrete composite mock-up with chevron-type braces equipped with HDR-based dampers. The second part of the research was focused on defining appropriate numerical models for the dissipative braces and relevant design methods. In particular, a direct DBD procedure for steel frames with dissipative braces, valid for both elastoplastic and elastomeric (viscoelastic) dampers and for pinned joints was developed. In order to obtain closed form solutions giving simple formulas that can be conveniently used in the preliminary design, the DBD procedure was applied to continuous models equivalent to the discrete dissipative bracing systems. Such continuous systems are cantilever beams

with bending and shear deformability, where the shear deformability is related to the dissipative braces and the flexural deformability is related to the columns of the bracing system.

2. EXPERIMENTAL CAMPAIGN

Mock-up

The mock up built at the Materials and Structures Testing Laboratory of University of Ancona is a steel-concrete composite structure, consisting of a couple of one-storey two-bay moment resisting frames: they are 3.00 m high with spans of 4.20 m. The six columns are realized with HE160A hot rolled grade S355 steel profiles. The composite beams are also obtained with HE160A grade S355 steel profiles and a 120 mm thick slab realised with C30/37 concrete cast on a collaborating EGB210 steel sheeting. The composite slab is directly supported by the main beams and connected with Nelson studs in order to ensure the full shear connection with the lower beam. The beam-to-column connections are composite, they are obtained by means of a beam end-plate bolted to the column flange and they are characterized by dissipative partial strength. In order to evaluate the stiffness of the frame and the storey drift at which the elastic limit is attained, a nonlinear static push over analysis was performed. The limit elastic drift obtained is about 15 mm and the static stiffness of the frame is about 8.0 kN/mm.

BRB devices

In Italy, unlike other countries in the world, dissipative braces have been originally developed to retrofit existing reinforced concrete structures with limited ductility. In this kind of structures small lateral displacements can be usually achieved, consequently short devices able to yield for small displacements must be employed, e.g., Buckling-Restrained Axial Damper (BRAD) devices developed by FIP-Industriale [20][21].



Figure 1. BRAD device developed by FIP Industriale.

To employ this kind of devices in the mock-up previously described, where very small yielding force values were necessary, standard BRAD manufactured by FIP Industriale with a special steel core were not feasible. Consequently, special BRAD device prototypes with an aluminum internal core were manufactured by FIP-Industriale only for the purpose of testing the mock-up (Fig. 1). The devices were connected in series with elastic braces and placed inside the real scale steel-concrete composite mock-up (Fig. 2).

The stiffness of the devices is $K=18$ kN/mm, whereas the stiffness of the global brace is about 15 kN/mm. The yield force is $F_y=20$ kN, whereas the maximum compressive force expected at maximum displacement is 34 kN. Since the behaviour of the elastoplastic devices is not time dependent, only quasi-static displacement-controlled tests are performed. An actuator, fixed to a reaction structure was used to apply the displacements.

The mock-up was instrumented so as to measure global forces (load cell C1) and displacements (inductive displacement transducers L1a,b,c) of the frame as well as the local forces (load cell C2) and strains (inductive displacement transducers L2a,b) of the devices, as shown in Figure 2.

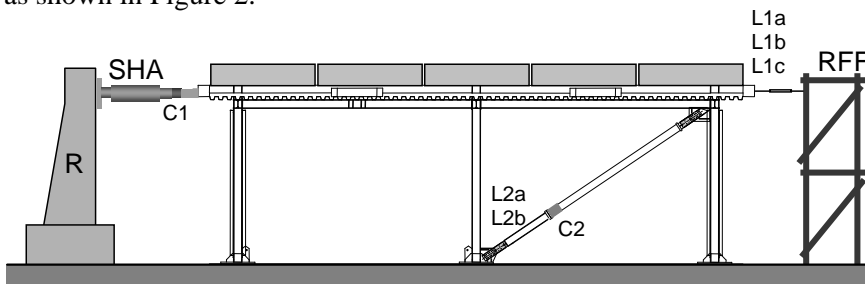


Figure 2. Test set-up: displacement-controlled cyclic tests.

Six devices were tested and the tests carried out are:

- test1: cyclic tests with displacement amplitude of 2 mm on the devices (2.5 mm on the frame slab) followed by cyclic tests at increasing displacements from 1 mm to 10 mm on the devices up to failure;
- test 2: cyclic tests with displacement amplitude of 6 mm on the devices (7.5 mm on the frame slab) up to failure;
- test 3: cyclic tests with displacement amplitude of 10 mm on the devices (13 mm on the frame slab) up to failure.

In the first part of test 1 the induced cyclic displacements are typical of damage limitation state (DLS) and both devices were capable of resisting numerous cycles, approximately 150 cycles (Fig. 3). Increasing displacements were enforced in the following cycles. In this second stage, one BRB immediately collapsed whereas the second one was able to reach cycles with amplitudes up to 10 mm. During the

second tests, which applied large displacements to the bracing system representative of a response at ultimate limit state (ULS), one of two BRBs reached failure after 43 cycles, the other supported about 27 cycles (Fig. 4). During the last test, which applied even larger displacements, one of two BRBs reached failure after 4 cycles, the other supported more than 10 cycles (Fig. 5).

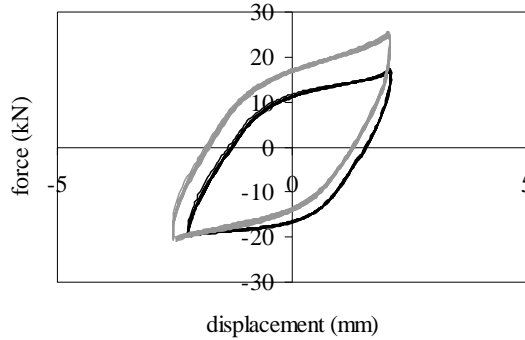


Figure 3. Cyclic tests on BRB 1 (grey line) and BRB 2 (black line) at 2 mm.

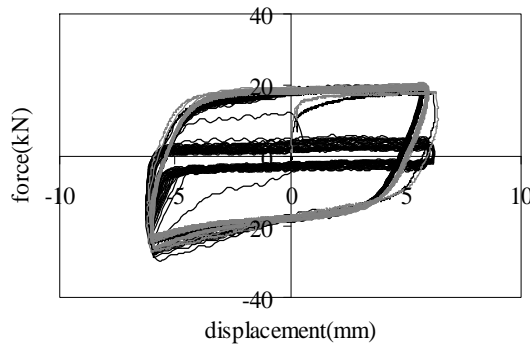


Figure 4. Cyclic tests on BRB 1 (grey line) and BRB 2 (black line) at 6 mm.

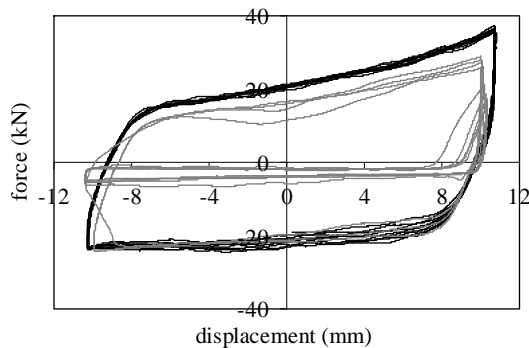


Figure 5. Cyclic tests on BRB 1 (grey line) and BRB 2 (black line) at 10 mm.

The experimental tests carried out confirmed that the devices have a large dissipation capacity, which increases by increasing displacement amplitude. Moreover the tested devices resulted able to sustain a large number of cycles for small and moderate displacements, however some fatigue problems occurred during largest displacement tests. This fact underlines the importance, for elastoplastic devices, of carrying out qualification tests aimed at demonstrating that the devices satisfied the requirements for strength and inelastic deformation under cyclic loading at the design displacement. Finally the shape of hysteretic cycles showed that the device behaviour is not symmetric. In fact, at the ULS-displacement test (test 2) the maximum force in compression is about 1.5 times the maximum force in traction and increases for larger displacements, due to the confinement of the steel core. This fact must be taken into account for the correct design of adjoining elements, such as columns, beams and brace connections.

HDR-based devices

The dissipating devices adopted are based on High Damping Rubber (HDR) and manufactured by T.A.R.R.C. (Tun Abdul Razak Research Center). The single device is made by the superposition of two $170 \times 230 \times 5$ mm rubber layers separated by an intermediate 2 mm thick steel shim. This device was coupled with the frame by means of Chevron-type bracings at the interior of the main moment resisting frames (Figs. 6-8). The dampers were placed horizontally and were directly bolted to the bottom flange of the steel beams and to the braces so as to undergo shear strain under the deck drift. In order to make the bracing system rigid with respect to the frame, and prevent undesirable movements between the frame and the dampers, the braces were stiffened by two prestressed cross-rods.

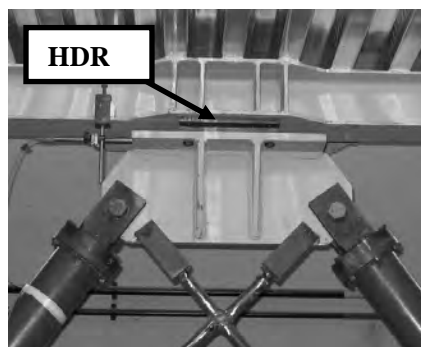


Figure 6. Mock-up equipped with HDR devices.

Free vibration tests were performed, followed by displacement-controlled cyclic tests at low frequencies and dynamic force-controlled cyclic tests at high frequency. The mock-up was instrumented so as to measure global forces and displacements of the frame as well as the local forces and strains in the HDR devices. In the case of free vibration tests and displacement controlled cyclic tests, an actuator fixed to a reaction structure was used to apply the displacements.

(Fig. 7). In the case of the force-controlled dynamic cyclic test an electro-hydraulic shaker consisting of a mobile mass of 0.9 t, a displacement actuator of 100 kN (± 100 mm) and a load cell (C3) were used (Fig. 8). In all cases three inductive displacement transducers (L1a,b,c) were used to measure the storey drift opposite the actuators. Strains in the HDR devices were determined by measuring the relative displacements between the plates bolted to the frame and brace (L2a,b) while a load cell (C2) was mounted on one of the brace struts.

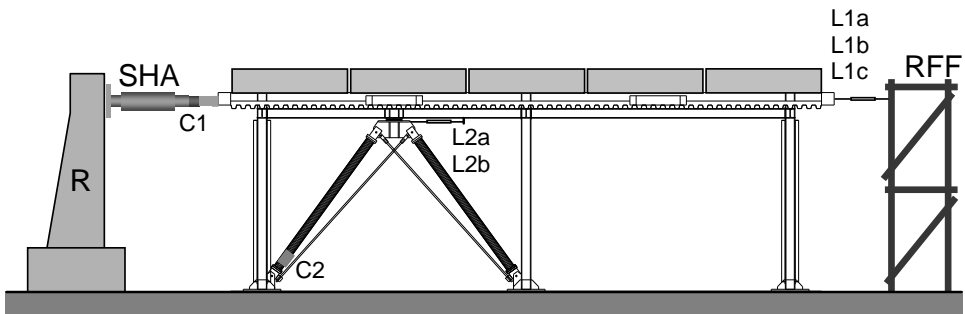


Figure 7. Test set-up: displacement-controlled cyclic tests.

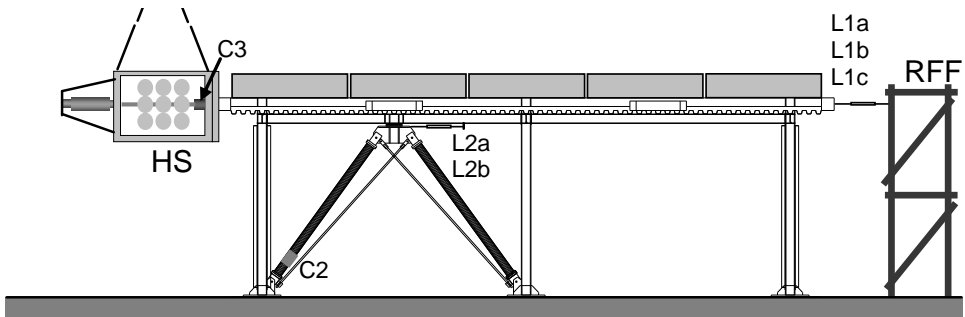


Figure 8. Test set-up: force-controlled cyclic tests.

Some results of the experimental campaign are illustrated in the following, while more details may be found in [13]. The first set of tests performed were snap back tests. The procedure adopted consisted of imposing a quasi-static linear displacement history to the systems. Once the desired displacement was attained, the loading force was instantaneously removed in order to monitor the free vibrations. Five levels of displacement were imposed below the elastic limit estimated for the frame. Figure 9a reports the displacement histories obtained by imposing different initial displacements. It is evident in this case that the system behaviour strongly depends on the displacement amplitude: this is increasingly stiffer as the displacements decrease. Since the rubber is a fading memory material, in all cases the displacement goes to zero in a sufficiently short period of time. In Figures 9b the free vibration test performed in the bare and braced frames are compared, in the case of the initial displacement of 10 mm. This graph shows the large increment of stiffness and dissipation capacity which occurs in the equipped frame.

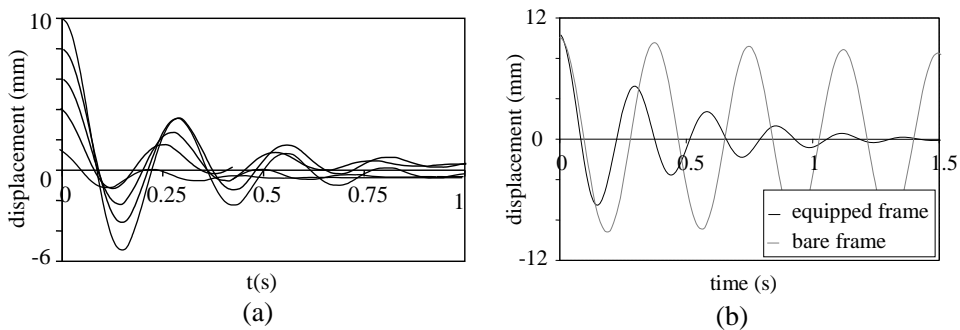


Figure 9. Free vibration tests at 10 mm: (a) load path; (b) free vibrations.

The second set of tests performed were force-controlled cyclic tests. They were carried out by means of the electro-hydraulic shaker in order to investigate the structure behaviour in a wide range of frequencies and force amplitudes. The test procedure was divided into two steps. The first step consisted of imposing frequency sweep tests with increasing and decreasing frequencies in order to identify the resonance condition. Successively cyclic tests at fixed frequency values, including the resonance frequency, were performed. This procedure was repeated for different force amplitudes (from 3 kN to 9 kN) in order to investigate the nonlinear behaviour of the system due to the HDR dissipation devices. The size of the range of frequencies investigated depends on the limits of the hydraulic system and consequently it varies for the different force intensities. Figures 10a and 10b show the results of the force-controlled cyclic tests. In particular, Figure 10a shows maximum displacement vs. frequency diagrams for different force amplitudes. It may be observed that the maximum displace-

ment nonlinearly increases and the resonance frequency decreases as the force amplitude increases, due to the softening behaviour of the rubber in the displacement range investigated. Figure 10b shows the force-displacement diagram of the devices at the resonance conditions at different force levels. These diagrams confirm the softening behaviour of the rubber, due to the different strain amplitudes, as well as the different strain rates of the tests performed at the resonance conditions.

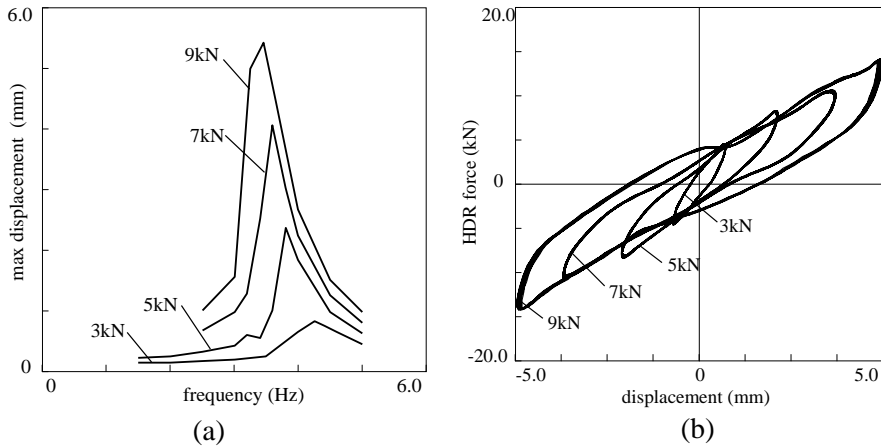


Figure 10. System total stiffness vs. maximum displacements (a); equivalent damping ratio vs. maximum displacements (b)

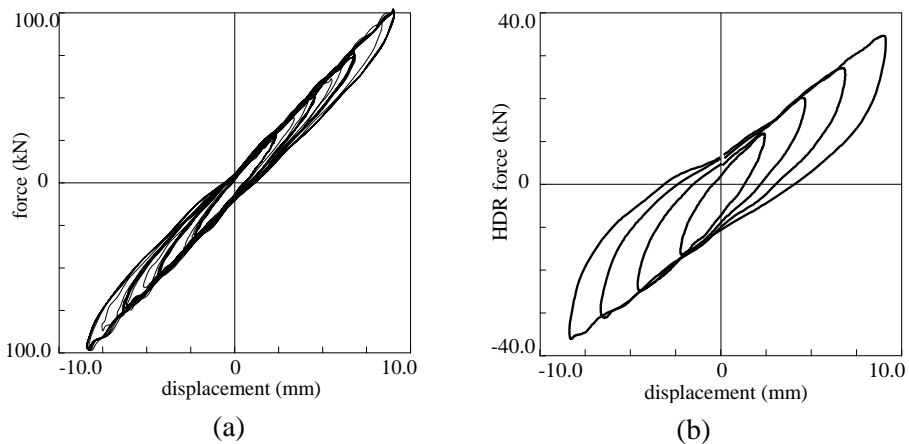


Figure 11. Total force-displacement diagram (a), force-displacement diagram of the devices (b).

Finally displacement-controlled cyclic tests were performed, in order to study the behaviour of the coupled system with increasing and decreasing displacements at a fixed frequency. Only low frequencies could be applied (quasi-static cyclic tests) because of the dimensions of the system tested and the limits of the hydraulic system and the reaction structure. In particular, the test consisted of a sinusoidal imposed displacement path with constant frequency of 0.5 Hz. The amplitude of the cycles was increased from 2 to 8 mm and then decreased from 8 to 2 mm, in steps of 2 mm. Figure 11b shows the total force versus displacement diagram, whereas Figure 11b shows the stable cycles, referring to the devices force vs. devices displacements. This last figure confirms that the rubber has a softening behaviour, due in this case only to the different strain amplitudes, being the test frequency assumed constant.

3. NUMERICAL MODELLING

BRB devices

Classical elastoplastic models, like the Bouc-Wen model [22] or the Menegotto-Pinto model [23], can be used to simulate the device response. A small hardening may be assumed, in this case a post-elastic stiffness equal to 0.01 times the initial device stiffness was used to simulate the tests carried out. Obviously, by using this model only the average device behaviour can be simulated, without taking into account the difference between maximum forces in tension and compression. The approximation is acceptable, as showed in Figure 12.

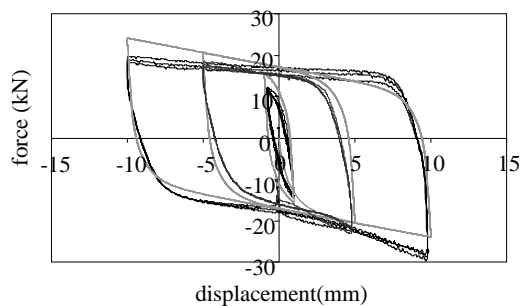


Figure 12. Cyclic tests (black line) and numerical simulations (grey line).

HDR-based devices

Tests carried out on the mock-up equipped with HDR-based devices were numerically simulated using for the HDR a constitutive model previously developed on the bases of a wide experimental campaign carried out on single devices [12]. Firstly, a multiplier factor which depends on the rubber area that

also takes into account secondary phenomena (such as brace deformations or slips at the connections) was experimentally calibrated by means of the displacement-controlled cyclic tests (Fig. 13). Successively, dynamic tests were simulated. Results of numerical simulations are reported in Figure 14, with reference to the snap back with a initial displacement of 10mm. Figure 15 reports the simulation force-displacement diagrams of the dissipation devices for the resonance conditions at 3kN and 9 kN. Experimental and numerical results are in good agreement in all the tests simulated.

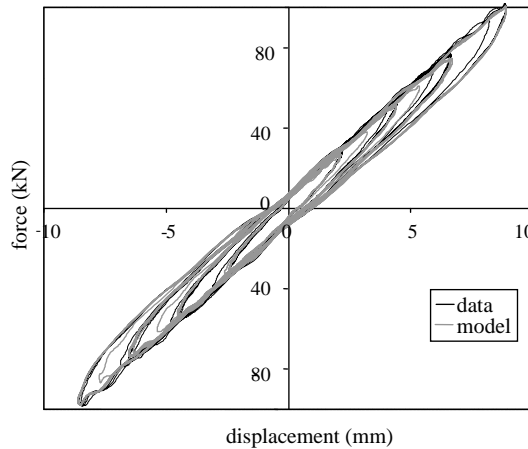


Figure 13. Experimental and numerical results of displacement-controlled cyclic test.

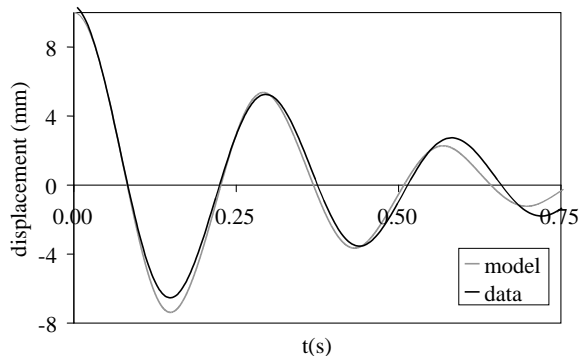


Figure 14. Experimental and numerical displacement histories of the snap-back test.

The rubber model used for numerical simulations, as well as other models available in the scientific literature for high damping rubbers [24] may be used to perform accurate nonlinear computations, even if they are usually quite

complex, require the calibration of many parameters and are not always available in commercial computational software. On the other hand, the description of the material behaviour by linear models is a simplified approach usually adopted in practical applications and accepted in recent guidelines [25] [26] [27] for both response spectrum analysis or linear time history analysis. This approach may be convenient because very few parameters need to be identified from the experimental data and structural analysis may be performed by means of very common commercial software.

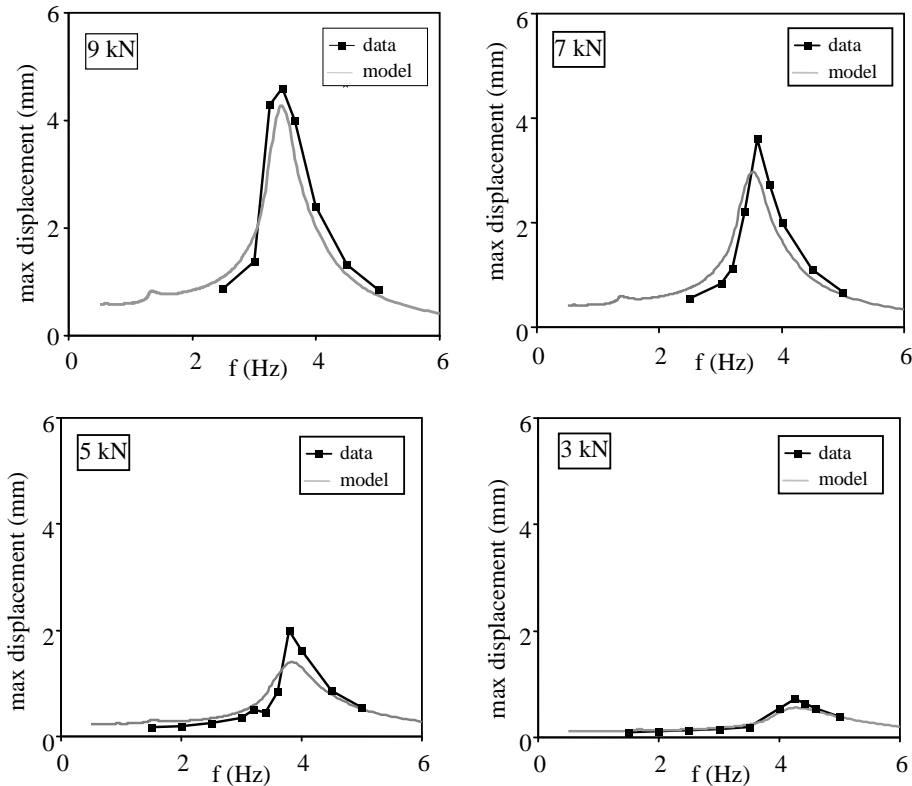


Figure 15. Experimental and numerical results of force controlled cyclic tests.

In Figure 16 some results referring to a Single Degree Of Freedom (SDOF) system, consisting of a mass m and a dissipating HDR-based device which provides the restoring force, subjected to different values of shear strain (γ) are reported. In particular, the maximum values of displacements and restoring forces per unit mass observed in the nonlinear system (solid line) together with the results of the linear approximation (dashed line) under sinusoidal excitations are reported in Figure 14a and Figure 14b, respectively. In general, the curves obtained for the approximated linear system adequately describe the

maximum values of displacements and forces. Large differences may be observed away from the peak response. More details may be found in [14].

Finally it should be observed that in the linear approach the transient behaviour of the rubber is generally neglected. However, by choosing appropriate equivalence criteria, equivalent stiffness and equivalent damping ratio, referring to the stable response and to the transient response may be obtained, for different values of frequency and displacement amplitude. It was observed that the linear model referring to the stationary behaviour generally shows a tendency to overestimate the displacements and underestimate the forces, whereas the linear model referring to the transient behaviour has the opposite tendency [14].

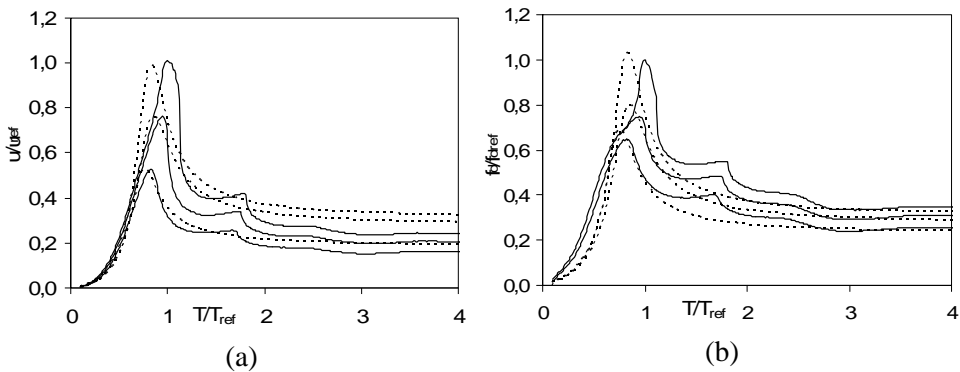


Figure 16. Harmonic analysis: non linear (solid line) and linear (dashed line) systems.

4. STRUCTURAL DESIGN

The central idea of the proposed design method is to apply the direct DBD procedure to a continuous model equivalent to a n -storey dissipative bracing system. Such continuous system is a cantilever with bending and shear deformability (Timoshenko beam formulation), where the shear deformability is related to the dissipative braces and the flexural deformability is related to the columns of the bracing system. In this way, closed form solutions are obtained giving simple design formulas that can be conveniently used in the preliminary design of this kind of structures. In order to obtain a one-parameter design procedure, only the first vibration mode is considered in the description of the dynamic behaviour of the continuous system. Based on this assumption and taking prescribed design values of strains due to shear and bending, the required distributions of shear and bending stiffness along the beam are obtained from the solution of an inverse problem. These stiffness functions are defined except for a unique multiplicative factor which can be evaluated by comparing the

seismic capacity with the seismic demand described using design response spectra. Finally, an equivalence is introduced between the continuous model and the discrete n-storey dissipative bracing system in order to use the closed form solutions in the real discrete cases.

Displacement-based design of continuous cantilever bracing systems

The balance equations and relevant boundary conditions of a cantilever beam including flexural and shear deformability are [28]:

$$\mu \ddot{u} - [(u' + \psi)K_s]' = q \quad (u' + \psi)K_s|_L = 0 \quad u|_0 = 0 \quad (1)$$

$$I_\mu \ddot{\psi} - (\psi' K_b)' + (u' + \psi)K_s = 0 \quad \psi' K_b|_L = 0 \quad \psi|_0 = 0 \quad (2)$$

where functions $u(\zeta; t), \psi(\zeta; t): [0, L] \times [0, \infty) \mapsto \mathfrak{R}$ describe the cross section transverse displacements and rotations respectively, L is the cantilever total height, $q(\zeta; t)$ is the time dependent transverse load distribution, $K_s(\zeta)$ and $K_b(\zeta)$ are the distribution of flexural and shear stiffness respectively, $\mu(\zeta)$ is the mass per unit length, $I_\mu(\zeta)$ is the rotational inertia, a prime denotes one differentiation with respect to ζ and a superposed dot denotes one differentiation with respect to time t . The strain field is described by the shear deformation $\gamma = u' + \psi$ and by the curvature $\theta = \psi'$. The solution is defined once the initial conditions are assigned. In the sequel the rotational inertia is neglected, the load distribution is taken equal to zero (free vibration problem) and only the first vibration mode is considered. Assuming that displacements and rotations of the first vibration mode are described as $u(\zeta; t) = v(\zeta)e^{i\omega t}$ and $\psi(\zeta; t) = \varphi(\zeta)e^{i\omega t}$ where ω is the first mode circular frequency, Equations (1) and (2) become:

$$(v' + \varphi)K_s|_L = 0 \quad v|_0 = 0 \quad (3)$$

$$(\varphi' K_b)' + (v' + \varphi)K_s = 0 \quad \varphi' K_b|_L = 0 \quad \varphi|_0 = 0 \quad (4)$$

A first vibration mode with uniform shear deformation $\bar{\gamma}$ and uniform curvature $\bar{\theta}$ along the cantilever is assumed as design objective. Transverse displacements and rotations describing such first vibration mode are obtained from the compatibility equations of the beam and relevant kinematic boundary conditions:

$$v' + \varphi = \bar{\gamma} \quad v|_0 = 0 \quad (5)$$

$$\varphi' = \bar{\theta} \quad \varphi|_0 = 0 \quad (6)$$

that integrated give:

$$v = \bar{\gamma}\zeta - \frac{1}{2}\bar{\theta}\zeta^2 \quad (7)$$

$$\varphi = \bar{\theta}\zeta \quad (8)$$

Substituting Equations (7) and (8) into Equations (3) and (4), the differential balance equations become:

$$-\mu\omega^2 v - K_s' \bar{\gamma} = 0 \quad K_s|_L = 0 \quad (9)$$

$$-K_b' \bar{\theta} + K_s' \bar{\gamma} = 0 \quad K_b|_L = 0 \quad (10)$$

As the unknown stiffness functions K_s and K_b are can be determined except for a unique scale factor, it is convenient to use as unknowns functions $a(\zeta) = K_s(\zeta)/K_{s0}$ and $j(\zeta) = K_b(\zeta)/K_{s0}$, where $K_{s0} = K_s|_0$ is the shear stiffness of the base section (scale factor). The function a is evaluated by integrating Equation (9); afterward the function j is obtained from Equation (10). In the case of uniform mass distribution the following analytical expressions are obtained:

$$a = \frac{1 + \frac{\beta}{3} - \left(\frac{\zeta}{L}\right)^2 - \frac{\beta}{3}\left(\frac{\zeta}{L}\right)^3}{1 + \frac{\beta}{3}} \quad (11)$$

$$\frac{j}{L^2} = \frac{1}{\frac{\beta}{2}\left(1 + \frac{\beta}{3}\right)} \left[\frac{1}{3} - \frac{1}{2}\frac{\zeta}{L} + \frac{1}{6}\left(\frac{\zeta}{L}\right)^3 + \beta \left(\frac{1}{8} - \frac{1}{6}\frac{\zeta}{L} + \frac{1}{24}\left(\frac{\zeta}{L}\right)^4 \right) \right] \quad (12)$$

where a dimensionless parameter $\beta = -\bar{\theta}L/\bar{\gamma}$ is introduced. It is observed that Equations (11) and (12) are polynomial expressions functions of the non dimensional abscissa ζ/L with shape depending on the parameter β only. The shear and flexural stiffness distributions a and j along the cantilever length in the case of uniform mass distribution are depicted in Figure 17(a) and Figure 17(b) respectively, normalized with respect to their relevant base values $a_0 = a|_0 = 1$ and:

$$j_0 = j|_0 = \frac{L^2 \left(\frac{\beta}{8} + \frac{1}{3} \right)}{\frac{\beta}{2} \left(1 + \frac{\beta}{3} \right)} \tag{13}$$

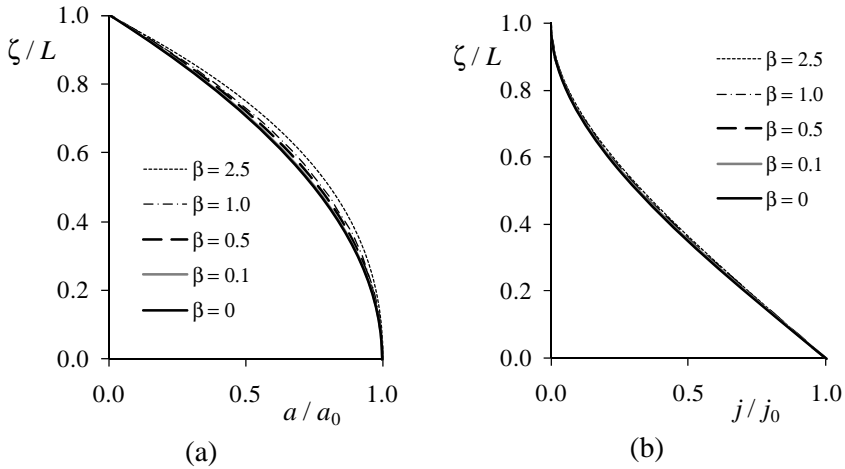


Figure 17. Distributions in the case of uniform mass of: (a) normalized shear stiffness; (b) normalized flexural stiffness.

In the first vibration mode, the mass m^* of the equivalent Single Degree of Freedom (SDOF) system, the modal participation factor Γ for the normalized displacement v/v_L , and the participating mass ratio η are respectively:

$$m^* = \frac{1}{v_L} \int_0^L \mu(\zeta)v(\zeta)d\zeta \tag{14}$$

$$\Gamma = \frac{v_L^2 m^*}{\int_0^L \mu(\zeta)v^2(\zeta)d\zeta} \tag{15}$$

$$\eta = \frac{\left[\int_0^L \mu(\zeta)v(\zeta)d\zeta \right]^2}{\int_0^L \mu(\zeta)\zeta d\zeta \cdot \int_0^L \mu(\zeta)v^2(\zeta)d\zeta} \tag{16}$$

Once the normalized flexural and shear stiffness distributions are known, the system circular frequency can be computed by means of the Rayleigh’s quotient [29]:

$$\omega^2 = K_{s0} \frac{\bar{\theta}^2 \int_0^L j d\zeta + \bar{\gamma}^2 \int_0^L a d\zeta}{\int_0^L \mu v^2 d\zeta} = K_{s0} \omega_{(1)}^2 \quad (17)$$

(except for the scale factor K_{s0}) where $\omega_{(1)}$ is the circular frequency corresponding to a unitary base shear stiffness.

The scale factor K_{s0} is determined for two cases: viscoelastic dissipation and elastoplastic dissipation. If a linear viscoelastic shear behaviour with a damping factor ξ_d associated to the shear stiffness is assumed for the cantilever beam, then the damping coefficient of the continuous system is:

$$\xi_s = \frac{\xi_d \bar{\gamma}^2 \int_0^L a d\zeta}{\bar{\theta}^2 \int_0^L j d\zeta + \bar{\gamma}^2 \int_0^L a d\zeta} + \xi_n \quad (18)$$

where the first term of the left hand side is the ratio between the dissipated energy in shear (the only structural dissipating source) and the total elastic deformation energy, i.e., strain energy method [4], while ξ_n is the inherent damping due to non structural elements. If the cantilever is assumed having linear elastic - perfect plastic shear behaviour with yield shear V_y attained for the design shear deformation $\bar{\gamma}$, i.e., $V_y = K_s \bar{\gamma}$, and with shear design ductility μ_d , i.e., the ultimate shear strain is given by $\gamma_u = \mu_d \bar{\gamma}$, then the system ductility μ_s for shear distribution proportional to V_y is:

$$\mu_s = \frac{v_{c,L} + \mu_d v_{d,L}}{v_{c,L} + v_{d,L}} \quad (19)$$

where $v_{c,L} = v_c|_L = -\bar{\theta}L^2/2$ is the flexural contribution of the displacement of the cantilever top end and $v_{d,L} = v_d|_L = \bar{\gamma}L$ is the shear contribution. As in the previous case, an inherent damping due to non structural elements ξ_n is also considered. It is observed that in both the two dissipation cases, an increase of the flexural deformability with respect to the shear deformability reduces the system dissipation. Consequently small value of β should be assumed in order to have highly dissipative systems. Once the modal parameters $\omega_{(1)}$ and Γ as well as the dissipative properties of the continuous viscoelastic or elastoplastic systems (ξ_s or μ_s) are known, the base shear stiffness K_{s0} can be designed by comparing the system capacity with the seismic demand. The capacity can be measured by means of the maximum displacement of the system (scale factor independent) and consequently the related demand can be deduced from di-

placement design spectra dependent upon K_{s0} through the circular frequency ω . In this way, the scale factor K_{s0} can be obtained by the equalities:

$$S_d(\sqrt{K_{s0}} \omega_{(1)}, \xi_s) = v_L \quad (20)$$

$$S_d(\sqrt{K_{s0}} \omega_{(1)}, \mu_s) = v_L \quad (21)$$

for the viscoelastic case and for the elastoplastic case respectively [30]. Otherwise, the capacity can be measured by means of the maximum acceleration achievable and the related demand can be deduced from design spectrum in terms of pseudo acceleration. In this case the scale factor K_{s0} can be obtained by the equalities:

$$S_a(\sqrt{K_{s0}} \omega_{(1)}, \xi_s) = \frac{K_{s0} \bar{\gamma}}{m^* \Gamma} \quad (22)$$

$$S_a(\sqrt{K_{s0}} \omega_{(1)}, \mu_s) = \frac{K_{s0} \bar{\gamma}}{m^* \Gamma} \quad (23)$$

for the viscoelastic case and for the elastoplastic case respectively [30]. The two approaches are equivalent even if the first one leads to simpler procedures and it is usually adopted in DBD procedures. After the determination of the scale factor K_{s0} , the design period together with design shear and flexural stiffness distributions can be calculated.

Displacement-based design of discrete cantilever bracing systems

In the case of a p -storey bracing system with constant floor mass m and constant inter-storey height h , the total length of the cantilever equal to $L = (p + 1/2)h$ and the uniform mass distribution equal to $\mu = m/h$ are assumed (Fig. 18). In the case of bracing systems with different floor masses or different inter-storey heights average values may be assumed for the preliminary design.

Given the design strains $\bar{\epsilon}_d$ and $\bar{\epsilon}_c$ of diagonals and columns respectively, the design shear strain $\bar{\gamma}$ and the design curvature $\bar{\theta}$ of the continuous system can be computed with geometric relations, depending on the configuration of bracing. For a V-bracing system, as such configuration is considered in the numerical applications (Fig. 19) equations are:

$$\bar{\gamma} = 2\bar{\epsilon}_d L_d^2 / bh \quad (24)$$

$$\bar{\theta} = -2\bar{\epsilon}_c / b \quad (25)$$

where b is the base of the bracing system, h is the storey height and L_d is the diagonal brace length given by $L_d = \sqrt{(b/2)^2 + h^2}$.

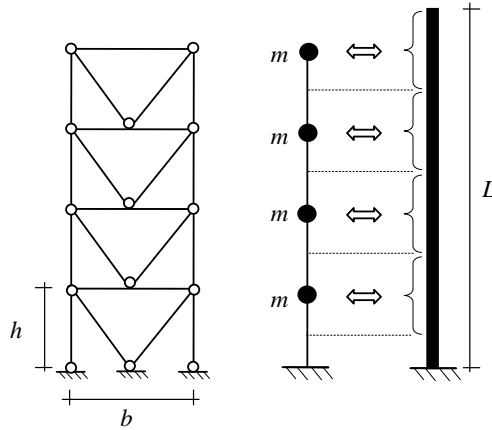


Figure 18. Equivalence between MDOF system and continuous system.

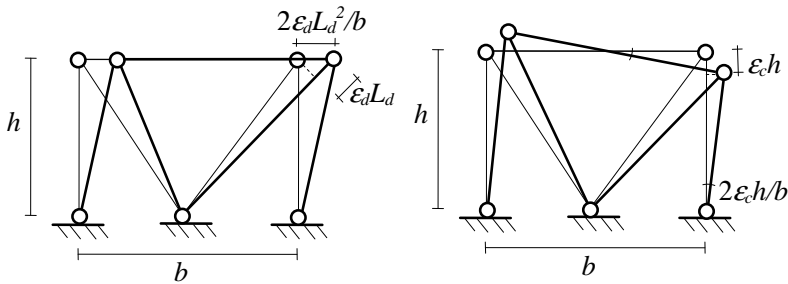


Figure 19. Shear and flexural strains of V-bracing systems.

Once strains are assigned, the displacement field can be obtained from Equation (7) and it is assumed that displacement at each storey is $v_i = v(\zeta_i)$, where ζ_i is the position of the i -th floor, with $i = 1 \dots p$. In the framework of the DBD procedure described in the previous section, design shear and flexural stiffness distributions are obtained from the solution of the assumed-strain inverse problem, where in the case of viscoelastic braces the brace damping coefficient ξ_d is the damping coefficient associated to the shear stiffness of the continuous cantilever, while in the case of elastoplastic braces the brace ductility μ_d is the shear design ductility of the continuous cantilever. In the bracing system the storey shear equilibrium is due to diagonals and the storey shear stiffness $K_{si} = K_s(\zeta_{si})$ can be obtained from the cantilever shear stiffness eva-

luated at the level ζ_{si} where the inertial force of discrete and continuous systems are equal:

$$\mu \int_{\zeta_s}^L v(\zeta) d\zeta = \sum_{k=i}^{k=p} m_k v_k \tag{26}$$

Similarly, the storey rotational equilibrium at particular bracing system sections (χ_i) is only due to columns and the storey bending stiffness associated to the columns $K_{bi} = K_b(\zeta_{bi})$ can be obtained from the cantilever bending stiffness evaluated at the level ζ_{bi} where the moments of inertial force of discrete and continuous systems are equal:

$$\mu \int_{\zeta_{bi}}^L \int_{\eta}^L v(\eta) d\eta d\zeta = \sum_{k=i}^{k=p} (\zeta_k - \chi_i) m_k v_k \tag{27}$$

In the case of V-bracing systems $\chi_i = \zeta_{i-1}$ can be assumed. From Equations (26) and (27) ζ_s and ζ_b can be obtained. However, when displacements due to column deformations are smaller than displacement due to diagonal deformation (like in the systems considered the paper) ζ_s and ζ_b result very close to the mid-height and to the base of the relevant storey, respectively. Consequently, the following storey stiffness values may be assumed (Fig. 20):

$$K_{si} = K_s ((\zeta_i - \zeta_{i-1})/2) = K_s (ih - h/2) \tag{28}$$

$$K_{bi} = K_b (\zeta_{i-1}) = K_b (ih - h) \tag{29}$$

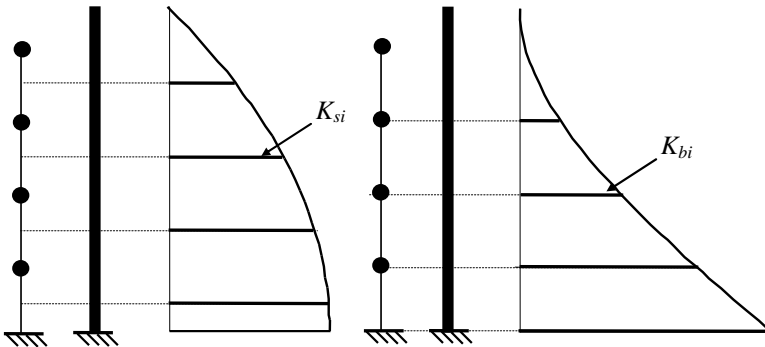


Figure 20. Shear and flexural stiffness equivalence between MDOF system and continuous system.

Therefore, for each floor:

$$K_{di} = \frac{2K_{si}L_d^2}{hb^2} \quad (30)$$

$$EA_{ci} = 2\frac{K_{bi}}{b^2} \quad (31)$$

Finally, if the dissipative braces are made of a dissipative device and an elastic link brace, appropriate equations must be adopted to design the dissipative brace components. For viscoelastic braces a spring placed in series with a Kelvin model can be adopted to evaluate the stiffness K_{0i} of viscoelastic device and the stiffness K_{bi} of link brace [31]:

$$K_{0i} = \beta(\xi_0, \xi_d)K_{di} \quad (32)$$

$$K_{bi} = \alpha(\xi_0, \xi_d)K_{0i} = \alpha(\xi_0, \xi_d)\beta(\xi_0, \xi_d)K_{di} \quad (33)$$

with

$$\alpha(\xi_0, \xi_d) = \frac{(1 + 4\xi_0^2)\xi_d}{(\xi_0 - \xi_d)} \quad (34)$$

$$\beta(\xi_0, \xi_d) = \frac{(1 + \alpha)^2 + 4\xi_0^2}{\alpha^2 + (1 + 4\xi_0^2)\alpha} \quad (35)$$

where ξ_0 is the damping coefficient of the viscoelastic material. For elastoplastic dissipative braces a model made by a spring placed in series with an elastoplastic model can be adopted [31]:

$$K_{0i} = K_{di} \frac{\mu_0 - 1}{\mu_d - 1} \quad (36)$$

$$K_{bi} = \frac{K_{0i}}{K_{0i}/K_{di} - 1} \quad (37)$$

where μ_0 is the ductility of the elastoplastic material. In both cases the dimensions of dampers and link braces may be evaluated from K_{0i} and K_{bi} .

Numerical applications

Approximations introduced by the proposed design method are: (i) vibration modes higher than the first mode are neglected; (ii) the real bracing system is modelled as an equivalent continuous system. In order to evaluate the effectiveness of this proposed design method, the seismic demand obtained in terms

of forces and displacements is compared with the results furnished by time history analyses of Multi Degrees Of Freedom (MDOF) models. Applications concerning bracings with different heights (4-storey and 8-storey) and both the dissipative brace typologies (viscoelastic elastomeric devices and elastoplastic BRBSs) are developed. In particular, a steel frames with five-bay times five-bay floors) are considered as testbed structures (Fig. 21). Storey height is $h = 3.4$ m and bay width is $b = 8$ m. The steel frames considered have pinned beam-column connections. Four V-bracing systems for each direction are the only seismic resistant components. Seismic floor masses, estimated from vertical live and superimposed dead loads, are $300 \text{ kNs}^2/\text{m}$ for each bracing system. For each frames two designs are considered for the dissipative bracings: (1) viscoelastic dissipative braces made of elastomeric dampers in series with elastic braces; (2) elastoplastic dissipative braces made of BRBs. The elastic spectrum type 1 given by the Eurocode 8 [26]for ground type B with a ground acceleration equal to $a_g = 0.35g$ is assumed in the design.

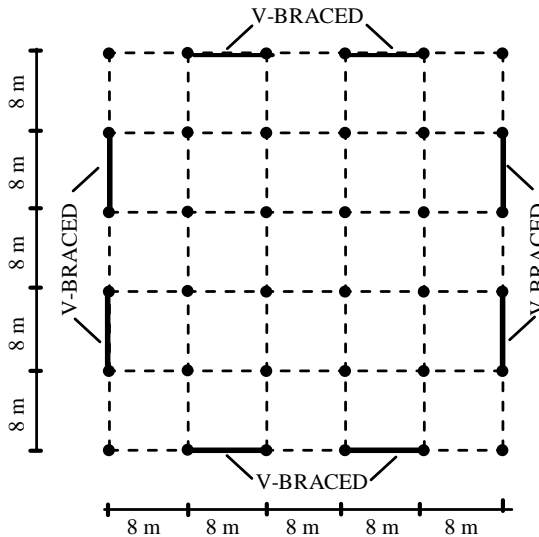


Figure 21. Floor configuration of the testbed steel frames.

For the time history analyses, seven ground motions were selected in order to obtain an average pseudo-acceleration spectrum matching the elastic spectrum assumed for the design, in accordance with Eurocode 8 [26][32]. Spectra of the selected ground motions are given in Figure 22 together with the average spectrum and the design spectrum. The response quantities (forces and displacements) hereafter presented are the average values over the seven time histories computed.

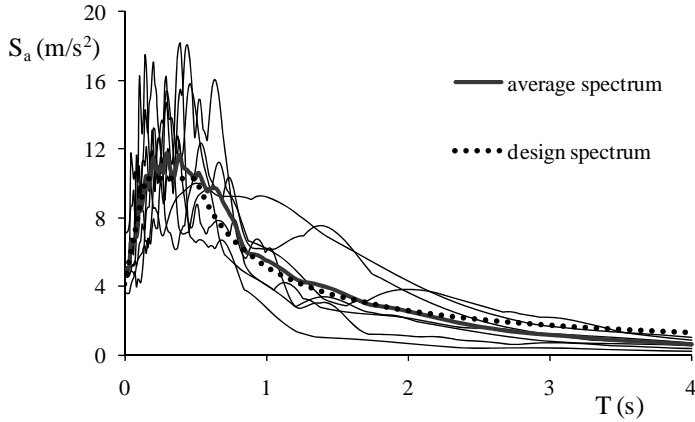


Figure 22. Pseudo-acceleration spectra of the seven selected ground motions and relevant average spectrum compared to the design spectrum.

Table 1. Seven selected ground motions for time history analyses.

Earthquake ID	Station ID	Earthquake name	Mw	Epicentre distance (km)	PGA (m/s ²)
1635	ST2484	South Iceland	6.5	7	4.45
1635	ST2482	South Iceland	6.5	15	3.56
250	ST205	Erzincan	6.6	13	5.03
93	ST67	Montenegro	6.9	16	4.54
93	ST62	Montenegro	6.9	25	4.68
2142	ST2488	South Iceland (aftershock)	6.4	11	5.02
286	ST60	Umbria Marche	6	11	7.07

As previously discussed, the starting point of the proposed design procedure is the assignment of the design strain $\bar{\epsilon}_d$ of diagonal braces and the design strain $\bar{\epsilon}_c$ of columns. In the case of elastomeric dampers, a design strain $\bar{\epsilon}_c = 0.33\epsilon_y$ was chosen for the columns of steel S355 (nominal yield strain $f_y = 355 \text{ N/mm}^2$), with the aim of limiting column deformations and at the same time of assuring the resistance and stability of columns under vertical and seismic loads, including bending moments due to the column continuity neglected in the design. For the diagonal braces, large values of $\bar{\epsilon}_d = \bar{u}_d/L_d$ may be adopted with adequate thickness of rubber, where \bar{u}_d is the design diagonal brace displacement. However, too high values of \bar{u}_d lead to excessively flexible structures, with resulting problems related to P- Δ effects, to non structural damages at the damage limit state or excessive deformations under wind

loads at the serviceability limit state. In the present benchmark structures with elastomeric dampers, design displacements equal to $\bar{u}_d = 23\text{mm}$ and $\bar{u}_d = 18\text{mm}$ were adopted in the 4-storey and 8-storey cases respectively, in order to limit the maximum inter-storey drift at the top storey of the bracing system to 1% of the inter-storey height. A damping coefficient $\xi_d = 0.17$ was assumed for diagonal braces; such value is very close to the rubber damping coefficient ξ_0 , for which a value of about 0.18 may be supposed [14], since elastic link braces are supposed to be sufficiently stiff. The values of β , the participating mass ratio η , the system damping coefficient ξ_s obtained from Equation (18) with $\xi_n = 0.05$, the mass m^* and the modal participation factor Γ , are given in Table 2. The base shear V_b , the scale factor K_{s0} and the natural period T obtained by applying the design procedure to the 4-storey and 8-storey cases are also reported in Table 2. Design storey displacements due to the columns (v_{ci}), to the diagonal braces (v_{di}) and total design displacements (v_i) are reported by Tables 3 and 4 for the 4-storey and 8-storey frames respectively. The storey shear stiffness (K_{si}), the flexural stiffness (K_{bi}), the relevant columns areas (A_{ci}), and diagonal brace stiffness (K_{di}) are also given. Dimensions of the designed symmetric wide-flanges cross sections of the columns (section height h_c , flange width b_f , flange thickness t_f , web height h_w , web thickness t_w) and relevant inertia properties (area A , strong axis I_y and weak axis I_z moments of inertia) are given in Tables 5 and 6 for the 4-storey and 8-storey frames respectively.

Table 2. Viscoelastic braces: design parameters and properties of the SDOF equivalent system.

Frame	β (-)	η (-)	ξ_s (-)	m^* (kNs ² /m)	Γ (-)	V_b (kN)	K_{s0} ($\times 10^3$ kN)	T (s)
4-storey	0.24	0.736	0.206	650.65	1.53	2616.20	294.7	1.22
8-storey	0.31	0.719	0.189	1178.70	1.55	3084.90	443.99	1.98

Table 3. Viscoelastic braces: design results for the 4-storey frame.

Floor	v_{ci} (mm)	v_{di} (mm)	v_i (mm)	K_{si} (kN)	K_{bi} ($\times 10^6$ kNmm)	A_{ci} (mm ²)	K_{di} (kN/mm)
4	13.0	120.7	133.8	119380	28790	4284	30.24
3	7.3	90.6	97.9	206750	72810	10836	52.37
2	3.3	60.4	63.6	263560	129030	19201	66.76
1	0.8	30.2	31.0	291280	191200	28452	73.78

Table 4. Viscoelastic braces: design results for the 8-storey frame.

Floor	v_{ci} (mm)	v_{di} (mm)	v_i (mm)	K_{si} (kN)	K_{bi} ($\times 10^6$ kNmm)	A_{ci} (mm ²)	K_{di} (kN/mm)
8	52.1	189.0	241.1	104970	19810	2947	26.59
7	39.9	165.4	205.3	194340	52290	7781	49.23
6	29.3	141.7	171.1	268820	97270	14475	68.09
5	20.4	118.1	138.5	329120	152370	22674	83.37
4	13.0	94.5	107.5	375940	215320	32042	95.23
3	7.3	70.9	78.2	410010	284000	42262	103.86
2	3.3	47.2	50.5	432020	356370	53031	109.43
1	0.8	23.6	24.4	442690	430530	64067	112.14

Table 5. Viscoelastic braces: designed column cross sections for the 4-storey frame.

Floor	h_c (mm)	b_f (mm)	t_f (mm)	h_w (mm)	t_w (mm)	A (cm ²)	I_y (cm ⁴)	I_z (cm ⁴)
4	180	180	10	160	6	45.6	2808.8	972.0
3	240	240	20	200	10	116	12314.6	4608.0
2	280	280	30	220	15	201	27707.0	10976.0
1	340	340	35	270	20	292	58873.3	22927.3

Table 6. Viscoelastic braces: designed column cross sections for the 8-storey frame.

Floor	h_c (mm)	b_f (mm)	t_f (mm)	h_w (mm)	t_w (mm)	A (cm ²)	I_y (cm ⁴)	I_z (cm ⁴)
8	150	150	10	130	6	37.8	1582.4	562.5
7	220	220	15	190	8	81.2	7403.8	2662.0
6	250	250	25	200	12	149.0	16685.4	6510.4
5	370	370	25	320	15	233.0	59241.4	21105.4
4	400	400	35	330	20	346.0	99532.8	37333.3
3	400	400	45	310	25	437.5	120236.5	48000.0
2	400	400	60	280	30	564.0	145648.0	64000.0
1	400	400	70	260	40	664.0	160605.3	74666.7

Two design arrangements were considered for each frame: (case *a*) the different designed profiles are adopted for each floor, and (case *b*) the same designed profile is assumed for two adjacent floors as common in many realistic situations. For the viscoelastic braces the stiffness equal to the design values were used in the finite element model. Figure 23 reports the maximum inter-storey drifts and maximum brace elongations at each level; Figure 24 gives the

maximum brace forces due to the seismic action; Figure 25 gives the maximum column axial forces due to the seismic action and vertical loads. Average values over the seven ground motions are depicted. In each figure both case *a* and case *b* are illustrated, while the dashed lines indicate the design values given by the proposed procedure. The agreement between design values and average results are satisfactory in both the 4-storey and 8-storey cases. Bending moments due to the continuity of the columns along the bracing height are negligible (about the 5% of yield moments of the columns) and column buckling verifications are satisfied.

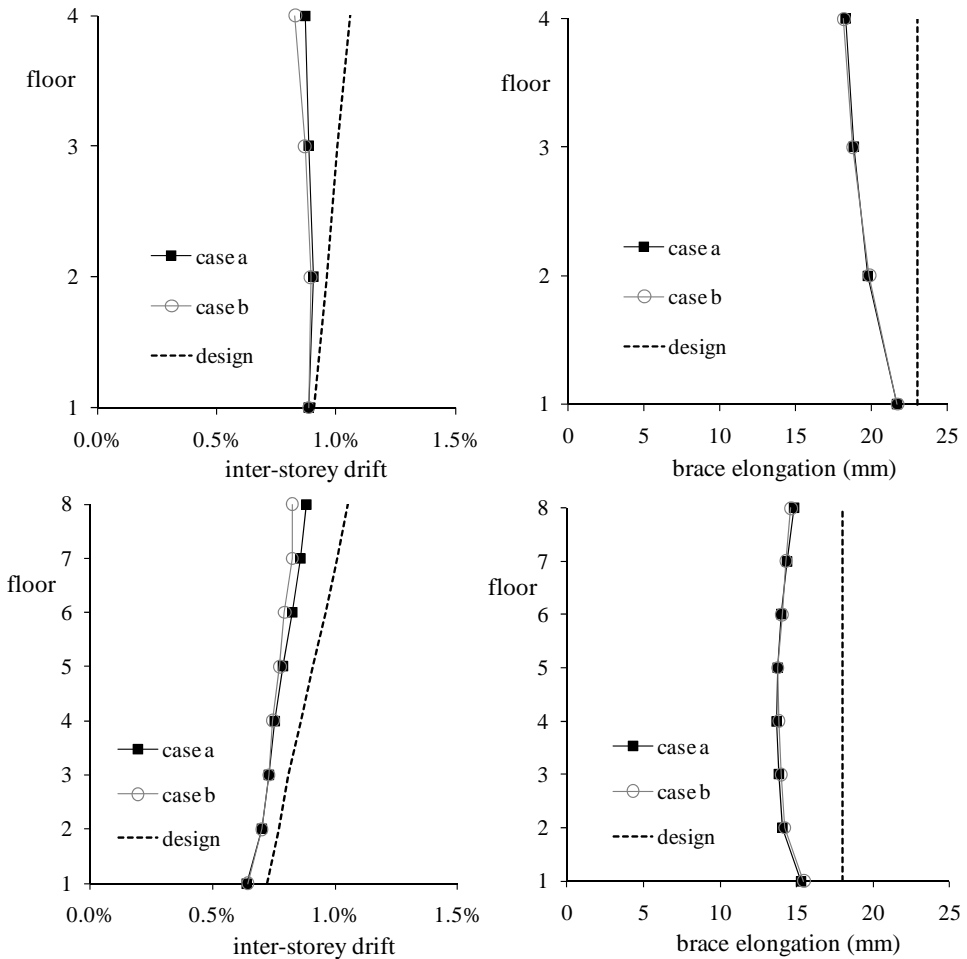


Figure 23. Viscoelastic braces: inter-storey drifts and brace elongations for the 4-storey and 8-storey frames.

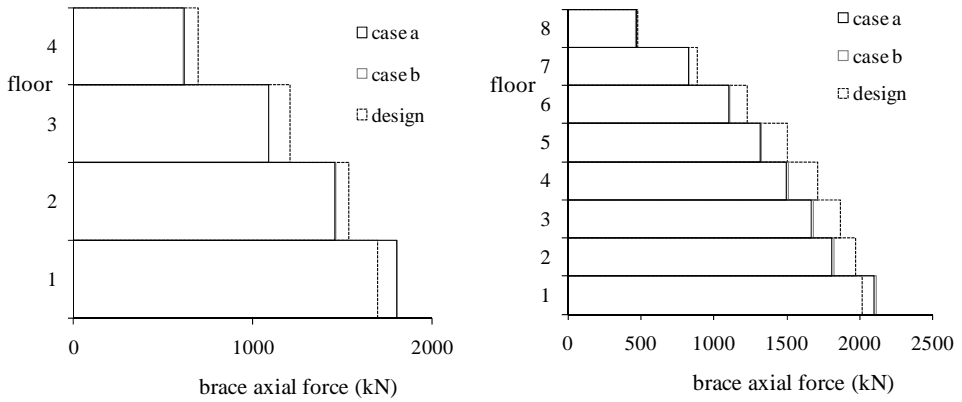


Figure 24. Viscoelastic braces: brace axial forces for the 4-storey and 8-storey frames.

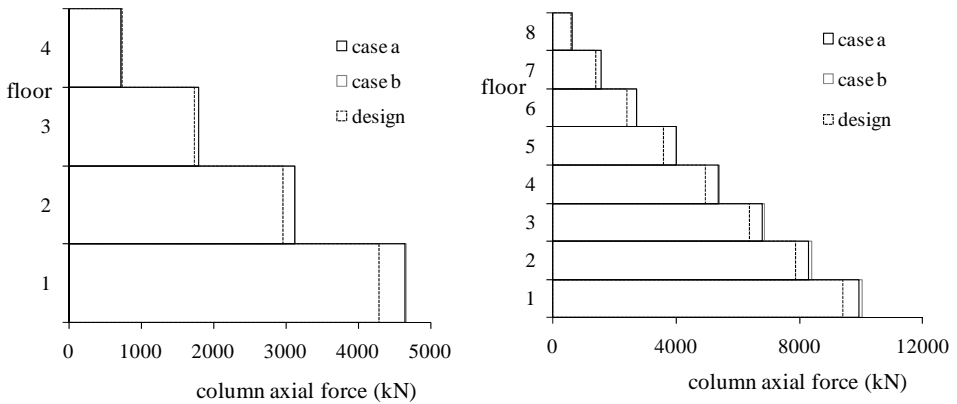


Figure 25. Viscoelastic braces: column axial forces for the 4-storey and 8-storey frames.

For completeness sake, the design of the elastomeric devices is also illustrated. Since at the end of the design procedure the system circular frequency ω is known, from the assigned design rubber strain γ_0 , the HDR properties $\xi_0(\gamma_0, \omega)$ and $G(\gamma_0, \omega)$ are known. A design rubber strain equal to $\gamma_0 = 1.5$ is here assumed and HDR properties equal to $G_0 = 0.7 \text{ N/mm}^2$ and $\xi_0 = 0.18$ can be considered, according to [14]. Therefore, device and brace stiffness may be determined with Equations (39) and (40). Results are reported by Tables 7 and 8. From these results dimensions of elastomeric devices and link braces can be obtained. In particular rubber areas at each storey level can be obtained through the following relation:

$$A_{ri} = K_{0i}h_0/G(\gamma_0, \omega) \quad (38)$$

where h_0 is rubber thickness given by the ratio between the device displacement and the design rubber strain.

Table 7. Viscoelastic braces: designed brace stiffness for the 4-storey frame.

Floor	K_{0i} (kN/mm)	K_{bi} (kN/mm)
4	31.77	610.20
3	55.03	1056.70
2	70.15	1347.10
1	77.53	1488.70

Table 8. Viscoelastic braces: designed brace stiffness for the 8-storey frame.

Floor	K_{0i} (kN/mm)	K_{bi} (kN/mm)
8	27.94	536.50
7	51.72	993.30
6	71.55	1373.90
5	87.60	1682.10
4	100.06	1921.50
3	109.13	2095.60
2	114.99	2208.10
1	117.82	2262.60

In the case of buckling restrained braces a design strain equal to $\bar{\epsilon}_c = 0.2\epsilon_y$ was adopted to limit column deformations and to assure resistance and stability of columns under vertical loads and seismic loads. This value is smaller than the corresponding value used for the design viscoelastic braces, due to the larger bending moments expected in this case. Steel S275 (nominal yield strain $f_y = 275 \text{ N/mm}^2$) was assumed for BRBs and the yield strain was assumed as design strain $\bar{\epsilon}_d = \epsilon_y = f_y / E = 275/210000 = 0.00131$. Regarding the value of μ_d , as demonstrated by different studies [8], BRBs with appropriate details are capable of sustaining a maximum ductility greater than 20. However, excessively flexible structures are obtained with high ductility values, leading to problems related to P- Δ effects, to non structural damages at the damage limit state or excessive deformations under wind loads at the serviceability limit state. On the other hand, small values of μ_d result in low dissipative systems. Design ductility parameters $\mu_d = 5.2$ and $\mu_d = 4.8$ were adopted in the 4-

storey and 8-storey frames respectively, in order to limit the maximum inter-storey drift at the bracing system of the top storey to the 1.5% of the inter-storey height. Values of β , the participating mass ratio η , the system ductility μ_s , the m^* mass and the modal participation factor Γ , are given in Table 9. The base shear V_b , the scale factor K_{s0} and the natural period T obtained are also given. Design storey displacements due to the columns (v_{ci}), to the diagonal braces (v_{di}) and total design displacements (v_i) are reported by Tables 10 and 11. Storey shear stiffness (K_{si}), flexural stiffness (K_{bi}), relevant columns areas (A_{ci}), and BRB areas (A_{di}) are also reported. Columns sections dimensions and properties are given in Tables 12 and 13. As in the previous examples, plate constituting columns profiles were selected among European commercial plates, so that the cross section areas are close to the design values. The same two design arrangements for the columns described in the previous section are considered, i.e., (case *a*) the different designed profiles are adopted for each floor, and (case *b*) the same designed profile is assumed for two adjacent floors. For the BRBs the design areas are the BRB areas used in the finite element model.

Table 9. Elastoplastic braces: design parameters and properties of the SDOF equivalent system.

Frame	β (-)	η (-)	μ_s (-)	m^* (kNs ² /m)	Γ (-)	V_b (kN)	K_{s0} ($\times 10^3$ kN)	T (s)
4-storey	0.49	0.723	4.38	630.92	1.55	1051.00	396.04	1.09
8-storey	0.92	0.705	3.60	1141.10	1.57	1309.20	493.36	1.96

Table 10. Elastoplastic braces: design results for the 4-storey frame.

Floor	v_{ci} (mm)	v_{di} (mm)	v_i (mm)	v_{ui} (mm)	K_{si} (kN)	K_{bi} ($\times 10^6$ kNmm)	A_{ci} (mm ²)	K_{di} (kN/m m)
4	13.0	120.7	133.8	195.5	163900	19690	2930	1038
3	7.3	90.6	97.9	145.1	281390	49540	7372	1782
2	3.3	60.4	63.6	95.8	356130	87380	13003	2255
1	0.8	30.2	31.0	47.4	391750	129040	19203	2481

Table 11. Elastoplastic braces: design results for the 8-storey frame.

Floor	v_{ci} (mm)	v_{di} (mm)	v_i (mm)	v_{ui} (mm)	K_{si} (kN)	K_{bi} ($\times 10^6$ kNmm)	A_{ci} (mm ²)	K_{di} (kN/mm)
8	52.1	189.0	241.1	377.7	14400	2142	30.4	119870
7	39.9	165.4	205.3	327.1	37890	5638	55.9	220790
6	29.3	141.7	171.1	277.4	70250	10455	77.0	303910
5	20.4	118.1	138.5	228.8	109720	16327	93.8	370360
4	13.0	94.5	107.5	181.1	154620	23009	106.7	421260
3	7.3	70.9	78.2	134.3	203430	30272	116.0	457750
2	3.3	47.2	50.5	88.6	254720	37904	121.8	480960
1	0.8	23.6	24.4	43.8	307190	45713	124.6	492030

Table 12. Elastoplastic braces: designed column sections for the 4-storey frame.

Floor	h_c (mm)	b_f (mm)	t_f (mm)	h_w (mm)	t_w (mm)	A (cm ²)	I_y (cm ⁴)	I_z (cm ⁴)
4	140	10	120	6	140	35.2	1271.7	457.3
3	200	15	170	10	200	77	5554.4	2000.0
2	270	20	230	12	270	135.6	18127.7	6561.0
1	320	25	270	15	320	200.5	37353.7	13653.3

Table 13. Elastoplastic braces: designed column sections for the 8-storey frame.

Floor	h_c (mm)	b_f (mm)	t_f (mm)	h_w (mm)	t_w (mm)	A (cm ²)	I_y (cm ⁴)	I_z (cm ⁴)
8	130	10	110	6	130	32.6	1004.7	366.2
7	210	10	190	8	210	57.2	4660.8	1543.5
6	220	20	180	12	220	109.6	9412.5	3549.3
5	320	20	280	15	320	170	31586.7	10922.7
4	370	25	320	18	370	242.6	60060.6	21105.4
3	400	30	340	20	400	308	88870.7	32000.0
2	400	40	320	25	400	400	110933.3	42666.7
1	400	50	300	25	400	475	128958.3	53333.3

In Figure 26 inter-storey drifts and brace required ductility are illustrated and compared with the design values given by the proposed procedure, while column axial forces together with the relevant design values are reported in Figure 27. In the case of BRBs, the response results of the analyses show lower agreement with the design values as compared to the viscoelastic braces. The reason is the well known large sensibility of elastoplastic braces to the localization of storey displacements, leading to a more important influence of higher vibration modes. However, results can be considered satisfactory since the

maximum inter-storey drift obtained is about 2% of the inter-storey height in both 4-storey and 8-storey cases. In addition the maximum BRB ductility does not exceed 8 at the considered design limit state. The large sensitivity to local storey plasticization leads also to non negligible bending moments due to column continuity (bending moments between the 20% and the 40% of the yield bending moment of the columns).

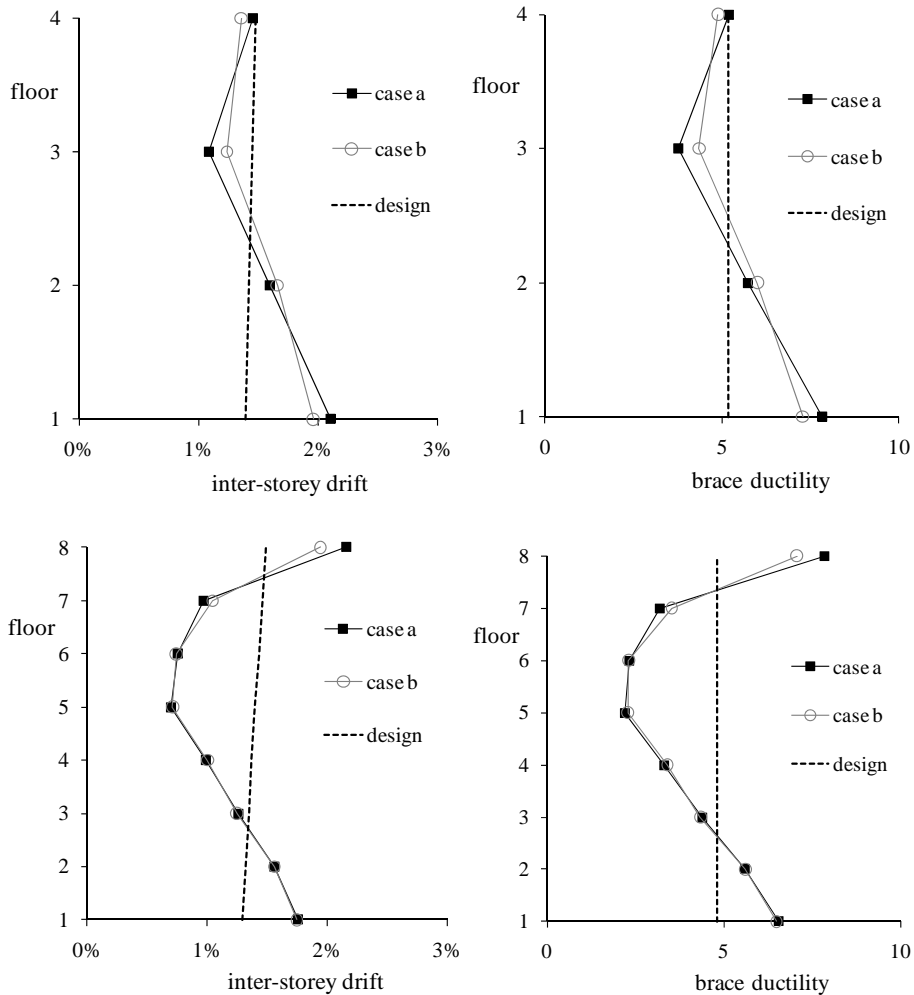


Figure 26. BRBs: inter-storey drifts and brace required ductility for the 4-storey and 8-storey frames.

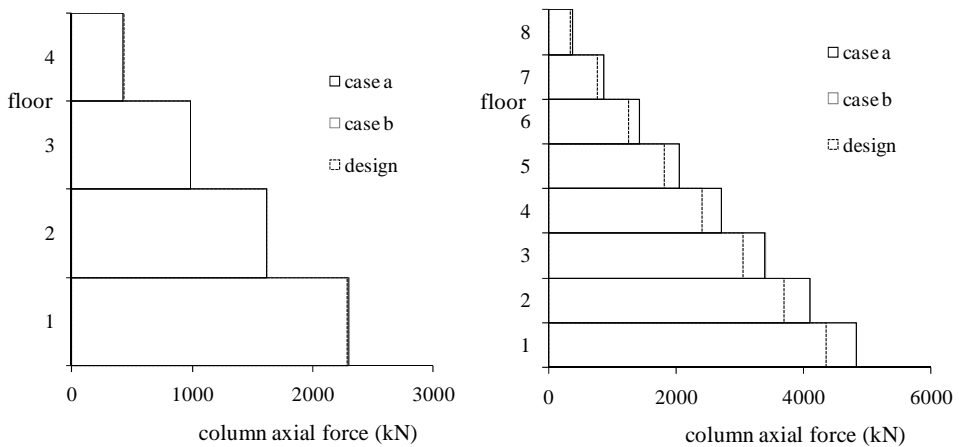


Figure 27. BRBs: column axial forces for the 4-storey and 8-storey frames.

5. CONCLUSION

Experimental tests carried out on a mock-up consisting of a full-scale composite frame with semi-rigid connections and equipped with dissipating braces based on elastoplastic BRAD devices and HDR devices demonstrated the efficiency of both typologies of dissipative bracings in increasing the stiffness and energy dissipation with respect to the bare frame. In particular, BRAD devices showed a large dissipation capacity, which increases by increasing displacement amplitude, despite some fatigue problems occurred for large displacement cyclic tests. A classical elastoplastic model can be used to simulate the behaviour of this kind of elastoplastic devices provided that the mean maximum force (average value between the maximum force in compression and the maximum force in tension) is used. In the case of HDR-based devices, a smaller dissipation capacity was observed. Both stiffness and dissipation capacity resulted strongly dependent on displacement amplitude and weakly dependent on the test frequency. On the other hand HDR devices supported an elevated number of cycles, even under large displacements, and without permanent deformations. The dynamic behaviour of this kind of devices is quite complex but simplified equivalent linear models are available.

A straightforward DBD method was proposed for structural systems made of a gravity load resistant system with pinned beam-column connections (which remain elastic) and dissipative viscoelastic or elastoplastic braces, based on continuous models consisting of a cantilever beams equivalent to the discrete bracing systems and relevant analytical expressions of flexural and shear stiffness distributions. The design method was applied to 4-storey and 8-storey steel frames with dissipative braces based on elastomeric dampers, as well as 4-

storey and 8-storey steel frames with buckling restrained braces. In the case of braces with elastomeric dampers satisfactory results were obtained and numerical simulations were carried out in order to investigate the limits of the model adopted for the design. In the cases of BRB-based bracing systems the accordance between design values and results of the time history analyses is less accurate (but still satisfactory) in consequence of the well-known large sensitivity of elastoplastic bracing systems due to the localization of storey displacements.

ACKNOWLEDGEMENTS

The authors wish to thank FIP Industriale (Italy) for providing them with their BRAD devices, and T.A.R.R.C. (Tun Abdul Razak Research Center, UK) for providing them with their elastomeric dampers. Partial support for this research from the Italian University Network of Seismic Engineering Laboratories (RELUIS) and the Italian Civil Protection Agency (Dipartimento della Protezione Civile), is gratefully acknowledged. Opinions expressed in this study are those of the authors and do not necessarily reflect those of the sponsors.

REFERENCES

- [1] Bruneau M, Uang CM, Whittaker A. Ductile design of steel structures. McGraw Hill; 1998.
- [2] Tremblay R. Inelastic response of steel bracing members. *Journal of Constructional Steel Research* 2002; 58(5-8): 665-701.
- [3] Tremblay R. Achieving a stable inelastic seismic response for braced steel frames. *Engineering Journal AISC* 2003; 40(2): 111-129.
- [4] Soong TT, Dargush GF. *Passive energy dissipation systems in structural engineering*. Wiley; 1997
- [5] Soong TT, Spencer BF. Supplemental energy dissipation: state-of-the-art and state-of-the-practice. *Engineering Structures* 2002; 24(3): 243-259.
- [6] Christopoulos C, Filiatrault A. *Principles of passive supplemental damping and seismic isolation*. IUSS Press; 2006.
- [7] Symans MD, Charney F, Whittaker AS, Constantinou MC, Kriker CA, Johnson MW, McNamara RJ. Energy dissipation systems for seismic application: current practice and recent developments. *Journal of Structural Engineering ASCE* 2008; 134(1): 3-21.
- [8] Uang CM, Nakashima M. Steel Buckling-Restrained Braced Frames. In Bertero VV, Bozorgnia Y, editors. *Earthquake Engineering, from Engineering Seismology to Performance-Based Engineering*. CRC Press; 2004.
- [9] Sabelli R, Mahin S, Chang C. Seismic demands on steel braced frame building with buckling-restrained braces. *Engineering Structures* 2003; 25(5): 655-666.

- [10] Lee KS, Fan CP, Sause R, Ricles J. Simplified design procedure for frame buildings with viscoelastic or elastomeric structural dampers. *Earthquake Engineering and Structural Dynamics* 2005; 34(10): 1271-1284.
- [11] Giacchetti R, Bartera F. Steel dissipating braces for upgrading existing building frames. *Journal of Constructional Steel Research* 2002; 60(3-5): 751-769.
- [12] Dall'Asta A, Ragni L. Experimental tests and analytical model of high damping rubber dissipating devices. *Engineering Structures* 2006; 28(13): 1874-1884.
- [13] Ragni L, Dezi L, Dall'Asta A, Leoni G. HDR devices for the seismic protection of frame structures: experimental results and numerical simulations. *Earthquake Engineering and Structural Dynamics* 2009; 38(10):1199-1217
- [14] Dall'Asta A, Ragni L. Dynamic systems with HDR: non linear behavior and linear approximation. *Earthquake Engineering and Structural Dynamics* 2008; 37(13): 1511-1526
- [15] BSSC, Building Seismic Safety Council. NEHRP recommended provisions for seismic regulations for new buildings and other structures. FEMA 450. Federal Emergency Management Agency; 2004.
- [16] Priestley MJN, Calvi GM, Kowalsky MJ. Displacement-based seismic design of structures. IUSS Press; 2007.
- [17] Kim J, Seo Y. Seismic design of low-rise steel frames with buckling-restrained braces. *Engineering Structures* 2004; 26(5): 543-551.
- [18] Lee KS, Ricles J, Sause R. Performance-based seismic design of steel MRFs with elastomeric dampers. *Journal of Structural Engineering ASCE* 2009; 135(5): 489-498.
- [19] Della Corte, G., Mazzolani, F.M., 2008. Theoretical developments and numerical verification of a displacement-based design procedure for steel braced structures - Proceedings of 14 WCEE – Beijing – China, 12-17 October 2008
- [20] Antonucci, R., Balducci, F., Castellano, M.G., Donà, F., "Pre-casted RC buildings with buckling restrained braces: the example of the new building of the faculty of engineering in Ancona", Proceedings of the Second International fib Congress, Napoli, Italy, June 5-8, 2006, paper No. 879.
- [21] Antonucci, R., Cappanera, F., Balducci, F., Castellano, M.G., "Adeguamento sismico del Liceo classico "Perticari" di Senigallia (AN)", Atti del XII Convegno Nazionale ANIDIS L'Ingegneria sismica in Italia, Pisa, Italy, 2007 (in Italian)
- [22] Wen YK. Method for Random Vibration of Hysteretic Systems, *Journal of the Engineering Mechanics Division ASCE*, 1976; 102 (EM2).
- [23] Menegotto M, Pinto PE. Method of analysis for cyclically loaded reinforced concrete plane frames including changes in geometry and nonelastic behavior of elements under combined normal force and bending. In: *Proceeding IABSE Symposium on Resistance and Ultimate Deformability of Structures Acted on by Well-Defined Repeated Loads*. Zurich, Switzerland; 1973, p. 112-123.
- [24] Grant D.N., Fenves G.L. and Auricchio F. Modelling and Analysis of High-damping Rubber Bearings for the Seismic Protection of Bridges, Iuss Press, Pavia, 2005.
- [25] Ministero delle Infrastrutture. Norme tecniche per le costruzioni. DM 2008, Rome , Italy (in Italian), 2008.

-
- [26] CEN, European Committee for Standardisation. Eurocode 8: design provisions for earthquake resistance of structures, Part 1.1: general rules, seismic actions and rules for buildings, EN 1998-1; 2004
 - [27] FEMA 356. Prestandard and commentary for the seismic rehabilitation of buildings. Federal Emergency Management Agency: Washington D.C., 2000.
 - [28] Timoshenko S. Vibration problems in engineering. Wiley; 1974.
 - [29] Chopra AK. Dynamics of structures: theory and applications to earthquake engineering, 2nd edition. Prentice-Hall; 2001.
 - [30] Fajfar P. Capacity spectrum method based on inelastic spectra. *Earthquake Engineering and Structural Dynamics* 1999; 28(9): 979-993.
 - [31] Kasai K, Fu Y, Watanabe A. Passive control systems for seismic damage mitigation. *Journal of Structural Engineering ASCE* 1998; 124(5): 501-512.
 - [32] Iervolino I, Galasso C, Cosenza E. REXEL: computer aided record selection for code-based seismic structural analysis. *Bulletin of Earthquake Engineering*, in print; DOI: 10.1007/s10518-009-9146-1.

NUMERICAL MODELLING AND SEISMIC ASSESSMENT OF STEEL AND STEEL-CONCRETE COMPOSITE FRAMES

Claudio Amadio¹, Maurizio Bella¹, Vanessa Bertoni¹, Lorenzo Macorini²

¹ *Department of Civil and Environmental Engineering, University of Trieste, Italy*

² *Department of Civil & Environmental Engineering, Imperial College London, UK*

Abstract. In the research, the seismic performance of steel and steel-concrete composite frames with partial strength connections has been analysed. An advanced modelling approach for partial strength joints has been developed and integrated into finite element models for nonlinear static and dynamic analysis of partially-restrained frames. The model, whose accuracy was confirmed in several experimental-numerical comparisons, is based on the component method and accounts for strength and stiffness degradation, which features the cyclic response of beam-to-column connections.

The advanced numerical model has then been used in probabilistic analyses of composite frames. The main sources of uncertainties, which affect the seismic behaviour of partially-restrained frames, have been defined and the Monte-Carlo method has been used in statistical simulations of joints and beams capacity. The results achieved established the consistency of the deterministic approach suggested by Eurocode 8 for designing steel-concrete seismic-resistant frames. Finally, in the last part of the research, the seismic upgrading of semi-continuous frames has been discussed and the enhanced responses that can be achieved using either steel X-braces or dissipative dampers were compared. The use of latter solution guaranteed better performance with low displacements, limited structural damage and reduced force demand on the foundations.

Keywords: steel and steel-concrete composite frames, partial strength connections, component method, probabilistic approach, Monte Carlo method, fragility and performance curves, visco-elastic dissipative bracings, seismic upgrading.

1. INTRODUCTION

The paper presents the main results achieved by the Research Unit of the University of Trieste in the RELUIS Project. In the research, the seismic performance of steel and steel-concrete composite frames with partial strength beam-to-column connections has been investigated using advanced numerical models.

The partially-restrained (PR) frames represent an attractive structural solution even when employed in earthquake-prone regions. They are more convenient than frames with full strength connections since the construction cost is markedly lower and, at the same time, they guarantee effective seismic performance, as the formation of plastic hinges in the beam-to-column connections with stable hysteresis loops, allows the structural system to dissipate a high quantity of energy.

In recent past, many efforts have been devoted to incorporate the connection characteristics into numerical models for PR frames. The current European codes of practice for steel [1] and composite structures [2] and for the seismic design of buildings [3] propose an accurate modelling approach for beam-to-column connections. The procedure is based on the use of mechanical model in which the joint structural response is schematised through an assembly of basic components. Using the Eurocodes provisions the monotonic moment-rotation curves for the joints can be calculated with high precision, while no specific rules are supplied for modelling the cyclic behaviour of the connection, which strongly affects the nonlinear response of PR frames under seismic loads.

In the research an advanced numerical model for the analysis of the steel and steel-concrete beam-to-column joints is presented. It has been developed on the basis of recent experimental results and accounts for strength and stiffness degradation with increasing deformation amplitude. The model is based on the component methods [4] and is capable of accurately predicting both the monotonic and cyclic behaviour of beam-to-column joints.

The dissipative response of the joints is analyzed employing a mechanical model based on the use of both rigid and flexible elements. The behaviour of each joint component is schematized through a mechanical law characterized by strength and stiffness deterioration. The accuracy of the proposed model has been checked performing numerical analyses and comparing the numerical responses with experimental results. Incorporating the proposed modelling approach in frame models, the seismic response of PR steel and steel-concrete composite frames can be assessed with high accuracy.

In the second part of the research, the seismic performance of PR frame has been investigated employing a probabilistic approach [5]. The main sources of uncertainties which influence the seismic behaviour of PR frames have been statistically defined [6,7,8] and the capacity of the analysed structures has been evaluated performing nonlinear dynamic analyses using the developed numerical model for beam-to-column connections. The seismic reliability of two frames has been evaluated drawing fragility curves [9] considering different performance objectives, which correspond to damage levels that are expected to not be exceeded when a structure is subjected to an earthquake ground motion of specified intensity. The consistency of the deterministic approach employed by Eurocode 8 (EC8) [3] for designing seismic resistant steel-concrete composite frames, has been checked comparing the probability of failure de-

terminated through the probabilistic analyses, assuming four limit states: Fully Operational (LS_0), Operational (LS_1), Life Safety (LS_2) and Near Collapse limit state (LS_3).

In the last part of this work, the seismic upgrading of semi-continuous PR frames has been dealt with and the enhanced performances that can be achieved using either steel X-braces or dissipative dampers were compared. In the former case concentric braced frames are used, they correspond to the more traditional structural system to resist lateral forces due to wind or earthquakes. Conversely, if viscoelastic dampers are employed, hybrid systems made of semi-continuous steel frames coupled with viscoelastic dissipative bracings are built. Such more advanced structural solution [10,11] benefits from the enhanced energy dissipation properties of viscoelastic dampers [12] that allow the interstorey drifts and plastic damage in the frames to be strongly limited, even in the case of severe earthquakes.

The results achieved can be useful to address the seismic upgrade of frames designed according to past codes (i.e. single level seismic criteria), frames built in regions assumed to be no-seismic at the time of the construction and now considered earthquake prone areas and, more in general, of existing structures whose seismic performance needs to be enhanced.

2. NUMERICAL MODELLING OF STEEL AND STEEL-CONCRETE JOINT

In recent past, it has been pointed out that, in addition to beams and columns, also the joints should be modelled when analysing steel and steel-concrete frames, since models with either pinned or rigid connections represent limit cases, which can be used only in simplified calculations [13].

At present, different modelling approaches can be employed to predict the actual response of beam-to-column connections:

- analytical models, based on mathematical formulations where the parameters of the moment-rotation curve are expressed as a function of mechanical and geometric properties [14,15,16,17];
- mechanical models, also called spring models or component models, based on the use of rigid and flexible elements appropriately connected [18,19,20,21,22,23];
- finite element models, mainly used to calibrate the different components employed in mechanical models [24,25,26,27].

The first strategy relies on the availability of experimental data on the joint behaviour under monotonic and cyclic loads in order to define material parameters for representing, through analytical expressions, the main features of the joint response, which include initial stiffness, maximum capacity as well as strength and stiffness degradation under cyclic loadings.

Using the last approach the nonlinear joint response can be estimated with high accuracy, controlling the stress distribution in the main joint resistant components. However 2D and 3D finite element models are restricted to the joint analysis and, because of the high computational cost, cannot be employed for modelling whole frames. The use of the component method, where the model parameters can be obtained in relatively cheap component tests, represents the best compromise between accuracy and computational demand.

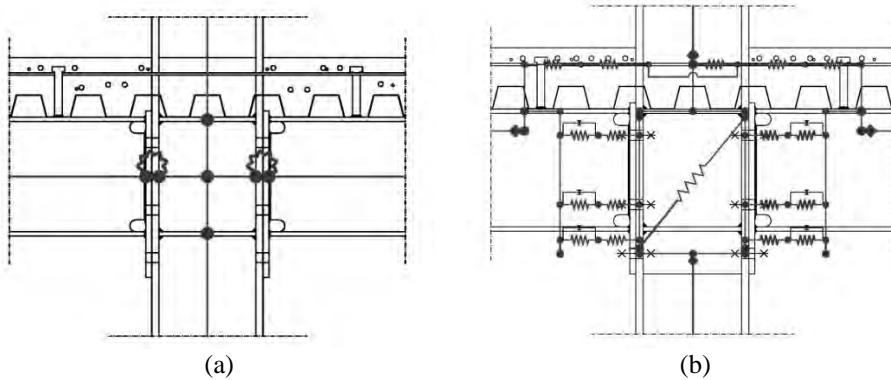


Figure 1. Beam-to-column connection modelling: (a) nonlinear rotational spring, (b) macro-model.

Such approach can be employed to determine maximum capacity and initial stiffness of beam-to-column connections by assembling the contribution, in term of strength and stiffness, of the different resistant components, modelled through axial springs. Following this procedure a nonlinear moment-rotation curve can be defined and used in frame models, where the whole joints response is associated to nonlinear rotational springs (Fig. 1a). However strength and stiffness degradation are not implicitly defined and should be derived from cyclic tests on whole joints. This reduces the advantage in using the component method and leads to employ such a strategy only in the case of monotonic loading, where a correct representation of the connection cyclic behaviour is not relevant.

In the research a macro-model for beam-to-column connections has been developed (Fig. 1b). With respect to previous component-based formulations [22,23], where the inelastic behaviour of each component is represented using trilinear kinematic hardening models, accurate mechanic laws characterized by strength and stiffness degradation are used in the proposed macro-model. Moreover particular attention has been paid on modelling the interaction between column and concrete slab in steel-concrete composite frames.

Following a brief description of the component approach used in the research, the mechanical laws for the main joint components are presented and

the accuracy of the proposed modelling approach is shown in several experimental-numerical comparisons, which comprise cyclic tests on single joints and a pseudo-dynamic test on a PR composite frame.

Component method

The components method can be divided into the following steps [20]:

- *component identification*: the contribution of the different active components, associated to basic resistant mechanisms (tension, compression, shear and bending) is identified (Fig. 2);
- *component characterisation*: definition of specific mechanical laws for the axial springs representing the basic resistant components;
- *component assembly*: assembly of the axial springs and definition of the rotational spring for the beam-to-column joint (Fig. 1a).

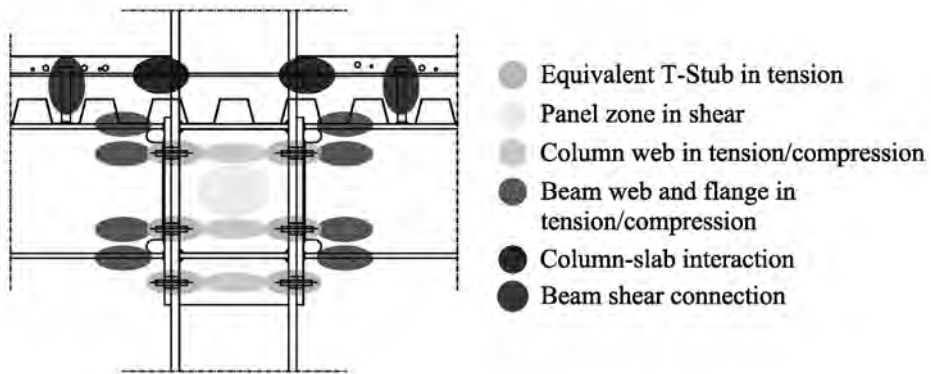


Figure 2. Component identification.

In models for steel joints, the resistant components are (Fig. 2):

- T-stub elements in tension;
- web panel in shear;
- column web in tension and/or compression;
- beam web and flange in tension and/or compression;
- bolts in shear and in bearing.

In the case of composite joints, in addition to the components aforementioned, those which refer to concrete slab and its interaction with the columns must be considered (Figs. 2 and 3). They correspond to:

- beam-to-slab connection in shear;
- concrete in compression against the column (mechanism 1);
- concrete struts in compression (mechanism 2);
- transversal steel bars in tension (mechanism 2);
- longitudinal bars in tension (mechanism 2) or slab in compression.

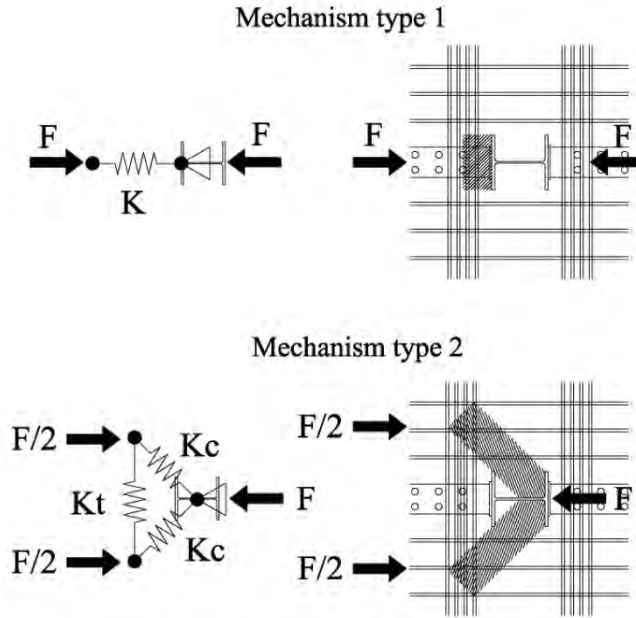


Figure 3. Mechanisms for transferring slab forces.

The assembly procedure is suggested by current codes of practice [28] to determine moment-rotation curves for representing the joints monotonic flexural behaviour. However, in the macro-model approach, such step is not considered, because each component is directly included in the joint model. With regard to the component characterisation, the Eurocodes [1][2][3][28] provide accurate expressions to calculate strength and elastic stiffness of the main resistant components, whereas they do not provide any specification to assess their cyclic behaviour.

Recently, it has been shown that, in seismic assessment of PR frames, where an accurate modelling of actual dissipative capacity of beam-to-column connections is essential, the component method can be effectively employed in macro-models where the different joint components are included in the frame model using specific plastic laws to represent their behaviour under cyclic loadings [29,30].

Macro-model for steel and steel-concrete beam-to-column joints

The model developed in the research, corresponds to a macro-model capable of predicting the monotonic and cyclic behaviour of beam-to-column connections. It corresponds to a refinement of previous models developed by the authors [23,29,30]. In the model, every resistant part of the joint is modelled using a set of nonlinear axial springs. Strength and initial stiffness of each spring are defined according to the Eurocode provisions [1][2][3][28], while specific plastic

laws are used to represent the actual cyclic response observed in experimental tests on components. The proposed modelling approach can be used to model any type of steel and steel-concrete joints, both welded and bolted. Herein after, for sake of conciseness, only composite joints with bolted end-plate, which represent one of the most effective connections for PR composite frames, are considered.

In Figure 4 the proposed macro-model for a composite beam-to-column connection is shown. In the following, a description for each component together with details on the mechanical relations employed for modelling the plastic behaviour under cyclic loads are provided.

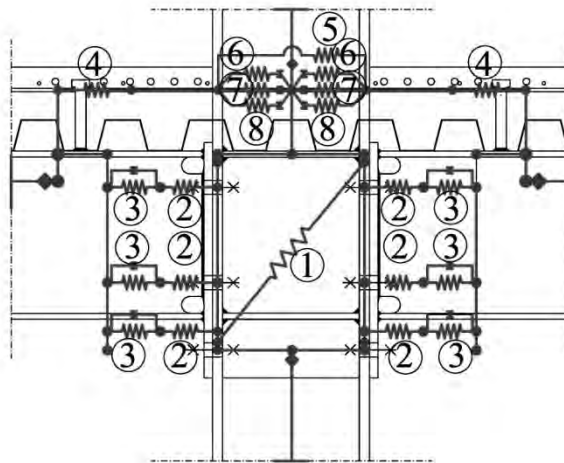


Figure 4. Macro-model for bolted end-plate composite beam-to-column connection.

The component represented by the spring No. 1 corresponds to the web panel in shear. The smooth hysteretic model developed by Kim & Engelhardt [31], which accounts for both bending and shear deformations, is used for modelling the elastic and plastic response. The monotonic model is based on quadric-linear relation between bending moment M and rotation γ and on Dafalias' bounding surface theory [32] combined with Cofie's rules [33] for movement of the bound line (Fig. 5). An elastic stiffness K_e , together with two post-elastic K_1 and K_2 and a hardening stiffness K_3 define the monotonic model. Such stiffness values can be calculated from material and geometric properties of the web column panel. With reference to the cyclic behaviour, accurate hysteretic rules are provided to predict panel zone response under cyclic loading [31].

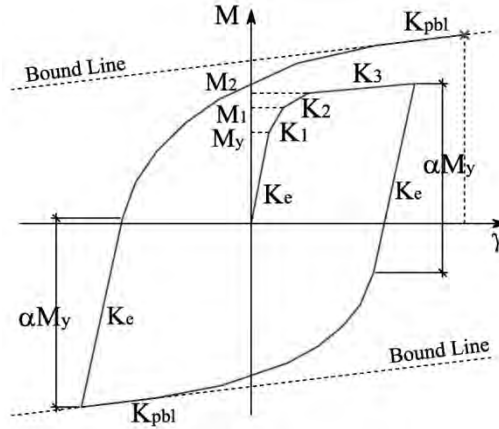


Figure 5. Monotonic curve and hysteresis rules for panel zone.

The unloading from the initial loading curve is described by an elastic branch with amplitude proportional to the initial elastic branch (αM_y). Finally the load reversal path is described by a smooth curve that tends to a bound line characterized by the same stiffness K_{pbl} of the hardening branch. The evolution of the bounding lines for the cyclic behaviour of the panel zone is defined using a cyclic steady state curve as defined in (1):

$$\frac{\gamma}{\gamma_n} = \frac{M^{pa}}{M_n^{pa}} + \left(\frac{M^{pa}}{\xi M_n^{pa}} \right)^c \quad \text{with } M_n^{pa} = M_y^{pa} + 2M_{pcf} \quad \text{and } \gamma_n = \frac{M^{pa}}{K_e} \quad (1)$$

where M_n^{pa} and γ_n are the normalizing panel moment and the corresponding elastic rotation respectively, while M_{pcf} is the plastic moment of the column flange and K_e is the elastic stiffness of the panel zone. The values of the two constants c and ξ , that define the cyclic steady state curve presented in (1), are assumed equal to 7 and 1.15 respectively, as found in [31] accounting for experimental data.

The relation between the shear force V and the bending moment acting on the panel zone M is defined in (2):

$$V = M \frac{1 - \rho}{d_b - t_{bf}} \quad \text{with } \rho = \frac{d_b - t_{bf}}{h_c} \quad (2)$$

where d_b is the panel zone height t_{bf} is the thickness of the beam flange and h_c is the column height.

The component modelled by the spring No. 2, represents beam and column webs in tension and/or transversal compression. A tri-linear hysteretic law with kinematic

hardening is used to model the hysteretic behaviour (Fig. 6). It corresponds to a polygonal hysteretic model which does not consider any strength and stiffness degradation and is characterized by an asymmetrical trilinear loading curve.

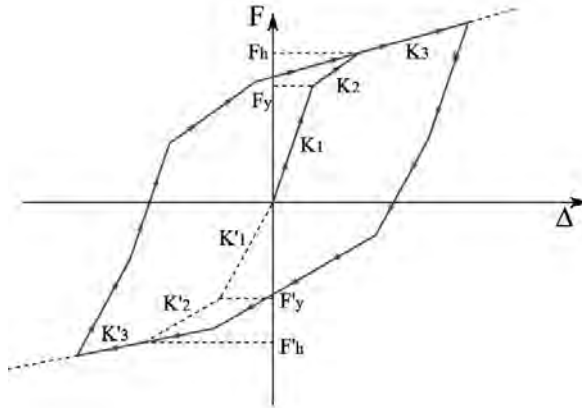


Figure 6. Trilinear hysteretic model with kinematic hardening.

Spring No. 3, corresponds to a T stub element for the end-plate and the column flange in bending. A specific nonlinear curve has been defined on the basis of the experimental results achieved by Clemente et al. [34] on T-stub specimens (Fig. 7). The proposed relationship is asymmetric; in compression the response is rigid, while the opening in tension is modelled by a curve with hardening and deterioration of strength and stiffness.

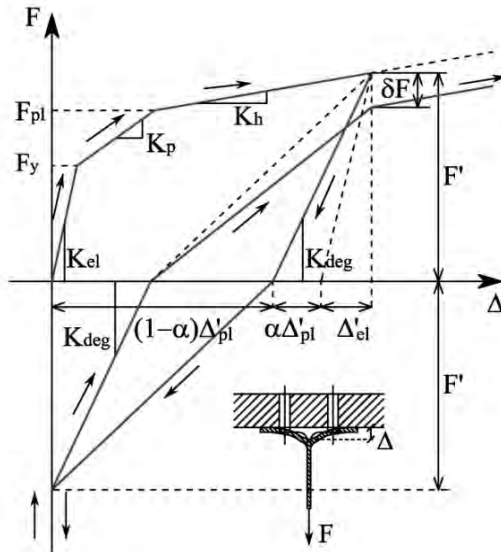


Figure 7. Nonlinear curve for T-stub component.

The elastic stiffness K_{el} in tension is calculated using the expression supplied by Eurocode 3 [28], whereas the stiffness along the unloading branch K'_{el} until the point of load inversion, is determined using the Takeda's model [35] to account for degradation. The stiffness K'_p , which defines the curve before the closure of the connection in compression, is evaluated considering that the closure is complete when a force in compression F' , equal to the maximum value experienced in tension before the load inversion, is reached. Finally, the stiffness K'_r for the reloading in tension, is calculated on the basis of a strength degradation $\delta F'$ [36]. The values K'_{deg} , K'_p , K'_r , $\delta F'$ are given by:

$$K'_{deg} = \frac{F'}{F'/K_{el} + \alpha \cdot \Delta'_{pl}}; \quad K'_p = \frac{F'}{(1-\alpha) \cdot \Delta'_{pl}}; \quad K'_r = \frac{F' - \delta F'}{\Delta' - F'/K'_{deg}} \quad (3)$$

$$\delta F' = F_y \cdot \gamma \cdot \left[1 - \left(1 - \left(\frac{E_{pl}}{E_{um} + E_{pl}} \right)^\delta \right) \cdot \left(1 - \left(\frac{\Delta'}{\Delta_{um}} \right)^\varepsilon \right) \right] \quad (4)$$

where Δ' , Δ'_{pl} , Δ_{um} , F_y , E_{um} and E_{pl} represent, respectively, the deformation corresponding to the force F' in tension, the plastic part of the deformation Δ' , the deformation at collapse, the force at yielding, the energy dissipated at collapse in a monotonic test and the plastic energy dissipated by the element in the previous step. In (3) and (4), α , γ , δ , ε are coefficients obtained by interpolation of experimental outcomes [34], minimizing the difference between experimental curves and the response determined using the mechanical model. Figure 8 shows a numerical-experimental comparison for a T-stub specimen, T120S in [34]. The good agreement between the two curves confirms the accuracy of the proposed cyclic model for T-stub components.

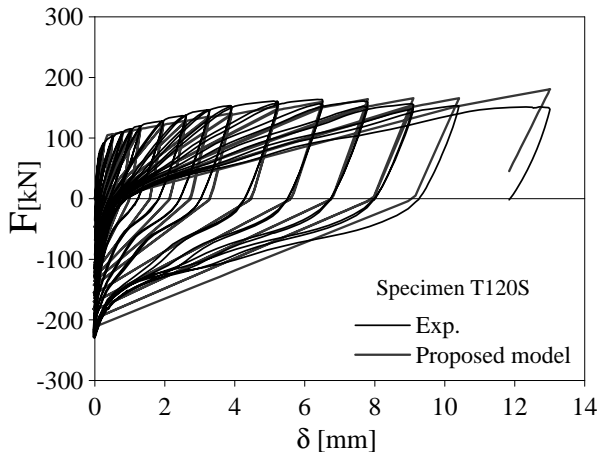


Figure 8. Experimental-numerical comparison for T-stub model.

Five nonlinear springs, No. 4-5-6-7-8 in Figure 4, have been employed to model the slab and the interaction between slab and column. The spring No. 4 models the shear connection in the composite beam. Only the connectors between the joint and the point of contraflexure in the beam are considered. A symmetric trilinear curve and the pivot degradation rule developed by Park [36] have been used to model the cyclic behavior (Fig. 9).

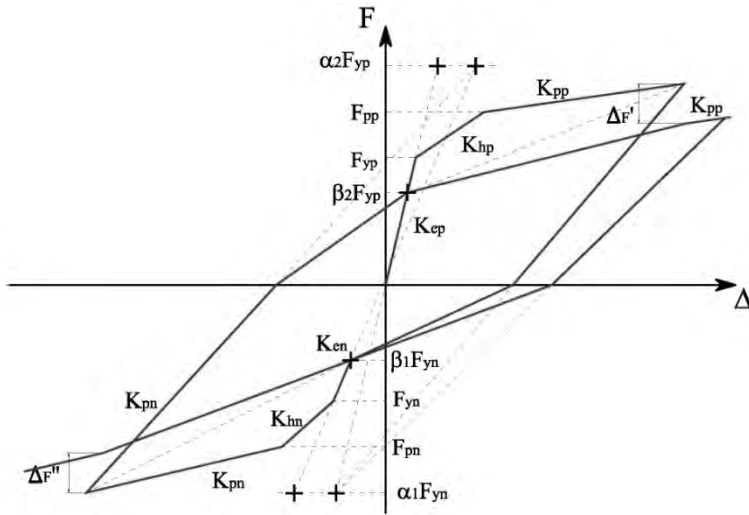


Figure 9. Trilinear curve with pivot stiffness degradation rule.

The spring No. 5 represents the longitudinal reinforcement bars and the concrete slab under tension. The asymmetric trilinear curve with no degradation shown in Figure 6 has been employed.

The spring No. 6 accounts for mechanism type 2 (Fig. 3) for slab-column interaction, which corresponds to a strut-and-tie mechanism with inclined struts against the column and transversal reinforcing bar ties.

Using the virtual work principle, the elastic stiffness K_{e2} for the interaction mechanism type 2 is given by:

$$K_{e2} = \frac{1}{\left[\frac{1}{K_c} + \frac{1}{4K_t} \right]} \quad (5)$$

where K_t and K_c are the elastic stiffness of the transverse bars and of the concrete strut respectively. With regard to the spring strength F_{r2} , it can be evaluated on the basis of the compressive strength of the concrete strut in and of the tensile strength of the transversal bars F_{rt} :

$$F_{r2} = \min\left(F_{rc}/\sqrt{2}; F_{rt}\right) \quad (6)$$

The cyclic behavior is represented through the pivot rule (Fig. 9).

Finally, springs No. 7-8 model mechanism type 1, which corresponds to confined and unconfined concrete layers in compression (Fig. 3). Again an asymmetric trilinear curve for modeling the monotonic response and the pivot rule for representing the hysteretic behavior has been considered.

Numerical analyses

The macro-model for beam-to-column connections has been implemented in the finite element code Abaqus [37]. Its accuracy has been checked through experimental-numerical comparisons, considering the cyclic response of steel and steel concrete composite joints and the behavior of PR composite frames under seismic loading.

In the first numerical analyses, the precision guaranteed by the Kim & Engelhardt's model in representing the hysteretic response of the column web panel component has been checked. Results achieved in cyclic tests on rigid joints, whose cyclic response mainly depends on plastic deformations in the panel zone, have been considered for numerical-experimental comparisons. In Figures 10 and 11 the welded and the rigid end-plate steel joints (specimen I1 and specimen J1 respectively) analyzed in [38] are shown together with experimental and numerical curves. The good agreement, in term of stiffness, strength and dissipative capacity, between experimental and numerical values confirms the accuracy of the models.

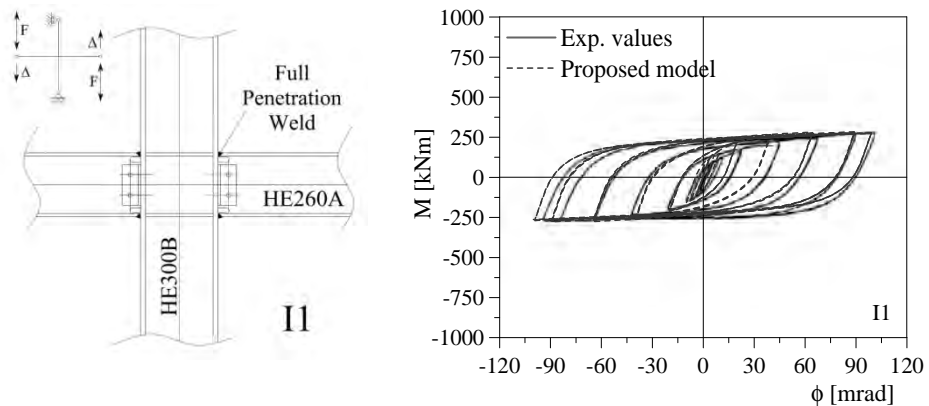


Figure 10. Experimental-numerical comparisons: welded joint [38].

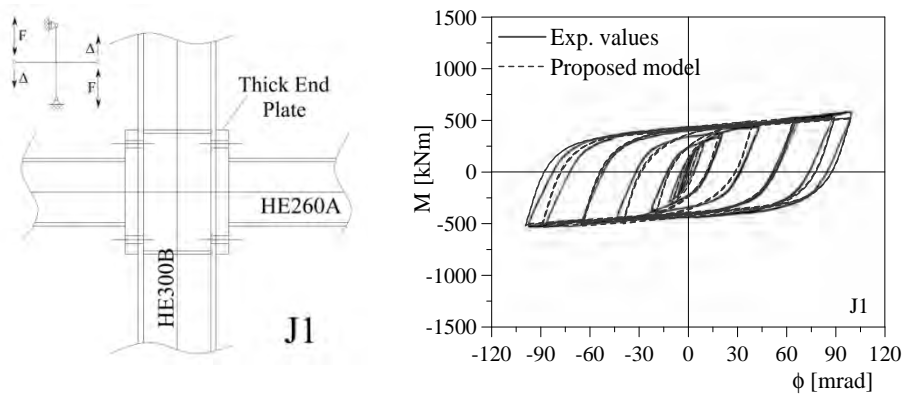


Figure 11. Experimental-numerical comparisons: rigid end-plate joint [38].

Some of the steel joints tested by Bernuzzi et al. [39], whose response is governed by equivalent T-stubs of bolted connections, have been analyzed to assess the effectiveness of the proposed cyclic model for T-stub elements when employed in macro-models for beam-to-column connections. In Figures 12-14 the results achieved for a flush end-plate bolted beam-to-column connection (specimen FPC), an asymmetric and a symmetric extended end-plate bolted joints (specimens EPC and EPBC-1) are shown. The experimental-numerical comparisons reveal a good agreement in terms of both strength and stiffness. The proposed model is able to describe strength degradation and pinching which characterize the cyclic response of this kind of connections.

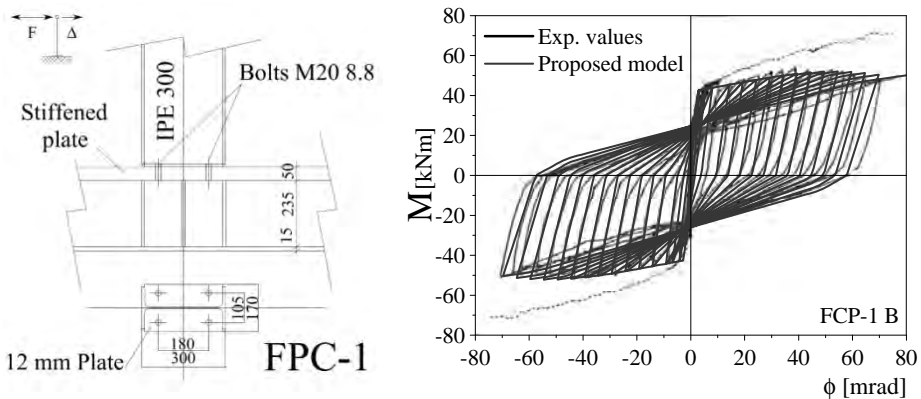


Figure 12. Experimental-numerical comparisons: flush end-plate beam-to-column connection [39].

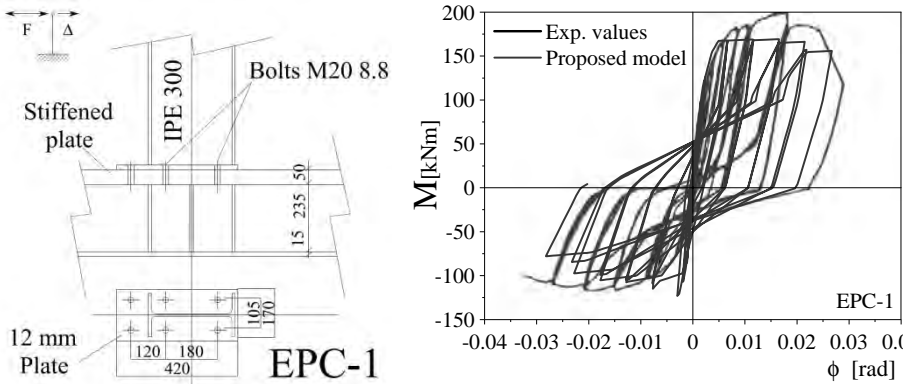


Figure 13. Experimental-numerical comparison: asymmetric extended end-plate beam-to-column connection [39].

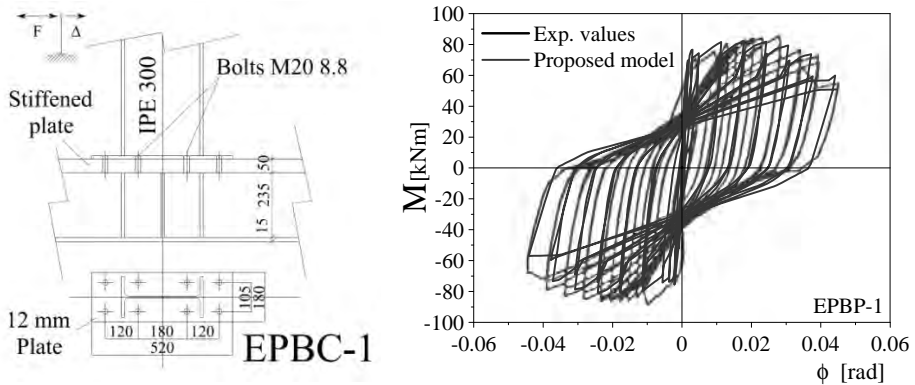


Figure 14. Experimental-numerical comparison: symmetric extended end-plate beam-to-column connection [39].

Further numerical simulations were performed on steel-concrete beam-to-column joints, where the behaviour under cyclic loading is strongly affected by the complex interaction between concrete slab and the steel column. In Figures 15 and 16 the three analysed composite joints, which correspond to the specimens CJ1-2 and CJ3 tested experimentally by Liew et al. [40], are shown.

The results of the numerical analyses show again a good agreement between numerical and experimental results also in the case of composite joints. The macro-model enables the cyclic behavior of the analyzed joints to be predicted with good accuracy.

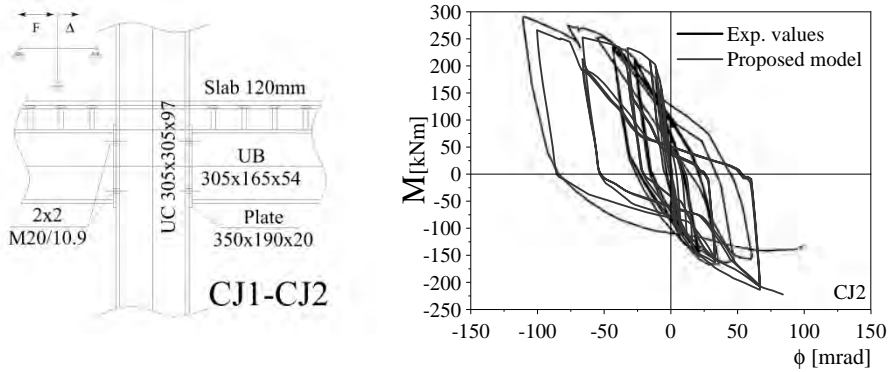


Figure 15. Experimental-numerical comparisons: steel-concrete composite joint with flush end-plate connection [40].

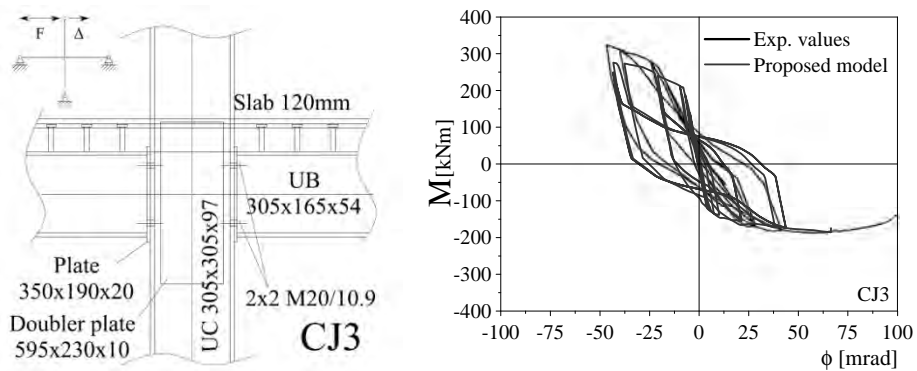


Figure 16. Experimental-numerical comparisons: steel-concrete composite joint with flush end-plate connection with strengthened web panel [40].

Finally, some results achieved in numerical analyses on a PR composite frame under lateral loading are presented. The effectiveness in using the proposed macro-model in numerical analyses for assessing the seismic response of whole steel-concrete composite frames is shown. As mentioned above, in such structural systems the beam-to-column connections play the fundamental role of dissipating the energy supplied by earthquakes through plastic hysteresis. Thus an accurate representation of the joint behavior under cyclic loading is fundamental to correctly predict the frame seismic response. Figures 17 and 18 display, respectively, the analysed composite frame and details of internal and external joints.

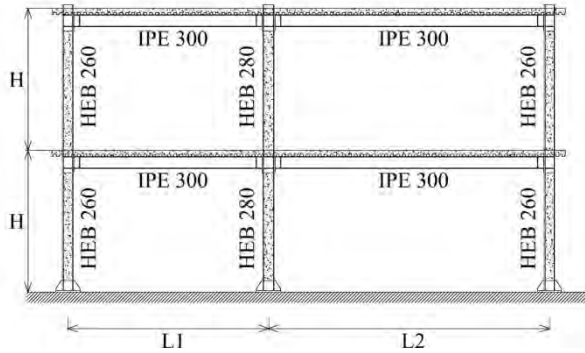


Figure 17. Elevation of the analysed PR steel-concrete composite frame.

The frame, tested at the ELSA Joint Research Centre in Ispra [41], represents a part of a full scale two-storey building made of three parallel two-bay frames with different span lengths: $L1=5$ m and $L2=7$ m spacing and $H=3.5$ m inter-storey height. External and internal joints were tested separately from the frame in order to investigate their response under cycle loading [42].

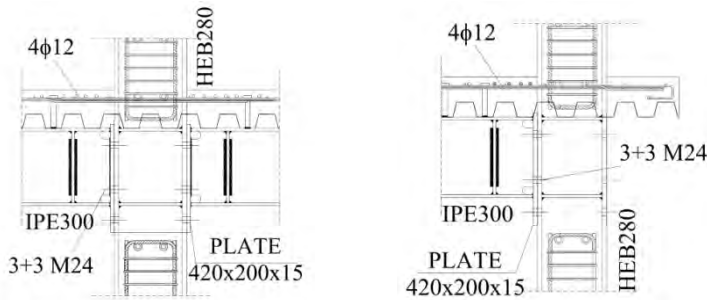


Figure 17. Details of internal and external composite joints [42].

Figures 19a and 19b show experimental-numerical comparisons on the joints cyclic behaviour. The figures confirm that the proposed refined model can adequately predict the cyclic response in terms of strength, stiffness and dissipated energy. Only the overstrength exhibited by the interior joint under sagging bending moment is not predicted with high precision, so as the abrupt drop in strength occurred in both the experimental tests once the plastic limit was reached.

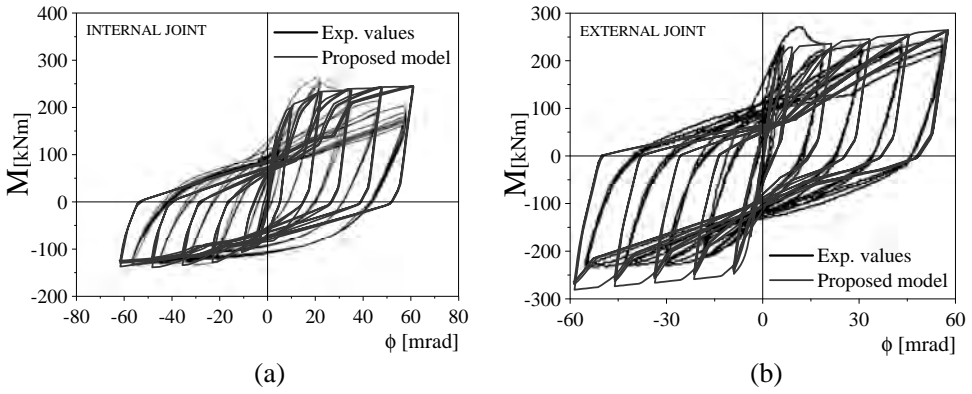


Figure 19. Numerical-experimental comparisons: (a) internal joint, (b) external joint.

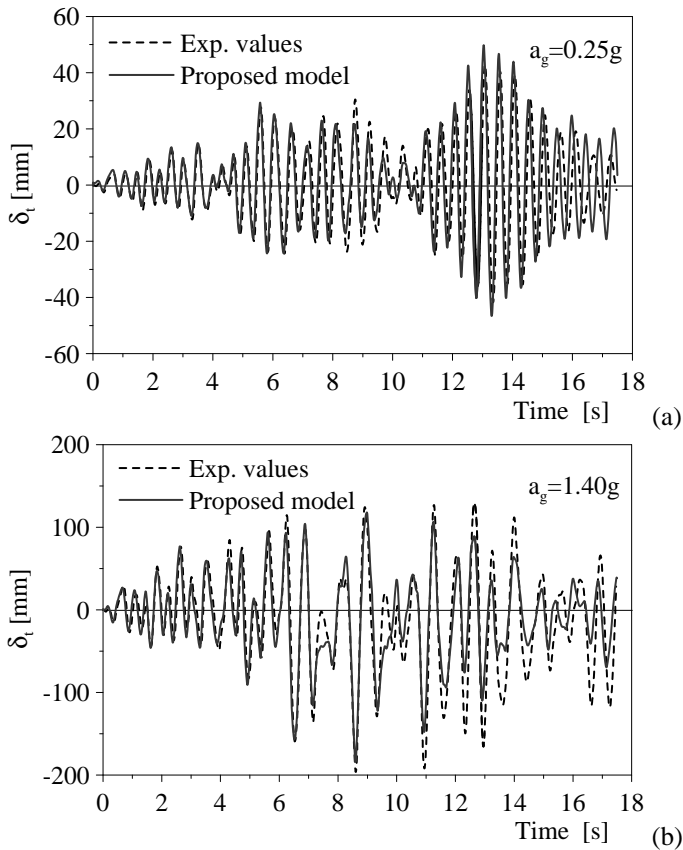


Figure 20. Numerical-experimental comparison, second floor displacements time history: (a) $a_g = 0.25g$, (b) $a_g = 1.40g$.

In Figures 20a and 20b experimental and numerical results are compared. They correspond to time-history second floor displacements, obtained by performing a static analysis under the history of experimental forces measured during the pseudo-dynamic test [41], carried out under an artificial earthquake ground motion compatible with the elastic spectrum proposed by the Eurocode 8 [3], for type 1 soil and peak ground acceleration $a_g = 0.25g$ and $a_g = 1.40g$.

An overall good correspondence between experimental and the numerical curves can be observed, which demonstrates the effectiveness guaranteed by using the proposed macro-model in predicting the actual seismic response of the frame even in the case of high peak ground accelerations.

3. SEISMIC ASSESSMENT OF PR COMPOSITE FRAMES USING THE PROBABILISTIC APPROACH

The advanced macro-model presented in “Component method” Section has been used to assess the seismic performance of PR composite frames design according Eurocode 8 [3]. A probabilistic approach [43] has been employed in the analyses. The main sources of uncertainties have been statistically defined and the capacity of the analysed structures has been evaluated performing nonlinear dynamic analyses. To limit the computational demand, only the most relevant sources of uncertainty have been considered:

- materials mechanical properties;
- characteristics of the seismic event;
- structural joints.

The probabilistic analysis has been carried out using the Monte Carlo (MC) method. In the analysis of a single frame, many structures are generated randomly with the same geometry but with different material properties. All the generated structures are analysed performing nonlinear dynamic analyses with different earthquake ground motions, so as to represent the randomness of the seismic event. Using the results of the nonlinear analyses the seismic reliability can be determined. It represents the complement to 1 of the seismic fragility $F_r(x)$, which is the probability of occurrence of a given limit state (characterised by a control variable LS) conditioned by a parameter representative of seismic hazard IM .

$$F_r(x) = P[LS | IM = x] \quad (7)$$

In general, in order to evaluate the reliability of a structure with reference to a specific limit state, a limit function $G(\mathbf{X}) = G(X_1, X_2, \dots, X_n)$ can be considered, where the variables X_i are random project variables (strength, stiffness, etc.). The structure complies with the limit state only if the function $G > 0$. According to the MC method, a set of values for \mathbf{X} is generated numerically to calculate G , considering their probability distribution and using a random gen-

erator. Repeating the process for a high number of sets the probability distribution for G can be determined. The number of simulated events required by MC method depends on the sampling technique. Even though the MC approach is usually associated with a *Simple Random Sampling* method for determining input values, in the research, the *Latin Hypercube Sampling* has been used, which allowed the reduction of the computational cost and generally the improvement of statistical efficiency.

Analysed frames

The first analysed frame (frame F1), corresponds to the PR steel-concrete frame tested at the ELSA Joint Research Centre, Ispra [41] and considered for numerical-experimental comparisons in “Numerical analyses” Section. The second structure (frame F2, Fig. 21), is a four-storey frame, geometrically similar to the former frame and designed according to Eurocode 4 and 8 [2][3]. The composite columns, partially encased, are made of steel profiles HEB 400, while the beams are steel profiles IPE 330 connected, through studs, to the upper concrete slab as in the first frame. The beam-to-column joints are extended end-plate bolted connections.

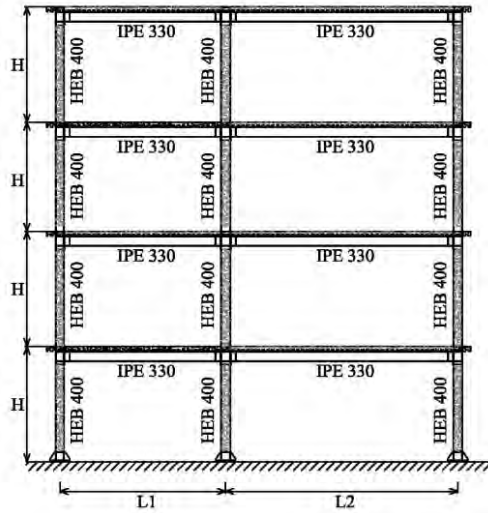


Figure 21. Elevation of the second frame analysed (F2 frame).

With regard to the materials properties, structural steel (Class S235JO) with $f_{yk,nom}=235$ MPa, bolts (Class 10.9; M24 M16) with $f_{yk,nom}=900$ MPa, $f_{uk,nom}=1000$ MPa and concrete with $f_{ck,nom}=25$ MPa, have been considered.

Seismic inputs

In the seismic assessment of structures, the earthquake ground motion represents the main source of uncertainty. In this work two series of recorded earthquake ground motions have been considered. The first series collects 10 recorded earthquake ground motions, which have been selected, according to Erberik & Elnashai [44], to represent a wide range of possible seismic events of significant intensity (magnitude ≥ 5.8). In Figure 22 the spectral accelerations are shown, while in Table 1 three seismic intensity indicators, namely peak ground acceleration a_g , magnitude M_s and modified Mercalli scale MM , which marks the earthquake ground motions are reported.

Table 1. Intensity indicators for the first set of earthquakes.

Earthquake	Date	Comp.	a_g [g]	Sd_{max} [cm]	Sa_{max} [g]
Imperial -Valley - El Centro(USA)	15/05/1940	S00E	0.348	28.0	0.935
Friuli - Buia (Italy)	15/09/1976	N-S	0.109	9.4	0.327
Alkoin - Xilikastro (Greece)	24/02/1981	N-S	0.290	20.1	1.018
Friuli - Tolmezzo (Italy)	06/05/1976	E-W	0.315	11.2	1.030
Tabas - Boshroych (Iran)	16/09/1978	N79E	1.004	10.3	0.339
Irpinia - Campano Lucano (Italy)	23/11/1980	E-W	0.175	18.6	0.595
Lazio- Abruzzo - Cassino-Sant'Elia (Italy)	07/05/1984	N-S	0.110	3.8	0.393
Kocaeli - Yesilkoy (Turkey)	17/08/1999	N-S	0.089	16.5	0.366
Gazli (Uzbekistan)	17/05/1976	E-W	0.720	50.4	2.008
Montenegro - Bar-S.O.	15/04/1979	E-W	0.363	40.6	1.305

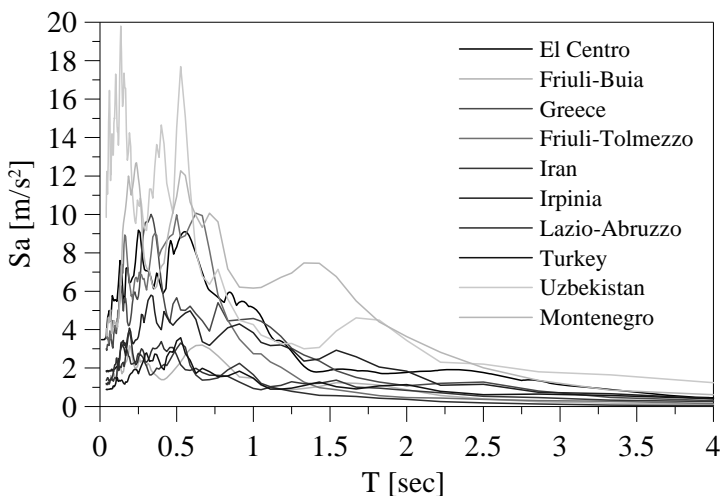
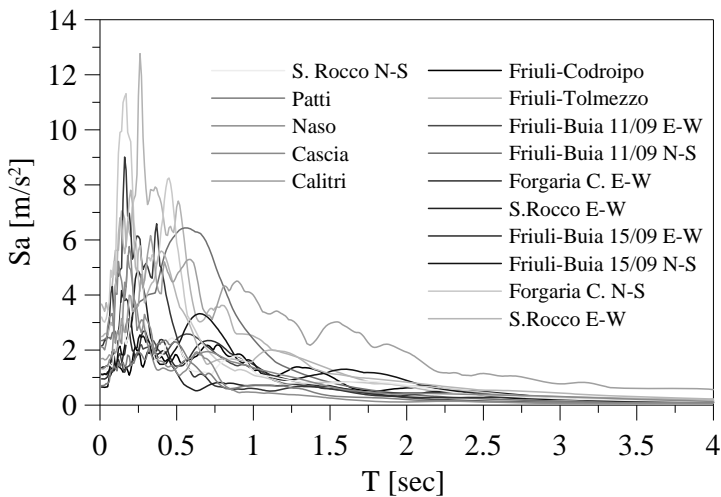


Figure 22. Spectral accelerations for the first set of earthquakes.

Table 2. Intensity indicators for the second set of earthquakes.

Earthquake	Date	Comp	a_g	Sd_{max}	Sa_{max}
			[g]	[cm]	[g]
0032 Codroipo	06/05/76	N-S	0.066	8.3	0.217
0038 Tolmezzo	06/05/76	N-S	0.366	7.5	1.060
0143 Buia	11/09/76	E-W	0.110	3.5	0.271
0143 Buia	11/09/76	N-S	0.234	7.3	0.639
0152 Forgaria C	15/09/76	E-W	0.218	7.0	0.858
0153 S.Rocco	15/09/76	E-W	0.135	7.7	0.513
0156 Buia	15/09/76	E-W	0.094	5.1	0.287
0156 Buia	15/09/76	N-S	0.109	9.4	0.327
0168 Forgaria C.	15/09/76	N-S	0.352	7.8	1.058
0169 S.Rocco	15/09/76	E-W	0.251	9.9	0.679
0169 S.Rocco	15/09/76	N-S	0.131	7.3	0.315
0301 Patti	15/04/78	N-S	0.071	2.6	0.271
0302 Naso	15/04/78	E-W	0.132	2.1	0.503
0350 Cascia	19/09/79	E-W	0.210	7.0	0.596
0636 Calitri	23/11/80	E-W	0.175	18.6	0.595


Figure 23. Spectral accelerations for the second set of earthquakes.

In the second series, 15 earthquake ground motions occurred in Italy has been taken into account (Fig. 23). Their pseudo-acceleration spectra fit in aver-

age the Eurocode 8 spectrum for soil A (Fig. 24). Table 2 summarizes their characteristics.

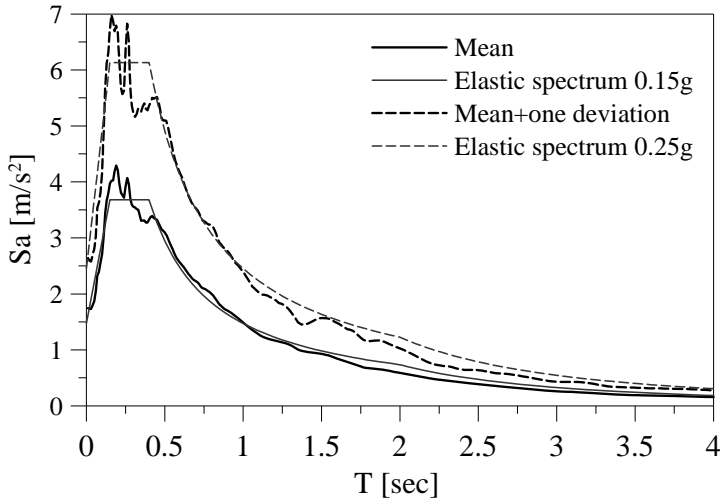


Figure 24. Mean and mean + one deviation spectra in terms of acceleration for the second set of earthquakes compared with code spectra.

Other sources of uncertainties

In the probabilistic analysis of the seismic performance of PR frames, the joints characterisation is fundamental to correctly evaluate the main source of energy dissipation. For this reason, the statistical distributions of joint materials properties have been considered, as well as statistical simulations of the joints and beams capacity have been carried out.

Material properties

With regard to the structural steel, two values for the yield stress: the first related to the flanges while the latter to the web of the cross section, have been assumed. Moreover, the Log-Normal statistical distribution for yield stress has been employed. The average of logarithmic yield stress has been considered dependent on the thickness t of the plates that form the section profile [45], as given in:

$$E(\ln f_y) = c_1 - c_2 t = 5.766 - 0.007t \quad (8)$$

where the constants c_1 and c_2 are based on steel type (Fe 360), t represents the thickness in mm and f_y is the yielding stress in N/mm^2 .

As far as steel bars are concerned, a Log-Normal distribution for tensile strength with a coefficient of variation $COV = 6\%$ has been considered in agree-

ement with [44]. Conversely, a Normal distribution for the concrete compressive strength f_c has been assumed according to [46], considering a coefficient of variation $COV=15\%$. The average value for f_c can be obtained from the characteristic value:

$$f_{c,m} = \frac{f_{c,k}}{1 - k \cdot COV} \text{ with } k=1.64 \quad (9)$$

For bolts ultimate strength, a Log-Normal distribution has been assumed, with an average value $E(f_u)=1.2 \cdot f_{u,k}$ and a $COV=2\%$. Finally, a Normal distribution has been employed for the ultimate strength f_{us} of the shear studs for the connection between concrete slab and steel beam. A $COV=4\%$ and an average value determined as a function of the characteristic value as in (9) have been assumed. More details on the statistical analysis of the material properties can be found in [43].

Capacity of beam and joints

The beam bending capacity has been characterized through the mean resistant values $M_{pl,m}$, the standard deviations s , and by means of the coefficient of variation COV , computed using the Monte Carlo method. Statistical tests have shown that the best probability distribution is the lognormal one. The results obtained in analyses for the two-storey frame are reported in Table 3 and Table 5. Statistical parameters for the joints of frame F1.

Table 3. Statistical parameters of the composite beam under sagging bending moment for frame F1.

$M_{pl,m}$ [KN/m]	s [KN/m]	λ	ξ	COV
426.62	20.38	6.055	0.048	0.05

Table 4. Statistical parameters of the composite beam under hogging bending moment for frame F1.

$M_{pl,m}$ [KN/m]	s [KN/m]	λ	ξ	COV
252.79	10.94	5.532	0.043	0.04

Table 5. Statistical parameters for the joints of frame F1.

Type of joint	Bending	Macro-model		
		M_r [kNm]	σ [kNm]	COV
External	M>0	263.86	16.87	0.06
	M<0	200.14	9.74	0.05
Internal	M>0	178.07	10.09	0.06
	M<0	107.34	8.61	0.08

The beam-to-column exterior and interior joints of both frames have been modelled using the macro-model based on the component approach, detailed in “Macro-model for steel and steel-concrete beam-to-column joints” Section. The stratified sampling technique, also known as the Latin Hypercube Sampling [47], has been employed. A number of 200 exterior and 200 interior joints subjected to positive and negative bending moments has been analysed. The statistical values of the resistant moment in terms of mean value M_r , variance σ and coefficient of variation COV are displayed in Table 5 for frame F1.

Damage evaluation

The destructive capacity of an earthquake is a complex combination between earthquake characteristic and structure properties, consequently earthquakes apparently similar can determine very different structural effects. For these reasons the definition of appropriate damage indexes is fundamental.

The damage definition and its evaluation is a complex problem that can be solved considering appropriate damage variables to describe the structural system state. One of the most relevant parameter, often used in seismic design, corresponds to the maximum inter-storey drift (δ_i) divided by the inter-storey height (h_i). This parameter, known as ISDA (Inter-storey Drift Angle), is strongly dependent on the structural typology and can be derived either from experimental tests or from inspection of real structures damaged by earthquakes. The ISDA values for four limit state are, used in seismic assessment and design of steel structures [48], reported in Table 6.

Table 6. Limit state and ISDA values for steel structures.

<i>Level of damage</i>	<i>ISDA %</i>	<i>Consequence</i>
LS ₀ : Fully Operational	0.5	Usable building
LS ₁ : Operational	1	Repairable building
LS ₂ : Life Safety	2	Irrecoverable building
LS ₃ : Near Collapse	5	Loss of the building

Table 7. Rotation limit (EC8) for assessing the damage in composite joints.

<i>Required performances</i>	<i>Rotation limit</i> [rads]
DL: Damage Limitation	0.013
SD: Significant Damage	0.030
NC: Near Collapse	0.050

Another relevant damage index for PR frames is the rotation in beam-to-column connections. The limits suggested by EC8 [3] for three limit states are presented in Table 7. In order to check the reliability in using the IDA limits (Tab. 6), for the seismic assessment of PR composite frames, pushover analyses have been carried out. Accurate numerical models with nonlinear springs to account for material nonlinearity in beam-to-column joints, in beams and at the base of the columns have been employed (details are given in the next Section). For each frame, two pushover analyses have been performed, considering either a uniform distribution of horizontal forces or a distribution proportional to the first mode of vibration. Using the numerical results, relations between the limit states based on IDA control and those related to the damage in the joints (rotation limit) has been sought. A very good agreement has been found both between the limited damage limit states LS_1 and DL (based on IDA values and rotation limits respectively) and the near collapse limit states LS_3 and NC . Conversely a minimal difference has been noticed in the case of severe damage. Thus a corrected value $IDA=2.5$ (instead of $IDA=2$, Tab. 5) has been used at LS_2 limit state, to achieved a maximum joint rotation equal to the limit at SD . Such modified limit has then been used in drawing fragility curves for the analysed frames.

Numerical analyses and fragility curves

After defining the earthquake ground motions together with the variability of joints and beam capacity and their statistical distributions, the statistical samples of the investigated structures have been determined. To this end, a specific program has been written in Python language. When running the code, the user is first asked to upload geometry, loads, mechanical properties and the arrangement of structural elements in the frame, as well as the sequence of earthquake ground motions. Then, a probability distribution is assigned to each random variables X_i , compatible with the cumulate probability curve. Using such data, the code generates a correlation matrix between random variables and samples.

In order to define a representative sample of the given statistical population, with a limited number of elements, the Latin Hypercube method [49] has been employed. For each earthquake ground motion, the program calculates the displacement spectrum S_d and for each expected spectral displacement, it determines the seismic intensity. Finally, it writes the input files compatible with the nonlinear finite element program used in the dynamic analyses. 1500 analyses have been carried out for each series of earthquakes: 15 frame models \times 10 earthquake ground motions \times 10 intensities for the first sequence of ground motions, 10 frame models \times 15 earthquake ground motions \times 10 intensities for the second one. The nonlinear analyses have been carried out using the nonlinear FE program Abaqus [37]. A sketch of the model employed for F1 frame is shown in Figure 25. The beam-to-column joints have been modelled as nonlin-

ear springs with bilinear asymmetric moment-rotation curves, whose elastic stiffness has been obtained through the component method. The bending resistance of the joint has been considered a random variable, and has been computed using the statistical simulation described in the previous paragraph, on the basis of the statistical distribution of the material mechanical properties. The joints behaviour, characterised by the presence of pinching and stiffness deterioration, as shown in Figures 19a and 19b in the case of F1 frame, has been modelled employing the pivot degradation rule (Fig. 9). Each composite beam span has been divided in 4 elastic beam elements connected one to another with rigid-plastic rotational springs. The resistance of such springs has been considered as a random variable and computed using the statistical simulation previously described. The columns have been modelled by means of linear beam elements and connected to the foundation with elasto-plastic rotational springs.

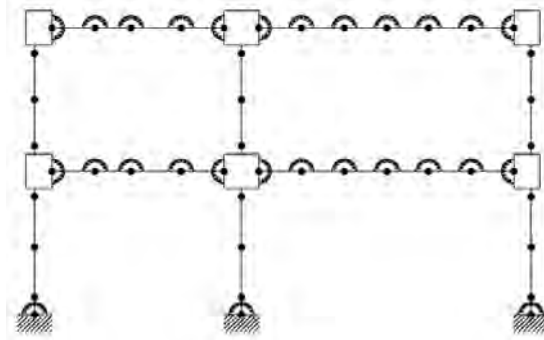


Figure 25. Finite element model for F1 frame used in nonlinear analyses.

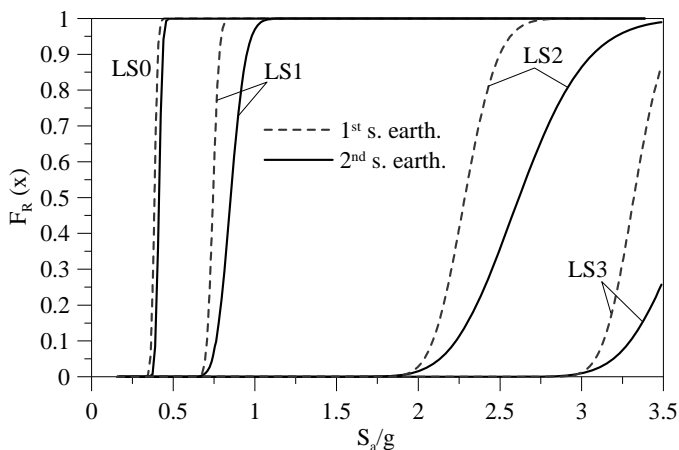


Figure 26. Fragility curves in terms of S_a for frame F1.

The stratified Latin Hypercube Sampling method, based on 9 random variables (strength of the column-to-foundation joint, positive and negative ultimate resistant moment for the 5 m and 7 m bay beams, positive and negative ultimate resistant moment for the interior and exterior beam-to-column joint) has been used. Each ground motion, described by the history of ground acceleration, has been scaled considering 10 values of seismic intensity, represented by the spectral displacement S_d evaluated using the natural period of the analysed structures. The fragility curves in terms of S_d for the frame F1 and for both earthquake series are displayed in Figure 26. They curves are similar for the two series. In particular, the starting points for each limit state are in good agreement, while the slope is more influenced by the series of ground motion, especially in the case of Life Safety and Near Collapse limit state.

In order to calculate the probability of failure P_f , the curve of seismic hazard $H(x)$ has been introduced, according to:

$$P_f = \sum_x P[LS|IM = x] \cdot P[IM = x] = \int_0^{+\infty} H(x) \cdot \frac{dF_r(x)}{dx} dx \tag{10}$$

Such curve provides the annual probability of exceeding of a given seismic intensity, which is generally measured by the spectral acceleration S_a . For the two frames, the seismic hazard curve proposed by Song & Ellingwood [50] for the state of California has been considered. It is represented in (11), where the parameters k and μ are equal to 2.38 and 0.045 respectively. These constant have been determined on the basis of the characteristics of the site and provides values of the seismic hazard compatible with those of the earthquake-prone region Irpinia in Italy.

$$H(x) = P[S_a > x] = 1 - \exp\left[-(x/\mu)^{-k}\right] \tag{11}$$

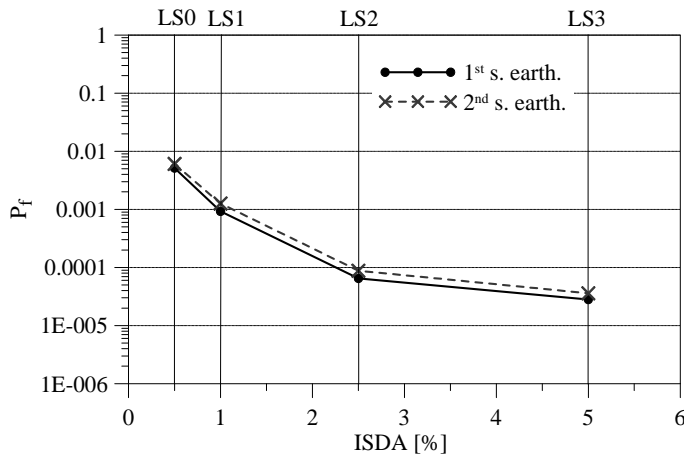


Figure 27. Performance curves for frame F1.

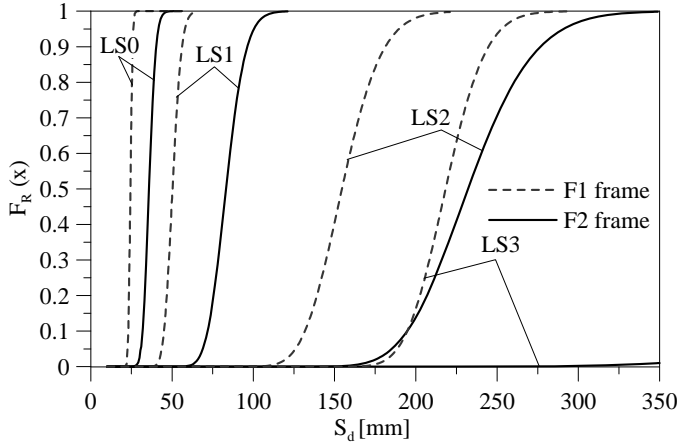


Figure 28. Fragility curves in terms of S_d for both frames, considering the second series of earthquake ground motions.

The performance curves, determined for the F1 frame, are displayed in Figure 27. They can be considered as the final outcome of the seismic reliability analysis carried out using a full probabilistic approach. It can be observed that the responses for the two series of earthquake ground motions are very similar; this confirms the stability and reliability of the obtained results.

In order to draw the fragility curves for frame F2 the same approach shown for the first frame was used. In Figure 28 the fragility curves in terms of S_d , drawn using the second series of earthquakes, are compared with those of frame F1.

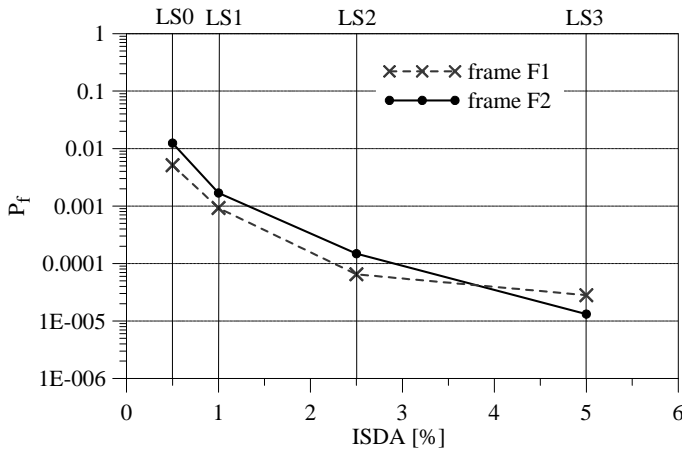


Figure 29. Comparison between the performance curves of the two analysed frames.

The two curves are similar for *LS0* and *LS1*, as both frames are equally conditioned by these damage limit states. Conversely, a strong separation between fragility curves can be observed in the case of the ultimate limit state *LS2* and *LS3*. The probability of failure at ultimate limit state is higher for frame F1 than for frame F2. This shows that, by increasing the height of the frame, the ultimate limit state checks become less crucial in the frame seismic design.

On the whole, the analyses carried out on the frame F1 have shown the stability of the results varying the series of earthquakes, which represents the maximum source of randomness. Moreover, the results achieved confirm a substantial validity of the design criteria proposed by the EC 8 (Figs. 27-29), as the annual probability of failure P_f , for each of the four damage limit states, assume acceptable values: $P_f \cong 10^{-2}$ for *LS0*, $P_f \cong 10^{-3}$ for *LS1*, $P_f \cong 10^{-4}$ for *LS2* and $P_f \cong 10^{-5}$ for *LS3*. In particular, increasing the height of the structure, it is evident as the frame becomes more strongly affected by the serviceability limit states, while the collapse is less relevant (Figs. 28 and 29).

4. SEISMIC UPGRADE OF EXISTING SEMI-CONTINUOUS FRAMES

In the last part of the research, the seismic upgrade of existing PR semi-continuous steel frames has been faced and the enhanced performance that can be achieved using different techniques are compared. The use of either steel X-braces or dissipative dampers has been considered. The effectiveness of the two solutions has been investigated analysing two case-studies. Two-level design criteria, which comprise checks under seismic events having a return period comparable with the service life of the structure (SLS) and under more severe earthquakes (ULS) have been considered.

After presenting the structural characteristics of the bare frames analysed, the design criteria employed for hybrid systems made of semi-continuous steel frames coupled with viscoelastic dissipative bracings are detailed. Finally, the results of nonlinear dynamic analyses, carried out using advanced numerical models are shown.

Analysed frames

The analysed structures correspond to a three-floor (3F) and to a six-floor (6F) PR frame respectively (Fig. 30). They were designed to withstand earthquakes according to specific performance (i.e. drift limits at SLS, specific behaviour factor at ULS). In both cases the seismic upgrade has been aimed at reducing both the drifts at SLS, so as to comply with lower lateral displacement limits, and the damage in the gravity-resistant systems (bare frames) at ULS, so as to avoid long downtime after earthquakes.

Both frames are regular and have beams with three equal bays $L=6.0$ m long. The former frame is 11.00 m height, whereas the latter is 21.50 m height. In both frames the interstorey height is $h_0=4.0$ m for the ground floor e $h_1=3.5$ m for the upper floors. The design of the two systems has been carried out following the rules supplied by the EC8 8 [3] with a peak ground acceleration $a_g=0.35g$, a type A soil and a behaviour factor $q=6$. The most critical condition for both frames was the check of lateral drifts at SLS. In order to comply with a limit drift of 0.75%, columns with a steel profile HEB300 for the 3F frame and HEB500 for the 6F frame have been employed. In both cases beams with a steel profile IPE300 have been determined. The semi-rigid beam-to-column joints, in both frames, correspond to web and flange bolted angles connections (Fig. 30). More details can be found in [51].

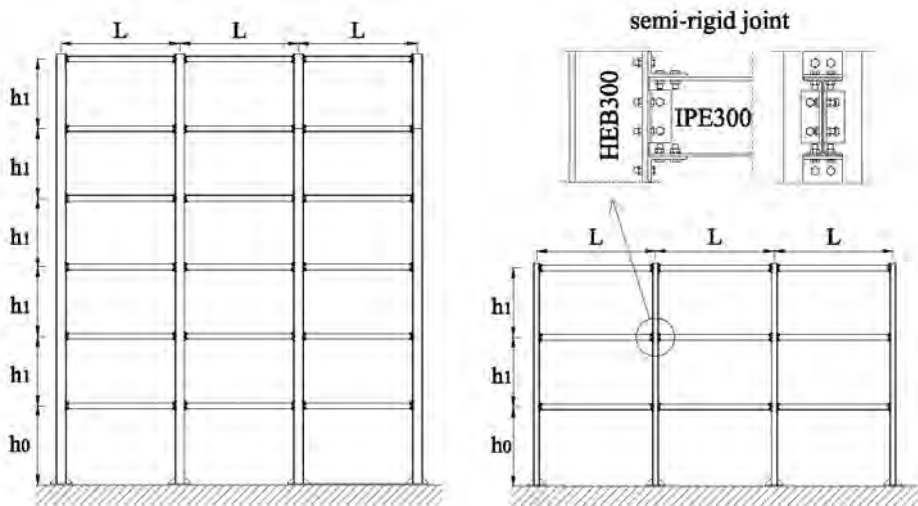


Figure 30. Elevation of the 3F and 6F bare frames together with beam-to-column connection details.

Design of seismic upgrading

Concentric bracings

The diagonal braces supply the frame with high lateral stiffness, so the design requirements at SLS can be easily satisfied. Conversely, the performance control at ULS, when the plastic dissipative capacity of the braced frames should be exploited, represents the most critical phase. In frames with concentric bracings the diagonals are the main dissipative components, while the other elements along the lateral load path, have to be dimensioned according to the capacity design rules. The compressive braces can either be considered or not in the structural model. However their slenderness represents one of the main

parameters that influences the seismic performance of the braced structure. Moreover, in order to achieve an effective global dissipative behaviour, floor collapse mechanisms must be always avoided.

The EC8 provisions have been employed and the braced structures were designed performing elastic analysis with a behaviour factor $q=4$ and considering only the contribution of the diagonal braces in tension. The non-dissipative elements have then been checked accounting for overstrength, as required by the capacity design method. The design results of the braced frames are presented in [51], where the dimensions of diagonal braces are reported. In Figure 31 the elevation of the F1 frame coupled with diagonal bracings is sketched.

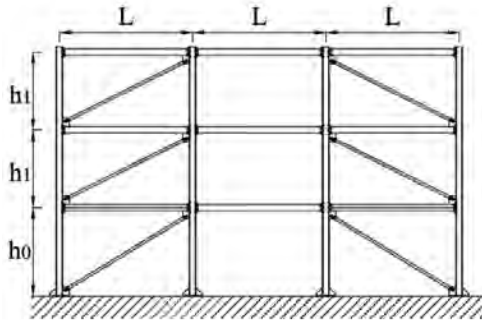


Figure 31. Elevation of the 3F frame with concentric braces.

Viscoelastic bracings

The coupling between steel semi-continuous frames and dissipative bracings lead to hybrid systems that combine effectively the typical advantages assured by frames with those of braced structures[10][11]. Even though a viscoelastic brace generally shows limited lateral stiffness, it dissipates the energy supplied by the earthquake through a visco-elastic behaviour by means of the use of rubber dampers, so limited lateral displacements are experienced by the structure even under severe earthquakes.

In such a system a viscoelastic dissipative bracing is arranged in parallel with a semi-rigid steel frame (Fig. 32). The viscoelastic dampers are made of two steel flanges with an inner natural rubber layer. It can be linked through bolts to the lower flange of the beam on top and to the joint plate for the two diagonal brace members at the bottom. The diagonal elements are two steel tubes coupled with two steel ties that assure the parallelism of the device to the beam.

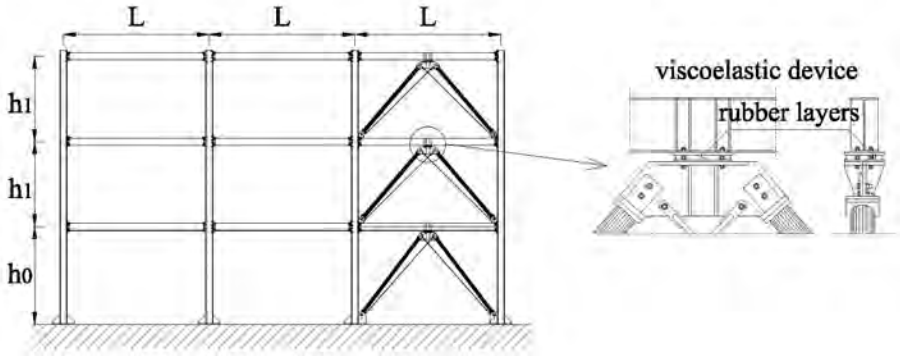


Figure 32. Elevation of the 3F frame with dissipative bracings and details a viscoelastic damper.

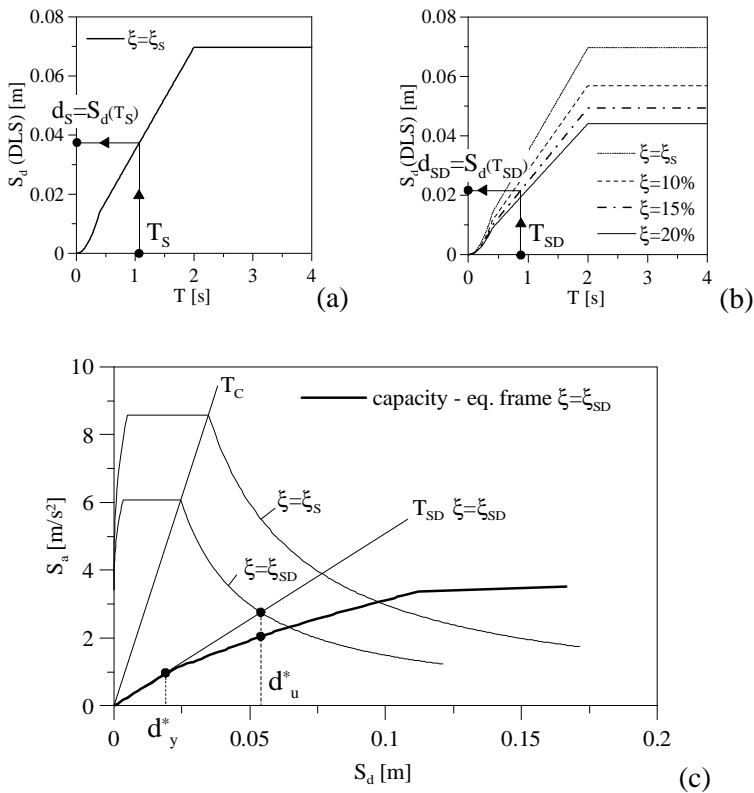


Figure 33. Displacement demand of the SDOF system equivalent to (a) the bare frame and to (b) the equipped structure. (c) ADRS curves for checks at ULS.

The design of the hybrid systems has been carried out determining the number and location of devices by checking the drifts of the equipped structures at SLS and controlling the ductility required at ULS [51]. A damping ratio $\xi_S = 5\%$ is usually employed to draw the elastic spectrum so as to consider the viscous dissipative properties of both the structural and non structural components of the analysed framed building. Then, the displacement demand d_S for the 1-DOF system, equivalent to the analysed structure, can be straightforwardly determined from either the natural period T_S or the natural frequency ω_S of the frame using the displacement spectrum at SLS (Fig. 33a). The displacements at the top floor d_t and at each floor d_i can be then calculated using the modal participation factor $\Gamma^{(1)}$ and the mode shape components $\phi_{Si}^{(1)}$ associated to the first mode of vibration of the bare frame, as given in:

$$d_t = \Gamma^{(1)} d_s, \quad d_i = \phi_{Si}^{(1)} d_t \quad (12)$$

If the interstorey drifts are higher than the limit value, a two-step design procedure can be used to design the visco-elastic dissipative system, necessary to enhance the seismic performance of the existing frame.

In the checks at SLS, some displacement spectra, for different values of the damping ratio ξ_D provided by the added dissipative devices, are considered (Fig. 33b). Such spectra can be achieved from the elastic spectrum using a damping correction factor (EC8). In previous research [12], it has been checked that values $\xi_D = 10\text{-}20\%$ lead to solutions of practical interest, being economically convenient.

The displacement demand for the 1-DOF system equivalent to the equipped frame first, and then the displacement at each floor of the real structure can be calculated using the same procedure employed for the bare frame. In the latter case, the natural period T_{SD} (or the natural frequency ω_{SD}) of the 1-DOF system equivalent to the equipped structure is the key parameter. This can be determined as a function of the total damping ratio $\xi_{SD} = \xi_S + \xi_D$, the dynamic properties of the bare frame and of the loss factor η_D of the rubber that forms the dampers [10]. The minimum value of ξ_D , that guarantees interstorey drifts lower than the design limit, is chosen.

Then the devices are designed in detail. If a constant distribution for the damping coefficient c_D , associated to the viscoelastic devices is used, it and the device stiffness k_D can be evaluated using eqs (13)-(14) respectively, where ϕ_{rSi} is the i^{th} floor interstorey drift for the first mode.

$$c_D = 2 \frac{\sum_{i=1}^N m_i \phi_{Si}^{(1)2}}{\sum_{i=1}^N \phi_{rSi}^{(1)2}} (\omega_{SD} \xi_{SD} - \omega_S \xi_S) \quad (13)$$

$$k_D = 2\omega_{SD} \frac{\sum_{i=1}^N m_i \phi_{S_i}^{(1)2}}{\eta_D \sum_{i=1}^N \phi_{rS_i}^{(1)2}} (\omega_{SD} \xi_{SD} - \omega_S \xi_S) \quad (14)$$

The calculation of the overall rubber height h_D for each device is carried out considering the maximum slip γ_D allowed for the viscoelastic material at SLS and the maximum demanded drift $d_{r,max}$ (15), whereas the area A_D of the rubber can be determined through the stiffness k_D according to (16).

$$h_D = d_{r,max} / \gamma_D \quad (15)$$

$$A_D = (k_D / G') h \quad (16)$$

where G' is the shear storage modulus of the rubber.

Under severe earthquakes, at ULS, a limited plastic damage in the frames is allowed, the structural checks correspond to evaluate the required ductility. It can be achieved drawing the A-D spectrum (pseudo-acceleration vs. displacement spectrum) and plotting both the demand diagram and the capacity curve. The structural capacity is determined by means of a nonlinear static analysis. The elastic limit displacement d_y^* of the structure is a result of the nonlinear pushover analysis, while, if $T_{SD} > T_C$ (Fig. 32c), the displacement demand d_u^* is equal to the abscissa of the performance point of the 1-DOF system with the same natural period and damping ratio of the equipped structure (Fig. 33c). The ratio d_u^*/d_y^* corresponds to the ductility required. This value can be compared with the same quantity calculated for the bare frame, so as to estimate the reduction in structural damage guaranteed by using viscoelastic devices. The damping ratio provided by the dampers can be increased to reduce plastic damage in the frame. In such a case the device details must be determined again, as specified above. Obviously, at ULS, the maximum drifts for the viscoelastic devices have to be checked as well.

Numerical analyses

After designing the strengthened frames so as to comply with an interstory drift limit equal to 5% at SLS[51], their seismic behaviour have been investigated, performing nonlinear dynamic analyses. An earthquake ground motion compatible with the elastic spectrum supplied by the Eurocode 8 for type A soil has been employed with different values for the peak ground acceleration $a_g = 0.10-0.20-0.30-0.40g$.

In Figures 34-37, the enhanced seismic performance, achieved through the two different strategies, are compared. The performance points of both 3F and 6F frames, the energy and the axial force demand in the columns for the 6F frame in the case of $a_g=0.4g$ are shown. In particular, the values of the total e-

energy E_{tot} , the viscous energy E_{visc} , the total plastic energy E_{pt} and the plastic energy demand in the existing frame E_{pj} are reported. All the seismic upgrading methods guarantee very low displacements, even in the case of severe earthquakes, and allowed the frames to behave elastically under seismic events with high probability to occur during the service life of the structures ($a_g=0.1-0.2g$).

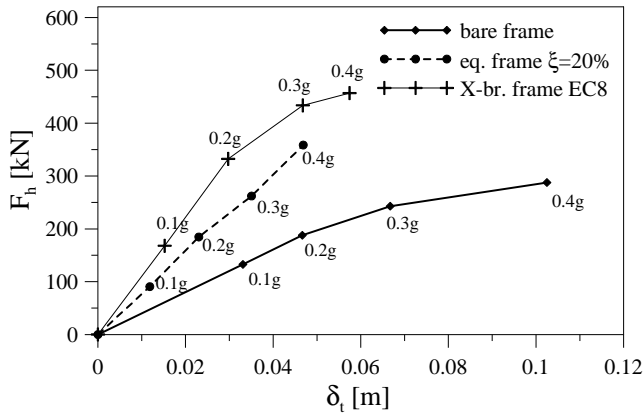


Figure 34. Performance points for the three-floor frame.

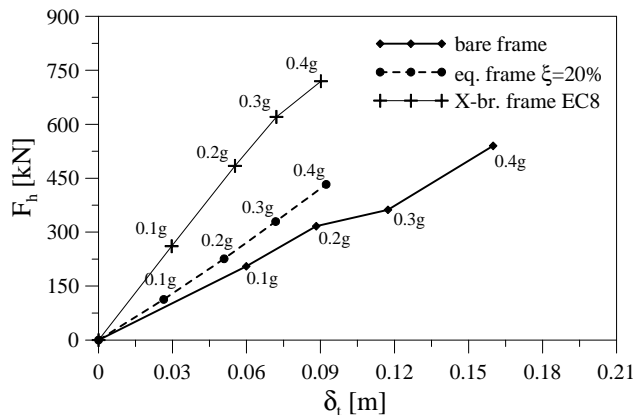


Figure 35. Performance points for the six-floor frame.

The use of viscoelastic dampers assures the highest performance. The maximum lateral displacement is very limited and the maximum base shear is noticeably lower than that calculates for both braced frames (Figs. 34 and 35), even lower than the base shear demand for the existing 6F frame. The base axial forces are reduced as well, this leads to no increase in strength demand on founda-

tions. As far the plastic energy demand is concerned, the use of viscoelastic dampers allows to strongly limit the structural damage even for $a_g=0.4$. Conversely, the energy supplied by severe earthquakes in the case of structures with added diagonal braces is dissipated not only by the hysteretic behaviour of the steel braces but also through a plastic damage of the beam-to-column connections of the existing frames.

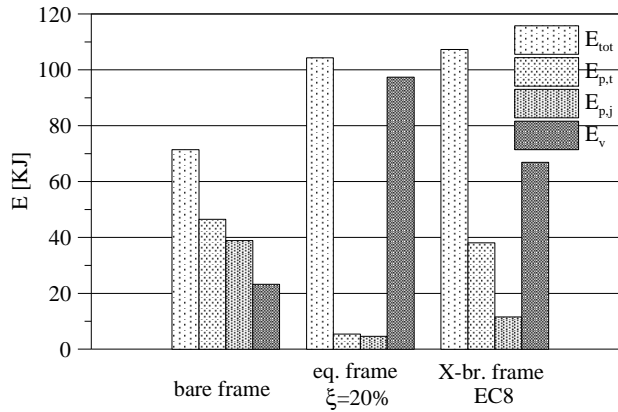


Figure 36. Six-floor frame, energy demand for $a_g=0.40g$.

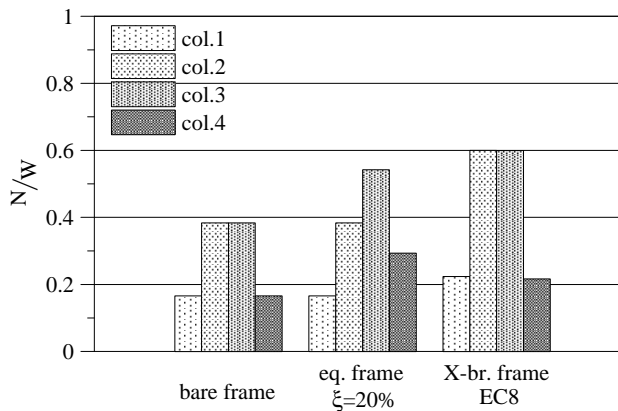


Figure 37. Six-floor frame, axial force demand for $a_g=0.40g$.

5. CONCLUSIONS

This paper reports the main results achieved in a research carried out to investigate the seismic performance of PR steel and steel-concrete composite frames. An advanced numerical model, which corresponds to a refinement of

previous macro-models for beam-to-column connections, has been developed. It enables the cyclic response of steel and composite joints to be predicted with high precision. The model has been implemented in a general finite element package and used in nonlinear static and dynamic analyses of PR frames. In particular the seismic performance of two composite frames have been analysed using the probabilistic approach. The results achieved confirm a substantial validity of the design criteria proposed by the Eurocodes as the calculated annual probability of failure is in good agreement with that considered by the European codes of practice. Finally, in the last part of the research, the seismic upgrading of existing semi-continuous steel frames was faced. The use of either viscoelastic dampers or traditional steel braces has been considered. A design procedure for frames with added energy dissipation devices has been presented and used for the seismic upgrading of two frames. The use of viscoelastic dampers results the most effective seismic upgrading technique. It guarantees low displacements, reduced structural damage, even in the case of severe earthquakes, and a limited force demand on the foundations.

ACKNOWLEDGEMENT

The authors gratefully acknowledge the support provided for this research by the Italian Government through the ReLUIIS 2005-08 grant.

REFERENCES

- [1] CEN 2003 prEN 1993-1-1 [2003] *Eurocode 3: Design of steel structures - Part 1-1: General rules and rules for buildings*, Brussels, Belgium.
- [2] CEN 2004 prEN1994-1-1 [2004] *Eurocode 4 Design of composite steel and concrete structures - Part 1.1: General rules and rules for buildings*, Brussels, Belgium.
- [3] CEN 2003 prEN 1998-1 [2003] *Eurocode 8: Design of structures for earthquake resistance - Part 1: General rules, seismic actions and rules for buildings*, Brussels, Belgium.
- [4] Tschammernegg, F., Queiroz, G. [1995] "Mechanical modelling of semi-rigid joints for the analysis of framed steel and composite structures," *Proceedings of 3rd International Workshop on connections in steel structures*. Trento Italy, 28-31 May 1995.
- [5] Augusti, G., Baratta, A., Casciati, F. [1984] *Probabilistic Methods in Structural Engineering*, Chapman & Hall, London, UK.
- [6] Dymitiotis, C., Kappos, A.J., Chryssanthopoulos. M.K. [1999] "Seismic reliability of RC frames with uncertain drift and member capacity," *Journal of structural Engineering*, ASCE; 125(9): 1038-47.
- [7] Song, J., Ellingwood, B.R. [1999] "Seismic reliability of special moment steel frames with welded connections : I," *Journal of Structural Engineering*, ASCE, 125(4): 357-371.

- [8] Song, J., Ellingwood, B.R. [1999] "Seismic reliability of special moment steel frames with welded connections : II," *Journal of Structural Engineering*, ASCE, 125(4): 372-384.
- [9] Ditlevsen, O., Madsen, H.O. [1996] *Structural Reliability Methods*, John Wiley & Sons Ltd, Chichester, UK.
- [10] Amadio, C., Bisetto, M., Macorini, L. [2008] "Seismic performance of steel frames coupled with visco-elastic bracings," *14th World Conference on Earthquake Engineering*, October 12-17, Beijing, China, (on CD).
- [11] Amadio, C., Clemente, I., Macorini L., Fragiaco, M. [2008]. "Seismic behaviour of hybrid systems made of PR composite frames coupled with dissipative bracings," *Earthquake Engineering and Structural Dynamics*, Wiley, 37(6): 861-879.
- [12] Soong, T.T., Dargush, G.F. [1997] *Passive energy dissipation systems in structural engineering*, John Wiley & Sons Ltd, Chichester, UK.
- [13] Tschemmerneegg, F., Huber, C. [1988] "The design of structural steel frames under consideration of the non-linear behaviour of joints," *Journal of Constructional Steel Research*, Elsevier, 11:73-103.
- [14] Nethercot, D., Zandonini, R. [1989] "Methods of prediction of joint behaviour: beam-to-column connections," in R. Narayanan (ed.) *Stability and Strength*, Elsevier Applied Science, 23-62.
- [15] Xiao, Y., Choo, B., Nethercot, D. [1996] "Composite connections in steel and concrete. Part 2 – Moment Capacity of End Plate Beam to Column Connections," *J. Construct. Steel Res.*, Elsevier, 37(1): 63-90.
- [16] Wong Y., Chan, S., Nethercot, D.A. [1996] "A simplified method for unbraced frames with semi-rigid connections," *International Conference on Advanced in Steel Structures*, Dec.11-14 1996, Hong Kong.
- [17] Faella, C., Pilluso, V., Rizzano, G. [2000]. *Structural Steel Semirigid Connections*, CRC PRESS, Boca Raton, Florida, USA.
- [18] Tschemmerneegg, F., Queiroz, G. [1995] "Mechanical modelling of semi-rigid joints for the analysis of framed steel and composite structures," *Proc. 3rd International Workshop on connections in steel structures.*, 28-31 May 1995 Trento Italy, Pergamon, Tarrytown, NY.
- [19] Wales, M.W., Rossow, E.C. [1983] "Coupled moment-axial force behavior in bolted joints," *Journal of Structural Engineering*, ASCE, 109(5): 1250-1266.
- [20] Tschemmerneegg, F., Huber, C. [1998] "Modelling of Beam-to-Column Joints," *J. Construct. Steel Res.*, Elsevier, 45(2): 199-216.
- [21] Benussi, F., Noè, S., Rassati, G.A., [1997] "Component-based modelling of semi-rigid joints in composite frames under monotonic and cyclic loads," *Proc. Giornate Italiane della Costruzione in Acciaio*, CTA, Abano Terme, Italy.
- [22] Rassati, G.A., Leon, R.T., Noè, S. [2004] "Component modelling of PR composite Joints under cyclic and dynamic loading," *Journal of Structural Engineering*, ASCE, 130(2): 343-351.
- [23] Amadio, C., Clemente, I., Fragiaco, M., Macorini, L., Noè, S., Pasquale, D. [2004] "Problems concerning semi-rigid steel frames modelling in seismic regions," *Costruzioni Metalliche*, (3): 46-53.

- [24] Kattener, M., Crisinel, M. [2000] "Finite element modelling of semi-rigid composite joints," *Computers and Structures*, Elsevier, (78):341-353.
- [25] Amadio, C., Fragiacommo, M. [2003] "Analysis of rigid and semi-rigid steel-concrete composite joints under monotonic loading, Part I: Finite element modelling and validation," *Steel & Composite Structures*, 3(5): 349-369.
- [26] Bursi, O.S., Ballerini, M. [1997] "Low-cycle Behaviour and Analysis of Steel-concrete Composite Substructures," *Proc. Int. Conf. on Composite Construction -Conventional and Innovative*, IABSE, September 16-18, Innsbruck, Austria, 1997.
- [27] Bursi, O.S., Gramola, G. [1997] "Smearred crack analysis of steel-concrete composite Substructures," *Int. Workshop and Seminar on the Behaviour of Steel Structures in Seismic Areas*, STESSA'97, August 3-8, Kyoto, Japan, 1997.
- [28] CEN, 2003 prEN 1993-1-8 [2003] *Eurocode 3: Design of steel structures - 1.8: Design of joints*, Brussels, Belgium.
- [29] Amadio, C., Bella, M., Clemente, I., Macorini, L. [2007] "Cyclic modelling of partial restrained bare steel and steel-concrete composite frames," *XII ANIDIS Conference*, Pisa June 2007, (on CD).
- [30] Amadio, C., Bella, M., Clemente, I., Macorini, L. [2007] "Cyclic modelling of bare steel and steel-concrete composite joints through the component method," *6th International Conference on Steel and Aluminium Structures ICSAS07*, Oxford (UK) July 24-27, 2007.
- [31] Kim, K. D., Engelhardt, M. D. [2002] "Monotonic and cyclic loading models for panel zones in steel moment frames," *Journal of Constructional Steel Research*, Elsevier, 58: 605-635
- [32] Dafalias, YF. [1975] "On cyclic and anisotropic plasticity: (I) A general model including material behavior under stress reversals. (II) Anisotropic hardening for initially orthotropic materials". *PhD thesis*, Department of Civil Engineering, University of California, Berkeley, CA; USA.
- [33] Cofie, N.G, Krawinkler, H. [1985] "Uniaxial cyclic stress-strain behavior of structural steel," *J. Engng. Mech.*, ASCE, 111(9):1105-1120.
- [34] Clemente, I., Noè, S., Rassati, G.A. [2005] "Experimental and numerical analyses of the cyclic behavior of T-stub components" *Proc. 20th CTA Conference*, Ischia, Italy 193-200.
- [35] Takeda, R.S., Sozen, M.A., Nielsen, N.N. [1970] "Reinforced concrete response to simulated earthquakes," *Journal of Structural Division ASCE*, 96 (12):2557-2573.
- [36] Park, Y.J., Reinhorn, A.M., Kunnath, S.K. [1987] "IDARC: Inelastic damage analysis of reinforced concrete frame-shear-wall structures," *Tech. Rep. NCEER-87-0008*, State University of New York at Buffalo, Buffalo NY.
- [37] ABAQUS user's manual - version 6.5-1 [2004] Hibbit, Karlsson & Sorenson.
- [38] Ballio, G., Calado, L., De Martino, A., Faella, C., Mazzolani, F.M. [1984] "Cyclic behaviour of steel beam-to-column joints experimental research," *Costruzioni Metalliche*, (2):69-90.
- [39] Bernuzzi, C., Zandonini, R., Zanon, P. [1996] "Experimental Analysis and Modelling of Semi-rigid Steel Joints under Cyclic Reversal Loading," *Journal of Constructional Steel Research*, 38(2):95-123.

- [40] Liew, J.Y.R., Teo, T.H., Shanmugam, N.E. [2004] "Composite joints subject to reversal of loading - Part 1: experimental study," *Journal of Constructional Steel Research*, 60:221-246.
- [41] Bursi, O.S., Caramelli, S., Fabbrocino, G., Molina, J., Salvatore, W., Taucer, F., Zandonini, R. "3D Full Scale Seismic Testing of a Steel-Concrete Composite Building at ELSA," *Report of ECOLADER project HPR-CT-1999-00059 and ECSC project 7210-PR-250*.
- [42] Caramelli, S., Lucchesi, D., Salvatore, W. "Dissipative beam-to-column connections of steel-concrete composite moment-resisting frames," *Report of ECOLADER project HPR-CT-1999-00059 and ECSC project 7210-PR-250*.
- [43] Amadio, C. [2008] "Probabilistic analysis of a partially-restrained steel-concrete composite frame," *Steel and Composite Structures*, 8(1): 35-52.
- [44] Erberik, M.A., Elnashai, A. S. [2004] "Fragility analysis of flat-slab structures", *Engineering Structures*, Elsevier, 26(7):937-947.
- [45] Piluso V., Rizzano G., Totoli G. (2003): "Progettazione a completo ripristino di resistenza di collegamenti flangiati trave colonna: approccio probabilistico," *Costruzioni metalliche*, 55(1): 33-41.
- [46] Dymitiotis, C., Kappos, A.J, Chryssanthopoulos, M.K, [1999] "Seismic reliability of RC frames with uncertain drift and member capacity," *Journal of structural Engineering*, ASCE, 125(9):1038-1047.
- [47] Olsson, A., Sandberg, G., Dahlblom, O. [2003] "On Latin hypercube sampling for structural reliability analysis," *Structural Safety*, Elsevier, 25:47-68.
- [48] Song J., Ellingwood B.R. (1999): "Seismic reliability of special moment steel frames with welded connections: I", *Journal of Structural Engineering*, ASCE, 125(4), 357-371.
- [49] Iman, R.L., Helton, J.C., Campbell, J.E. [1981] "An approach to sensitivity analysis of computer models, Part 1. Introduction, input variable selection and preliminary variable assessment," *Journal of Quality Technology*, 13 (3):174-183.
- [50] Song, J., Ellingwood, B.R. [1999] "Seismic reliability of special moment steel frames with welded connections: II," *Journal of Structural Engineering*, ASCE, 125(4):372-384.
- [51] Amadio, C., Bella, M., Macorini, L. [2009] "Seismic upgrade of existing semi-continuous steel frames: a comparison between the use of concentric steel braces and viscoelastic dissipative systems," *Proc. 6th International Conference STESSA 2009*, Philadelphia (USA), August 16-20, Behaviour of Steel Structures in Seismic Areas, Stessa 2009, Mazzolani, Ricles and Sause, (eds), CRC Press, Taylor & Francis Group, London, 527-533.

Finito di stampare nel mese di ottobre 2011 per conto di DoppiaVoce
presso Officine Grafiche Francesco Giannini & Figli S.p.A. – Napoli